In presenting the dissertation as a partial fulfillment of the requirements for an advanced degree from the Georgia Institute of Technology, I agree that the Library of the Institute shall make it available for inspection and circulation in accordance with its regulations governing materials of this type. I agree that permission to copy from, or to publish from, this dissertation may be granted by the professor under whose direction it was written, or, in his absence, by the Dean of the Graduate Division when such copying or publication is solely for scholarly purposes and does not involve potential financial gain. It is understood that any copying from, or publication of, this dissertation which involves potential financial gain will not be allowed without written permission.

7/25/68

TWO APPROACHES TO THE THREE-DIMENSIONAL JET-IN-CROSS-WIND PROBLEM: A VORTEX LATTICE MODEL AND A NUMERICAL SOLUTION OF THE NAVIER-STOKES EQUATIONS

A THESIS

Presented to

The Faculty of the Graduate Division

by

Joe Floyd Thompson, Jr.

In Partial Fulfillment

of the Requirements for the Degree

Doctor of Philosophy

in the School of Aerospace Engineering

Georgia Institute of Technology

June, 1971

TWO APPROACHES TO THE THREE-DIMENSIONAL JET-IN-CROSS-WIND PROBLEM: A VORTEX LATTICE MODEL AND A NUMERICAL SOLUTION OF THE NAVIER-STOKES EQUATIONS

Approved:

Chairman

Date approved by Chairman: 5/18/71

NOTE:

Special permission was received from the Division of Graduate Studies to vary the thesis format so that the headings could fit the needs of the report.

ACKNOWLEDGMENTS

The author wishes to express his appreciation especially to his thesis advisor, Dr. J. C. Wu, for encouragement and assistance throughout the course of this research and to his readers, Dr. L. H. Bangert and Dr. H. M. McMahon, for their valuable suggestions. Appreciation is also due the personnel of the Rich Electronic Computer Center, especially Mr. Jerry Sieger.

The author is also grateful to Mrs. Cassandra Breland for preparing the figures, to Mrs. Glinda Dinkelacker and Mrs. Judy Gasaway for typing the rough draft, and to Mrs. Lou Ann Vasek for typing the final draft.

Finally the author is appreciative of the financial support of project Themis (U. S. Army Research Office, Durham) and a National Science Foundation Science-Faculty Fellowship.

TABLE OF CONTENTS

TABLE OF CONTENTS (Continued)

TABLE OF CONTENTS (Continued)

TABLE OF CONTENTS (Continued)

TABLE OF CONTENTS (Continued)

TABLE OF CONTENTS (Continued)

LIST OF TABLES

LIST OF ILLUSTRATIONS

SUMMARY

A three-dimensional numerical solution of the time-dependent, incompressible Navier-Stokes equations based on an integro-differential formulation of these equations is developed. With this formulation it is possible to obtain the complete solution in the entire flow field while restricting the actual computational field to the region of significant vorticity magnitude at each time. This allows a considerable reduction in the computer storage required, since only the field points having significant vorticity at any time need be stored at that time, and calculations are actually performed only at those points at that time. The computational field thus expands in time. The specification of conditions at infinity is unnecessary in the present formulation, these conditions being contained implicitly, so that it is not necessary to artificially locate "infinity" at the boundaries of a finite computational field. The solution is obtained on a field that is, in effect, infinite.

The solution uses the vorticity and velocity as dependent variables, the former being calculated at each time from an explicit difference equation, and the latter being subsequently calculated from a summation over the vorticity distribution. The method is thus explicit, and the time step and Reynolds number must be kept within a certain stability region. The stability criteria are determined from a

linearized stability analysis, and a general comparison of the von Neumann and matrix methods of stability analysis is given, the two methods being shown to be equivalent for mixed initial value-boundary value problems.

The validity of the numerical solution is established by comparison of the results with the exact solution for the time-dependent, one-dimensional flow over a suddenly accelerated infinite flat plate moving parallel to itself at constant velocity, and by comparison of surface pressure and drag coefficients with experimental results and with the results of other numerical solutions for the two-dimensional flow about a circular cylinder. A discussion and comparison of the results of other numerical solutions for this case is also given. The accurate determination of surface pressures and drag coefficients by the present solution and all other numerical solutions is shown to be restricted to small Reynolds numbers unless very small grid spacing is used in the vicinity of the surface. The larger scale wake phenomena, however, may be obtained at much higher Reynolds numbers. Periodic vortex shedding and the formation of a vortex street, as exhibited by the solution, are presented and are shown to be suppressed in the solution by the addition of a splitter plate behind the cylinder.

The numerical solution is applied to the flow field of an infinite jet in a cross-flow and to the flow field of a jet issuing perpendicularly from an infinite plane wall into

a cross-flow parallel to the wall. The former case is two-dimensional, in the sense of having a direction of invariance, but with three variable vorticity and velocity components. The latter case is fully three-dimensional. Solutions are given for this case for two types of starts: (1) the start from the opening of the jet exit, and (2) the start from a cylindrical discontinuity standing on the jet exit, separating the jet and cross-flow.

A three-dimensional nonlinear numerical instability that results from a coupling of a velocity component and the vorticity components in the plane perpendicular to the velocity component is detected and analyzed in detail. The time development of the three-dimensional flow from both of the above types of starts is presented in the form of vorticity and velocity profiles and vector plots and is discussed in detail. The numerical method shows the deflection and deformation of the jet into the expected kidney shape, a recirculation within the jet in the form of counter-rotating vortices, and entrainment of the cross-flow into the rear of the jet. The method also shows the low pressure region behind the jet to be expected from experimental results, the emission of a vortex ring from the jet exit, and vorticity waves propagating up the jet from the exit. The effects and appropriate values of several numerical parameters involved in the solution are determined from comparisons of the results for various cases.

A vortex lattice potential flow model of the jet in cross-wind is also developed and evaluated. This model consists of a lattice of straight vortex segments forming a series of rings with connecting columns. The lattice deforms as time passes according to the velocities induced on itself by the vortex segments forming the lattice. Although the lattice deforms into the expected kidney shape and is deflected downstream by the cross-wind, the model is shown to be incapable of producing the viscous wall pressure distribution about the jet.

NOMENCLATURE

Symbols
English Letters

a	(a). constant coefficient used in Appendices G and H, defined in Equation (H-1), in numerical solution (b). perpendicular distance from vortex segment to point of velocity calculation in vortex lattice model (Figure 55)
$\underline{A}$	matrix used in Appendix H, defined by Equation (H-8)
$\underset{\sim}{A}$	general vector used to define vector identities
A	constant coefficient used in Appendices G and I, defined above Equation (I-1)
$\underset{\sim}{a}_1, \underset{\sim}{a}_2$	vectors from ends of vortex segment to point of velocity calculation in vortex lattice model (Figure 55)
A_f, A_p	x and y projections, respectively, of the portion of the cylinder surface curve lying in a boundary cell (Figure 12)
$\underset{\sim}{b}$	vector displacement due to velocity induced by vortex segment in vortex lattice model (Figure 56)
b	(a). constant coefficient used in Appendices G and H, defined in Equation (H-1), in numerical solution (b). magnitude of $\underset{\sim}{b}$ in vortex lattice model (c). magnitude of $\underset{\sim}{B}$ used in Appendix I
$\underset{\sim}{B}$	general vector used to define vector identities
$\underline{B}$	matrix used in Appendix H, defined by Equation (H-26)
B	constant coefficient used in Appendices G and I, defined above Equation (I-1)
b_1, b_2, b_3, b_4	functions used and defined in Appendix N in vortex lattice model

$\underset{\sim}{C}$	(a). cross-product vector defined above Equation (VI-17), components given by Equation (VI-17) (b). general vector used to define vector identities
C	constant coefficient used in Appendices G and I, defined above Equation (I-1)
C_D	total drag coefficient
C_{D_f}	friction drag coefficient
C_{D_p}	pressure drag coefficient
C_p	surface pressure coefficient
$C_{\pm}$	constant coefficients used in Appendix H, defined in Equation (H-29)
C_k^+, C_k^-	constant coefficients used in Appendix H, defined in Equation (H-9)
d	function used and defined in Appendix N in vortex lattice model
D	circular cylinder diameter
$d\underset{\sim}{l}$	increment of length in circuit
dS	increment of surface
$d\nu$	increment of volume
dx, dy, dz	increments in x, y, z directions, respectively
$d\phi$	increment of angle in vortex lattice model
$d\Omega$	increment of solid angle
d_1, d_2, d_3, d_4	functions used and defined in Appendix N in vortex lattice model
$\underset{\sim}{e}$	outward unit normal to jet exit curve in boundary plane
$\underset{\sim}{e}_1$	unit vector in direction of velocity induced by vortex segment in vortex lattice model (Figure 55)

$\underset{\sim}{e}_2$	unit vector perpendicular to both vortex segment and velocity induced thereby in vortex lattice model (Figure 56)
e_1, e_2, e_3, e_4	functions used and defined in Appendix N in vortex lattice model
f	general function used in Appendix H, defined in Equation (H-1)
f(x,y)	function defining jet exit bounding curve, f(x,y) = 0 (Figure 12)
F_1, F_2, F_3	functions defined below Equation (VI-18) and below Equation (VI-20)
g	(a). parameter used in Appendix G, defined above Equation (G-1) (b). general function used in Appendix H, defined in Equation (H-1)
h	(a). mesh width in numerical solution (b). vortex ring initial spacing in vortex lattice model
h_1, h_2, h_3	scale factors for the curvilinear coordinates, x_1, x_2, x_3, respectively, in Appendix B in numerical solution
h_1, h_2, h_3, h_4	functions used and defined in Appendix N in vortex lattice model
$\underset{\sim}{i}$	unit vector in x-direction
i	(a). number of cells from origin in x-direction (b). $\sqrt{-1}$ where indicated
$\underline{I}$	unit matrix used in Appendices G and H
I	field extent in x-direction used in Appendix G
$\underset{\sim}{j}$	unit vector in y-direction
j	number of cells from origin in y-direction
J	field extent in y-direction used in Appendix G
$\underset{\sim}{k}$	unit vector in z-direction

k	(a). number of cells from origin in z-direction (b). component index of Fourier expansion used in Appendix H, defined in Equation (H-19b) (c). eigenvalve and eigenvector index used in Appendix H, defined by Equation (H-32)
k_1, k_2	constants used in Appendix G, defined by Equation (G-3)
$\underset{\sim}{l}$	vector length of vortex segment
$\underline{L}$	matrix used in Appendices G and H, defined above Equation (H-8)
L, L_x, L_y	lengths defined on Figure 23 and Figure 16
L	difference operator used in Appendix H, defined by Equation (H-4)
l_1, l_2, l_3	dimensions of triangular source element used in Appendix N in vortex lattice model (Figure 105)
m_1, m_2, m_3, m_4	functions used and defined in Appendix N in vortex lattice model
$\underset{\sim}{n}$	unit vector normal to surface, directed outward from enclosed volume
n	number of time steps from start
N_D	number of cells across major axis of cylinder or jet exit, as the case may be
p	(a). pressure (b). eigenvalve index used in Appendix G, defined by Equation (G-7)
q	(a). eigenvalve index used in Appendix G, defined by Equation (G-8) (b). parameter used in Appendices G and H, defined above Equation (H-3)
q_1, q_2	functions used and defined in Appendix N in vortex lattice model
$\underset{\sim}{r}$	position vector

r	(a). parameter used in Appendix G, defined above Equation (G-1) (b). parameter used in Appendices G and H, defined above Equation (H-3)
$\underset{\sim}{R}$	image of position vector $\underset{\sim}{r}$ in infinite plane, defined by Equation (II-9), (Figure 1)
R_c	cell Reynolds number in numerical solution, based on cross-flow velocity and mesh width
R	(a). Reynolds number based on cross-flow velocity and cylinder or jet exit diameter, as the case may be (b). jet exit radius in vortex lattice model
r_m	range about point of velocity calculation beyond which vorticity is neglected
r_f	radius beyond which no vortex cells are created
$\underset{\sim}{r}_p$	position vector of point of velocity calculation in vortex lattice model (Figure 55)
$\underset{\sim}{r}_1$, $\underset{\sim}{r}_2$	position vectors of ends of vortex segment in vortex lattice model (Figure 55)
r_1, r_2, r_3, r_4	functions used and defined in Appendix N in vortex lattice model
t	time
T	(a). time, nondimensionalized with respect to cross-flow velocity and cylinder radius (b). function only of t used in Appendix G, defined above Equation (G-2)
u	component of velocity in x-direction
$\underset{\sim}{v}$	velocity
v	component of velocity in y-direction
V	(a). magnitude of velocity, $\underset{\sim}{v}$ (b). representative velocity magnitude in stability analysis
v_n	component of velocity normal to general solid body surface in Appendix B

$\underset{\sim}{v}_1$, $\underset{\sim}{v}_2$	solutions used in Appendix A, defined above Equations (A-8)
$\underset{\sim}{v}_1'$, $\underset{\sim}{v}_2'$	solutions used in Appendix A, defined above Equations (A-9)
v_1, v_2, v_3	components of velocity in the x_1, x_2, x_3 directions, respectively, in Appendix B
V_c	magnitude of cross-flow velocity infinitely remote from jet and plate
$\underset{\sim}{V}_j$	velocity on jet exit
V_j	magnitude of $\underset{\sim}{V}_j$
V_r	velocity ratio, $V_r = \frac{V_j}{V_c}$
$\underset{\sim}{V}_s$	velocity on plane boundary
$\underset{\sim}{V}_o$	(a). potential velocity distribution about two-dimensional cylinder for start from cylindrical discontinuity (b). potential velocity distribution induced by a uniform source distribution on the jet exit for start from opening of the jet exit.
$\underset{\sim}{V}_\infty$	velocity at infinite distance from jet, jet exit, or solid cylinder, as the case may be
w	component of velocity in z-direction
x	cartesian coordinate
$\underline{X}$	matrix used in Appendix G, defined below Equation (G-6)
X	function only of x used in Appendix G, defined above Equation (G-2)
x_1, x_2, x_3	curvilinear coordinates used in Appendix B
x_1, x_2, x_3, x_4	x-coordinates of source element in Appendix N
y	cartesian coordinate
y_1, y_2, y_3, y_4	y-coordinates of source element in Appendix N
Y	function only of y used in Appendix G, defined above Equation (G-2)

z	cartesian coordinate

Greek Letters

α_k	constant coefficient used in Appendix H, defined by Equation (H-9)
β_k^+, β_k^-	constant coefficients used in Appendix H, defined by Equation (H-9)
β, $\beta_\pm$	quadratic roots used in Appendix G, defined above Equation (G-4)
$\gamma_\pm$	constant used in Appendix H, defined in Equation (H-29)
Γ	circulation
Γ_a, Γ_b	circulations defined on Figure 23
δ_{ij}	Kroniker delta: $\delta_{ij} = 0$ if $i \neq j$; $\delta_{ii} = 1$
Δt	time step
Δx	(a). mesh width in Appendix H (b). displacement in x-direction due to induced velocity in vortex lattice model
Δy	displacement in y-direction due to induced velocity in vortex lattice model
Δz	displacement in z-direction due to induced velocity in vortex lattice model
$\Delta\alpha$	angular displacement due to velocity induced by vortex segment in vortex lattice model (Figure 56)
$\Delta\phi$	angular spacing of vortex columns in vortex lattice solution (Figure 104)
$\underline{\varepsilon}$	matrix used in Appendix H, defined above Equation (H-8)
ε	(a). error in difference approximation in Appendix H in numerical solution (b). increment of distance normal to jet exit bounding curve in Appendix L in vortex lattice model

$\varepsilon(x,y)$	function defined below Equation (VI-18)
ζ	component of vorticity in z-direction
ζ_k, ζ_{kl}, ζ_{klm}	discrete functions of t used in Appendix H
η	component of vorticity in y-direction
θ_1, θ_2	angles between vortex segment and vectors from ends thereof to the point of velocity calculation in vortex lattice model (Figure 55)
θ	angle from front stagnation point of cylinder
λ	(a). constant used in Appendix G, defined by Equation (G-3) (b). eigenvalue of matrix $\underline{A}$ used in Appendix H
λ'	eigenvalue of matrix $\underline{B}$ in Appendix H
ν	kinematic viscosity
ξ	component of vorticity in x-direction
ξ_k	discrete function of x used in Appendix H
π	pi
ρ	(a). density (b). spectral radius of matrix $\underline{A}$ used in Appendix H
σ	angle of source element x'-axis from x-axis in vortex lattice solution
τ_i, $\underset{\sim}{\tau}$	eigenvector of matrix $\underline{B}$ used in Appendix H
τ	truncation error
ϕ	(a). initial angle of vortex column from positive x-axis in vortex lattice model (Figure 104) (b) general function used in Appendix L to illustrate vector theorem
ψ	initial angle between vortex ring segments in vortex lattice model (Figure 105)

ω	vorticity
ω_m	minimum vorticity for creation of new vortex cell

Subscripts

body	indicates surface integration on solid body surface
c	indicates cross-flow velocity infinitely remote from cylinder or jet, as the case may be
cal	indicates actual calculated velocity induced on vertices of undeformed lattice at great distance above plane boundary by the vortex segments of the lattice in vortex lattice model
eff	indicates effective value of jet velocity after accounting is made for discretization error in matching exit source strength to vortex lattice strength in vortex lattice solution
exit	indicates surface integration on jet exit
i	refers to position in x-direction, defined as number of cells in x-direction from origin
image	indicates integral in image field in vortex lattice solution
I	value of subscript i at maximum extent of field from origin in x-direction in Appendix H
I_o	value subscript i at front stagnation point on cylinder
j	refers to position in y-direction, defined as number of cells in y-direction from origin
J	(a). refers to infinite jet in cross-wind sub-solution when affixed to velocity or vorticity (b). value of subscript j at maximum extent of field from origin in y-direction in Appendix H

J_o	value of subscript j at front stagnation point on cylinder
k	(a). refers to position in z-direction, defined as number of cells in z-direction from origin (b). Fourier expansion component index in Appendix H (c). eigenvalue and eigenvector index in Appendix H
m	(a). indicates number of boundary cell in numerical solution (b). indicates number of vortex column in vortex lattice model
min	refers to minimum value
n	refers to time value, defined as number of time steps from start
o	(a). refers to limit of integration in Equation (IV-10) (b). indicates potential flow velocity when affixed to velocity
object	indicates integral in image field in vortex lattice solution
p	(a). value of subscript i as summational variable (b). eigenvalue index used in Appendix G, defined by Equation (G-7)
P	refers to infinite plate sub-solution
plane	indicates surface integration on infinite plane boundary
q	(a). value of subscript j as summational variable (b). eigenvalue index used in Appendix G, defined by Equation (G-8)
r	value of subscript k as summational variable
s	(a). indicates surface value of velocity (b). indicates stagnation point value of pressure
x	indicates component in x-direction

y	indicates component in y-direction
z	indicates component in z-direction
0-	indicates limit approached from negative side
0+	indicates limit approached from positive side
0	refers to value 0^{o} from negative of cross-flow direction
90	refers to value 90^{o} from negative of cross-flow direction
1	refers to image field in Appendix L in vortex lattice model
∞	(a). indicates value at infinite distance from the jet, jet exit, or solid cylinder, as the case may be (b). indicates surface integration over surface at infinite distance from jet, jet exit, or solid cylinder, as the case may be, when affixed to integral

Superscripts

n	refers to time value, defined as number of time steps from start
T	indicates matrix transpose
'	(a). indicates variable of integration when affixed to position vector or coordinate (b). refers to prime sub-solution when affixed to velocity or vorticity (c). refers to coordinate system in source triangle as used and defined in Appendix N
"	indicates variable of integration

Notation

0	order of magnitude
Re	real part
Im	imaginary part

$\frac{\partial}{\partial n}$	derivative normal to surface
$\underset{\sim}{\nabla}$	vector del operator
∇^2	Laplacian operator
$\sim$	vector
$\_$	matrix
x	vector cross product
$\cdot$	vector dot product
$\lvert\ \rvert$	magnitude
$\lVert\ \rVert$	natural matrix norm

Notes:

1. Subscripts and superscripts that form integral parts of a symbol are not identified separately.

2. Nondimensionalization is used without change of symbol when noted in each chapter or appendix. All quantities are nondimensionalized with respect to the mesh width h, the cross-flow velocity V_c, and the cross-flow dynamic pressure $\frac{1}{2}\rho V_c^2$ except as specifically noted in the above list of symbols or in the location concerned. All quantities used in the figures are nondimensionalized accordingly.

CHAPTER I

INTRODUCTION

The problem of the incompressible jet issuing from a wall into a cross-flow parallel to the wall is of significance in several areas of engineering, ranging from STOL/VTOL aircraft design to pollution control. The problem involves considerable interaction between the jet and the cross-flow, the jet being deformed and deflected backward by the cross-flow, and some of the cross-flow being entrained into the rear of the jet. The result is the formation of a low pressure region on the wall behind the jet. The nonlinearity of the Navier-Stokes equations makes an analytical solution in this case, as in many others of interest, highly improbable. Furthermore, the three-dimensionality of the problem requires computer memory storage and computation time much too large for practical solution by the difference equation algorithms that have been applied successfully in two-dimensional problems.

Attention, therefore, has been directed either to simplified models of the flow, constructed of line vortices and/or other distributed singularities {1-10}*, or to the semi-empirical prediction of various characteristics of the flow,

---

*Numbers enclosed in these brackets refer to references listed under Literature Cited.

such as the deflected jet path and mass entrainment, using experimental data and a number of simplifying assumptions {10-19}. Both of these approaches have yielded results of value, in that certain effects of the flow can be predicted with some degree of accuracy if enough experimental data is available. However, since neither is based directly on the differential equations of motion, it is not to be expected that either is capable of refinement to the extent as to predict the fine details and development of the complete flow.

The present investigation encompasses the development and evaluation of the following:

(a) a numerical solution for the flow, based on an integro-differential form of the Navier-Stokes equations, formulated to minimize the computer storage required,

(b) a vortex lattice potential flow model of the flow.

The scope of the first of these is much broader than that of the second, and a far greater portion of the total effort naturally was concentrated on the numerical solution. The numerical solution proved to be capable of predicting the wall pressure distribution to be expected from experimental results, while the potential flow model did not. The importance of the numerical solution in the formulation used extends beyond the present problem in that this approach brings three-dimensional numerical solutions of the Navier-Stokes equations on large fields at least into the realm of possibility.

Related Work - Numerical Solution

The range of numerical solutions of the Navier-Stokes equations has been expanding quite rapidly in the last few years but still is confined to two-dimensional or axi-symmetric flows, with only a few exceptions. In two dimensions, calculations for flow fields with boundaries coinciding with the coordinate lines of some curvilinear system are well advanced and now quite numerous.

The time-dependent and/or steady two-dimensional flow about rectangular bodies {20-23}, circular cylinders {24-36}, oblate spheroids {37}, elliptic cylinders {36}, and finite flat plates {36, 38, 39}, as well as the axi-symmetric flow about spheres {40}, has been considered in various Reynolds number ranges. Numerical solutions for the two-dimensional internal flow in straight channels {41}, slant {42} and step {43} diffusers, channels with rectangular or curved bends {44}, square cavities {43, 45, 46}, and the axi-symmetric flow in curved channels with swirl {47} and in circular cavities {48} have also been developed. Finally, solutions for free flows such as the two-dimensional free jet {49}, the axi-symmetric impinging jet {50}, the emerging vortex ring {51}, and the many varied two-dimensional free surface and multi-fluid flows treated by the group at Los Alamos Scientific Laboratories in the past several years {52-56} and others {57} have been presented.

Three-dimensional solutions, however, have been at a premium and have been confined primarily to free convection heat transfer {58, 76, 77}, where the velocities are very small and coarse grids can be used. Other examples are the Taylor vortex instability in the flow between concentric rotating cylinders {59, 60} and the flow in a very short section of a square pipe {61}. One type of three-dimensional solution {60} uses a Fourier expansion in one coordinate, with only a single term retained, and thus might not truly be classed as three-dimensional.

Of the time-dependent solutions presented for various flow geometries all but a few {23, 24, 33, 39, 51, 58, 61} have been explicit in time. In two cases {23, 24} reductions in computer time of as much as 95% of that required by ordinary Gauss-Seidel iteration were achieved by the theoretical determination of the optimum acceleration parameter for the particular equations involved.

Stability problems are always encountered in the explicit methods at high Reynolds numbers, and some researchers {26, 30, 36, 42, 43, 50} have used one-sided upstream space differences in order to reach higher Reynolds numbers. However, one-sided differences introduce a numerical viscosity through their larger truncation error as compared with central differences, yet it is precisely in the higher Reynolds number range, where the physical diffusion is reduced, that the errors thus introduced become most serious.

This can be reduced by using higher-order one-sided differences {42} or iterating the complete solution at each time step {36}, thus achieving the accuracy of central differences but with better stability.

Most solutions have been based on forms of the Navier-Stokes equations not involving the pressure as a primary variable, and the vorticity-stream function form has been the most widely used, the few exceptions being the use of a vorticity-velocity form {25, 49} and, in three-dimensions, the vorticity-vector potential form {58}. In many of these the pressure is calculated subsequently by a line integral of the original Navier-Stokes equations {27-30, 32-35, 37, 38, 40, 47}, but a few have used the Poisson equation for the pressure obtained from the divergence of the Navier-Stokes equations {20, 40}. The Los Alamos group {52-56} and a few others {26, 45, 57} have used the original Navier-Stokes equations simultaneously with the Poisson equation for the pressure. The use of the Poisson equation for the pressure, however, is questionable, for the boundary conditions for the pressure are at best ambiguous, but must be specified on the entire boundary since the equation is elliptic. The solution, therefore, cannot be guaranteed to be properly posed. This is merely a reflection of the fact that the pressure should be considered a function linking the simultaneous differential equations, rather than a primary variable, in the solution of the equations.

Boundary conditions are always a problem in representing infinite flow fields on finite grids, and various methods of specification have been proposed. The most commonly used boundary conditions at "infinity" have been simply uniform flow with zero vorticity {23, 24, 27, 29, 30, 32, 33, 35, 36, 37, 40}, although others have attempted to better represent the true condition of infinity by using asymptotic expansions at the boundary with iteration {28, 31, 38, 57}. The latter, however, is apparently equivalent in accuracy to the former applied farther out {38}.

A wider variation in the downstream boundary conditions is evident, with most researchers using zero streamwise gradients {26, 30, 43, 47, 52, 53, 55, 57}, but others using extrapolation {22}, one-sided differences {42}, periodic upstream and downstream boundaries {20, 21, 61}, zero vorticity {23, 50}, or specified profiles {44}. Several different specifications of the boundary conditions on the body surface have also been employed. Two methods are most common for vorticity: the use of central differences on the boundary with the values at virtual points inside the wall determined from the no-slip condition {20, 21, 27, 28, 38, 42-46, 48}, and higher-order one-sided differences on the boundary {23, 24, 25, 33, 37, 40, 58, 61}. In two cases {23, 58} these specifications have been compared and the latter found to be less perturbing to the solution. In cases where

the point at which a tangential velocity was evaluated did not fall on a boundary line, reflective boundary conditions have been used {52, 53, 55}.

There is always the question of accuracy of a numerical solution, and there is no guarantee that the nonlinear difference system converges to the solution of the differential equations, rather than to that of some other differential equations, even when the solution is stable. Unfortunately analogous experimental situations are not always attainable, and detailed results are not always available for comparison. Some results have, however, compared fairly well with drag and surface pressure data for circular cylinders {27, 28, 30, 32, 33, 34, 40}. These solutions and results are discussed more fully in Chapter IV in connection with those of the present solution.

There are two principal limiting factors in numerical solutions—computer time and storage capacity, there being no doubt that accuracy can be achieved in the absence of these two limits. The goal then is to develop methods which possess the greatest economy in time and storage. The integro-differential formulation used in the present effort allows significant reduction in the storage required, especially in three-dimensions, and thereby makes three-dimensional numerical solutions on large fields practical. This storage economy is achieved by taking advantage of the particular

nature of the Navier-Stokes equations, i.e., the tendency of large velocity gradients to occur only in relatively small regions of the flow for small values of the viscosity. All of the three-dimensional numerical solutions of the Navier-Stokes equations reported have been restricted to small flow fields. The present formulation, however, allows the consideration of fields of meaningful size.

Of the two-dimensional solutions reported, those of Payne {49} for the plane jet and Whitehead {51} for the emerging vortex ring are applied to flow situations most similar to those considered in the present effort. Neither of these problems, however, involves a cross-wind, and the latter involves a time-dependent jet exit velocity which eventually vanishes. The numerical formulation of Payne {25, 49} bears some surface resemblance to the present formulation, but is fundamentally different, being based on the use of discrete line vortices and their images in any solid surfaces present, rather than on the integro-differential formulation of the governing equation. It is thus necessary in the formulation of Payne that the image points in any curved solid surfaces be located, a requirement that is difficult to fulfill for general surfaces. It is not clear how such use of vortices and images could be extended to three-dimensional solutions. These two solutions do, however, provide certain comparisons with the present results as noted in Chapter VI.

Related Work—Vortex Lattice Model

Various approximate methods have been proposed for the determination of the deflected jet path, all based in some way on average or integral momentum-force balances. The most simplistic of these simply add the jet and cross-wind mean velocity vectors {11} or stream functions {12}. Others are based on a balance between the drag perpendicular to the jet axis and the centrifugal force of the jet {13-15}. Some slightly more sophisticated methods attempt also the prediction of the jet axial velocity variation and entrainment by application of the integral momentum equations to control volumes containing the jet {10, 16, 17, 18}. All of these methods require a considerable amount of empirical data. In addition all of the quantities assumed constant in the various methods must, of course, be determined empirically. Still another approach considers the jet deflection as due to inelastic collision {19}.

The heavy dependence on empirical data and the numerous assumptions make some of these methods little more than curve-fits of experimental data for the jet path, axial velocity, and entrainment. Furthermore none of the fits has been shown to be universal enough to give reliable predictions in all ranges of the data. Such approaches, therefore, are of limited value in the prediction of the properties of the jet in a cross flow.

Most recent attempts have been directed toward the representation of the jet by distributed singularities of various types. Several two-dimensional or quasi-two-dimensional representations have been considered {1, 2, 10} which consider the jet to be undeflected {1, 2} or use singularities confined to the plane formed by the jet axis and the cross-wind {10}.

The representation of the jet and wake by an elliptic cylinder with an afterbody, the dimensions of which are determined to fit the wall pressure distribution, gives fairly good agreement with the experimental wall pressure distribution outside the region directly behind the jet. The inclusion of a sink in the afterbody {2} to take account of the entrainment gives even better agreement with experimental results. The use of a plane lattice of straight vortex segments located on the plane formed by the jet axis and the cross-wind velocity {10} does not give very close agreement with the experimental wall pressures. A similar approach is the use of two-dimensional doublets placed on the empirical jet path {10} with the strengths varying along the path in such a way as to cause the jet cross-section parallel to the wall to change from a circle through a series of ellipses, with a line of two-dimensional sinks of pre-determined strengths located on the major axes of the ellipses. This representation attempts to take some account of both the jet deflection and the entrainment.

Several three-dimensional singularity distributions have also been proposed {3-9}, the simplest of which uses two vortex lines with a sink line half-way between, the three lines having a common tangent plane at each point {3}. A rather extensive model designed to represent not only the jet but also adjoining three-dimensional bodies such as wings, nacelles, fans, and the like, by a three-dimensional distribution of sources and doublets has also been developed {4, 5}. Here the solid surfaces are covered with quadrilateral source panels, fan inlets are covered by quadrilateral doublet panels, and the jet is represented by a fixed tube of pre-determined geometry covered by quadrilateral doublet panels and placed on the empirical jet path. Bound and trailing vortices are added to the wing to allow lifting forces. This method is the best available for at least approximate calculation of the aerodynamic coefficients for complicated three-dimensional fan-in-wing combinations. However, its accuracy still leaves much to be desired because of the fact that the jet itself is not too well represented. The entire jet geometry is pre-determined from empirical data and kept very nearly cylindrical.

A similar but less complete approach uses only bound and trailing vortices to represent a wing of zero thickness, and a three-dimensional lattice of straight vortex segments of predetermined geometry placed on the empirical jet path

to represent the jet {6}. Yet another variation uses specified normal velocity on the surface of the jet tube and includes trailing vortices from the jet {7}.

None of the above methods allows for the deformation of the jet cross-section into the characteristic "kidney" shape. Some attempts at this are in progress. One proposal is a stack of two-dimensional vortex rings, each of which deforms under its own influence as time progresses {8}, those farther from the jet exit having been deforming for a longer time. This model, however, takes no account of the mutual influence of the rings, nor does it allow them to rotate about an axis perpendicular to the jet axis and cross-wind. Another proposal is the use of a three-dimensional lattice of short unconnected vortex segments which move under their mutual influence {9}. This, however, suffers from violation of Kelvin's theorems {73, Chapter 9}.

In the above-mentioned work several researchers have included three-dimensional vortex lattices in their models {4-9}. However, in most of these the lattice is of fixed geometry and is kept in a predetermined configuration rather than being left free to determine its own configuration {4-7}. The lattice in these cases cannot represent the true jet but only serves to supply some influences of the jet on associated bodies. In another case only vortex rings, with no connecting column vortices, have been used {8}. Here the

rings are allowed to deform, but only under their individual, not mutual influences. The last work cited {9} is most similar to the model of this proposal. The use of discrete vortex elements, however, makes that model differ significantly from the model investigated here.

CHAPTER II

INTEGRO-DIFFERENTIAL FORMULATION

Mathematical Formulation

Incompressible fluid motion is governed by the Navier-Stokes equation with constant density and fluid properties:

$$\frac{\partial \underset{\sim}{v}}{\partial t} + (\underset{\sim}{v} \cdot \underset{\sim}{\nabla})\underset{\sim}{v} = -\frac{1}{\rho}\underset{\sim}{\nabla} p + \nu \nabla^2 \underset{\sim}{v} \tag{1}$$

together with the continuity equation

$$\underset{\sim}{\nabla} \cdot \underset{\sim}{v} = 0 \tag{2}$$

The pressure may be eliminated as a dependent variable by taking the curl of Equation (1) and introducing the vorticity as a dependent variable (Appendix A). The system of differential equations governing the motion is then

$$\frac{\partial \underset{\sim}{\omega}}{\partial t} = \underset{\sim}{\nabla} \times (\underset{\sim}{v} \times \underset{\sim}{\omega}) + \nu \nabla^2 \underset{\sim}{\omega} \tag{3}$$

$$\underset{\sim}{\nabla} \times \underset{\sim}{v} = \underset{\sim}{\omega} \tag{4}$$

$$\underset{\sim}{\nabla} \cdot \underset{\sim}{v} = 0 \tag{5}$$

The last two equations together imply the equation (Appendix A)

$$\nabla^2 \underset{\sim}{v} = -\underset{\sim}{\nabla} \times \underset{\sim}{\omega} \tag{6}$$

and, as is shown in Appendix A, the solution of this equation subject to given boundary conditions and specified vorticity distribution and the solution of the simultaneous equations (4) and (5) subject to the same boundary conditions and vorticity distribution are both unique and, therefore, identical. It then follows that the solution of the differential system defined by Equations (3), (4), and (5) can be obtained by solving the differential system composed of Equations (3) and (6).

The second of these equations, being a Poisson equation, can be expressed in integral representation by Green's Theorem (Appendix B):*

$$\underset{\sim}{v}(\underset{\sim}{r}) = \frac{1}{4\pi} \iint \left[\frac{\frac{\partial \underset{\sim}{v}}{\partial n}}{|\underset{\sim}{r}' - \underset{\sim}{r}|} + \frac{(\underset{\sim}{r}' - \underset{\sim}{r}) \cdot \underset{\sim}{n}}{|\underset{\sim}{r}' - \underset{\sim}{r}|^3} \underset{\sim}{v} \right] dS + \frac{1}{4\pi} \iiint \frac{\nabla \underset{\sim}{} \times \underset{\sim}{\omega}}{|\underset{\sim}{r}' - \underset{\sim}{r}|} d\nu \qquad (7)$$

where the integrations are over $\underset{\sim}{r}'$, with $\underset{\sim}{v}$, $\underset{\sim}{\omega}$, and the normal to the surface $\underset{\sim}{n}$ being functions thereof. The volume integral is over the entire flow field, and the surface integral is over the boundary thereof. This equation expresses the velocity in the field as a function of the normal derivative of the velocity on the surface, the velocity itself on the surface and the vorticity distribution in the field.

---

*Dependence on time is understood throughout this chapter.

Formulation with a Porous Infinite Plane Boundary

Green's Theorem also implies the following integral relation for a point $\underset{\sim}{r}$ outside the flow field (Appendix B):

$$\iint \left[\frac{\frac{\partial \underset{\sim}{v}}{\partial n}}{|\underset{\sim}{r}' - \underset{\sim}{r}|} + \frac{(\underset{\sim}{r}' - \underset{\sim}{r}) \cdot \underset{\sim}{n}}{|\underset{\sim}{r}' - \underset{\sim}{r}|^3} \underset{\sim}{v}\right] dS + \iiint \frac{\nabla \times \underset{\sim}{\omega}}{|\underset{\sim}{r}' - \underset{\sim}{r}|} d\nu = 0 \quad (8)$$

For any problem involving an infinite plane boundary, porous or impervious, Equation (8) can be used to eliminate the term involving the derivative normal to that boundary from the surface integral of Equation (7). Referring to Figure 1, for every point $\underset{\sim}{r}$ in the flow field define an image point $\underset{\sim}{R}$ beyond the plane boundary:

$$\underset{\sim}{R} \equiv \underset{\sim}{r} - 2(\underset{\sim}{k} \cdot \underset{\sim}{r})\ \underset{\sim}{k} \quad (9)$$

where $\underset{\sim}{k}$ is the unit vector perpendicular to the plane boundary, directed into the flow field.

Combination of Equations (7) and (8), with $\underset{\sim}{r}$ in Equation (8) replaced by $\underset{\sim}{R}$, yields the following replacement for Equation (7), the integrals over the surface at infinity having vanished (Appendix B):

$$\underset{\sim}{v}(\underset{\sim}{r}) = \frac{\underset{\sim}{k} \cdot \underset{\sim}{r}}{2\pi} \iint \frac{\underset{\sim}{v}\, dS}{|\underset{\sim}{r}' - \underset{\sim}{r}|^3} +$$

$$+ \frac{1}{4\pi} \iiint \left(\frac{1}{|\underset{\sim}{r}' - \underset{\sim}{r}|} - \frac{1}{|\underset{\sim}{r}' - \underset{\sim}{R}|}\right) (\nabla \times \underset{\sim}{\omega})\, d\nu \quad (10)$$

Here, from Equation (9),

$$|\underset{\sim}{r}' - \underset{\sim}{R}| = [|\underset{\sim}{r}' - \underset{\sim}{r}|^2 + 4(\underset{\sim}{k} \cdot \underset{\sim}{r})\ (\underset{\sim}{k} \cdot \underset{\sim}{r}')]^{1/2} \qquad (11)$$

The surface integral is now over only the plane boundary, but the volume integral is still over the entire flow field. The only requirement that has been imposed to secure the vanishing of the surface integrals over the boundary at infinity is that the derivative of the velocity normal to that boundary be non-zero only over a finite portion of the boundary and/or over a portion of finite vertical extent above the plane boundary. This certainly will be the case at any finite time after the start of the flow.

Using the properties of the particular function $|\underset{\sim}{r}' - \underset{\sim}{r}|^{-1}$ employed here, the volume integral of Equation (10) can be expressed in a form not requiring the derivative of the vorticity (Appendix B). The final integro-differential system to be solved is then

$$\frac{\partial \underset{\sim}{\omega}}{\partial t} = \underset{\sim}{\nabla} \times (\underset{\sim}{v} \times \underset{\sim}{\omega}) + \nu \nabla^2 \underset{\sim}{\omega} \qquad (12)$$

$$\underset{\sim}{v}(\underset{\sim}{r}) = \frac{\underset{\sim}{k} \cdot \underset{\sim}{r}}{2\pi} \iint \frac{\underset{\sim}{V}_s \, dS}{|\underset{\sim}{r}' - \underset{\sim}{r}|^3}$$

$$+ \frac{1}{4\pi} \iiint \left(\frac{\underset{\sim}{r}' - \underset{\sim}{r}}{|\underset{\sim}{r}' - \underset{\sim}{r}|^3} - \frac{\underset{\sim}{r}' - \underset{\sim}{R}}{|\underset{\sim}{r}' - \underset{\sim}{R}|^3} \right) \times \underset{\sim}{\omega} d\nu \qquad (13)$$

where the surface velocity $\underset{\sim}{V}_s$ is specified by the boundary

conditions. The boundary conditions at infinity are contained implicitly in the formulation so that no further specification is necessary.

Formulation with a Finite Closed Solid Boundary

As shown in Appendix B, the normal gradient of the velocity on the surface of a body of any shape can be written in terms of the surface vorticity:

$$\frac{\partial \underset{\sim}{v}}{\partial n} = \underset{\sim}{\omega} \times \underset{\sim}{n}$$

Also in Appendix B it is shown that, with this expression for $\frac{\partial \underset{\sim}{v}}{\partial n}$, the surface integral of Equation (7) can be combined with the volume integral (specifying $\underset{\sim}{v} = 0$ on the body surface), so that Equation (7) may be rewritten as

$$\underset{\sim}{v}(\underset{\sim}{r}) = \underset{\sim}{V}_{\infty} + \frac{1}{4\pi}\iiint \left(\frac{\underset{\sim}{r}' - \underset{\sim}{r}}{|\underset{\sim}{r}' - \underset{\sim}{r}|^3}\right) \times \underset{\sim}{\omega} d\nu \qquad (14)$$

Here the conditions at infinity have been taken to be zero vorticity and uniform velocity.* The integro-differential system to be solved in this case then is

$$\frac{\partial \underset{\sim}{\omega}}{\partial t} = \underset{\sim}{\nabla} \times (\underset{\sim}{v} \times \underset{\sim}{\omega}) + \nu \nabla^2 \underset{\sim}{\omega} \qquad (15)$$

$$\underset{\sim}{v}(\underset{\sim}{r}) = \underset{\sim}{V}_{\infty} + \frac{1}{4\pi}\iiint \left(\frac{\underset{\sim}{r}' - \underset{\sim}{r}}{|\underset{\sim}{r}' - \underset{\sim}{r}|^3}\right) \times \underset{\sim}{\omega} d\nu \qquad (16)$$

where $\underset{\sim}{V}_{\infty}$ is the uniform velocity at an infinite distance from the body.

*Specifically, the vorticity must approach zero at least as fast as the inverse square of the radius.

Reduction of Volume Integrals in One and Two Dimensions

As shown in Appendix B, the volume integral of Equation (16) may be reduced to a surface integral for two-dimensional solutions by carrying out the integration over the direction of invariance. In two-dimensional problems then Equation (16) is replaced by the equation

$$\underset{\sim}{v}(\underset{\sim}{r}) = \underset{\sim}{V}_{\infty} + \frac{1}{2\pi}\iint\left(\frac{\underset{\sim}{r}' - \underset{\sim}{r}}{|\underset{\sim}{r}' - \underset{\sim}{r}|^2}\right) \times \underset{\sim}{\omega} dS \qquad (17)$$

where the surface integral extends over the entire two-dimensional flow field.

Also in Appendix B it is shown that the volume integral of Equation (13) may be reduced to a line integral for one-dimensional solutions by performing the integration in the plane of invariance. Therefore, in one-dimensional problems Equation (13) is replaced by the equation

$$u(z) = V_{\infty} + \int_{o}^{z} \eta dz' \qquad (18)$$

Numerical Solution in the Integro-Differential Formulation

Computation Procedure

The explicit numerical solution consists of a two-part procedure at each time step: (a) first the new vorticity is calculated at the new time from the parabolic (in time)

differential equation, and (b) then the new velocity is calculated from the appropriate integral over the new vorticity distribution. Now only those field points with non-zero vorticity need be considered in the calculation of the velocity from the integral over the vorticity distribution, since the integrand is zero where the vorticity is zero. Furthermore, with the space derivatives in the differential equation for the vorticity expressed as three-point central differences, the vorticity can change at each time step only at, or adjacent to, points that already have non-zero vorticity at that time. Therefore, the velocity is required for the actual calculation only at points having non-zero vorticity. This then means that the solution in the entire flow field can be obtained while actually performing calculations only in the region of non-zero vorticity at each time. Therefore, only the points with non-zero vorticity at a given time need be stored at that time, rather than all the field points as would be required if the numerical solution were based on the differential formulation.

It should be noted that all of the information contained in the differential system, Equations (1) and (2), is also contained in the integro-differential system, Equations (12) and (13) or Equations (15) and (16). In particular, the effect of the boundary conditions at infinity, i.e., the free stream, have not been lost, but are contained implicitly in

the integro-differential formulation. In fact, the finite numerical calculation field in the integro-differential formulation is, in effect, infinite, and the necessity of locating "infinity" at a finite distance, as is required in numerical methods based on the differential formulation, is avoided. The restriction of the field of actual computation to the region of non-zero vorticity at each time is not an approximation in itself.

This formulation thus takes advantage of the particular nature of the Navier-Stokes equations, i.e., their tendency to produce solutions having large gradients, and hence vorticity, over relatively small regions of the flow field for fluids of small viscosity. This property of the equations is a distinct impediment to numerical solution of the differential system, but is exploited to advantage in the numerical solution of the integro-differential system, with considerable savings in computer storage.

In the numerical solution the flow field is divided into elementary cells (which are cubes, squares, or simply line segments in three, two, and one dimensional flow problems, respectively), each of which is centered on a point of a rectangular grid of constant mesh width. For purposes of identification the following definitions are introduced:

vortex cell—a cell centered on a point having non-zero vorticity,

border cell—a cell centered on a point having zero vorticity, but being adjacent to a vortex cell,

boundary cell—a cell containing a portion of a solid surface boundary,

aggregate of vortex cells—the group of all the vortex cells in the flow field.

At each time step the new vorticity of each vortex cell is calculated from the finite difference representation of the differential equation, Equation (3). New vorticity is also calculated for each border cell from the same equation. If the sum of the magnitude of the vorticity of a border cell and that of any vortex cell adjacent to the border cell in question exceeds a specified value, the border cell is reclassified as a vortex cell. If not, the vorticity calculated for the border cell is instead distributed evenly among the adjacent vortex cells, and the border cell remains a border cell. The velocity is then calculated in each current vortex cell from the integral over the vorticity distribution in the aggregate of vortex cells. Values of vorticity and velocity are stored only for the vortex cells. The cell cataloging procedure necessary to implement the economy in storage requirements is described in Appendix C, and typical comparisons with the storage requirements of the differential formulation are also given therein.

Computer Time Required (UNIVAC 1108 Computer)

The computer time required increases as time progresses since the computational field becomes larger at each time step as more vortex cells are added. The computer time is also strongly dependent on the influence range beyond which vorticity is neglected in the velocity calculation, since the velocity calculation accounts for the majority of the computation time required at each time step. For the longest two-dimensional run made, the solution required about 7.5 minutes per time step with 3408 vortex cells and an influence range of 24 cells. In that case the aggregate of vortex cells extended 40 cells normal to the cross-flow and 140 cells parallel to the cross-flow. However, since the region of non-zero vorticity, i.e., the aggregate of vortex cells, is only a small portion of the entire flow field, the same solution using a differential formulation would have required, conservatively, an 80 x 280 rectangular field containing some 22,400 points as opposed to the 3400 required in the present case. Comparison of time required by the present solution with that of a solution based on differential formulation in this case should therefore assume that about seven times as many points would be required with the differential formulation.

In the longest three-dimensional run made, the solution required about 13.8 minutes per time step with 2256

vortex cells and an influence range of 12 cells. The aggregate of vortex cells in this case extended 13 cells above the plane boundary and 24 cells both normal and parallel to the cross-flow. The same solution with differential formulation thus would have required at least a 20 x 50 x 50 field with 50,000 points, or about twenty times the number of points required in the present solution. It should be noted also that these estimates of the size of the field required with the differential formulation are conservative, assuming as they do that the infinity conditions can be imposed at distances about half the extent of the region of non-zero vorticity from the edge of that region.

The large computer time required by the evaluation of the velocity from the integral over the vorticity field makes the numerical method based on the integro-differential formulation, however, non-competitive with methods based on differential formulation in two-dimensional problems. (The calculation of the velocity at each point truly requires a summation over all other points having non-zero vorticity, though only those points within a certain distance are actually included.) This arises from the fact that the integral solution of Poisson's equation is equivalent, in finite methods, to inverting a matrix having as many elements as there are calculation points in the field. The differential solution of Poisson's equation, however, is equivalent, in

finite methods, to solving the matrix equation by iteration rather than by inversion. For matrices of any appreciable size, iterative methods of solution, especially with convergence acceleration, are much more efficient than matrix inversion.

There is another point, however, for the field involved in the integro-differential method, including as it does only the points with non-zero vorticity at any time, is smaller than that necessary for differential methods. (The above-mentioned restriction of the summation to points within a certain distance of the point in question reduces the size still farther.) The latter must, of course, include at all times the entire field ever to be used at any time. Therefore, the matrix to be inverted in the integro-differential method is smaller than the matrix to be solved by iteration in the differential methods. There is, then, a cross-over point, the integro-differential method being faster at the earlier time steps than the differential. The situation is reversed, however, as the computational field of the integro-differential method increases with time and the matrix being inverted becomes larger. Though always smaller than the matrix of fixed size that is solved iteratively in the differential methods, the matrix of the integro-differential method eventually requires more time for inversion than is required for iterative solution of the larger matrix of the differential methods.

It would seem that the velocity calculation could be done more efficiently if the geometry factors involved were calculated only once and read from storage as needed. This, of course, is true if the retrieval from storage can be done faster than the needed values can be calculated. Such, however, is not the case with magnetic tape storage, the only alternative available in the present effort. Calculations showed that tape storage of the geometry factors in blocks small enough to be kept in core with the rest of the program, i.e., of the order of the field size, offers no time savings in the present case. Disc storage, however, has retrieval time faster by several orders of magnitude than tape storage and would allow a considerable savings in computer time.

Even if the retrieval from storage required no time at all, a cross-over point would still exist in comparison with differential methods. The storing of the geometry factors amounts to storing the inverse of the matrix rather than recalculating it at each time. However, with very large matrices the number of calculations necessary just to perform the matrix multiplication with the inverse exceeds that involved in the iterative solution of the matrix. Thus, although speed could be gained with the use of more rapid data retrieval storage, the differential methods would still eventually become faster as time progressed, the cross-over point being postponed to a later time.

In three dimensions, however, the integro-differential method is superior in speed at the present state of the art. The primary reason for this is that the significant storage reduction achieved by the integro-differential method allows three-dimensional problems of large field size to be considered without the use of any low-speed storage, i.e., completely in the high-speed core. This is a result, of course, of confining the calculation to the region of non-zero vorticity at any time. The addition of the third dimension causes the field required for the differential methods to become so large that the solution can no longer be kept in core, but must be read from the low-speed storage at each iteration. The same retrieval time discussed above, but even larger here due to the large field, then must be considered in these methods at each iteration.

In addition the relative field matrix size advantage of the integro-differential method over that of the differential is increased by an order of magnitude in three dimensions, as compared with two dimensions. The point at which the inversion of the smaller matrix requires more calculations than the iterative solution of the larger matrix is thus postponed to much larger times in three-dimensional problems.

The result of both these factors then is a significant speed advantage of the integro-differential method in three

dimensions at the present time—witness the dearth of differential method solutions in three dimensions that have been presented.

Applications Developed

This numerical method based on the integro-differential formulation is applied first to the time-dependent, one-dimensional flow over a suddenly accelerated infinite plane wall (Chapter III) for comparison with an exact solution of the Navier-Stokes equations. The method is then applied to the time-dependent, two-dimensional flow about an infinite solid cylinder with its axis normal to the cross-flow (Chapter IV) for comparison with experimental data and the results of other numerical methods. The comparisons made in these two chapters serve to establish the validity of the numerical method before application to the jet in cross-wind.

The time-dependent, three-dimensional jet in cross-wind (Chapter VI) is treated with two different types of initial conditions. In the first case, the flow is considered to start from the opening of the jet exit. The initial velocity distribution for this case is the superposition of a uniform flow parallel to the wall and the velocity induced by a uniform source distribution on the jet exit (Figure 2a). With this type of start the jet penetrates more deeply into the cross-flow, while being deflected backward, as time passes until a steady state is reached

(Figure 2a).

The initial vorticity distribution for this case then is simply a plane sheet of vorticity on the wall, resulting from the satisfaction of the no-slip condition at the wall (Figure 2b). Since this sheet of vorticity extends to infinity in the two directions parallel to the wall, the region of non-zero vorticity is already of infinite extent at the start, so that the number of vortex cells is infinite from the start. However, the solution at an infinite distance parallel to the wall from the jet exit at all times is simply that of the one-dimensional flow above an infinite plane wall. This is simply the solution developed in Chapter III superposed with a uniform flow parallel and opposite in direction to the velocity of the infinite plane. This one-dimensional solution thus supplies the conditions at infinity at all times for the complete three-dimensional solution for the jet in cross-wind with this type of start.

Therefore, the difference between the complete solution and this one-dimensional solution is a three-dimensional solution having zero vorticity at infinity, and thus having only a finite region of non-zero vorticity at any finite time. The initial vorticity distribution for this latter solution is then a circular plane sheet of finite extent on the wall surrounding the jet exit, resulting from the application of the no-slip condition to the velocity induced

parallel to the wall by the uniform source distribution on the jet exit (Figure 2c). The complete numerical solution is therefore obtained with this type start by performing simultaneously the one-dimensional solution of Chapter III and a three-dimensional solution (Chapter VI) having a finite extent of non-zero vorticity.

The other case treated is that in which the flow is considered to start from the dissolving of a hypothetical pipe standing on the jet exit, separating an interior uniform vertical flow of infinite vertical extent from the exterior potential cross-flow about the pipe normal to its axis (Figure 3a). In this case the jet penetrates without deformation to infinity normal to the wall at the start. As time passes, the jet is deformed and deflected backward, the portion at infinity above the wall remaining normal to the wall as its vertical velocity is reduced to zero (Figure 3a). Each type of start leads eventually to the same steady state.

The initial vorticity distribution in this case is a plane sheet of vorticity on the wall, resulting from the satisfaction of the no-slip condition at the wall, and a cylindrical sheet of vorticity standing on the jet exit, resulting from the velocity discontinuity created at the dissolution of the pipe (Figure 3b). Now both of these sheets of vorticity are of infinite extent, the plane sheet extending to infinity normal to the wall. However, the solution

at an infinite distance parallel to the wall from the jet exit is again that of the one-dimensional flow above an infinite plane wall. Also, the solution at infinite vertical distance above the wall is that corresponding to the dissipation of an infinite column of fluid by the cross-flow (with no variation along the column), the column having been located over the jet exit at the start and having had at that time the uniform vertical velocity of the above-mentioned flow inside the hypothetical pipe (Figure 4). As time passes, the column is deformed and displaced backward by the cross-flow, and the vertical velocity is gradually dissipated (Figure 4). At infinite time this solution is reduced to that of the undisturbed uniform cross-flow, with no vertical velocity. This is a time-dependent, two-dimensional problem (but with three variable components of velocity and vorticity) and is developed in Chapter V for use in the solution with this type start as described below. The solution of Chapter V thus supplies the conditions at infinity normal to the wall in this case.

The sum of the solutions developed in Chapters III and V supplies all of the infinity conditions for the complete three-dimensional solution in this case. The difference between the complete solution in this case and this combination of solutions then is a three-dimensional solution having zero vorticity at infinity, and thus having only a finite

region of non-zero vorticity at any finite time. The initial vorticity distribution for this latter solution is then a plane sheet of finite extent on the wall surrounding the jet exit, resulting from the application of the no-slip condition to the velocity induced parallel to the wall by the doublet distribution on the jet exit diameter that, with the uniform cross flow, forms a closed streamline corresponding to the jet exit curve, e.g., a single doublet at the center of a circular exit (Figure 3c). The complete numerical solution is therefore obtained in this case by performing simultaneously the one-dimensional solution of Chapter III, the two-dimensional solution of Chapter V, and a three-dimensional solution (Chapter VI) having a finite extent of non-zero vorticity.

CHAPTER III

NUMERICAL SOLUTION FOR THE FLOW ABOVE A SUDDENLY ACCELERATED INFINITE FLAT PLATE

In this chapter the numerical method is applied to the time-dependent, one-dimensional flow above a suddenly accelerated infinite plane moving parallel to itself at constant velocity. This solution was developed for two purposes: to provide a test of the numerical method against an exact solution and to provide a sub-solution for use in developing the three-dimensional solution for the jet in cross-wind in Chapter VI.

Numerical Formulation

Vorticity-Velocity Solution

The one-dimensional solution for the flow above an infinite flat plate moving parallel to itself in an otherwise quiescent fluid is determined by the nondimensional equations (Chapter II)

$$\frac{\partial \eta}{\partial t} = \frac{1}{R_c} \frac{\partial^2 \eta}{\partial z^2} \qquad (1)^*$$

$$u(z, t) = 1 + \int_0^z \eta(z', t)\, dz' \qquad (2)$$

---

*All quantities in this chapter are nondimensionalized as noted in the Nomenclature.

where the cell Reynolds number R_c is based on the constant plate velocity. The boundary condition is

$$u(0, t) = 1$$

and the initial condition is

$$\eta(z, 0) = \begin{cases} -1, & z = 0 \\ 0, & z > 0 \end{cases}$$

which correspond to the initial solution

$$u(z, 0) = \begin{cases} 1, & z = 0 \\ 0, & z > 0 \end{cases}$$

The numerical approximation of Equation (1) is, using a two-point forward time difference and three-point central space differences (Appendix D),

$$\eta_k^{n+1} = (1 - 2\frac{\Delta t}{R})\eta_k^n + \frac{\Delta t}{R_c}(\eta_{k+1}^n + \eta_{k-1}^n) \qquad (3)$$

in the straight explicit form, or

$$\eta_k^{n+1} = \left(\frac{\frac{1}{2} - \frac{\Delta t}{R_c}}{\frac{1}{2} + \frac{\Delta t}{R_c}} \right) \eta_k^{n-1} + \frac{\frac{\Delta t}{R_c}}{(\frac{1}{2} + \frac{\Delta t}{R_c})}(\eta_{k+1}^n + \eta_{k-1}^n) \qquad (4)$$

in the Dufort-Frankel form. Here the superscript and subscript refer to time and space, respectively: $\eta_k^n \equiv \eta(z_k, t_n)$.

The integral of Equation (2) is approximated by the summation

$$u_k^n = 1 + \sum_{r=1}^{k-1} \eta_r^n \tag{5}$$

Boundary Conditions and Initial Conditions

Since

$$\lim_{z \to \infty} u(z, t) = 0$$

Equation (2) implies that

$$\int_0^\infty \eta(z, t)\, dz = -1$$

so that, from Equation (5),

$$\sum_{k=1}^{\infty} \eta_k^n = -1, \text{ all } n$$

But, in the straight explicit formulation,

$$\sum_{k=1}^{\infty} \eta_k^n = \eta_1^n + \sum_{k=2}^{\infty} \eta_k^n$$

$$= \eta_1^n + \sum_{k=2}^{\infty} [\eta_k^{n-1} + \frac{\Delta t}{R_c}(\eta_{k+1}^{n-1} - 2\eta_k^{n-1} + \eta_{k-1}^{n-1})]$$

where Equation (3) has been used to express η_k^n in terms of

the previous values for the summation. Then,

$$\sum_{k=1}^{\infty} \eta_k^n = \eta_1^n + \sum_{k=2}^{\infty} \eta_k^{n-1} + \frac{\Delta t}{R_c}\Big[\sum_{k=2}^{\infty} \eta_k^{n-1} - \eta_2^{n-1} - 2\sum_{k=2}^{\infty} \eta_k^{n-1} + \sum_{k=2}^{\infty} \eta_k^{n-1} + \eta_1^{n-1}\Big]$$

$$= \eta_1^n + \sum_{k=1}^{\infty} \eta_k^{n-1} - \eta_1^{n-1} + \frac{\Delta t}{R_c}(\eta_1^{n-1} - \eta_2^{n-1})$$

Then, since it is required above that

$$\sum_{k=1}^{\infty} \eta_k^n = \sum_{k=1}^{\infty} \eta_k^{n-1}$$

it must be that

$$0 = \eta_1^n - \eta_1^{n-1} + \frac{\Delta t}{R_c}(\eta_1^{n-1} - \eta_2^{n-1})$$

But from Equation (3) applied on the boundary,

$$\eta_1^n = (1 - 2\frac{\Delta t}{R_c})\eta_1^{n-1} + \frac{\Delta t}{R_c}(\eta_2^{n-1} + \eta_o^{n-1})$$

These last two equations are both satisfied if the vorticity at the virtual point below the boundary is defined to be equal to the value on the boundary:

$$\eta_o^n \equiv \eta_1^n$$

This requirement then satisfies the conservation of vorticity that is implied by Equation (2), and the boundary condition on the velocity is implicit in this equation.

The proper representation of the boundary condition is thus achieved by the specification of a value of vorticity at a virtual point one cell width below the boundary, this value being taken equal to that on the boundary ($z_1 = 0$):

$$\eta_o^n = \eta_1^n$$

The initial conditions are simply

$$\eta_1^o = -1$$

$$\eta_k^o = 0 \quad , \quad k \neq 1$$

Computation Procedure

At each successive time step new values of the vorticity are calculated from Equation (3) or (4), depending on formulation being used, and new velocity values are then obtainable from Equation (5). Only those cells with non-zero vorticity, i.e., vortex cells,* and one border cell* need be included in the calculation, for only in these cells can the vorticity change at a given time step. If the

*Vortex cells and border cells are defined in Chapter II.

magnitude of the newly calculated vorticity in the border cell (which had zero vorticity at the previous time) is sufficiently large, the border cell is reclassified as a vortex cell and the extent of non-zero vorticity is thus increased by one cell. Otherwise, the extent of non-zero vorticity remains unchanged, and the vorticity of the border cell in question remains zero. Two criteria for making this determination were examined:

(1) The vorticity field is extended if the magnitude of the vorticity calculated for the border cell exceeds a specified minimum, ω_m. Otherwise this vorticity is added to that of the topmost vortex cell.

(2) The vorticity field is extended if the sum of the magnitude of the vorticity calculated for the border cell and that of the topmost vortex cell exceeds a specified minimum, ω_m. Otherwise this vorticity is added to that of the topmost vortex cell.

Thus no vorticity is ever lost from the field. (The simple discarding of the vorticity calculated for the border cell in the event of no reclassification results in vorticity flowing out of the field of computation, so that the viscous effects of the wall are eventually obliterated.) These two schemes amount to a spacial averaging, whereby the total

vorticity present is not altered, but the distribution at the outer edge of the field is averaged over adjacent points in the field.

Comparison With Exact Solution

From the comparisons given in Figure 5* it is clear that the solution using the above minimum vorticity scheme #1 does not converge as the time step is reduced at constant cell size. The solution with scheme #2, however, does converge to the exact solution of Equations (1) and (2), {67, Chapter 5}, as is demonstrated in Figure 6.

The effect at large times of the minimum vorticity, ω_m, is shown in Figures 7 and 8 for the two schemes. Comparison of Figures 7 and 8 shows that both schemes are accurate with a minimum vorticity of 0.001. Scheme #1, however, shows a much more rapid loss of accuracy as the minumum vorticity is increased. The accuracy with each scheme naturally deteriorates in time with a large minimum vorticity, since the error thus introduced is cumulative. With larger values of the minimum vorticity the transition of a border cell to a vortex cell becomes less likely, so that the vorticity tends to be artificially confined and its spread away from the wall is inhibited.

---

*Parameters used in all results presented are given in Table 4.

The lack of convergence with a decrease in time step that results with scheme #1 is reflected in the loss of accuracy as time progresses that is evident in Figure 9a. Scheme #2, however, suffers no such loss (Figure 9b).

CHAPTER IV

NUMERICAL SOLUTION FOR THE FLOW ABOUT A TWO-DIMENSIONAL SOLID CYLINDER

In this chapter the numerical method is applied to the time-dependent, two-dimensional flow normal to the axis of an infinite solid circular cylinder with and without a rear splitter plate. This solution was developed to provide a comparison of the results of the numerical method for the surface pressure distribution, the pressure, friction, and total drag coefficients, the length of the standing vortices behind the cylinder, and the vortex shedding frequency with those of other numerical methods and with experimental data. Since the purpose of this comparison was to verify the method to be applied to the three-dimensional jet in cross-wind, for which cartesian coordinates are appropriate, a cartesian system was used also for this comparison, even though cylindrical coordinates are, of course, more appropriate to the analysis of the flow about a circular cylinder. In the jet in cross-wind problem, the portion of the jet near the exit is essentially cylindrical, so that the cartesian coordinate system used must be capable of treating essentially cylindrical geometries as well as geometries that are predominantly rectangular.

Numerical Formulation

Vorticity-Velocity Solution

The two-dimensional solution for the flow of an unbounded free stream about a cylinder with its axis perpendicular to the free stream is determined by the equations (Chapter II)

$$\frac{\partial \underset{\sim}{\omega}}{\partial t} = \underset{\sim}{\nabla} \times (\underset{\sim}{v} \times \underset{\sim}{\omega}) + \nu \nabla^2 \underset{\sim}{\omega} \tag{1}$$

$$\underset{\sim}{v} = \underset{\sim}{V}_{\infty} + \frac{1}{2\pi} \iint \frac{(\underset{\sim}{r}' - \underset{\sim}{r})}{|\underset{\sim}{r}' - \underset{\sim}{r}|^2} \times \underset{\sim}{\omega}(\underset{\sim}{r}')\, dS \tag{2}$$

where the integral is over the entire two-dimensional region exterior to the cylinder, and $\underset{\sim}{V}_{\infty}$ is the uniform velocity at an infinite distance from the cylinder. After nondimensionalization with respect to the free stream velocity V_{∞} and the cell size h, Equations (1) and (2) become, for the coordinate system shown in Figure 10,

$$\frac{\partial \zeta}{\partial t} = -\frac{\partial}{\partial x}(u\zeta) - \frac{\partial}{\partial y}(v\zeta) + \frac{1}{R_c}\left(\frac{\partial^2 \zeta}{\partial x^2} + \frac{\partial^2 \zeta}{\partial y^2}\right) \tag{3}*$$

$$u = -1 + \frac{1}{2\pi} \iint \frac{(y' - y)\, \zeta(x', y')}{(x' - x)^2 + (y' - y)^2}\, dx'dy' \tag{4a}$$

---

*Hereafter all quantities in this chapter are nondimensionalized as noted in the Nomenclature.

$$v = -\frac{1}{2\pi}\iint \frac{(x' - x)\,\zeta\,(x', y')}{(x' - x)^2 + (y' - y)^2}\,dx'dy' \qquad (4b)$$

with the cell Reynolds number defined as $R_c = \frac{V_\infty h}{\nu}$, and all quantities in Equations (3) and (4) taken as dimensionless.

With the space derivatives replaced by three-point central differences and the time derivative by a two-point forward difference, Equation (3) is approximated (Appendix D) by the difference equation,

$$\zeta^{n+1}_{i,j} = \left(1 - \frac{4\Delta t}{R_c}\right)\zeta^n_{i,j} - \frac{\Delta t}{2}\left[(u\zeta)^n_{i+1,j} - (u\zeta)^n_{i-1,j} + (v\zeta)^n_{i,j+1} - (v\zeta)^n_{i,j-1}\right] + \frac{\Delta t}{R_c}\left[\zeta^n_{i+1,j} + \zeta^n_{i-1,j} + \zeta^n_{i,j+1} + \zeta^n_{i,j-1}\right] \qquad (5)$$

in the straight explicit form, or by the difference equation, (Appendix D)

$$\zeta^{n+1}_{i,j} = \left(\frac{\frac{1}{2} - 2\frac{\Delta t}{R_c}}{\frac{1}{2} + 2\frac{\Delta t}{R_c}}\right)\zeta^{n-1}_{i,j} - \frac{\frac{\Delta t}{2}}{\left(\frac{1}{2} + 2\frac{\Delta t}{R_c}\right)}\left[(u\zeta)^n_{i+1,j} - (u\zeta)^n_{i-1,j} + (v\zeta)^n_{i,j+1} - (v\zeta)^n_{i,j-1}\right] + \frac{\frac{\Delta t}{R_c}}{\left(\frac{1}{2} + 2\frac{\Delta t}{R_c}\right)}\left[\zeta^n_{i+1,j} + \zeta^n_{i-1,j} + \zeta^n_{i,j+1} + \zeta^n_{i,j-1}\right] \qquad (6)$$

in the Dufort-Frankel form. Here Δt is the (nondimensional) time step, and the subscripts and superscripts refer to space and time coordinates, respectively:

$$\zeta^n_{i,j} \equiv \zeta(x_i, y_j, t_n)$$

The integrals of Equation (4) are approximated numerically by

$$u^n_{i,j} = -1 + \frac{1}{2\pi} \sum_{\substack{p \\ (p,q)\neq(i,j)}} \sum_{q} \frac{(y_q - y_j)\,\zeta^n_{p,q}}{(x_p - x_i)^2 + (y_q - y_j)^2} \tag{7a}$$

$$v^n_{i,j} = -\frac{1}{2\pi} \sum_{\substack{p \\ (p,q)\neq(i,j)}} \sum_{q} \frac{(x_p - x_i)\,\zeta^n_{p,q}}{(x_p - x_i)^2 + (y_q - y_j)^2} \tag{7b}$$

The summations need be taken only over those points having $\zeta^n_{p,q} \neq 0$. A square grid is used, and the cells are squares of unit width centered on the grid points as shown in Figure 11. The velocities are evaluated at the centers of the square cells.

Surface Pressure

The pressure on the cylinder surface is calculated from the Navier-Stokes equations, which in two dimensions and nondimensional form are

$$\frac{\partial u}{\partial t} + u\frac{\partial u}{\partial x} + v\frac{\partial u}{\partial y} = -\frac{1}{2}\frac{\partial p}{\partial x} + \frac{1}{R_c}\left(\frac{\partial^2 u}{\partial x^2} + \frac{\partial^2 u}{\partial y^2}\right) \tag{8a}$$

$$\frac{\partial v}{\partial t} + u\frac{\partial v}{\partial x} + v\frac{\partial v}{\partial y} = -\frac{1}{2}\frac{\partial p}{\partial y} + \frac{1}{R_c}\left(\frac{\partial^2 v}{\partial x^2} + \frac{\partial^2 v}{\partial y^2}\right) \tag{8b}$$

where the pressure is nondimensionalized with respect to the free stream dynamic pressure, $\frac{1}{2}\rho V_\infty^2$. Using the continuity equation and definition of vorticity, Equation (8) may be rewritten as

$$\frac{1}{2}\frac{\partial p}{\partial x} = -\frac{1}{R_c}\frac{\partial \zeta}{\partial y} - \frac{1}{2}\frac{\partial (u^2 + v^2)}{\partial x} + v\zeta - \frac{\partial u}{\partial t} \tag{9a}$$

$$\frac{1}{2}\frac{\partial p}{\partial y} = \frac{1}{R_c}\frac{\partial \zeta}{\partial x} - \frac{1}{2}\frac{\partial (u^2 + v^2)}{\partial y} - u\zeta - \frac{\partial v}{\partial t} \tag{9b}$$

The line integrals of Equation (9) in the x and y directions, respectively, are

$$p(x,y) - p(x_o,y) = 2\int_{x_o}^{x}\left(-\frac{1}{R_c}\frac{\partial \zeta}{\partial y} + v\zeta - \frac{\partial u}{\partial t}\right) dx$$

$$- [V^2(x,y) - V^2(x_o,y)] \tag{10a}$$

$$p(x,y) - p(x,y_o) = 2\int_{y_o}^{y}\left(\frac{1}{R_c}\frac{\partial \zeta}{\partial x} - u\zeta - \frac{\partial v}{\partial t}\right) dy$$

$$- [V^2(x,y) - V^2(x,y_o)] \tag{10b}$$

Equation (10a) applied between the forwardmost point of the cylinder and a point at an infinite distance upstream of the cylinder yields the stagnation point pressure coefficient:

$$(Cp)_s = p_s - p_\infty = 2\int_\infty^x \left(-\frac{1}{R_c}\frac{\partial \zeta}{\partial y} + v\zeta - \frac{\partial u}{\partial t}\right) dx + 1 \qquad (11)$$

This may be rewritten

$$(Cp)_s = 1 + \frac{2}{R_c}\frac{\partial}{\partial y}\int_x^\infty \zeta dx + 2\frac{\partial}{\partial t}\int_x^\infty u dx$$
$$- 2\int_x^\infty v\zeta dx \qquad (12)$$

Then with (x_{I_o}, y_{J_o}) for the coordinates of the stagnation point, the numerical approximation of Equation (12), using trapezoidal integration and central differences for both derivatives, is

$$(Cp)_s^n = 1 + \frac{1}{R_c}\left[\left(\frac{1}{2}\zeta^n_{I_o,J_o+1} + \sum_{i=I_o+1}^{\infty} \zeta^n_{i,J_o+1}\right) -\right.$$

$$\left. - \left(\frac{1}{2}\zeta^n_{I_o,J_o-1} + \sum_{i=I_o+1}^{\infty} \zeta^n_{i,J_o-1}\right)\right]$$

$$+ \left(\sum_{i=I_o+1}^{\infty} u^{n+1}_{i,J_o} - \sum_{i=I_o+1}^{\infty} u^{n-1}_{i,J_o}\right)$$

$$- 2\sum_{i=I_o+1}^{\infty} v^n_{i,J_o}\,\zeta^n_{i,J_o} \qquad (13)$$

Here the summations involving vorticity extend only as far upstream as the extent of non-zero vorticity. The summation

over the x-velocity extends sufficiently beyond the region of non-zero vorticity for the velocity to be negligibly different from the undisturbed value of -1.

The pressure coefficient around the surface of the cylinder is calculated from Equation (10) applied around the layer of boundary cells,* with the velocity taken as zero in the boundary cells. Again using trapezoidal integration, with one-sided differences for the derivatives, these become, in the first quadrant,

$$C_{p_{i,j}} = C_{p_{i+1,j}} + \frac{1}{R_c}(\zeta_{i,j+1} + \zeta_{i+1,j+1} - \zeta_{i,j} - \zeta_{i+1,j}) \quad (14a)$$

$$C_{p_{i,j}} = C_{p_{i,j-1}} + \frac{1}{R_c}(\zeta_{i+1,j} + \zeta_{i+1,j-1} - \zeta_{i,j} - \zeta_{i,j-1}) \quad (14b)$$

with similar expressions in the other quadrants. Here the first two vorticity values in the parentheses are values in the layer of cells adjacent to the boundary cells, and the last two values are those in the boundary cells. The procedure is similar in the other quadrants.

Drag Coefficients

The pressure drag coefficient is calculated from the pressure coefficient according to the expression

$$C_{D_p} = \frac{1}{D} \oint C_p \, dy \quad (15)$$

---

*Boundary cells are defined in Chapter II.

where D is the cylinder diameter, $\underset{\sim}{n}$ is the unit outward normal to the surface, and the integral is taken around the cylinder surface. This is approximated numerically by the summation

$$C_{D_p} = \frac{1}{D} \sum_m C_{p_m} A_{p_m} \tag{16}$$

where the summation is over all the boundary cells, and A_p is the y-projection of the portion of the surface curve lying in each boundary cell, the rear boundary cells having negative values (Figure 12). The friction drag coefficient is calculated according to

$$C_{D_f} = \frac{1}{D} \oint \frac{2}{R_c} \zeta dx \tag{17}$$

which is approximated numerically as

$$C_{D_f} = \frac{2}{DR_c} \sum_m \zeta_m A_{f_m} \tag{18}$$

with A_f the x-projection of the portion of the surface curve contained in each boundary cell as is indicated in Figure 12 as well.

Computation Procedure*

At each time step new values of the vorticity are

---

*Reference to Equation (6) assumes the use of the Dufort-Frankel form. In the straight explicit form, Equation (6) is replaced by Equation (5).

calculated for each vortex cell* and each border cell* from Equation (6). In this equation the vorticity is taken as zero at all points not corresponding to vortex cells. If the sum of the magnitude of the vorticity calculated for a border cell and that of any adjacent vortex cell is greater than the specified minimum vorticity, ω_m, then the border cell is reclassified as a vortex cell. Otherwise the vorticity calculated for the border cell is distributed evenly among the adjacent vortex cells, so that no vorticity is ever simply discarded.

The current set of vortex cells, including those added at the current time step, is then cataloged and a new set of border cells surrounding the aggregate† of vortex cells is created. Finally, the velocity components are calculated for each vortex cell from Equation (7), with the summation being taken only over those vortex cells within a prescribed range, r_m, of the cell in question. This process is repeated at each succeeding time step for the duration of the calculations.

Initial Conditions

The cells through which the curve defining the surface of the cylinder passes, designated as boundary cells,

---

*Vortex cells and border cells are defined in Chapter II.

†The aggregate of vortex cells is defined in Chapter II.

are the only cells having non-zero vorticity at the start and, therefore, constitute the initial aggregate of vortex cells (Figure 12). The initial vorticity in each of these cells is calculated from the relation between circulation and vorticity:

$$\Gamma = \oint \underset{\sim}{v} \cdot d\underset{\sim}{l} = \int \underset{\sim}{\omega} \cdot d\underset{\sim}{S}$$

Since initially the irrotational potential velocity solution prevails, the initial circulation and also the initial vorticity (the cell area being unity) of each boundary cell is equal to the line integral of the potential velocity over that portion of the cylinder surface curve that lies within the cell (Figure 12). Equation (7) would then reproduce, at the start, the potential velocity solution, to within the error involved in the discretization, at all points exterior to the cylinder, the summation being taken over the boundary cells.

The fact that a portion of each boundary cell lies within the cylinder might seem somewhat unreal. However, the definition of cells containing vorticity is merely a device used to represent the integrals of Equation (4) numerically. In the strictest sense neither this solution nor any other numerical solution is meant to represent the flow field on a scale smaller than the mesh size. The precise placement of the cells is, therefore, not particularly important as long as the boundary conditions can be adapted to the particular

placement used and are well represented. The current scheme was chosen in preference to alternatives that would place initial vorticity in cells lying entirely in regions actually having no vorticity at the start, i.e., not containing any of the surface curve so that the surface vorticity is not confined well enough to the surface region.

Boundary Conditions

By far the greatest problem in applying the present scheme, based as it is on a rectangular coordinate system, to the flow about curved solid bodies is the proper representation of the boundary conditions. The normal component of the velocity on the boundary, as well as the tangential component, is a problem here, since the usual device of specifying a constant stream function on the boundary as a boundary condition, and thereby guaranteeing a zero normal component, is not available. It should be emphasized again that vorticity images in the boundary are not employed in the present solution and are therefore not available for guaranteeing a zero normal velocity component.

The representation of the boundary conditions is then even more critical in the present integro-differential approach, for since the velocity is calculated from an integral over the vorticity distribution throughout the entire field, the velocity boundary conditions are entirely implicit, i.e., neither the normal nor the tangential velocity component can be forced to be zero on the boundary; the vorticity

distribution must be such as to produce zero values of velocity on the boundary through the integrals of Equation (4). The vorticity in the fluid adjacent to the boundary, i.e., in the boundary cells, is especially critical to the maintenance of zero normal velocity on the boundary, since these cells contain the highest vorticity in the field and that most recently generated at the boundary. It is in these cells, however, that the convection and diffusion are most difficult to represent with this rectangular approximation to a curved boundary. A total of fifteen different boundary treatments were evaluated in the present study, and the results are discussed in Appendix E where the reasons for the scheme chosen are given.

Results and Comparisons with Other Numerical Solutions*

Survey of Other Numerical Solutions

The two-dimensional flow about a circular cylinder has been the subject of much numerical effort in the past several years [24-35]. (Two of these references are recalculations using older solutions: [31] uses the older solution of Kawaguti [35], and [34] uses the solution of Payne [25].) Most of the solutions presented are very similar in basic

*The convergence of the solution and the effects of the various parameters involved are discussed in Appendix F.

numerical approach but differ in regard to the type of matrix solution employed, the treatment of boundary conditions, the method of drag calculation, and other such details. All of the recent solutions, both steady and time-dependent, are formulated using an expanding circular grid, so that the radial mesh size decreases as the surface of the cylinder is approached. Only one solution {30} differs at all from this grid structure, through the joining of the expanding circular grid with a rectangular grid at large radius. All except one {34} use the stream function and vorticity as dependent variables, the exception replacing the stream function with the velocity components. Most solutions also use the non-conservative form of the vorticity equation with central differences. The conservative form is used in two solutions, however, in one case with central differences {34} and in one case with streamwise one-sided differences {30}.

Of the time-dependent solutions, only that of Dey {24} and that of Son and Hanratty {33} are implicit in time. The latter, however, is not completely implicit, because the stream function and vorticity are evaluated by separate matrix solutions, rather than simultaneously. This means that the calculation of the vorticity at the current time step involves the values of the stream function at the previous time step, not the current values. This solution also assumes symmetry about the center line. Dey's solution,

which employs an optimized acceleration of the convergence of the matrix iterative solution for both the vorticity and the stream function developed and applied in rectangular coordinates by the present author {23}, is completely implicit. Here, as in the present author's solution for the flow about rectangular bodies, the vorticity at the current time step at each point depends on the adjacent values of both the vorticity and the stream function at the current time step. Similarly the stream function at the current time step at each point depends on the adjacent values of the stream function and the coincident value of the vorticity, both at the current time step.

That the completely implicit time-dependent solution approaches more closely the solution of the nonlinear differential equations is evidenced by the fact that none of the explicit solutions has been able to achieve vortex shedding without forcing the shedding to start by external perturbation. This is the case for the explicit solution of Fromm {21} for the flow about a rectangular body as well. However, in the completely implicit solution of Dey for the circular cylinder, and in that of the present author for rectangular bodies, shedding begins and the vortex street is formed without the necessity of external disturbance of the solution. This is most likely due to the fact that the difference equation representation of the nonlinearity of the differential equation is superior in the completely implicit solution,

since there the nonlinear terms are evaluated at the current time step, rather than at the previous step as in the explicit methods. The formation of the vortices and subsequent shedding and vortex street creation are all effects of the nonlinear terms, since these phenomena disappear when the linear terms dominate at low Reynolds number, and therefore would be expected to reflect the accuracy with which the nonlinearity of the differential equation is represented in the difference equation. It is probably for this reason that explicit methods must be perturbed to shed.

Surface Pressure and Drag Coefficients

Results of Other Solutions. Drag determinations have been made in most solutions by calculating the surface pressures from the line integral of the Navier-Stokes equations, the exceptions making the determination from the Blasius drag equation applied around a circuit enclosing the cylinder {28} or from momentum considerations {34}. Three solutions {27, 28, 31} employ an extrapolation to infinite outer boundary in an attempt to remove the "wall" effect on the drag coefficient introduced by the necessity of using a finite field of calculation. The results of the various solutions are compared in Figure 13, which includes also experimental data and the results of the present solution. The values given here for the time-dependent solutions are taken at supposedly large enough times for the change in time to be negligible.

Since the surface pressure is dependent on the derivative of vorticity normal to the surface, the accuracy of the surface pressure is no better than that with which the boundary layer is represented by the solution. It is possible for a numerical solution to give a quite good representation of the large-scale phenomena of the wake, including the vortex shedding and street formation, and still give very inaccurate surface pressure and drag because of poor representation of the small-scale details of the boundary layer. For this reason the drag predicted by all numerical solutions at a fixed radial mesh size becomes less accurate as the Reynolds number* increases and the boundary layer thickness decreases.

This tendency is exhibited in Figure 13a by all the solutions given in which a constant radial mesh size was used. (The field size and the ratio of mesh size at the cylinder surface to the cylinder radius are given for each solution in Table 1.) Also in two solutions in which the mesh size was reduced as the Reynolds number increased {27, 33}, the reduction was insufficient and the points again fall below the experimental curve at the higher Reynolds numbers in Figure 13a.

The only solution to maintain accuracy in the surface pressure, and hence drag, at Reynolds number above 60 is that

---

*Throughout this chapter the Reynolds number referred to is the cylinder Reynolds number based on the cylinder diameter.

of Thoman and Szewczyk {30}, in which the mesh size was set at a certain fraction of the steady-state boundary layer thickness at the forward stagnation point, as predicted by boundary layer theory, at each Reynolds number. This relating of the mesh size to the expected boundary layer thickness allowed successful drag prediction even at Reynolds number of 40,000, but required an extremely small mesh at such values, of course.

Hamielec and Raal {27} show a strong effect of the extent of the field, the drag coefficient tending to decrease as the radius of the outer boundary, where the flow is taken as uniform, increases. The drag coefficients given in Figure 13a for Reynolds numbers of 50 and 100 from this solution were obtained with significantly smaller computational fields than those used for Reynolds numbers of 30 and below. (The field for Reynolds number of 30 was five times as large.) Even with the extrapolation employed, the values at these two highest Reynolds numbers lie above the curve established by their values for Reynolds number of 30 and below. It is probable then that the values presented for Reynolds numbers of 50 and 100 are too high, and that lower values would have been obtained had the field been larger. The agreement of the point at Reynolds number of 50 with the experimental curve in Figure 13a thus is deceptive, for both it and the point at Reynolds number of 100 should probably be lower,

conforming to the trend of the points for Reynolds number of 30 and below.

In the solution of Takami and Keller {28} a semi-empirical asymptotic formula relating the stream function and the vorticity on the outer boundary to the drag coefficient is used in an iterative procedure to provide boundary conditions for these dependent variables on the outer boundary. This results in much less variation with the position of the outer boundary, but the variation that does remain is somewhat erratic. Furthermore, with this device the accuracy of the solution is dependent on the validity of the asymptotic formula, which, of course, varies with the Reynolds number. The evaluation of the drag from the Blasius contour integral used in this solution leads to variations with the contour chosen, which tend to increase and become erratic as the Reynolds number or the mesh size increases. Here also a much smaller field was used at the higher Reynolds numbers (30-60). The drag coefficient, however, is shown to decrease as the outer boundary recedes at higher Reynolds number, the rate of decrease increasing with the Reynolds number. This fact, together with the somewhat erratic positioning of the points for this solution in Figure 13a, suggests that the drag given at Reynolds number of 30 and above, where only one value of the outer radius was considered, may be too high as a result of wall effect.

The very small field used by Takaisi {31} gave apparent agreement with the experimental curve. However, in view of the findings of the above authors in regard to the effect of field size, Takaisi's results would probably have been lower had a larger field been used.

The field size used by Thoman and Szewczyk {30} was comparable to that used in the above two solutions at the higher Reynolds numbers, but the mesh size was considerably smaller. Their drag results thus could also be a bit high due to wall effect but, even allowing for such error, the improvement with the smaller mesh size is apparent.

Jain and Rao {29} used a field larger by an order of magnitude, but terminated their calculations at a much earlier time at Reynolds number of 200. Their true value of drag at this Reynolds number thus would be expected to be lower than indicated. The earlier work of Kawaguti and Jain {32}, which differs from that cited immediately above only by the imposition of symmetry about the center line, was terminated at even earlier times.

The solution of Son and Hanratty {33}, for which both the field size and the final time were adequate, probably shows the truest trend in the absence of wall effect and transient effects of all these solutions at the higher Reynolds numbersfor the mesh sizes used. It thus appears that a cell Reynolds number (based on the mesh width at the

cylinder surface) of about 3 is the maximum for which accurate calculation of surface pressure and drag can be obtained.

In summary, at the low Reynolds numbers, when the boundary layer is thick, all the solutions agree quite closely with each other and with the experimental curve. What variation there is is within the range caused by differences in time-step and time of evaluation in the time-dependent cases and differences in the treatment of the boundary at infinity in all cases. At higher Reynolds numbers, however, it is necessary to reduce the mesh size considerably, or else all solutions predict drag that is too low. This is evident from the results actually given in Figure 13a for the various solutions, but would be evident to an even greater extent were the effects of too small a field and insufficient approach to the steady-state removed.

Present Results.* The agreement of the present results in Figure 13 with the pressure, friction, and total drag coefficients predicted by other numerical solutions and by experimental results is good for Reynolds numbers less than 10, corresponding to a cell Reynolds number of 0.833 for the cell size used. Table 1 shows the cell Reynolds numbers (based on the mesh size at the cylinder surface for expanding grids) used in the other numerical solutions cited to be

---

*The parameters used in all the results presented in each figure are given in Table 4.

comparable to this value in most cases. Except for the solution of Jain and Rao {29} the cell Reynolds numbers used were about five or less. In the present case the angularity of the boundary requires a somewhat smaller cell Reynolds number for accuracy.

The above-mentioned Reynolds number effects are more pronounced in the present solution because of the angular representation of the curved boundary of the cylinder. (This angularity of the boundary is, of course, not inherent in the integro-differential formulation but resulted from the desire to use cartesian coordinates throughout.) Better accuracy at the higher Reynolds numbers could, of course, be obtained in the present case with a smaller cell size, as is illustrated in the time development results cited below. The excessive computer time required, however, was not justifiable, since the purpose of consideration of the circular cylinder was only to verify the numerical approach and not to analyze the cylinder itself. The results obtained demonstrate that the drag prediction of the present method is accurate for a cell Reynolds number of unity or less even with the rectangular representation of the circular boundary.

The time development of the pressure and friction drag coefficients of the present solution is shown in Figure 14. With the larger cell size the initial development is much more rapid than that of other solutions because of the

angularity of the boundary. With the smaller cell size, however, the initial fall of the pressure coefficient to a minimum and the subsequent rise are in agreement with the prediction of Thoman and Szewczyk {30}, who show the minimum at Reynolds number 200 to be reached at about time t = 13, and that of Ingham {34}, who gives the minimum at about time t = 11 for Reynolds number 100. The angularity of the boundary is much reduced at the smaller step size given here, and the details of the viscous layer at the surface are much better represented as a result. The effect on the friction drag coefficient is much less pronounced, since it depends on the value of the vorticity rather than the derivative thereof.

The surface pressure distribution is compared with that predicted by other solutions and with experimental values in Figure 15. The large kinks in the curve at the very low Reynolds number of 2 are a result of the large truncation error in the Laplacian at such a Reynolds number. The same effect causes the friction drag to be a bit high (Figure 13c). Considering the angularity of the boundary used, the general shape and level of the curves show satisfactory agreement at the lower Reynolds numbers with the predictions of solutions using cylindrical coordinates. From Figure 15b, the tendency of the pressure decrease on the forward portion of the cylinder predicted by numerical results to be less rapid than that observed experimentally is shared by other solutions as well.

Length of Standing Vortices

Results of Other Solutions. The results of the various solutions for the length of the vortices behind the cylinder are compared in Figure 16 with the results of the present solution and with experimental data. The length of the standing vortices behind the cylinder is even more dependent on the field size than is the drag. The prediction of Takami and Keller {28} is probably too short as a result of too small a field. (The experimental prediction of Taneda {63} is also influenced by wall effect, of course.) The length predicted by the time-dependent solution of Kawaguti and Jain {32} approaches the steady-state prediction of Hamielec and Raal {27} at Reynolds number of 30, the fields being large in both solutions. The close approach of the solution of Thoman and Szewczyk {30}, with a smaller field, to these solutions is probably the tendency of the streamwise differencing used in the former to lengthen the vortices. This is also suggested by the fact that this solution is later in leveling off than that of Kawaguti and Jain. The solution of Jain and Rao {29} and that of Son and Hanratty {33}, all approach a value above that predicted by Takami and Keller. A comparison of these with results of the present solution is given below.

Present Results. (The aft extent of the standing vortices was determined in the present solution by locating

on the centerline the point on either side of which the velocity vectors were oppositely directed.) The present solution gives a better prediction of the length of the vortices than it does for the drag at higher Reynolds numbers because the former is a result of much larger scale phenomena and not as dependent on conditions at the surface. The present results for Reynolds number of 36 agree with the results of other numerical solutions and appear to approach closely the steady-state experimental values which are also given for comparison in Figure 16.

Development of Vortex Street

Cylinder Only. The development of a vortex street behind the circular cylinder is shown in Figure 17.* The flow was perturbed at T = 10.67 and again at T = 12.00, the vorticity on the centerline behind the cylinder being increased in magnitude by a factor of 100 in each instance. At the first perturbation the vorticity on the centerline was so near zero that the perturbation had little visible effect on the flow pattern (Figure 17b). However, it did serve to cause the vorticity on the centerline to begin to increase, so that the second perturbation was effective (Figure 17c) and caused the shedding to begin.

---

*The scale factors for the vector plots are given in Table 5. The magnitude of a vector is indicated by the length of the stem of the arrow, the size of the arrowheads being the same throughout. Spurious lines on the plots are the result of plotter error.

The first vortex is shed from the top at T = 14.67 and rapidly disappears after that time (Figures 17d-17g). Meanwhile, the bottom vortex grows and moves rearward, and a new vortex is formed at the top (Figure 17h). This new vortex then grows and moves rearward, and the bottom vortex is shed at T = 20.67 (Figure 17l).

The pressure coefficients at the points 0° and 90° from the negative of the free stream direction on the cylinder and the pressure drag are given in Figure 18. Here the vortex shedding is evident from the waveforms assumed, especially at the 90° point. The peaks of the wave (both upper and lower) correspond to the moment of shedding. Shedding from the top is thus accompanied by an increase in the pressure at the top of the cylinder, while shedding from the bottom results in a decrease in pressure at the top of the cylinder.

The effect of the perturbation was to launch the flow rather abruptly into the shedding mode, and the pressure waveform at the 90° point is quite well formed from the moment of its sudden appearance after the second perturbation. The pressure at the 0° point requires more time to assume its final waveform, since the flow at this point is little influenced by the flow behind the cylinder until the street becomes more developed. The drag also has not assumed its final form, but does exhibit the increase to be expected upon formation of the street.

An unperturbed case was also run as a control and the results are given by the dashed lines in Figure 18. It is clear that the shedding was not about to start without the perturbation.

The Strouhal number calculated from the shedding frequency as indicated by the pressure at the 90° point is 0.17 which, for this cylinder Reynolds number of 120, agrees well with experimental results {67, Chapter 2}.

The shed vortices, and hence the developing vortex street, are visible behind the cylinder when the velocity vectors are plotted in a coordinate system moving with the velocity of the vortices (83% of the remote fluid velocity {23}) as shown in Figure 19.

Cylinder with Splitter Plate. The wake development with a splitter plate, of length two cylinder diameters, extending from the rear of the cylinder is shown in Figure 20. Here perturbations of the same type discussed above were introduced at T = 9.67 and T = 11.33. The disordered flow resulting from these perturbations is evident in Figures 20f and 20h. However, in both instances the flow recovers and assumes its standing vortex form, with no tendency to shed.

The lack of shedding is evident also in the pressure and drag coefficients given in Figure 21 and compared with the results without the splitter plate. The disturbances introduced by the perturbations are evident but are smoothed

in time, and a steady state is being approached.

The fact that the drag with the splitter plate is larger than that without from the beginning is a numerical effect and has no physical meaning. As shown in Figure 13a the drag predicted by the solution with the cell size employed is too low at this high a cylinder Reynolds number, as a result of the inadequate representation of the thin boundary layer. The splitter plate, however, causes the boundary layer to thicken in the region near the 180° point on the cylinder. Therefore the ratio of cell size to boundary layer thickness is decreased in this region, and the normal gradient of the vorticity, and hence the pressure, are better represented in this region with the splitter plate than without. This results in lower pressures in the rear of the cylinder with the splitter plate and hence larger drag. (The pressures in the rear of the cylinder both with and without the splitter plate are too high as a result of the large cell size/boundary layer thickness ratio.) The point then is that with the splitter plate the drag coefficient is calculated more accurately and hence is increased relative to the value calculated without the splitter plate. In both cases the drag is still too low at this Reynolds number with this cell size.

CHAPTER V

NUMERICAL SOLUTION FOR THE INFINITE JET IN CROSS-WIND

In this chapter the numerical method is applied to the time-dependent, two-dimensional infinite jet in cross-wind. This is a two-dimensional problem in the sense of there being a direction of invariance (along the jet axis). There are, however, three variable components of both the velocity and the vorticity. This problem represents the flow field infinitely above the jet exit when the flow is started from the dissolution of a hypothetical pipe separating an interior uniform jet flow from an exterior potential cross-flow as discussed in Chapter II. It may be visualized at the start as an infinitely long column of vertically moving fluid surrounded by a cross-flow normal to the axis of the column (Figure 4). As time passes the discontinuity is dissipated and the column is swept backward, mixing with the cross-flow, so that the vertical velocity is spread out and eventually reduced to zero.

This solution was developed to provide a sub-solution for use in developing the three-dimensional solution for the jet in cross-wind starting from a cylindrical discontinuity in Chapter VI. However, the solution proved to be of considerable interest in itself, revealing a nonlinear

instability arising from a coupling of the vertical velocity and the horizontal vorticity. This instability is discussed in detail in a later section.

Numerical Formulation

Vorticity-Velocity Solution

The flow of an unbounded cross-wind about an infinite jet with its axis perpendicular to the cross-wind is governed by the same vector equations of motion given in connection with the problem of the two-dimensional cylinder (Chapter II):

$$\frac{\partial \underset{\sim}{\omega}}{\partial t} = \underset{\sim}{\nabla} \times (\underset{\sim}{v} \times \underset{\sim}{\omega}) + \nu \nabla^2 \underset{\sim}{\omega} \tag{1}$$

$$\underset{\sim}{v} = \underset{\sim}{V}_{\infty} + \frac{1}{2\pi} \iint \frac{(\underset{\sim}{r}' - \underset{\sim}{r})}{|\underset{\sim}{r}' - \underset{\sim}{r}|^2} \times \underset{\sim}{\omega}(\underset{\sim}{r}') \, dS \tag{2}$$

but with the surface integral now extending over the entire field, there being no boundaries.

This flow is two-dimensional in the sense that there are no variations in one direction. The velocity in that direction, however, is not zero and varies in both time and the other two space directions. Physically this solution represents the smoothing out of the cylindrical discontinuity between a flow inside an infinite cylinder, parallel to its axis (with constant velocity across the cylinder), and the two-dimensional potential flow of an unbounded cross-wind about the cylinder, perpendicular to its axis. There are

thus no boundary conditions involved, the conditions at infinity being contained implicitly in the integro-differential formulation.

Again with non-dimensionalization with respect to the cross-wind velocity and the cell size, Equations (1) and (2) become, for the coordinate system shown in Figure 22,

$$\frac{\partial \xi}{\partial t} = \frac{\partial}{\partial y}(u\eta - v\xi) + \frac{1}{R_c}\left(\frac{\partial^2 \xi}{\partial x^2} + \frac{\partial^2 \xi}{\partial y^2}\right) \tag{3a}*$$

$$\frac{\partial \eta}{\partial t} = -\frac{\partial}{\partial x}(u\eta - v\xi) + \frac{1}{R_c}\left(\frac{\partial^2 \eta}{\partial x^2} + \frac{\partial^2 \eta}{\partial y^2}\right) \tag{3b}$$

$$\frac{\partial \zeta}{\partial t} = \frac{\partial}{\partial x}(w\xi - u\zeta) - \frac{\partial}{\partial y}(v\zeta - w\eta) + \frac{1}{R_c}\left(\frac{\partial^2 \zeta}{\partial x^2} + \frac{\partial^2 \zeta}{\partial y^2}\right) \tag{3c}$$

and

$$u = -1 + \frac{1}{2\pi}\iint \frac{(y' - y)\,\zeta(x', y')}{(x' - x)^2 + (y' - y)^2}\,dx'\,dy' \tag{4a}$$

$$v = -\frac{1}{2\pi}\iint \frac{(x' - x)\,\zeta(x', y')}{(x' - x)^2 + (y' - y)^2}\,dx'\,dy' \tag{4b}$$

$$w = \frac{1}{2\pi}\iint \frac{(x' - x)\eta(x', y') - (y' - y)\xi(x', y')}{(x' - x)^2 + (y' - y)^2}\,dx'\,dy' \tag{4c}$$

---

*Hereafter all quantities in this chapter are nondimensionalized as noted in the Nomenclature.

All quantities in these equations are dimensionless, and the cell Reynolds number is based on the cross-wind velocity:

$$R_c = \frac{V_c h}{\nu}.$$

With the space derivatives replaced by three-point central differences and the time derivative by a two-point forward difference, Equations (3) are approximated (Appendix D) by the difference equations,

$$\xi^{n+1}_{i,j} = (1 - \frac{4\Delta t}{R_c})\xi^n_{i,j} + \frac{\Delta t}{2}[(u\eta - v\xi)^n_{i,j+1} - (u\eta - v\xi)^n_{i,j-1}]$$

$$+ \frac{\Delta t}{R_c}[\xi^n_{i+1,j} + \xi^n_{i-1,j} + \xi^n_{i,j+1} + \xi^n_{i,j-1}] \qquad (5a)$$

$$\eta^{n+1}_{i,j} = (1 - \frac{4\Delta t}{R_c})\eta^n_{i,j} - \frac{\Delta t}{2}[(u\eta - v\xi)^n_{i+1,j} - (u\eta - v\xi)^n_{i-1,j}]$$

$$+ \frac{\Delta t}{R_c}[\eta^n_{i+1,j} + \eta^n_{i-1,j} + \eta^n_{i,j+1} + \eta^n_{i,j-1}] \qquad (5b)$$

$$\zeta^{n+1}_{i,j} = (1 - \frac{4\Delta t}{R_c})\zeta^n_{i,j} + \frac{\Delta t}{2}[(w\xi - u\zeta)^n_{i+1,j} - (w\xi - u\zeta)^n_{i-1,j}$$

$$- (v\zeta - w\eta)^n_{i,j+1} + (v\zeta - w\eta)^n_{i,j-1}]$$

$$+ \frac{\Delta t}{R_c}[\zeta^n_{i+1,j} + \zeta^n_{i-1,j} + \zeta^n_{i,j+1} + \zeta^n_{i,j-1}] \qquad (5c)$$

in the straight explicit form, or by the difference equations,

$$\xi_{i,j}^{n+1} = \left(\frac{\frac{1}{2} - 2\frac{\Delta t}{R_c}}{\frac{1}{2} + 2\frac{\Delta t}{R_c}}\right)\xi_{i,j}^{n-1} + \frac{\frac{\Delta t}{2}}{(\frac{1}{2} + 2\frac{\Delta t}{R_c})}[(u\eta - v\xi)_{i,j+1}^{n} - (u\eta - v\xi)_{i,j-1}^{n}]$$

$$+ \frac{\frac{\Delta t}{R_c}}{(\frac{1}{2} + 2\frac{\Delta t}{R_c})}[\xi_{i+1,j}^{n} + \xi_{i-1,j}^{n} + \xi_{i,j+1}^{n} + \xi_{i,j-1}^{n}] \qquad (6a)$$

$$\eta_{i,j}^{n+1} = \left(\frac{\frac{1}{2} - 2\frac{\Delta t}{R_c}}{\frac{1}{2} + 2\frac{\Delta t}{R_c}}\right)\eta_{i,j}^{n-1} - \frac{\frac{\Delta t}{2}}{(\frac{1}{2} + 2\frac{\Delta t}{R_c})}[(u\eta - v\xi)_{i+1,j}^{n} - (u\eta - v\xi)_{i-1,j}^{n}]$$

$$+ \frac{\frac{\Delta t}{R_c}}{(\frac{1}{2} + 2\frac{\Delta t}{R_c})}[\eta_{i+1,j}^{n} + \eta_{i-1,j}^{n} + \eta_{i,j+1}^{n} + \eta_{i,j-1}^{n}] \qquad (6b)$$

$$\zeta_{i,j}^{n+1} = \left(\frac{\frac{1}{2} - 2\frac{\Delta t}{R_c}}{\frac{1}{2} + 2\frac{\Delta t}{R_c}}\right)\zeta_{i,j}^{n-1} + \frac{\frac{\Delta t}{2}}{(\frac{1}{2} + 2\frac{\Delta t}{R_c})}[(w\xi - u\zeta)_{i+1,j}^{n} - (w\xi - u\zeta)_{i-1,j}^{n} - (v\zeta - w\eta)_{i,j+1}^{n} + (v\zeta - w\eta)_{i,j-1}^{n}]$$

$$+ \frac{\frac{\Delta t}{R_c}}{(\frac{1}{2} + 2\frac{\Delta t}{R_c})}[\zeta_{i+1,j}^{n} + \zeta_{i-1,j}^{n} + \zeta_{i,j+1}^{n} + \zeta_{i,j-1}^{n}] \qquad (6c)$$

in the Dufort-Frankel form. Here Δt is the (nondimensional)

time step, and the subscripts and superscripts refer to the space and time coordinates, respectively: $\zeta^n_{i,j} \equiv \zeta(x_i, y_j, t_n)$, etc.

The integrals of Equation (4) are approximated numerically by

$$u^n_{i,j} = -1 + \frac{1}{2\pi} \sum_{\substack{p \\ (p,q)\neq(i,j)}} \sum_{q} \frac{(y_q - y_j)\zeta^n_{p,q}}{(x_p - x_i)^2 + (y_q - y_j)^2} \tag{7a}$$

$$v^n_{i,j} = -\frac{1}{2\pi} \sum_{\substack{p \\ (p,q)\neq(i,j)}} \sum_{q} \frac{(x_p - x_i)\zeta^n_{p,q}}{(x_p - x_i)^2 + (y_q - y_j)^2} \tag{7b}$$

$$w^n_{i,j} = \frac{1}{2\pi} \sum_{\substack{p \\ (p,q)\neq(i,j)}} \sum_{q} \frac{(x_p - x_i)\eta^n_{p,q} - (y_q - y_j)\xi^n_{p,q}}{(x_p - x_i)^2 + (y_q - y_j)^2} \tag{7c}$$

The summations extend over all points having non-zero vorticity. The square grid and cell configuration are the same as those used in the two-dimensional cylinder solution and are shown in Figure 11. Again the velocities are evaluated at the center of each cell.

Computation Procedure

The computation procedure is the same as that described in Chapter IV for the two-dimensional cylinder, except that no solid surface vortices are involved in this application.

Both of the two criteria discussed in Chapter II for the creation of a new vortex cell* from a border cell*—(1) the magnitude of the vorticity calculated for a border cell exceeding the specified minimum vorticity, ω_m, and (2) the sum of the magnitude of the vorticity calculated for a border cell and that of any adjacent vortex cell exceeding the specified minimum vorticity, ω_m—were evaluated and found to be only negligibly different at the practical total times and time steps actually used. In the one-dimensional results of Chapter II, however, the second of these criteria was superior at very long times or very small time steps. Since the velocity in the one-dimensional solution is calculated from a line integral, the vorticity of each cell in that case represents an infinite plane of vorticity. However, the vorticity of a cell in the two-dimensional solution represents only an infinite column of vorticity, and in three dimensions a cell represents only a finite cube of vorticity. Therefore, the spacial averaging of vorticity accomplished by the distinction between vortex and border cells is progressively less critical in two and three dimensions, and the two minimum vorticity schemes discussed above are progressively less different. Some latitude may be taken, therefore, in the choice of scheme to be used.

---

*Vortex cells and border cells are defined in Chapter II.

Initial Conditions

Only those cells through which the curve defining the initial discontinuity between the jet and cross-wind passes have non-zero vorticity at the start. This initial aggregate* of vortex cells is set up exactly as described in Chapter IV for the two-dimensional cylinder, these initial cells being the same as the "boundary cells" in that case (Figure 12). The initial value of the z-component of vorticity in these cells is the same as that calculated for the two dimensional cylinder.

The initial values of the x and y components of vorticity are also determined from the circulation, but an additional consideration is necessary because of the variation of vorticity in these directions. The volume integral of Equation (II-16), from which the integral of Equation (2) was obtained by integration over the z-direction, would be represented numerically by a summation over cubes of unit width, just as the surface integral is represented by a summation over squares of unit width. If the product of the vorticity, $\underset{\sim}{\omega}$, in a unit cube and the volume of the cube, unity, is to represent the effect of a portion of length, $\underset{\sim}{1}$, of a vortex line of circulation, Γ, (as should be the case from the Biot-Savart relation {73, Chapter 18}) then the

---

*The aggregate of vortex cells is defined in Chapter II.

relation $(\underset{\sim}{\omega})\ (1) = (\Gamma)\ (\underset{\sim}{1})$ must hold. The components of vorticity then are $\xi = \Gamma\ \underset{\sim}{i} \cdot \underset{\sim}{1}$ and $\eta = \Gamma\ \underset{\sim}{j} \cdot \underset{\sim}{1}$. This calculation is illustrated in Figure 23. The circulation is the line integral of the velocity around the circuit shown and is thus equal to the z-component of the velocity, the cell width being unity. The x and y components of vorticity in the initial cells thus are equal to the product of the jet velocity and the projections in the x and y directions, respectively, of the portion of the discontinuity curve contained in each cell.

Equation (7) would then reproduce, at the start, the potential solution for the flow about the cylindrical discontinuity curve for the x and y velocity components, and the jet velocity for the z-component within the discontinuity curve, with zero z-component elsewhere. This is to within the limit of the discretization, of course, and is shown in Figure 24.*

The lack of boundaries eliminates the problems encountered in the two-dimensional cylinder solution in relation to the representation of a curved boundary by rectangular segments. Here the initial discontinuity curve is so represented, but this introduces only some perturbation at the

---

*The scale factors for the vector plots are given in Table 5. The magnitude of a vector is indicated by the length of the stem of the arrow, the size of the arrowheads being the same throughout. Spurious lines on the plots are the result of plotter error.

start, since the discontinuity is smoothed out as time passes. All cells contain fluid exclusively in this application.

Stability

As shown in Appendix G the stability requirements, based on a linearized stability analysis of Equations (5) and (6), are

(a) straight explicit:

$$\Delta t \leq \frac{2}{R_c}\sqrt{\frac{4}{R_c^2} - 1} \text{ if } R_c \leq 2$$

$$\Delta t \leq \frac{2}{R_c} \text{ if } R_c \geq 2 \tag{8}$$

(b) Dufort-Frankel:

All Δt if $R_c \leq 2$

$$\Delta t \leq \frac{R_c}{2\sqrt{R_c^2 - 4}} \text{ if } R_c \geq 2 \tag{9}$$

These limits are shown in Figures 25 and 26, respectively, for a comparison with the results of computer experimentation. The determination of stability or instability was made in most cases from observation of the velocity vector plots. Other determinations were based on whether or not the vorticity components were amplified in time. Borderline cases in which no definite determination could be made are indicated.

Straight Explicit Formulation

Referring to Figure 25, for cell Reynolds number below 1.5 the actual stability of the nonlinear straight explicit algorithm follows very closely the linearized prediction of Equation (8). The boundary of the stable region is sharp in this range of Reynolds numbers,* as illustrated by the velocity vector plots at the same Reynolds number but different time steps in Figure 27.† Comparison of Figure 27b and Fugure 78a gives an even sharper definition of the boundary, the time steps here being the same but with different Reynolds numbers. The stability boundary becomes less distinct as the Reynolds number increases. The high peak in the stable region predicted by the linearized analysis is not attained, but the actual stable region does exhibit a lower and more broad maximum around a Reynolds number of 3.25 and extends above the linearized boundary. The stability boundary becomes very indistinct, approaches and possibly falls below the linearized prediction as the Reynolds number increases further.

The early disorder evident in Figure 28 is due to a nonlinear instability resulting from a coupling between the

---

*Throughout this chapter the Reynolds number referred to is the cell Reynolds number based on the cell width and the cross-wind velocity.

†Parameters used in all results presented are given in Table 4.

vertical velocity and the horizontal vorticity through the convective terms of Equation (5). This nonlinear coupling is a three-dimensional process and does not occur in completely two-dimensional flow, i.e., flows with zero velocity in the direction of invariance, since then only one component of vorticity is non-zero. This instability is localized in regions of large gradients of vertical velocity and, being so localized, is more apt to produce a lasting perturbation of the solution than a divergence, although the latter is also possible. This perturbation is evident in Figure 28b. The solution here was quite stable with no amplification of vorticity. However, the solution is rendered meaningless by the large perturbation generated by this nonlinear instability at the start. This nonlinear instability is analyzed in some detail in Appendix J where its time development and response to various parameters are given.

Dufort-Frankel Formulation

Figure 26 shows that the stability boundary of the actual nonlinear algorithm in the Dufort-Frankel formulation deviates markedly from the linearized prediction at low cell Reynolds number, the nonlinear solution having a finite time step limit even at Reynolds number below 2. As the Reynolds number increases above 2 the actual stability boundary crosses above the linearized prediction, and a stable region above the linearized boundary occurs. The stability boundary

then approaches the linearized prediction as the Reynolds number increases further.

The finite stability limit on the time step at low Reynolds number is due to the same nonlinear coupling of the equations described above, for the convective terms in the Dufort-Frankel and the straight explicit formulations differ only by their coefficients and not in form. The Dufort-Frankel formulation, however, removes the linear instability, which arises from the diffusional terms, at cell Reynolds number below 2, so that the time step may be increased in this Reynolds number range to the point where the amplification of vorticity by the nonlinear mechanism is too great for even the strong diffusion to overcome. In the straight explicit formulation diffusional instability leads to divergence in this range of Reynolds number at time steps below that at which the nonlinear disturbance becomes appreciable. Since the damping due to diffusion decreases as the Reynolds number increases, the nonlinear instability is the primary cause of divergence at all Reynolds numbers in the Dufort-Frankel formulation.

Results and Discussion*

The time development of the solution is shown in

---

*The convergence of the solution and the effects of the various parameters involved in the solution are discussed in Appendix F.

Figures 29 and 30 for two different gradual starts,* the cases being otherwise the same. With the more rapid of the two starts, the nonlinear disturbance discussed in Appendix J results in significant residual perturbation even though the disturbance is damped and the solution is stable. The nonlinear disturbance causes the jet boundary, as indicated by the circuit of maximum horizontal vorticity magnitude, to become pinched in, as it were, in the forward portion so that the jet cross-section develops into a distinctive "Y" shape. This "Y" shape of the jet is evident in the perspective view of the vertical velocity as well.

With the more gradual start the initial gradients are sufficiently reduced before the onset of significant convection that the nonlinear disturbance is much less effective. The jet cross-section now develops into more of the expected "kidney" shape {79}, the effect of the disturbance being reduced to the tendency of the cross-section to be somewhat pointed in front. With a smaller cell size (Figure 31) the jet cross-section is much smoother. Similarly a reduction in the jet velocity also results in a smoother jet cross-section (Figure 32). Both of the latter figures exhibit the distinctive kidney shape that has been observed in experimental investigation.

---

*As discussed in Appendix J, the gradual start consists of doubling the velocities at each time step until the final value is reached.

The nonlinear disturbance is more pronounced for an elliptic jet with its major axis parallel to the cross-wind (Figure 33) than for a circular jet of the same diameter as the minor axis of the ellipse (Figure 29). Again the jet boundary tends to become pinched in, and two vertical velocity maxima are evident. Again a more gradual start eliminates most of the perturbation (Figure 34). Finally, the solution for an elliptic jet with the major axis perpendicular to the cross-wind is shown in Figure 35. The kidney-shaped cross-section is clearly evident in this case.

CHAPTER VI

NUMERICAL SOLUTION FOR THE THREE-DIMENSIONAL JET IN CROSS-WIND

In this chapter the numerical method is applied to the time-dependent, three-dimensional jet in cross-wind, using two different types of initial conditions: the start from the opening of the jet exit and the start from the dissolution of a hypothetical pipe standing on the jet exit, separating a uniform vertical flow of infinite vertical extent from the potential cross-flow about the pipe normal to its axis. (These two starts are discussed in more detail at the end of Chapter II.) In the first of these cases the jet penetrates more deeply into the field as time passes, there having been no penetration at the start. In the second case the jet penetrates to infinity above the wall at the start, but the vertical flow far above the wall is gradually dissipated, so that the penetration decreases as time passes. Both starts should lead eventually to the same steady state with finite penetration.

Numerical Formulation

Start from a Cylindrical Discontinuity

The three-dimensional flow field of a jet issuing perpendicularly from an infinite solid plane wall into a cross-

wind parallel to the wall and bounded only by the wall is governed by the equations of motion (Chapter II)

$$\frac{\partial \underset{\sim}{\omega}}{\partial t} = \underset{\sim}{\nabla} \times (\underset{\sim}{v} \times \underset{\sim}{\omega}) + \nu \nabla^2 \underset{\sim}{\omega} \tag{1}$$

$$\underset{\sim}{v}(\underset{\sim}{r}) = \frac{\underset{\sim}{k} \cdot \underset{\sim}{r}}{2\pi} \iint \frac{\underset{\sim}{V}_s}{|\underset{\sim}{r}' - \underset{\sim}{r}|^3} \, dS + \frac{1}{4\pi} \iiint \left(\frac{\underset{\sim}{r}' - \underset{\sim}{r}}{|\underset{\sim}{r}' - \underset{\sim}{r}|^3} - \frac{\underset{\sim}{r}' - \underset{\sim}{R}}{|\underset{\sim}{r}' - \underset{\sim}{R}|^3} \right) \times \underset{\sim}{\omega} d\nu \tag{2}$$

where $\underset{\sim}{R} = \underset{\sim}{r} - 2(\underset{\sim}{k} \cdot \underset{\sim}{r})\underset{\sim}{k}$. The surface integral is taken over the plane boundary, and the volume integral is taken over the entire flow field above the plane boundary. The boundary conditions on the boundary plane are, for the coordinate system shown in Figure 36,

$$\underset{\sim}{v}(x, y, 0, t) = \begin{cases} 0 , & f(x, y) > 0 \\ \underset{\sim}{k}V_j , & f(x, y) < 0 \end{cases} \tag{3}$$

where $\underset{\sim}{k}V_j$ is the constant uniform jet exit velocity, and $f(x, y) = 0$ is the equation of the jet exit curve. The conditions at infinity are implicit in the integro-differential formulation: the cross-flow velocity at an infinite distance above the plane boundary is both constant and uniform.

Here the flow is taken to start from a cylindrical discontinuity perpendicular to the plane boundary and standing on the jet exit curve. The flow within the cylinder is

uniform and parallel to its axis, and the exterior flow is the two-dimensional potential flow of an unbounded stream about the cylinder, perpendicular to its axis. The initial conditions then are, with the vorticity evaluated from two-point, one-sided differences,

$$\underset{\sim}{\omega}(x, y, z, 0) = \begin{cases} 0 \ , \ f(x, y) \neq 0 \\ \left| \frac{1}{h} V_j \ \underset{\sim}{k} \times \underset{\sim}{e}(x, y) + \frac{1}{h} \underset{\sim}{e}(x, y) \times \underset{\sim o}{V}(x, y), \right. \\ \qquad\qquad f(x, y) = 0 \end{cases}$$

$$+ \begin{cases} 0 \ , \ z > 0 \\ \frac{1}{h} \underset{\sim}{k} \times \underset{\sim o}{V} (x, y), \ z = 0 \end{cases} \qquad (4)$$

which correspond to

$$\underset{\sim}{v}(x, y, z, 0) = \begin{cases} \underset{\sim}{k} V_j \ , \ f(x, y) < 0 \\ \underset{\sim o}{V} \ , \ f(x, y) > 0, \ z > 0 \\ 0 \ , \ f(x, y) > 0, \ z = 0 \end{cases} \qquad (5)$$

Here h is the cell width, $\underset{\sim}{e}(x, y)$ is the outward unit normal to the jet exit curve,

$$\underset{\sim}{e}(x, y) = \frac{\underset{\sim}{\nabla} f(x, y)}{\left| \underset{\sim}{\nabla} f(x, y) \right|}$$

and $\underset{\sim o}{V}(x, y)$ is the velocity field of the two-dimensional potential flow of a constant uniform free stream, with

velocity $-i\underset{\sim}{V}_c$, about a cylinder having the shape of the jet exit, perpendicular to the axis of the cylinder. Thus

$$\lim_{x^2 + y^2 \to \infty} \underset{\sim}{V}_o(x, y) = - i\underset{\sim}{V}_c$$

In Equation (4) the terms $\frac{1}{h}V_j \underset{\sim}{k} \times \underset{\sim}{e}$ and $\frac{1}{h}\underset{\sim}{e} \times \underset{\sim}{V}_o$ represent, respectively, the vorticity generated on the cylindrical discontinuity by the jet inside and by the cross-flow outside. The term $\frac{1}{h}\underset{\sim}{k} \times \underset{\sim}{V}_o$ represents the vorticity generated by the cross-flow on the plane boundary to satisfy the no-slip condition. All three of these terms have non-zero values at infinity, since both the jet and plane boundary are of infinite extent, so that the initial aggregate of vortex cells* would be infinite.

This however, is avoided by writing the solution as the sum of three solutions:

$$\begin{aligned} \underset{\sim}{v}(x, y, z, t) &= \underset{\sim}{v}_p(z, t) + \underset{\sim}{v}_J(x, y, t) + \underset{\sim}{v}'(x, y, z, t) \\ \underset{\sim}{\omega}(x, y, z, t) &= \underset{\sim}{\omega}_p(z, t) + \underset{\sim}{\omega}_J(x, y, t) + \underset{\sim}{\omega}'(x, y, z, t) \end{aligned} \tag{6}$$

where $\underset{\sim}{v}_p$, $\underset{\sim}{\omega}_p$ is the solution for the flow above an impervious infinite flat plate moving parallel to itself with a velocity equal in magnitude, but opposite in direction, to the cross-flow velocity. Also, $\underset{\sim}{v}_J$, $\underset{\sim}{\omega}_J$ is the solution for

---

*Vortex cells and the aggregate of vortex cells are defined in Chapter II.

an infinite jet in cross-wind with no wall present. These two solutions supply the conditions approached at infinite distances parallel and perpendicular, respectively, to the plane boundary by the complete solution. Thus

$$\lim_{x^2 + y^2 \to \infty} \underset{\sim}{\omega}(x, y, z, t) = \underset{\sim}{\omega}_p(z, t)$$

$$\lim_{z \to \infty} \underset{\sim}{\omega}(x, y, z, t) = \underset{\sim}{\omega}_J(x, y, t)$$

Then

$$\lim_{x^2 + y^2 + z^2 \to \infty} \underset{\sim}{\omega}'(x, y, z, t) = 0$$

and the extent of non-zero values of $\underset{\sim}{\omega}'$ is finite.

Infinite Plate Sub-Solution. The boundary conditions for the first of these solutions are given by

$$\underset{\sim}{v}_p(0, t) = \underset{\sim}{i}V_c \tag{7}$$

and the initial conditions by

$$\underset{\sim}{\omega}_p(z, 0) = \begin{cases} 0 , & z > 0 \\ -\frac{1}{h}\underset{\sim}{k} \times \underset{\sim}{i}V_c , & z = 0 \end{cases} \tag{8}$$

where V_c is the magnitude of the constant cross-flow velocity of the complete solution at an infinite distance above the plane boundary. These initial conditions correspond to

$$\underset{\sim}{v}_p(z, 0) = \begin{cases} 0 \ , & z > 0 \\ i\underset{\sim}{V}_c, & z = 0 \end{cases} \tag{9}$$

This problem is one-dimensional and has an exact solution. However, in the interest of consistency, this was also done numerically in the integro-differential formulation as discussed in Chapter II.

Infinite Jet in Cross-Wind Sub-Solution. The second of these solutions has no boundaries and therefore no boundary conditions. (The condition that the velocity approach at infinity that of the undisturbed constant cross-flow of the complete solution,

$$\lim_{x^2 + y^2 \to \infty} \underset{\sim}{v}_J(x, y, t) = - i\underset{\sim}{V}_c$$

is contained implicitly in the integro-differential formulation for this solution.) The initial conditions are

$$\underset{\sim}{\omega}_J(x, y, 0) = \begin{cases} 0 \ , & f(x, y) \neq 0 \\ \frac{1}{h} V_j \underset{\sim}{k} \times \underset{\sim}{e}(x, y) + \frac{1}{h} \underset{\sim}{e}(x, y) \times \underset{\sim}{V}_o(x, y), & f(x, y) = 0 \end{cases} \tag{10}$$

which correspond to

$$\underset{\sim}{v}_J(x, y, 0) = \underset{\sim}{V}_o(x, y) + \begin{cases} 0 \ , & f(x, y) > 0 \\ k\underset{\sim}{V}_j, & f(x, y) < 0 \end{cases} \tag{11}$$

This solution is two-dimensional and is discussed in Chapter V.

Prime Sub-Solution. The boundary conditions for the remaining solution are, from Equation (6),

$$\underset{\sim}{v}'(x, y, 0, t) = \underset{\sim}{v}(x, y, 0, t) - \underset{\sim}{v}_p(0, t) - \underset{\sim}{v}_J(x, y, t)$$

$$= \begin{Bmatrix} 0 , & f(x, y) > 0 \\ \underset{\sim}{kV}_j , & f(x, y) < 0 \end{Bmatrix} - \underset{\sim}{iV}_c - \underset{\sim}{v}_J(x, y, t) \qquad (12)$$

and are thus time-dependent. Similarly the initial conditions are

$$\underset{\sim}{\omega}'(x, y, z, 0) = \underset{\sim}{\omega}(x, y, z, 0) - \underset{\sim}{\omega}_p(z, 0) - \underset{\sim}{\omega}_J(x, y, 0)$$

$$= \begin{cases} 0, & z > 0 \\ \frac{1}{h}\underset{\sim}{k} \times [\underset{\sim}{V}_o(x, y) + \underset{\sim}{iV}_c], & z = 0 \end{cases} \qquad (13)$$

The equations of motion for this solution are obtained by substitution of Equation (6) into Equations (1) and (2). Thus, from Equation (1)

$$\frac{\partial \underset{\sim}{\omega}_p}{\partial t} + \frac{\partial \underset{\sim}{\omega}_J}{\partial t} + \frac{\partial \underset{\sim}{\omega}'}{\partial t} = \underset{\sim}{\nabla} \times [(\underset{\sim}{v}_p + \underset{\sim}{v}_J + \underset{\sim}{v}') \times (\underset{\sim}{\omega}_p + \underset{\sim}{\omega}_J + \underset{\sim}{\omega}')]$$

$$+ \nu(\nabla^2 \underset{\sim}{\omega}_p + \nabla^2 \underset{\sim}{\omega}_J + \nabla^2 \underset{\sim}{\omega}')$$

But

$$\frac{\partial \underset{\sim}{\omega}_p}{\partial t} = \underset{\sim}{\nabla} \times (\underset{\sim}{v}_p \times \underset{\sim}{\omega}_p) + \nu\nabla^2 \underset{\sim}{\omega}_p$$

$$\frac{\partial \underset{\sim}{\omega}_J}{\partial t} = \underset{\sim}{\nabla} \times (\underset{\sim}{v}_J \times \underset{\sim}{\omega}_J) + \nu\nabla^2 \underset{\sim}{\omega}_J$$

so that

$$\frac{\partial \underset{\sim}{\omega}'}{\partial t} = \underset{\sim}{\nabla} \times (\underset{\sim}{v}' \times \underset{\sim}{\omega}') + \nu \nabla^2 \underset{\sim}{\omega}' + \underset{\sim}{\nabla} \times [\underset{\sim}{v}_p \times \underset{\sim}{\omega}_J + \underset{\sim}{v}_J \times \underset{\sim}{\omega}_p + (\underset{\sim}{v}_p + \underset{\sim}{v}_J) \times \underset{\sim}{\omega}' + \underset{\sim}{v}' \times (\underset{\sim}{\omega}_p + \underset{\sim}{\omega}_J)] \quad (14)$$

Equation (2), being linear, is unchanged in form:

$$\underset{\sim}{v}'(\underset{\sim}{r}) = \frac{\underset{\sim}{k} \cdot \underset{\sim}{r}}{2\pi} \iint \frac{\underset{\sim}{V}'_s}{|\underset{\sim}{r}' - \underset{\sim}{r}|^3} \, dS + \frac{1}{4\pi} \iiint \left(\frac{\underset{\sim}{r}' - \underset{\sim}{r}}{|\underset{\sim}{r}' - \underset{\sim}{r}|^3} - \frac{\underset{\sim}{r}' - \underset{\sim}{R}}{|\underset{\sim}{r}' - \underset{\sim}{R}|^3} \right) \times \underset{\sim}{\omega}' d\nu \quad (15)$$

The velocity in the integrand of the surface integral is that given by the boundary conditions in Equation 12.

The three-dimensional, time-dependent solution of Equations (1) and (2), subject to the boundary conditions given by Equation (3) and the initial conditions given by Equation (4), is thus obtained by adding the one-dimensional solution of Chapter II and the two-dimensional solution of Chapter V to the three-dimensional solution of Equations (14) and (15), subject to the boundary conditions given by Equation (12) and the initial conditions given by Equation (13).

With nondimensionalization with respect to the cross-wind velocity V_c and the cell width h, Equation (14) becomes

$$\frac{\partial \xi'}{\partial t} = \frac{\partial C_z}{\partial y} - \frac{\partial C_y}{\partial z} + \frac{1}{R_c}\left(\frac{\partial^2 \xi'}{\partial x^2} + \frac{\partial^2 \xi'}{\partial y^2} + \frac{\partial^2 \xi'}{\partial z^2}\right) \qquad (16a)^*$$

$$\frac{\partial \eta'}{\partial t} = \frac{\partial C_x}{\partial z} - \frac{\partial C_z}{\partial x} + \frac{1}{R_c}\left(\frac{\partial^2 \eta'}{\partial x^2} + \frac{\partial^2 \eta'}{\partial y^2} + \frac{\partial^2 \eta'}{\partial z^2}\right) \qquad (16b)$$

$$\frac{\partial \zeta'}{\partial t} = \frac{\partial C_y}{\partial x} - \frac{\partial C_x}{\partial y} + \frac{1}{R_c}\left(\frac{\partial^2 \zeta'}{\partial x^2} + \frac{\partial^2 \zeta'}{\partial y^2} + \frac{\partial^2 \zeta'}{\partial z^2}\right) \qquad (16c)$$

where

$$\underset{\sim}{C} \equiv \underset{\sim}{v}_p \times \underset{\sim}{\omega}_J + \underset{\sim}{v}_J \times \underset{\sim}{\omega}_p + (\underset{\sim}{v}_p + \underset{\sim}{v}_J) \times \underset{\sim}{\omega}' + \underset{\sim}{v}' \times (\underset{\sim}{\omega}_p + \underset{\sim}{\omega}_J)$$

or

$$C_x = v'\zeta' - w'\eta' - w_J\eta_p + v_J\zeta' - w_J\eta' + v'\zeta_J - w'(\eta_p + \eta_J) \qquad (17a)$$

$$C_y = w'\xi' - u'\zeta' - u_p\zeta_J + w_J\xi' - (u_p + u_J)\zeta' + w'\xi_J - u'\zeta_J \qquad (17b)$$

$$C_z = u'\eta' - v'\xi' + u_p\eta_J + (u_p + u_J)\eta' - v_J\xi' + u'(\eta_p + \eta_J) - v'\xi_J \qquad (17c)$$

Here

$$\underset{\sim}{v}_p = \underset{\sim}{i}u_p, \quad \underset{\sim}{\omega}_p = \underset{\sim}{i}\eta_p$$

$$\underset{\sim}{v}_J = \underset{\sim}{i}u_j + \underset{\sim}{j}v_J + \underset{\sim}{k}w_J, \quad \underset{\sim}{\omega}_J = \underset{\sim}{i}\xi_J + \underset{\sim}{j}\eta_J + \underset{\sim}{k}\zeta_J$$

Similarly, Equation (15) becomes

---

*Hereafter in this chapter all quantities are nondimensionalized as noted in the Nomenclature.

$$u' = -\frac{z}{2\pi}\iint\frac{1 + u_J(x', y')}{F_1}\,dx'dy'$$

$$+\frac{1}{4\pi}\iiint\frac{(y' - y)\zeta'(x', y', z') - (z' - z)\eta'(x', y', z')}{F_2}dx'dy'dz'$$

$$-\frac{1}{4\pi}\iiint\frac{(y' - y)\zeta'(x', y', z') - (z' + z)\eta'(x', y', z')}{F_3}dx'dy'dz' \qquad (18a)$$

$$v' = -\frac{z}{2\pi}\iint\frac{v_J(x', y')}{F_1}\,dx'dy'$$

$$+\frac{1}{4\pi}\iiint\frac{(z' - z)\xi'(x', y', z') - (x' - x)\zeta'(x', y', z')}{F_2}dx'dy'dz'$$

$$-\frac{1}{4\pi}\iiint\frac{(z' + z)\xi'(x', y', z') - (x' - x)\zeta'(x', y', z')}{F_3}dx'dy'dz' \qquad (18b)$$

$$w' = -\frac{z}{2\pi}\iint\frac{w_J(x', y') - V_r\varepsilon(x', y')}{F_1}dx'dy'$$

$$+\frac{1}{4\pi}\iiint\frac{(x' - x)\eta'(x', y', z') - (y' - y)\xi'(x', y', z')}{F_2}dx'dy'dz'$$

$$-\frac{1}{4\pi}\iiint\frac{(x' - x)\eta'(x', y', z') - (y' - y)\xi'(x', y', z')}{F_3}dx'dy'dz' \qquad (18c)$$

where

$$F_1 \equiv [(x' - x)^2 + (y' - y)^2 + z^2]^{3/2}$$

$$F_2 \equiv [(x' - x)^2 + (y' - y)^2 + (z' - z)^2]^{3/2}$$

$$F_3 \equiv [(x' - x)^2 + (y' - y)^2 + (z' + z)^2]^{3/2}$$

$$\varepsilon(x', y') \equiv \begin{cases} 0 , & f(x', y') > 0 \\ 1 , & f(x', y') < 0 \end{cases}$$

Here the primes denoting the variables of integration are not to be confused with those referring to the prime solution ($\underset{\sim}{v}'$, $\underset{\sim}{\omega}'$). All quantities in these equations are dimensionless, and the cell Reynolds number is based on the cross-flow velocity:

$$R_c = \frac{V_c h}{\nu}$$

With the space derivatives replaced by three-point central differences and the time derivatives by a two-point forward difference, Equations (16) are approximated (Appendix D) by the following difference equations, the primes now being understood:

$$\xi^{n+1}_{i,j,k} = (1 - 6\frac{\Delta t}{R_c})\xi^{n}_{i,j,k}$$

$$+ \frac{\Delta t}{2}[(C_z)^{n}_{i,j+1,k} - (C_z)^{n}_{i,j-1,k} - (C_y)^{n}_{i,j,k+1}$$

$$+ (C_y)^{n}_{i,j,k-1}]$$

$$+ \frac{\Delta t}{R_c}[\xi^{n}_{i+1,j,k} + \xi^{n}_{i-1,j,k} + \xi^{n}_{i,j+1,k} + \xi^{n}_{i,j-1,k}$$

$$+ \xi^{n}_{i,j,k+1} + \xi^{n}_{i,j,k-1}] \qquad (19a)$$

$$\eta^{n+1}_{i,j,k} = (1 - 6\frac{\Delta t}{R_c})\eta^{n}_{i,j,k} + \frac{\Delta t}{2}[(C_x)^{n}_{i,j,k+1} - (C_x)^{n}_{i,j,k-1}$$

$$- (C_z)^{n}_{i+1,j,k} + (C_z)^{n}_{i-1,j,k}]$$

$$+ \frac{\Delta t}{R_c}[\eta^{n}_{i+1,j,k} + \eta^{n}_{i-1,j,k} + \eta^{n}_{i,j+1,k} + \eta^{n}_{i,j-1,k}$$

$$+ \eta^{n}_{i,j,k+1} + \eta^{n}_{i,j,k-1}] \qquad (19b)$$

$$\zeta^{n+1}_{i,j,k} = (1 - 6\frac{\Delta t}{R_c})\zeta^{n}_{i,j,k} + \frac{\Delta t}{2}[(C_y)^{n}_{i+1,j,k} - (C_y)^{n}_{i-1,j,k}$$

$$- (C_x)^{n}_{i,j+1,k} + (C_x)^{n}_{i,j-1,k}]$$

$$+ \frac{\Delta t}{R_c}[\zeta^{n}_{i+1,j,k} + \zeta^{n}_{i-1,j,k} + \zeta^{n}_{i,j+1,k} + \zeta^{n}_{i,j-1,k}$$

$$+ \zeta^{n}_{i,j,k+1} + \zeta^{n}_{i,j,k-1}] \qquad (19c)$$

in straight explicit form. Here Δt is the (nondimensional) time step, and the subscripts and superscripts refer to the space and time coordinates, respectively: $\zeta^{n}_{i,j,k} \equiv \zeta(x_i, y_j, z_k, t_n)$.

The integrals of Equation (18) are approximated numerically by

$$u^n_{i,j,k} = -\frac{z_k}{2\pi}\sum_p\sum_q \frac{1 + (u_J)^n_{p,q}}{F_1}$$

$$+\frac{1}{4\pi}\sum_p\sum_q\sum_r{}_{(p,q,r)\neq(i,j,k)} \frac{(y_q - y_j)\zeta^n_{p,q,r} - (z_r - z_k)\eta^n_{p,q,r}}{F_2}$$

$$-\frac{1}{4\pi}\sum_p\sum_q\sum_r{}_{(p,q,r)\neq(i,j,k)} \frac{(y_q - y_j)\zeta^n_{p,q,r} - (z_r + z_k)\eta^n_{p,q,r}}{F_3} \qquad (20a)$$

$$v^n_{i,j,k} = -\frac{z_k}{2\pi}\sum_p\sum_q \frac{(v_J)^n_{p,q}}{F_1}$$

$$+\frac{1}{4\pi}\sum_p\sum_q\sum_r{}_{(p,q,r)\neq(i,j,k)} \frac{(z_r - z_k)\xi^n_{p,q,r} - (x_p - x_i)\zeta^n_{p,q,r}}{F_2}$$

$$-\frac{1}{4\pi}\sum_p\sum_q\sum_r{}_{(p,q,r)\neq(i,j,k)} \frac{(z_r + z_k)\xi^n_{p,q,r} - (x_p - x_i)\zeta^n_{p,q,r}}{F_3} \qquad (20b)$$

$$w^n_{i,j,k} = -\frac{z_k}{2\pi}\sum_p\sum_q \frac{(w_J)^n_{p,q} - V_r\varepsilon_{p,q}}{F_1}$$

$$+\frac{1}{4\pi}\sum_p\sum_q\sum_r{}_{(p,q,r)\neq(i,j,k)} \frac{(x_p - x_i)\eta^n_{p,q,r} - (y_q - y_j)\xi^n_{p,q,r}}{F_2}$$

$$-\frac{1}{4\pi}\sum_p\sum_q\sum_r{}_{(p,q,r)\neq(i,j,k)} \frac{(x_p - x_i)\eta^n_{p,q,r} - (y_q - y_j)\xi^n_{p,q,r}}{F_3} \qquad (20c)$$

where now

$$F_1 \equiv [(x_p - x_i)^2 + (y_q - y_j)^2 + z_k^2]^{3/2}$$

$$F_2 \equiv [(x_p - x_i)^2 + (y_q - y_j)^2 + (z_r - z_k)^2]^{3/2}$$

$$F_3 \equiv [(x_p - x_i)^2 + (y_q - y_j)^2 + (z_r + z_k)^2]^{3/2}$$

$$\varepsilon_{p,q} \equiv \begin{cases} 0 \ , & (x_p, y_q) \text{ not on jet exit} \\ 1 \ , & (x_p, y_q) \text{ on jet exit} \end{cases}$$

The summations extend over all points having non-zero vorticity.

The above relations for the velocity apply for $z_k \neq 0$. On the boundary plane the velocity is given by the boundary conditions from Equation (12), so that Equation (20) is replaced by

$$u^n_{i,j,1} = -1 - (u_J)^n_{i,j} \tag{21a}$$

$$v^n_{i,j,1} = -(v_J)^n_{i,j} \tag{21b}$$

$$w^n_{i,j,1} = V_r \varepsilon_{i,j} - (w_J)^n_{i,j} \tag{21c}$$

From the initial conditions given by Equation (13) the initial aggregate of vortex cells consists of a layer of finite extent, one cell in thickness, lying on the boundary plane. The lateral extent of this layer is determined by

the minimum vorticity, ω_m, below which cells are considered to have zero vorticity. Initial surface vorticity at greater distances from the exit is neglected.

Surface Pressure Coefficient. The pressure on the plane boundary is calculated from the line integral of the Navier-Stokes equations. On the boundary plane the velocity components parallel to the plane are zero, and the normal component is also zero, except on the jet exit where the normal derivatives of the velocity are zero. The convective terms therefore vanish on the boundary plane, and the Navier-Stokes equations may be written (with pressure nondimensionalized relative to the remote cross-flow dynamic pressure) as

$$\frac{1}{2}\nabla p = \frac{1}{R_c}\nabla^2 \underset{\sim}{v} = -\frac{1}{R_c}\nabla \underset{\sim}{} \times \underset{\sim}{\omega} \tag{22}$$

Then

$$\frac{\partial p}{\partial x} = \frac{2}{R_c}\frac{\partial \eta}{\partial z} \tag{23}$$

since

$$\frac{\partial \zeta}{\partial y} = \frac{\partial^2 v}{\partial x \partial y} - \frac{\partial^2 u}{\partial y^2} = 0$$

on the boundary plane.

Then, from the integral of Equation (23),

$$p(x, y, 0, t) - p_\infty = \frac{2}{R_c}\frac{\partial}{\partial z}\int_\infty^x \eta(x', y, z, t)dx' \tag{24}$$

where the derivative is evaluated at z = 0. This integral is approximated using two-point, one-sided differences and trapezoidal numerical integration as

$$p^n_{i,j,1} - p_\infty = -\frac{2}{R_c}\left[\frac{1}{2}\left(\eta^n_{i,j,2} - \eta^n_{i,j,1}\right) + \sum_{p=i+1}^{\infty}\left(\eta^n_{p,j,2} - \eta^n_{p,j,1}\right)\right] \tag{25}$$

where the vorticity used is that of the prime solution above, since $\frac{\partial \eta}{\partial z} = 0$ at z = 0 for the one and two-dimensional solutions above. The summations then actually extend only over the prime vortex cells, rather than to infinity as in the continuous case.

Start from the Opening of the Jet Exit

The initial conditions for the start from the opening of the jet exit are given by

$$\underset{\sim}{\omega}(x, y, z, 0) = \begin{Bmatrix} 0\ ,\ z > 0 \\ \\ \frac{1}{h}\underset{\sim}{k} \times \underset{\sim o}{V}(x, y, 0) - \frac{1}{h}\underset{\sim}{k} \times \underset{\sim}{i}V_c,\ z = 0 \end{Bmatrix} + \begin{Bmatrix} 0\ ,\ f(x, y) \neq 0,\ z = 0 \\ \\ \frac{1}{h}V_j \underset{\sim}{k} \times \underset{\sim}{e}(x, y),\ f(x, y) = 0,\ z = 0 \end{Bmatrix} \tag{26}$$

where $\underset{\sim o}{V}(x, y, 0)$ here is the potential velocity distribution on the boundary plane induced by a uniform source distribution on the jet exit with strength equal to the jet exit

velocity. As before, $-i\underset{\sim}{V}_c$ is the constant cross-flow, and $\underset{\sim}{e}(x, y)$ is the outward unit normal to the jet exit curve. These conditions correspond to an initial velocity distribution given by

$$\underset{\sim}{v}(x, y, z, 0) = \begin{cases} \underset{\sim}{V}_o(x, y, z) - i\underset{\sim}{V}_c & , z > 0 \\ k\underset{\sim}{V}_j & , f(x, y) < 0, z = 0 \\ 0 & , f(x, y) > 0, z = 0 \end{cases} \quad (27)$$

In these relations the velocity induced by the source distribution on the jet exit is given by {73, Chapter 11}

$$\underset{\sim}{V}_o = -\frac{V_j}{2\pi}\int\int \frac{\underset{\sim}{r}' - \underset{\sim}{r}}{|\underset{\sim}{r}' - \underset{\sim}{r}|^3} dS \quad (28)$$

Again the extent of non-zero vorticity on the boundary plane is infinite, so that the solution is advantageously broken into two parts: (a) the one-dimensional solution for the flow over an infinite solid plate, parallel to the plate, with constant velocity at an infinite distance from the plate equal to that of the cross-flow, and (b) the difference between the complete solution and the above solution. Thus the complete solution is written

$$\begin{aligned} \underset{\sim}{v}(x, y, z, t) &= \underset{\sim}{v}_p(z, t) + \underset{\sim}{v}'(x, y, z, t) \\ \underset{\sim}{\omega}(x, y, z, t) &= \underset{\sim}{\omega}_p(z, t) + \underset{\sim}{\omega}'(x, y, z, t) \end{aligned} \quad (29)$$

where $\underset{\sim}{v}_p, \underset{\sim}{\omega}_p$ represent solution (a) above, and $\underset{\sim}{v}', \underset{\sim}{\omega}'$ solution (b). The former thus supplies the conditions approached by the complete solution at infinite laterial distances at each time:

$$\lim_{x^2 + y^2 \to \infty} \underset{\sim}{\omega}(x, y, z, t) = \underset{\sim}{\omega}_p(z, t)$$

Then, as before,

$$\lim_{x^2 + y^2 + z^2 \to \infty} \underset{\sim}{\omega}'(x, y, z, t) = 0$$

and the extent of non-zero values of $\underset{\sim}{\omega}'$ is finite in the prime solution.

Infinite Plate Sub-Solution. The solution $\underset{\sim}{\omega}_p, \underset{\sim}{v}_p$ used here is simply that of the same notation used with the start from the cylindrical discontinuity discussed above, but with the constant velocity, $-\underset{\sim}{i}V_c$, added to the latter. The boundary is thus at rest in the present usage, the remote fluid being in motion with velocity $-\underset{\sim}{i}V_c$.

Prime Sub-Solution. The boundary conditions for the prime solution are, from Equation (29),

$$\underset{\sim}{v}'(x, y, 0, t) = \underset{\sim}{v}(x, y, 0, t) - \underset{\sim}{v}_p(0,t)$$

$$= \begin{cases} 0 , & f(x, y) > 0 \\ \underset{\sim}{k}V_j, & f(x, y) < 0 \end{cases} \qquad (30)$$

and are not time-dependent in this case. Similarly the initial conditions are

$$\underset{\sim}{\omega}'(x, y, z, 0) = \underset{\sim}{\omega}(x, y, z, 0) - \underset{\sim}{\omega}_p(z, 0)$$

$$= \begin{Bmatrix} 0 \ , \ z > 0 \\ \frac{1}{h}\underset{\sim}{k} \times \underset{\sim}{V}_o(x, y, 0), \ z = 0 \end{Bmatrix}$$

$$+ \begin{Bmatrix} 0 \ , \ f(x, y) \neq 0, \ z = 0 \\ \frac{1}{h}V_j \underset{\sim}{k} \times \underset{\sim}{e}(x, y), \ f(x, y) = 0, \ z = 0 \end{Bmatrix} \quad (31)$$

The equations of motion and their numerical approximations are the same as those given above for the start from the cylindrical discontinuity, except that all variables subscripted "J" are omitted, and the surface integrals of Equations (18a) and (18b) and the double summations of Equations (20a) and (20b) are also omitted. Similarly Equations (21a) and (21b) are omitted, the velocity parallel to the boundary being zero on the boundary in the present case. The pressure calculation is unchanged and is performed in the same manner described above.

Computation Procedure

With each type of start the vorticities of the sub-solutions, other than the prime sub-solution, are evaluated first at each new time from the appropriate parabolic difference equation. (The infinite plate sub-solution and the

infinite jet in cross-wind sub-solution are independent of each other, as well as of the prime sub-solution, so that the order in which these two sub-solutions are evaluated is immaterial.) The velocity of these sub-solutions is then evaluated from the appropriate integral over the respective vorticity. The calculation procedures for the infinite jet in cross-wind sub-solution and the infinite plate sub-solution are the same as those given in Chapter V and Chapter II, respectively.

Finally, using these results, the vorticity of the prime sub-solution is evaluated from the appropriate parabolic difference equation, and the velocity of this sub-solution is then evaluated from the integral over this vorticity distribution. (The restriction of the field of integration over the vorticity distribution for the velocity calculation to a specified range from the point of evaluation is also used for the prime solution.) The sub-solutions are then added to produce the complete solution at the current time.

In view of the negligible differences between the results with the two minimum vorticity schemes for the two-dimensional solutions at the total times actually reached, the scheme requiring the fewer calculations was chosen for use in three dimensions. Thus a border cell* is changed to a

---

*Border cells and vortex cells are defined in Chapter II.

vortex cell* if the magnitude of the vorticity calculated for the border cell exceeds the specified minimum vorticity, ω_m. Otherwise this vorticity is distributed evenly among the adjacent vortex cells.

In order to reduce the computer time required, border cells beyond a specified radius r_f from the jet exit axis are not allowed to change to vortex cells, their vorticity being distributed evenly among the adjacent vortex cells. This radius was taken as three or four exit radii, as indicated in the results presented. This restriction affects primarily the spread of prime vorticity on and just above the plane boundary, since in the total times considered the spread of vorticity above the plane boundary was largely confined within this range by the minimum vorticity criterion for creation of a vortex cell from a border cell. The specification of this maximum limit for the spread of prime vorticity causes the rectangularity of the edge of the vorticity field evident near the plane boundary in some of the vector plots.

Since the boundary here is plane, the difficulty of boundary condition representation encountered with the circular cylinder does not arise, and no special treatment of the equations for evaluation in the boundary cells† is necessary.

---

*Border cells and vortex cells are defined in Chapter II.

†Boundary cells are defined in Chapter II.

The values of all terms at virtual points inside the boundary are taken as equal to the corresponding surface value at the point of calculation. The surface values are calculated from the appropriate boundary conditions given in the preceding discussion.

Since the nonlinear instability discussed in Chapter V eliminates much of the advantage of the Dufort-Frankel formulation, the simpler straight explicit formulation was used exclusively for the three-dimensional solution.

Results and Discussion

Results were obtained for circular jets with velocity ratios of 8 and 4 with cross-flow Reynolds numbers of 12 and 6 (based on the jet exit diameter). Profiles of vorticity and velocity are presented and analyzed in Appendix K for velocity ratio of 8 and Reynolds number of 12 for each type of start. A number of interactions among various components of vorticity and velocity were noted and are analyzed in detail in this appendix. The emission of a vortex ring from the jet exit in the case of the start from the opening of the exit is evident in these profiles, as are vorticity waves propagating up the jet from the exit with both types of start. The time development of these upward propagating vorticity waves is discussed in some detail in Appendix K and the effects of various parameters thereon are presented.

Vorticity and Velocity

Vorticity and velocity vectors for the start from the opening of the jet exit are shown in Figures 37-42.* (Here vectors are shown only for prime vortex cells, i.e., cells having non-zero vorticity in the prime solution. This was done simply to economize the plotter time required and does not imply that the flow is uniform outside the regions shown.) Figures 37 and 38 give the horizontal (parallel to the boundary plane) vectors, and Figures 39 and 40 give the vertical vectors. In addition Figures 41 and 42 show the velocity vectors in planes through the center of the jet exit, perpendicular and parallel, respectively, to the remote cross-flow. It should be realized that the upstream (relative to the cross-flow) inclination of the vectors in the latter figure simply reflects the forward flow of the recirculation within the jet and does not imply that the overall jet is so inclined.

The development and upward convection of the vortex ring emitted at the exit at the start that is characterized by the vorticity and outward velocity peaks in Figures 89,

---

*The scale factors for the vector plots are given in Table 5. The magnitude of a vector is indicated by the length of the stem of the arrow, the size of the arrowheads being the same throughout. Spurious lines on the plots are the result of plotter error. Parameters used in all results presented are given in Table 4.

91, and 92, discussed in Appendix K, is evident upon close inspection of the vectors. In particular, the strong outward inclination of the velocity vectors in Figures 37 and 41 occurs just above the vortex ring, and there follows a fairly abrupt shift in inclination beneath the ring.

The recirculation within the jet, characterized by the forward horizontal velocity peaks in Figure 91, discussed in Appendix K, that develops at the later times is quite evident in the vector plots. This recirculation is retarded near the jet exit because of the boundary condition there, and dies out in the upper portion of the jet.

The vorticity and velocity vectors for the start from the cylindrical discontinuity standing on the jet exit are shown in Figures 43-48. The progress of the above-mentioned vorticity waves up the jet is quite evident, particularly in Figures 47 and 48. In this case the magnitude of the horizontal velocity within the jet is much smaller than that encountered with the other type of start and the rather complicated horizontal velocity patterns within the jet thus involve primarily velocity of very small magnitude. It should be recalled that the arrowheads of the vectors are all of the same size, the magnitude of the vector being indicated only by the length of the shaft. The pattern shifts from simple recirculation within the jet, involving two counter-rotating vortices, to a pattern involving four vortices—two

of which are the extensions of the two mentioned above, but displaced to the rear, and two additional counter-rotating vortices in the forward portion of the jet, these rotating oppositely to those in the rear. Between the two sets of vortices the cross-flow penetrates the jet. Again the horizontal flow is retarded near the plane boundary because of the boundary condition so that the internal vortices die out as the boundary is approached.

Stability

As shown in Appendix G the linearized stability criteria for Equation (19) are

$$\Delta t \leq \frac{1}{V_r^2}\left(\frac{4}{3R_c} - \frac{2}{3}\sqrt{\frac{4}{R_c^2} - V_r^2}\right) \text{ if } R_c \leq \frac{2}{V_r}$$

$$\Delta t \leq \frac{4}{3V_r^2 R_c} \text{ if } R_c \geq \frac{2}{V_r}$$

These criteria, being based on a maximum field velocity equal to the jet exit velocity (Appendix G), are conservative since the velocity only attains that maximum value in a relatively small portion of the field. The linearized stability analysis given, however, is developed as if the velocity in the entire field were equal to this maximum value. Therefore, although violation of the above criteria would lead to divergence if the velocity in the entire field were equal to the maximum value, if the region of violation is not

too great the instability will be local in origin and may be damped as it propagates into other regions of the flow.

The time steps used did exceed the above limits, but were well below the corresponding limits obtained with the cross-flow velocity taken as the field maximum to be used in the stability criteria. It is for this reason that the vorticity waves running up the jet occur (Appendix K). These waves are the result of local linear instability generated in the region of high jet velocity near the exit. They then propagate up the jet but are damped in the process as a result of the decrease in velocity up the jet. In the two unstable cases discussed in Appendix K, however, the violation of the above stability criteria was great enough that the local instability was of sufficient amplitude as to lead to divergence. Such vorticity waves were observed also in the numerical solution of Payne for the two-dimensional jet {49} and in that of Whitehead for the axi-symmetric emission of a vortex ring {51}, but were not recognized as the result of local linear instability. Neither of these solutions involved a cross-flow but were simple jets issuing into a quiescent surrounding.

Surface Pressure Distribution

Surface pressure coefficients for the above-mentioned cases are shown in Figures 49-53. Although the low Reynolds numbers of these cases preclude direct comparison with

available experimental data, the low pressure region behind the jet observed and to be expected in viscous flow {68, 79} is evident. (The precise location of the contours in these figures is less significant than their shape, since the former was affected by restriction of the lateral extent of the spread of vorticity near the boundary applied to conserve computer time in these cases.) With the start from the opening of the jet exit, the surface pressure contours are originally circles about the exit, the pressure being positive at all points and decreasing with increasing radius, since the initial solution is the superposition of a uniform exit source distribution and a constant pressure uniform cross-flow. As time progresses the pressures, particularly in the rear of the jet are reduced, and a region of negative pressure (coefficient) appears in the rear portion of the jet (Figure 49, T = 0.67). The negative pressure region expands and eventually encompasses the positive pressure region in front of the jet (Figure 49, T = 0.93), the latter having been reduced considerably. The pattern at the later times shown exhibits a region of positive pressure in front of the jet that is surrounded by a region of negative pressure, the lowest pressures occurring in the rear of the jet.

With a reduction of the velocity ratio, the flow develops less rapidly, and the positive pressure region in the front of the jet is not surrounded at the last time

given (Figure 50). The pattern is generally the same but with greater downstream extent of the low pressure lobes behind the jet.*

With the start from the dissolution of the cylindrical discontinuity (Figure 51), the region of negative pressure behind the jet is established immediately after the start. The later stages are quite similar with both types of start. It is clear that the development into the eventual pressure contour pattern is more rapid with the start from the discontinuity, as would be expected since the jet penetrates from the start in that case. (The loss of most of the contours for T = 1.00, 1.20, 1.33 was due to plotter error). With a reduction in velocity ratio the pattern is similar but less compact overall (Figure 52). The region of lowest pressure is more extensive, however, with the larger velocity ratio (cf. Figures 51 and 52, T = 0.93).

A reduction in the cross-flow Reynolds number increases the extent of the low pressure region and also results in a lower minimum pressure behind the jet (Figure 53). This is indicative of the importance of the viscous effects associated with the presence of the solid wall in the development of the low pressure region behind the jet, since these effects are stronger at lower Reynolds numbers.

---

*This trend with the velocity ratio is in agreement with the experimental results of Mosher [30].

CHAPTER VII

VORTEX LATTICE MODEL OF THE THREE-DIMENSIONAL JET IN CROSS-WIND

It was recognized from the start that no potential flow model could represent completely the viscous effects that are prominent in the jet in cross-wind, in particular the entrainment of the cross-wind and the low pressure region behind the jet. However, since numerous proposals have been put forward for representing the jet at least approximately by a lattice of vortices of fixed geometry, the evaluation of a lattice of variable geometry determined by velocities induced by the lattice on itself was considered to be of value. With this model, the deformation and backward deflection of the jet and some entrainment are included, developing in time from within the model itself without being prescribed beforehand. Thus it would seem that a model with such freedom would incorporate many of the features of the jet in cross-wind, even representing in effect some of the viscous features.

Vortex Lattice Model

It is shown in Appendix L that the representation of a jet issuing normally from an infinite plane wall into a cross-flow parallel to the wall by a lattice of vortex segments

must include also a uniform source distribution on the jet exit. The velocity then is the resultant of the velocities induced by the vortex segments, their solid-wall images in the infinite plane, and the source distribution. These singularities are depicted in Figure 54. At each time step the velocities induced at each vertex of the lattice by the vortex segments, their images, and the source distribution are calculated, and the vertices are moved accordingly. The lattice thus deforms as time progresses and the vertices are moved about.

Original Lattice Configuration

The original configuration of the lattice (at time zero) has all vortex segments either parallel or perpendicular to the wall. The segments that are parallel to the wall form a set of equally spaced closed rings and are here denoted as "ring segments." All the rings are identical, and the vertices of the ring segments forming each ring lie on the projection of the jet exit curve in the plane of that ring. Any shape exit is permitted.

The segments that are perpendicular to the wall connect the vertices of the ring segments, thus forming columns, perpendicular to the wall, standing on the jet exit curve. The spacing of these columns around the jet exit curve is arbitrary, but symmetry about the plane parallel to the cross-wind and perpendicular to the wall, bisecting the jet

exit, is required. The lengths of the ring segments are determined by the column spacing and may or may not be constant around the ring. The lengths of all column segments are, however, the same since the rings are equally spaced.

The circulation of each vortex segment is constant in time and is determined from the original lattice configuration as follows: The circulations of all the ring segments are the same and are determined by the jet velocity. Taking the line integral around the path indicated in Figure 54,

$$\Gamma = \oint \underset{\sim}{v} \cdot d\underset{\sim}{l} = V_j h \tag{1}$$

This expression holds for any jet exit shape and any column spacing. The circulations of all column segments in the same column are the same, but there is variation from one column to another. Taking the line integral around the path indicated in Figure 54,

$$\Gamma_m = \oint_m \underset{\sim}{v} \cdot d\underset{\sim}{l} \tag{2}$$

For arbitrary jet exit shape or experimental velocity distribution around the jet exit this expression must be evaluated to suit the particular case. In the case of equally spaced columns around a circular exit with a potential flow velocity distribution for a circular cylinder this becomes

$$\Gamma_m = \int_{\phi_m - \frac{\Delta\phi}{2}}^{\phi_m + \frac{\Delta\phi}{2}} (2V_c \sin\phi) R d\phi = 4V_c R \sin\frac{\Delta\phi}{2} \sin\phi_m \qquad (3)$$

The front and rear columns thus have zero circulation, while those at 90° have the largest circulation.

The jet exit is covered by a uniform source distribution of a constant strength determined by the jet exit velocity as indicated in Appendix N. The equation for the velocity induced thereby is also given in this appendix.

Time Development

The velocity induced at $\underset{\sim}{r}_p$ by a straight vortex segment between $\underset{\sim}{r}_1$ and $\underset{\sim}{r}_2$ (see Figure 55), with positive circulation reckoned as clockwise when viewed from $\underset{\sim}{r}_1$ to $\underset{\sim}{r}_2$, is given by (Appendix N).

$$\underset{\sim}{v} = \underset{\sim}{e}_1 \frac{\Gamma}{4\pi a}(\cos\theta_1 - \cos\theta_2) \qquad (4)$$

where

$$\underset{\sim}{e}_1 \equiv \frac{\underset{\sim}{l} \times \underset{\sim}{a}_1}{|\underset{\sim}{l} \times \underset{\sim}{a}_1|}, \quad \underset{\sim}{l} \equiv \underset{\sim}{r}_2 - \underset{\sim}{r}_1$$

$$a \equiv \frac{|\underset{\sim}{l} \times \underset{\sim}{a}_1|}{l}, \quad \underset{\sim}{a}_1 = \underset{\sim}{r}_p - \underset{\sim}{r}_1, \quad \underset{\sim}{a}_2 = \underset{\sim}{r}_p - \underset{\sim}{r}_2$$

$$\cos\theta_1 = \frac{\underset{\sim}{l} \cdot \underset{\sim}{a}_1}{l a_1}, \quad \cos\theta_2 = \frac{\underset{\sim}{l} \cdot \underset{\sim}{a}_2}{l a_2}$$

The use of this velocity with a finite time step, however, results in a spiralling effect. To avoid this the movement resulting from this induced velocity may be based on the

angular velocity about the vortex segment as follows (Appendix N, see Figure 56). (This has also been used in {9}.)

$$a\frac{\Delta\alpha}{\Delta t} = V \text{ or } \Delta\alpha = \frac{V\Delta t}{a}$$

Then

$$b = 2(a \sin \frac{\Delta\alpha}{2})$$

and

$$\underset{\sim}{b} = \underset{\sim}{e}_1 b \cos \frac{\Delta\alpha}{2} + \underset{\sim}{e}_2 b \sin \frac{\Delta\alpha}{2}$$

with

$$\underset{\sim}{e}_2 \equiv \frac{\underset{\sim}{1} \times \underset{\sim}{e}_1}{1}$$

so that

$$\underset{\sim}{b} = \underset{\sim}{e}_1 a \sin \Delta\alpha + \underset{\sim}{e}_2 a(1 - \cos \Delta\alpha) \qquad (5)$$

This vector $\underset{\sim}{b}$ is then the displacement of point $\underset{\sim}{r}_p$ due to the velocity induced by the vortex segment. If the displacement were taken as $\underset{\sim}{v}\Delta t$, instead, the perpendicular distance from the vortex segment to the point $\underset{\sim}{r}_p$ would increase. But the velocity field of a straight vortex segment is a circular field, so that this distance should not change. The above form of the displacement achieves this desired effect. Note that for small $\Delta\alpha$, i.e., small Δt,

$$\underset{\sim}{b} = \underset{\sim}{e}_1 a\Delta\alpha + \underset{\sim}{e}_2 a\frac{(\Delta\alpha)^2}{2}$$

$$= \underset{\sim}{e}_1 V\Delta t + \underset{\sim}{e}_2 \frac{(V\Delta t)^2}{2a} = \underset{\sim}{v}\Delta t + O(\Delta t)^2 \qquad (6)$$

as expected.

The spiralling effect is pronounced only in the immediate vicinity of the vortex, and only there is it necessary to resort to the use of angular velocity. Elsewhere displacements are better calculated directly from the velocity in the interest of economy of computer time.

At each vertex the displacement vectors induced by each ring segment, each column segment, their images in the wall, and the source distribution on the jet exit are calculated and summed. The vertex is then moved by the resultant of these displacement vectors. The lattice thus deforms in time, and the length and orientation of each vortex segment changes. The circulations, however, do not change.

Several rings and their columns are added beyond the top ring in the field to simulate conditions at infinity. These rings are equally spaced and are kept directly above the top ring of the field.

At each time step a new undeformed ring is formed on the jet exit. All the rings move upward, of course, under their mutual influence and that of the source distribution, so that a new ring, and its associated column segments, is added at each time step. This new ring is initially undeformed and enters at the jet exit. It in turn becomes deformed as it moves upward under the influence of all the induced velocities of the lattice.

Results and Discussion*

Appropriate values for the spacing of the rings and columns of the lattice were determined by comparing the wall pressure distribution about the undeformed lattice with the exact solution for the potential flow about a circular cylinder {73, Chapter 12}. Practical limits on computer time, however, limit the spacings that can actually be used. The results with several values of these parameters are shown in Figures 57-59.

The discretization involved causes the matching of the velocities induced by the exit source distribution and the vortex segments to be slightly imperfect. With the vertical velocities induced near the exit by the sources and the vortices matched as discussed in Appendix N, there still remains a slight imbalance in the other velocity components. This imbalance causes the first emitted ring to contract slightly after emission. Since vortex sheets are unstable, tending to roll up as a result of small displacements normal to the sheet, this contraction initiates a rolling up of the sheet as shown in Figure 60.

Only the first few rings emitted experience significant contraction from this imbalance between the source

---

*All quantities used on the figures discussed in this chapter are nondimensionalized with respect to the exit radius, the cross-flow velocity, and the cross-flow dynamic pressure.

distribution and the vortex segments, since after the lattice becomes deformed the velocities induced by the various vortex segments of the lattice are no longer ordered as at the start. The lattice thus attempts to reach a steady state below the rolled-up portion. However, vortex segments in the region of the roll-up become so stretched as to no longer give an adequate representation of the vortex sheet. Therefore, although in principle the initial roll-up could be tolerated and simply allowed to pass upward out of the field of interest, this is not practically possible because of the stretching and extreme distortion of the lattice.

Therefore, a number of expedients were considered to stabilize the lattice during the first few steps and thus eliminate the roll-up. The method finally selected was to calculate the displacement of each vertex from a weighted average of the velocity actually induced at the vertex and that induced at a corresponding vertex a great distance above the plane boundary, the weight of the latter decreasing linearly down the jet from unity for the first ring emitted. The vertices of each successively emitted ring thus are displaced more according to the velocity actually induced at those vertices. Since one ring is discarded from the top at each time step, this initial stabilization procedure gradually becomes less effective and finally becomes inoperative as time progresses.

The success of this initial stabilization of the lattice is evident upon comparison of Figures 61 and 60. The results of the same procedure applied with other values of the ring and column spacing are shown in Figure 62. The time shown is the longest for which the lattice was not stretched to the point of not being an adequate representation of the vortex sheet. (The stretching alluded to here is a result of the roll-up of the jet into two counter-rotating vortices.) Longer times could, of course, be reached with closer spacing of the vortex segments in the lattice, but at the expense of a rapid increase in computer time.

The deformation of the jet into the expected "kidney" shape {68, 79} is evident in Figure 62. However, the surface pressure distribution resulting from the deformed lattice (Figure 62e) is not greatly different from that before deformation (Figure 62f) because of the dominant influence of the lower portion of the lattice. This potential flow model thus does not give even an approximate match of the experimental data in the rear of the jet even though the deformation and deflection of the jet are included.

The data presented here for this potential flow model are only an illustrative sample of the large amount of data obtained. It was concluded from the study of this freely deforming vortex lattice model that such a model, even

though it does represent to some extent the experimentally observed deformation and deflection of the jet, is not at all capable of representing the causes of the low pressure region behind the jet. As stated previously, this conclusion was not unexpected. The low pressure region behind the jet thus may be attributed to viscous effects arising from the presence of the solid wall, and not to the deformation and deflection of the jet.

CHAPTER VIII

CONCLUSIONS AND RECOMMENDATIONS

Conclusions

The principal conclusions of the present investigation are as follows:

1. The numerical method based on an integro-differential formulation of the Navier-Stokes equations is a valid method of numerical solution of the Navier-Stokes equations, yielding the solution in the entire flow field while actual computation is confined to the region of significant vorticity magnitude. This method requires two orders of magnitude less computer storage for three-dimensional problems than do methods based on differential formulation.

2. The large computer time required by the evaluation of the velocity from the integral over the vorticity field makes the numerical method based on the integro-differential formulation non-competitive with methods based on differential formulation in two-dimensional problems. In three dimensions, the integro-differential method is superior in speed at the present state of the art. The primary reason for this speed advantage is that the significant storage reduction achieved by the integro-differential method allows three-dimensional problems of large field size to be considered without the use of any low-speed storage, i.e.,

completely in the high-speed core. This feature is a result, of course, of confining the calculation to the region of non-zero vorticity at any time.

3. The specification of conditions at infinity is unnecessary in the present formulation, these conditions being contained implicitly, so that it is not necessary to artificially locate "infinity" at the boundaries of a finite computational field. The solution is obtained on a field that is, in effect, infinite.

4. Care must be taken in the integro-differential formulation to represent the integral over the vorticity distribution accurately in the numerical approximation, especially in the region of highest vorticity near solid boundaries. For this reason the proper numerical representation of boundary conditions is even more critical in the present formulation than in differential formulations. It is thus of great advantage to have a coordinate line coincident with any solid boundary that is present. However, a moderately successful method of representing the boundary conditions for the integral with the boundary and coordinate lines not coincident has been developed.

5. The numerical method is convergent with decreasing time step and, for the one-dimensional flow above a suddenly accelerated infinite flat plate, is known to converge to the exact solution.

6. The numerical method is capable of predicting the drag coefficients for a two-dimensional solid circular cylinder with good accuracy. The cell size must be reduced, however, to maintain accuracy as the cylinder Reynolds number increases. Other numerical methods share the same feature. With cartesian coordinates the cell Reynolds number must be unity or less for accurate drag prediction. The numerical method with cartesian coordinates is capable of predicting the surface pressure distribution also, but with some irregularity due to the angularity of the boundary, for cell Reynolds numbers of unity or less.

7. The numerical method is capable of predicting the time history of the length of the standing vortices behind a two-dimensional solid circular cylinder with accuracy for cell Reynolds numbers of 3 or less, and possibly higher. The method does produce periodic vortex shedding, at a frequency close to the expected value if a vorticity perturbation is introduced, and shows the establishment of a vortex street. The shedding and street formation are surpressed by the addition of a rear splitter plate.

8. The stability of the numerical method follows generally the linearized prediction given, but with some significant differences. In two-dimensional flow with only two variable components of vorticity and velocity the linearized stability region is followed very closely (exactly for one-

dimensional flow), and there is no upper limit on the cell Reynolds number. However, in flow with three variable components of velocity and vorticity, even with a direction of invariance, a nonlinear instability occurs through a convective coupling between a velocity component and the two vorticity components normal thereto. This nonlinear instability arises in the parabolic differential equation for the rate of change of vorticity and is not peculiar to the integro-differential formulation itself. This instability is dependent more on the cell Reynolds number than on the time step. There still is not necessarily an upper limit, per se, on the cell Reynolds number, but impulsive starts are highly susceptible to nonlinear instability and a progressively more gradual start is necessary as the cell Reynolds number increases and/or the velocity ratio increases. As with all explicit methods the time step is rather severely limited by the stability requirements.

9. The numerical solution for the problem of the jet issuing normally from an infinite plane wall into a cross-flow parallel to the wall may be constructed in such a manner that the three-dimensional calculation is confined to a field of vorticity of finite extent, both in the case of a start from the opening of the jet exit and in the case of a start from the dissolution of a cylindrical discontinuity standing on the jet exit, separating a uniform interior jet

flow from the exterior potential flow around the cylindrical discontinuity.

10. The numerical method shows the deflection and deformation of the jet into the expected kidney shape, a recirculation within the jet in the form of counter-rotating vortices, and entrainment of the cross flow into the rear of the jet. The method also shows the low pressure region behind the jet to be expected from experimental results, the emission of a vortex ring from the jet exit and, vorticity waves propagating up the jet from the exit. These waves are generated by local linear instability, as predicted, in the high velocity region near the exit and may be damped upon propagation upward.

11. The potential flow model—a freely deforming lattice of straight vortex segments, their images in the infinite wall, and a uniform source distribution on the jet exit—of the jet issuing normally from an infinite plane wall into a cross-flow parallel to the wall is not capable of representing even approximately the causes of the low pressure region behind the jet, even though this model does represent to some extent the deflection and deformation of the jet. The low pressure region behind the jet may be attributed to viscous effects arising from the presence of the solid wall, and not to the deformation and deflection of the jet.

Recommendations

The integro-differential numerical formulation should be immediately applicable to the flow about three-dimensional solid bodies, as well as to jet flows. Future efforts using the integro-differential formulation should be made using disc storage of the geometric factors in the integral over the vorticity distribution. Also the coordinate system used should be a curvilinear system having a coordinate line coincident with the field boundary. The use of such a curvilinear system with general shaped solid bodies should be investigated. Also the use of a coordinate system in which relatively more coordinate lines are concentrated near the solid boundaries should be considered in order to extend the range of Reynolds numbers for which accurate surface pressures can be obtained.

Consideration should also be given to the use of an implicit system of difference equations rather than the present explicit form. Implicit schemes have less restrictive stability criteria and thus allow the use of larger time steps. However, the iteration required may destroy the time advantage unless optimized acceleration of the convergence of the iteration can be achieved. This optimization in the integro-differential formulation must be accomplished on an expanding field of non-rectangular shape if the essential storage reduction feature of the formulation is to be preserved.

APPENDIX A

VARIOUS FORMS OF THE EQUATIONS OF MOTION

Vorticity Equation

The Navier-Stokes equations for an incompressible fluid are

$$\frac{\partial \underset{\sim}{v}}{\partial t} + (\underset{\sim}{v} \cdot \underset{\sim}{\nabla})\underset{\sim}{v} = - \frac{1}{\rho}\underset{\sim}{\nabla} p + \nu \nabla^2 \underset{\sim}{v} \tag{1}$$

But using the vector identities {69, Chapter IV},

$$(\underset{\sim}{A} \cdot \underset{\sim}{\nabla})\underset{\sim}{A} = \frac{1}{2}\underset{\sim}{\nabla} A^2 - \underset{\sim}{A} \times (\underset{\sim}{\nabla} \times \underset{\sim}{A}) \tag{2a}$$

$$\nabla^2 \underset{\sim}{A} = \underset{\sim}{\nabla}(\underset{\sim}{\nabla} \cdot \underset{\sim}{A}) - \underset{\sim}{\nabla} \times (\underset{\sim}{\nabla} \times \underset{\sim}{A}) \tag{2b}$$

and the continuity equation,

$$\underset{\sim}{\nabla} \cdot \underset{\sim}{v} = 0 \tag{3}$$

Equation (1) may be rewritten

$$\frac{\partial \underset{\sim}{v}}{\partial t} + \frac{1}{2}(\underset{\sim}{v} \cdot \underset{\sim}{v}) - \underset{\sim}{v} \times (\underset{\sim}{\nabla} \times \underset{\sim}{v}) = - \frac{1}{\rho}\underset{\sim}{\nabla} p - \nu \underset{\sim}{\nabla} \times (\underset{\sim}{\nabla} \times \underset{\sim}{v}) \tag{4}$$

Then defining the vorticity by

$$\underset{\sim}{\omega} \equiv \underset{\sim}{\nabla} \times \underset{\sim}{v} \tag{5}$$

and taking the curl of Equation (4), we have (since the curl of any gradient is zero)

$$\frac{\partial \underset{\sim}{\omega}}{\partial t} - \underset{\sim}{\nabla} \times (\underset{\sim}{v} \times \underset{\sim}{\omega}) = \nu \nabla^2 \underset{\sim}{\omega} \tag{6}$$

Here the vector identity (2b) has again been used.

Using the continuity equation (3) and the definition of vorticity (5) in the vector identity (2b), we have the Poisson equation for the velocity,

$$\nabla^2 \underset{\sim}{v} = \underset{\sim}{\nabla}(\underset{\sim}{\nabla} \cdot \underset{\sim}{v}) - \underset{\sim}{\nabla} \times (\underset{\sim}{\nabla} \times \underset{\sim}{v}) = - \underset{\sim}{\nabla} \times \underset{\sim}{\omega} \tag{7}$$

Uniqueness and Identity of Solutions

Let $\underset{\sim}{v}_1$ and $\underset{\sim}{v}_2$ be two solutions of Equation (7) satisfying the same boundary conditions, the vorticity distribution being the same for both. Then

$$\nabla^2(\underset{\sim}{v}_1 - \underset{\sim}{v}_2) = 0 \text{ in the field} \tag{8a}$$

$$\underset{\sim}{v}_1 - \underset{\sim}{v}_2 = 0 \text{ on the boundary} \tag{8b}$$

But by the extremum principle for the Laplace equation {70, Chapter III} the extrema of any solution of the Laplace equation must occur on the boundary. Therefore, the only solution of Equation (8a) with the boundary conditions specified by Equation (8b) is

$$\underset{\sim}{v}_1 - \underset{\sim}{v}_2 = 0$$

on both the field and boundary. The solution of Equation (7) with specified boundary conditions and vorticity distribution is therefore unique for these boundary

conditions and vorticity distribution.

Now let $\underset{\sim}{v}_1'$ and $\underset{\sim}{v}_2'$ be two solutions of the set of equations, (3) and (5), satisfying the same boundary conditions with the same vorticity distribution. Then

$$\left.\begin{aligned} \underset{\sim}{\nabla} \times (\underset{\sim}{v}_1' - \underset{\sim}{v}_2') &= 0 \qquad (9a) \\ \underset{\sim}{\nabla} \cdot (\underset{\sim}{v}_1' - \underset{\sim}{v}_2') &= 0 \qquad (9b) \end{aligned}\right\} \text{ in the field}$$

$$\underset{\sim}{v}_1' - \underset{\sim}{v}_2' = 0 \qquad \text{on the boundary} \qquad (9c)$$

But any vector having both its curl and divergence equal to zero must also have its Laplacian equal to zero by the vector identity (2b). Therefore, the vector $\underset{\sim}{v}_1' - \underset{\sim}{v}_2'$ must satisfy

$$\nabla^2(\underset{\sim}{v}_1' - \underset{\sim}{v}_2') = 0 \quad \text{in the field} \qquad (10)$$

Then, in view of the boundary conditions for the vector $\underset{\sim}{v}_1' - \underset{\sim}{v}_2'$ specified by Equation (9c), it follows again from the extremum principle for the Laplace equation cited above that the only vector satisfying both Equation (10) and (9c) is the zero vector:

$$\underset{\sim}{v}_1' - \underset{\sim}{v}_2' = 0$$

in the field and boundary. Therefore, the solution of the set of equations, (3) and (5), with specified boundary conditions and vorticity distribution is also unique.

But any solution of the set of equations, (3) and (5), must also be a solution of the equation (7) because of the vector identity (2b). Then since the solution of the set, (3) and (5), and that of the equation (7) with the same specified boundary conditions and vorticity distribution are both unique, it follows that they must be identical.

APPENDIX B

INTEGRAL REPRESENTATION OF POISSON EQUATION SOLUTION

General Solution

The equation

$$\nabla^2 \underset{\sim}{v} = - \underset{\sim}{\nabla} \times \underset{\sim}{\omega}$$

with a specified vorticity distribution is a Poisson equation for the velocity. The solution may, therefore, be written for a bounded volume in the form of an integral representation by Green's Theorem {71, Chapter 7}:

$$\underset{\sim}{v}(\underset{\sim}{r}) = \frac{1}{4\pi}\iint\left[\frac{\frac{\partial \underset{\sim}{v}(\underset{\sim}{r}')}{\partial n}}{|\underset{\sim}{r}' - \underset{\sim}{r}|} + \frac{(\underset{\sim}{r}' - \underset{\sim}{r}) \cdot \underset{\sim}{n}(\underset{\sim}{r}')}{|\underset{\sim}{r}' - \underset{\sim}{r}|^3}\underset{\sim}{v}(\underset{\sim}{r}')\right] dS$$

$$+ \frac{1}{4\pi}\iiint \frac{\underset{\sim}{\nabla} \times \underset{\sim}{\omega}(\underset{\sim}{r}')}{|\underset{\sim}{r}' - \underset{\sim}{r}|} d\nu \qquad (1)$$

where the volume integral extends over the entire field, and the surface integral over the boundary thereof. The variable of integration in each integral is $\underset{\sim}{r}'$. The unit vector $\underset{\sim}{n}$ is defined to be normal to the boundary of the field, directed outward.

Specialization to Field with An Infinite Plane Boundary

Equation (1) applies for a point $\underset{\sim}{r}$ within the field. For a point outside the field we have

$$\iint \left[\frac{\frac{\partial \underset{\sim}{v}(\underset{\sim}{r}')}{\partial n}}{|\underset{\sim}{r}' - \underset{\sim}{r}|} + \frac{(\underset{\sim}{r}' - \underset{\sim}{r}) \cdot \underset{\sim}{n}(\underset{\sim}{r}')}{|\underset{\sim}{r}' - \underset{\sim}{r}|^3} \underset{\sim}{v}(\underset{\sim}{r}') \right] dS$$

$$+ \iiint \frac{\nabla \times \underset{\sim}{\omega}(\underset{\sim}{r}')}{|\underset{\sim}{r}' - \underset{\sim}{r}|} d\nu = 0 \qquad (2)$$

Let the boundary of the field consist of a plane and a hemisphere centered at the origin. The velocity is zero on the plane except on a portion termed the jet exit, the velocity thereon being specified as $\underset{\sim}{V}_j$. The velocity at an infinite distance above the plane boundary is specified as $\underset{\sim}{V}_\infty$. Then Equation (1) becomes

$$\underset{\sim}{v}(\underset{\sim}{r}) = \frac{1}{4\pi} \iint_{\text{plane}} \frac{\frac{\partial \underset{\sim}{v}}{\partial n}}{|\underset{\sim}{r}' - \underset{\sim}{r}|} dS + \frac{1}{4\pi} \iint_{\text{exit}} \frac{(\underset{\sim}{r}' - \underset{\sim}{r}) \cdot \underset{\sim}{n}}{|\underset{\sim}{r}' - \underset{\sim}{r}|^3} \underset{\sim}{V}_j dS$$

$$+ \frac{1}{4\pi} \iint_\infty \left[\frac{\frac{\partial \underset{\sim}{v}}{\partial n}}{|\underset{\sim}{r}' - \underset{\sim}{r}|} + \frac{(\underset{\sim}{r}' - \underset{\sim}{r}) \cdot \underset{\sim}{n}}{|\underset{\sim}{r}' - \underset{\sim}{r}|^3} \underset{\sim}{v} \right] dS + \frac{1}{4\pi} \iiint \frac{\nabla \times \underset{\sim}{\omega}}{|\underset{\sim}{r}' - \underset{\sim}{r}|} d\nu \qquad (3)^*$$

Here the surface integral over the plane boundary includes the jet exit. The third surface integral extends over all the field boundary not included in the plane boundary. Note that the velocity is not constant over this portion of the boundary, since the zero value specified at the intersection of this portion of the boundary with the plane boundary results in a velocity gradient above the plane boundary. Similarly for a

---

*The notation ∞ on the third surface integral implies the limit of the integral over the hemispherical surface as its radius approaches infinity.

point $\underset{\sim}{R}$ outside the flow field, Equation (2) becomes

$$\frac{1}{4\pi}\iint_{\text{plane}} \frac{\frac{\partial \underset{\sim}{v}}{\partial n}}{|\underset{\sim}{r}' - \underset{\sim}{R}|} dS + \frac{1}{4\pi}\iint_{\text{exit}} \frac{(\underset{\sim}{r}' - \underset{\sim}{R}) \cdot \underset{\sim}{n}}{|\underset{\sim}{r}' - \underset{\sim}{R}|^3} \underset{\sim}{V}_j dS$$

$$+ \frac{1}{4\pi}\iint_{\infty} \left[\frac{\frac{\partial \underset{\sim}{v}}{\partial n}}{|\underset{\sim}{r}' - \underset{\sim}{R}|} + \frac{(\underset{\sim}{r}' - \underset{\sim}{R}) \cdot \underset{\sim}{n}}{|\underset{\sim}{r}' - \underset{\sim}{R}|^3} \underset{\sim}{v}\right] dS$$

$$+ \frac{1}{4\pi}\iiint \frac{\nabla \underset{\sim}{x} \underset{\sim}{\omega}}{|\underset{\sim}{r}' - \underset{\sim}{R}|} d\nu = 0 \qquad (4)$$

Now let the point $\underset{\sim}{R}$ be the image in the plane boundary of the point $\underset{\sim}{r}$ (Figure 1):

$$\underset{\sim}{R} = \underset{\sim}{r} - 2(\underset{\sim}{k} \cdot \underset{\sim}{r})\underset{\sim}{k} \qquad (5)$$

where $\underset{\sim}{k}$ is the unit vector normal to the plane boundary, directed into the flow field. Then

$$(\underset{\sim}{r}' - \underset{\sim}{R}) = (\underset{\sim}{r}' - \underset{\sim}{r}) + 2(\underset{\sim}{k} \cdot \underset{\sim}{r})\underset{\sim}{k} \qquad (6a)$$

and

$$|\underset{\sim}{r}' - \underset{\sim}{R}|^2 = |\underset{\sim}{r}' - \underset{\sim}{r}|^2 + 4(\underset{\sim}{k} \cdot \underset{\sim}{r})(\underset{\sim}{k} \cdot \underset{\sim}{r}') \qquad (6b)$$

Thus for points of integration, i.e., $\underset{\sim}{r}'$, on the plane boundary we have, since there $\underset{\sim}{k} \cdot \underset{\sim}{r}' = 0$,

$$|\underset{\sim}{r}' - \underset{\sim}{R}| = |\underset{\sim}{r}' - \underset{\sim}{r}|$$

Therefore

$$\iint_{\text{plane}} \frac{\frac{\partial \underset{\sim}{v}}{\partial n}}{|\underset{\sim}{r}' - \underset{\sim}{r}|} dS = \iint_{\text{plane}} \frac{\frac{\partial \underset{\sim}{v}}{\partial n}}{|\underset{\sim}{r}' - \underset{\sim}{R}|} dS \qquad (7)$$

Then combining Equations (3) and (4) through Equation (7) we have

$$\underset{\sim}{v}(\underset{\sim}{r}) = -\frac{1}{4\pi}\iint_{\text{exit}} \frac{(\underset{\sim}{r}' - \underset{\sim}{R}) \cdot \underset{\sim}{n}}{|\underset{\sim}{r}' - \underset{\sim}{R}|^3} \underset{\sim}{V}_j \, dS$$

$$-\frac{1}{4\pi}\iint_{\infty}\left[\frac{\frac{\partial \underset{\sim}{v}}{\partial n}}{|\underset{\sim}{r}' - \underset{\sim}{R}|} + \frac{(\underset{\sim}{r}' - \underset{\sim}{R}) \cdot \underset{\sim}{n}}{|\underset{\sim}{r}' - \underset{\sim}{R}|^3}\underset{\sim}{v}\right] dS$$

$$-\frac{1}{4\pi}\iiint \frac{\nabla \times \underset{\sim}{\omega}}{|\underset{\sim}{r}' - \underset{\sim}{R}|} d\nu + \frac{1}{4\pi}\iint_{\text{exit}} \frac{(\underset{\sim}{r}' - \underset{\sim}{r}) \cdot \underset{\sim}{n}}{|\underset{\sim}{r}' - \underset{\sim}{r}|^3} \underset{\sim}{V}_j \, dS$$

$$+\frac{1}{4\pi}\iint_{\infty}\left[\frac{\frac{\partial \underset{\sim}{v}}{\partial n}}{|\underset{\sim}{r}' - \underset{\sim}{r}|} + \frac{(\underset{\sim}{r}' - \underset{\sim}{r}) \cdot \underset{\sim}{n}}{|\underset{\sim}{r}' - \underset{\sim}{r}|^3}\underset{\sim}{v}\right] dS$$

$$+\frac{1}{4\pi}\iiint \frac{\nabla \times \underset{\sim}{\omega}}{|\underset{\sim}{r}' - \underset{\sim}{r}|} d\nu \qquad (8)$$

Now combine the two integrals over the exit;

$$\iint_{\text{exit}} \left[\frac{(\underset{\sim}{r}' - \underset{\sim}{r}) \cdot \underset{\sim}{n}}{|\underset{\sim}{r}' - \underset{\sim}{r}|^3} - \frac{(\underset{\sim}{r}' - \underset{\sim}{R}) \cdot \underset{\sim}{n}}{|\underset{\sim}{r}' - \underset{\sim}{R}|^3}\right] \underset{\sim}{V}_j \, dS$$

$$= \iint_{\text{exit}} \frac{(\underset{\sim}{R} - \underset{\sim}{r}) \cdot \underset{\sim}{n}}{|\underset{\sim}{r}' - \underset{\sim}{r}|^3} \underset{\sim}{V}_j \, dS$$

$$= 2(\underset{\sim}{k} \cdot \underset{\sim}{r}) \iint_{\text{exit}} \frac{\underset{\sim}{V}_j \, dS}{|\underset{\sim}{r}' - \underset{\sim}{r}|^3} \qquad (9)$$

using Equation (5) and the fact that $\underset{\sim}{k} \cdot \underset{\sim}{n} = -1$ on the exit.

The integrals of $\frac{\partial \underset{\sim}{v}}{\partial n}$ over the surface at infinity* may also be combined as follows:

$$\iint_{\infty} \left(\frac{1}{|\underset{\sim}{r}' - \underset{\sim}{r}|} - \frac{1}{|\underset{\sim}{r}' - \underset{\sim}{R}|}\right) \frac{\partial \underset{\sim}{v}}{\partial n} dS = \iint_{\infty} \frac{|\underset{\sim}{r}' - \underset{\sim}{R}| - |\underset{\sim}{r}' - \underset{\sim}{r}|}{|\underset{\sim}{r}' - \underset{\sim}{R}| \cdot |\underset{\sim}{r}' - \underset{\sim}{r}|} \frac{\partial \underset{\sim}{v}}{\partial n} dS \tag{10}$$

But, by Equation (6b),

$$|\underset{\sim}{r}' - \underset{\sim}{R}| = [|\underset{\sim}{r}' - \underset{\sim}{r}|^2 + 4(\underset{\sim}{k} \cdot \underset{\sim}{r})(\underset{\sim}{k} \cdot \underset{\sim}{r}')]^{1/2}$$

$$= \{|\underset{\sim}{r}' - \underset{\sim}{r}|^2 [1 + \frac{4(\underset{\sim}{k} \cdot \underset{\sim}{r})(\underset{\sim}{k} \cdot \underset{\sim}{r}')}{|\underset{\sim}{r}' - \underset{\sim}{r}|^2}]\}^{1/2}$$

$$\cong |\underset{\sim}{r}' - \underset{\sim}{r}| [1 + \frac{2(\underset{\sim}{k} \cdot \underset{\sim}{r})(\underset{\sim}{k} \cdot \underset{\sim}{r}')}{|\underset{\sim}{r}' - \underset{\sim}{r}|^2}] \text{ as } \underset{\sim}{r}' \to \infty \tag{11}$$

Then, with this relation in Equation (10),

$$\iint_{\infty} \left(\frac{1}{|\underset{\sim}{r}' - \underset{\sim}{r}|} - \frac{1}{|\underset{\sim}{r}' - \underset{\sim}{R}|}\right) \frac{\partial \underset{\sim}{v}}{\partial n} dS = 2(\underset{\sim}{k} \cdot \underset{\sim}{r}) \iint_{\infty} \frac{(\underset{\sim}{k} \cdot \underset{\sim}{r}')}{|\underset{\sim}{r}' - \underset{\sim}{r}|^3} \frac{\partial \underset{\sim}{v}}{\partial n} dS \tag{12}$$

But since $dS \sim |\underset{\sim}{r}' - \underset{\sim}{r}|^2$ we have

$$\iint_{\infty} \frac{1}{|\underset{\sim}{r}' - \underset{\sim}{r}|^3} \frac{\partial \underset{\sim}{v}}{\partial n} dS = 0$$

if $\frac{\partial \underset{\sim}{v}}{\partial n}$ is bounded. Equation (12) may then be written

---

*The terminology "surface at infinity" refers to the hemispherical surface in the limit as its radius approaches infinity.

$$\iint_{\infty}\left(\frac{1}{|\underset{\sim}{r}' - \underset{\sim}{r}|} - \frac{1}{|\underset{\sim}{r}' - \underset{\sim}{R}|}\right)\frac{\partial \underset{\sim}{v}}{\partial n}dS = 2(\underset{\sim}{k} \cdot \underset{\sim}{r})\iint_{\infty}\frac{\underset{\sim}{k} \cdot (\underset{\sim}{r}' - \underset{\sim}{r})}{|\underset{\sim}{r}' - \underset{\sim}{r}|^3}\frac{\partial \underset{\sim}{v}}{\partial n}dS \tag{13}$$

Thus this integral does not vanish in general unless $\frac{\partial \underset{\sim}{v}}{\partial n} = 0$ at infinity. However, if $\frac{\partial \underset{\sim}{v}}{\partial n} \neq 0$ over only a portion of the surface of finite extent above the boundary plane, $\underset{\sim}{k} \cdot \underset{\sim}{r}'$ is bounded in the region of non-zero $\frac{\partial \underset{\sim}{v}}{\partial n}$, and from Equation (12) the integral does vanish if $\frac{\partial \underset{\sim}{v}}{\partial n}$ is bounded since $dS \sim |\underset{\sim}{r}' - \underset{\sim}{r}|^2$. It is therefore assumed in the present application that $\frac{\partial \underset{\sim}{v}}{\partial n}$ is zero over the surface at infinity except on a portion of finite extent above the boundary plane, so that the integral of $\frac{\partial \underset{\sim}{v}}{\partial n}$ over the surface at infinity does vanish:

$$\iint_{\infty}\left(\frac{1}{|\underset{\sim}{r}' - \underset{\sim}{r}|} - \frac{1}{|\underset{\sim}{r}' - \underset{\sim}{R}|}\right)\frac{\partial \underset{\sim}{v}}{\partial n}dS = 0 \tag{14}$$

The integrals of $\underset{\sim}{v}$ over the surface at infinity may be combined to yield

$$\iint_{\infty}\left[\frac{(\underset{\sim}{r}' - \underset{\sim}{r}) \cdot \underset{\sim}{n}}{|\underset{\sim}{r}' - \underset{\sim}{r}|^3} - \frac{(\underset{\sim}{r}' - \underset{\sim}{R}) \cdot \underset{\sim}{n}}{|\underset{\sim}{r}' - \underset{\sim}{R}|^3}\right]\underset{\sim}{v}dS$$

$$= \iint_{\infty}\left\{\left[\frac{|\underset{\sim}{r}' - \underset{\sim}{R}|^3(\underset{\sim}{r}' - \underset{\sim}{r}) - |\underset{\sim}{r}' - \underset{\sim}{r}|^3(\underset{\sim}{r}' - \underset{\sim}{R})}{|\underset{\sim}{r}' - \underset{\sim}{r}|^3\,|\underset{\sim}{r}' - \underset{\sim}{R}|^3}\right] \cdot \underset{\sim}{n}\right\}\underset{\sim}{v}dS \tag{15}$$

The numerator may be rewritten, using Equation (5), as

$$|\underset{\sim}{r}' - \underset{\sim}{R}|^3 (\underset{\sim}{r}' - \underset{\sim}{r}) - |\underset{\sim}{r}' - \underset{\sim}{r}|^3 [(\underset{\sim}{r}' - \underset{\sim}{r}) + 2(\underset{\sim}{k} \cdot \underset{\sim}{r})\underset{\sim}{k}]$$

$$= |\underset{\sim}{r}' - \underset{\sim}{r}|^3 \{[1 + \frac{4(\underset{\sim}{k} \cdot \underset{\sim}{r})(\underset{\sim}{k} \cdot \underset{\sim}{r}')}{|\underset{\sim}{r}' - \underset{\sim}{r}|^2}]^{3/2} - 1\}(\underset{\sim}{r}' - \underset{\sim}{r})$$

$$- 2|\underset{\sim}{r}' - \underset{\sim}{r}|^3 (\underset{\sim}{k} \cdot \underset{\sim}{r})\underset{\sim}{k}$$

$$\cong |\underset{\sim}{r}' - \underset{\sim}{r}|^3 [\frac{6(\underset{\sim}{k} \cdot \underset{\sim}{r})(\underset{\sim}{k} \cdot \underset{\sim}{r}')}{|\underset{\sim}{r}' - \underset{\sim}{r}|^2}](\underset{\sim}{r}' - \underset{\sim}{r})$$

$$- 2|\underset{\sim}{r}' - \underset{\sim}{r}|^3 (\underset{\sim}{k} \cdot \underset{\sim}{r})\underset{\sim}{k} \qquad (16)$$

as $\underset{\sim}{r}'$ approaches infinity. Then using Equation (16) in Equation (15) we have

$$\iint_\infty [\frac{(\underset{\sim}{r}' - \underset{\sim}{r}) \cdot \underset{\sim}{n}}{|\underset{\sim}{r}' - \underset{\sim}{r}|^3} - \frac{(\underset{\sim}{r}' - \underset{\sim}{R}) \cdot \underset{\sim}{n}}{|\underset{\sim}{r}' - \underset{\sim}{R}|^3}]\underset{\sim}{v}dS$$

$$\cong \iint_\infty \{[\frac{6(\underset{\sim}{k} \cdot \underset{\sim}{r})(\underset{\sim}{k} \cdot \underset{\sim}{r}')(\underset{\sim}{r}' - \underset{\sim}{r})}{|\underset{\sim}{r}' - \underset{\sim}{r}|^5} - \frac{2(\underset{\sim}{k} \cdot \underset{\sim}{r})\underset{\sim}{k}}{|\underset{\sim}{r}' - \underset{\sim}{r}|^3}] \cdot \underset{\sim}{n}\}\underset{\sim}{v}dS \qquad (17)$$

But since $dS \sim |\underset{\sim}{r}' - \underset{\sim}{r}|^2$ this integral vanishes for any bounded $\underset{\sim}{v}$. Therefore

$$\iint_\infty [\frac{(\underset{\sim}{r}' - \underset{\sim}{r}) \cdot \underset{\sim}{n}}{|\underset{\sim}{r}' - \underset{\sim}{r}|^3} - \frac{(\underset{\sim}{r}' - \underset{\sim}{R}) \cdot \underset{\sim}{n}}{|\underset{\sim}{r}' - \underset{\sim}{R}|^3}]\underset{\sim}{v}dS = 0 \qquad (18)$$

Then, using Equations (9), (14), and (18), Equation (8) reduces to

$$\underset{\sim}{v}(\underset{\sim}{r}) = \frac{\underset{\sim}{k} \cdot \underset{\sim}{r}}{2\pi} \iint_{exit} \frac{\underset{\sim}{V}_j \, dS}{|\underset{\sim}{r}' - \underset{\sim}{r}|^3}$$

$$+ \frac{1}{4\pi} \iiint \left(\frac{1}{|\underset{\sim}{r}' - \underset{\sim}{r}|} - \frac{1}{|\underset{\sim}{r}' - \underset{\sim}{R}|} \right) (\underset{\sim}{\nabla} \times \underset{\sim}{\omega}) \, d\nu \qquad (19)$$

This equation reflects the following boundary conditions:

$\underset{\sim}{v} = 0$ on the plane boundary, except on the exit

$\underset{\sim}{v} = \underset{\sim}{V}_j$ on the jet exit

$\frac{\partial \underset{\sim}{v}}{\partial n} = 0$ on the surface at infinity (not including the plane boundary) except on a portion of finite vertical extent above the plane boundary.

Here it is not necessary to specify constant velocity on the jet exit. Also no assumption of constant velocity over the surface at infinity has been made. Indeed the velocity over this surface is not constant but varies on a portion of finite vertical extent above the plane boundary as a result of the viscous layer above that solid boundary.

Note that for points on the plane boundary not on the exit, $\underset{\sim}{k} \cdot \underset{\sim}{r} = 0$ and $|\underset{\sim}{r}' - \underset{\sim}{r}|$ is never zero in the integral over the exit in Equation (19). This integral, therefore, vanishes for $\underset{\sim}{r}$ on the plane boundary but not on the exit. Furthermore, $\underset{\sim}{R} = \underset{\sim}{r}$, from Equation (5), on the plane boundary, so that the volume integral of Equation (19) also vanishes for $\underset{\sim}{r}$ on the plane boundary. Equation (19) thus yields $\underset{\sim}{v} = 0$ for points on the plane boundary and not on the exit,

as expected. Points on the jet exit require a slightly different treatment.

For points on the exit the volume integral again vanishes since $\underset{\sim}{R} = \underset{\sim}{r}$. The surface integral is, however, improper, with a singularity at $\underset{\sim}{r}' = \underset{\sim}{r}$. The integral must, therefore, be evaluated by surrounding the singularity with a hemisphere as shown in Figure 63a. The integral vanishes on all of the surface except on the hemisphere since $\underset{\sim}{k} \cdot \underset{\sim}{r} = 0$. Now the combined integrals over the exit as developed in Equation (9) cannot be used for this evaluation on the hemisphere because the image point $\underset{\sim}{R}$ is now inside the field since $\underset{\sim}{R} = \underset{\sim}{r}$ here. Rather, the original two integrals, i.e., the left hand side of Equation (9) must be used. The hemisphere shown in Figure 63a then applies only to the first of these two integrals, and the construction shown in Figure 63b must be used for the second. Then for the first integral we have, referring to Figure 63a,

$$\underset{\sim}{n} = \frac{\underset{\sim}{r}' - \underset{\sim}{r}}{|\underset{\sim}{r}' - \underset{\sim}{r}|}, \quad dS = |\underset{\sim}{r}' - \underset{\sim}{r}|^2 \, d\Omega$$

so that

$$\frac{1}{4\pi} \iint_{\text{exit}} \frac{(\underset{\sim}{r}' - \underset{\sim}{r}) \cdot \underset{\sim}{n}}{|\underset{\sim}{r}' - \underset{\sim}{r}|^3} \underset{\sim}{V}_j \, dS = \lim_{|\underset{\sim}{r}' - \underset{\sim}{r}| \to 0} \frac{1}{4\pi} \int_0^{2\pi} \underset{\sim}{V}_j \, d\Omega = \frac{1}{2} \underset{\sim}{V}_j(\underset{\sim}{r}) \qquad (20)$$

For the second integral we have, from Figure 63b,

$$\underset{\sim}{n} = -\frac{\underset{\sim}{r}' - \underset{\sim}{R}}{|\underset{\sim}{r}' - \underset{\sim}{R}|}, \quad dS = |\underset{\sim}{r}' - \underset{\sim}{R}|^2 \, d\Omega$$

so that

$$\frac{1}{4\pi} \iint_{\text{exit}} \frac{(\underset{\sim}{r}' - \underset{\sim}{R}) \cdot \underset{\sim}{n}}{|\underset{\sim}{r}' - \underset{\sim}{R}|^3} \underset{\sim}{V}_j \, dS = \lim_{|\underset{\sim}{r}' - \underset{\sim}{R}| \to 0} \frac{1}{4\pi} \int_0^{2\pi} (-\underset{\sim}{V}_j) \, d\Omega = -\frac{1}{2} \underset{\sim}{V}_j(\underset{\sim}{r})$$

The two integrals together then yield

$$\frac{1}{4\pi} \iint_{\text{exit}} \left[\frac{(\underset{\sim}{r}' - \underset{\sim}{r}) \cdot \underset{\sim}{n}}{|\underset{\sim}{r}' - \underset{\sim}{r}|^3} - \frac{(\underset{\sim}{r}' - \underset{\sim}{R}) \cdot \underset{\sim}{n}}{|\underset{\sim}{r}' - \underset{\sim}{R}|^3} \right] \underset{\sim}{V}_j \, dS = \underset{\sim}{V}_j(\underset{\sim}{r}) \tag{21}$$

for $\underset{\sim}{r}$ on the exit as expected.

The form of the volume integral of Equation (19) may be modified as follows:

$$\iiint \frac{\underset{\sim}{\nabla} \times \underset{\sim}{\omega}}{|\underset{\sim}{r}' - \underset{\sim}{r}|} d\nu = \iiint \left[\underset{\sim}{\nabla} \times \frac{\underset{\sim}{\omega}}{|\underset{\sim}{r}' - \underset{\sim}{r}|} - \left(\underset{\sim}{\nabla} \frac{1}{|\underset{\sim}{r}' - \underset{\sim}{r}|} \right) \times \underset{\sim}{\omega} \right] d\nu \tag{22}$$

But

$$\iiint \underset{\sim}{\nabla} \times \frac{\underset{\sim}{\omega}}{|\underset{\sim}{r}' - \underset{\sim}{r}|} d\nu = \iint \underset{\sim}{n} \times \frac{\underset{\sim}{\omega}}{|\underset{\sim}{r}' - \underset{\sim}{r}|} dS \tag{23}$$

by a variation of Gauss' Divergence Theorem of vector analysis {69, Chapter VI}. Now the surface integral in Equation (23) must include an integral over the surface of an infinitesmal sphere surrounding the singularity of the volume integral of Equation (23) at $\underset{\sim}{r}' = \underset{\sim}{r}$. This surface integral over the sphere, however, vanishes since there

we have

$$\iint_{\text{sphere}} \underset{\sim}{n} \times \frac{\underset{\sim}{\omega}}{|\underset{\sim}{r}' - \underset{\sim}{r}|} dS = \int_0^{4\pi} - \left(\frac{\underset{\sim}{r}' - \underset{\sim}{r}}{|\underset{\sim}{r}' - \underset{\sim}{r}|}\right) \times \frac{\underset{\sim}{\omega}}{|\underset{\sim}{r}' - \underset{\sim}{r}|} |\underset{\sim}{r}' - \underset{\sim}{r}|^2 d\Omega$$

$$= - \int_0^{4\pi} (\underset{\sim}{r}' - \underset{\sim}{r}) \times \underset{\sim}{\omega} d\Omega$$

and the integrand of this integral approaches zero as $\underset{\sim}{r}' \to \underset{\sim}{r}$.

Then using Equations (22) and (23) in Equation (19), we have

$$\underset{\sim}{v}(\underset{\sim}{r}) = \frac{\underset{\sim}{k} \cdot \underset{\sim}{r}}{2\pi} \iint_{\text{exit}} \frac{\underset{\sim}{V}_j dS}{|\underset{\sim}{r}' - \underset{\sim}{r}|^3}$$

$$+ \frac{1}{4\pi} \iint_{\text{plane}} \left(\frac{1}{|\underset{\sim}{r}' - \underset{\sim}{r}|} - \frac{1}{|\underset{\sim}{r}' - \underset{\sim}{R}|}\right) (\underset{\sim}{n} \times \underset{\sim}{\omega}) dS$$

$$+ \frac{1}{4\pi} \iint_{\infty} \left(\frac{1}{|\underset{\sim}{r}' - \underset{\sim}{r}|} - \frac{1}{|\underset{\sim}{r}' - \underset{\sim}{R}|}\right) (\underset{\sim}{n} \times \underset{\sim}{\omega}) dS$$

$$+ \frac{1}{4\pi} \iiint \left(\frac{\underset{\sim}{r}' - \underset{\sim}{r}}{|\underset{\sim}{r}' - \underset{\sim}{r}|^3} - \frac{\underset{\sim}{r}' - \underset{\sim}{R}}{|\underset{\sim}{r}' - \underset{\sim}{R}|^3}\right) \times \underset{\sim}{\omega} d\nu \qquad (24)$$

Since in Equation (22)

$$\underset{\sim}{\nabla} \frac{1}{|\underset{\sim}{r}' - \underset{\sim}{r}|} = - \frac{\underset{\sim}{r}' - \underset{\sim}{r}}{|\underset{\sim}{r}' - \underset{\sim}{r}|^3}$$

the gradient being taken with respect to $\underset{\sim}{r}'$.

Now the surface integral on the plane boundary in Equation (24) vanishes since there we have $|\underset{\sim}{r}' - \underset{\sim}{R}| = |\underset{\sim}{r}' - \underset{\sim}{r}|$. The surface integral over the surface at infinity is of the same form as the left hand side of Equation (13), $\frac{\partial \underset{\sim}{v}}{\partial n}$ being replaced by $\underset{\sim}{n} \times \underset{\sim}{\omega}$. Therefore this integral vanishes if $\underset{\sim}{\omega}$ is zero on the surface at infinity (not including the plane boundary), except on a portion of finite vertical extent above the plane boundary and/or on any finite portion of the surface.

Therefore Equation (24) reduces to

$$\underset{\sim}{v}(\underset{\sim}{r}) = \frac{\underset{\sim}{k} \cdot \underset{\sim}{r}}{2\pi} \iint_{\text{exit}} \frac{\underset{\sim}{V}_j \, dS}{|\underset{\sim}{r}' - \underset{\sim}{r}|^3}$$

$$+ \frac{1}{4\pi} \iiint \left(\frac{\underset{\sim}{r}' - \underset{\sim}{r}}{|\underset{\sim}{r}' - \underset{\sim}{r}|^3} - \frac{\underset{\sim}{r}' - \underset{\sim}{R}}{|\underset{\sim}{r}' - \underset{\sim}{R}|^3} \right) \times \underset{\sim}{\omega} \, d\nu \qquad (25)$$

and this is the equivalent of Equation (19).

Specialization to Field with a Finite Closed Solid Body

With $\underset{\sim}{v} = 0$ specified on the surface of a finite closed solid boundary, Equation (1) becomes, for a bounded spherical volume centered at the origin*

$$\underset{\sim}{v}(\underset{\sim}{r}) = \frac{1}{4\pi} \iint_{\text{body}} \frac{\frac{\partial \underset{\sim}{v}}{\partial n}}{|\underset{\sim}{r}' - \underset{\sim}{r}|} dS + \frac{1}{4\pi} \iint_{\infty} \frac{\frac{\partial \underset{\sim}{v}}{\partial n}}{|\underset{\sim}{r}' - \underset{\sim}{r}|} dS$$

---

*Here the notation ∞ on the second integral implies the limit of the integral over the spherical surface as its radius approaches infinity.

$$+ \frac{1}{4\pi}\iint_{\infty}\frac{(\underset{\sim}{r}' - \underset{\sim}{r}) \cdot \underset{\sim}{n}}{|\underset{\sim}{r}' - \underset{\sim}{r}|^3}\underset{\sim}{v}dS$$

$$+ \frac{1}{4\pi}\iiint\frac{\underset{\sim}{\nabla} \times \underset{\sim}{\omega}}{|\underset{\sim}{r}' - \underset{\sim}{r}|}d\nu \qquad (26)$$

Now let $\underset{\sim}{v}$ be specified to be constant and $\frac{\partial \underset{\sim}{v}}{\partial n}$ to be zero on the surface at infinity.* Then the second surface integral above vanishes and the third becomes

$$\frac{1}{4\pi}\iint_{\infty}\frac{(\underset{\sim}{r}' - \underset{\sim}{r}) \cdot \underset{\sim}{n}}{|\underset{\sim}{r}' - \underset{\sim}{r}|^3}\underset{\sim}{v}dS = \frac{\underset{\sim}{V}_{\infty}}{4\pi}\iint_{\infty}\frac{(\underset{\sim}{r}' - \underset{\sim}{r}) \cdot \underset{\sim}{n}}{|\underset{\sim}{r}' - \underset{\sim}{r}|^3}dS \qquad (27)$$

where $\underset{\sim}{V}_{\infty}$ is the constant value of $\underset{\sim}{v}$ at infinity. No loss of generality is incurred by taking the surface at infinity to be spherical about the point $\underset{\sim}{r}$. Then

$$\underset{\sim}{n} = \frac{\underset{\sim}{r}' - \underset{\sim}{r}}{|\underset{\sim}{r}' - \underset{\sim}{r}|} \text{ and } dS = |\underset{\sim}{r}' - \underset{\sim}{r}|^2 d\Omega$$

so that the integral becomes

$$\frac{1}{4\pi}\iint_{\infty}\frac{(\underset{\sim}{r}' - \underset{\sim}{r}) \cdot \underset{\sim}{n}}{|\underset{\sim}{r}' - \underset{\sim}{r}|^3}\underset{\sim}{v}dS = \frac{\underset{\sim}{V}_{\infty}}{4\pi}\int_0^{4\pi} d\Omega = \underset{\sim}{V}_{\infty} \qquad (28)$$

Equation (26) then reduces to

$$\underset{\sim}{v}(\underset{\sim}{r}) = \frac{1}{4\pi}\iint_{\text{body}}\frac{\frac{\partial \underset{\sim}{v}}{\partial n}}{|\underset{\sim}{r}' - \underset{\sim}{r}|}dS + \frac{1}{4\pi}\iiint\frac{\underset{\sim}{\nabla} \times \underset{\sim}{\omega}}{|\underset{\sim}{r}' - \underset{\sim}{r}|}d\nu + \underset{\sim}{V}_{\infty} \qquad (29)$$

*The terminology "surface at infinity" refers to the spherical surface in the limit as its radius approaches infinity. The normal derivative must approach zero at least as fast as the inverse square of the radius.

But by Equations (22) and (23) the volume integral may be written

$$\iiint \frac{\nabla \times \omega}{|r' - r|} d\nu = \iint \frac{n \times \omega}{|r' - r|} dS + \iiint \frac{(r' - r)}{|r' - r|^3} \times \omega d\nu \qquad (30)$$

and since $\omega = 0$ on the surface at infinity*, Equation (29) may then be rewritten as

$$v(r) = V_\infty + \frac{1}{4\pi} \iint_{body} \frac{\frac{\partial v}{\partial n} + n \times \omega}{|r' - r|} dS + \frac{1}{4\pi} \iiint \frac{(r' - r)}{|r' - r|^3} \times \omega d\nu \qquad (31)$$

But

$$\frac{\partial v}{\partial n} + n \times \omega = (n \cdot \nabla) v + n \times (\nabla \times v)$$

$$= [\nabla(n \cdot v) - (v \cdot \nabla) n - n \times (\nabla \times v) - v \times (\nabla \times n)]$$

$$+ n \times (\nabla \times v) \qquad (32)$$

Then, since $v = 0$ on the body surface, we have

$$\frac{\partial v}{\partial n} + n \times \omega = \nabla (n \cdot v) = \nabla v_n \qquad (33)$$

on the body surface. Here v_n is the velocity component normal to the body surface. Now the continuity equation

$$\nabla \cdot v = 0 \qquad (34)$$

may be expressed in orthogonal curvilinear coordinates as

---

*Specifically, the vorticity must approach zero at least as fast as the inverse square of the radius.

{69, Chapter VII},

$$\frac{\partial}{\partial x_1}(h_2 h_3 v_1) + \frac{\partial}{\partial x_2}(h_1 h_3 v_2) + \frac{\partial}{\partial x_3}(h_1 h_2 v_3) = 0 \qquad (35)$$

where the h's are the scale factors in the respective directions, i.e.,

$$h_i \equiv \left| \frac{\partial \underset{\sim}{r}}{\partial x_i} \right| \qquad i = 1, 2, 3$$

Let the x_3 direction be defined as normal to the body surface. Then since $\underset{\sim}{v} = 0$ on the body surface we have

$$v_1 = v_2 = v_3 = \frac{\partial v_1}{\partial x_1} = \frac{\partial v_2}{\partial x_2} = 0$$

on the body surface. Then

$$\frac{\partial}{\partial x_1}(h_2 h_3 v_1) = v_1 \frac{\partial}{\partial x_1}(h_2 h_3) + h_2 h_3 \frac{\partial v_1}{\partial x_1} = 0$$

on the body surface. Similarly,

$$\frac{\partial}{\partial x_2}(h_1 h_3 v_2) = 0$$

on the body surface. Then Equation (35) reduces to

$$\frac{\partial}{\partial x_3}(h_1 h_2 v_3) = 0 \qquad (36)$$

on the body surface. But $v_3 = 0$ also on the body surface so that Equation (36) implies that

$$\frac{\partial v_3}{\partial x_3} = 0 \tag{37}$$

on the body surface as well. Also since $v_3 = 0$ on the body surface

$$\frac{\partial v_3}{\partial x_1} = \frac{\partial v_3}{\partial x_2} = 0$$

on the body surface, or finally

$$\underset{\sim}{\nabla} v_n = 0 \tag{38}$$

on the body surface for any shape surface. Therefore by Equation (33)

$$\frac{\partial \underset{\sim}{v}}{\partial n} + \underset{\sim}{n} \times \underset{\sim}{\omega} = 0 \tag{39}$$

on a body surface of any general shape.

Equation (31) then reduces to

$$\underset{\sim}{v}(\underset{\sim}{r}) = \underset{\sim}{V}_\infty + \frac{1}{4\pi}\iiint \frac{(\underset{\sim}{r}' - \underset{\sim}{r})}{|\underset{\sim}{r}' - \underset{\sim}{r}|^3} \times \underset{\sim}{\omega} d\nu \tag{40}$$

Reduction of Volume Integral in Two-Dimensional Flow

If $\underset{\sim}{\omega}$ is invarient in the z direction we have

$$\iiint \frac{(\underset{\sim}{r}' - \underset{\sim}{r}) \times \underset{\sim}{\omega}}{|\underset{\sim}{r}' - \underset{\sim}{r}|^3} d\nu = \int_{-\infty}^{\infty} dz' \iint_{xy\text{-plane}} dS \frac{(\underset{\sim}{r}' - \underset{\sim}{r}) \times \underset{\sim}{\omega}(x', y')}{|\underset{\sim}{r}' - \underset{\sim}{r}|^3}$$

$$= - \iint_{xy\text{-plane}} dS \underset{\sim}{\omega}(x', y') \times \int_{-\infty}^{\infty} \frac{(\underset{\sim}{r}' - \underset{\sim}{r})}{|\underset{\sim}{r}' - \underset{\sim}{r}|^3} dz' \qquad (41)$$

But

$$\int_{-\infty}^{\infty} \frac{(\underset{\sim}{r}' - \underset{\sim}{r}) dz'}{|\underset{\sim}{r}' - \underset{\sim}{r}|^3} = \int_{-\infty}^{\infty} \frac{\underset{\sim}{i}(x' - x) + \underset{\sim}{j}(y' - y) + kz'}{[(x' - x)^2 + (y' - y)^2 + z'^2]^{3/2}} dz'$$

$$= [\underset{\sim}{i}(x' - x) + j(y' - y)] \cdot \int_{-\infty}^{\infty} \frac{dz'}{[(x' - x)^2 + (y' - y)^2 + z'^2]^{3/2}}$$

$$- \underset{\sim}{k} \int_{-\infty}^{\infty} \frac{z' dz'}{[(x' - x)^2 + (y' - y)^2 + z'^2]^{3/2}} \qquad (42)$$

The last integral vanishes since the integrand is odd. The remaining integration may be performed with the result

$$\int_{-\infty}^{\infty} \frac{dz'}{[(x' - x)^2 + (y' - y)^2 + z'^2]^{3/2}}$$

$$= \frac{1}{(x' - x)^2 + (y' - y)^2} \frac{z'}{[(x' - x)^2 + (y' - y)^2 + z'^2]^{1/2}} \Bigg|_{-\infty}^{\infty}$$

$$= \frac{2}{(x' - x)^2 + (y' - y)^2} \qquad (43)$$

Then

$$\int_{-\infty}^{\infty} \frac{(\underset{\sim}{r}' - \underset{\sim}{r})}{|\underset{\sim}{r}' - \underset{\sim}{r}|^3} dz' = 2 \frac{\underset{\sim}{i}(x' - x) + \underset{\sim}{j}(y' - y)}{(x' - x)^2 + (y' - y)^2} \tag{44}$$

and

$$\iiint \frac{(\underset{\sim}{r}' - \underset{\sim}{r}) \times \underset{\sim}{\omega}}{|\underset{\sim}{r}' - \underset{\sim}{r}|^3} d\nu = 2 \iint_{xy\text{-plane}} \frac{[\underset{\sim}{i}(x' - x) + \underset{\sim}{j}(y' - y)] \times \underset{\sim}{\omega}(x', y')}{(x' - x)^2 + (y' - y)^2} dS \tag{45}$$

Then, with $\underset{\sim}{r}'$ restricted to the x-y plane, Equation (40) becomes

$$\underset{\sim}{v}(\underset{\sim}{r}) = \underset{\sim}{V}_\infty + \frac{1}{2\pi} \iint \frac{(\underset{\sim}{r}' - \underset{\sim}{r})}{|\underset{\sim}{r}' - \underset{\sim}{r}|^2} \times \underset{\sim}{\omega} dS \tag{46}$$

Reduction of Volume Integral in One-Dimensional Flow

If $\underset{\sim}{\omega}$ is invariant in the x and y directions we have

$$\iiint \frac{(\underset{\sim}{r}' - \underset{\sim}{r}) \times \underset{\sim}{\omega}}{|\underset{\sim}{r}' - \underset{\sim}{r}|^3} d\nu = \int_0^\infty dz' \int_{-\infty}^{\infty} dx' \int_{-\infty}^{\infty} dy' \frac{(\underset{\sim}{r}' - \underset{\sim}{r}) \times \underset{\sim}{\omega}(z')}{|\underset{\sim}{r}' - \underset{\sim}{r}|^3}$$

$$= - \int_0^\infty dz' \, \underset{\sim}{\omega}(z') \times \int_{-\infty}^{\infty} dx' \int_{-\infty}^{\infty} dy' \frac{(\underset{\sim}{r}' - \underset{\sim}{r})}{|\underset{\sim}{r}' - \underset{\sim}{r}|^3} \tag{47}$$

Now

$$\int_{-\infty}^{\infty} \int_{-\infty}^{\infty} \frac{(\underset{\sim}{r}' - \underset{\sim}{r})}{|\underset{\sim}{r}' - \underset{\sim}{r}|^3} dx' dy' = \int_{-\infty}^{\infty} \int_{-\infty}^{\infty} \frac{\underset{\sim}{i}\, x' + \underset{\sim}{j}\, y' + \underset{\sim}{k}(z' - z)}{[x'^2 + y'^2 + (z' - z)^2]^{3/2}} dx' dy' \tag{48}$$

But the $\underset{\sim}{i}$ and $\underset{\sim}{j}$ components of this integral vanish because of odd integrands. Therefore,

$$\int_{-\infty}^{\infty}\int_{-\infty}^{\infty}\frac{(\underset{\sim}{r}' - \underset{\sim}{r})}{|\underset{\sim}{r}' - \underset{\sim}{r}|^3}dx'dy'$$

$$= \underset{\sim}{k}(z' - z)\int_{-\infty}^{\infty}\int_{-\infty}^{\infty}\frac{dx'dy'}{[x'^2 + y'^2 + (z' - z)^2]^{3/2}}$$

$$= \underset{\sim}{k}(z' - z)\int_{-\infty}^{\infty}\frac{1}{y'^2 + (z' - z)^2}\ \frac{x'}{[x'^2 + y'^2 + (z' - z)^2]^{1/2}}\Bigg|_{-\infty}^{\infty}dy'$$

$$= 2\underset{\sim}{k}(z' - z)\int_{-\infty}^{\infty}\frac{dy'}{y'^2 + (z' - z)^2}$$

$$= 2\underset{\sim}{k}(z' - z)\frac{1}{|z' - z|}\tan^{-1}\left(\frac{y'}{|z' - z|}\right)\Bigg|_{-\infty}^{\infty}$$

$$= 2\pi\underset{\sim}{k}\frac{z' - z}{|z' - z|} \qquad (49)$$

Since $\underset{\sim}{r}' - \underset{\sim}{R}$ differs from $\underset{\sim}{r}' - \underset{\sim}{r}$ only in the sign of z, we have immediately that

$$\int_{-\infty}^{\infty}\int_{-\infty}^{\infty}\frac{(\underset{\sim}{r}' - \underset{\sim}{R})}{|\underset{\sim}{r}' - \underset{\sim}{R}|^3}dx'dy' = 2\pi\underset{\sim}{k}\frac{z' + z}{|z' + z|} = 2\pi\underset{\sim}{k} \qquad (50)$$

Then

$$\iiint \frac{(\underset{\sim}{r}' - \underset{\sim}{r}) \times \underset{\sim}{\omega}}{|\underset{\sim}{r}' - \underset{\sim}{r}|^3} d\nu = 2\pi \int_0^\infty \frac{z' - z}{|z' - z|} (\underset{\sim}{k} \times \underset{\sim}{\omega}) dz'$$

$$= -2\pi \int_0^z (\underset{\sim}{k} \times \underset{\sim}{\omega}) dz' + 2\pi \int_z^\infty (\underset{\sim}{k} \times \underset{\sim}{\omega}) dz' \qquad (51)$$

and

$$\iiint \frac{(\underset{\sim}{r}' - \underset{\sim}{R}) \times \underset{\sim}{\omega}}{|\underset{\sim}{r}' - \underset{\sim}{R}|^3} d\nu = 2\pi \int_0^\infty (\underset{\sim}{k} \times \underset{\sim}{\omega}) dz' \qquad (52)$$

Then, using Equations (51) and (52),

$$\iiint \left(\frac{\underset{\sim}{r}' - \underset{\sim}{r}}{|\underset{\sim}{r}' - \underset{\sim}{r}|^3} - \frac{\underset{\sim}{r}' - \underset{\sim}{R}}{|\underset{\sim}{r}' - \underset{\sim}{R}|^3} \right) \times \underset{\sim}{\omega} d\nu = -4\pi \int_0^z (\underset{\sim}{k} \times \underset{\sim}{\omega}) dz' \qquad (53)$$

If the velocity is zero on the infinite plane at z = 0, Equation (25) then reduces to

$$\underset{\sim}{v}(z) = -\int_0^z (\underset{\sim}{k} \times \underset{\sim}{\omega}) dz' = -\underset{\sim}{k} \times \int_0^z \underset{\sim}{\omega} dz' \qquad (54)$$

If, however, the plane is in motion at velocity $\underset{\sim}{V}_\infty$ then, reading "plane" for "exit" and "$\underset{\sim}{V}_\infty$" for "$\underset{\sim}{V}_j$" in Equation (25), the first integral therein becomes

$$\frac{\underset{\sim}{k} \cdot \underset{\sim}{r}}{2\pi} \iint_{\text{plane}} \frac{\underset{\sim}{V}_\infty dS}{|\underset{\sim}{r}' - \underset{\sim}{r}|^3}$$

$$= \underset{\sim}{V}_{\infty} \frac{z}{2\pi} \int_{-\infty}^{\infty} \int_{-\infty}^{\infty} \frac{dx'dy'}{[(x' - x)^2 + (y' - y)^2 + z^2]^{3/2}}$$

$$= \underset{\sim}{V}_{\infty} \frac{z}{2\pi} \frac{2\pi}{z} = \underset{\sim}{V}_{\infty} \tag{55}$$

the integration being the same as that performed above in Equation (49). Therefore Equation (25) reduces in this case to

$$\underset{\sim}{v}(z) = \underset{\sim}{V}_{\infty} - \underset{\sim}{k} \times \int_{o}^{z} \underset{\sim}{\omega} dz' \tag{56}$$

If the non-zero component of $\underset{\sim}{\omega}$ is $\underset{\sim}{j}\eta$ this reduces to

$$u(z) = V_{\infty} + \int_{o}^{z} \eta dz' \tag{57}$$

APPENDIX C

CATALOGING OF CELLS WITH NON-ZERO VORTICITY

Since only the cells with non-zero vorticity, hereafter referred to as "vortex cells"* for purposes of identification, are to be stored, it is necessary to catalog the vortex cells in a manner which will allow the determination of which, if any, vortex cells are adjacent to any given cell. The convenience of subscript notation, by which an adjacent cell can be identified by simply incrementing a subscript, is not available here, since its use would require storing an array containing all points in the field, thus defeating the purpose of confining the storage to the points with non-zero vorticity.

Each vortex cell is assigned a number, beginning with 1, when it is created, and it retains the same number for all time. The vorticity and velocity of each cell are subscripted with the cell number and stored in one-dimensional arrays. The cataloging procedure then provides a means of determining the number of the vortex cell located at any given location in the field. The second function of the cataloging procedure is to create a layer of border* cells, one

---

*Vortex cells, border cells, and the aggregate of vortex cells are defined in Chapter II.

cell in thickness, surrounding the aggregate* of vortex cells. It is only these border cells that have the possibility of becoming vortex cells, i.e., acquiring non-zero vorticity, at the next time step. Since the border cells have zero vorticity, cell numbers are not assigned to them, and no values of vorticity or velocity are stored for them.

Two-Dimensional Catalog

Catalog Procedure

The cell numbers, L, of the vortex cells are arranged in a one-dimensional array, TCEL (LE), in columns of cells having the same Y-coordinate, the columns being placed in the array successively according to ascending Y-values. Within each column the cells are arranged successively according to ascending X-values. The border cells are located between each of the columns in the array. This is illustrated in Figure 64. Here the vortex cells are enclosed by the heavy line and the border cells by the dotted line. The center numbers are the vortex cell numbers, L, which are permanent and occur in order of creation and not by position, and the corner numbers refer to the position, LE, in the array TCEL. Thus TCEL (3) = 10, TCEL (8) = 8, TCEL (9) = 9, TCEL (10) = 11, TCEL (24) = 6, etc. A common value NWJ is stored in the

---

*Vortex cells, border cells, and the aggregate of vortex cells are defined in Chapter II.

positions in the array TCEL corresponding to border cells, e.g., TCEL (1) = NWJ, TCEL (2) = NWJ, TCEL (4) = NWJ, TCEL (26) = NWJ, etc.

Finally the difference between the X-coordinate of the first border cell in each column and the position of that cell in the array TCEL is stored against the column number, J, in an array TXMIN (J), e.g., TXMIN (3) = 5 - 1 = 4, TXMIN (7) = 2 - 18 = - 16, etc. The cell number of a cell with X and Y-coordinates I and J, respectively, can then be determined in two steps. First the operation LE = I - TXMIN (J) gives the position, LE, of the cell in the array TCEL. The cell number, L, is then immediately available from L = TCEL (LE). For example, consider the cell with coordinates I = 4, J = 7. As noted above, TXMIN (7) = - 16 so that LE = 4 - (- 16) = 20. Then L = TCEL (20) = 2, which is the cell number of the cell at X = 4, Y = 7 in the figure. These two steps will produce the value NWJ, common to all border cells, if the coordinates are those of a border cell.

In addition, the position in the array TCEL of the first vortex cell in each column is stored against the column number, J (which is equal to the Y-coordinate), in an array TCϕL 1 (J). Similarly the positions in the array TCEL of the first border cell in each column and the first border cell after the vortex cells in each column are stored against the column number in the arrays TCϕL (J) and TCϕL 2 (J),

respectively. Thus, TCϕL (5) = 6, TCϕL 1 (5) = 8, TCϕL 2 (5) = 11, etc. For columns containing no vortex cells, a common value is stored in TCϕL 1 and TCϕL 2. Thus TCϕL 1 (1) = TCϕL 2 (1) and TCϕL 1 (9) = TCϕL 2 (9), etc. This procedure is followed throughout.

Comparison of Storage Requirements

The storage requirements then are four arrays (TCϕL, TCϕL 1, TCϕL 2, TXMIN) of dimension equal to the maximum lateral (perpendicular to the free stream) extent of non-zero vorticity, one array (TCEL) of dimension equal to the maximum number of vortex cells and border cells, and six arrays for velocity and vorticity of dimension equal to the maximum number of vortex cells. All these arrays are one-dimensional. By contrast, conventional storing of the entire field would require only the six arrays for velocity and vorticity, but they would be two-dimensional arrays of dimension equal to the number of points in the entire field.

For example, consider a typical arrangement using a 100 x 50 field (5000 points). It is reasonable that only a fourth of these points would have sufficient vorticity to be considered vortex cells, and the lateral extent of these cells would likely be no more than half the lateral field extent. With 1250 vortex cells there would be about 125 border cells. The storage required by the two schemes is

Only Vortex Cells Stored	Entire Field Stored
4 x 25 = 100	6 x 5,000 = 30,000
1 x 1375 = 1375	
6 x 1250 = 7500	
8975	

The saving in storage achieved by storing only the cells with non-zero vorticity is thus quite significant and becomes even more so for larger fields.

Three-Dimensional Catalog

Catalog Procedure

The three-dimensional cataloging procedure is an extension of the two-dimensional procedure with the cell number, L, of the vortex cells arranged in a one-dimensional array, CEL (LE), in columns of cells having the same Y and Z coordinates. The columns are numbered consecutively in order of creation and are placed in the array in groups of columns having the same Z coordinates, the groups being ordered successively according to ascending Z values. The columns within each group and the cells within each column are arranged successively according to ascending Y and X values, respectively. Again border cells are located between each of the columns in the array. In addition border columns, i.e., columns composed exclusively of border cells, are located between each of the groups of columns in the array.

Finally the differences between the Y-coordinate of the first border column in each group and the number of that column are stored against the group number, K, in an array YMIN (K).

The cell number of a cell with coordinates I, J, K then can be determined in three steps. First, C = J - YMIN (K) gives the number of the column containing the cell. Then, LE = I - XMIN (C) gives the position of the cell in the array CEL. The cell number is then immediately available from L = CEL (LE).

The position in the array CEL of the first vortex cell in each column is again stored against the column number (now designated C and not being related to the Y-coordinate as in two dimensions) in an array CϕL 1 (C). Similarly the positions in the array CEL of the first border cell in each column and the first border cell after the vortex cells in each column are stored against the column number in the arrays CϕL (C) and CϕL 2 (C), respectively. The difference between the X-coordinate of the first border cell in each column and the position of that cell in the array CEL is stored against the column number, C, in an array XMIN (C).

In turn, the number of the first vortex column, i.e., column containing vortex cells, in each group of columns is stored against the group number, K, which is equal to the Z-coordinate, in an array PLA 1 (K). Similarly, the numbers

of the first border column in each group and the first border column after the vortex columns in each group are stored against the group number in the arrays PLA (K) and PLA 2 (K), respectively. This procedure is followed throughout the three-dimensional catalog.

Comparison of Storage Requirements

The storage requirements are then four arrays (CϕL, CϕL 1, CϕL 2, XMIN) of dimension equal to the maximum number of vortex and border columns, four arrays (PLA, PLA 1, PLA 2, YMIN) of dimension equal to the maximum extent of non-zero vorticity in the Z-direction, one array (CEL) of dimension equal to the maximum number of vortex and border cells, and six arrays for velocity and vorticity of dimension equal to the maximum number of vortex cells. Again all these arrays are one-dimensional.

The storage economy is even greater in three dimensions. Continuing the previous example, let there be 50 steps in the Z-direction also. Then the total number of points in the field is 5,000 x 50 = 250,000. In three dimensions it is reasonable to assume that the proportion of cells with significant vorticity will be less than in two dimensions, say one-tenth. Then with 25,000 vortex cells, 2500 border cells, and 500 columns we have, assuming extent in the Z-direction no more than half the field,

Only Vortex Cells Stored			Entire Field Stored
4	x 500	= 2,000	6 x (250,000) =
4	x 25	= 100	1,500,000
1	x 27,500	= 27,500	
6	x 25,000	= 150,000	
		179,600	

APPENDIX D

DIFFERENCE EQUATIONS AND TRUNCATION ERROR

Two-Dimensional Solid Cylinder

Straight Explicit Form

The time derivative is approximated by a two-point forward difference expression,

$$\frac{\partial \zeta}{\partial t} \sim \frac{\zeta_{i,j}^{n+1} - \zeta_{i,j}^{n}}{\Delta t} \qquad (1)^*$$

and the space derivatives by three-point central difference expressions, of which the following are representative:

$$\frac{\partial \zeta}{\partial x} \sim \frac{\zeta_{i+1,j}^{n} - \zeta_{i-1,j}^{n}}{2(1)} \qquad (2)$$

$$\frac{\partial^2 \zeta}{\partial x^2} \quad \frac{\zeta_{i+1,j}^{n} - 2\zeta_{i,j}^{n} + \zeta_{i-1,j}^{n}}{(1)^2} \qquad (3)$$

(The nondimensional spacial mesh width is equal to unity since the mesh width has been taken as the reference length.) Substitutions of these forms in Equation (IV - 3) yields the straight explicit difference equation (IV - 5).

Expansion of each of the above values of ζ by Taylor

---

*All quantities in this appendix are nondimensionalized as noted in the Nomenclature except as specifically noted here.

series after substitution in Equation (IV - 3) yields an expression for the truncation error, i.e., the amount by which the solution of the differential equation (IV - 3) fails to satisfy the difference equation (IV - 5):

$$\tau = -\frac{1}{2}\left[\frac{\partial^2 \zeta}{\partial t^2}\right]\Delta t - \frac{1}{6}\left[\frac{\partial^3 (u\zeta)}{\partial x^3} + \frac{\partial^3 (v\zeta)}{\partial y^3}\right] + \frac{1}{12R_c}\left[\frac{\partial^4 \zeta}{\partial x^4} + \frac{\partial^4 \zeta}{\partial y^4}\right] \qquad (4)$$

the derivatives being evaluated at some point in the calculation field. This is the nondimensional truncation error, with the cell size as the reference length, and all quantities on the right are likewise nondimensional. A clearer statement of the expected error is given by converting Equation (4) to dimensional form:

$$\tau = -\frac{1}{2}\left[\frac{\partial^2 \zeta}{\partial t^2}\right]\Delta t - \frac{1}{6}\left[\frac{\partial^3 (u\zeta)}{\partial x^3} + \frac{\partial^3 (v\zeta)}{\partial y^3}\right]h^2 + \frac{\nu}{12}\left[\frac{\partial^4 \zeta}{\partial x^4} + \frac{\partial^4 \zeta}{\partial y^4}\right]h^2 \qquad (5)$$

where all quantities are dimensional. The dimensional truncation error thus approaches zero with the time and spacial step sizes. This is true regardless of the manner in which the limits are approached.

Dufort-Frankel Form

The time derivative is approximated by a three-point central difference expression:

$$\frac{\partial \zeta}{\partial t} \sim \frac{\zeta_{i,j}^{n+1} - \zeta_{i,j}^{n-1}}{2\Delta t} \qquad (6)$$

The spacial derivatives are again approximated by three-point central difference expressions as in Equations (2) and (3), but with the $\zeta^n_{i,j}$ of Equation (3) expressed as a time average:

$$\zeta^n_{i,j} = \frac{1}{2}(\zeta^{n+1}_{i,j} + \zeta^{n-1}_{i,j}) \tag{7}$$

Substitution of these forms in Equation (IV - 3) yields the Dufort-Frankel difference equation (IV - 6).

The dimensionless truncation error obtained in the manner prescribed above is (all quantities here being non-dimensional)

$$\tau = -2\left[\frac{\Delta t}{R_c}\frac{\partial^2\zeta}{\partial t^2}\right]\Delta t - \frac{1}{6}\left[\frac{\partial^3(u\zeta)}{\partial x^3} + \frac{\partial^3(v\zeta)}{\partial y^3}\right] + \frac{1}{12R_c}\left[\frac{\partial^4\zeta}{\partial x^4} + \frac{\partial^4\zeta}{\partial y^4}\right] \tag{8}$$

The dimensional truncation error is then, with dimensional quantities,

$$\tau = -2\left[\frac{\Delta t}{h^2}\frac{\partial^2\zeta}{\partial t^2}\right]\Delta t - \frac{1}{6}\left[\frac{\partial^3(u\zeta)}{\partial x^3} + \frac{\partial^3(v\zeta)}{\partial y^3}\right]h^2 + \frac{\nu}{12}\left[\frac{\partial^4\zeta}{\partial x^4} + \frac{\partial^4\zeta}{\partial y^4}\right]h^2 \tag{9}$$

Thus the truncation error vanishes as Δt and h approach zero with a constant ratio $\frac{\Delta t}{h^2}$.

Infinite Jet in Cross-Wind

Straight Explicit Form

With the time derivatives approximated by two-point forward difference expressions, and the space derivatives by three-point central difference expressions as in Equations (1) - (3), Equation (V - 3) is approximated by the straight explicit difference equation (V - 5). The dimensional truncation error is

$$\tau_\xi = -\frac{1}{2}\left[\frac{\partial^2 \xi}{\partial t^2}\right]\Delta t + \frac{1}{6}\left[\frac{\partial^3 (u\eta)}{\partial y^3} - \frac{\partial^3 (v\xi)}{\partial y^3}\right]h^2 + \frac{\nu}{12}\left[\frac{\partial^4 \xi}{\partial x^4} + \frac{\partial^4 \xi}{\partial y^4}\right]h^2 \tag{10a}$$

$$\tau_\eta = -\frac{1}{2}\left[\frac{\partial^2 \eta}{\partial t^2}\right]\Delta t + \frac{1}{6}\left[\frac{\partial^3 (v\xi)}{\partial x^3} - \frac{\partial^3 (u\eta)}{\partial x^3}\right]h^2 + \frac{\nu}{12}\left[\frac{\partial^4 \eta}{\partial x^4} + \frac{\partial^4 \eta}{\partial y^4}\right]h^2 \tag{10b}$$

$$\tau_\zeta = -\frac{1}{2}\left[\frac{\partial^2 \zeta}{\partial t^2}\right]\Delta t + \frac{1}{6}\left[\frac{\partial^3 (w\xi)}{\partial x^3} - \frac{\partial^3 (u\zeta)}{\partial x^3} - \frac{\partial^3 (v\zeta)}{\partial y^3} + \frac{\partial^3 (w\eta)}{\partial y^3}\right]h^2 + \frac{\nu}{12}\left[\frac{\partial^4 \zeta}{\partial x^4} + \frac{\partial^4 \zeta}{\partial y^4}\right]h^2 \tag{10c}$$

where all quantities are dimensional. The dimensionless form may be easily inferred by comparison with Equations (4) and (5). Again the truncation error approaches zero with the space and time steps.

Dufort-Frankel Form

With the time derivatives approximated by three-point

central difference expressions, and the space derivatives by three-point central difference expressions with the time averaging of the central term as in Equations (6), (2), (3), and (7), Equations (V - 3) are approximated by the Dufort-Frankel difference equations (V - 6). The dimensional truncation error is the same as that given by Equation (10) except that the factor $\frac{1}{2}$ of the time-derivative term is replaced by the factor $2\frac{\Delta t}{h^2}$ and all quantities are considered dimensional.

Three-Dimensional Jet in Cross-Wind

With the time derivatives approximated by two-point forward difference expressions, and the space derivatives by three-point central difference expressions as in Equations (1) - (3), Equations (VI - 16) are approximated by the straight explicit difference equations (VI - 19). The dimensional truncation error is

$$\tau_\xi = -\frac{1}{2}\left[\frac{\partial^2 \xi}{\partial t^2}\right]\Delta t + \frac{1}{6}\left[\frac{\partial^3 C_z}{\partial y^3} - \frac{\partial^3 C_y}{\partial z^3}\right]h^2 + \frac{\nu}{12}\left[\frac{\partial^4 \xi}{\partial x^4} + \frac{\partial^4 \xi}{\partial y^4} + \frac{\partial^4 \xi}{\partial z^4}\right]h^2 \qquad (11a)$$

$$\tau_\eta = -\frac{1}{2}\left[\frac{\partial^2 \eta}{\partial t^2}\right]\Delta t + \frac{1}{6}\left[\frac{\partial^3 C_x}{\partial z^3} - \frac{\partial^3 C_z}{\partial x^3}\right]h^2 + \frac{\nu}{12}\left[\frac{\partial^4 \eta}{\partial x^4} + \frac{\partial^4 \eta}{\partial y^4} + \frac{\partial^4 \eta}{\partial z^4}\right]h^2 \qquad (11b)$$

$$\tau_\zeta = -\frac{1}{2}\left[\frac{\partial^2 \zeta}{\partial t^2}\right]\Delta t + \frac{1}{6}\left[\frac{\partial^3 C_y}{\partial x^3} - \frac{\partial^3 C_x}{\partial y^3}\right]h^2 + \frac{\nu}{12}\left[\frac{\partial^4 \zeta}{\partial x^4} + \frac{\partial^4 \zeta}{\partial y^4} + \frac{\partial^4 \zeta}{\partial z^4}\right]h^2$$

all quantities being dimensional.

APPENDIX E

EVALUATION OF SOLID SURFACE BOUNDARY TREATMENTS

Representation of Convection in Boundary Cells

The velocity actually calculated from Equation (IV - 7) in the boundary cells* is not zero since the boundary cells, being square, cannot represent the true curved boundary exactly and some lie well out into the fluid, containing only a small portion of the surface. This is true even for the initial solution. There arises then the question as to whether this actual calculated velocity should properly be used in the convective terms of Equation (IV - 6), or whether a zero velocity should be substituted. This velocity influences the calculation of the vorticity in both the boundary cells and the adjacent layer of cells.

Referring to Figure (65) and Equation (IV - 6), the calculation of the vorticity in the fluid at points 1 and 4 involves the product of the vorticity and y-velocity in the boundary cells at points 2 and 5, respectively, this product representing convection of vorticity across the interface between the points involved.

Similarly, the calculation of the vorticity in the boundary cells at 2 and 5 involves the product of the

---

*Boundary cells are defined in Chapter II.

vorticity and y-velocity at points 1 and 3 and at points 4 and 6, respectively. Now there is obviously no convection between points 3 and 2, since the interface between is in the solid wall. Therefore, the above-mentioned product at point 3 is omitted in the calculation in the boundary cell at 2. The inclusion of the product at point 6 implies convection across the interface between 5 and 6.

The presence of non-zero velocity in the boundary cells at points 2, 5, and 6 thus admits several alternatives in the representation of convection near the boundary. Five alternatives for the convective terms were evaluated in the course of this study and are discussed below in the light of the above explanation and Figure 65. These convection schemes were compared using diffusion scheme A, surface vorticity scheme A, and corner scheme A, as defined in later sections. The effects of each of these schemes are in turn evaluated below.

Convection Scheme A - Use of Zero Velocity in Boundary Cells

The use of zero velocity in the boundary cells causes the above-mentioned products at points 2, 5, and 6 in Figure 65 to be zero, so that the cells at 1 and 4 experience no convection with the cells at 2 and 5. However, the cells at 2 and 5 still experience convection with the cells at 1 and 4 since the products in the latter cells are unaffected. This is an anomalous situation, since the convection into

any cell certainly must be supplied by the adjacent cell. In the present solution the boundary cells do contain fluid, and convection to or from them is not unphysical. This alternative then is not as attractive as it might seem at first thought.

With this scheme the vorticity generated at the surface must move from the boundary cells to the adjacent layer of cells by pure diffusion before it can be convected into the remainder of the fluid. While this in itself is not unphysical in a continuous field, it becomes unrealistic in the discretetized field necessary in numerical solution, for at high Reynolds numbers the diffusion becomes insufficient to transmit the vorticity generated at the surface to the adjacent layer of cells unless the cell size is extremely small. This vorticity thus never becomes available for convection downstream, so that no wake forms and the flow remains essentially unchanged from the potential flow that existed at the start. The results of this scheme at a cylinder Reynolds number of 12,000 at a time well beyond the expected onset of separation and vortex formation showed no vortices.

While the failure of this scheme to represent the flow accurately at high Reynolds number is due partly to the inadequate representation of the thin boundary layer by the finite grid, it has been shown by several investigators

{21, 23, 24} that numerical solutions can represent the wake accurately, including the formation and shedding of vortices, even when the grid is too coarse to represent the boundary layer. If the boundary layer is thinner than the cell size, the numerical solution should incorporate an average effect of the boundary layer on the fluid in general into the first layer of cells—here the boundary cells. Since the effect of the boundary layer is to make the vorticity generated at the surface available for convection downstream, it follows that in the present solution the boundary cells must be capable of representing the overall effect of the boundary layer, and that there must therefore be convection from the boundary cells to the adjacent layer of cells.

At low Reynolds numbers, or with sufficiently small cell size at higher Reynolds numbers, the diffusion from the boundary cells to the adjacent layer overshadows the convection anyway, so that the value of the velocity in the boundary cells is of less importance. In the light of this and the above conclusions, the use of the actual calculated velocity in the boundary cells would seem to be a better choice. This also removes the bothersome anomaly of convection into one cell but not out of the adjacent cell.

Convection Scheme B - Use of Calculated Velocity in Boundary Cells

The occurrence of non-zero velocities in the boundary cells is a result of the rectangular representation of the boundary curve, which causes some boundary cells to contain more fluid than boundary. Since the boundary cells are intended to represent the vorticity of the fluid immediately adjacent to the surface these cells are fluid cells, and thus their velocities can be viewed as a kind of average velocity of the fluid contained therein. In this sense the calculated velocities in the boundary cells are not unreal, at least within the finite representation of the field, and are not necessarily to be rejected.

Again referring to Figure 65, with the velocity not equal to zero in the boundary cells the cells at 1 and 4 experience convection from the boundary cells, so that the anomaly mentioned in the previous section is removed, and the vorticity generated at the boundary can be convected downstream to form a wake even at high Reynolds numbers. However, the boundary cell at point 5 now experiences convection from the boundary cell at 6, as well as from the cell at 4, while the boundary cell at 2, of course, still experiences no convection from point 3 within the wall. The corner boundary cells thus experience convection on two sides, while the other boundary cells have convection on only one side.

Since the existence of the corners is a result of the rectangular representation of the curved boundary, it would seem well to keep special effects of the corners at a minimum.

The boundary cell at 2 also experiences convection from the boundary cells on either side in the x-direction, so that now vorticity is convected along the layer of boundary cells. While this convection along the layer of boundary cells might be considered to represent convection parallel to the boundary in the fluid adjacent to the boundary, the presence of the corners allows such convection to cause vorticity generated at the surface to flow along the layer of boundary cells to the corners and from there out into the fluid at an abnormally high rate. The result was an almost complete loss of vorticity in the boundary cells, which then allowed upstream penetration of the boundary, with consequent detachment of the entire wake from the body. This pattern was little affected by the cell size in any case.

Convection Scheme C - Use of Zero Velocity in Boundary Cells Only for Calculation in Boundary Cells

This scheme combines parts of the two previously discussed schemes. The cells at 1 and 4 do experience convection from the boundary cells, since the calculated velocities at 2 and 5 are used for the calculation of the new vorticity

at 1 and 4, and the anomaly of convection scheme A is thus removed. However, when new vorticities are calculated in the boundary cells, zero velocities are substituted for the calculated values in the boundary cells, so that there is no convection between the boundary cells at 5 or 6, nor any between the boundary cell at 2 and the boundary cells on either side in the x-direction, thus removing the special effects of the corners mentioned in the above section. This then allows the vorticity generated at the surface to be convected away from the surface but not along the surface.

The presence of the convection away from the surface allows the formation of the vortices and wake, while the elimination of the convection parallel to the surface in the boundary cells prevents the loss of vorticity in the boundary cells by convection to the corners and thence off into the fluid. The results of this scheme were an improvement over the two previously discussed schemes in all cases that were evaluated.

Convection Scheme D - No Convection in Boundary Cells

Here the calculated velocities are used in the boundary cells, so that the cells at 1 and 4 experience convection from the boundary cells at 2 and 4, but no convection is used in the calculation of the new vorticities in the boundary cells. This scheme contains an anomaly opposite to that of convection scheme A, for now the cell at 1 experiences

convection with the boundary cell at 2, but the boundary cell at 2 does not experience convection with the cell at 1. Vorticity generated at the surface is convected downstream, but the vorticity in the fluid adjacent to the surface is not diminished thereby, so that non-conservation of vorticity would be expected. The boundary cells here developed too large a vorticity, since none was lost by convection, so that the boundary was penetrated from the rear as a result of this spurious vorticity.

Convection Scheme E - No Convection in Boundary Cells and Use of Zero Velocity in Boundary Cells

This is a combination of schemes A and D. The anomalies of both schemes are removed since there is no convection at all between the boundary cells and the adjacent layer of cells. This scheme produced no wake or vortices, since, as with scheme A, there is no convection away from the surface of vorticity generated at the surface, and this scheme is therefore also unattractive and was given no further consideration.

Selection of Convection Scheme

These comparisons then indicate that the most reasonable treatment of convection in the vicinity of the surface is convection scheme C, which allows convection of vorticity generated at the surface away from the surface but not along the surface. Accordingly, it was determined to use

convection scheme C, employing the actual calculated velocities in the boundary cells except for calculations in the boundary cells, where zeros are substituted.

Representation of Diffusion in Boundary Cells*

Diffusion Scheme A - Use of Calculated Vorticity in Boundary Cells

There might appear to be less question of the vorticity values in the boundary cells, and in the above comparison of convection schemes the calculated vorticity in the boundary cells was used in the diffusion terms of Equation (IV - 6). However, with this diffusion scheme (designated diffusion scheme A) vorticity in the boundary cells was diminished at low cylinder Reynolds number by diffusion to the extent that it was insufficient to prevent penetration of the upstream surface. (Comparisons of diffusion schemes were made using convection scheme C, surface vorticity scheme A, and corner scheme A, except as noted.) This was the case, in fact, for all four convection schemes discussed above. In each case the vorticity in the boundary cells was severely depleted by the strong diffusion prevalent at low Reynolds numbers.

---

*When required, the value of the vorticity at virtual points inside the boundary is taken equal to the surface value corresponding to the boundary cell for which the calculation is being made, i.e., for calculation in cell 2, the vorticity at point 3 is taken as the surface value at point 2

This is a result of the numerical approximation of the integrals over the vorticity distribution in Equation (IV - 4). Since the largest vorticity occurs at the surface, it is of paramount importance that the region in the immediate vicinity of the surface be well represented in the numerical integration. Unfortunately, this region is also the location of the largest vorticity gradients. Now in the solution of the differential equation the fluid vorticity approaches the surface value continuously, so that the integral of Equation (IV - 4) includes vorticity values up to, and including, the surface value. In the summation over the vorticity cells in Equation (IV - 7), the summation over the boundary cells must represent the integral over the region immediately adjacent to the surface and hence must supply some direct influence of the surface value of the vorticity. It is the failure of the integral to include this direct influence of the surface vorticity that causes the penetration of the surface that occurs with this diffusion scheme in this case.

Diffusion Scheme B - Use of Surface Vorticity in Boundary Cells

It was found necessary in order to better represent the integral over the region adjacent to the surface to use the surface values of the vorticity, rather than the actual values in the boundary cells, in the diffusion terms of

Equation (IV - 6) for calculating the new values of vorticity in the boundary cells. In addition, the change calculated for the vorticity in the boundary cells over the time step is assumed to be a change from the previous surface value at that point, rather than from the previous actual value of the vorticity in the boundary cells. This treatment of the diffusion terms for calculation in the boundary cells is referred to for comparison purposes as diffusion scheme B.

This scheme is compatible with the location of the boundary cells on the surface used in the present method, for it becomes exact as the surface is approached since the true fluid vorticity is continuous to the surface. The important point in this argument, and also in the above question of the velocity to be used in the boundary cells, is, in fact, that the boundary cells are located astride the surface, as indicated in Figure 65, rather than adjacent to the surface as would be the case if in Figure 65 the dotted surface were displaced one-half cell width down and to the left. Properties in the boundary cells are thus meant to represent the properties of fluid in the immediate vicinity of the surface.

It also should be noted that this treatment of the diffusion terms for calculation of vorticity in the boundary cells is a natural companion to the treatment of the

convection terms discussed above as convection scheme C. In each case, for calculation of the change in vorticity in the boundary cells the actual surface value of the property in question is used in the adjacent boundary cells, i.e., zero for velocity and the surface value for vorticity.

The use of diffusion scheme B reduced the upstream penetration at low Reynolds number somewhat, but significant penetration still remained. A reduction of the time step showed no significant change in the results, thus eliminating the possibility of the loss of vorticity in the boundary cells and consequent upstream penetration with diffusion scheme A being due to a too large a time step. The vortices formed too high above the center line, and there was significant penetration of the downstream boundary. Both of these features indicate that the vorticity in the boundary cells was too high. The penetration of the downstream surface and the associated outflow through the upstream boundary is caused by excess vorticity in the boundary cells around 90°, especially on the highest corners. With this diffusion scheme there was very little difference between the solution using the convection schemes C and B, the results being very nearly identical.

Selection of Diffusion Scheme

The diffusion scheme using surface values of the vorticity for calculation in the boundary cells (scheme B) does

reduce the upstream penetration by maintaining the vorticity in the boundary cells and therefore was selected. However, it results in too large a vorticity on the higher corners of the boundary cells, thereby causing the vortices to form too high on the cylinder, with consequent penetration of the downstream boundary and outflow through the upstream boundary. Consideration was therefore given to the method of calculation of the surface vorticity as discussed in the next section.

Representation of Surface Vorticity

Surface Vorticity Scheme A - Use of Zero Velocity in Boundary Cells

In all results discussed above, the surface vorticity was located on the boundary cells and was calculated from the curl of the velocity using two-point, one-sided differences between the boundary cells and the adjacent layer of cells, with the velocity in the boundary cells taken as zero, this being referred to as surface vorticity scheme A.

Referring again to Figure 65, in this scheme the surface vorticity at 2 is equal to the x-velocity at point 1; the surface vorticity at 6 is equal to the negative of the y-velocity at 7; and the surface vorticity at 5 is equal to the sum of the x-velocity at 4 and the negative of the y-velocity at 8. This scheme results in large vorticity on the

outside (convex) corners and zero vorticity on the inside (concave) corners so that the presence of the corners is felt to too great an extent.

Surface Vorticity Scheme B - Use of Calculated Velocity in Boundary Cells

An obvious variation, designated surface vorticity scheme B, of this scheme is to use the actual calculated velocity in the boundary cells in the evaluation of the curl, e.g., the surface vorticity at 2 is set equal to the difference between the x-velocity at points 1 and 2, etc. This gives non-zero vorticity on the inside corners, but reduces the surface vorticity at all other points, not just at the outside corners and resulted in inadequate surface vorticity with no vortices having been formed at cylinder Reynolds number of 120. This is not surprising, for since the vorticity in the boundary cells is not equal to the surface vorticity, a difference taken between the boundary cells and the adjacent layer of cells must represent actually a derivative in the fluid and not at the surface.

Representation of Corner Vorticity

Corner Scheme A - No Special Consideration of Corners

Corner scheme A refers simply to the calculation of the vorticity in the corner cells from the curl with no special consideration given to the corners. This scheme

resulted in too large a vorticity in the outside corner cells, as mentioned above.

Two schemes, designated as corner schemes B and C, respectively, for reducing the surface vorticity at the outside corners only were tried: (a) dividing the surface vorticity on the corners by two, and (b) calculating only the surface vorticity on the corner using non-zero velocity in the boundary cells. Both of these corner schemes are evaluated below.

Corner Scheme B - Use of Central Differences with Zero Velocity in Boundary Cells

The first of these schemes might be justified by arguing that, since the derivatives involved in the curl at the corners are parallel to part of the surface, rather than perpendicular as at the other points, the differences there should be central rather than one-sided. If zero velocity is to be used in the boundary cells, this then results simply in divisions of the curl, as calculated from the one-sided differences, by two. The surface vorticity of the outside corners is thus reduced, but that of the inside corners remains zero. The reduction in surface vorticity at the outside corners caused the vortices to form later and closer to the center line, with less penetration of the downstream surface, and also less upstream penetration.

Corner Scheme C - Use of Central Differences with Calculated Velocity in Boundary Cells

The second treatment of the surface vorticity on the corners, corner scheme C, mentioned above, depends for justification on the argument that, since the corners are abnormal projections away from the true curved boundary, central differences involving the actual calculated velocity in the boundary cells should be used in the curl. This scheme reduces the surface vorticity at the outside corners and gives non-zero vorticity on the inside corners. The upstream penetration was less, and the flow did separate and begin to form a wake with corner scheme C, both of which features favor this scheme.

Corner Scheme D - Modification of Scheme C on Inside Corners

A variation of corner scheme C, designated as corner scheme D, has the corner surface vorticity evaluated exactly as in scheme C, but in the calculation of the vorticity in the boundary cells on the inside corners the change over the time step was taken to be the change from zero, rather than from the surface value on the inside corners. This was considered to combine some of the aspects of schemes B and C, the value of the surface vorticity on the inside corners being zero in the former. The vector plots showed almost no noticeable difference from those of scheme C, except that separation occurred later than with scheme C.

Surface Pressures and Drag Coefficients*

Again the rectangular representation of the curved surface raises a question as to what value to use for the vorticity in the boundary cells in the calculation of the surface pressure coefficient and the drag coefficients—the actual calculated value in the boundary cells, designated coefficient scheme A; or the surface value, coefficient scheme B. Both choices were evaluated and the results for the pressure and drag coefficients, together with the minimum pressure coefficient on the surface, are given in Table 3 at time T = 2.0, except as noted, for several of the boundary treatments.

A comparison of coefficient schemes A and B is also given in the time development of the coefficients in Figures 66-68 for Reynolds numbers 6, 24, and 120. The effect of the time step on the pressure coefficient is much greater with coefficient scheme B, and increases as time progresses. The effect of the time step is greater with scheme A for the friction coefficient, but no such increase with time is evident. These trends are understandable, since the time step affects the vorticity in the boundary cells and

---

*All quantities used in figures and tables discussed in this appendix are nondimensionalized as noted in the Nomenclature. Parameters used in all results presented are given in Table 4.

adjacent cells directly, but affects the surface vorticity only indirectly through the velocity. The pressure coefficient with scheme B then is more affected by the time step, since one of the vorticities involved therein is more sensitive to the time step than is the other. Since only one vorticity is involved in the friction drag coefficient, scheme B is less sensitive to the time step in that case.

The existence of the corners causes the steady-state pressure distribution to be reached much faster than with a smooth curved surface, with the result that little change occurs in the drag coefficients given after time T = 2.0, except at Reynolds number 120. For this reason the time histories of the drag coefficients given do not match those of solutions obtained in cylindrical coordinates, although the asymptotic values agree fairly well at low Reynolds numbers. This also is the reason for the large effect of the cell size on the early time development of the drag coefficient. The smaller cell size gives a better representation of the curve and hence the true time development.

The pressure distributions of Figure 69 also tend to favor scheme A, since scheme B produces a more severe pressure drop. The drag coefficients with scheme B are, therefore, larger than with scheme A, and the agreement with the other numerical solutions and the experimental data given in Figure 13b is not as good. The choice of scheme A for the

pressure coefficient is logical, since its use of the actual calculated values of the vorticity in the boundary cells more closely represents the derivative of the vorticity in the fluid. Scheme A also gives friction drag coefficients in better agreement with the other numerical solutions shown in Figure 13c.

Final Selection of Schemes

Of the five convection schemes evaluated only schemes B and C produced vortices at high Reynolds numbers. These two schemes produced very similar results for both the flow pattern and the drag coefficients, the only noticeable difference being a slightly more rapid development of the flow with scheme B. However, convection scheme C produced a reasonable flow pattern at high Reynolds number even with diffusion scheme A, while convection scheme B allowed complete penetration of the surface. Although diffusion scheme A is not to be chosen, this does seem to indicate that convection scheme C is more reasonable.

The choice of diffusion scheme is more clear, since diffusion scheme A allowed considerable penetration of the surface at low Reynolds number with all convection schemes. The surface vorticity scheme is also clearly indicated to be scheme A since scheme B did not produce vortex formation. Diffusion scheme A was therefore selected as more representative of the physical flow field.

The first corner scheme is eliminated by penetration of the downstream surface. Of the remaining three, both B and D involve zeros for vorticity on some of the corners and result in insufficient pressure drop around the cylinder.

The final selection then is

convection scheme C

diffusion scheme B

surface vorticity scheme A

corner scheme C

coefficient scheme A.

APPENDIX F

CONVERGENCE AND EFFECT OF PARAMETERS*

Two-Dimensional Flow About Solid Cylinder

Convergence

Convergence of the solution as the time step decreases at constant cell size is demonstrated for the Dufort-Frankel formulation in Figure 70. Some differences are evident as the time step is reduced from 0.4 to 0.2, but the second reduction by half produced little change. The convergence was quantitatively evident in the numerical results which were checked extensively on a point-by-point comparison basis.

Effect of Parameters

Figure 71 shows the effect of the influence range r_m used in the velocity calculation. (It is recalled that vorticity more distant than r_m from the point at which the velocity is being calculated is not included in the calculation at that point.) The drastic error introduced by too

---

*All quantities used on figures discussed in this appendix are nondimensionalized as noted in the Nomenclature. The scale factors for the vector plots are given in Table 5. The magnitude of a vector is indicated by the length of the stem of the arrow, the size of the arrowheads being the same throughout. Spurious lines on the plots are the result of plotter error. Parameters used in all results presented are given in Table 4.

small an influence range is evident in Figure 71a where the range was one cylinder diameter. A range of two cylinder diameters, however, yields results very nearly the same as those obtained with a range of four diameters and was thus considered adequate.

Figures 72 and 71b show the effect of the minimum vorticity ω_m necessary for creation of a new vortex cell.* (It is recalled that a new vortex cell is created from a border cell* only if the sum of the magnitude of the prospective vorticity calculated for that border cell and the magnitude of the vorticity of any adjacent vortex cell exceeds ω_m. Otherwise the vorticity is distributed evenly among the adjacent vortex cells.) Very little effect, other than the varying number of vortex cells, is evident even at the largest value of ω_m used. The effect of this parameter, however, increases with time, as is noted for the one-dimensional infinite flat plate results of Chapter III. The value of 0.01 was considered adequate for the total times considered for the three-dimensional jet.

Infinite Jet in Cross-Wind

Convergence

The convergence of the solution as the time step decreases at constant cell size is demonstrated for the straight explicit formulation in Figure 73. Similar

*Vortex cells and border cells are defined in Chapter II.

convergence was obtained with the Dufort-Frankel formulation. Small changes occurred upon a reduction of the time step from 0.4 to 0.2, but further reduction produced only very slight change as evident from these figures. Again the convergence was quantitatively evident in the numerical results which were checked point by point.

Effect of Parameters

The effect of the influence range r_m used in the velocity calculation is shown in Figure 74. (It is recalled that vorticity more distant than r_m from the point at which the velocity is being calculated is not included in the calculation at that point.) Large differences are evident between the results with ranges of one and two exit diameters. However, the effect of a further increase to four diameters is slight except to eliminate most of the misdirected downward vertical velocity. The magnitude of this downward velocity is very small, however. (Recall that the arrowheads are all of one size. The magnitude of the velocity is indicated only by the length of the shaft of the arrow.) A range of two exit diameters was, therefore, considered adequate.

Figures 75 and 74b show the effect of the minimum vorticity ω_m necessary for creation of a new vortex cell. (It is recalled that a new vortex cell is created from a border cell only if the sum of the magnitude of the

prospective vorticity calculated for that border cell and the magnitude of the vorticity of any adjacent vortex cell exceeds ω_m. Otherwise the vorticity is distributed evenly among the adjacent vortex cells.) The effect of ω_m in the range considered is small at this time, being confined to a change in the number of vortex cells. As shown in Chapter III, the effect of this parameter increases with time as the vorticity spreads more widely. The choice of 0.01 was considered adequate for the total times considered.

APPENDIX G

LINEARIZED STABILITY CRITERIA*

Straight Explicit Formulation

Two-Dimensional

Applying the results of the stability analysis in two-dimensions given in Appendix H to Equation (IV - 5) of Chapter IV and Equation (V - 5) of Chapter V we have

$$a = V, \quad b = \frac{1}{R_c}$$

where V is a representative (nondimensional) velocity magnitude in the field, and R_c is the cell Reynolds number. Use of the largest velocity in the field for V will give the most conservative stability criteria, of course.

Then with the cell size as the reference length we have, in the notation of Appendix H,

$$r = \frac{\Delta t}{(1)^2}, \quad q = \frac{\Delta t}{2(1)}$$

and, from the two-dimensional results of Appendix H, two regions of stability:

$$\text{(a)} \quad \Delta t \leq \frac{R_c}{4} \text{ and } \frac{\Delta t}{2} < \frac{1}{V}\sqrt{\frac{\Delta t}{2R_c}}$$

---

*All quantities in this appendix are nondimensionalized as noted in the Nomenclature.

$$(b)\quad \frac{R_c}{4} \leq \Delta t < \frac{R}{2} \text{ and } \frac{1}{V}\sqrt{\frac{\Delta t}{R_c} - \frac{1}{4}} < \frac{\Delta t}{2} < \frac{1}{V}\sqrt{\frac{\Delta t}{2R_c}}$$

The first of these may be reduced to

$$\Delta t < \min\left(\frac{R_c}{4}, \frac{2}{V^2 R_c}\right)$$

and, therefore, may be stated as

$$(a)\quad \begin{cases} R_c \leq \dfrac{2\sqrt{2}}{V} \text{ and } \Delta t \leq \dfrac{R_c}{4} \\ R_c \geq \dfrac{2\sqrt{2}}{V} \text{ and } \Delta t \leq \dfrac{2}{V^2 R_c} \end{cases}$$

since $\quad \dfrac{R_c}{4} \leq \dfrac{2}{V^2 R_c}$ for $R_c \leq \dfrac{2\sqrt{2}}{V}$.

The stability region (b) above may be given as

$$\frac{R_c}{4} \leq \Delta t \leq \frac{R_c}{2} \text{ and } \frac{\Delta t}{R_c} - \frac{1}{4} \leq \frac{\Delta t^2 V^2}{4} \text{ and } \frac{\Delta t^2 V^2}{4} \leq \frac{\Delta t}{2R_c}$$

The last of these was encountered above and reduces to

$$\Delta t \leq \frac{2}{V^2 R_c}$$

The second becomes

$$\Delta t^2 V^2 - \frac{4}{R_c}\Delta t + 1 \geq 0$$

The roots of this quadratic are

$$\Delta t = \frac{1}{V^2}\left[\frac{2}{R_c} \pm \sqrt{\frac{4}{R_c^2} - V^2}\right]$$

Both of these roots are real and positive for $R_c \leq \frac{2}{V}$ so that, since the quadratic is positive at infinity, it is positive in the following two ranges of Δt:

$$\left.\begin{aligned} \Delta t &\leq \frac{1}{V^2}\left[\frac{2}{R_c} - \sqrt{\frac{4}{R_c^2} - V^2}\right] \\ \Delta t &\geq \frac{1}{V^2}\left[\frac{2}{R_c} + \sqrt{\frac{4}{R_c^2} - V^2}\right] \end{aligned}\right\} \quad R_c \leq \frac{2}{V}$$

If, however, $R_c > \frac{2}{V}$ then there are no real roots, and the quadratic must be positive for all values of Δt. This condition, therefore, does not restrict Δt for $R_c > \frac{2}{V}$.

Since $\Delta t \leq \frac{2}{V^2 R_c}$ is also required, there are no acceptible values of Δt in the range above the larger root of the quadratic. Also the range of Δt below the smaller root is smaller than that defined by $\Delta t \leq \frac{2}{V^2 R_c}$. Therefore, the stability region (b) may be stated as

$$\text{(b)} \quad \begin{cases} R_c \leq \frac{2}{V} \text{ and } \frac{R_c}{4} \leq \Delta t \leq \frac{R_c}{2} \text{ and } \Delta t \leq \frac{1}{V^2}\left[\frac{2}{R_c} - \sqrt{\frac{4}{R_c^2} - V^2}\right], \\ R_c \geq \frac{2}{V} \text{ and } \frac{R_c}{4} \leq \Delta t \leq \frac{R_c}{2} \text{ and } \Delta t \leq \frac{2}{V^2 R_c} \end{cases}$$

These conditions for region (b) may be combined further, however. The first set requires that

$$\frac{R_c}{4} \leq \frac{1}{V^2}\left(\frac{2}{R_c} - \sqrt{\frac{4}{R_c^2} - V^2}\right) ,$$

or

$$\sqrt{\frac{4}{R_c^2} - V^2} \leq \frac{2}{R_c} - \frac{R_c V^2}{4}$$

which requires that

$$\frac{2}{R_c} - \frac{R_c V^2}{4} \geq 0$$

else the square root is not real. This requires that $R_c \leq \frac{2\sqrt{2}}{V}$. This, however, is already satisfied since $R_c \leq \frac{2}{V}$ for this set of conditions. It then is only required that

$$\frac{4}{R_c^2} - V^2 \leq \left(\frac{2}{R_c} - \frac{R_c V^2}{4}\right)^2$$

which reduces to $\frac{R_c V^2}{4} \geq 0$, and is thus trivial.

The second set of conditions of (b) above require that

$$\frac{R_c}{4} \leq \frac{2}{V^2 R_c}$$

which requires that $R_c \leq \frac{2\sqrt{2}}{V}$. Then, since

$$\frac{1}{V^2}\left(\frac{2}{R_c} - \sqrt{\frac{4}{R_c^2} - V^2}\right) \leq \frac{R_c}{2} \text{ for } R_c \leq \frac{2}{V}$$

and

$$\frac{2}{V^2 R_c} \leq \frac{R_c}{2} \text{ for } R_c \geq \frac{2}{V}$$

the conditions for region (b) may be further restated as

$$\text{(b)} \quad \begin{cases} R_c \leq \frac{2}{V} \text{ and } \frac{R_c}{4} \leq \Delta t \leq \frac{1}{V^2}\left(\frac{2}{R_c} - \sqrt{\frac{4}{R_c^2} - V^2}\right) \\ \frac{2}{V} \leq R_c \leq \frac{2\sqrt{2}}{V} \text{ and } \frac{R_c}{4} \leq \Delta t \leq \frac{2}{V^2 R_c} \end{cases}$$

But now the stability regions defined by (a) and (b) overlap and may be combined. The regions of stability then may be stated finally as

$$R_c \leq \frac{2}{V} \text{ and } \Delta t \leq \frac{1}{V^2}\left(\frac{2}{R_c} - \sqrt{\frac{4}{R_c^2} - V^2}\right)$$

$$R_c \geq \frac{2}{V} \text{ and } \Delta t \leq \frac{2}{V^2 R_c}$$

With no variation in the direction of the jet axis, the appropriate value for the maximum field velocity is that of the cross-wind, i.e., unity in the present nondimensional form. For V = 1 the stability criteria become

$$R_c \leq 2 \text{ and } \Delta t \leq \frac{2}{R_c} - \sqrt{\frac{2}{R_c^2} - 1}$$

$$R_c \geq 2 \text{ and } \Delta t \leq \frac{2}{R_c}$$

Three-Dimensional

By the same development applied to the three-dimensional results from Appendix H, the stability regions for Equation (VI - 19) of Chapter VI are defined by

$$R_c \leq \frac{2}{V} \text{ and } \Delta t \leq \frac{1}{V^2}\left(\frac{4}{3R_c} - \frac{2}{3}\sqrt{\frac{4}{R_c^2} - V^2}\right)$$

$$R_c \geq \frac{2}{V} \text{ and } \Delta t \leq \frac{4}{3V^2 R_c}$$

Here the appropriate value for the maximum field velocity is the jet exit velocity (the velocity ratio in the present nondimensional form) for velocity ratios greater than unity.

Dufort-Frankel Formulation

With $r \equiv \frac{\Delta t}{R}$ and $g \equiv \frac{\Delta t}{2}$ Equation (IV - 6) of Chapter IV and Equation (V - 6) of Chapter V may be written as

$$\begin{aligned}(\tfrac{1}{2} + 2r)\zeta_{i,j}^{n+1} = (\tfrac{1}{2} - 2r)\zeta_{i,j}^{n-1} &- gV(\zeta_{i+1,j}^{n} - \zeta_{i-1,j}^{n} \\ &+ \zeta_{i,j+1}^{n} - \zeta_{i,j-1}^{n}) \\ &+ r(\zeta_{i+1,j}^{n} + \zeta_{i-1,j}^{n} + \zeta_{i,j+1}^{n} + \zeta_{i,j-1}^{n}) \qquad (1)\end{aligned}$$

(Again V is a representative (nondimensional) velocity magnitude in the field.) Let the solution be written in the form

$$\zeta^{n}_{i,j} = X_i Y_j T_n$$

where the functions X, Y, and T are functions only of x, y, and t, respectively. Then

$$(\tfrac{1}{2} + 2r)\frac{T_{n+1}}{T_n} = (\tfrac{1}{2} - 2r)\frac{T_{n-1}}{T_n} - gV(\frac{X_{i+1}}{X_i} - \frac{X_{i-1}}{X_i} + \frac{Y_{j+1}}{Y_j} - \frac{Y_{j-1}}{Y_j})$$

$$+ r(\frac{X_{i+1}}{X_i} + \frac{X_{i-1}}{X_i} + \frac{Y_{j+1}}{Y_j} + \frac{Y_{j-1}}{Y_j}) \qquad (2)$$

From this equation and the functional form of X, Y, and T it follows that

$$r(\frac{X_{i+1}}{X_i} + \frac{X_{i-1}}{X_i}) - gV(\frac{X_{i+1}}{X_i} - \frac{X_{i-1}}{X_i}) = \text{constant} \equiv k_1 \qquad (3a)$$

$$r(\frac{Y_{j+1}}{Y_j} + \frac{Y_{j-1}}{Y_j}) - gV(\frac{Y_{j+1}}{Y_j} - \frac{Y_{j-1}}{Y_j}) = \text{constant} \equiv k_2 \qquad (3b)$$

$$(\tfrac{1}{2} + 2r)\frac{T_{n+1}}{T_n} - (\tfrac{1}{2} - 2r)\frac{T_{n-1}}{T_n} = \text{constant} \equiv \lambda = k_1 + k_2 \qquad (3c)$$

Equation (3c) may be solved by the substitution of $T_n = \beta^n$ where β is a constant. Thus β must satisfy

$$(\tfrac{1}{2} + 2r)\beta^2 - \lambda\beta + (2r - \tfrac{1}{2}) = 0 \qquad (4)$$

so that there are two acceptable values:

$$\beta_{\pm} = \frac{\lambda \pm \sqrt{\lambda^2 - 4(4r^2 - \frac{1}{4})}}{1 + 4r} \qquad (5)$$

For stability it must be required that

$$|\beta_{\pm}| < 1$$

This then requires consideration of the properties of quadratic roots as given in Appendix I. In the notation of Appendix I we have

$$A = \frac{1}{2} + 2r$$

$$B = -\lambda$$

$$C = 2r - \frac{1}{2}$$

But the constant λ is the sum of the two constants, k_1 and k_2, defined in Equation (3a) and (3b): $\lambda = k_1 + k_2$. Using the matrices $\underline{I}$, $\underline{L}$ and $\underline{L}^T$, as defined in Appendix H, Equation (3a) may be written as a matrix equation:

$$[k_1\underline{I} - r(\underline{L}^T + \underline{L}) + gV(\underline{L}^T - \underline{L})]\underline{X} = \underline{0} \qquad (6)$$

where $\underline{X}$ is a column matrix:

$$\underline{X} \equiv \begin{pmatrix} X_1 \\ X_2 \\ \cdot \\ \cdot \\ \cdot \\ X_{I-1} \end{pmatrix}$$

Thus k_1 is an eigenvalue of the matrix $[r(\underline{L}^T + \underline{L}) - gV(\underline{L}^T - \underline{L})]$. This matrix is the same as the matrix $\underline{B}$ defined by Equation (H - 26) of Appendix H, except for the two constant coefficients. The eigenvalues, therefore, may be inferred from the results of Appendix H, as stated by

Equation (H - 33) of that appendix. Thus

$$(k_1)_p = 2\sqrt{r^2 - g^2V^2}\cos\frac{\pi p}{I} \qquad p = 1, 2, \cdots, I - 1 \qquad (7)$$

where p = 0, I corresponds to the field boundaries in the x-direction. Similarly the eigenvalues of Equation (3b) are

$$(k_2)_q = 2\sqrt{r^2 - g^2V^2}\cos\frac{\pi q}{J} \qquad q = 1, 2, \cdots, J - 1 \qquad (8)$$

where q = 0, J corresponds to the field boundaries in the y-direction. Then the acceptable values of the constant λ are

$$\lambda_{p,q} = (k_1)_p + (k_2)_q = 2\sqrt{r^2 - g^2V^2}\left(\cos\frac{\pi p}{I} + \cos\frac{\pi q}{J}\right) \qquad (9)$$

so that

$$B = -2\sqrt{r^2 - g^2V^2}\left(\cos\frac{\pi p}{I} + \cos\frac{\pi q}{J}\right)$$

Now according to the results of Appendix I the magnitudes of the roots of the quadratic equation

$$A\beta^2 + B\beta + C = 0$$

will be less than unity in the following four cases:

(a) A, B, C real

$$B^2 - 4AC \geq 0$$

$$\left|\frac{C}{A}\right| < 1$$

$$|B| < |A + C|$$

(b) A, B, C real

$$B^2 - 4AC < 0$$

$$\left|\frac{C}{A}\right| < 1$$

(c) A, C real; B imaginary $\quad |B|^2 + 4AC \geq 0$

$$\left|\frac{C}{A}\right| < 1$$

$$|B| < |A - C|$$

(d) A, C real; B imaginary $\quad |B|^2 + 4AC < 0$

$$\left|\frac{C}{A}\right| < 1$$

In the present application, B is real if $r^2 - g^2V^2 \geq 0$. If this is the case then $B^2 - 4AC \geq 0$ if

$$(r^2 - g^2V^2)(\cos \frac{\pi p}{I} + \cos \frac{\pi q}{J})^2 \geq 4r^2 - \frac{1}{4}$$

Then if

$$(r^2 - g^2V^2)(2)^2 \geq 4r^2 - \frac{1}{4}$$

which reduces to

$$gV \leq \frac{1}{4}$$

we have $B^2 - 4AC \geq 0$ for some p,q for all values of r such that $r \geq gV$. Then referring to cases (a) and (b) defined above, if $r \geq gV$ and $gV \leq \frac{1}{4}$ we must require that $|B| < |A + C|$ and $\left|\frac{C}{A}\right| < 1$, while if $gV > \frac{1}{4}$ only the latter is required.

Now $|B| < |A + C|$ is satisfied if

$$2\sqrt{r^2 - g^2V^2}\ |\cos \frac{\pi p}{I} + \cos \frac{\pi q}{J}| < |2r + \frac{1}{2} + 2r - \frac{1}{2}|$$

This will be satisfied for all p,q if

$$4\sqrt{r^2 - g^2V^2} < 4r$$

which reduces to

$$g^2V^2 > 0$$

which is always satisfied. Also $\left|\frac{C}{A}\right| < 1$ is satisfied if

$$\left|\frac{2r - \frac{1}{2}}{2r + \frac{1}{2}}\right| < 1$$

This also is always satisfied. Therefore the solution is stable if $r \geq gV$. No restriction is imposed on the value of gV.

If, however, $r^2 - g^2V^2 < 0$, we have B imaginary; then $|B|^2 + 4AC \geq 0$ if

$$(g^2V^2 - r^2)(\cos \tfrac{\pi p}{I} + \cos \tfrac{\pi q}{J})^2 \geq \tfrac{1}{4} - 4r^2$$

Then, if

$$(g^2V^2 - r^2)\ (2)^2 \geq \tfrac{1}{4} - 4r^2$$

which reduces to

$$gV \geq \tfrac{1}{4}$$

we have $|B|^2 + 4AC \geq 0$ for some p,q for all values of r such that $r < gV$. Thus, referring to cases (c) and (d) defined above, if $r < gV$ and $gV \geq \frac{1}{4}$ we must satisfy $|B| < |A - C|$ and $\left|\frac{C}{A}\right| < 1$, while for $gV < \frac{1}{4}$ only the latter is required.

Now $|B| < |A - C|$ is satisfied if

$$2\sqrt{g^2V^2 - r^2}\ |\cos \tfrac{\pi p}{I} + \cos \tfrac{\pi q}{J}| < |2r + \tfrac{1}{2} - 2r + \tfrac{1}{2}|$$

This will be satisfied for all p,q if

$$4\sqrt{g^2V^2 - r^2} < 1$$

which reduces to

$$r^2 > g^2V^2 - \frac{1}{16}$$

Again $\left|\frac{C}{A}\right| < 1$ is always satisfied as above.

Therefore, if $r < gV$ the solution is stable if

$$gV < \frac{1}{4} \text{ and } r < gV$$

$$gV \geq \frac{1}{4} \text{ and } \sqrt{g^2V^2 - \frac{1}{16}} < r < gV$$

But since the solution is stable for all values of gV when $r \geq gV$ we have for the final statement of the stability criteria:

$$gV < \frac{1}{4} \text{ , stable for all } r$$

$$gV \geq \frac{1}{4} \text{ , stable for } r > \sqrt{g^2V^2 - \frac{1}{16}}$$

Applying these criteria to Equation (IV - 6) of Chapter IV and Equation (V - 6) of Chapter V we have

$$r = \frac{\Delta t}{R_c} , \quad g = \frac{\Delta t}{2}$$

so that the stability conditions become

$$\frac{\Delta t}{2}V < \frac{1}{4} \text{ , stable for all } \frac{\Delta t}{R_c}$$

$$\frac{\Delta t}{2}V \geq \frac{1}{4} \text{ , stable for } \frac{\Delta t}{R_c} > \sqrt{\frac{\Delta t^2}{4}V^2 - \frac{1}{16}}$$

These conditions may be restated as

$$\Delta t < \frac{1}{2V} \text{ , stable for all } R_c$$

$$\Delta t \geq \frac{1}{2V} \text{ , stable for } \Delta t^2\left(\frac{V^2}{4} - \frac{1}{R_c^2}\right) < \frac{1}{16}$$

Now for $R_c \leq \frac{2}{V}$ the last condition is satisfied for all Δt, since then $\frac{V^2}{4} - \frac{1}{R_c^2} \leq 0$. For $R_c > \frac{2}{V}$ this condition may be stated as

$$\Delta t < \frac{R_c}{2\sqrt{V^2R_c^2 - 4}}$$

The stability criteria then may be stated as

$$R_c \leq \frac{2}{V} \text{ , stable for all } \Delta t$$

$$R_c > \frac{2}{V} \text{ , stable for } \Delta t < \frac{R_c}{2\sqrt{V^2R_c^2 - 4}}$$

With V = 1 these become

$$R_c \leq 2 \text{ , stable for all } \Delta t$$

$$R_c > 2, \text{ stable for } \Delta t < \frac{R_c}{2\sqrt{R_c^2 - 4}}$$

APPENDIX H

COMPARISON OF VON NEUMANN AND MATRIX METHODS OF STABILITY ANALYSIS

Consider the differential equation

$$\frac{\partial f}{\partial t} = a\frac{\partial f}{\partial x} + b\frac{\partial^2 f}{\partial x^2} + g(x, t) \tag{1}$$

where a and b are constants and g(x, t) is a known function. Let the differential equation be approximated by a difference equation as follows:

$$\frac{f_i^{n+1} - f_i^n}{\Delta t} = a\frac{f_{i+1}^n - f_{i-1}^n}{2\Delta x} + b\frac{f_{i+1}^n - 2f_i^n + f_{i-1}^n}{(\Delta x)^2} + g_i^n$$

or

$$f_i^{n+1} = f_i^n + \frac{a}{2}\frac{\Delta t}{\Delta x}(f_{i+1}^n - f_{i-1}^n) + b\frac{\Delta t}{(\Delta x)^2}(f_{i+1}^n - 2f_i^n + f_{i-1}^n) + g_i^n\Delta t \tag{2}$$

Here the subscript refers to space and the superscript to time. This difference equation is straight explicit, in that the values at each space point at each new time step are predicted from values at the same and neighboring space points at the previous time.

Now define $\frac{\Delta t}{2\Delta x} \equiv q$, $\frac{\Delta t}{(\Delta x)^2} \equiv r$. Then

$$f_i^{n+1} = Lf_i^n + g_i^n \Delta t \tag{3}$$

where the difference operation L is defined by

$$Lf_i^n \equiv f_i^n + aq(f_{i+1}^n - f_{i-1}^n) + br(f_{i+1}^n - 2f_i^n + f_{i-1}^n)$$

$$= (1 - 2br)f_i^n + aq(f_{i+1}^n - f_{i-1}^n) + br(f_{i+1}^n + f_{i-1}^n) \tag{4}$$

Now the values actually obtained by computation with the difference equation will contain some computational error. Thus the values actually obtained at step n are $f_i^n + \varepsilon_i^n$ where f_i^n represents the true value, and ε_i^n the error. Then operation at the next time step produces $L(f_i^n + \varepsilon_i^n) + g_i^n \Delta t$, which then differs from the true solution at that time step by ε_i^{n+1}. Thus

$$f_i^{n+1} + \varepsilon_i^{n+1} = L(f_i^n + \varepsilon_i^n) + g_i^n \Delta t \tag{5}$$

But since f_i^n is the true solution, we have, using Equation (3) in Equation (5),

$$\varepsilon_i^{n+1} = L\varepsilon_i^n \tag{6}$$

so that the error satisfies the homogeneous difference equation:

$$\varepsilon_i^{n+1} = (1 - 2br)\varepsilon_i^n + aq(\varepsilon_{i+1}^n - \varepsilon_{i-1}^n) + br(\varepsilon_{i+1}^n + \varepsilon_{i-1}^n) \tag{7}$$

If there are boundary conditions imposed in the problem, at say i = 0 and i = I, we then have f_0^n and f_I^n given, so that no error is present on the boundaries, since the values there are known and are not calculated. Then

$$\varepsilon_0^n = \varepsilon_I^n = 0$$

The presence of boundaries thus imposes a restriction on the types of errors that may arise, i.e., there will never be any errors on the boundaries. In the pure initial value problem, with no boundary conditions, no such restriction on the error is present, and errors of a completely arbitrary nature may occur. The range of errors that may arise in mixed initial value-boundary value problems is thus smaller than in pure initial value problems, and the stability restrictions of the latter may, therefore, be expected to be more severe.

Now if boundary conditions are imposed, Equation (7) may be written as a matrix equation by defining the following I - 1 order matrices:

$$\underline{L} \equiv \begin{pmatrix} 0 & . & . & . & . & . & . \\ 1 & 0 & . & . & . & . & . \\ 0 & 1 & 0 & . & . & . & . \\ . & 0 & 1 & 0 & . & . & . \\ . & . & . & . & . & . & . \\ . & . & . & . & . & . & . \end{pmatrix}, \qquad \underline{\varepsilon}^n \equiv \begin{pmatrix} \varepsilon_1^n \\ \varepsilon_2^n \\ \varepsilon_3^n \\ . \\ . \\ . \end{pmatrix}$$

Thus $\underline{L}$ has zero elements except on the lower sub-diagonal where the elements are unity. The elements of these matrices are given by

$$(\underline{L})_{ij} = \delta_{i-1,j}, \quad (\underline{\varepsilon}^n)_i = \varepsilon_i^n$$

Then Equation (7) becomes $\underline{\varepsilon}^{n+1} = \underline{A}\,\underline{\varepsilon}^n$ with

$$\underline{A} \equiv (1 - 2br)\underline{I} + aq(\underline{L}^T - \underline{L}) + br(\underline{L}^T + \underline{L}) \tag{8}$$

where $\underline{I}$ is the unit matrix and the superscript "T" indicates the matrix transpose. Thus

$$\underline{L}^T = \begin{pmatrix} 0 & 1 & 0 & . & . & . & . \\ . & 0 & 1 & 0 & . & . & . \\ . & . & 0 & 1 & . & . & . \\ . & . & . & . & . & . & . \\ . & . & . & . & . & . & . \end{pmatrix} \quad \text{or} \quad (\underline{L}^T)_{ij} = \delta_{i+1,j}$$

In the absence of boundary conditions the matrices are of infinite order, so that the matrix formulation is thus useful only for mixed initial value-boundary value problems. Therefore, pure initial value problems are treated by the von Neumann (Fourier expansion) stability analysis, but mixed initial value-boundary value problems may be treated either by the von Neumann analysis or by matrix stability analysis as shown below.

Von Neumann Stability Analysis

Expand the error in a general Fourier Series:

$$\varepsilon_i^n = \mathrm{Re} \sum_{k=1}^{\infty} (C_k^+ e^{i\beta_k^+ x_i} + C_k^- e^{-i\beta_k^- x_i}) e^{i\alpha_k t_n} \tag{9}$$

where C_k^+, C_k^-, β_k^+, β_k^-, and α_k are all complex constants. For stability we must have $\mathrm{Im}(\alpha_k) > 0$ or, equivalently,

$$|e^{i\alpha_k}| < 1$$

Now $x_i = i\Delta x$ and $t_n = n\Delta t$ (with the "i" here not to be confused with the above usage as $\sqrt{-1}$) so that if we define

$$\xi_k^{\pm} \equiv e^{i\beta_k^{\pm}\Delta x} \text{ and } \zeta_k \equiv e^{i\alpha_k \Delta t}$$

we have

$$\varepsilon_i^n = \mathrm{Re} \sum_{k=1}^{\infty} [C_k^+ (\xi_k^+)^i + C_k^- (\xi_k^-)^{-i}] (\zeta_k)^n \tag{10}$$

(Here the i and n are exponents, the i being the space coordinate index and <u>not</u> $\sqrt{-1}$.) Then for stability

$$|\zeta_k| < 1$$

Now substitute Equation (10) into Equation (7) and rearrange. Then

$$\sum_{k=1}^{\infty} \{C_k^+ (\xi_k^+)^i (\zeta_k)^n [\zeta_k - (1 - 2br) - aq(\xi_k^+ - \xi_k^{+-1}) - br(\xi_k^+ + \xi_k^{+-1})]$$

$$+ C_k^-(\xi_k^-)^{-i}(\zeta_k)^n[\zeta_k - (1 - 2br)$$

$$- aq(\xi_k^{-\,-1} - \xi_k^-) - br(\xi_k^{-\,-1} + \xi_k^-)]\} = 0 \tag{11}$$

Now since this must hold for all i we must have

$$\zeta_k - (1 - 2br) - aq[(\xi_k^+) - (\xi_k^+)^{-1}]$$

$$- br[(\xi_k^+) + (\xi_k^+)^{-1}] = 0 \tag{12a}$$

and

$$\zeta_k - (1 - 2br) + aq[(\xi_k^-) - (\xi_k^-)^{-1}]$$

$$- br[(\xi_k^-) + (\xi_k^-)^{-1}] = 0 \tag{12b}$$

Subtracting these and rearranging, we obtain

$$aq[(\xi_k^+) - (\xi_k^+)^{-1}] + br[(\xi_k^+) + (\xi_k^+)^{-1}]$$

$$= - aq[(\xi_k^-) - (\xi_k^-)^{-1}] + br[(\xi_k^-) + (\xi_k^-)^{-1}]$$

or

$$(br + aq)[(\xi_k^+) - (\xi_k^-)^{-1}] = (br - aq)[(\xi_k^-) - (\xi_k^+)^{-1}]$$

or

$$\frac{(\xi_k^+) - (\xi_k^-)^{-1}}{(\xi_k^-) - (\xi_k^+)^{-1}} = \frac{br - aq}{br + aq}$$

Then multiplying the numerator and denominator on the left by $\xi^+\xi^-$, we obtain

$$\frac{(\xi_k^+)^2(\xi_k^-) - (\xi_k^+)}{(\xi_k^-)^2(\xi_k^+) - (\xi_k^-)} = \frac{br - aq}{br + aq}$$

or, finally

$$\xi_k^- = (\frac{br + aq}{br - aq})\xi_k^+ \tag{13}$$

Note that this relation is a consequence of the difference equation only and has nothing to do with any boundary conditions. It is, therefore, to be satisfied in pure initial value problems as well as in mixed initial value-boundary value problems.

Using Equation (13), drop the superscript from ξ_k^+ and write Equation (10) now as

$$\varepsilon_i^n = \mathrm{Re} \sum_{k=1}^{\infty} [C_k^+ \xi_k^i + C_k^-(\frac{br + aq}{br - aq})^{-i}\xi_k^{-i}](\zeta_k)^n \tag{14}$$

with ζ_k from Equation (12a):

$$\zeta_k = 1 - 2br + aq(\xi_k - \xi_k^{-1}) + br(\xi_k + \xi_k^{-1}) \tag{15}$$

or using the definition of ξ_k,

$$\zeta_k = 1 - 2br + aq(e^{i\beta_k\Delta x} - e^{-i\beta_k\Delta x}) + br(e^{i\beta_k\Delta x} + e^{-i\beta_k\Delta x})$$

$$= 1 - 2br + i2aq \sin(\beta_k\Delta x) + 2br \cos(\beta_k\Delta x) \tag{16}$$

Now for the pure initial value problem there are no other conditions to be satisfied, and β_k may be taken to be

real. We then have for the stability criterion of the pure initial value problem, from Equation (16),

$$[1 - 2br + 2br\cos(\beta_k \Delta x)]^2 + 4a^2q^2\sin^2(\beta_k \Delta x) < 1$$

which may be rewritten as

$$[1 - 2br + 2br\cos(\beta_k \Delta x)]^2 + 4a^2q^2 - 4a^2q^2\cos^2(\beta_k \Delta x) < 1 \tag{17}$$

for all β_k.

Note that this same result is obtained when only a single component of the Fourier series is taken. In that case Equation (12b) is eliminated, and the error is given by Equation (14) with all $C_k^- = 0$ and all but one C_k^+ equal to zero. Equation (17) is unchanged. The same result is likewise obtained by taking all $C_k^+ = 0$ and all but one C_k^- equal to zero. In that case, Equation (12a) instead of Equation (12b) is eliminated.

If, however, boundary conditions are imposed we have further conditions to be satisfied by the β_k. Thus applying the conditions $\varepsilon_0^n = \varepsilon_I^n = 0$ we have

$$\mathrm{Re} \sum_{k=1}^{\infty} [C_k^+ + C_k^-](\zeta_k)^n = 0 \tag{18a}$$

and

$$\mathrm{Re} \sum_{k=1}^{\infty} [C_k^+ \xi_k^I + C_k^-(\frac{br + aq}{br - aq})^{-I} \xi_k^{-I}](\zeta_k)^n = 0 \tag{18b}$$

Since these must hold for all n, we must have

$$C_k^- = - C_k^+ \tag{19a}$$

and then

$$\xi_k^{2I} = \left(\frac{br - aq}{br + aq}\right)^I$$

or

$$\xi_k = \left(\frac{br - aq}{br + aq}\right)^{1/2} e^{i\frac{k\pi}{I}} \quad k = 1, 2, \ldots, I - 1 \tag{19b}$$

This then requires that β_k be complex, for

$$e^{i\beta_k \Delta x} = \xi_k = \left(\frac{br - aq}{br + aq}\right)^{1/2} e^{i\frac{k\pi}{I}}$$

or

$$i\beta_k \Delta x = i\frac{k\pi}{I} + \frac{1}{2}\ln\left(\frac{br - aq}{br + aq}\right)$$

so that

$$\beta_k = \frac{k\pi}{I\Delta x} - i\frac{1}{2}\ln\left(\frac{br - aq}{br + aq}\right) \tag{20}$$

Using Equation (19b), we have from Equation (14), for the mixed initial value-boundary value problem,

$$\varepsilon_i^n = \mathrm{Re} \sum_{k=1}^{I-1} C_k \left[\left(\frac{br - aq}{br + aq}\right)^{i/2} e^{i\frac{k\pi i}{I}} - \left(\frac{br + aq}{br - aq}\right)^{-i} \left(\frac{br - aq}{br + aq}\right)^{-i/2} e^{-i\frac{k\pi i}{I}}\right] (\zeta_k)^n$$

where only the first "i" in the exponentials is $\sqrt{-1}$. Then

$$\varepsilon_i^n = \mathrm{Re} \sum_{k=1}^{I-1} C_k \left(\frac{br - aq}{br + aq}\right)^{i/2} \left(e^{i\frac{k\pi i}{I}} - e^{-i\frac{k\pi i}{I}}\right) (\zeta_k)^n$$

or, including the 2i in the constants, C_k,

$$\varepsilon_i^n = \mathrm{Re} \sum_{k=1}^{I-1} C_k \left(\frac{br - aq}{br + aq}\right)^{i/2} \sin\left(\frac{k\pi i}{I}\right) (\zeta_k)^n \tag{21}$$

Also, substituting Equation (19b) in Equation (12a), we have

$$\zeta_k = 1 - 2br + aq\left[\left(\frac{br - aq}{br + aq}\right)^{1/2} e^{i\frac{k\pi}{I}} - \left(\frac{br - aq}{br + aq}\right)^{-1/2} e^{-\frac{ik\pi}{I}}\right]$$

$$+ br\left[\left(\frac{br - aq}{br + aq}\right)^{1/2} e^{i\frac{k\pi}{I}} + \left(\frac{br - aq}{br + aq}\right)^{-1/2} e^{-\frac{ik\pi}{I}}\right]$$

or

$$\zeta_k = 1 - 2br + \sqrt{(br)^2 - (aq)^2}\left(e^{i\frac{k\pi}{I}} + e^{-i\frac{k\pi}{I}}\right)$$

$$= 1 - 2br + 2\sqrt{(br)^2 - (aq)^2} \cos\frac{k\pi}{I} \tag{22}$$

The stability criterion for the mixed initial value-boundary value problem then is one of the following:

$$\left|1 - 2br + 2\sqrt{(br)^2 - (aq)^2} \cos\frac{k\pi}{I}\right| < 1 \text{ if } |br| \geq |aq| \tag{23a}$$

for all $k = 1, 2, \cdots, I - 1$

$$(1 - 2br)^2 + 4[(aq)^2 - (br)^2] \cos^2\frac{k\pi}{I} < 1 \text{ if } |aq| \geq |br| \tag{23b}$$

for all $k = 1, 2, \cdots, I - 1$. Note that for the mixed initial value-boundary value problem the Fourier series is finite, k running from 1 to I - 1.

In summary, by the von Neumann analysis, the error is given in general by Equation (14) for the pure initial value problem, with the stability criterion given by Equation (17), with β_k unrestricted. For the mixed initial value-boundary value problem the error is given in general by Equation (21), and the stability criterion by Equation (23), with k running from 1 to I - 1.

Matrix Stability Analysis

With $\underline{\varepsilon}^{n+1} = \underline{A}\underline{\varepsilon}^{n}$ and $\underline{A}$ given by Equation (8) we have

$$\underline{\varepsilon}^{n+1} = \underline{A}(\underline{A}\ \underline{\varepsilon}^{n-1}) = \underline{A}^2\underline{\varepsilon}^{n-1}$$

Carrying this out repetitively we obtain finally

$$\underline{\varepsilon}^{n} = \underline{A}^{n}\underline{\varepsilon}^{o} \tag{24}$$

Then using matrix norms induced by the vector norm (natural norms) we have

$$||\underline{\varepsilon}^{n}|| \leq ||\underline{A}^{n}|| \cdot ||\underline{\varepsilon}^{o}|| \leq ||\underline{A}||^{n} \cdot ||\underline{\varepsilon}^{o}||$$

Now it may be shown* that the maximum eigenvalue in magnitude of a matrix is the limit inferior of its norms. Using this fact and requiring for stability that $||A|| < 1$ for some norm, we have as a necessary and sufficient

---

*{72, Chapter 1 }

condition for stability that

$$\rho(\underline{A}) < 1 \tag{25}$$

where $\rho(\underline{A})$ is the spectral radius, i.e., maximum eigenvalue in magnitude, of $\underline{A}$:

$$\rho(\underline{A}) \equiv \max |\lambda|$$

where λ is an eigenvalue of $\underline{A}$. It is thus necessary to determine the eigenvalues of $\underline{A}$ as given by Equation (8). These eigenvalues are determined as follows:

Define the matrix $\underline{B}$ as

$$\underline{B} \equiv aq(\underline{L}^T - \underline{L}) + br(\underline{L}^T + \underline{L}) \tag{26}$$

Then $\underline{A} = (1 - 2br)\underline{I} + \underline{B}$, and the eigenvalues of $\underline{A}$ then are the eigenvalues of $\underline{B}$ plus $(1 - 2br)$. Now the eigenvalues of $\underline{B}$ are determined by

$$\underline{B}\ \underline{\tau} = \lambda'\underline{\tau} \tag{27}$$

where $\underline{\tau}$ is a column matrix of the same order as $\underline{B}$, and λ' is the eigenvalue. Using the definition of the matrix $\underline{L}$, we have the elements of $\underline{B}$ given by

$$(\underline{B})_{ij} = aq[(\underline{L}^T)_{ij} - (\underline{L})_{ij}] + br[(\underline{L}^T)_{ij} + (\underline{L})_{ij}]$$

$$= aq(\delta_{i+1,j} - \delta_{i-1,j}) + br(\delta_{i+1,j} + \delta_{i-1,j})$$

Then

$$(\underline{B}\underline{\tau})_i = \sum_{j=1}^{I-1} (\underline{B})_{ij}(\underline{\tau})_j$$

$$= \sum_{j=1}^{I-1} [aq(\delta_{i+1,j} - \delta_{i-1,j}) + br(\delta_{i+1,j} + \delta_{i-1,j})]\tau_j$$

$$= aq(\tau_{i+1} - \tau_{i-1}) + br(\tau_{i+1} + \tau_{i-1})$$

Then Equation (27) represents the set of I - 1 equations

$$aq(\tau_{i+1} - \tau_{i-1}) + br(\tau_{i+1} + \tau_{i-1}) = \lambda'\tau_i$$

$$i = 1, 2, \cdots, I - 1 \qquad (28)$$

with boundary conditions $\tau_o = \tau_I = 0$.

Now take a solution of the form

$$\tau_i = C_+\gamma_+^i + C_-\gamma_-^{-i} \qquad (29)$$

where i is <u>not</u> $\sqrt{-1}$ in the exponents. Then substituting in Equation (28) and rearranging,

$$C_+\gamma_+^i[aq(\gamma_+ - \gamma_+^{-1}) + br(\gamma_+ + \gamma_+^{-1}) - \lambda']$$

$$+ C_-\gamma_-^{-i}[aq(\gamma_-^{-1} - \gamma_-) + br(\gamma_- + \gamma_-^{-1}) - \lambda'] = 0$$

Since this must apply for all i, we must have

$$aq(\gamma_+ - \gamma_+^{-1}) + br(\gamma_+ + \gamma_+^{-1}) - \lambda' = 0 \qquad (30a)$$

and

$$aq(\gamma_-^{-1} - \gamma_-) + br(\gamma_- + \gamma_-^{-1}) - \lambda' = 0 \qquad (30b)$$

Combining these,

$$aq(\gamma_+ - \gamma_+^{-1}) + br(\gamma_+ + \gamma_+^{-1}) = aq(\gamma_-^{-1} - \gamma_-) + br(\gamma_- + \gamma_-^{-1})$$

and after rearrangement,

$$\gamma_- = \left(\frac{br + aq}{br - aq}\right)\gamma_+ \qquad (31)$$

Also the boundary conditions require that

$$C_+ + C_- = 0$$

$$C_+\gamma_+^I + C_-\gamma_-^{-I} = 0$$

Then

$$C_- = - C_+ \text{ and } \gamma_+^I - \gamma_-^{-I} = 0$$

Using Equation (31), the second of these becomes

$$\gamma_+^I - \left(\frac{br + aq}{br - aq}\right)^{-I} \gamma_+^{-I} = 0$$

or

$$\gamma_+^{2I} = \left(\frac{br - aq}{br + aq}\right)^I$$

or

$$\gamma_+ = \left(\frac{br - aq}{br + aq}\right)^{1/2} e^{i\frac{k\pi}{I}} \quad k = 1, 2, \cdots, I - 1 \qquad (32a)$$

Then

$$\gamma_- = \left(\frac{br + aq}{br - aq}\right)^{1/2} e^{i\frac{k\pi}{I}} \qquad (32b)$$

Using these values in Equation (30a) or Equation (30b), we have

$$\lambda_k' = aq\left[\left(\frac{br - aq}{br + aq}\right)^{1/2} e^{i\frac{k\pi}{I}} - \left(\frac{br - aq}{br + aq}\right)^{-1/2} e^{-i\frac{k\pi}{I}}\right]$$

$$+ br\left[\left(\frac{br - aq}{br + aq}\right)^{1/2} e^{i\frac{k\pi}{I}} + \left(\frac{br - aq}{br + aq}\right)^{-1/2} e^{-i\frac{k\pi}{I}}\right]$$

$$= \sqrt{(br)^2 - (aq)^2}\left(e^{i\frac{k\pi}{I}} + e^{-i\frac{k\pi}{I}}\right)$$

$$= 2\sqrt{(br)^2 - (aq)^2}\cos\frac{k\pi}{I} \qquad k = 1, 2, \cdots, I - 1 \qquad (33)$$

which are the eigenvalues of $\underline{B}$. Using Equation (32a) and Equation (32b) in Equation (29), we have

$$\tau_i = C_+\left[\left(\frac{br - aq}{br + aq}\right)^{i/2} e^{i\frac{k\pi i}{I}} - \left(\frac{br + aq}{br - aq}\right)^{-i/2} e^{-i\frac{k\pi i}{I}}\right]$$

$$= C_+\left(\frac{br - aq}{br + aq}\right)^{i/2} \sin\frac{k\pi i}{I} \qquad (34)$$

(Here only the first "i" in the exponentials is $\sqrt{-1}$ in the first equation. In the second, the $2\sqrt{-1}$ has been incorporated in C_+.) We now have that the eigenvalues of $\underline{A}$ are

$$\lambda_k = (1 - 2br) + \lambda_k'$$

$$= (1 - 2br) + 2\sqrt{(br)^2 - (aq)^2}\cos\frac{k\pi}{I}$$

$$k = 1, 2, \cdots, I - 1 \qquad (35)$$

and the eigenvectors of $\underline{A}$, being common with those of $\underline{B}$, are

$$(\underline{\tau}_k)_i = \left(\frac{br - aq}{br + aq}\right)^{i/2} \sin \frac{k\pi i}{I} \tag{36}$$

The stability criterion for the mixed initial value-boundary value problem by the matrix analysis is, from Equation (35) and Equation (25), one of the following:

$$\left|1 - 2br + 2\sqrt{(br)^2 - (aq)^2}\cos\frac{k\pi}{I}\right| < 1 \quad \text{if } |br| \geq |aq| \tag{37a}$$

for all $k = 1, 2, \cdots, I - 1$

$$(1 - 2br)^2 + 4[(aq)^2 - (br)^2]\cos^2\frac{k\pi}{I} < 1 \text{ if } |aq| \geq |br| \tag{37b}$$

for all $k = 1, 2, \cdots, I - 1$

These are the same as Equations (23a) and (23b) obtained from the von Neumann analysis with boundary conditions.

Also since the eigenvectors of $\underline{A}$ form a complete set, $\underline{A}$ being real and symmetric, we may expand the initial error in terms of these eigenvectors. Using Equation (36),

$$(\underline{\varepsilon}^o)_i = \sum_{k=1}^{I-1} C_k \left(\frac{br - aq}{br + aq}\right)^{i/2} \sin\frac{k\pi i}{I} = \sum_{k=1}^{I-1} C_k (\underline{\tau}_k)_i \tag{38}$$

Then by Equation (24)

$$\underline{\varepsilon}^n = \underline{A}^n \underline{\varepsilon}^o = \underline{A}^n \sum_{k=1}^{I-1} C_k \underline{\tau}_k = \sum_{k=1}^{I-1} C_k \underline{A}^n \underline{\tau}_k = \sum_{k=1}^{I-1} C_k \lambda_k^n \underline{\tau}_k$$

since $\underline{\tau}_k$ is an eigenvector of $\underline{A}$ so that $\underline{A}\underline{\tau}_k = \lambda_k \underline{\tau}_k$. Then

$$(\underline{\varepsilon}^n)_i = \sum_{k=1}^{I-1} C_k \left(\frac{br - aq}{br + aq}\right)^{i/2} \sin\frac{k\pi i}{I} (\lambda_k)^n \qquad (39)$$

with λ_k given by Equation (35). This also agrees with the expansion in Equation (21) obtained by the von Neumann analysis with boundary conditions.

Stability Criteria

One-Dimensional

Now consider the mixed initial value-boundary value problem. The stability condition is then given by Equation (23):

$$\left|1 - 2br + 2\sqrt{(br)^2 - (aq)^2}\cos\frac{k\pi}{I}\right| < 1 \text{ if } |br| \geq |aq|$$

$$(1 - 2br)^2 + 4[(aq)^2 - (br)^2]\cos^2\frac{k\pi}{I} < 1 \text{ if } |aq| \geq |br|$$

Now b is positive for problems of interest, and the sign of a does not matter. Therefore take both a and b positive. If $aq \leq br$ and $1 - 2br \geq 0$ we must have

$$1 - 2br + 2\sqrt{(br)^2 - (aq)^2} < 1$$

or

$$\sqrt{(br)^2 - (aq)^2} < br$$

which is already satisfied since $aq \leq br$ here. Therefore the

solution is stable for $r \leq \frac{1}{2b}$ and $aq \leq br$.

If $aq \leq br$ and $1 - 2br \leq 0$ we must have

$$2br - 1 + 2\sqrt{(br)^2 - (aq)^2} < 1$$

or

$$br + \sqrt{(br)^2 - (aq)^2} < 1$$

or

$$\sqrt{(br)^2 - (aq)^2} < 1 - br$$

But this requires that $1 - br > 0$ or $r < \frac{1}{b}$. Then

$$(br)^2 - (aq)^2 < 1 - 2br + (br)^2$$

is required, or $(aq)^2 > 2br - 1$. The solution then is also stable for

$$\frac{1}{2b} \leq r < \frac{1}{b} \text{ and } \sqrt{2br - 1} < aq \leq br$$

If $aq \geq br$ we must have

$$(1 - 2br)^2 + 4[(aq)^2 - (br)^2] < 1$$

or

$$1 - 4br + 4(br)^2 + 4(aq)^2 - 4(br)^2 < 1$$

or

$$-4br + 4(aq)^2 < 0$$

or

$$(aq)^2 < br$$

Then

$$br \leq aq < \sqrt{br}$$

But this then requires that $br < \sqrt{br}$, or that $br < 1$. We then also have stability for

$$r < \frac{1}{b} \text{ and } br \leq aq < \sqrt{br}$$

In summary the solution is stable under any of the following three conditions:

(1) $r \leq \frac{1}{2b}$ and $q \leq \frac{br}{a}$

(2) $\frac{1}{2b} \leq r < \frac{1}{b}$ and $\frac{\sqrt{2br - 1}}{a} < q \leq \frac{br}{a}$

(3) $r < \frac{1}{b}$ and $\frac{br}{a} \leq q < \frac{1}{a}\sqrt{br}$

But conditions (1) and (3) can be combined to give stability for

$$r \leq \frac{1}{2b} \text{ and } q < \frac{1}{a}\sqrt{br}$$

and conditions (2) and (3) can be combined to give stability for

$$\frac{1}{2b} \leq r < \frac{1}{b} \text{ and } \frac{\sqrt{2br}}{a} < q < \frac{1}{a}\sqrt{br}$$

We thus finally have two regions of stability:

(a) $r \leq \frac{1}{2b}$ and $q < \frac{\sqrt{br}}{a}$

$$(b)\ \frac{1}{2b} \leq r < \frac{1}{b} \text{ and } \frac{\sqrt{2br - 1}}{a} < q < \frac{\sqrt{br}}{a}$$

Two-Dimensional

For two-dimensional mixed initial value-boundary value problems, Equation (22) is replaced by

$$\zeta_{k,l} = 1 - 4br + 2\sqrt{(br)^2 - (aq)^2}\ (\cos\frac{k\pi}{I} + \cos\frac{l\pi}{J})$$

$$k = 1, 2, \cdots, I - 1;\ l = 1, 2, \cdots, J - 1$$

Then if $aq \leq br$ and $1 - 4br \geq 0$ we must have

$$1 - 4br + 4\sqrt{(br)^2 - (aq)^2} < 1$$

or

$$\sqrt{(br)^2 - (aq)^2} < br$$

which is already satisfied since $aq \leq br$ here. Therefore the solution is stable for $r \leq \frac{1}{4b}$ and $aq \leq br$.

If $aq \leq br$ and $1 - 4br \leq 0$ we must have

$$4br - 1 + 4\sqrt{(br)^2 - (aq)^2} < 1$$

or

$$br + \sqrt{(br)^2 - (aq)^2} < \frac{1}{2}$$

or

$$\sqrt{(br)^2 - (aq)^2} < \frac{1}{2} - br$$

But this requires that $\frac{1}{2} - br > 0$, or $r < \frac{1}{2b}$. Then

$$(br)^2 - (aq)^2 < \frac{1}{4} - br + (br)^2$$

is required, or $(aq)^2 > br - \frac{1}{4}$. The solution then is also stable for

$$\frac{1}{4b} \leq r < \frac{1}{2b} \text{ and } \sqrt{br - \frac{1}{4}} < aq \leq br$$

If $aq \geq br$ we must have

$$(1 - 4br)^2 + 16[(aq)^2 - (br)^2] < 1$$

or

$$1 - 8br + 16(br)^2 + 16(aq)^2 - 16(br)^2 < 1$$

or

$$(aq)^2 < \frac{br}{2}$$

Then

$$br \leq aq < \sqrt{\frac{br}{2}}$$

But this then requires that $br < \sqrt{\frac{br}{2}}$, or that $br < \frac{1}{2}$. We then also have stability for

$$r < \frac{1}{2b} \text{ and } br \leq aq < \sqrt{\frac{br}{2}}$$

Then after combining the 1st and 3rd, and 2nd and 3rd, of these regions we have as above two regions of stability:

(a) $r \leq \frac{1}{4b}$ and $q < \frac{1}{a}\sqrt{\frac{br}{2}}$

(b) $\frac{1}{4b} \leq r < \frac{1}{2b}$ and $\frac{1}{a}\sqrt{br - \frac{1}{4}} < q < \frac{1}{a}\sqrt{\frac{br}{2}}$

Three-Dimensional

In three dimensions Equation (22) is replaced by

$$\zeta_{k,l,m} = 1 - 6br + 2\sqrt{(br)^2 - (aq)^2}\left(\cos\frac{k\pi}{I} + \cos\frac{l\pi}{J} + \cos\frac{m\pi}{K}\right)$$

$k = 1, 2, \cdots, I - 1;\ l = 1, 2, \cdots, J - 1;$

$m = 1, 2, \cdots, K - 1$

Then if $aq \leq br$ and $1 - 6br \geq 0$ we must have

$$1 - 6br + 6\sqrt{(br)^2 - (aq)^2} < 1$$

or

$$\sqrt{(br)^2 - (aq)^2} < br$$

which is already satisfied since $aq \leq br$ here. Therefore the solution is stable for $r \leq \frac{1}{6b}$ and $aq \leq br$.

If $aq \leq br$ and $1 - 6br \leq 0$, we must have

$$6br - 1 + 6\sqrt{(br)^2 - (aq)^2} < 1$$

or

$$br + \sqrt{(br)^2 - (aq)^2} < \frac{1}{3}$$

or

$$\sqrt{(br)^2 - (aq)^2} < \frac{1}{3} - br$$

But this requires that $\frac{1}{3} - br > 0$ or $r < \frac{1}{3b}$. Then

$$(br)^2 - (aq)^2 < \frac{1}{9} - \frac{2}{3}br + (br)^2$$

is required, or $(aq)^2 > \frac{2}{3}br - \frac{1}{9}$. The solution then is also stable for

$$\frac{1}{6b} \leq r < \frac{1}{3b} \text{ and } \sqrt{\frac{2}{3}br - \frac{1}{9}} < aq \leq br$$

If $aq \geq br$, we must have

$$(1 - 6br)^2 + 36[(aq)^2 - (br)^2] < 1$$

or

$$1 - 12br + 36(br)^2 + 36(aq)^2 - 36(br)^2 < 1$$

or

$$(aq)^2 < \frac{br}{3}$$

Then

$$br \leq aq \leq \sqrt{\frac{br}{3}}$$

But this then requires that $br < \sqrt{\frac{br}{3}}$ or that $br < \frac{1}{3}$. We then also have stability for

$$r < \frac{1}{3b} \text{ and } br \leq aq < \sqrt{\frac{br}{3}}$$

Then after combining the 1st and 3rd, and 2nd and 3rd, of

these regions, we again have two regions of stability:

(a) $r \leq \frac{1}{6b}$ and $q < \frac{1}{a}\sqrt{\frac{br}{3}}$

(b) $\frac{1}{6b} \leq r < \frac{1}{3b}$ and $\frac{1}{a}\sqrt{\frac{2}{3}br - \frac{1}{9}} < q < \frac{1}{a}\sqrt{\frac{br}{3}}$

APPENDIX I

SOME PROPERTIES OF QUADRATIC ROOTS

Let the roots of the quadratic equation

$$A\beta^2 + B\beta + C = 0$$

be required to be less than unity in magnitude. Thus

$$\left| \frac{-B \pm \sqrt{B^2 - 4AC}}{2A} \right| < 1$$

or

$$\left| -B \pm \sqrt{B^2 - 4AC} \right| < 2|A| \qquad (1)$$

Four combinations of real and complex coefficients of interest in the present application are considered below.

Case 1 - A, B, C Real and $B^2 - 4AC \geq 0$

In this case the inequality (1) may be written

$$|B| + \sqrt{B^2 - 4AC} < 2|A| \qquad (2)$$

or

$$\sqrt{B^2 - 4AC} < 2|A| - |B|$$

This then requires that $|B| < 2|A|$, and also that

$$B^2 - 4AC < 4A^2 + B^2 - 4|A| \cdot |B|$$

or

$$|A| \cdot |B| < A(A + C) \qquad (3)$$

But this requires that $A(A + C) > 0$ or

$$A^2(1 + \frac{C}{A}) > 0$$

Since A is real, this then reduces to $\frac{C}{A} > -1$. Then the inequality (3) may be written

$$|B| < \frac{A^2}{|A|}(1 + \frac{C}{A}) = |A(1 + \frac{C}{A})|$$

or finally,

$$|B| < |A + C|$$

There are thus three conditions necessary for the satisfaction of the inequality (2):

$$|B| < 2|A|$$

$$\frac{C}{A} > -1$$

$$|B| < |A + C|$$

together with the originally stated condition $B^2 \geq 4AC$. From the first of these conditions we have $B^2 < 4A^2$ so that

$$4AC \leq B^2 < 4A^2$$

But this requires that

$$4AC \leq 4A^2$$

or that $\frac{C}{A} < 1$. This, then, with the second condition above,

requires that $\left|\frac{C}{A}\right| < 1$. This being the case, the first condition above is redundant, in view of the third condition. Therefore, the conditions for the satisfaction of the inequality (1) in this case may be reduced to

$$\left|\frac{C}{A}\right| < 1 \text{ and } |B| < |A + C|$$

Case 2 - A, B, C Real and $B^2 - 4AC < 0$

In this case the inequality (1) may be stated as

$$B^2 + (4AC - B^2) < 4A^2 \tag{4}$$

so that it is required that $\frac{C}{A} < 1$. But since $B^2 < 4AC$ and B is real, we must have $AC > 0$. Therefore, the satisfaction of the inequality (1) requires in this case only that

$$\left|\frac{C}{A}\right| < 1$$

Case 3 - A, C Real; B Imaginary; $|B|^2 + 4AC \geq 0$

Let the imaginary B be written as $B = ib$, where b is real. Then inequality (1) may be stated as

$$|-ib \pm \sqrt{-b^2 - 4AC}| < 2|A|$$

Then, since $b^2 + 4AC \geq 0$, this may be written as

$$|b| + \sqrt{b^2 + 4AC} < 2|A| \tag{5}$$

which requires that $|b| < 2|A|$. Then

$$b^2 + 4AC < 4A^2 + b^2 - 4|A| \cdot |B|$$

or

$$|A| \cdot |b| < A(A - C) \tag{6}$$

But this requires that $A(A - C) > 0$ or

$$A^2(1 - \frac{C}{A}) > 0$$

Therefore it is required that $\frac{C}{A} < 1$. This being the case, the inequality (6) becomes

$$|b| < \frac{A^2}{|A|} (1 - \frac{C}{A}) = |A(1 - \frac{C}{A})|$$

so that $|b| < |A - C|$ is required.

There are then three conditions for the satisfaction of the inequality (5), together with the originally stated condition $b^2 \geq - 4AC$:

$$|b| < 2|A|$$

$$\frac{C}{A} < 1$$

$$|b| < |A - C|$$

From the first of these conditions we have $b^2 < 4A^2$ so that

$$- 4AC \leq b^2 < 4A^2$$

This then requires that

$$-4AC < 4A^2$$

or that $\frac{C}{A} > -1$. This, with the second condition above, requires that $\left|\frac{C}{A}\right| < 1$ and, the first condition becomes redundant in view of the third condition. Therefore the conditions for satisfaction of the inequality (1) in this case reduce to

$$\left|\frac{C}{A}\right| < 1$$

$$|B| < |A - C|$$

Case 4 - A, C Real; B Imaginary; $|B|^2 + 4AC < 0$

Again with $B = ib$, b being real, the inequality (1) may be stated in this case as

$$b^2 + (-b^2 - 4AC) < 4A^2$$

so that it is required that $\frac{C}{A} > -1$. But since $b^2 < -4AC$ and b is real, we must have $AC < 0$. Therefore the satisfaction of the inequality (1) requires, in this case, only that

$$\left|\frac{C}{A}\right| < 1$$

APPENDIX J

NONLINEAR INSTABILITY*

Source of Nonlinear Instability

The nonlinear instability arises from the derivatives in the convective terms involving the z-velocity component of Equation (V - 3c):

$$\frac{\partial}{\partial x}(w\xi) \text{ and } \frac{\partial}{\partial y}(w\eta)$$

Since the flow starts with a velocity discontinuity at the interface between the jet and cross-wind, the gradients of z-velocity and x-y vorticity are quite large in the vicinity of this original interface for several time steps. This results in very large values of the above derivatives, which may persist for several time steps.

The large tangential (to the interface, or jet edge) derivatives of the product of the z-velocity and the x-y vorticity in Equation (V - 3c) amplify the magnitude of the

---

*All quantities used on figures discussed in this appendix are nondimensionalized as noted in the Nomenclature. The scale factors for the vector plots are given in Table 5. The magnitude of a vector is indicated by the length of the stem of the arrow, the size of the arrowheads being the same throughout. Spurious lines on the plots are the result of plotter error. Parameters used in all results presented are given in Table 4.

z-vorticity on the jet edge and reverse the direction at some points at the first time step. Similarly the large normal derivatives of the same product create large z-vorticity at the points adjacent to the original interface, especially inside the jet, at some of which points the new vorticity is opposite in direction to the initial values at the adjacent points on the interface. The result at the first time step is shown in Figure 76a.

The gradients of x-y velocity are much smaller, however, so that no amplification occurs through Equation (V - 3a) or (V - 3b) at the start. The x-y vorticity thus exhibits only a normal spread from the interface (Figure 76b). The z-velocity, which is induced by the x-y vorticity, therefore is quite regular (Figure 76c), but the amplified and misdirected z-vorticity induces an irregular x-y velocity distribution with large gradients, especially inside the jet, and with a tendency toward inflow into the jet on all sides (Figure 76d).

In the following time steps the large z-vorticity from the first time step is reversed and reduced in magnitude by the normal (to the jet edge) derivatives of the product of z-velocity and x-y vorticity. The normal derivatives also cause large z-vorticity to spread out to the sides and rear of the jet. Though some misdirection still remains, the z-vorticity distribution has now assumed mostly its original

direction, but with amplification (Figure 76e). This results in an x-y velocity distribution more closely resembling the original, but with outflow from the jet ahead of the 90° point and inflow behind because of the amplified z-vorticity around the sides of the jet. The region of amplified z-vorticity at the rear of the jet causes a similar region of outflow and inflow across the jet to exist near the center line at the rear of the jet (Figure 76h). (Though the figure shows the results at the third time step, this pattern was already formed at the second step.)

This x-y velocity distribution involves large tangential gradients of the normal velocity at the edge of the jet on the sides and at the rear. This then causes the tangential derivative of the product of the normal velocity and tangential vorticity to be large in these regions, resulting in amplification of the normal vorticity through Equations (V - 3a) and (V - 3b), (Figure 76f). This again is a nonlinear coupling of the equations, for the tangential vorticity here couples with the normal velocity to amplify the normal vorticity through the $\frac{\partial}{\partial y}(u\eta)$ term of Equation (V - 3a) and the $\frac{\partial}{\partial x}(v\xi)$ term of Equation (V - 3b). This misdirection of the x-y vorticity results in an irregular z-velocity distribution, with large z-velocity being induced at the sides of the jet. Close examination of Figure 76g shows the z-

velocity near the front and rear of the jet to be larger at the sides than on the centerline.

This increased z-velocity and x-y vorticity at the sides of the jet then couple to amplify the z-vorticity in that region, while the originally amplified z-vorticities are being reduced by convection and diffusion (Figure 76i). Simultaneously the x-y vorticity at the sides is being amplified by the coupling of the large x-y velocity gradients and x-y vorticity in that region (Figure 76j). The increased z-vorticity at the sides of the jet maintains the x-y velocity pattern (Figure 76l), with strong flow away from the jet at the sides followed closely by return flow to the jet, that causes the amplification of the x-y vorticity. Similarly, the increased x-y vorticity in the same region maintains the large z-velocity at the sides of the jet which causes the amplification of the z-vorticity (Figure 76k). The largest jet velocities then occur in the wings of the jet rather than in the central portion. The result of this nonlinear coupling of the equations is divergence unless the large vorticity generated can be dissipated by convection and diffusion rapidly enough.

This nonlinear coupling of the equations for the vorticity thus arises through "convection" of velocity along vortex lines, as represented by the term $(\underset{\sim}{\omega} \cdot \underset{\sim}{\nabla})\underset{\sim}{v}$, rather than convection due to fluid motion, represented by $(\underset{\sim}{v} \cdot \underset{\sim}{\nabla})\underset{\sim}{\omega}$. In fact the latter process, through the convective

terms involving ξ, η, and ζ in Equations (V - 3a), (V - 3b), and (V - 3c), respectively, tends to aid diffusion in dissipating the gradients generated. The nonlinear coupling is a three-dimensional process and does not occur in completely two-dimensional flow, i.e., with zero velocity in the direction of invariance, since there only one component of vorticity is non-zero.

The entirely different character of linear instability, due to the diffusion terms, is illustrated in Figure 77. Diffusional instability tends to produce general amplification of all vorticity components, with a wave-like velocity field, rather than the localized amplification and disturbance characteristic of the nonlinear instability.

Characteristics of Nonlinear Instability

This disturbance due to the convective terms is dependent only on the time step and not the Reynolds number. Whether the process leads to significant perturbation of the flow or even divergence, however, is dependent on the Reynolds number since diffusion serves to damp the sustaining gradients. Thus, the divergence shown in Figure 27b is due to linear instability, the nonlinear disturbance being damped completely by diffusion at this low Reynolds number. Above a cell Reynolds number of about 3 for a velocity ratio of 8, it is the nonlinear instability that leads to divergence unless a gradual start is used. Such a gradual

start renders the flow much more smooth. At higher velocity ratio, however, the nonlinear disturbance becomes severe at lower Reynolds number as in Figure 78b, which shows the wave-like linear disturbance upstream, but with the strong flow away from and then back to the jet characteristic of the nonlinear disturbance.

Instability from this source is more severe in the present case because the representation of the curved initial interface between the jet and cross-flow by square cells as shown in Figure 12 requires evaluating derivatives oblique to a discontinuity. In this representation the z-velocity and the component of vorticity parallel to the line of these interface cells both vary along the line of cells, and it is the values of the above-mentioned derivatives parallel to the line of interface cells that are excessive. In a curvilinear coordinate system composed of lines parallel and perpendicular to the curved interface, however, there would be no variation tangential to the interface of either the z-velocity or the tangential vorticity component, and there would be no normal component of vorticity. Since the derivatives in question would be replaced in that case by derivatives parallel and perpendicular to the interface, their values would be zero at the start and less than those occurring in the present case thereafter. The instability could still develop after the start, however, since the

vorticity would not remain parallel to the coordinate lines. The irregularity of the original interface in the present case served only to initiate the original amplification of the z-vorticity. The sustentation of the process thereafter cannot be attributed to the form of the original interface, since no such discontinuity exists after the start. A sufficiently large disturbance in vorticity would trigger the process in any case.

The severity of the perturbation caused by this nonlinear instability increases with the velocity ratio (Figure 78) since it arises from the z-velocity. It also increases with the cell Reynolds number since the efficacy of the diffusion terms in dissipating the gradients decreases as the Reynolds number increases.

Setting the z-velocity in the interface cells to zero at the start reduces the destabilizing effect of the nonlinear instability considerably at low cell Reynolds number. This procedure is justified on the grounds that the z-velocity is zero outside the discontinuity curve, and this outside value may as well be taken in the interface cells through which the discontinuity curve passes. However, as the Reynolds number increases, the reduction in the gradients by diffusion in the first time step becomes insufficient to prevent amplification of the z-vorticity at the following steps. Reducing the time step at the start does not help

greatly because the relative magnitudes of the convective and diffusive terms remains the same. The instability can be reduced, however, by starting the flow gradually rather than impulsively, but at larger cell Reynolds numbers the start must be very gradual indeed as is shown in the results presented in Chapter V.

Figure 79 shows the flow pattern for elliptic jets with the same major diameter as the circular jet of Figure 79a and with the same cell Reynolds number and time step, the z-velocity in the interface cells again being set to zero at the start. As would be expected, the nonlinear instability is more severe for the elliptic jet with its major axis perpendicular to the cross-wind than for the circular jet, since the gradients 90° from the cross-flow direction are more severe in the former case as a result of the larger curvature of the ellipse in those regions. Similarly the gradients in these regions are less severe with the ellipse major axis parallel to the cross-wind, so that the nonlinear instability is less pronounced in this case than with a circular jet of the same minor diameter.

The nonlinear instability is reduced as the time step decreases at the lower Reynolds number, cf. Figures 80 and 81, but the time step has less effect as the Reynolds number increases and the diffusion becomes less effective. Again a significant residual perturbation is left for cell Reynolds

number greater than about 2 at a velocity ratio of 8. The damping of a strong early disturbance is illustrated in Figure 82 for a case in which the z-velocity was not set to zero in the interface cells at the start and the flow was started impulsively. At the later time the outward deflection fartherest downstream is the residual perturbation.

That a gradual start that is not gradual enough can be worse than an impulsive start is illustrated in Figure 83, which shows the same case as in Figure 82 but with a gradual start through which the jet and cross-wind velocities were doubled at each time step, the full values being reached in 20 steps. The flow at the early time step is much smoother with the gradual start since the velocities at that time were much smaller in that case. However, at the later time, 20 steps after the attainment of full velocity, the flow is more disordered than that with the impulsive start. The reason for this is that at this Reynolds number the diffusion is so small that it alone cannot achieve sufficient dissipation of the gradients before the velocities near their full values in the twenty-step start. The result then is effectively a delayed rapid, though not impulsive, start, and, as far as the instability is concerned, a given number of time steps after the attainment of full velocity with the twenty-step start corresponds more closely to the same number of time steps from the start with the

impulsive start. Thus Figure 83b is more similar to Figure 82b than to 82c, although in time it corresponds to the latter. In the same manner, five and ten-step starts at this Reynolds number gave less disturbance at a given time than did the twenty-step start, the five being superior to the ten. The disturbance was still dissipated faster with the impulsive start.

At a Reynolds number of 2.5 a two-step start was sufficient to completely eliminate the perturbation. The gradual start thus is effective against the nonlinear disturbance, especially at the lower Reynolds numbers where it gives diffusion a change to achieve significant dissipation of the gradients before the convection terms become appreciable. However, at higher Reynolds number the start must be extremely slow, since the diffusion is much reduced. An insufficiently gradual start simply delays the onset of the disturbance. Linear starts were also examined but found to be less effective than the type discussed above for the same number of steps in the period of velocity increase. The reason for the superiority of the latter type is that it provides an initial period when essentially no convection is in effect. At high Reynolds number, however, this period must be very long to allow the low diffusion to achieve sufficient dissipation.

APPENDIX K

VORTICITY AND VELOCITY INTERACTIONS IN THE THREE-DIMENSIONAL JET IN CROSS-WIND*

Profiles of the vorticity and velocity are shown in Figures 84-95 for the jet starting from the opening of the exit and in Figures 94-103 for the jet starting from the cylindrical discontinuity above the jet exit. In all cases both the jet and the cross-flow velocities were gradually increased to their final values by doubling the value at each time step, until the final value was reached at the time step indicated. Figures 84-88 and 94-98 show unstable cases for the two types of start, and these are used for the detailed analysis below since the features are more marked. Throughout the following discussion the terms "horizontal" and "vertical" are applied to planes parallel and perpendicular, respectively, to the boundary plane. Also, "front" and "rear" refer, respectively, to the upstream and downstream directions of the remote cross-flow.

---

*All quantities used on figures discussed in this appendix are nondimensionalized as noted in the Nomenclature. The scale factors for the vector plots are given in Table 5. The magnitude of a vector is indicated by the length of the stem of the arrow, the size of the arrowheads being the same throughout. Spurious lines on the plots are the result of plotter error. Parameters used in all results presented are given in Table 4.

Start from the Opening of the Jet Exit

Considering first the start from the opening of the jet exit, at the start the vorticity distribution consists of the superposition on the boundary plane of straight lines of vorticity anti-parallel to the y-axis and concentric vorticity rings centered on the jet exit axis. The straight lines of vorticity have no variation in the x-direction and are the result of the cross-flow, while the rings are due to the source flow from the jet exit and thus increase from zero strength at the exit axis to maximum strength on the edge of the exit, with continual decrease thereafter. This type of start thus has no vorticity in the fluid above the boundary. The fluid on the jet exit, however, does have non-zero horizontal vorticity. The initial velocity distribution is formed by the superposition of the uniform cross-flow parallel to the boundary and the velocity due to a distribution of sources of strength equal to the jet exit velocity located on the jet exit as discussed in Chapter VI.

Unstable Case - $V_r = 8$

During the first portion of the gradual start the convective terms are insignificant compared with the diffusion terms, so that the vorticity spreads upward from the boundary by diffusion, with a resultant decrease in magnitude of the

vorticity on the boundary. In the last few starting steps, however, the convection becomes significant and begins to spread the vorticity downstream over the entire boundary and also upward and outward over the jet exit. The vertical convection on the exit reverses the diffusional decline in horizontal vorticity magnitude there, as vorticity is convected up from below, and tends to increase the magnitude of the horizontal vorticity on and above the exit. This trend continues in the steps following the attainment of full velocity and is evident in the η-profiles of Figure 84b.

The vertical convection from below is absent on the edges of the exit, the exit velocity being zero there, so that the horizontal vorticity continues to be reduced in magnitude by diffusion during and immediately following the start period as shown in Figures 84a and 84c. The decrease in magnitude is accelerated at the rear edge after significant negative vorticity has been convected above the edge and the negative peak is formed as discussed below. The presence of the peak and the accompanying increase in vertical velocity causes significant upward convection of negative vorticity away from the exit edge, thus accelerating the trend toward lower negative vorticity on the edge (Figure 84a, $t = 2.2$).

The large horizontal velocity above the exit rear edge, due to the combination of the cross-flow and the large

outward horizontal velocity of the jet at this early time, causes considerable rearward convection of negative horizontal vorticity from over the exit into this region. This convection parallel to the boundary, aided by vertical convection from below as the vorticity rises over the edge, causes the rising negative peak in the η-profile in Figure 84a. Over the exit front edge the horizontal convection is reduced, since the cross-flow and the outward horizontal velocity of the jet are in opposition. The resultant horizontal convection is forward, since the horizontal velocity of the jet is larger in magnitude at this early time than that of the cross-flow. Also, the horizontal vorticity on and over the forward portion of the exit is positive as a result of the large source velocity, so that there is horizontal convection of positive vorticity from over the exit into the region above the forward edge, as well as vertical convection from below as the vorticity rises. The reduction in the horizontal convection, however, results in only a positive protuberance on the η-profile in Figure 84c, over the forward edge, rather than a peak as over the rear edge.

The negative peak in Figure 84a and the positive protuberance in Figure 84c represent the expected emission of the vortex ring from the exit, as influenced in the present case by the downstream sweep of the cross-flow, which tends to strengthen the ring in the rear and weaken it in front.

This causes the ring to rise from the front to the rear of the jet, so that the rear portion of the ring is both higher and stronger than the front.

Also during this period following the attainment of full velocity, vertical vorticity is generated around the exit edges as a result of the horizontal gradients of the vertical velocity along lines of horizontal vorticity (Figure 85a).

The horizontal velocity over the center of the exit at first tends to increase negatively as a result of the increase in negative η-vorticity on the exit (Figure 86c). However, the vertical vorticity being generated around the exit edges induces positive horizontal velocity over the exit center, with the result that the u-profile develops a bend back toward positive values after sufficient vertical vorticity has been generated (Figure 86c, t = 2.2).

The behavior of the horizontal velocity profiles at the exit edge is due to the passage of the rising vortex ring: an increase in velocity away from the jet axis above the ring, followed by a decrease below the ring (Figures 86b, 86d, 87a). The vertical velocity peaks also reflect the passage of the ring, the effect being stronger toward the rear as a result of the convectional strengthening of the rear of ring by the cross-flow. This is evident in Figures 88a-c.

The vortex ring around the edge of the jet is influenced both by horizontal and vertical convection, and the relative importance of the two varies with position of the ring. This causes the ring to broaden vertically, with horizontal convection tending to strengthen the upper portion of the ring and vertical convection the lower. At the early times the horizontal convection is the stronger, since the jet still possesses a strong radial flow, so that the maximum vorticity magnitude occurs on the upper portion of the ring (Figure 84a, t = 2.2; Figure 84d, t = 2.4, 2.6; Figure 84f, t = 2.4, 2.6).

However, the ring increases the vertical velocity of the jet and decreases the radial velocity just below the ring. Therefore, the horizontal convection is overshadowed by vertical convection in the lower portion of the ring. As the ring rises, the jet radial velocity is reduced and its vertical velocity is increased, so that the vertical convection becomes dominant, and the vorticity magnitude maximum shifts from the upper to the lower portion of the ring (Figures 84d and 84f, t = 2.8). The further decline in jet radial velocity as the ring rises farther causes the effect of horizontal convection to be reduced to such an extent that the upper portion of the vorticity crest gradually disappears (Figures 84d and 84f, t = 3.4). The effect of the cross-flow is again evident in the more rapid decline in the horizontal

convection effect upstream.

The vorticity of the ring initially amplifies itself as it rises, since an increase in the vorticity of the ring tends to increase the vertical convection into the region just above the ring, both by virtue of the vorticity increase itself and through the consequent increase in vertical velocity. As the vertical velocity above the exit edge increases, the upward convection from the exit increases, with a resultant decrease in the magnitude of the horizontal vorticity on the exit edge (Figures 84d and 84f). The decrease in magnitude of vorticity above the exit edge after passage of the ring, however, decreases this convection, so that a constant value of horizontal vorticity at the exit edge is approached.

The large vertical gradient of horizontal vorticity in the region immediately below the ring combines with the increase in vertical velocity in this region caused by the ring to produce large upward convection of vorticity out of this region. This results in a significant decrease in the magnitude of the horizontal vorticity after passage of the ring, as is demonstrated by the large reversals in the η-profiles in Figures 84d and 84f. This trough in the horizontal vorticity around the jet edge rises behind the ring and is even more amplified by vertical convection than is the ring, since the presence of the large vorticity of the ring

above continues to produce upward convection of vorticity out of the region between the ring and the trough, while the trough itself reduces the convection of vorticity into this region from below. In the present unstable case this amplification proceeds to the point of reversing the direction of the horizontal vorticity in the trough and thus replacing the trough with a ring of opposite vorticity following the primary ring.

In a similar manner the deficit of vorticity in the trough reduces the upward convection out of the region below the trough, so that convection of horizontal vorticity from below into this region causes another reversal in the horizontal vorticity below the trough, and thus a ring of vorticity of the same sense as the primary ring following the trough or ring of opposite sense, as the case may be (Figures 84d and 84f, t = 3.4).

The increase in vertical velocity in the plane of the vortex ring emitted at start causes an increase in vertical convection over the jet exit and a consequent increase in negative horizontal vorticity above the exit center as vorticity is convected from below (Figure 84e, t = 2.6). This negative vorticity peak rises and is amplified by vertical convection from below in the same manner as is the ring discussed above. Also in the manner discussed above, the negative vorticity peak causes large upward convection of

negative vorticity out of the region below the peak and creates a deficit in vorticity there. In the present case the upward convection of negative vorticity out of this region is sufficient to drive the deficit to a positive vorticity peak (Figure 84e, t = 3.0). This peak is then strongly amplified, since the region between it and the negative peak above experiences both the loss of negative vorticity through upward convection to the negative peak above and the gain of positive vorticity through convection from the positive peak below.

There also is large upward convection of positive vorticity out of the region below the positive peak, which creates first a deficit in vorticity and eventually a second negative peak in that region (Figure 84e, t = 3.2). This peak is also strongly amplified by vertical convection, through the combined influence of its own vorticity and the positive peak above in the same manner as is the positive peak.

The amplification is enhanced by horizontal convection, since the horizontal velocity induced by these horizontal vorticity peaks is in such a direction as to convect vorticity into the regions of the peaks following the first. This effect, however, is overshadowed by the stronger amplification produced by vertical convection as a result of the very large gradients of vorticity. The amplification of these

horizontal vorticity peaks within the jet is not unlike that of the peaks around the jet edges, except that the much larger vertical velocity within the jet drives the amplification to a much greater degree within the jet. The destabilization therefore occurs within the jet.

On the exit center the horizontal vorticity reverses its early negative increase as the vertical velocity above the exit increases and the vertical convection of vorticity from below is thus balanced. Diffusion then decreases the magnitude of the vorticity (Figure 84e, t = 2.8). However, with the development of the second negative peak of vorticity above the exit, the negative vorticity on the exit is reduced in magnitude as the upward convection of negative vorticity away from the exit is increased by the presence of this peak. In the present unstable case this vorticity deficit is driven to positive vorticity (Figure 84e, t = 3.0). The vorticity on the exit center then increases positively at a greater rate, being influenced both by upward convection of negative vorticity to the peak above and convection of positive vorticity from below.

The vertical vorticity is subject to much less variation as shown in Figure 85b and continues to be generated primarily by gradients of vertical velocity along lines of horizontal vorticity. The amplification is a result of prior amplification of horizontal vorticity. The trough evident at

t = 3.4 is due to a diffusional decrease when the convective terms balance. The decrease at the boundary at the later times is a result of diffusion.

The horizontal velocity profiles (Figures 86 and 87) reflect primarily the effect of the horizontal vorticity distribution, since the amplification thereof causes the effect of the vertical vorticity to be overshadowed. The peaks of the horizontal velocity profiles lie generally between those of the horizontal vorticity at the same location. The outward directed horizontal velocity immediately above the exit edge is due to the horizontal vorticity around the edge that results from the presence of the jet. This outflow is eventually to be balanced by inward velocity induced by horizontal vorticity above the boundary plane. In particular, the excessively large forward velocity above both the center and front of the jet exit at the later times (Figures 86h and 86i, t = 3.4) is due to the positive horizontal vorticity generated at those times on the exit by vertical convection of negative vorticity away from the exit into the second negative horizontal vorticity peak as discussed above.

The vertical velocity (Figure 88) generally follows the rise of the horizontal vorticity around the jet edge, especially over the exit axis. However, the strong peak just above the exit axis at the later times (Figure 88e,

t = 3.4) is due to the presence of strong negative horizontal vorticity just downstream, corresponding to the lower negative peak in the η-profile over the exit center in Figure 84e. All of these features are reduced in the stable case considered below.

Stable Case - $V_r = 8$

The reduction of convectional instability by a decrease in the time step is evident upon comparison of the results discussed above with those presented in Figures 89-93. Most of the same features discussed above are present, but the magnitudes are greatly reduced and some significant alteration of form results.

The primary effect at the early times of the time-step reduction is to significantly decrease the contribution of horizontal convection to the formation of the vortex ring emitted from the exit. Thus the sharp peak on the upper part of the negative crest of the η-profile of Figure 84a at t = 2.2 is eliminated (Figure 89a). A similar effect, but to a much lesser degree, occurs at the front of the jet (Figure 89c). Otherwise, the forms of both the horizontal and vertical vorticity distributions at the early times are not altered, though the magnitudes are decreased somewhat (Figures 89a-c, 90a).

The forms of the velocity distributions at the early times (Figures 91a-c, 92a, 93a-c) are altered only by the

above-mentioned reduction of the upper part of the horizontal vorticity crest. This causes a corresponding reduction of the outward horizontal velocity above the ring (most noticeable in Figure 92a at t = 2.2) and of the vertical velocity. The overall magnitudes are also somewhat reduced, of course.

Even at the later times the forms of the horizontal vorticity distributions are not greatly altered (Figures 89 d-f). Comparison of Figures 84d and 89d shows the negative peaks, which correspond to the vortex ring emitted from the exit at the start, to be in the same locations with each time step (comparison should be with the lower part of the crest in Figure 84d in view of the reduction in the upper part mentioned above). The same conclusions are reached by comparison of the positive crests at the front of the jet (Figures 84f and 89f). The speed of propagation of the ring is thus unaltered by the time step reduction. The primary effect is, as mentioned above, the reduction of the upper part of the vorticity crest that constitutes the ring, as a result of the reduction of the effect of horizontal convection. The self-amplification of the ring by vertical convection is also significantly reduced, but this affects only the magnitude, not the form.

Of more significance to stability is the alteration of the vorticity trough that follows the ring. In the

unstable case this vorticity deficit is amplified and driven to a reversal in direction of vorticity by vertical convection across the large vorticity gradient from the trough to the ring above. This amplification is reduced with the smaller time step to the extent that a balance is achieved with damping (Figures 89d and 89f). This then leaves only moderate vertical gradient of vorticity below the trough, so that no vortex ring follows the trough.

The reversal of the η-profile below the trough at the front of the jet (Figure 89f, $t = 3.4$) is caused by forward horizontal convection of positive vorticity from over the exit. This convection is a result of the forward horizontal velocity still being induced in the lower forward part of the jet by the positive horizontal vorticity that is created on the forward edge of the exit by the presence of the jet. This horizontal convection is thus increasing the positive vorticity in the forward part of the jet above the exit. This increase in positive vorticity in this region will then serve to balance that on the exit edge below and to reduce the forward velocity. Such a balance has already been more nearly achieved at the rear of the jet (Figure 89d).

The reduction of convectional instability has its greatest effect in the interior of the jet, however, as evidenced by the sharp contrast between Figure 84e and Figure 89e. Again the form and location of the crests are

esentially the same. Here, as at the jet edge, the reduced time step allows the amplification by vertical convection to be arrested by diffusion before the large vertical gradients that power the amplification by vertical convection can develop.

The vertical vorticity shows the least alteration, it being simply reduced and smoothed at the lower time step (Figure 90b). The positive crest occurring at t = 3.4 with the larger time step (Figure 85b), is, of course, removed, since the large horizontal vorticity that led to its creation has been eliminated. The boundary values of all vorticity components show little effect of the time step reduction.

The primary effect, other than a general magnitude reduction, of the reduction of the time step on the horizontal velocity distribution (Figures 91 and 92) is the change in form of the profiles below the ring emitted at the start. Since the severity of the horizontal vorticity trough following the ring has been greatly reduced, the upper part of the horizontal velocity crest below the ring, i.e., between the ring and the trough, is correspondingly reduced (Figures 91 g-i). The lower part of the horizontal velocity distribution reflects the elimination of the severe horizontal vorticity gradients in that region which induced this horizontal velocity in the previous case.

The form of these velocity distributions is due to the combined effects of the horizontal and vertical vorticity distributions. The outward velocity above the rising vortex ring emitted at the start is due to the ring. Similarly the inward velocity induced by the ring below itself accounts for the abrupt upper portion of the velocity crest in that region evident especially in Figures 91g and 92b at t = 3.4. These effects are less marked at the front of the jet because of both the opposition of the cross-flow and the reduced strength of the ring in that region (Figure 91i).

The lower portion of the velocity distribution, except for the region just above the boundary, is affected primarily by the vertical vorticity that has been generated around the jet edge, and generally follows the shape of the vertical vorticity distribution (Figure 90b). This causes a forward recirculation within the jet. In the region immediately above the boundary the horizontal vorticity on the boundary, which exists because of the presence of the jet, is also effective and tends to produce forward velocity in the forward portion of the jet and outward velocity around the jet edge. These velocities are, however, being reduced by the diffusion and convection of vorticity of like sign into the region above the boundary as discussed above. This vorticity tends to induce velocities in the opposite direction.

The vertical velocity distribution (Figure 93) is affected primarily by the large horizontal vorticity around the edge of the jet, and the crest reflects the passage of the vortex ring emitted at the start. The secondary crest at t = 3.4 above the exit (Figure 93e) is due to the negative horizontal vorticity crest just aft, corresponding to the lower negative crest of Figure 89e. The reduction of the upper portion of the horizontal vorticity crests at the lower time step is reflected by a corresponding reduction of the upper portion of the vertical velocity crests.

Start from a Cylindrical Discontinuity

With the start from the cylindrical discontinuity above the jet exit, the initial vorticity distribution on the boundary plane consists of lines of vorticity perpendicular to the streamlines of the two-dimensional potential flow about the cylinder. In addition there is a cylindrical vortex sheet standing on the exit and extending upward to infinity with no vertical variation. The vorticity on this sheet consists of horizontal rings of vorticity around the sheet and vertical vortex lines parallel to the cylinder axis, the former being due to the jet within the cylindrical discontinuity and the latter to the cross-flow without. The initial vorticity of the fluid both inside and outside the discontinuity is zero.

The fluid on the jet exit at the start

theoretically has zero vorticity also but, due to the discretization, a small amount of non-zero vorticity is present there. The initial velocity distribution consists of a uniform vertical jet within the cylindrical discontinuity, and the two-dimensional potential flow about the discontinuity, perpendicular to its axis, outside as discussed previously in Chapter VI.

Unstable Case - $V_r = 8$

During the first part of the gradual starting period the convective terms are negligible, and diffusion spreads the vorticity, reducing the sharp initial gradients. Thus the vorticity profiles at the end of the starting period (t = 0.8 in Figures 94 and 95) reflect primarily this diffusive effect. The differences between the front and rear of the jet near the boundary (Figures 93a, 93c) are the result primarily of the vorticity generated on the boundary by the cross-flow, which tends to be in conjunction with that due to the jet in the rear, but in opposition in front. The generation of horizontal vorticity on the boundary tends to counter the diffusional dissipation there, with the result that a vertical gradient in horizontal vorticity develops above the edge of the exit, especially in the rear where the vorticity generated on the edge by the jet and that generated by the cross-flow are in conjunction (Figure 94a, t = 0.8) and thus augment each other.

When the full velocities are attained, the existence of this vertical gradient causes horizontal vorticity to be convected upward from the exit edge, especially in the rear of the jet. This effect accounts for the peak in the η-profile at the rear of the jet (Figure 94a; t = 1.2, 1.6) that forms just above the boundary immediately after the starting period. This horizontal vorticity crest is then convected upward in the same manner as the starting vortex ring emitted from the exit with the other type of start discussed above. As with the ring in that case, the crest in the present case amplifies itself primarily by vertical convection as it rises, there being amplification to a lesser degree by horizontal convection, from upstream, of vorticity that had diffused from the jet edge. The rearward velocity causing this horizontal convection is the outward velocity induced by the crest above itself.

Also by the same process discussed for the other type of start, a vorticity trough develops behind the crest (Figure 94a, t = 2.4) and follows it upward, being amplified by vertical convection across the steep gradient of vorticity from trough to crest above. The development, rise, and amplification of the crest and trough in the present case are thus completely analogous to that of the vortex ring and trough formed with the start from the opening of the jet exit, but with much smaller amplitudes since the engendering

gradients are much smaller. Indeed, the use of "crest" here, as opposed to "ring" with the other start, has no significance other than to recall the difference in amplitude. The term "ring" was used before only in deference to common usage.

The vorticity crest is much less marked in the front of the jet, but is evident at the latest time shown (Figure 94c, t = 2.8). The crest here is amplified by vertical convection resulting from the stronger vertical gradient in vertical velocity, as well as from the gradient of horizontal vorticity, and, therefore, becomes significant only after the vertical velocity crest is formed. The vorticity crest then appears in the region of strong vertical velocity gradient above the vertical velocity crest.

As with the other start, the crest is both higher and stronger in the rear of the jet. (The trough above the crest in front of the jet is due to the excessive loss of vorticity to downstream horizontal convection resulting from the creation of vertical vorticity between the center and sides of the jet as discussed below in connection with the horizontal velocity profiles.) At the exit edge the horizontal vorticity decreases by diffusion until a balance is reached with vertical convection from below, and a steady-state is approached (Figure 94a, 94c). The general vertical decrease in horizontal vorticity at the edge of the jet is

due both to diffusion and downstream convection, the latter being relatively important in the front of the jet.

The only other noteworthy feature of the η-profiles at the jet edge is the small protuberance in the upper portion of the profiles (above the vorticity crest discussed previously, with the same direction as this crest) (Figures 94a, 94c; t = 2.8). This perturbation is a result of an approximation in the solution whereby the velocity in the border cells (cells having vorticity that differs from the value at an infinite distance above the point in question by less than a specified minimum) is taken to be the asymptotic value approached at an infinite distance above the point in question. This causes the vertical velocity above the topmost vortex cell to be slightly less than its true value, and thus allows a small excess of convection of vorticity from below to produce the protuberance in the vorticity profile. A comparison with a larger minimum vorticity is given in Figure 94 at t = 2.8. Here the above-mentioned uppermost vorticity crest at the rear of the jet is clearly more severe with the larger minimum vorticity. Otherwise the effect of the change in the minimum vorticity at this time is quite small.

The protuberance in the upper portion of the horizontal vorticity at the rear of the jet in Figure 94c, resulting as discussed above from the minimum vorticity effect, is

illustrative of the possible destabilizing influence of the use of too large a value for the minimum vorticity. The effect of the minimum vorticity is naturally greatest near the boundary of the region of non-zero vorticity and in this case a change of the minimum vorticity from 0.1 to 0.01 had almost no effect at all in the lower portion of the jet. At larger time steps the effect is more pronounced and hastens the destabilization.

The horizontal vorticity over the exit center is initially near zero, but some positive vorticity is soon acquired by horizontal convection from the front of the jet (Figure 94b, t = 0.8), resulting from the vertical vorticity generated between the center and sides of the jet as discussed below in connection with the velocity profiles. This convection causes a positive crest to form which rises and is amplified, both by its own tendency to increase the upward convection of positive vorticity into the region toward which it moves and by continued horizontal convection of positive vorticity from the front of the jet.

The vertical convection of positive vorticity out of the region below this crest causes a region of negative vorticity to develop below the crest (Figure 94b, t = 1.6). This negative crest is then strongly amplified as it rises by vertical convection across the large vertical gradient between it and the positive crest above. The negative crest

then causes large vertical convection of negative vorticity out of the region below and thus leads to the formation of a second positive crest (Figure 94b, t = 2.0). This second positive crest in turn rises and is amplified by vertical convection across the vertical vorticity gradient between it and the negative crest above. This process continues with the formation of a second negative crest (t = 2.4) followed by a third positive crest (t = 2.8), etc., all being strongly amplified by vertical convection. This is exactly the same behavior described above for the interior of the jet with the other type of start and rapidly leads to divergence. The behavior of the vorticity on the exit center is controlled primarily by upward convection across the gradients created above the boundary by this oscillation.

The behavior of the vertical vorticity on the edge of the jet (Figure 95) differs somewhat from that observed with the other type of start because of the differences in the vertical velocity distribution. With the present start the jet is already established at the start, so that there is strong vertical velocity throughout the region of the horizontal vorticity variation described above. Significant horizontal gradients in vertical velocity then can exist along all the lines of horizontal vorticity. The vertical vorticity on the jet edge thus follows closely the horizontal vorticity in the interior of the jet. Comparison of Figures

94b and 95 shows this correspondence at the later times, with the phase lag of the vertical vorticity behind the horizontal vorticity to be expected since variations in the former are generated by the latter. At the early times the profile at the rear of the jet is more representative of the horizontal vorticity just inside the sides of the jet than is the profile in the center of the jet, so that the initial crest of the vertical vorticity corresponds more closely to the crest in the profile in Figure 94a.

The general vertical decrease is due primarily to diffusion. There is also general downstream convection of vertical vorticity, but this and the diffusion are overpowered locally by the above effects. With the start from the opening of the exit, however, the jet must develop from the start, and, at the times shown, significant vertical velocity has not yet spread too great a distance above the exit. Therefore, the horizontal vorticity in the upper part of the developing jet is ineffective in generating vertical vorticity, since insufficient vertical velocity is there available.

With the present type of start the horizontal velocity is affected more by the vertical vorticity than was the case with the other type of start, since significant vertical vorticity exists at the sides of the jet from the beginning along the entire length of the jet. The values approached by

all the velocities at large distance above the boundary are due entirely to vertical vorticity. Also, the strong outward horizontal velocity above the exit edge is absent with the present start, since horizontal vorticity is also established from the beginning along the entire jet. The horizontal velocity in the rear and sides of the jet, however, reflects primarily the rise of the horizontal vorticity crest at the edge of the jet— outward velocity above the crest and inward below (Figures 96a and 97). The small bulge due to the horizontal vorticity protuberance caused by the minimum vorticity effect is discernable at t = 2.8 just below the top of the velocity profile at the sides of the jet (Figure 97).

The rearward horizontal velocity in the forward portion of the jet at the early times (Figures 96c, 96d) is due to vertical vorticity between the center and sides of the jet directed opposite to that on the jet sides. This vertical vorticity is generated by the convective terms as a result of the gradients in y-vorticity and vertical velocity normal to the centerline at the front of the jet. These gradients are prominent at the start because of the curvature of the jet edge. This vertical vorticity is realigned with that on the jet sides as time passes, as a result of the corrective influence of the gradient in vertical velocity along x-vorticity lines.

Vertical vorticity directed opposite to that on the jet sides is also created in the interior of the jet between the center and the sides in the same manner. The causative horizontal vorticity gradient here is initially a result, however, of diffusion of y-vorticity inward from the sides of the jet. This horizontal vorticity is convected upward and causes a rising horizontal gradient until significant vorticity has reached the center of the jet.

At the later times the large horizontal vorticity in the center of the jet discussed above (Figure 94b) is the cause of the gradient. At these times this vertical vorticity gradually shifts to become in phase with that on the jet sides, but with larger amplitude. There is then considerable horizontal variation of the vertical vorticity, with different patterns in different planes, so that the separate effects on the horizontal velocity profile at the front of the jet are obscured. However, the general trend at the later times is toward a positive crest above the boundary and a negative crest above that, as reflected in the horizontal velocity profiles at the front of the jet (Figure 96d). It is the negative velocity due to the negative crest, which of course emerges before the following positive crest, that increases the rearward horizontal convection and causes the upper horizontal vorticity trough at the front of the jet mentioned above (Figure 94c). The generation of this

vertical vorticity between the center and sides of the jet is accentuated by the small number of cells per radius used. A smaller cell size would result in smaller gradients.

The decrease in horizontal vorticity in the front of the jet (Figure 94c) causes an excess in positive vorticity at, and just above, the exit edge, and this tends to induce forward horizontal velocity above the boundary at the front of the jet. This effect is accentuated at the later times by the increase in horizontal vorticity just behind the front of the jet, corresponding to the increase on the boundary that occurs in conjunction with the lowest positive crest in the horizontal velocity profile at the jet center (Figure 94b).

The horizontal velocity above the jet center is negative at the early times, because of the above-mentioned oppositely directed vertical vorticity between the center and the sides of the jet, and horizontal convection therefrom is the cause of the formation of the initial horizontal vorticity crest in the interior of the jet mentioned above (Figure 94b, $t = 1.6$).

However, the crests in the horizontal vorticity exert a dominant effect when they achieve sufficient amplification, and the horizontal velocity in the jet center then follows the horizontal vorticity there (Figures 96c and 94b, at $t = 2.8$). The horizontal velocity in the jet center is

in phase with the vertical vorticity at the jet sides at the later times (Figures 95 and 96c) and must also, therefore, be influenced by this vorticity at those times. However, the phase relationship between this vertical vorticity and the horizontal vorticity in the jet center is such that their effects on the horizontal velocity are not separable. The stronger horizontal vorticity must, however, dominate.

The vertical velocity distribution in the center of the jet (Figure 98b) conforms primarily to the horizontal vorticity in the rear (and sides) of the jet (Figure 94a). The decrease in vertical velocity after the increase above the exit at the early times is due to the vertical decrease in horizontal vorticity magnitude. As the crest in the horizontal vorticity at the jet edge develops and rises, a corresponding vertical velocity crest follows inside the jet. The subsequent development of the horizontal vorticity trough around the jet then causes a similar trough in the interior vertical velocity. These correspondences are quite evident at the latest time in Figures 98b and 94a. The small uppermost crest of vertical velocity is due to the corresponding vorticity crest caused by the minimum vorticity effect discussed above.

The strong crest just above the boundary is due to x-vorticity on either side of the centerline which diffuses from the exit edge into the jet and then is convected upward.

This effect is accentuated in the present case by the small number of cells per exit radius, which causes the x-vorticity in the cell next to the centerline to be larger than would be the case if the cell size were reduced. Horizontal convection tends to increase this effect in the front portion of the jet and decrease it in the rear by conveying the x-vorticity into the jet in front, but out in the rear.

The vertical velocity at the edge of the jet is influenced primarily by the horizontal vorticity within the jet and, therefore, follows to some degree the η-profile above the center of the exit (Figure 94b). This is true to a greater extent in the rear of the jet (Figure 98a, especially $t = 2.8$) than in the front (Figure 98c) because of the rearward convection due to the cross-flow.

The initial decrease in vertical velocity above the boundary at both the front and rear of the jet, as well as the initial increase in the interior, is due to the inward diffusion of horizontal vorticity generated on the exit edge by the jet. The general decrease in vertical velocity in the front portion of the jet is due to the rearward convection of vorticity by the cross-flow. The crest that develops at the later times in this region is due to x-vorticity to the sides of the centerline as discussed above. This effect is reduced in the stable case that is discussed below.

A comparison of the effect of the range of integration r_m in the velocity calculation is given in Figures 96-98 at t = 2.4. As would be expected an increase in the integration range tends to increase the rearward horizontal velocity and the vertical velocity. The effect on the former is stronger in the lower portion of the jet as a result of the significant rearward and lateral spread of vertical vorticity. The effect on the vertical velocity is stronger in the upper portion of the jet because of the dominant influence of the exit source integral in the lower portion of the jet.

Stable Case - $V_r = 8$

The stabilizing effect of a reduction in time step is evident upon comparison of Figures 94-98 with Figures 99-103. The horizontal vorticity distribution at the edges of the jet has the same basic form with the smaller time step, but the peaked nature prevalent at the larger time step is reduced to a smooth waveform (Figure 99a, 99c; Figures 94a, 94c). Again the negative crest at the rear of the jet and the positive crest at the front are both due primarily to vertical convection and are formed initially from the vertical gradients of horizontal vorticity created by diffusive dissipation above the boundary. (The stronger vertical gradient of vertical velocity is also significant at the front of the jet as mentioned above.) The crest is enhanced in the rear and

degraded in the front by horizontal convection due to the cross-flow, and is therefore both stronger and higher in the rear of the jet.

The reduction of the convectional instability also eliminates the vorticity trough that develops in the upper portion of the horizontal vorticity profile at the front of the jet with the larger time step (Figures 99c and 94c) as a result of excessive rearward horizontal convection caused by the generation of oppositely directed vertical vorticity between the center and sides of the jet discussed above.

The smaller negative crest in the upper portion of the horizontal vorticity profile at the rear of the jet (Figure 99a) caused by the minimum vorticity effect as discussed above is still present but reduced. A comparison with a smaller minimum vorticity is given in Figure 99 at t = 2.2. Again the effect is slight except in the upper portion where the above-mentioned crest is eliminated.

In the interior of the jet the pattern of the horizontal vorticity distribution is altered significantly in form as well as magnitude by the reduction in time step (Figures 99b and 94b). The early development of the positive crest followed by a negative crest is essentially the same, the former crest again being formed as a result of rearward horizontal convection, and the latter by vertical convection across the vertical gradient thus created. However, the

subsequent amplification is much reduced and the wavelength of the disturbance is increased, so that the catastrophic divergence evident with the larger time step does not occur. The increase in wavelength is significant, since disturbances of wavelengths equal to twice the cell size, as occurred with the larger time step, are the most destructive with central differences for first derivatives, since then the opposite wave crests fall on the two points used for evaluation of the derivative.

The broad nature of the positive crest at the later times in Figure 99b is due to the combined effects of horizontal and vertical convection, the former being dominant in the lower portion of the crest and the latter in the upper portion. This form develops because the vertical convection tends to spread the crest upward. In the unstable case considered previously, the divergent amplification from vertical convection far overshadowed the effects of horizontal convection and distorted the upper portion of the crest into an overpowering sharp peak. The minimum vorticity effect discussed above also tends to make the upper portion of the crest more abrupt by reducing the vertical convection of vorticity away from the top of the crest.

Again the vertical vorticity distribution at the sides of the jet is influenced primarily by the horizontal vorticity in the interior of the jet, and is created by gradients

of vertical velocity along horizontal vorticity lines. There is, therefore, close correspondence between the wave forms of Figures 100a and 99b, the former having a phase lag relative to the latter. The contrast with the unstable case in Figure 95 is marked and agrees with the corresponding contrast between the horizontal vorticity profiles in the interior of jet. As with the horizontal vorticity, the time step reduction achieves an increase in wavelength as well as a decrease in amplitude of the disturbance waveform.

The behavior of both the horizontal and vertical vorticity on the boundary is not greatly affected by the time step, though the magnitude of the variation is reduced, especially in the interior of the jet after the unstable case begins to diverge (Figures 99a, 99c, 100a; Figures 94a, 94c, 95).

The horizontal velocity distribution at the edge of the jet has a similar form with each of the two time steps (cf. Figures 101b, 101d, 102a, with Figures 96b, 96d, 97), but with reduced magnitude of the variation at the smaller time step. The sharp horizontal vorticity peaks are reduced, so that the velocity profile at the rear of the jet (Figure 101b) has a smooth wave form with the smaller time step. With the reduced amplitude of the horizontal vorticity variations in the rear of the jet, there is also a significant contribution to the horizontal velocity there

by the vertical vorticity generated on the sides of the jet and convected downstream by the cross-flow, as illustrated by the phase coincidence of Figures 101b and 100a at the later times. The outward velocity is the result of the horizontal vorticity crest, but the positive velocity crest below is due largely to the vertical vorticity crest above the boundary.

In the front portion of the jet the rearward crest of the horizontal velocity is much reduced. This crest, it is recalled, is a result of vertical vorticity generated between the center and sides of the jet that is directed opposite to that on the sides (see the discussion of the unstable case above). The positive crest is due to the corresponding crest of the vertical vorticity at the sides of the jet (Figure 100a) and also to the positive horizontal vorticity at the forward edge of the exit.

In the interior of the jet the horizontal velocity distribution is greatly altered by the time step reduction (cf. Figures 101c and 96c), as a result of the alteration of the vorticity distributions. The initial rearward velocity induced by the vertical vorticity generated between the center and sides mentioned above is still present but reduced. At the later times the horizontal velocity in the center of the jet follows closely the vertical vorticity distribution on the sides of the jet (Figure 100a), with modifications

due to the horizontal vorticity distribution in the interior of the jet (Figure 99b) that cause the velocity wave to lag slightly behind the vertical vorticity wave.

The initial decrease in vertical velocity above the exit at the front and rear of the jet, as well as the increase in the interior (Figures 103a-c), is again due to the diffusion of horizontal vorticity generated on the exit edge into the jet. The vertical velocity at the rear of the jet (Figure 103a) reflects primarily the horizontal vorticity distribution in the interior of the jet and hence follows roughly the profile of Figure 99b.

The variation in horizontal vorticity at the edge of the jet is too small with the smaller time step to have a noticeable effect on the vertical velocity over the exit center. The profile there (Figure 103b) therefore exhibits a general vertical decrease as a result of the decrease in horizontal vorticity at the sides of the jet, with none of the severe oscillation present with the larger time step (Figure 98b).

In the forward portion of the jet (Figure 103c) the vertical velocity generally decreases vertically because of the reduction in horizontal vorticity in the forward portion of the jet by horizontal convection and diffusion. The crest just above the boundary is again due to x-vorticity to the sides of the centerline as discussed in the unstable

case. Again a comparison is given of the effect of an increase in the range of integration in the velocity calculation (Figures 101-103, t = 1.8), the increase tending to increase the rearward horizontal velocity and the vertical velocity.

The horizontal vorticity distributions at later times (Figures 99d-f) exhibit generally a continuation of the pattern of vertically moving waves, with only a few modifications. Vertical convection across the gradients that result above the exit with the upward passage of the waves continue to generate the waves at the rear of the jet (cf. small crest two radii above the boundary at t = 5.0 in Figure 99d) and in the interior of the jet (Figure 99e). The latter profile is subject to some distortion near the boundary resulting from truncation error in the velocity calculation. In order to conserve computer time the range used in the velocity calculation in the present case of long duration was chosen to be only one exit diameter. This introduces no great error until the later times when significant vorticity is widely spread near the boundary. The error then is greatest in the lower portion of the jet near the center and front of the jet, since the predominant horizontal movement of vorticity is rearward and to the sides. Some rather sharp horizontal gradients of velocity, therefore, develop in the jet interior and the results shown for

the last two times are suspect in the lower forward portion of the jet.

The uppermost crest at the rear of the jet, resulting from the minimum vorticity effect discussed above, causes the creation and amplification of the trough which follows. This trough develops primarily because of the loss of vorticity through vertical convection across the gradient caused by the crest above, but is amplified by losses due to downstream convection resulting from the horizontal vorticity gradient created by the uppermost positive crest in the jet interior. Both this trough and the crest above exist only because of the minimum vorticity approximation and are, therefore, removable. Horizontal convection is the cause of the broadening of the primary crest. Here negative vorticity is convected downstream from the interior of the jet.

At the front of the jet, the crest generated at the start becomes more apparent as time passes and it moves upward. The crest is maintained by vertical convection from below because of the vertical gradients of both the horizontal vorticity and the vertical velocity, the latter gradient being more significant in the front of the jet than elsewhere, and thus is located in the region of large velocity gradient above the vertical velocity crest (Figure 103f). The amplification of the trough behind at the last two time steps is due to horizontal convection that is directed

upstream in front and downstream behind—a result of the above-mentioned truncation error in the integration. The narrowing of the negative crest in the jet interior is due to downstream horizontal convection of positive vorticity into the upper portion of the crest. This is a result of the uppermost rearward velocity crest in the interior of the jet.

The vertical vorticity at the jet sides (Figure 100b) continues to follow the horizontal vorticity in the interior of the jet in a vertically moving wave with little distortion.

The horizontal velocity (Figure 101) continues to reflect the combined influence of both the horizontal and vertical vorticity, with the latter being dominant. There is thus a close phase coincidence with the vertical vorticity (Figure 100b). The topmost velocity crest in the rear of the jet is raised a bit by the vorticity trough following the crest created by the minimum vorticity effect (Figure 99d). Also the larger horizontal vorticity variations in the interior of the jet (Figure 99e) are such as to amplify the effect of the vertical vorticity in that region. Since the vertical vorticity lags the horizontal, the velocity contributions of each are in phase here and, therefore, the effects are not separable. The large negative velocity near the boundary at the later times is probably excessive as a result

of the above-mentioned truncation error in the integration, since a considerable body of vertical vorticity directed opposite to that nearest the exit center (negative at these times) is not being included in the calculation here.

The horizontal velocity in the front of the jet (Figure 101i) is also influenced to an increasing degree by the vertical vorticity, and at the latter times is in phase with the horizontal velocity at the center and rear of the jet (Figures 101g, 101h). However, as noted above, the horizontal velocity in the interior of the jet also has the proper phase relationship with the velocity here.

The horizontal velocity at the sides of the jet shows less variation and reflects the passage of the horizontal vorticity wave up the sides of the jet. The outward horizontal velocity just above the edge of the exit on all sides is due to the horizontal vorticity generated on the exit edge by the jet. This is to be balanced by the effect of vorticity of like sign above the boundary, but such a balance cannot be achieved perfectly due to the discretization. Again a smaller cell size, i.e., more cells per jet radius, would improve the results.

The vertical velocity just above the boundary continues to be influenced strongly by the horizontal vorticity generated at the exit edge by the jet and diffused onto the jet on the boundary as discussed above. The vertical

velocity in the interior of the jet decreases vertically as a result of the general decrease in horizontal vorticity at the sides of the jet.

At the front and rear of the jet, however, the vertical velocity continues to reflect the influence of the horizontal vorticity in the interior of the jet. The wave form of Figure 103d thus corresponds generally to that of Figure 99e. (Recall that the profile of Figure 99e is over the exit center and is only representative, not definitive, of the horizontal vorticity distribution in the entire jet interior.) At the front of the jet (Figure 103f) the results are more complicated, involving also the effect of the x-vorticity distribution to the sides of the centerline, which is the cause of the crest as discussed above. This effect decreases in time as the vorticity is dissipated.

APPENDIX L

DEVELOPMENT OF SINGULARITY DISTRIBUTION FOR VORTEX LATTICE MODEL

As shown in Appendix B the velocity induced by a specified vorticity distribution may be calculated from the integral relation (B - 1) for a bounded volume:

$$\underset{\sim}{v}(\underset{\sim}{r}) = \frac{1}{4\pi}\iint\left[\frac{\frac{\partial \underset{\sim}{v}}{\partial n}}{|\underset{\sim}{r}' - \underset{\sim}{r}|} + \frac{(\underset{\sim}{r}' - \underset{\sim}{r}) \cdot \underset{\sim}{n}}{|\underset{\sim}{r}' - \underset{\sim}{r}|^3}\underset{\sim}{v}\right]dS + \frac{1}{4\pi}\iiint\frac{\underset{\sim}{\nabla} \times \underset{\sim}{\omega}}{|\underset{\sim}{r}' - \underset{\sim}{r}|}d\nu \tag{1}$$

This may be rewritten, using Equation (B - 30), as

$$\underset{\sim}{v}(\underset{\sim}{r}) = \frac{1}{4\pi}\iint\left[\frac{\frac{\partial \underset{\sim}{v}}{\partial n}}{|\underset{\sim}{r}' - \underset{\sim}{r}|} + \frac{(\underset{\sim}{r}' - \underset{\sim}{r}) \cdot \underset{\sim}{n}}{|\underset{\sim}{r}' - \underset{\sim}{r}|^3}\underset{\sim}{v} + \frac{\underset{\sim}{n} \times \underset{\sim}{\omega}}{|\underset{\sim}{r}' - \underset{\sim}{r}|}\right]dS$$

$$+ \frac{1}{4\pi}\iiint\frac{(\underset{\sim}{r}' - \underset{\sim}{r}) \times \underset{\sim}{\omega}}{|\underset{\sim}{r}' - \underset{\sim}{r}|^3}d\nu \tag{2}$$

The volume integral extends over the entire flow field, and the surface integral covers the entire boundary of the flow field. The unit vector $\underset{\sim}{n}$ is the outward normal to the boundary of the flow field (Figure 1).

Let part of the fluid boundary be a plane located at $z = 0$, which is impervious except for a finite area of arbitrary shape on which the normal velocity is uniform. This finite area of non-zero normal velocity on the $z = 0$

plane is here referred to as the "exit." The remainder of the boundary of the flow field is taken to be a he isphere located above the z = 0 plane, with its center at the origin. The flow field thus comprises the entire region above the z = 0 plane, this region being designated the "object field."

Now for every point $\underset{\sim}{r}$ in the object field define a corresponding point $\underset{\sim}{r}_1$ in the region below the z = 0 plane (this region being designated the "image field") having the same x and y components as $\underset{\sim}{r}$, but with the z component reversed. Thus

$$\underset{\sim}{r}_1 \equiv \underset{\sim}{r} - 2(\underset{\sim}{k} \cdot \underset{\sim}{r})\underset{\sim}{k} \tag{3}$$

Also define an image vorticity $\underset{\sim}{\omega}_1$ at each point in the image field, this image vorticity having the same z component as the vorticity at the corresponding point in the object field, but with the other components reversed:

$$\underset{\sim}{\omega}_1(\underset{\sim}{r}_1) \equiv \underset{\sim}{\omega}(\underset{\sim}{r}) - 2[\underset{\sim}{i} \cdot \underset{\sim}{\omega}(\underset{\sim}{r})]\underset{\sim}{i} - 2[\underset{\sim}{j} \cdot \underset{\sim}{\omega}(\underset{\sim}{r})]\underset{\sim}{j} \tag{4}$$

with $\underset{\sim}{r}_1$ and $\underset{\sim}{r}$ related by Equation (3). Finally, define the normal velocity on the common plane boundary in the image field to be opposite to that in the object field:

$$\underset{\sim}{k} \cdot \underset{\sim}{v}_1(x_1, y_1, 0) = - \underset{\sim}{k} \cdot \underset{\sim}{v}(x, y, 0) \tag{5}$$

where, by Equation (3), $x_1 = x$ and $y_1 = y$.

Then the velocity induced at points within the image field by the image vorticity is given by (cf. Equation (2))

$$\underset{\sim}{v}_1(\underset{\sim}{r}_1) = \frac{1}{4\pi}\iint\left[\frac{\frac{\partial \underset{\sim}{v}_1}{\partial n_1}}{|\underset{\sim}{r}'' - \underset{\sim}{r}_1|} + \frac{(\underset{\sim}{r}'' - \underset{\sim}{r}_1)\cdot \underset{\sim}{n}_1}{|\underset{\sim}{r}'' - \underset{\sim}{r}_1|^3}\underset{\sim}{v}_1 + \frac{\underset{\sim}{n}_1 \times \underset{\sim}{\omega}_1}{|\underset{\sim}{r}'' - \underset{\sim}{r}_1|}\right]dS_1$$

$$+ \frac{1}{4\pi}\iiint\frac{(\underset{\sim}{r}'' - \underset{\sim}{r}_1)\times \underset{\sim}{\omega}_1}{|\underset{\sim}{r}'' - \underset{\sim}{r}_1|^3}d\nu_1 \qquad (6)$$

where the integration is now over the image field, the variable of integration being $\underset{\sim}{r}''$. If Equations (4) and (5) are substituted in the integrals of Equation (6), and the points of integration $\underset{\sim}{r}''$ in the image field are converted to the corresponding points $\underset{\sim}{r}'$ in the object field by application of Equation (3),

$$\underset{\sim}{r}'' = \underset{\sim}{r}' - 2(\underset{\sim}{k}\cdot\underset{\sim}{r}')\underset{\sim}{k} \qquad (7)$$

The integrals over the image field may then be transformed to integrals over the object field, and it may then be shown that Equation (6) reduces to (Appendix M)

$$\underset{\sim}{v}_1(\underset{\sim}{r}_1) = \underset{\sim}{v}(\underset{\sim}{r}) - 2[\underset{\sim}{k}\cdot\underset{\sim}{v}(\underset{\sim}{r})]\underset{\sim}{k} \qquad (8)$$

with $\underset{\sim}{r}_1$ and $\underset{\sim}{r}$ related by Equation (3), and $\underset{\sim}{v}(\underset{\sim}{r})$ given by Equation (2). The velocity in the image field induced by the image vorticity is thus the same as that at corresponding points in the object field, except that the z component is

reversed.

Now if in the integrals over the image field in Equation (6), the point $\underset{\sim}{r}$ is located outside the image field, i.e., outside the field of integration, the equation is equal to zero. Then, since all points in the object field are outside the image field, we may write, using Equation (2) and Equation (6) with $\underset{\sim}{r}$ in the object field,

$$\underset{\sim}{v}(\underset{\sim}{r}) = \frac{1}{4\pi}\iint_{\text{object}}\left[\frac{\frac{\partial \underset{\sim}{v}}{\partial n}}{|\underset{\sim}{r}' - \underset{\sim}{r}|} + \frac{(\underset{\sim}{r}' - \underset{\sim}{r}) \cdot \underset{\sim}{n}}{|\underset{\sim}{r}' - \underset{\sim}{r}|^3}\underset{\sim}{v} + \frac{\underset{\sim}{n} \times \underset{\sim}{\omega}}{|\underset{\sim}{r}' - \underset{\sim}{r}|}\right]dS$$

$$+ \frac{1}{4\pi}\iiint_{\text{object}}\frac{(\underset{\sim}{r}' - \underset{\sim}{r}) \times \underset{\sim}{\omega}}{|\underset{\sim}{r}' - \underset{\sim}{r}|^3}d\nu$$

$$+ \frac{1}{4\pi}\iint_{\text{image}}\left[\frac{\frac{\partial \underset{\sim}{v}_1}{\partial n_1}}{|\underset{\sim}{r}'' - \underset{\sim}{r}|} + \frac{(\underset{\sim}{r}'' - \underset{\sim}{r}) \cdot \underset{\sim}{n}_1}{|\underset{\sim}{r}'' - \underset{\sim}{r}|^3}\underset{\sim}{v}_1 + \frac{\underset{\sim}{n}_1 \times \underset{\sim}{\omega}_1}{|\underset{\sim}{r}'' - \underset{\sim}{r}|}\right]dS_1$$

$$+ \frac{1}{4\pi}\iiint_{\text{image}}\frac{(\underset{\sim}{r}'' - \underset{\sim}{r}) \times \underset{\sim}{\omega}_1}{|\underset{\sim}{r}'' - \underset{\sim}{r}|^3}d\nu_1 \qquad (9)$$

with $\underset{\sim}{\omega}_1$ and $\underset{\sim}{v}_1$ given by Equations (4) and (8), respectively, and $\underset{\sim}{r}''$ related to $\underset{\sim}{r}'$ by Equation (7). The first two integrals are over the object field, and the last two are over the image field, the sum of the latter being zero since $\underset{\sim}{r}$ is outside the image field.

Let the velocity approach at infinity a uniform value that is parallel to the common plane boundary, except

possibly on a finite portion of the surface at infinity.* With the uniform velocity at infinity indicated by $\underset{\sim}{V}_\infty$ we have, using $\underset{\sim}{v} = \underset{\sim}{V}_\infty$ and $\underset{\sim}{v}_1 = \underset{\sim}{V}_\infty$, since $\underset{\sim}{V}_\infty$ has no z component,

$$\frac{1}{4\pi}\iint_{\substack{\text{object}\\ \infty}} \frac{(\underset{\sim}{r}' - \underset{\sim}{r})\cdot\underset{\sim}{n}}{|\underset{\sim}{r}' - \underset{\sim}{r}|^3}\underset{\sim}{v}dS + \frac{1}{4\pi}\iint_{\substack{\text{image}\\ \infty}} \frac{(\underset{\sim}{r}'' - \underset{\sim}{r})\cdot\underset{\sim}{n}_1}{|\underset{\sim}{r}'' - \underset{\sim}{r}|^3}\underset{\sim}{v}_1 dS_1$$

$$= \frac{\underset{\sim}{V}_\infty}{4\pi}\Bigg[\iint_{\substack{\text{object}\\ \infty}} \frac{(\underset{\sim}{r}' - \underset{\sim}{r})\cdot\underset{\sim}{n}}{|\underset{\sim}{r}' - \underset{\sim}{r}|^3}dS + \iint_{\substack{\text{image}\\ \infty}} \frac{(\underset{\sim}{r}'' - \underset{\sim}{r})\cdot\underset{\sim}{n}_1}{|\underset{\sim}{r}'' - \underset{\sim}{r}|^3}dS_1\Bigg]$$

$$= \frac{\underset{\sim}{V}_\infty}{4\pi}\iint\frac{(\underset{\sim}{r}' - \underset{\sim}{r})\cdot\underset{\sim}{n}}{|\underset{\sim}{r}' - \underset{\sim}{r}|^3}dS = \underset{\sim}{V}_\infty \qquad (10)\dagger$$

The last step follows from the development of Equation (B - 28) of Appendix B from Equation (B - 27). The left hand side of Equation (10) vanishes when $\underset{\sim}{v}$, and hence $\underset{\sim}{v}_1$, is replaced by the deviation of the velocity from the uniform value, since then the total solid angle subtended by the finite area of non-zero velocity deviation approaches zero at infinity.

With the above specification of the velocity at infinity and the additional stipulation of no variation of velo-

---

*The terminology "surface at infinity" refers to the hemispherical surface in the limit as its radius approaches infinity.

†The notation ∞ on the surface integrals implies the limit of the integral over the hemispherical surface as its radius approaches infinity.

city normal to the surface on the finite area of deviation from uniformity,* we have the first surface integrals in both the object and image spaces of Equation (9) vanishing on the surface at infinity. Similarly, if the vorticity at infinity is specified to be either zero or normal to the surface, the last surface integral in each space vanishes on the surface at infinity.†

It is shown in Appendix M that the surface integrals on the plane boundary may be combined and reduced, so that Equation (9) becomes

$$\underset{\sim}{v}(\underset{\sim}{r}) = \underset{\sim}{V}_\infty - \frac{1}{2\pi} \iint_{\substack{\text{object}\\\text{plane}}} \frac{\underset{\sim}{i}\frac{\partial v_z}{\partial x} + \underset{\sim}{j}\frac{\partial v_z}{\partial y}}{|\underset{\sim}{r}' - \underset{\sim}{r}|} dS + \underset{\sim}{k}\frac{(\underset{\sim}{k} \cdot \underset{\sim}{r})}{2\pi} \iint_{\substack{\text{object}\\\text{plane}}} \frac{v_z \, dS}{|\underset{\sim}{r}' - \underset{\sim}{r}|^3}$$

$$+ \frac{1}{4\pi} \iiint_{\text{object}} \frac{(\underset{\sim}{r}' - \underset{\sim}{r}) \times \underset{\sim}{\omega}}{|\underset{\sim}{r}' - \underset{\sim}{r}|^3} d\nu + \frac{1}{4\pi} \iiint_{\text{image}} \frac{(\underset{\sim}{r}'' - \underset{\sim}{r}) \times \underset{\sim}{\omega}_1}{|\underset{\sim}{r}'' - \underset{\sim}{r}|^3} d\nu_1 \qquad (11)$$

where the surface integrals are over the $z = 0$ plane. Now the derivatives $\frac{\partial v_z}{\partial x}$ and $\frac{\partial v_z}{\partial y}$ are zero everywhere on the $z = 0$ plane except on the edge of the exit. Therefore, if $\underset{\sim}{e}$ is a unit outward normal to the exit area boundary curve and lies in the $z = 0$ plane and ε is an infinitesmal distance parallel to $\underset{\sim}{e}$, we have

---

*More specifically, the normal derivative must vanish at least as fast as the inverse square of the radius, a condition that is fulfilled for velocities induced by vortices and sources.

†This condition is fulfilled by specification since the vorticity is confined to the lattice and thus has all its derivatives zero elsewhere.

$$\underset{\sim}{i}\frac{\partial v_z}{\partial x} + \underset{\sim}{j}\frac{\partial v_z}{\partial y} = -\frac{V_j}{\varepsilon}\underset{\sim}{e} \quad \text{and} \quad dS = \varepsilon \; dl$$

where V_j is the uniform z-velocity on the exit area, and dl is an increment of arc length along the exit area bounding curve. Then the first surface integral of Equation (11) becomes

$$\iint \frac{\underset{\sim}{i}\frac{\partial v_z}{\partial x} + \underset{\sim}{j}\frac{\partial v_z}{\partial y}}{|\underset{\sim}{r}' - \underset{\sim}{r}|} dS = -V_j \oint \frac{\underset{\sim}{e}\; dl}{|\underset{\sim}{r}' - \underset{\sim}{r}|} \tag{12}$$

with the line integral taken around the exit area boundary curve. If $\underset{\sim}{dl}$ is a vector of magnitude dl, directed tangent to the exit area bounding curve in the direction of positive line integration, i.e., exit area on the left, we have

$$\underset{\sim}{e}\, dl = \underset{\sim}{dl} \times \underset{\sim}{k}$$

so that the right hand side of Equation (12) may be written

$$-V_j \oint \frac{\underset{\sim}{e}\; dl}{|\underset{\sim}{r}' - \underset{\sim}{r}|} = V_j \underset{\sim}{k} \times \oint \frac{\underset{\sim}{dl}}{|\underset{\sim}{r}' - \underset{\sim}{r}|} \tag{13}$$

But by a vector integral theorem {69, Chapter 6}

$$\oint \phi \, d\underset{\sim}{r} = \iint (\underset{\sim}{n} \times \underset{\sim}{\nabla}\phi) dS \tag{14}$$

where the surface integral is taken over the area enclosed by the circuit of the line integral, and $\underset{\sim}{n}$ is a unit normal

to the surface directed in the positive sense of traverse of a circuit. Then applying Equation (14) to Equation (13) we have

$$- V_j \oint \frac{d\underset{\sim}{l} \times \underset{\sim}{k}}{|\underset{\sim}{r}' - \underset{\sim}{r}|} = V_j \underset{\sim}{k} \times \iint_{exit} [\underset{\sim}{k} \times \underset{\sim}{\nabla}(\frac{1}{|\underset{\sim}{r}' - \underset{\sim}{r}|})]dS$$

$$= - V_j \underset{\sim}{k} \times [\underset{\sim}{k} \times \iint_{exit} \frac{\underset{\sim}{r}' - \underset{\sim}{r}}{|\underset{\sim}{r}' - \underset{\sim}{r}|^3} dS]$$

$$= V_j \underset{\sim}{k}(\underset{\sim}{k} \cdot \underset{\sim}{r}) \iint_{exit} \frac{dS}{|\underset{\sim}{r}' - \underset{\sim}{r}|^3} + V_j \iint_{exit} \frac{\underset{\sim}{r}' - \underset{\sim}{r}}{|\underset{\sim}{r}' - \underset{\sim}{r}|^3} dS \qquad (15)$$

In the last step the vector identity {69, Chapter 2},

$$\underset{\sim}{A} \times (\underset{\sim}{B} \times \underset{\sim}{C}) = (\underset{\sim}{A} \cdot \underset{\sim}{C})\underset{\sim}{B} - (\underset{\sim}{A} \cdot \underset{\sim}{B})\underset{\sim}{C} \qquad (16)$$

has been used. Substitution of Equation (15) in Equation (11), via Equations (12) and (13), then yields

$$\underset{\sim}{v}(\underset{\sim}{r}) = \underset{\sim}{V}_\infty - \frac{V_j}{2\pi} \iint_{exit} \frac{\underset{\sim}{r}' - \underset{\sim}{r}}{|\underset{\sim}{r}' - \underset{\sim}{r}|^3} dS + \frac{1}{4\pi} \iiint_{object} \frac{(\underset{\sim}{r}' - \underset{\sim}{r}) \times \underset{\sim}{\omega}}{|\underset{\sim}{r}' - \underset{\sim}{r}|^3} d\nu$$

$$+ \frac{1}{4\pi} \iiint_{image} \frac{(\underset{\sim}{r}'' - \underset{\sim}{r}) \times \underset{\sim}{\omega}_1}{|\underset{\sim}{r}'' - \underset{\sim}{r}|^3} d\nu_1 \qquad (17)$$

The surface integral in this equation is just the velocity induced by a uniform source distribution of strength V_j located on the exit area {73, Chapter 11}. The second volume integral is the velocity induced by the solid-wall images of the vorticity in the flow field.

APPENDIX M

DEVELOPMENT OF CERTAIN RELATIONS CITED IN APPENDIX L

Development of Equation (L - 8) from Equation (L - 6)

If Equation (L - 8) is true, then

$$\underset{\sim}{v}_1 = \underset{\sim}{i}v_x + \underset{\sim}{j}v_y - \underset{\sim}{k}v_z \tag{1}$$

Now, since $\underset{\sim}{n}_1 = \underset{\sim}{k}$ on the plane boundary,

$$\frac{\partial \underset{\sim}{v}_1}{\partial n_1} = \underset{\sim}{i}\frac{\partial v_{1_x}}{\partial z}\bigg|_{o-} + \underset{\sim}{j}\frac{\partial v_{1_y}}{\partial z}\bigg|_{o-} + \underset{\sim}{k}\frac{\partial v_{1_z}}{\partial z}\bigg|_{o-} \tag{2}$$

where the derivatives are those obtained as z approaches zero from below. But if Equation (L - 8), and hence Equation (1) above, is true, the x and y velocity components vary continuously at the plane boundary from the object to the image field, but their gradients in the z-direction are discontinuous. Conversely the z velocity component is discontinuous at the plane boundary, but its z-gradient is continuous. Therefore

$$\frac{\partial v_{1_x}}{\partial z}\bigg|_{o-} = -\frac{\partial v_x}{\partial z}\bigg|_{o+}, \quad v_{1_x} = +v_x \tag{3a}$$

$$\frac{\partial v_{1_y}}{\partial z}\bigg|_{o-} = -\frac{\partial v_y}{\partial z}\bigg|_{o+}, \quad v_{1_y} = +v_y \tag{3b}$$

$$\left.\frac{\partial v_{1_z}}{\partial z}\right|_{o-} = + \left.\frac{\partial v_z}{\partial z}\right|_{o+}, \quad v_{1_z} = - v_z \tag{3c}$$

if Equation (L - 8) is true.

Also from Equations (L - 3) and (L - 7)

$$\underset{\sim}{r}'' - \underset{\sim}{r}_1 = \underset{\sim}{r}' - \underset{\sim}{r} - 2[\underset{\sim}{k} \cdot (\underset{\sim}{r}' - \underset{\sim}{r})]\underset{\sim}{k} \tag{4}$$

so that

$$|\underset{\sim}{r}'' - \underset{\sim}{r}_1| = |\underset{\sim}{r}' - \underset{\sim}{r}| \tag{5}$$

for $\underset{\sim}{r}''$ and $\underset{\sim}{r}_1$ related to $\underset{\sim}{r}'$ and $\underset{\sim}{r}$ by Equations (L - 3) and (L - 7), respectively. This relation is true throughout the field.

Now using Equation (4) on the $z = 0$ plane,

$$\begin{aligned}(\underset{\sim}{r}'' - \underset{\sim}{r}_1) \cdot \underset{\sim}{n}_1 &= (\underset{\sim}{r}'' - \underset{\sim}{r}_1) \cdot \underset{\sim}{k} \\ &= (\underset{\sim}{r}' - \underset{\sim}{r}) \cdot \underset{\sim}{k} - 2(\underset{\sim}{r}' - \underset{\sim}{r}) \cdot \underset{\sim}{k} \\ &= - (\underset{\sim}{r}' - \underset{\sim}{r}) \cdot \underset{\sim}{k} \\ &= (\underset{\sim}{r}' - \underset{\sim}{r}) \cdot \underset{\sim}{n}\end{aligned} \tag{6}$$

since $\underset{\sim}{n}_1 = \underset{\sim}{k} = - \underset{\sim}{n}$. Also on the $z = 0$ plane, from Equation (L - 4),

$$\begin{aligned}\underset{\sim}{n}_1 \times \underset{\sim}{\omega}_1 = \underset{\sim}{k} \times (- \underset{\sim}{i}\omega_x - \underset{\sim}{j}\omega_y + \underset{\sim}{k}\omega_z) &= - \underset{\sim}{k} \times (\underset{\sim}{i}\omega_x + \underset{\sim}{j}\omega_y + \underset{\sim}{k}\omega_z) \\ &= \underset{\sim}{n} \times \underset{\sim}{\omega}\end{aligned} \tag{7}$$

Finally, from Equations (4) and (L - 4) we have

$$(\underset{\sim}{r}'' - \underset{\sim}{r}_1) \times \underset{\sim}{\omega}_1 = \begin{vmatrix} \underset{\sim}{i} & \underset{\sim}{j} & \underset{\sim}{k} \\ (\underset{\sim}{r}' - \underset{\sim}{\dot{r}})_x & (\underset{\sim}{r}' - \underset{\sim}{\dot{r}})_y & -(\underset{\sim}{r}' - \underset{\sim}{\dot{r}})_z \\ -\omega_x & -\omega_y & +\omega_z \end{vmatrix} \tag{8}$$

Then, using Equations (1), (3), (5), (6), (7), and (8) in Equation (L - 6) we have

$$\underset{\sim}{v}_1(\underset{\sim}{r}_1) = \frac{1}{4\pi}\iint\Bigg[\frac{-\underset{\sim}{i}\frac{\partial v_x}{\partial z} - \underset{\sim}{j}\frac{\partial v_y}{\partial z} + \underset{\sim}{k}\frac{\partial v_z}{\partial z}}{|\underset{\sim}{r}' - \underset{\sim}{r}|}$$

$$- \frac{(\underset{\sim}{r}' - \underset{\sim}{r})_z}{|\underset{\sim}{r}' - \underset{\sim}{r}|^3}(\underset{\sim}{i}v_x + \underset{\sim}{j}v_y - \underset{\sim}{k}v_z) + \frac{\underset{\sim}{i}\omega_y - \underset{\sim}{j}\omega_x}{|\underset{\sim}{r}' - \underset{\sim}{r}|}\Bigg]dS$$

$$+ \frac{1}{4\pi}\iiint\frac{\underset{\sim}{i}[(\underset{\sim}{r}'-\underset{\sim}{r})_y\omega_z-(\underset{\sim}{r}'-\underset{\sim}{r})_z\omega_y] + \underset{\sim}{j}[(\underset{\sim}{r}'-\underset{\sim}{r})_z\omega_x-(\underset{\sim}{r}'-\underset{\sim}{r})_x\omega_z]}{|\underset{\sim}{r}' - \underset{\sim}{r}|^3}d\nu$$

$$- \frac{1}{4\pi}\iiint\frac{\underset{\sim}{k}[(\underset{\sim}{r}' - \underset{\sim}{r})_x\omega_y - (\underset{\sim}{r}' - \underset{\sim}{r})_y\omega_x]}{|\underset{\sim}{r}' - \underset{\sim}{r}|^3}d\nu = \underset{\sim}{i}v_x + \underset{\sim}{j}v_y - \underset{\sim}{k}v_z \tag{9}$$

by comparison with Equation (L - 2).

Reduction of Surface Integrals of Equation (L - 9)

From Equation (3), on the z = 0 plane

$$\frac{\partial \underset{\sim}{v}_1}{\partial n_1} = -\underset{\sim}{i}\frac{\partial v_x}{\partial z} - \underset{\sim}{j}\frac{\partial v_y}{\partial z} + \underset{\sim}{k}\frac{\partial v_z}{\partial z} \tag{10}$$

But also

$$\frac{\partial \underset{\sim}{v}}{\partial n} = - \underset{\sim}{i}\frac{\partial v_x}{\partial z} - \underset{\sim}{j}\frac{\partial v_y}{\partial z} - \underset{\sim}{k}\frac{\partial v_z}{\partial z} \tag{11}$$

since $\underset{\sim}{n} = - \underset{\sim}{k}$. Therefore

$$\frac{\partial \underset{\sim}{v}_1}{\partial n} + \frac{\partial \underset{\sim}{v}}{\partial n} = - 2(\underset{\sim}{i}\frac{\partial v_x}{\partial z} + \underset{\sim}{j}\frac{\partial v_y}{\partial z}) \tag{12}$$

Also on the z = 0 plane we have from Equation (L - 7), since $\underset{\sim}{k} \cdot \underset{\sim}{r}' = 0$, $\underset{\sim}{r}'' = \underset{\sim}{r}'$. Then on the z = 0 plane,

$$|\underset{\sim}{r}'' - \underset{\sim}{r}| = |\underset{\sim}{r}' - \underset{\sim}{r}| \tag{13}$$

and

$$(\underset{\sim}{r}'' - \underset{\sim}{r}) \cdot \underset{\sim}{n}_1 = - (\underset{\sim}{r}' - \underset{\sim}{r}) \cdot \underset{\sim}{n} \tag{14}$$

Then using Equations (2), (7), (12), (13), and (14) we have the sum of the surface integrals on the z = 0 plane in Equation (L - 9) reduced to

$$\frac{1}{4\pi} \iint_{\text{plane}} \left[\frac{-2(\underset{\sim}{i}\frac{\partial v_x}{\partial z} + \underset{\sim}{j}\frac{\partial v_y}{\partial z})}{|\underset{\sim}{r}' - \underset{\sim}{r}|} + \frac{2(\underset{\sim}{r}' - \underset{\sim}{r}) \cdot \underset{\sim}{n}}{|\underset{\sim}{r}' - \underset{\sim}{r}|^3}\underset{\sim}{k}v_z + 2\frac{\underset{\sim}{i}\omega_y - \underset{\sim}{j}\omega_x}{|\underset{\sim}{r}' - \underset{\sim}{r}|}\right] dS$$

But since $\underset{\sim}{k} \cdot \underset{\sim}{r}' = 0$ we have $\underset{\sim}{r}' \cdot \underset{\sim}{n} = 0$ on the z = 0 plane. Also

$$\omega_y - \frac{\partial v_x}{\partial z} = (\frac{\partial v_x}{\partial z} - \frac{\partial v_z}{\partial x}) - \frac{\partial v_x}{\partial z} = - \frac{\partial v_z}{\partial x} \tag{15a}$$

$$- \omega_x - \frac{\partial v_y}{\partial z} = - (\frac{\partial v_z}{\partial y} - \frac{\partial v_y}{\partial z}) - \frac{\partial v_y}{\partial z} = - \frac{\partial v_z}{\partial y} \tag{15b}$$

Therefore the above surface integral finally reduces to

$$-\frac{1}{2\pi}\iint_{\text{plane}}\left[\frac{\underset{\sim}{i}\frac{\partial v_z}{\partial x}+\underset{\sim}{j}\frac{\partial v_z}{\partial y}}{|\underset{\sim}{r}'-\underset{\sim}{r}|}-\underset{\sim}{k}(\underset{\sim}{k}\cdot\underset{\sim}{r})\frac{v_z}{|\underset{\sim}{r}'-\underset{\sim}{r}|^3}\right]dS$$

APPENDIX N

VELOCITY INDUCED BY THE LINEAR VORTEX SEGMENTS AND BY THE EXIT SOURCE DISTRIBUTION

Linear Vortex Segments

As noted in Chapter VII the velocity induced at $\underset{\sim}{r}_p$ by a straight vortex segment between $\underset{\sim}{r}_1$ and $\underset{\sim}{r}_2$ (Figure 55), with positive circulation reckoned as clockwise when viewed from $\underset{\sim}{r}_1$ to $\underset{\sim}{r}_2$, is given by

$$\underset{\sim}{v} = \underset{\sim}{e}_1 \frac{\Gamma}{4\pi a}(\cos\theta_1 - \cos\theta_2)$$

where

$$\underset{\sim}{e}_1 \equiv \frac{\underset{\sim}{l} \times \underset{\sim}{a}_1}{|\underset{\sim}{l} \times \underset{\sim}{a}_1|} \qquad a \equiv \frac{|\underset{\sim}{l} \times \underset{\sim}{a}_1|}{l}$$

$$\cos\theta_1 = \frac{\underset{\sim}{l} \cdot \underset{\sim}{a}_1}{l a_1} \qquad \cos\theta_2 = \frac{\underset{\sim}{l} \cdot \underset{\sim}{a}_2}{l a_2}$$

with

$$\underset{\sim}{l} \equiv \underset{\sim}{r}_2 - \underset{\sim}{r}_1$$

$$\underset{\sim}{a}_1 \equiv \underset{\sim}{r}_p - \underset{\sim}{r}_1$$

$$\underset{\sim}{a}_2 \equiv \underset{\sim}{r}_p - \underset{\sim}{r}_2$$

With the coordinates of the point of calculation taken as (x_p, y_p, z_p) and those of the ends of the vortex segment taken as (x_1, y_1, z_1) and (x_2, y_2, z_2) we have

$$e_{1_x} = \frac{1}{q_1}[(y_2 - y_1)(z_p - z_1) - (z_2 - z_1)(y_p - y_1)]$$

$$e_{1_y} = \frac{1}{q_1}[(z_2 - z_1)(y_p - y_1) - (y_2 - y_1)(x_p - x_1)]$$

$$e_{1_z} = \frac{1}{q_1}[(x_2 - x_1)(y_p - y_1) - (y_2 - y_1)(x_p - x_1)]$$

where

$$q_1 = \{[(y_2 - y_1)(z_p - z_1) - (z_2 - z_1)(y_p - y_1)]^2 + [(z_2 - z_1)(x_p - x_1) - (x_2 - x_1)(z_p - z_1)]^2 + [(x_2 - x_1)(y_p - y_1) - (y_2 - y_1)(x_p - x_1)]^2\}^{1/2}$$

Also

$$a = \frac{q_1}{q_2}$$

where

$$q_2 \equiv [(x_2 - x_1)^2 + (y_2 - y_1)^2 + (z_2 - z_1)^2]^{1/2}$$

Also

$$\cos\theta_1 = \frac{(x_2-x_1)(x_p-x_1)+(y_2-y_1)(y_p-y_1)+(z_2-z_1)(z_p-z_1)}{q_2[(x_p-x_1)^2+(y_p-y_1)^2+(z_p-z_1)^2]^{1/2}}$$

$$\cos\theta_2 = \frac{(x_2-x_1)(x_p-x_2)+(y_2-y_1)(y_p-y_2)+(z_2-z_1)(z_p-z_2)}{q_2[(x_p-x_2)^2+(y_p-y_2)^2+(z_p-z_2)^2]^{1/2}}$$

Then

$$v_x = \frac{\Gamma}{4\pi} \frac{e_{1_x}}{a}(\cos \theta_1 - \cos \theta_2)$$

$$v_y = \frac{\Gamma}{4\pi} \frac{e_{1_y}}{a}(\cos \theta_1 - \cos \theta_2)$$

$$v_z = \frac{\Gamma}{4\pi} \frac{e_{1_z}}{a}(\cos \theta_1 - \cos \theta_2)$$

and

$$V \equiv |\underset{\sim}{v}| = \frac{\Gamma}{4\pi a}(\cos \theta_1 - \cos \theta_2)$$

$$\Delta\alpha \equiv \frac{V\Delta t}{a}$$

also

$$e_{2_x} = \frac{1}{q_2}[(y_2 - y_1)e_{1_z} - (z_2 - z_1)e_{1_y}]$$

$$e_{2_y} = \frac{1}{q_2}[(z_2 - z_1)e_{1_x} - (x_2 - x_1)e_{1_z}]$$

$$e_{2_z} = \frac{1}{q_2}[(x_2 - x_1)e_{1_y} - (y_2 - y_1)e_{1_x}]$$

and

$$b_x = e_{1_x}\, a \sin \Delta\alpha + e_{2_x}\, a(1 - \cos \Delta\alpha)$$

$$b_y = e_{1_y}\, a \sin \Delta\alpha + e_{2_y}\, a(1 - \cos \Delta\alpha)$$

$$b_z = e_{1_z}\, a \sin \Delta\alpha + e_{2_z}\, a(1 - \cos \Delta\alpha)$$

The contribution of this vortex segment to the motion of point $\underset{\sim}{r}_p$ for this time interval then is given by

$$\Delta x = v_x \Delta t$$

$$\Delta y = v_y \Delta t$$

$$\Delta z = v_z \Delta t$$

if the spiral correction is not used, or by

$$\Delta x = b_x$$

$$\Delta y = b_y$$

$$\Delta z = b_z$$

if the spiral correction is used.

Exit Source Distribution

From {74} the velocity induced at a point (x, y, z) by a uniform source distribution of unit density on a quadrilateral lying in the xy-plane with corner points (x_1, y_1), (x_2, y_2), (x_3, y_3), and (x_4, y_4) is given by

$$v'_x = \frac{y_2 - y_1}{d_1} \ln\left(\frac{r_1 + r_2 - d_1}{r_1 + r_2 + d_1}\right) + \frac{y_3 - y_2}{d_2} \ln\left(\frac{r_2 + r_3 - d_2}{r_2 + r_3 + d_2}\right)$$

$$+ \frac{y_4 - y_3}{d_3} \ln\left(\frac{r_3 + r_4 - d_3}{r_3 + r_4 + d_3}\right) + \frac{y_1 - y_4}{d_4} \ln\left(\frac{r_4 + r_1 - d_4}{r_4 + r_1 + d_4}\right)$$

$$v'_y = \frac{x_1 - x_2}{d_1} \ln\left(\frac{r_1 + r_2 - d_1}{r_1 + r_2 + d_1}\right) + \frac{x_2 - x_3}{d_2} \ln\left(\frac{r_2 + r_3 - d_2}{r_2 + r_3 + d_2}\right)$$

$$+ \frac{x_3 - x_4}{d_3} \ln\left(\frac{r_3 + r_4 - d_3}{r_3 + r_4 + d_3}\right) + \frac{x_4 - x_1}{d_4} \ln\left(\frac{r_4 + r_1 - d_4}{r_4 + r_1 + d_4}\right)$$

$$v'_z = \tan^{-1}\left(\frac{m_1 e_1 - h_1}{z r_1}\right) - \tan^{-1}\left(\frac{m_1 e_2 - h_2}{z r_2}\right)$$

$$+ \tan^{-1}\left(\frac{m_2 e_2 - h_2}{z r_2}\right) - \tan^{-1}\left(\frac{m_2 e_3 - h_3}{z r_3}\right)$$

$$+ \tan^{-1}\left(\frac{m_3 e_3 - h_3}{z r_3}\right) - \tan^{-1}\left(\frac{m_3 e_4 - h_4}{z r_4}\right)$$

$$+ \tan^{-1}\left(\frac{m_4 e_4 - h_4}{z r_4}\right) - \tan^{-1}\left(\frac{m_4 e_4 - h_1}{z r_1}\right)$$

where

$$d_1 \equiv [(x_2 - x_1)^2 + (y_2 - y_1)^2]^{1/2}$$

$$d_2 \equiv [(x_3 - x_2)^2 + (y_3 - y_2)^2]^{1/2}$$

$$d_3 \equiv [(x_4 - x_3)^2 + (y_4 - y_3)^2]^{1/2}$$

$$d_4 \equiv [(x_1 - x_4)^2 + (y_1 - y_4)^2]^{1/2}$$

and

$$m_1 \equiv \frac{y_2 - y_1}{x_2 - x_1} \qquad m_2 \equiv \frac{y_3 - y_2}{x_3 - x_2}$$

$$m_3 \equiv \frac{y_4 - y_3}{x_4 - x_3} \qquad m_4 \equiv \frac{y_1 - y_4}{x_1 - x_4}$$

and

$$r_k \equiv [(x - x_k)^2 + (y - y_k)^2 + z^2]^{1/2}$$

$$e_k \equiv z^2 + (x - x_k)^2$$

$$h_k \equiv (y - y_k)(x - x_k)$$

for k = 1, 2, 3, 4.

Since the vortex sheet surrounding the jet is represented by discrete linear vortex segments, it is appropriate to replace the true exit area by an area bounded by straight lines connecting the column vortex segments on the plane boundary as shown in Figure 104. This area can then be divided into triangular segments, and the velocity induced by each triangle calculated from the above relations. The sum of the velocities induced by all the triangles then is the total velocity induced by the uniform source distribution on exit area that lies inside the vortex sheet. If the exit area is circular, the triangular segments are isoceles triangles, and it is convenient to calculate the induced velocity components in a coordinate system having its origin at the vertex of the triangle and its x'-axis along the bisector of the vertex angle (Figure 105a), and then to transform to the basic coordinate system. Thus

$$v_{x'} = \frac{l_2}{d} \ln\left[\left(\frac{r_1 + r_2 - d}{r_1 + r_2 + d}\right)\left(\frac{r_4 + r_1 - d}{r_4 + r_1 + d}\right)\right]$$

$$- \ln\left[\left(\frac{r_2 + r_3 - l_2}{r_2 + r_3 + l_2}\right)\left(\frac{r_3 + r_4 - l_2}{r_3 + r_4 + l_2}\right)\right]$$

$$v'_{y'} = \frac{l_1}{d} \ln\left[\left(\frac{r_4 + r_1 - d}{r_4 + r_1 + d}\right)\left(\frac{r_1 + r_2 + d}{r_1 + r_2 - d}\right)\right.$$

$$v'_{z'} = \tan^{-1}\left(\frac{\frac{l_2}{l_1}e_1 - h_1}{zr_1}\right) - \tan^{-1}\left(\frac{\frac{l_2}{l_1}e_2 - h_2}{zr_2}\right)$$

$$+ \tan^{-1}\left(\frac{-\frac{l_2}{l_1}e_4 - h_4}{zr_4}\right) - \tan^{-1}\left(\frac{-\frac{l_2}{l_1}e_1 - h_1}{zr_1}\right)$$

where

$$d \equiv \sqrt{l_1^2 + l_2^2}$$

and

$$r_1 = (x'^2 + y'^2 + z'^2)^{1/2}$$

$$r_2 = [(x' - l_1)^2 + (y' - l_2)^2 + z'^2]^{1/2}$$

$$r_3 = [(x' - l_1)^2 + y'^2 + z'^2]^{1/2}$$

$$r_4 = [(x' - l_1)^2 + (y' + l_2)^2 + z'^2]^{1/2}$$

$$e_1 = x'^2 + z'^2$$

$$e_2 = e_3 = e_4 = (x' - l_1)^2 + z'^2$$

$$h_1 = x'y' \qquad h_3 = (x' - l_1)y'$$

$$h_2 = (x' - l_1)(y' - l_2) \qquad h_4 = (x' - l_1)(y' + l_2)$$

Then

$$v'_x = v'_x, \cos\sigma - v'_y, \sin\sigma$$

$$v'_y = v'_x, \sin\sigma + v'_y, \cos\sigma$$

$$v'_z = v'_z,$$

In the case of a general shaped exit area it is convenient to take the initial x-axis along one side of the triangle (Figure 105b). Thus

$$v'_x, = \frac{l_3}{d_1} \ln\left(\frac{r_1 + r_2 - d_1}{r_1 + r_2 + d_1}\right) - \frac{l_3}{d_2} \ln\left(\frac{r_2 + r_3 - d_2}{r_2 + r_3 + d_2}\right)$$

$$v'_y, = - \frac{l_2}{d_1} \ln\left(\frac{r_1 + r_2 - d_1}{r_1 + r_2 + d_1}\right) + \frac{l_2 - l_1}{d_2} \ln\left(\frac{r_2 + r_3 - d_2}{r_2 + r_3 + d_2}\right)$$

$$+ \ln\left(\frac{r_3 + r_4 - d_3}{r_3 + r_4 + d_3}\right) + \ln\left(\frac{r_4 + r_1 - d_4}{r_4 + r_1 + d_4}\right)$$

$$v'_z, = \tan^{-1}\left(\frac{\frac{l_3}{l_2} e_1 - b_1}{z' r_1}\right) - \tan^{-1}\left(\frac{\frac{l_3}{l_2} e_2 - b_2}{z' r_2}\right)$$

$$+ \tan^{-1}\left(\frac{\frac{l_3}{l_2 - l_1} e_2 - b_2}{z' r_2}\right) - \tan^{-1}\left(\frac{\frac{l_3}{l_2 - l_1} e_3 - b_3}{z' r_3}\right)$$

where

$$d_1 = (l_2^2 + l_3^2)^{1/2}$$

$$d_2 = [(l_1 - l_2)^2 + l_3^2]^{1/2}$$

$$d_3 = \frac{1}{3}(2l_1 - l_2)$$

$$d_y = \frac{1}{3}(l_1 + l_2)$$

and

$$r_1 = (x'^2 + y'^2 + z'^2)^{1/2}$$

$$r_2 = [(x' - l_2)^2 + (y' - l_3)^2 + z'^2]^{1/2}$$

$$r_3 = [(x' - l_1)^2 + y'^2 + z'^2]^{1/2}$$

$$r_4 = [(x' - d_4)^2 + y'^2 + z'^2]^{1/2}$$

$$e_1 = x'^2 + z'^2$$

$$e_2 = (x' - l_2)^2 + z'^2$$

$$e_3 = (x' - l_1)^2 + z'^2$$

$$e_4 = (x' - d_4)^2 + z'^2$$

$$b_1 = x'y' \qquad b_3 = (x' - l_1)y'$$

$$b_2 = (x' - l_2)(y' - l_3) \qquad b_4 = (x' - d_4)y'$$

Then

$$v'_x = v'_x, \cos\sigma - v'_y, \sin\sigma$$

$$v'_y = v'_x, \sin\sigma + v'_y, \cos\sigma$$

$$v'_z = v'_z,$$

The above relations apply for a source distribution of unit density. The velocity induced by the source distribution in the present application is then given by

$$\underset{\sim}{v} = \frac{(v_z)_o}{2\pi} \underset{\sim}{v}'$$

Ideally the exit velocity $(v_z)_o$ should be the prescribed jet velocity. Similarly at infinite distance above the plane boundary the undeformed vortex lattice above should induce the same prescribed jet velocity at points inside the lattice. This, however, cannot be precisely the case since the lattice is composed of discrete elements, rather than being a continuous vortex sheet. It is, however, necessary that the vertical velocity induced by the source match that actually induced by the discrete vortex lattice before deformation, else the vortex rings near the exit will move initially at a vertical velocity different from that at an infinite distance above the plane boundary. Therefore, the source strength is determined from the vertical velocity actually induced by the undeformed lattice at a great distance above the plane boundary, rather than from the ideal jet velocity. This determination is made as follows: The vertical velocity induced by continuous infinite circular cylinder vortex sheet of strength V_j on itself is equal to $\frac{V_j}{2}$ {75}. The velocity induced on itself by an infinite sheet

composed of plane segments parallel to the axis is then approximated as $\frac{\psi}{2\pi}V_j$, where ψ is the average angle between the planes forming the sheet (Figure 104). Therefore, if V_{cal} is the vertical velocity actually induced on the lattice vertices at a great distance above the plane boundary by the discrete lattice before deformation, the effective jet velocity may be approximated as

$$(V_j)_{eff} = \frac{2\pi}{\psi} V_{cal}$$

The source strength is then based on $(V_j)_{eff}$, rather than the prescribed jet velocity V_j. This procedure was found to produce an excellent matching of the initial vertical velocity of the rings near the exit with that at a great distance above the exit for both 16 and 32 column vortices spaced evenly around a circular exit.

Table 1. Parameters Used in Various Numerical Solutions for Circular Cylinder

Hamielec and Raal {27}

Mesh size: 0.0513 for R = 1, 10, 50 (R_c = 0.0256, 0.256, 1.28)
0.105 for R = 2, 4, 15 (R_c = 0.105, 0.210, 0.788)
0.0618 for R = 30 (R_c = 0.928)
0.0253 for R = 100 (R_c = 1.26)

Field size: 90.0 for R = 1, 2, 4
66.5 for R = 10, 15, 30
20.1 for R = 50
12.2 for R = 100

Takami and Keller {28}

Mesh size: 0.0816 for R from 1 to 60 (R_c from 0.0408 to 2.45)

Field size: 59.4 for R from 1 to 20
16.9 for R from 30 to 60

Takaisi {31}

Mesh size: 0.111 for R from 0.5 to 100 (R_c from 0.0278 to 5.56)

Field size: 10 for R from 0.5 to 100

Thoman and Szewczyk {30}

Mesh size: 1/12 of boundary layer thickness at forward stagnation point.

Field size: 10 laterally, 18 downstream for R from 40 to 40,000

Final time: 24 for R = 40
160 for R = 200

Jain and Rao {29}

Mesh size: 0.1102 for R from 40 to 200 (R_c = 2.2 to 11.0)

Field size: 111.3 for R from 40 to 200

Final time: 24 for R = 40
32 for R = 60, 200
52 for R = 100

Table 1 (Continued)

Kawaguti and Jain {32}

Mesh size:	0.1102	for R from 1 to 100	(R_c = 0.0551 to 5.51)
Field size:	111.3	for R from 1 to 100	
Final time:	1.2	for R = 1	
	12	for R = 10, 20, 60	
	16	for R = 30	
	24	for R = 40, 50, 100	

Son and Hanratty {33}

Mesh size:	0.0816	for R = 40	(R_c = 1.63)
	0.0319	for R = 200	(R_c = 3.19)
	0.0222	for R = 500	(R_c = 5.55)
Field size:	111.3	for R = 40	
	152.4	for R = 200	
	157.3	for R = 500	
Final time:	50	for R = 40	
	56.1	for R = 200	
	67.4	for R = 500	

Note: Mesh sizes given are ratios of physical radial increment at the cylinder surface to the cylinder radius. Field sizes given are ratios of the physical maximum field radius to the cylinder radius. Final times are given as nondimensionalized with respect to the cylinder radius and free stream velocity. The cell Reynolds numbers here are based on the mesh size given.

Table 2. Combinations Evaluated for Cylinder Boundary Treatments

Convection Scheme														
A	x				x									
B		x				x							x	
C			x				x			x	x	x	x	x
D				x				x						
E									x					
Diffusion Scheme														
A	x	x	x	x										x
B					x	x	x	x	x	x	x	x	x	
Surface Vorticity Scheme														
A	x	x	x	x	x	x	x	x	x		x	x	x	x
B										x				
Corner Scheme														
A	x	x	x	x	x	x	x	x	x	x				
B											x			
C												x	x	x
D														

Convection Schemes

A : $v = 0$ in boundary cells
B : $\tilde{v} \neq 0$ in boundary cells
C : $\tilde{v} = 0$ in boundary cells only for calculation there
D : No convection in boundary cells
E : No convection in boundary cells, $\underset{\sim}{v} = 0$ in boundary cells

Diffusion Schemes

A : Calculated vorticity used for calculation in boundary cells
B : Surface vorticity used for calculation in boundary cells

Table 2 (Continued)

Surface Vorticity Schemes

A : $\underset{\sim}{\omega} = 0$ in boundary cells
B : $\tilde{\underset{\sim}{\omega}} \neq 0$ in boundary cells

Corner Schemes

A : $\underset{\sim}{\omega} = 0$ in boundary cells, one-sided difference
B : $\underset{\sim}{\omega} = 0$ in boundary cells, central difference
C : $\underset{\sim}{\omega} \neq 0$ in boundary cells, central difference
D : $\underset{\sim}{\omega} \neq 0$ in boundary cells, central differences, zero vorticity used on inside corners for calculation there

Table 3. Drag Coefficients and Minimum Pressures for Various Cylinder Boundary Treatments

	Scheme				(A)	(B)	(A)	(B)	(A)	(B)
	convection	diffusion	surface vorticity	corners	C_{D_p}	C_{D_p}	C_D	C_D	$(C_p)_{min}$	$(C_p)_{min}$
R = 12	C	B	A	C	1.29	2.24	1.25	1.49	-0.89	-2.13
	B	B	A	C	1.25	2.16	1.25	1.47	-0.93	-2.18
(t = 10)	E	B	A	C	1.57	2.51	1.34	1.58	-1.05	-2.21
	C	B	A	D	0.12	2.02	1.14	1.42	+0.46	-1.84
(Δt = 0.2, t = 6)	C	A	A	A	0.55	10.25	1.01	2.47	-0.09	-12.55
(Δt = 0.2, t = 6)	C	A	A	C	1.69	3.74	1.40	1.78	-1.17	-3.58
(Δt = 0.2, t = 6)	C	B	A	C	1.78	2.47	1.60	1.78	-1.25	-2.25
(t = 10)	C	B	A	C	1.35	2.31	1.30	1.54	-0.94	-2.19
R = 24	C	B	A	C	0.98	1.48	0.76	0.88	-0.51	-1.23
(Δt = 0.2)	C	B	A	C	0.97	1.26	0.81	0.89	-0.63	-1.08
(Δt = 0.1)	C	B	A	C	0.96	1.12	0.85	0.90	-0.68	-0.93
	B	B	A	C	0.90	1.36	0.75	0.86	-0.55	-1.30
	C	B	A	D	0.48	1.41	0.71	0.85	+0.04	-1.13
	C	A	A	A	0.39	5.42	0.45	1.21	+0.28	-5.98
	C	A	A	C	0.96	2.39	0.63	0.88	-0.46	-2.14
(Δt = 0.2)	C	A	A	A	0.38	5.41	0.45	1.22	+0.28	-5.97
R = 48	C	B	A	C	0.78	1.03	0.46	0.51	-0.23	-0.59
	C	B	A	D	0.58	1.00	0.43	0.49	+0.02	-0.52

(Continued)

Table 3 (Continued)

	Scheme				(A) C_{D_p}	(B) C_{D_p}	(A) C_D	(B) C_D	(A) $(C_p)_{min}$	(B) $(C_p)_{min}$
R = 120	C	B	A	C	0.58	0.67	0.22	0.23	+0.23	+0.12
(t = 42)	C	B	A	C	0.30	0.38	0.14	0.16	+0.44	+0.34
	B	B	A	C	0.34	0.44	0.19	0.21	+0.33	+0.19
	C	B	A	D	0.53	0.65	0.21	0.23	+0.29	+0.14
($t = 20$, $N_D = 24$)	C	B	A	C	0.002	0.14	0.26	0.28	-0.12	-0.43
($\Delta t = 0.2$, $t = 20$, $N_D = 24$)	C	B	A	C	-0.007	0.06	0.28	0.29	-0.18	-0.36
($t = 20$, $N_D = 24$)	B	B	A	C	-0.19	-0.10	0.24	0.25	-0.02	-0.32
R = 6	C	B	A	C	1.82	3.67	2.04	2.51	-1.35	-3.48
($\Delta t = 0.2$)	C	B	A	C	1.87	3.26	2.16	2.52	-1.41	-3.11

All values obtained with $\Delta t = 0.4$, $N_D = 12$ at time t = 12, except as noted.

Table 4. Values of Parameters Used in Results Presented

Figure	R_c	Δt	N_D	r_m	ω_m	r_f	t	formu-lation
5	1	*	--	--	0.001		*	D
6	1	*	--	--	0.001		*	D
7	1	0.4	--	--	*		*	D
8	1	0.4	--	--	*		*	D
9	1	0.1	--	--	0.001		*	D
13	*	0.4	12	24	0.01		---	D
14	*	0.4	*	$2.N_D$	0.01		---	D
15	*	0.4	12	24	0.01		---	D
16	*	0.4	*	$2.N_D$	0.01		---	D
17	10	0.4	12	24	0.01		*	D
18	10	0.4	12	24	0.01		---	D
19	10	0.4	12	24	0.01		*	D
20	10	0.4	12	24	0.01		*	D
21	10	0.4	12	24	0.01		---	D
24	10	0.4	12	24	0.01		---	D
27	1.35	*	6	12	0.001		5.6	S
28	2.5	0.65	6	12	0.001		15.6	S
29	5.0	0.2	6	24	0.01		*	S
30	5.0	0.2	6	24	0.01		*	S
31	2.5	0.4	12	24	0.01		*	S
32	5.0	0.2	6	24	0.01		*	S
33	5.0	0.2	6	24	0.01		*	S
34	5.0	0.2	6	24	0.01		*	S
35	2.5	0.4	6	24	0.01		*	S
37-42	2.0	0.05	6	12	0.001	9	*	S
43-48	2.0	0.1	6	6	0.10	9	*	S
49	2.0	0.05	6	12	0.001	9	*	S
50	2.0	0.1	6	12	0.01	12	*	S
51	2.0	0.1	6	6	0.10	9	*	S
52	2.0	0.2	6	12	0.01	12	*	S
53	1.0	0.1	6	12	0.01	12	*	S
66	0.5	*	12	24	0.01		*	D
67	2	*	*	$2.N_D$	0.01		*	D
68	10	*	*	$2.N_D$	0.01		*	D
69	*	0.4	12	24	0.01		14	D
70	2	*	12	24	0.01		12	D
71	10	0.4	12	*	0.001		16	D
72	10	0.4	12	24	*		16	D
73	2.0	*	6	12	0.01		8	S
74	2.5	0.4	6	*	0.001		12	D
75	2.5	0.4	6	12	*		12	D
76	3.5	0.70	6	12	0.001		*	S
77	1.0	0.30	6	12	0.001		2.4	S

Table 4 (Continued)

78	1.5	0.40	6	12	0.001		4.0	S
79	3.0	0.65	12	24	0.001		7.8	S
80	2.5	0.40	12	24	0.001		*	D
81	2.5	0.60	12	24	0.001		*	D
82	10.0	0.4	6	24	0.01		*	D
83	10.0	0.4	6	24	0.001		*	D
84- 88	2.0	0.1	6	12	0.01	9	*	S
89- 93	2.0	0.05	6	12	0.001	9	*	S
94- 98	2.0	0.2	6	6	0.01	9	*	S
99-103	2.0	0.1	6	6	0.10	9	*	S

Notes:

1. An asterisk indicates a quantity given on the figure.
2. In Figures 13-15, $\Delta t = 0.2$ for $R_c = 2$.
3. D indicates the Dufort-Frankel formulation.
4. S indicates the straight explicit formulation.

Table 5. Scale Factors for Vector Plots

Figure	1a	1b	2a	2b	3a	3b	4a	4b
17	0.045	0.045	---	---	---	---	---	---
19	0.045	0.045	---	---	---	---	---	---
20	0.045	0.045	---	---	---	---	---	---
24	0.15	0.15	0.1207	0.1207	0.15	0.15	0.2414	0.1207
27	0.15	0.15	---	---	---	---	---	---
28	0.15	0.15	---	---	---	---	---	---
29	0.1125	0.1125	0.0923	0.0923	0.1125	0.1125	---	---
30	0.1125	0.1125	0.0923	0.0923	0.1125	0.1125	---	---
31	0.0900	0.0900	0.0682	0.0682	0.0900	0.0900	---	---
32	0.1125	0.1125	0.0923	0.0923	0.1125	0.1125	---	---
33	0.0900	0.0900	0.0682	0.0682	0.0900	0.0900	---	---
34	0.0900	0.0900	0.0682	0.0682	0.0900	0.0900	---	---
35	0.0900	0.0900	0.0682	0.0682	0.0900	0.0900	---	---
37- 42	0.0900	0.0900	0.0682	0.0682	0.0900	0.0900	0.1363	0.0682
43- 48	0.0900	0.0900	0.0682	0.0682	0.0900	0.0900	0.1363	0.0682
70- 72	0.0900	0.0900	---	---	---	---	---	---
73	0.1125	0.1125	0.0923	0.0923	0.1125	0.1125	---	---
74	0.1125	0.1125	0.0923	0.0923	0.1125	0.1125	---	---
75	0.1125	0.1125	0.0923	0.0923	0.1125	0.1125	---	---
76	0.15	0.15	0.1207	0.1207	0.15	0.15	0.2414	0.1207
77	0.15	0.15	0.1207	0.1207	0.15	0.15	0.2414	0.1207
78	0.15	0.15	---	---	---	---	---	---
79	0.15	0.15	---	---	---	---	---	---
80	---	---	---	---	0.1125	0.1125	---	---
81	---	---	---	---	0.1125	0.1125	---	---
82	0.1125	0.1125	---	---	---	---	---	---
83	0.1125	0.1125	---	---	---	---	---	---

Table 5 (Continued)

Notes:

1. The columns contain the following scale factors:

   Column 1a: inches per unit horizontal velocity
   Column 1b: inches per cell on horizontal velocity plot
   Column 2a: inches per unit vertical velocity
   Column 2b: inches per cell on vertical velocity plot
   Column 3a: inches per unit horizontal vorticity
   Column 3b: inches per cell on horizontal vorticity plot
   Column 4a: inches per unit vertical vorticity
   Column 4b: inches per cell on vertical vorticity plot

2. Plots are unretouched computer plots of a Cal-Comp Incremental Plotter. Spurious lines are the results of plotter failure.

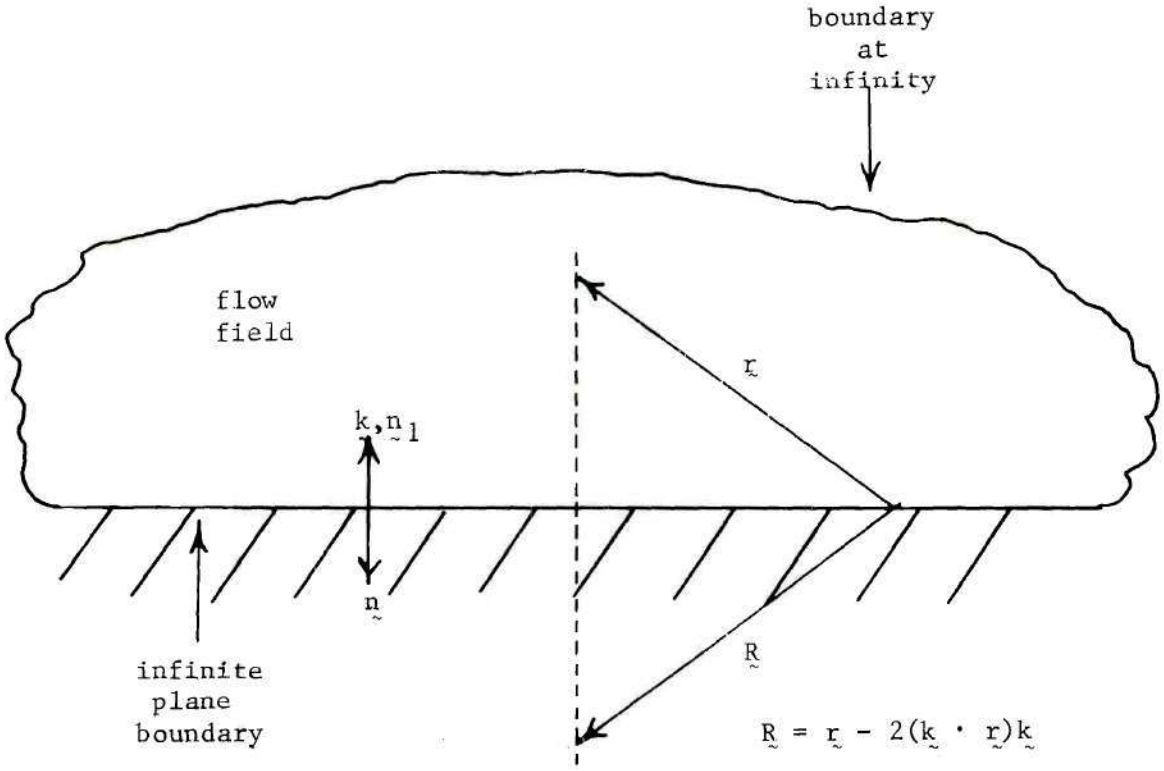

Figure 1. Integration Field and Image

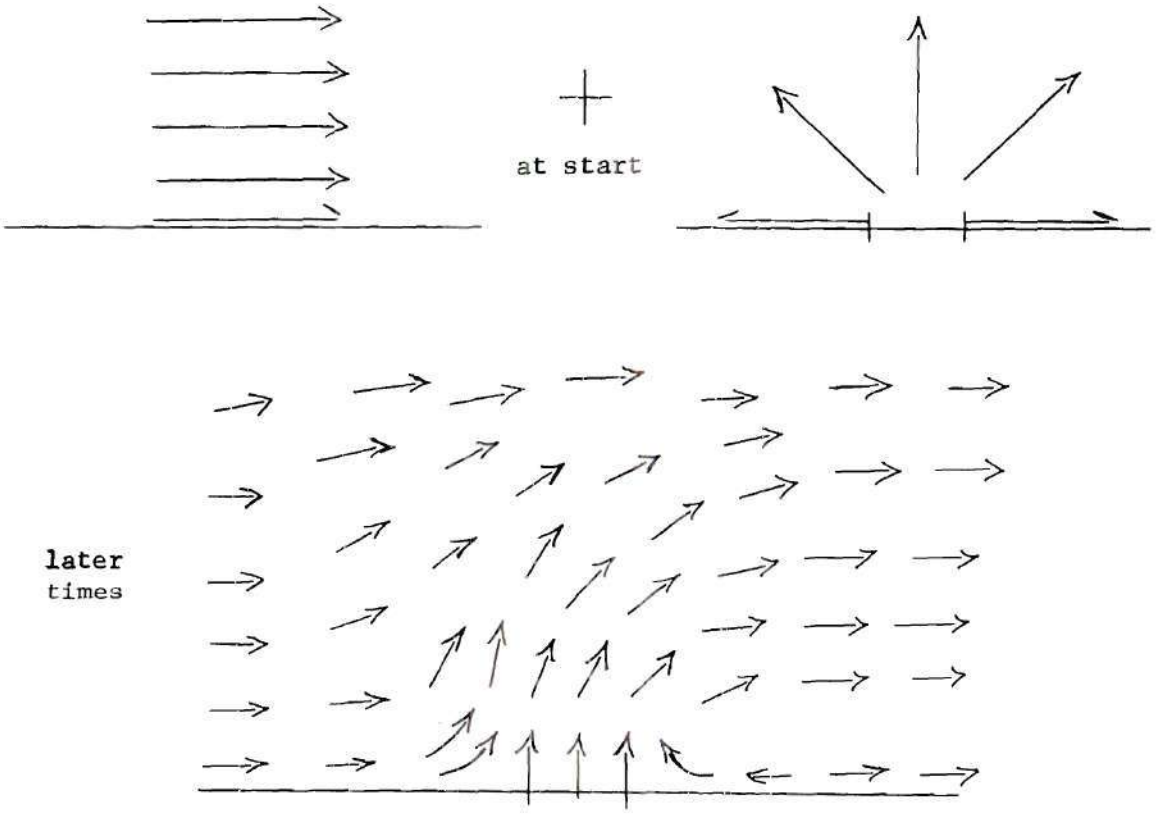

(a) Velocity Field Development

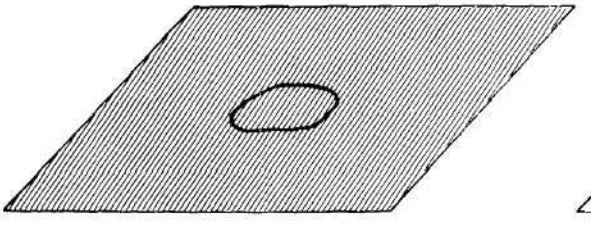

(b) Initial Vorticity Distribution for Complete Solution

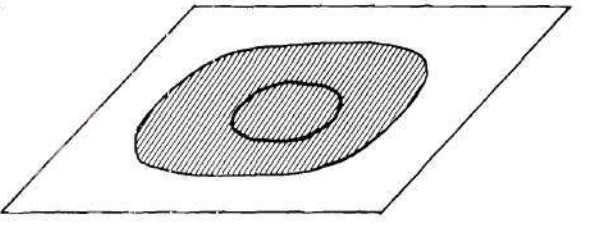

(c) Initial Vorticity Distribution for Three-Dimensional Sub-Solution

Figure 2. Illustration of Jet in Cross-Wind Problem with Start from Opening of Jet Exit

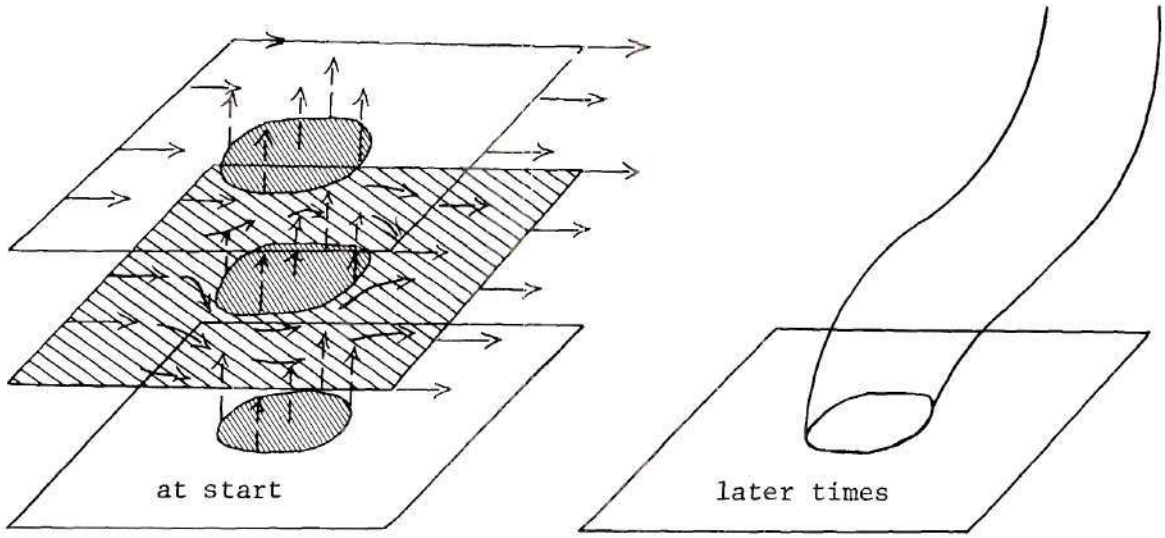

(a) Velocity Field Development

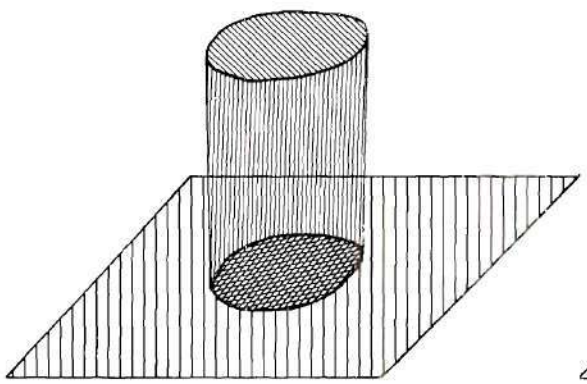

(b) Initial Vorticity Distribution for Complete Solution

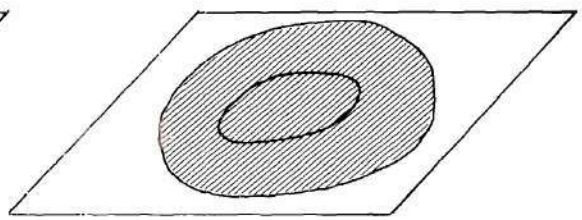

(c) Initial Vorticity Distribution for Three-Dimensional Sub-Solution

Figure 3. Illustration of Jet in Cross-Wind Problem with Start from Dissolution of Cylindrical Discontinuity

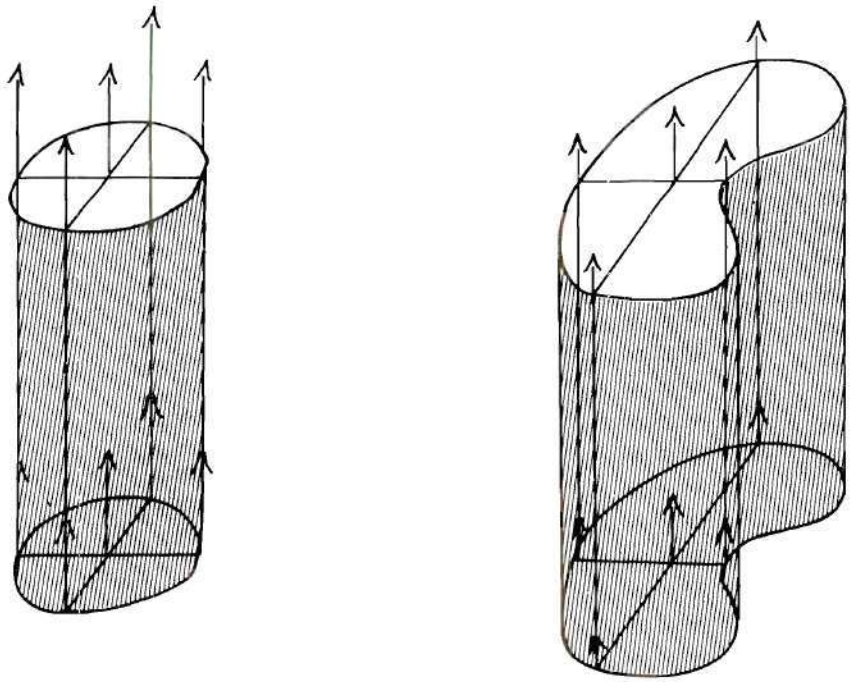

Figure 4. Illustration of Infinite Jet in Cross-Wind Problem

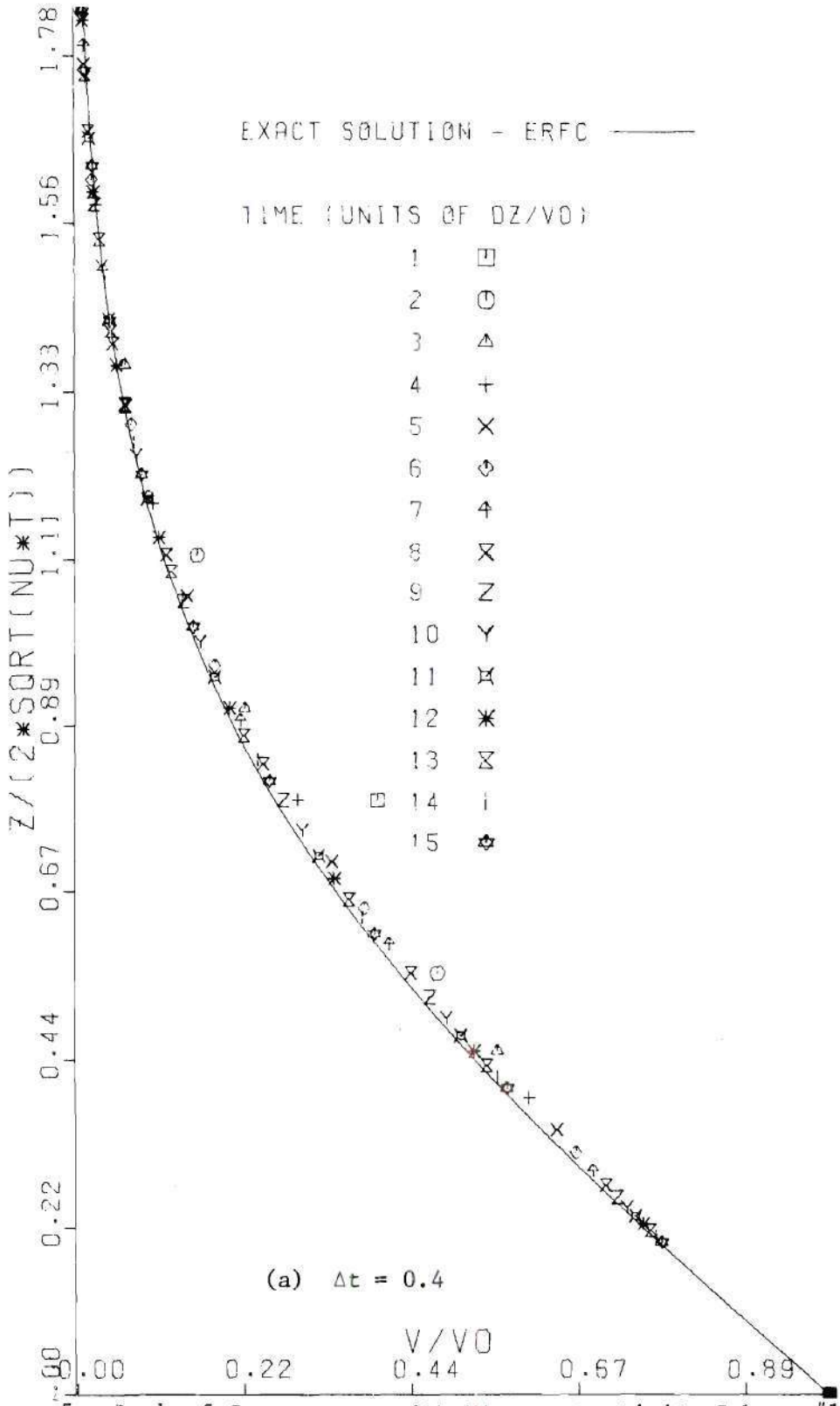

(a) $\Delta t = 0.4$

Figure 5. Lack of Convergence with Minimum Vorticity Scheme #1 for Decreasing Time Step at Fixed Cell Size - Suddenly Accelerated Infinite Flat Plate

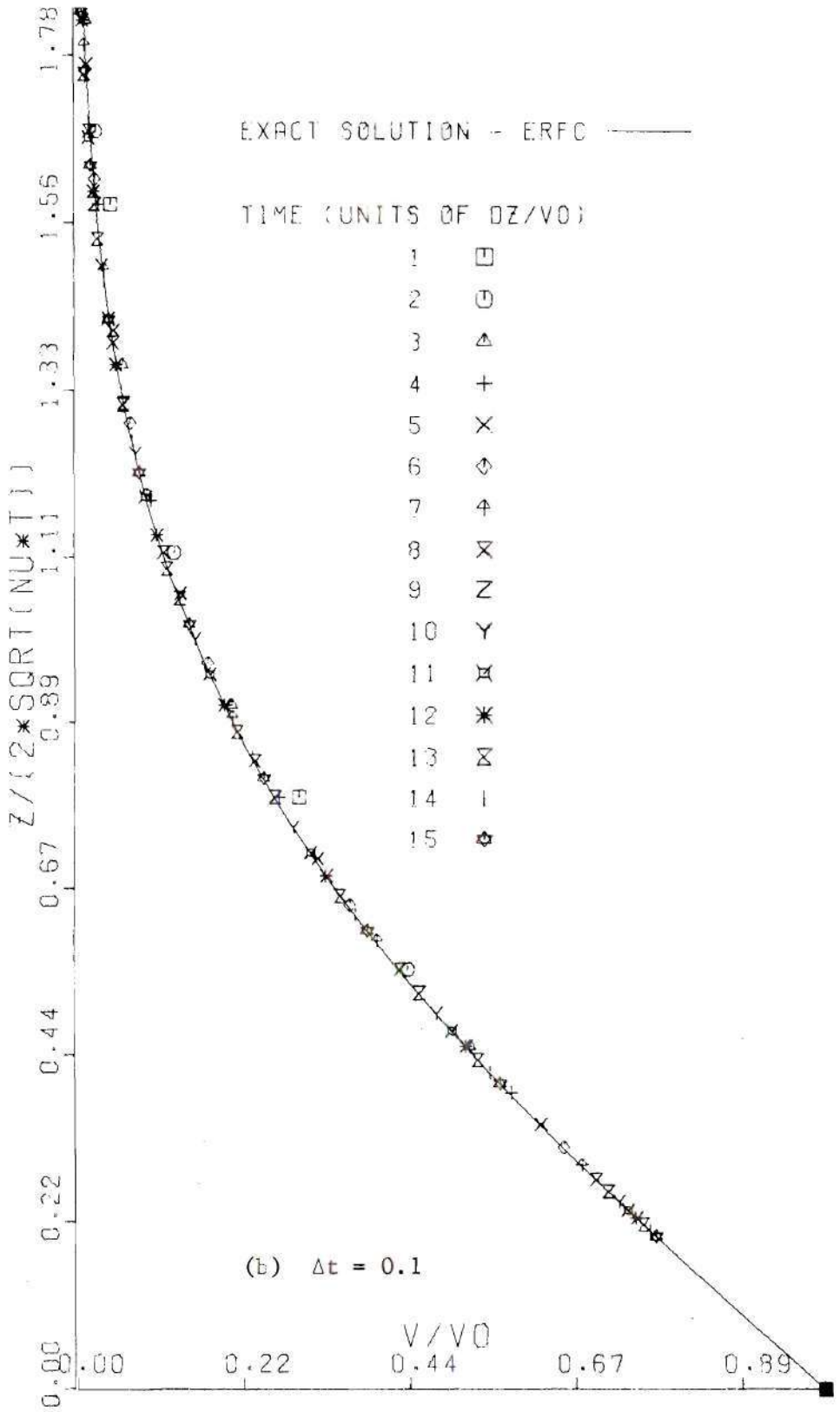

Figure 5. (cont.)

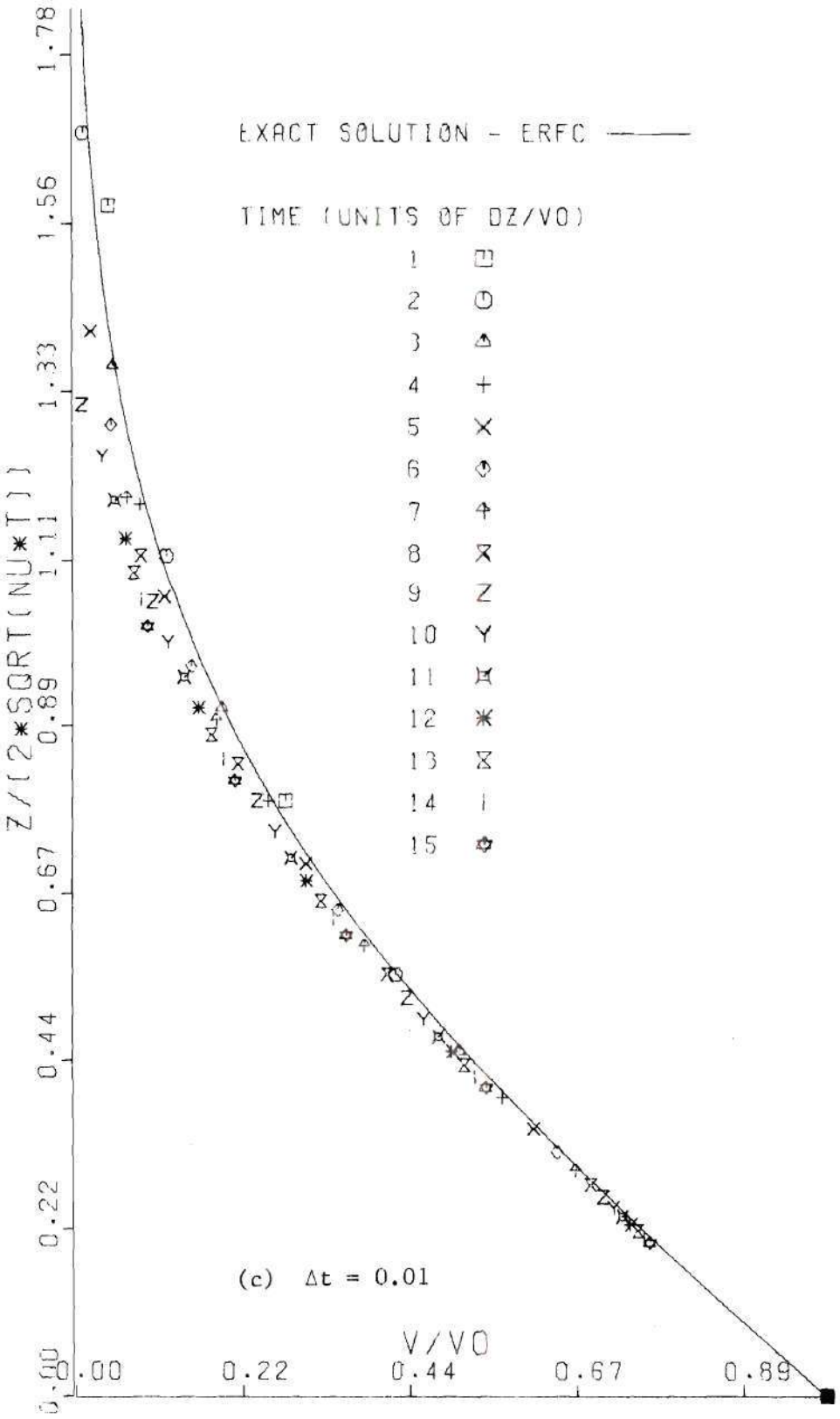

Figure 5. (cont.)

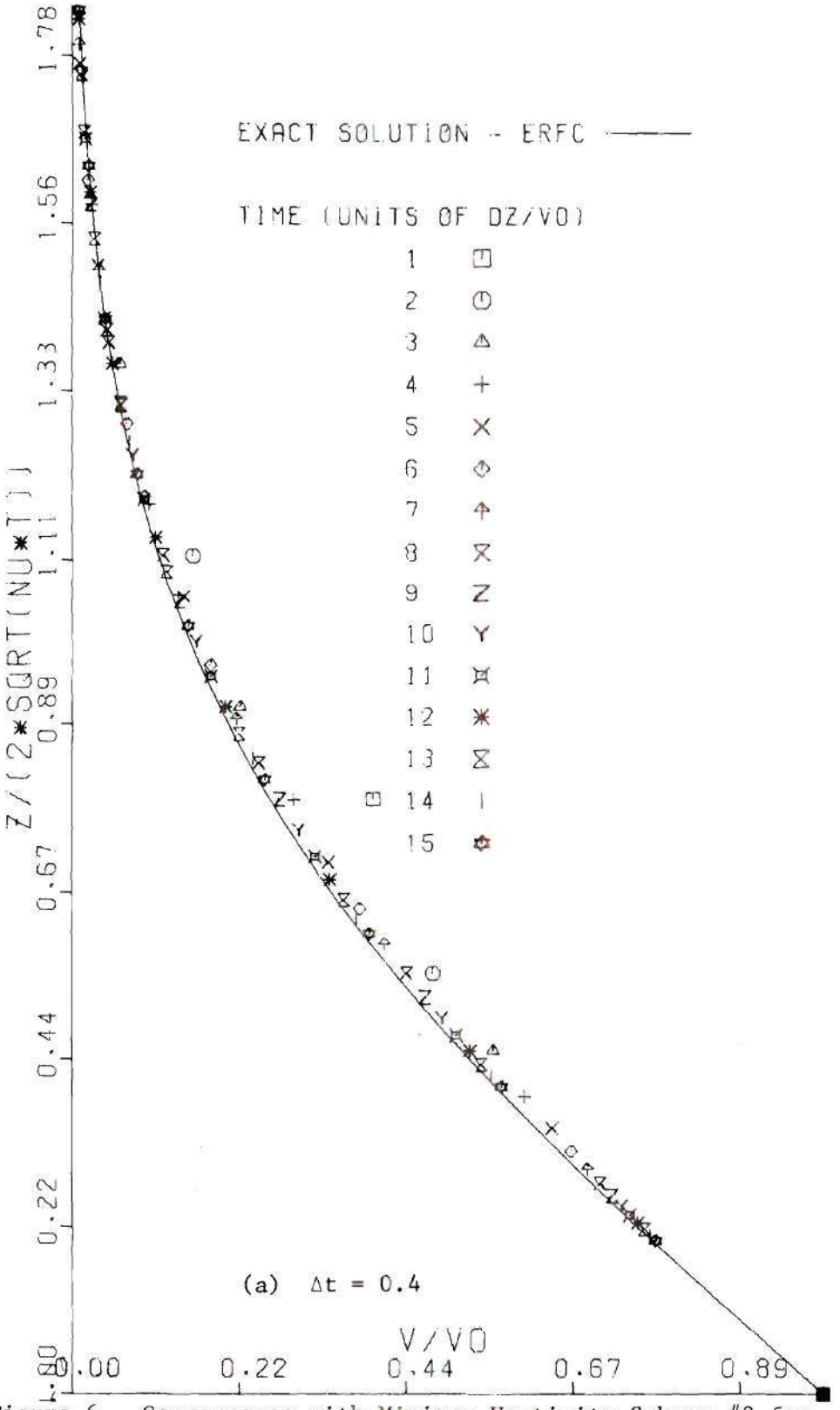

Figure 6. Convergence with Minimum Vorticity Scheme #2 for Decreasing Time Step at Fixed Cell Size - Suddenly Accelerated Infinite Flat Plate

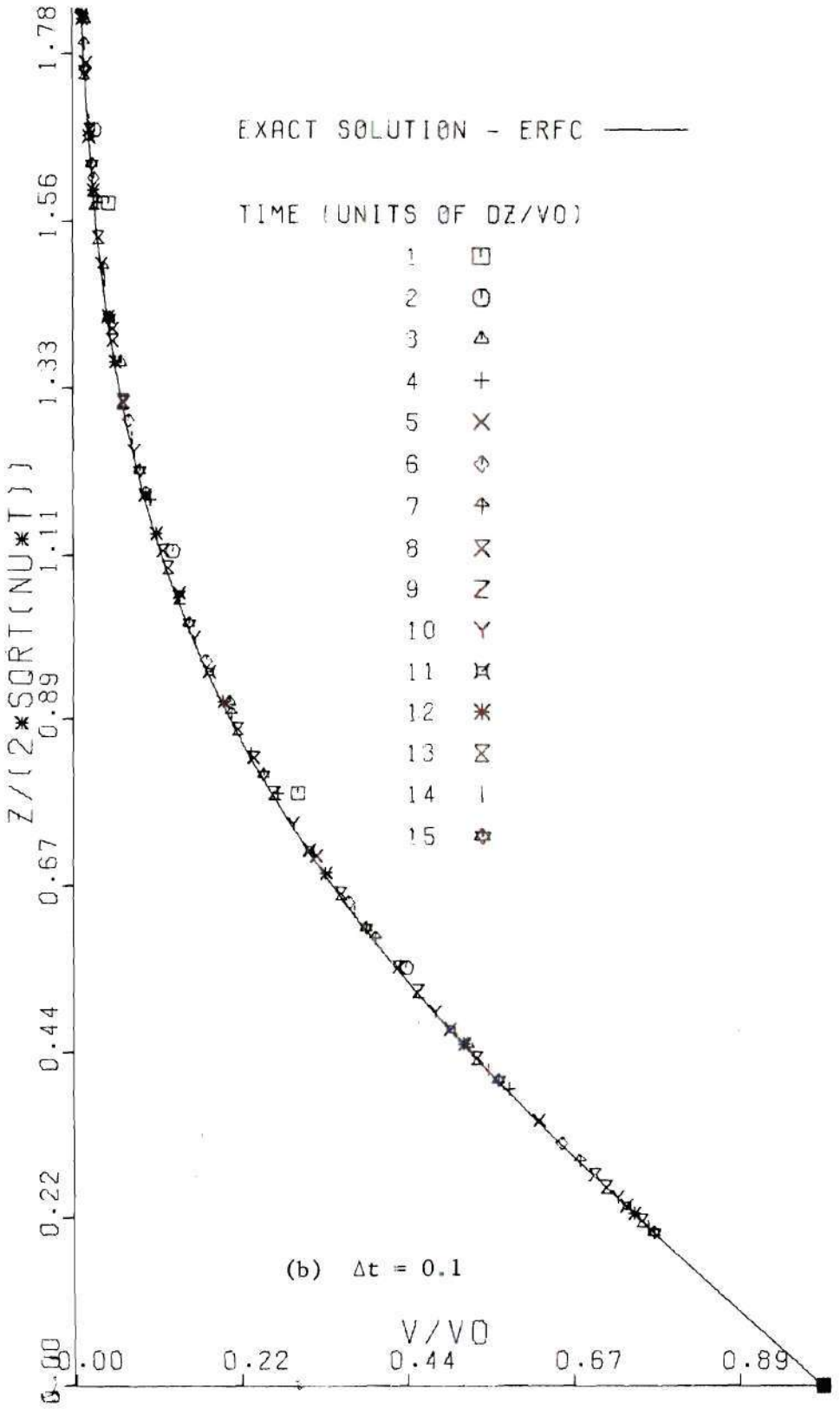

(b) $\Delta t = 0.1$

Figure 6. (cont.)

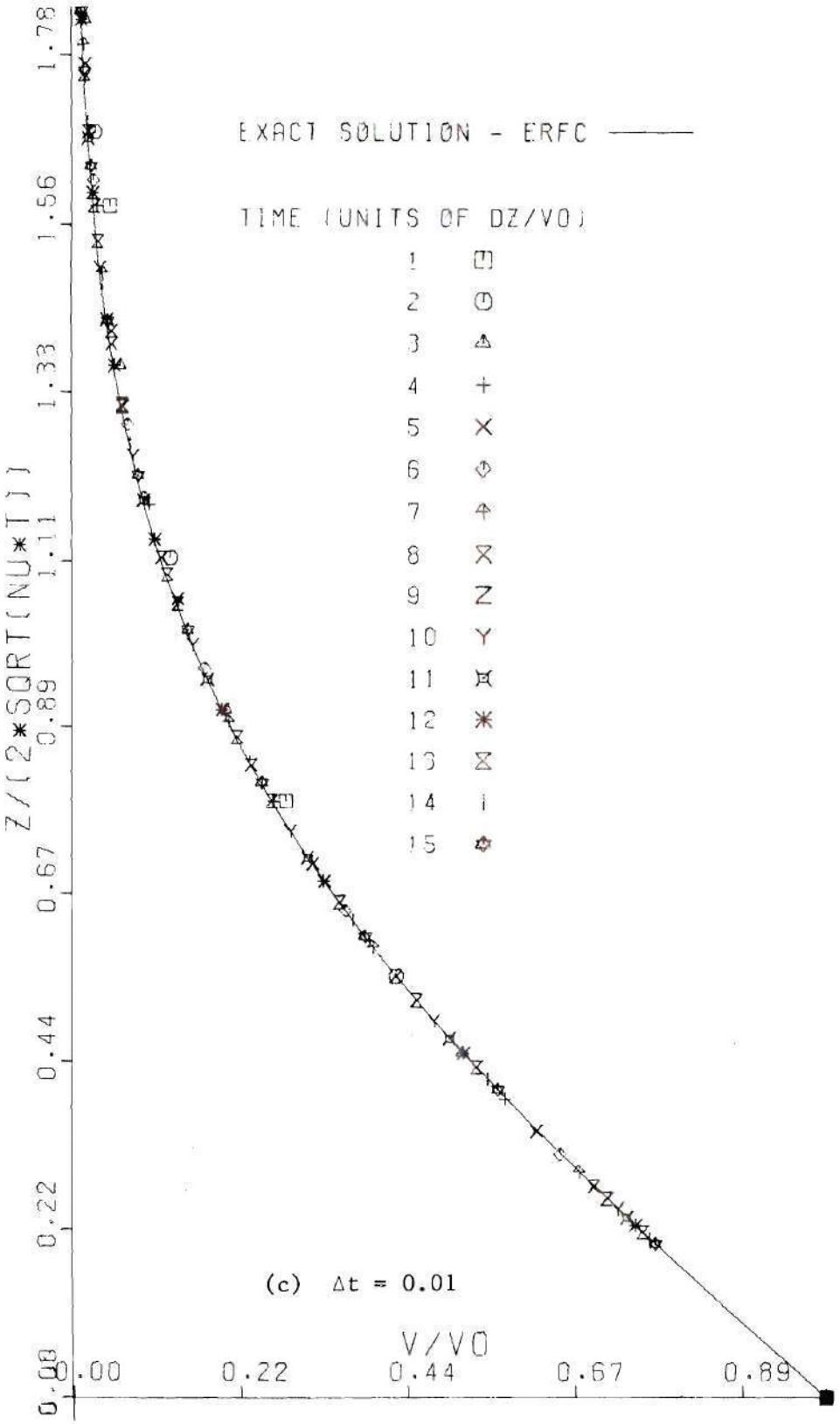

(c) $\Delta t = 0.01$

Figure 6. (cont.)

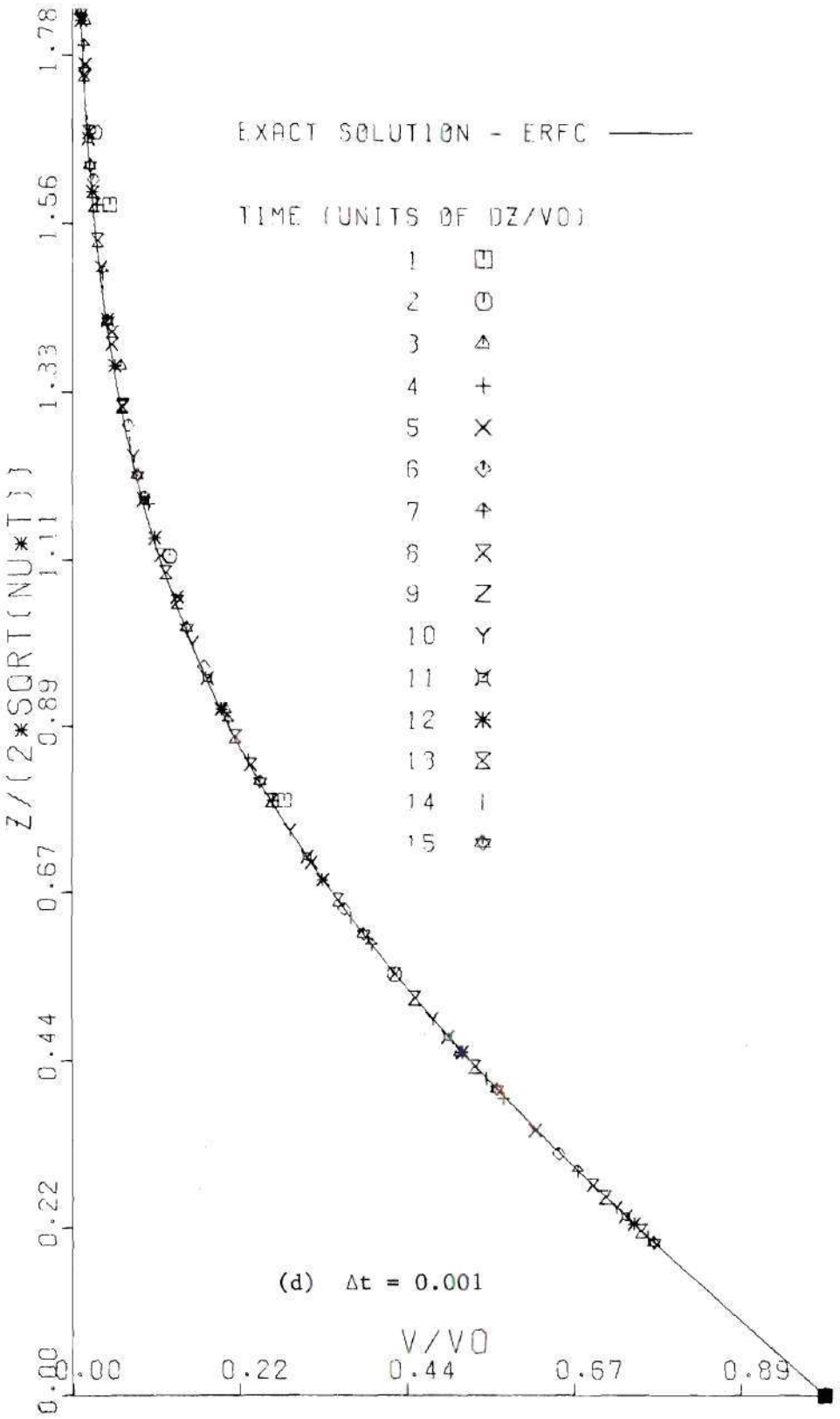

Figure 6. (cont.)

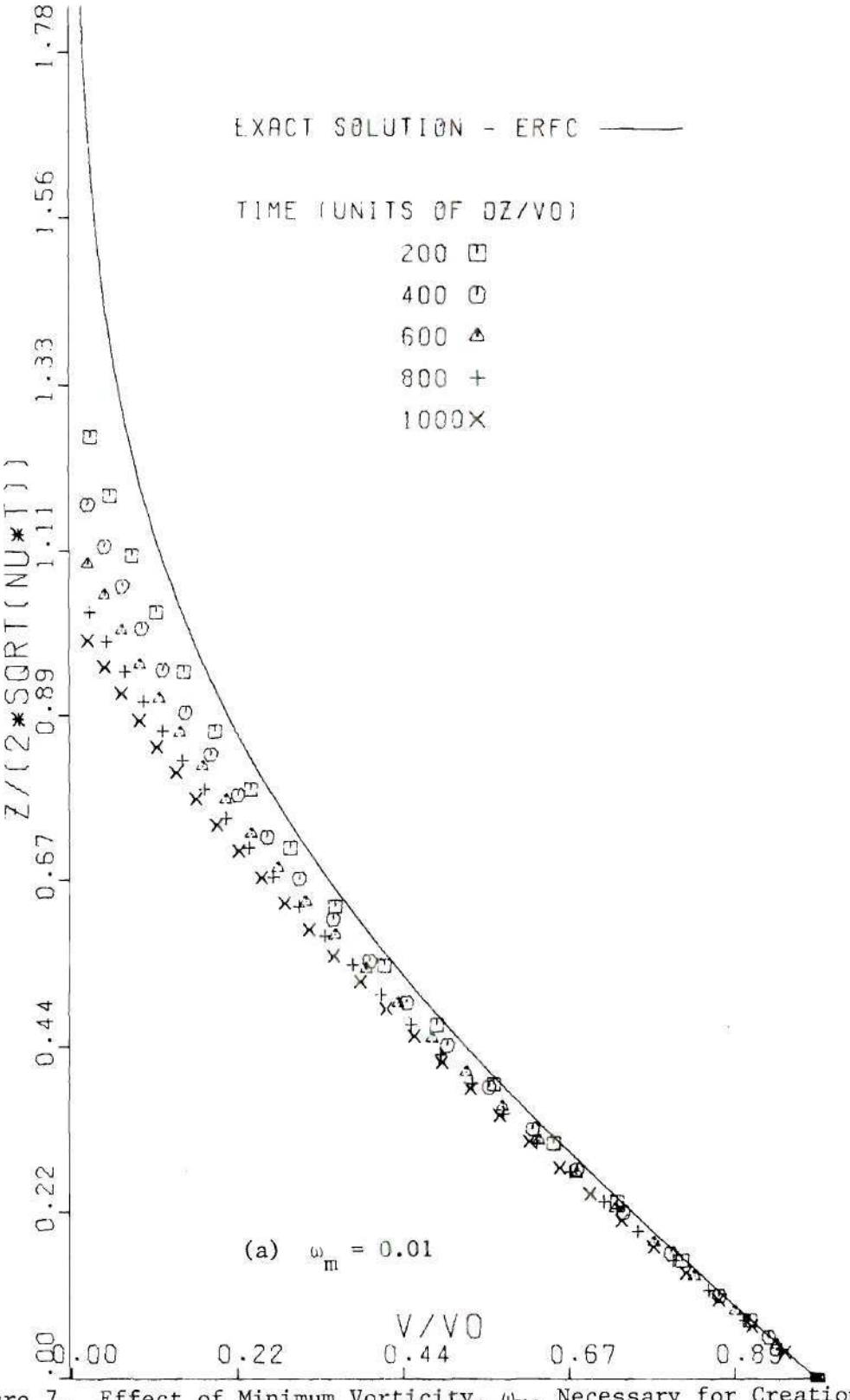

Figure 7. Effect of Minimum Vorticity, ω_m, Necessary for Creation of New Vortex Cells with Minimum Vorticity Scheme #1 - Suddenly Accelerated Infinite Flat Plate

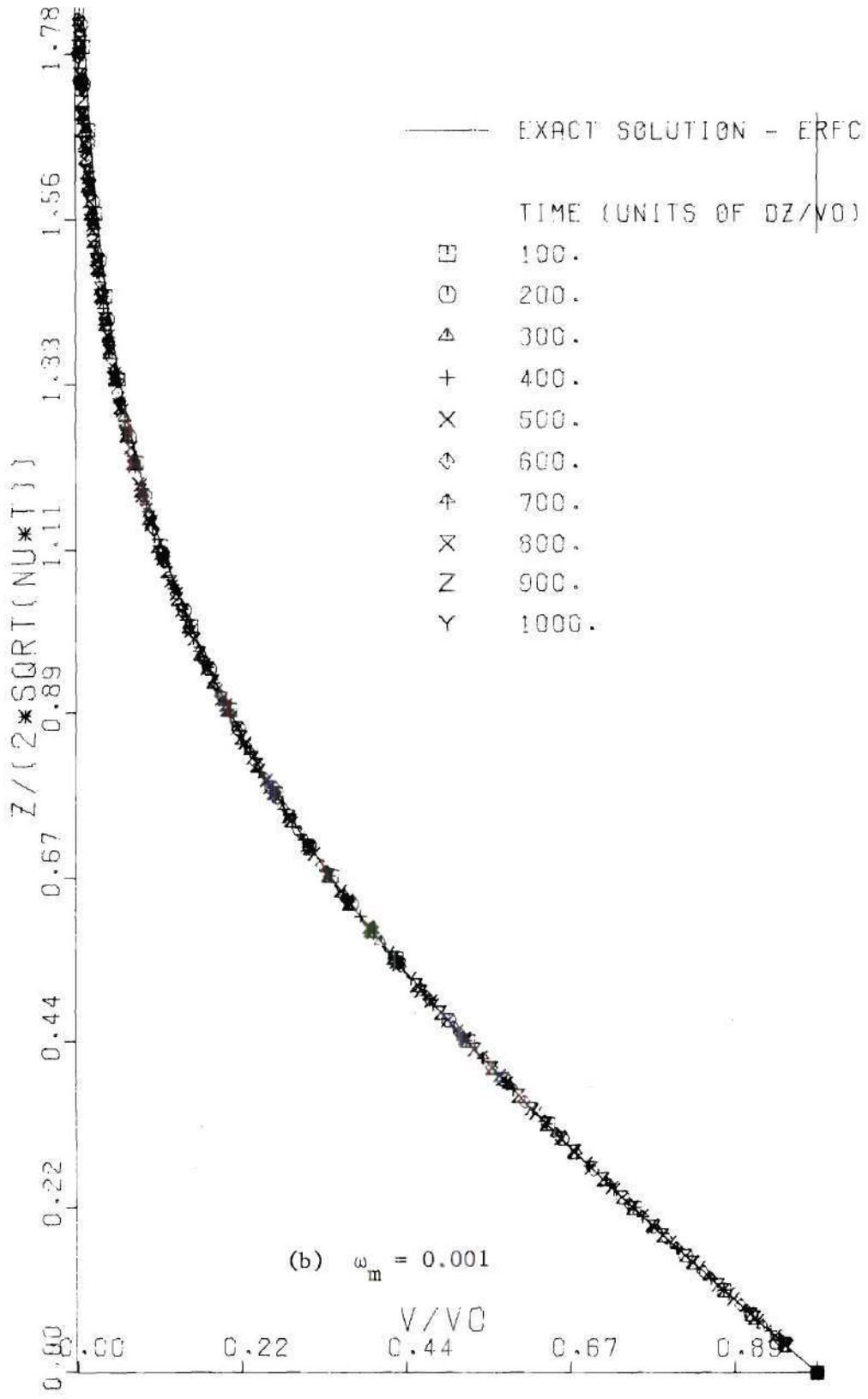

(b) $\omega_m = 0.001$

Figure 7. (cont.)

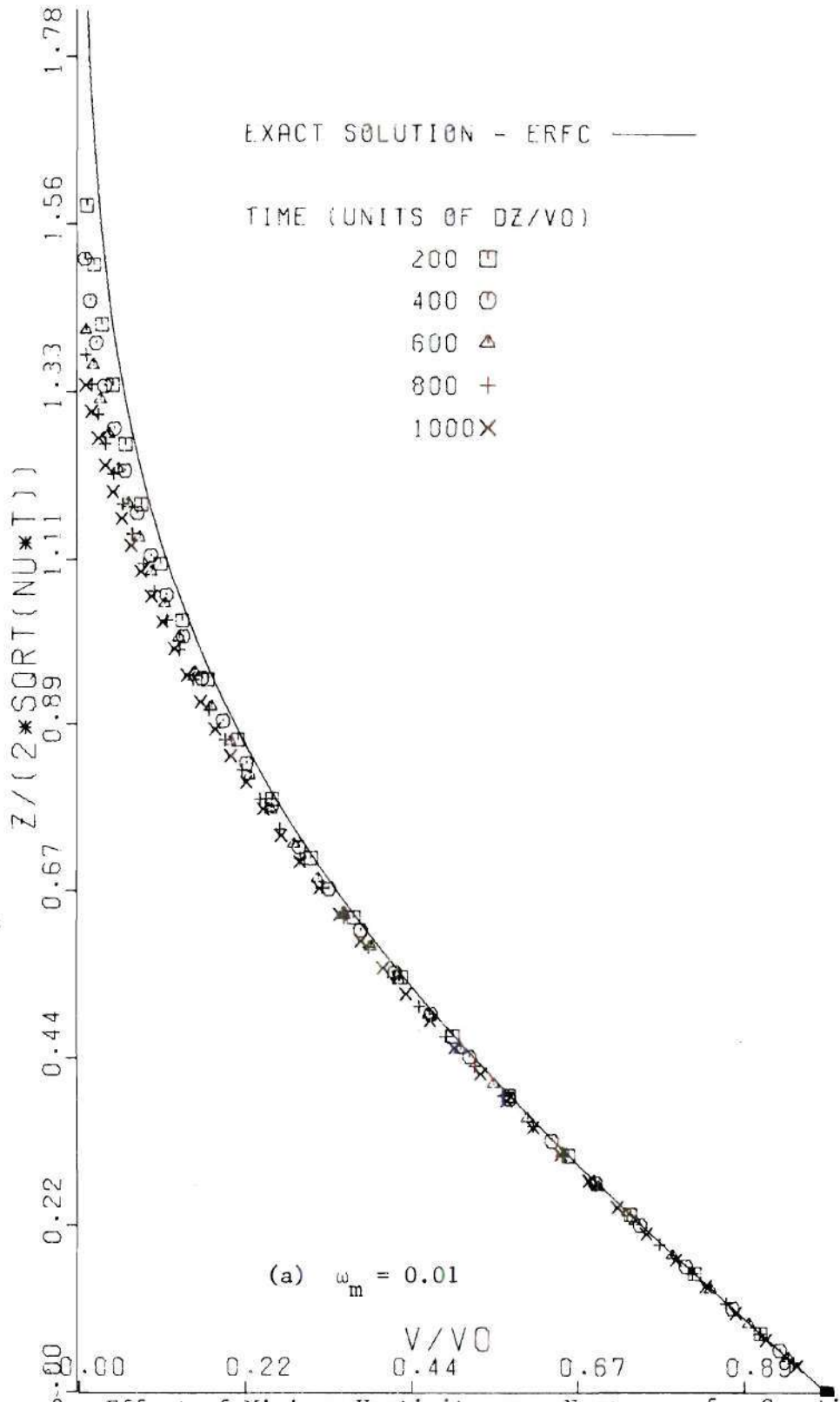

Figure 8. Effect of Minimum Vorticity, ω_m, Necessary for Creation of New Vortex Cells with Minimum Vorticity Scheme #2 - Suddenly Accelerated Infinite Flat Plate

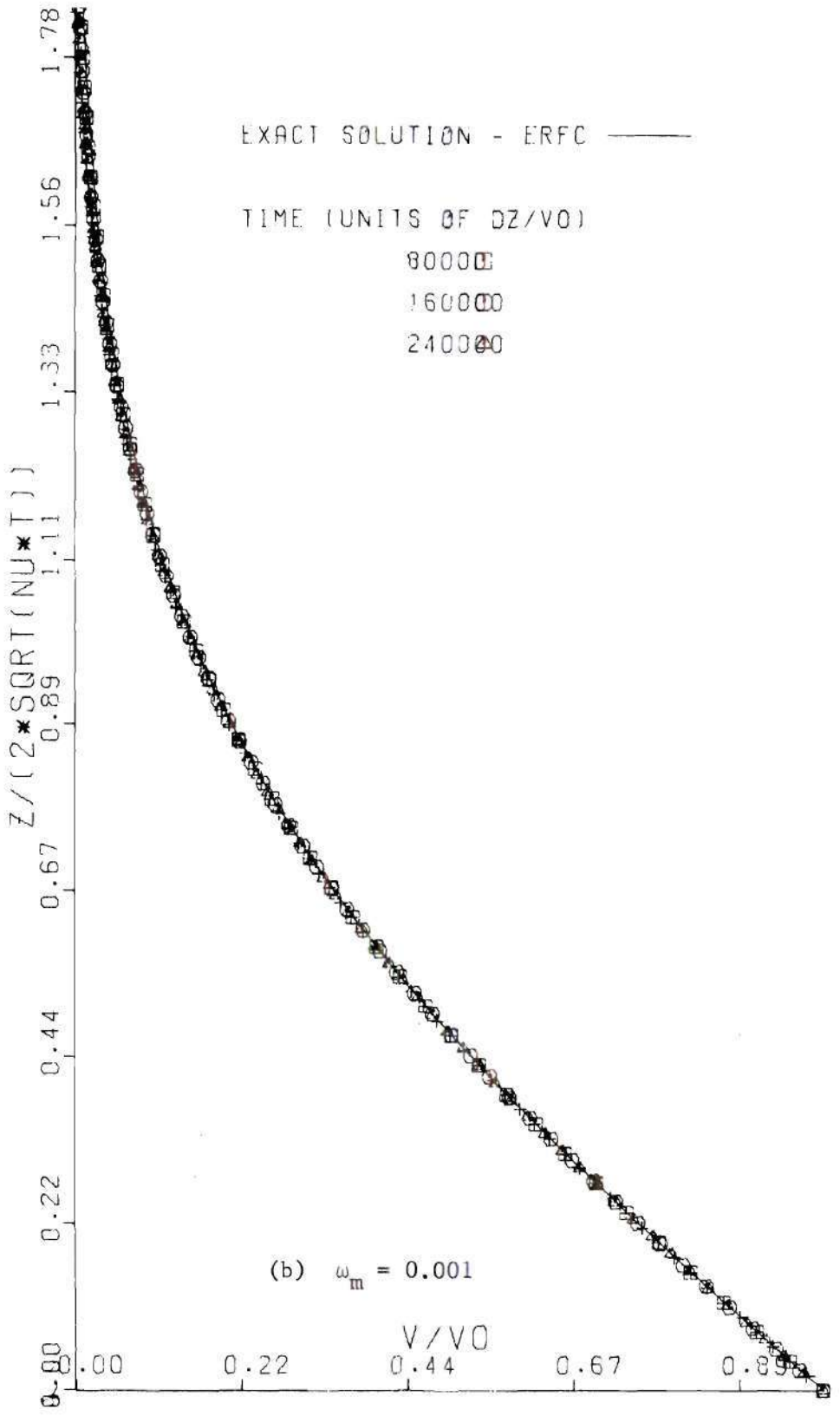

(b) $\omega_m = 0.001$

Figure 8. (cont.)

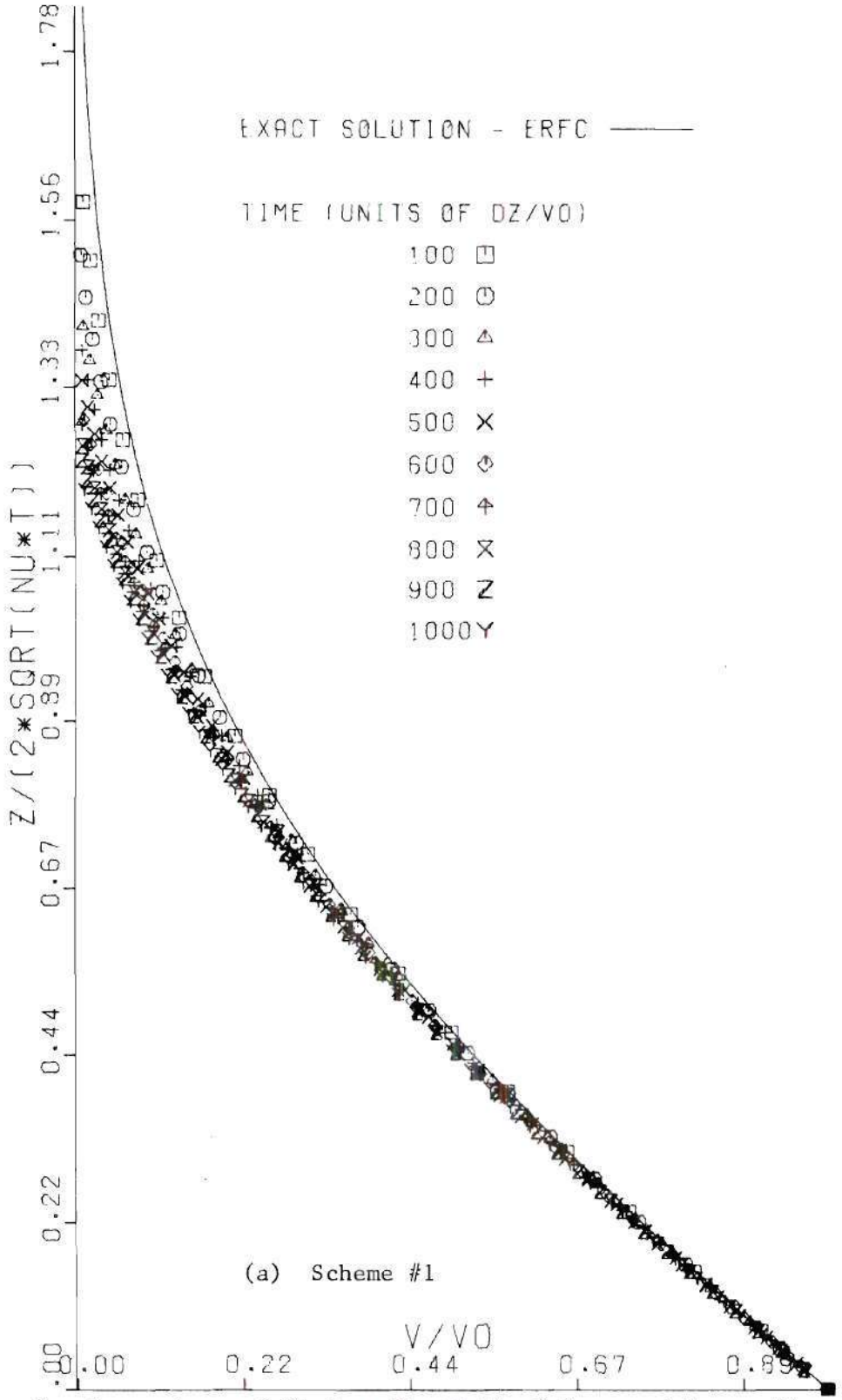

Figure 9. Comparison of Minimum Vorticity Schemes at Large Times - Suddenly Accelerated Infinite Flat Plate

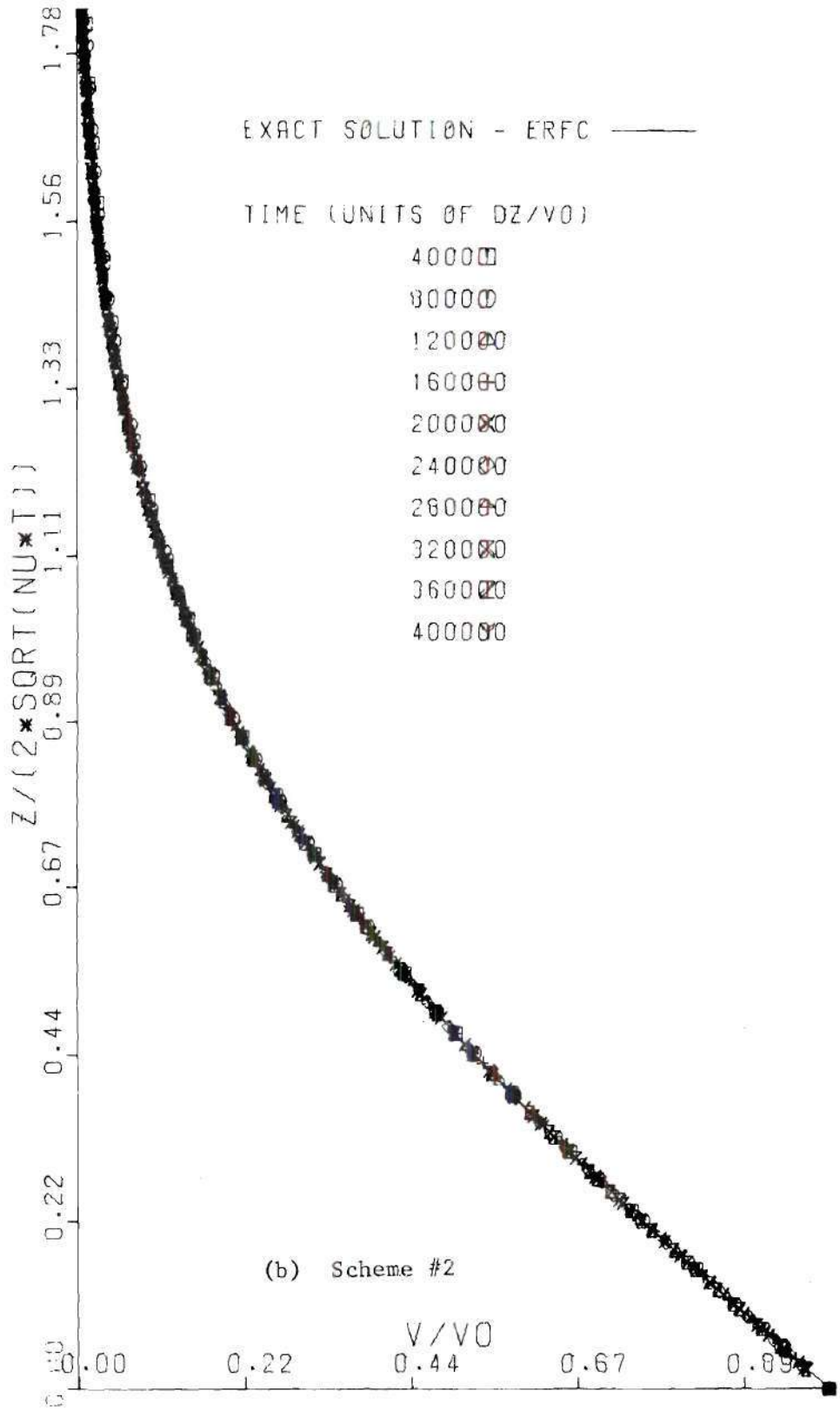

(b) Scheme #2

Figure 9. (cont.)

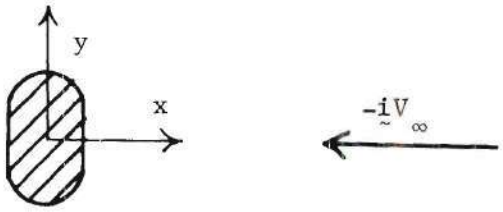

Figure 10. Coordinate System for Two-Dimensional Solid Body Solution

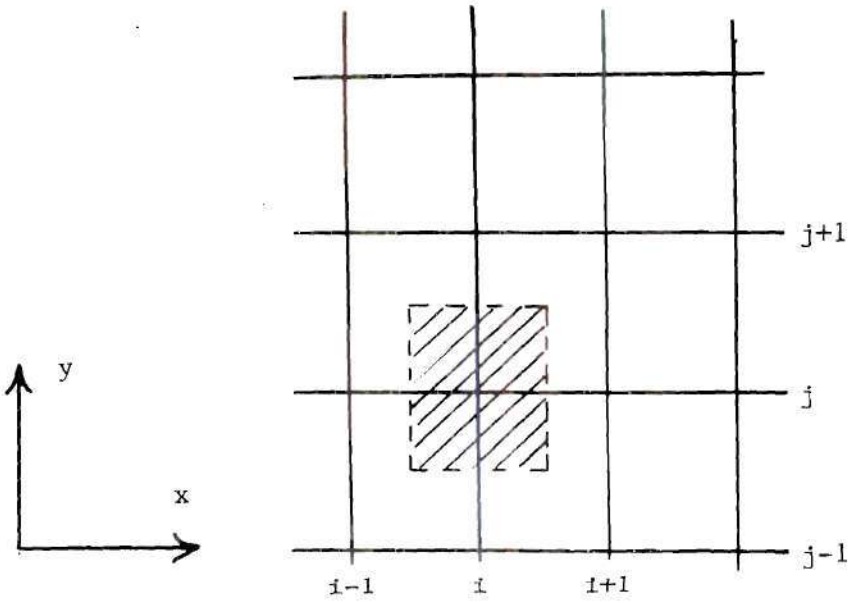

Figure 11. Grid and Cell Configuration

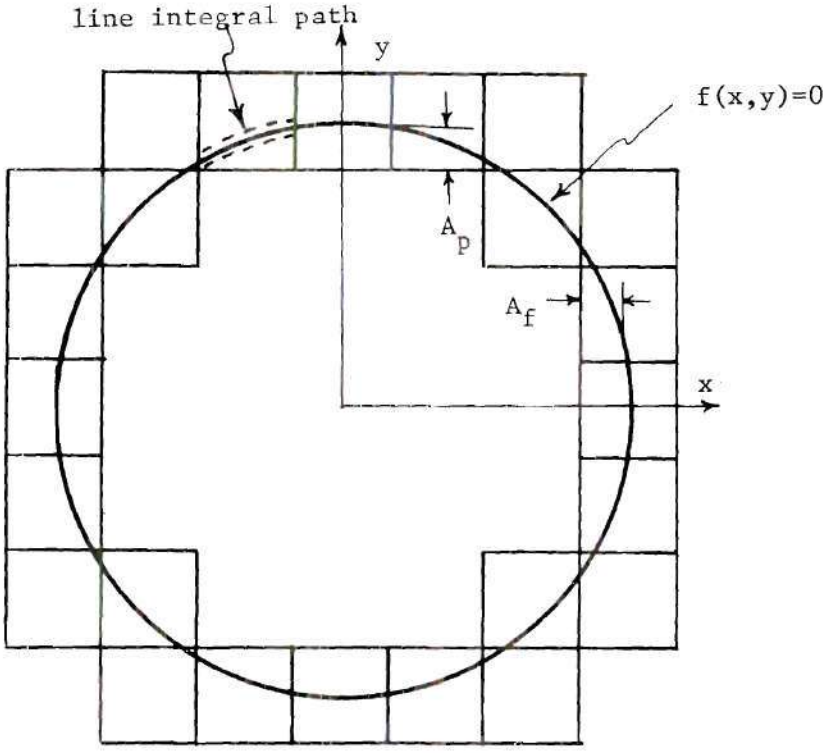

Figure 12. Boundary Cells and Initial Vortex Cells for the Two-Dimensional Solutions

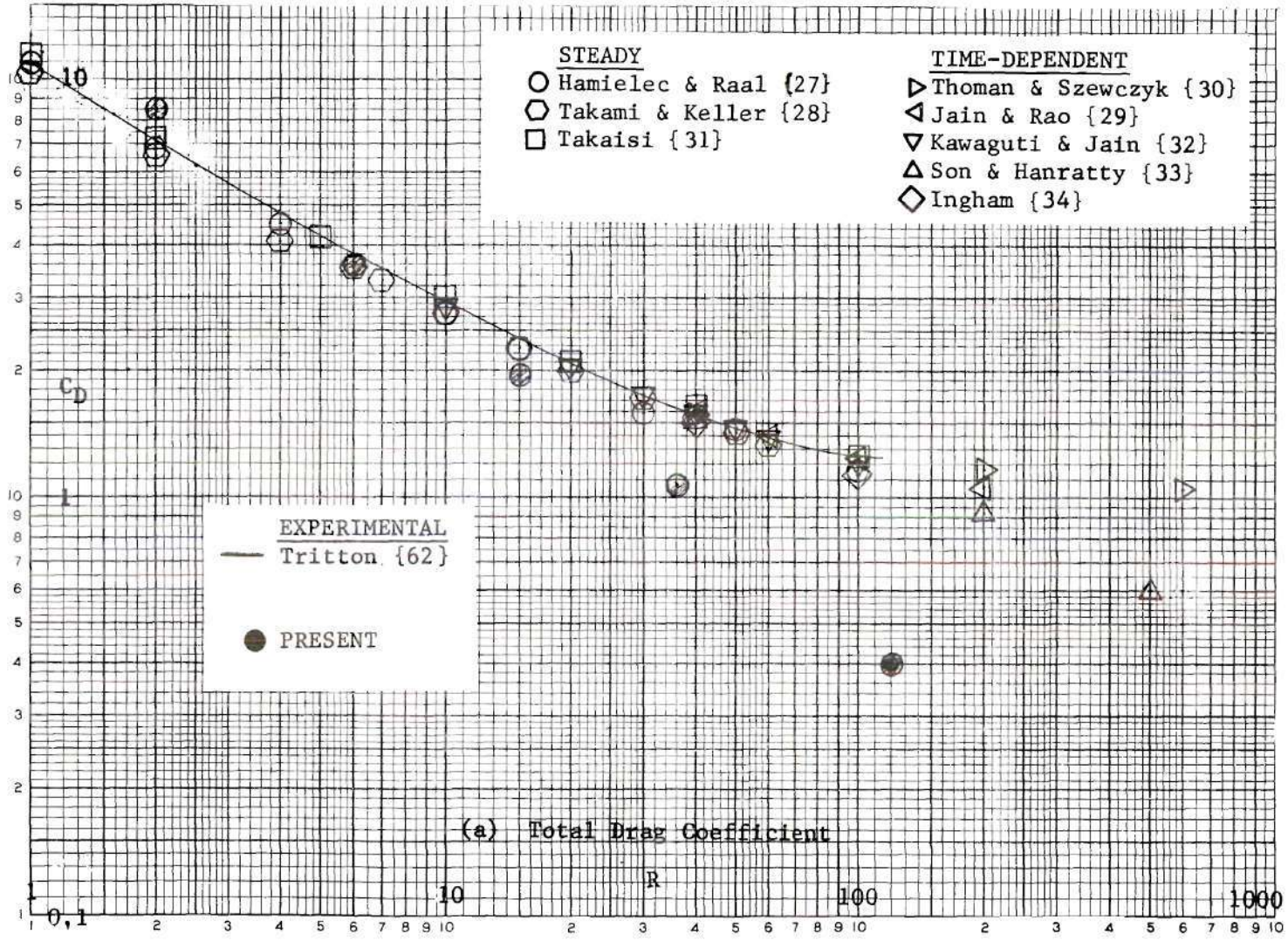

Figure 13. Comparison of Results for Circular Cylinder Drag with other Numerical Solutions and Experimental Results

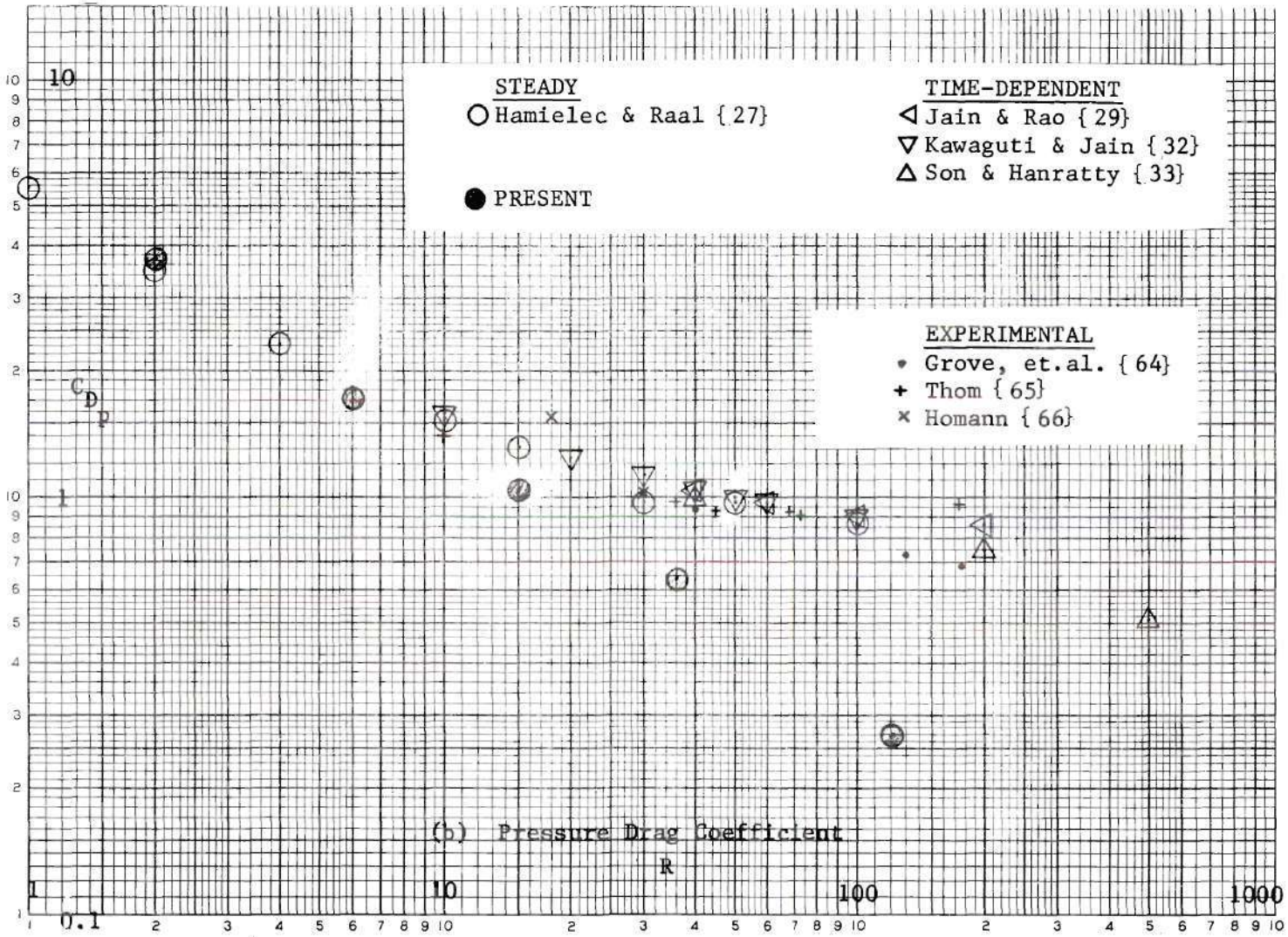

Figure 13. (cont.)

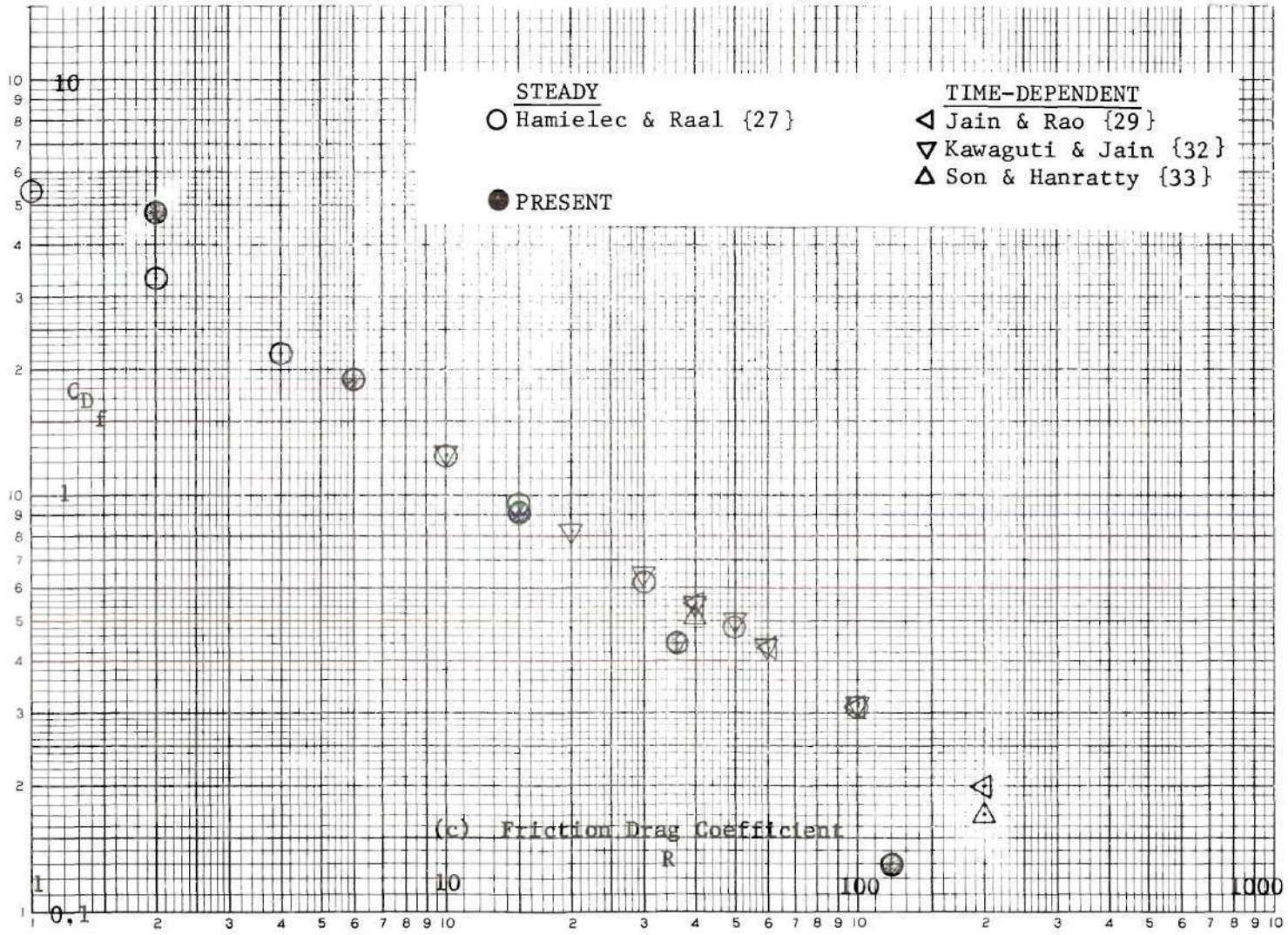

Figure 13. (cont.)

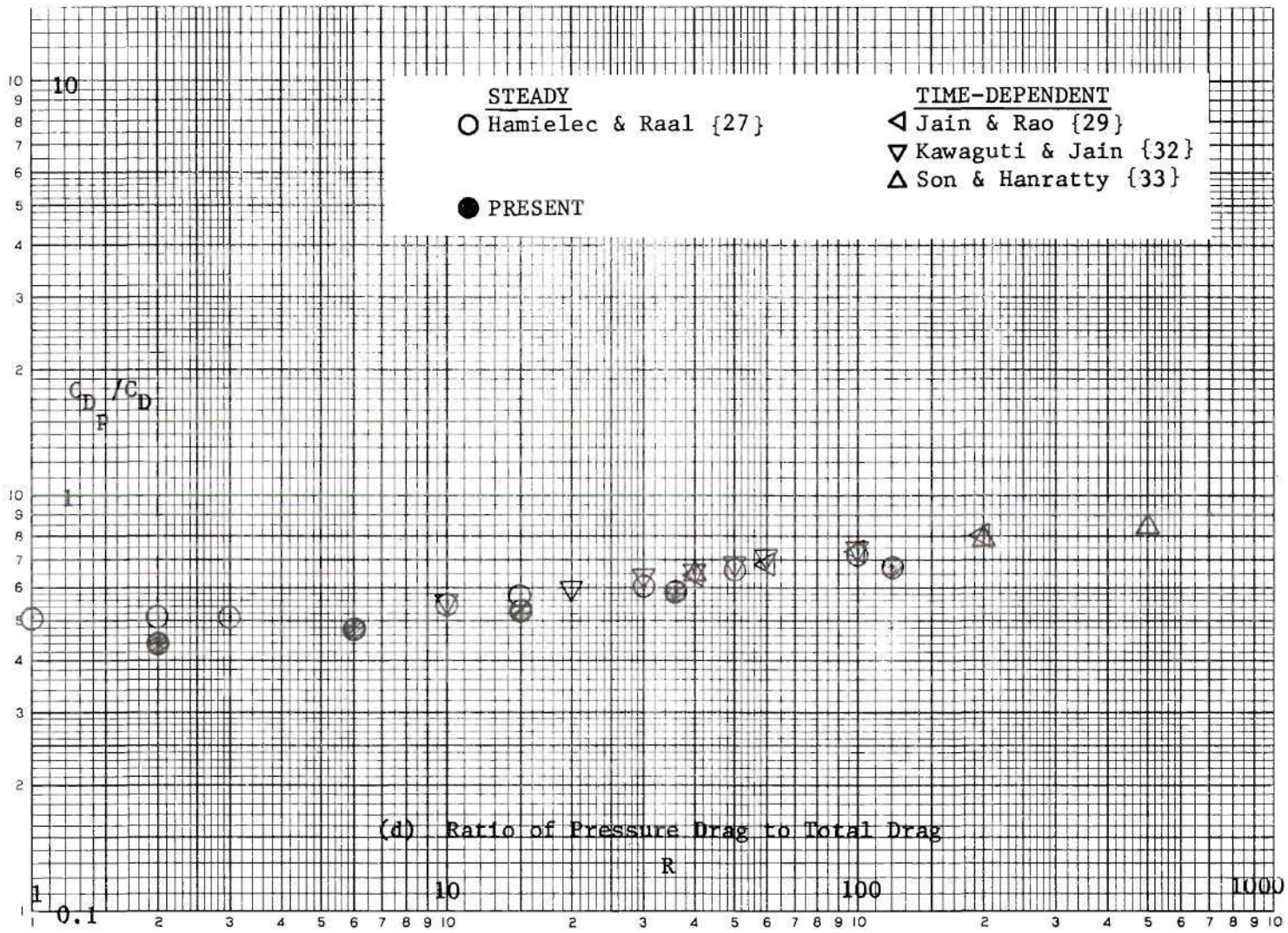

Figure 13. (cont.)

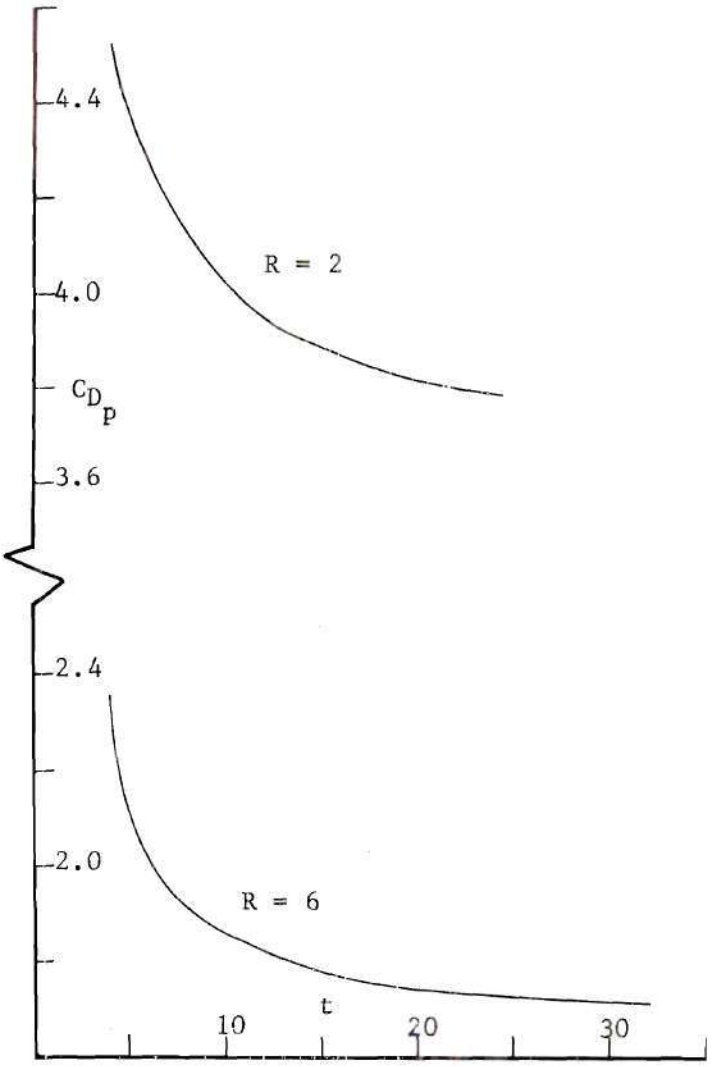

(a) Pressure Drag Coefficient
(continued on next page)

Figure 14. Time Development of Circular Cylinder Drag

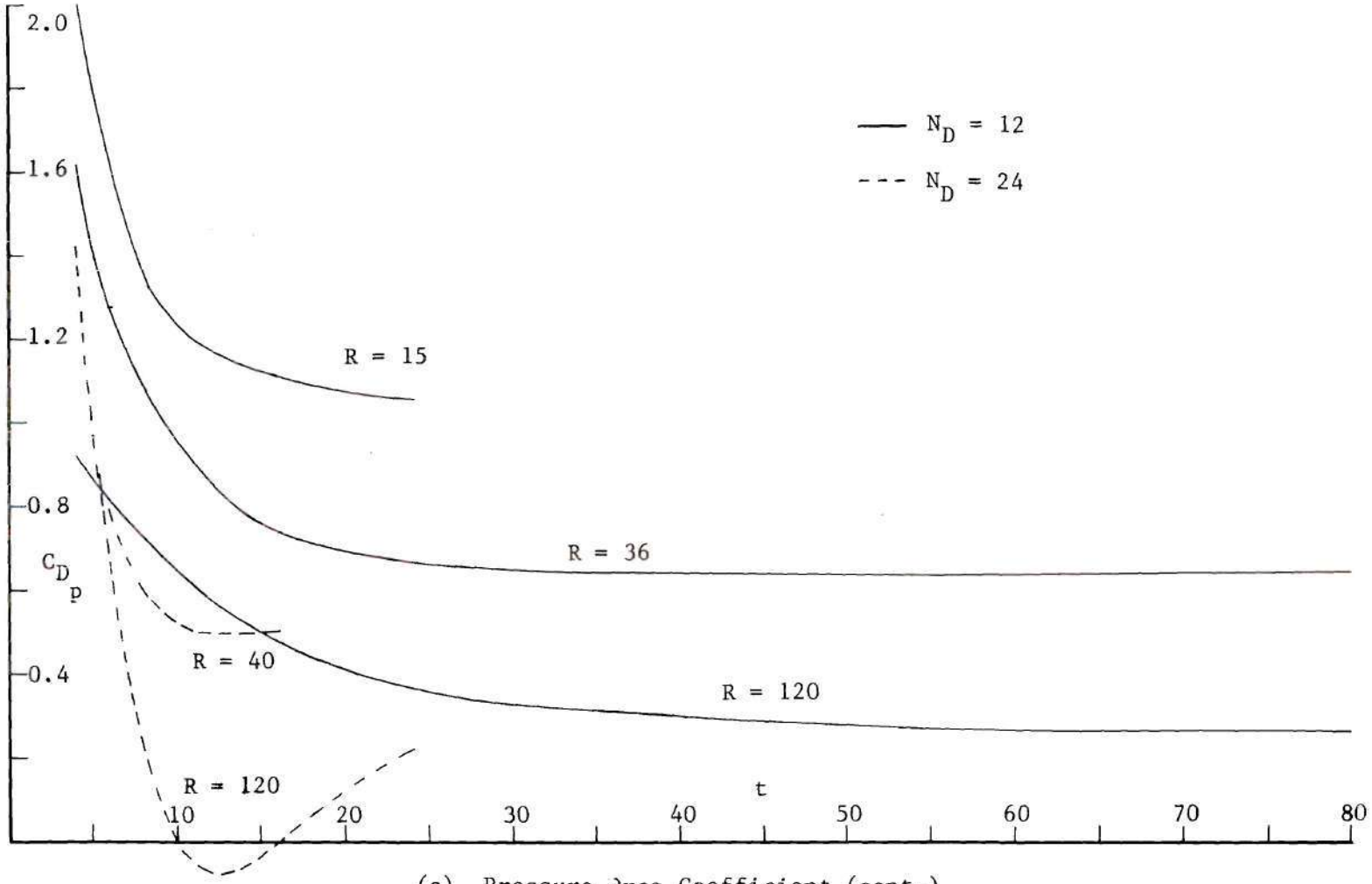

(a) Pressure Drag Coefficient (cont.)

Figure 14. (cont.)

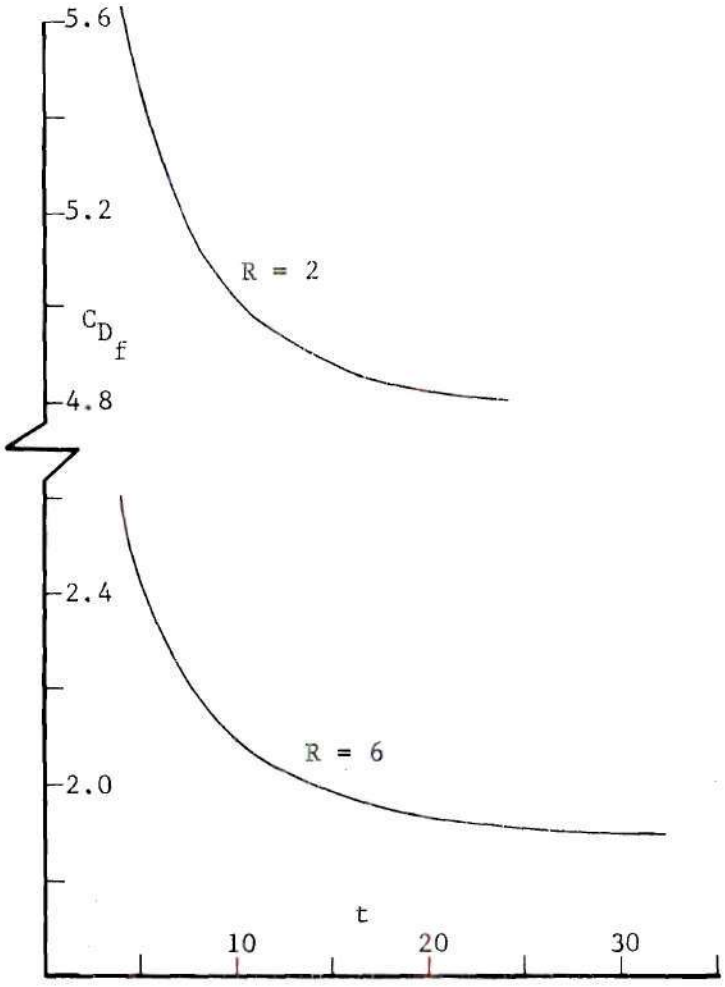

(b) Friction Drag Coefficient
(continued on next page)

Figure 14. (cont.)

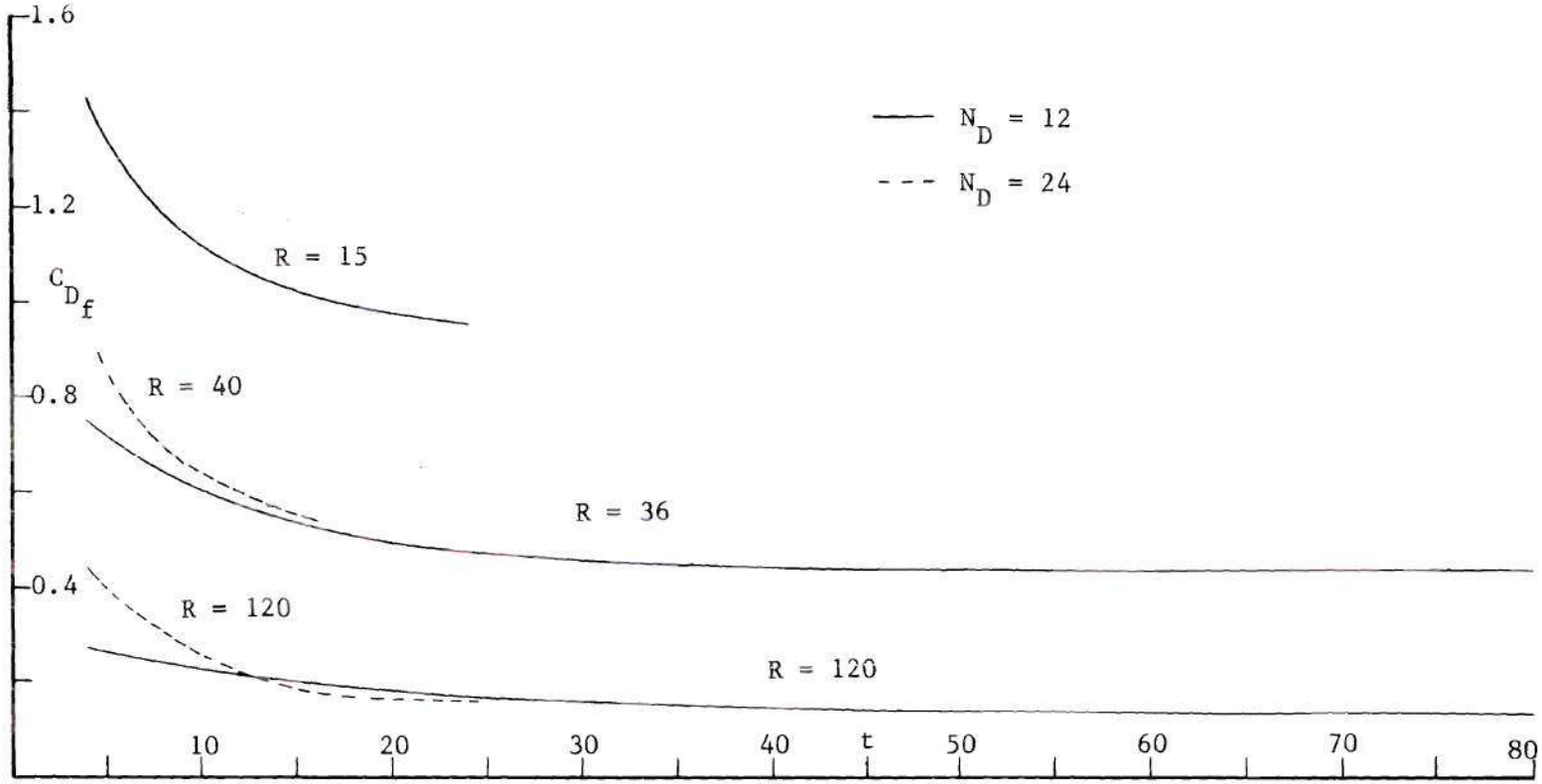

(b) Friction Drag Coefficient (cont.)

Figure 14. (cont.)

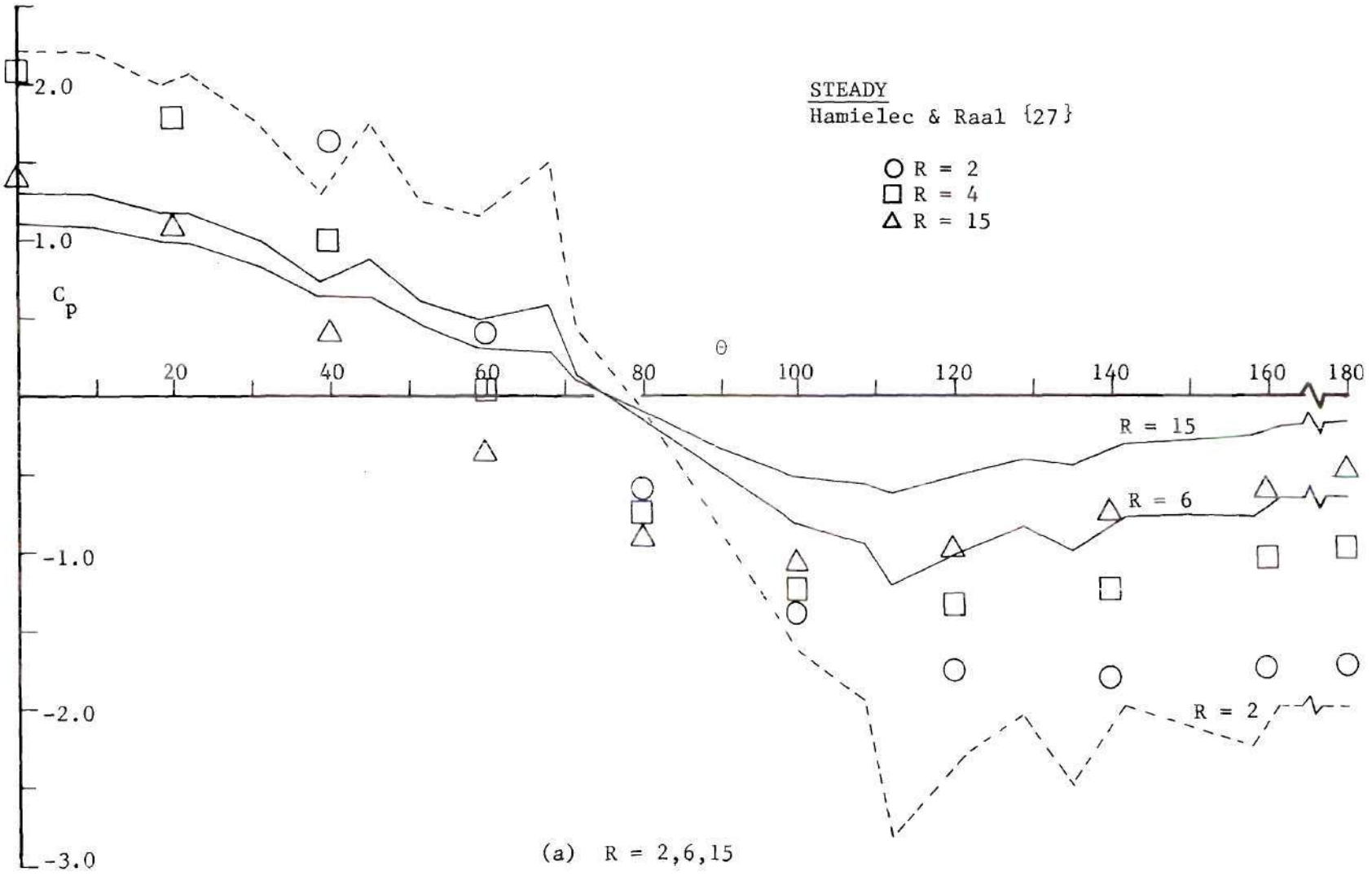

(a) R = 2,6,15

Figure 15. Surface Pressure Distribution on Circular Cylinder

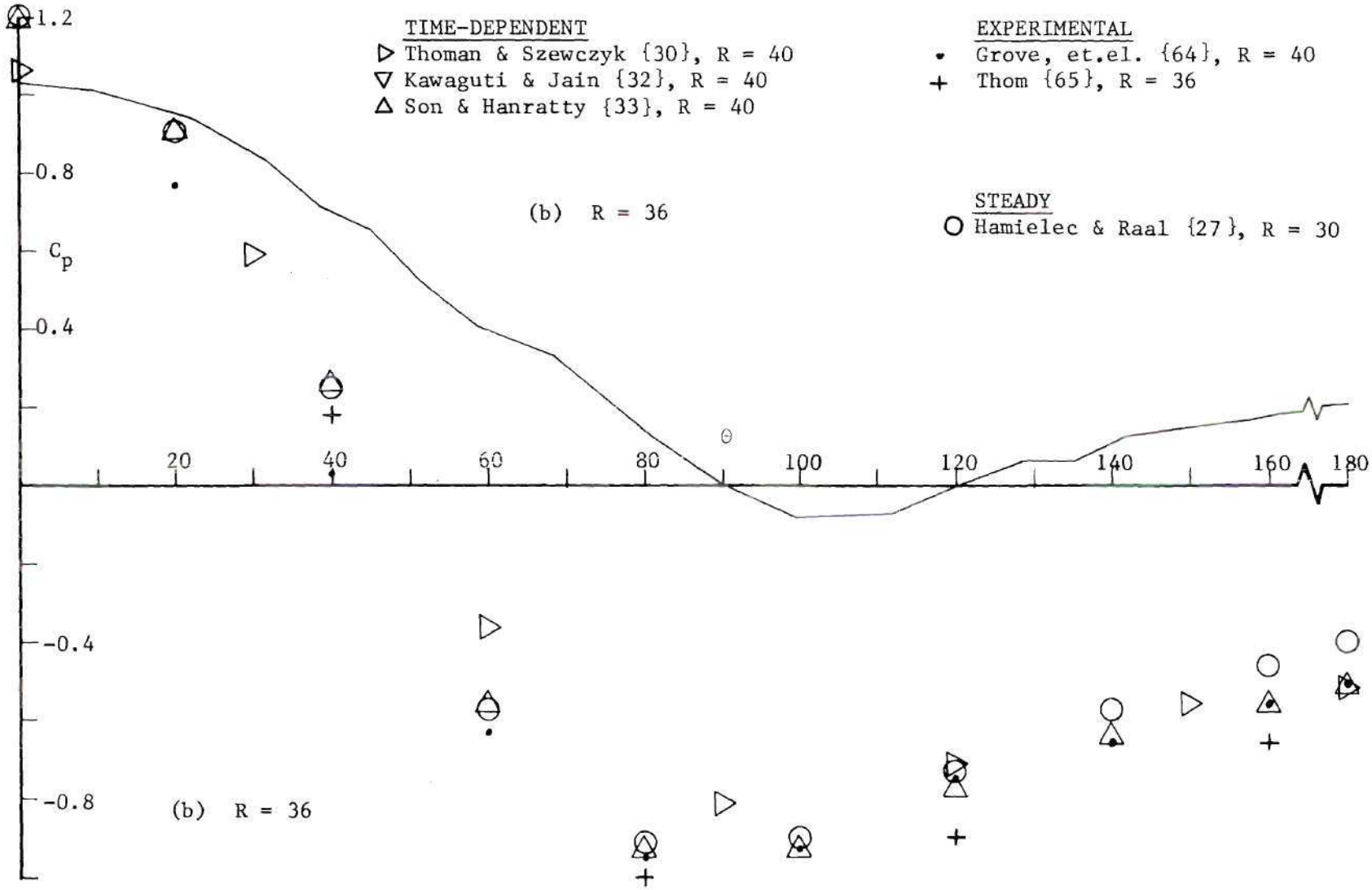

Figure 15. (cont.)

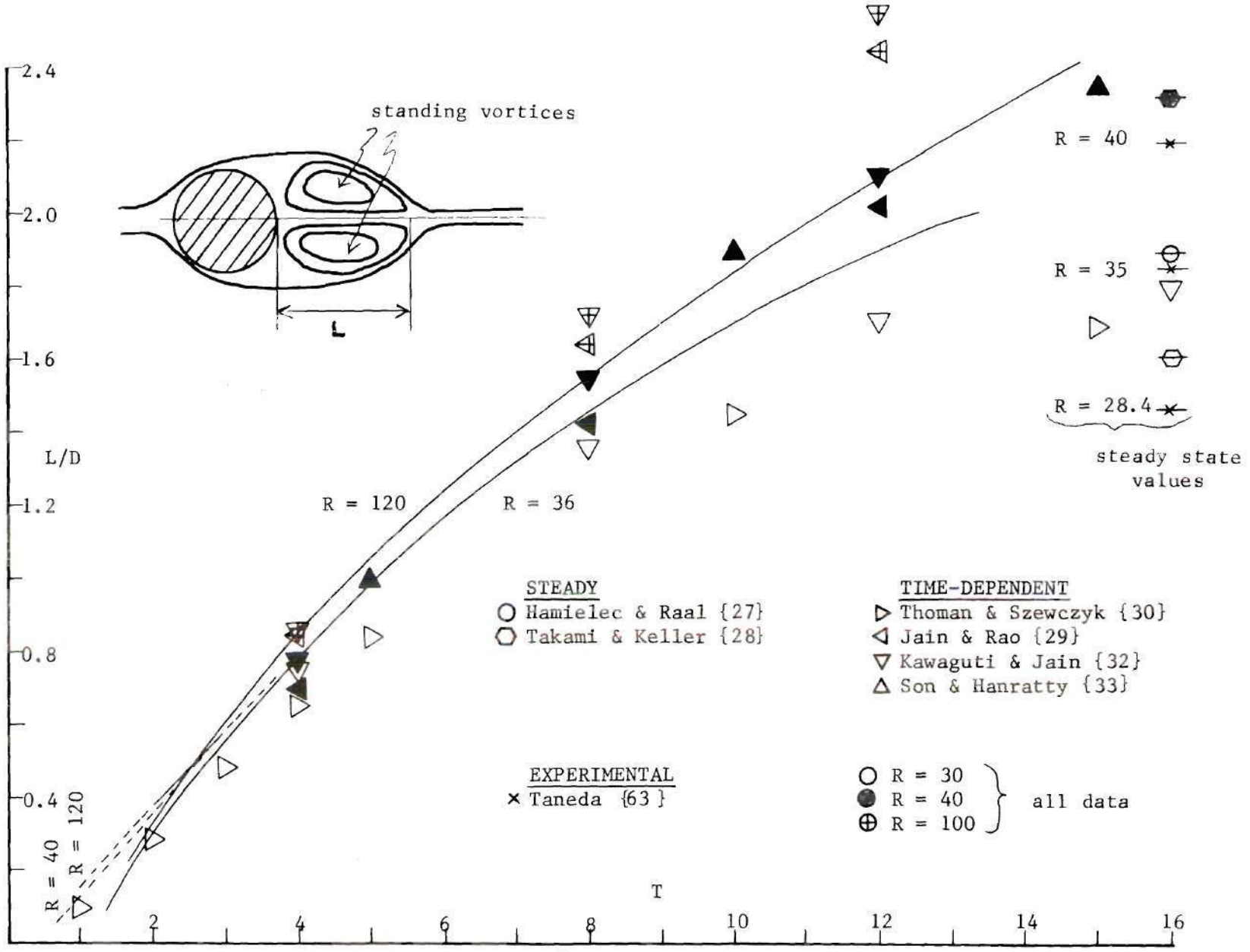

Figure 16. Time Development of Length of Standing Vortices Behind Circular Cylinder

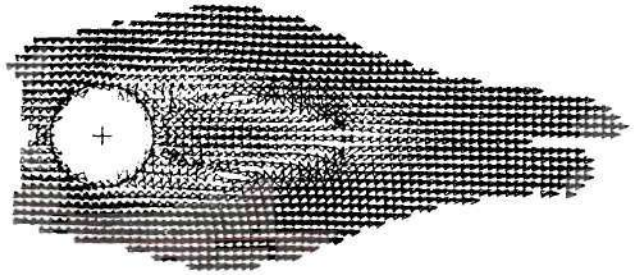

(a) T = 10.00

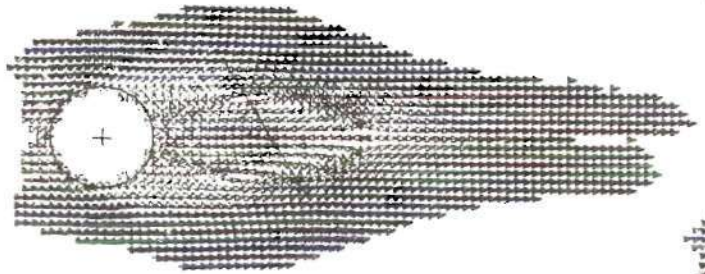

(b) T = 11.33

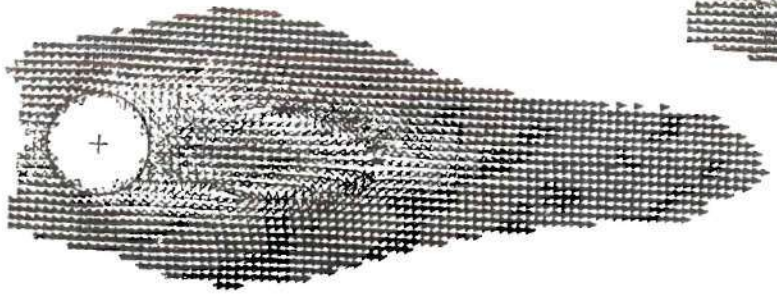

(c) T = 12.67

(d) T = 14.67

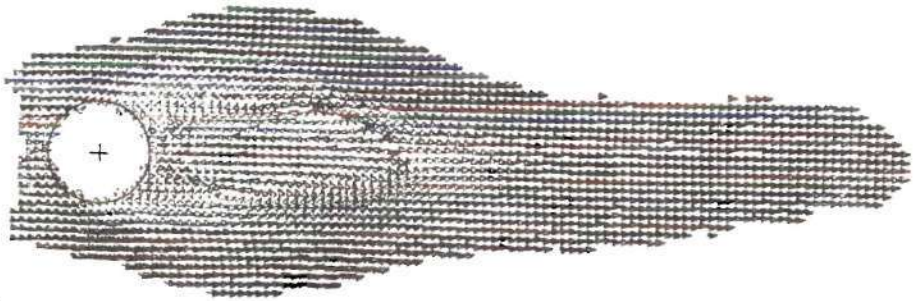

(e) T = 15.33

Figure 17. Vortex Shedding and Street Formation Behind Circular Cylinder - R = 120

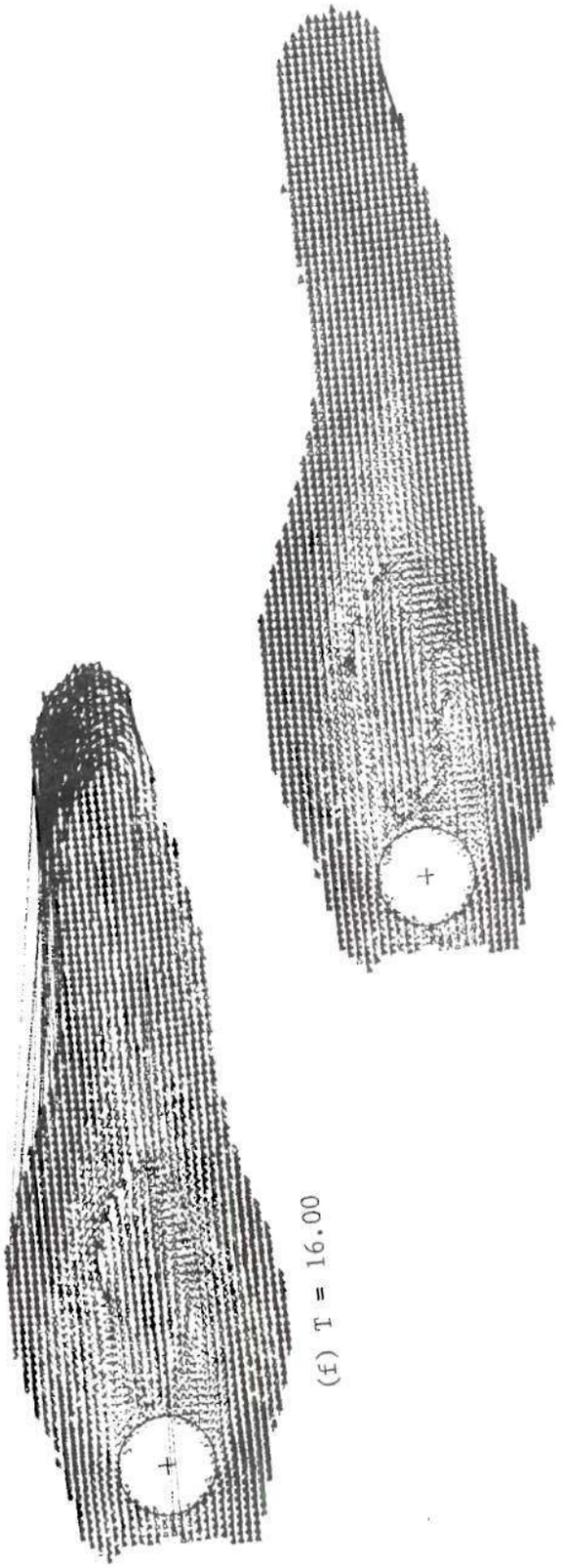

(f) T = 16.00

(g) T = 17.33

(h) T = 18.00

Figure 17. (cont.)

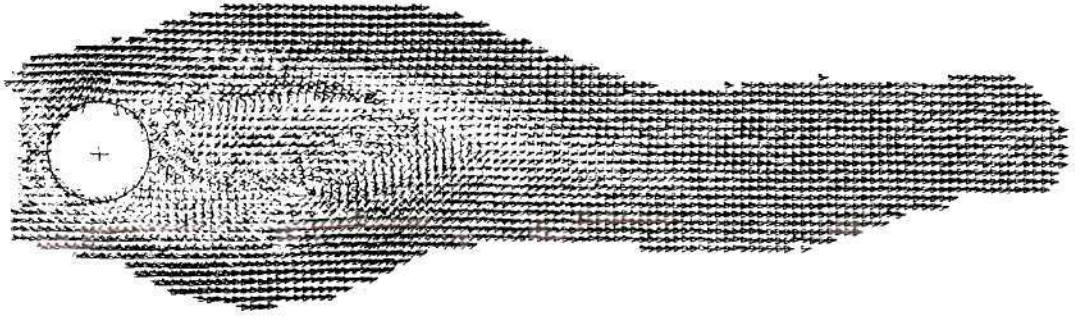

(i) T = 18.67

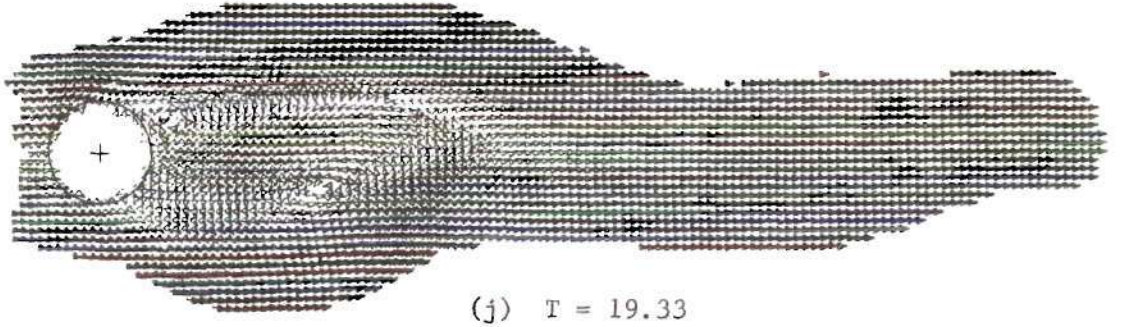

(j) T = 19.33

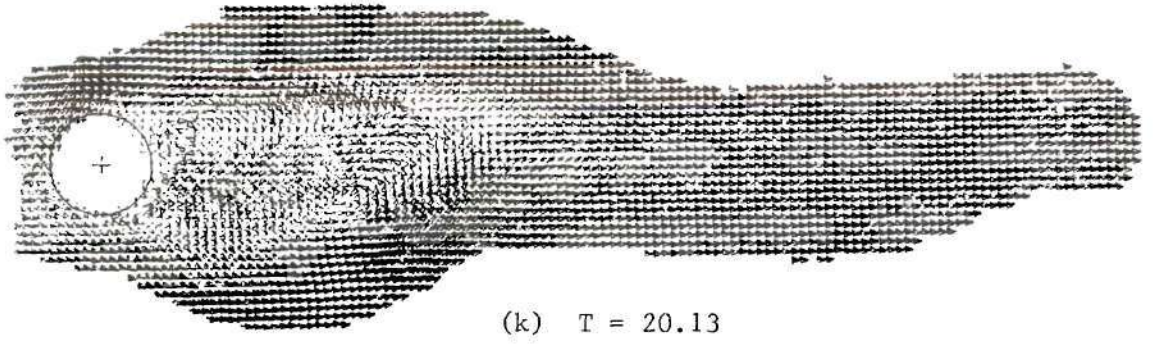

(k) T = 20.13

Figure 17. (cont.)

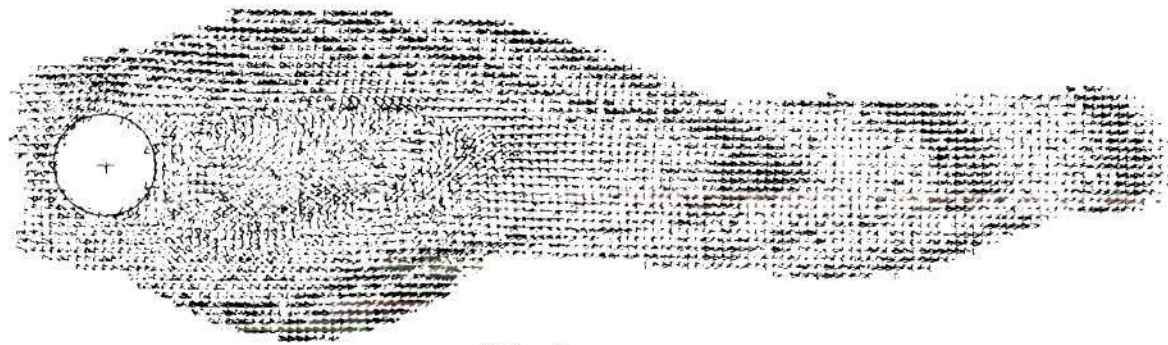

(l) T = 20.67

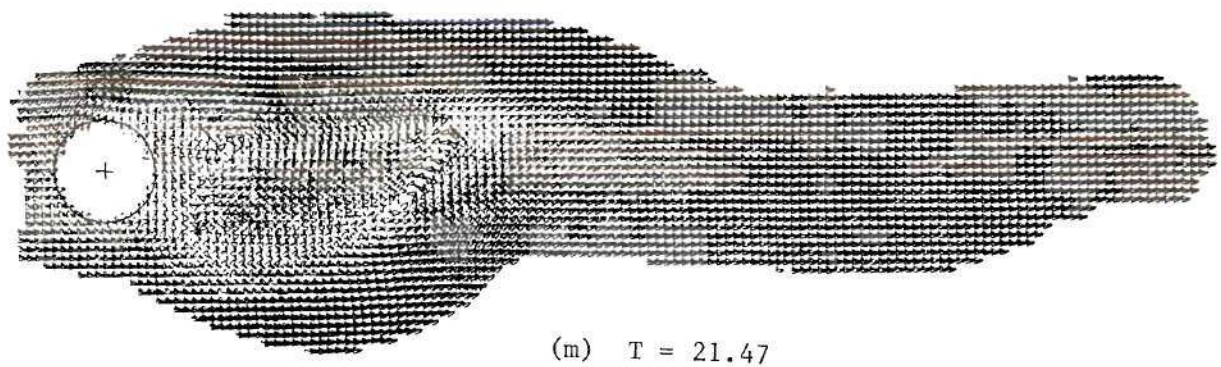

(m) T = 21.47

Figure 17. (cont.)

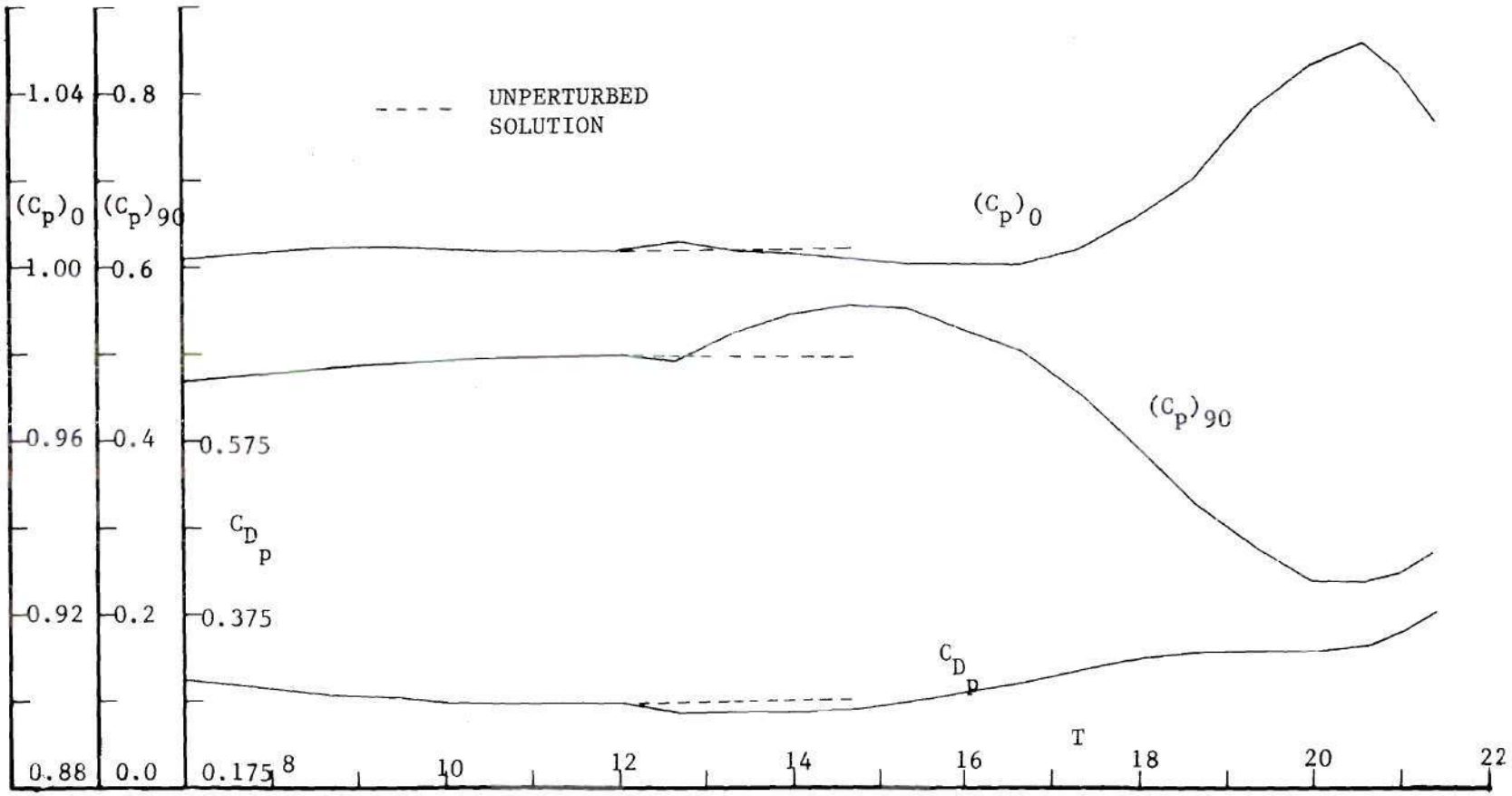

Figure 18. Time Development of Circular Cylinder Pressure Drag and Surface Pressure During Vortex Shedding - R = 120

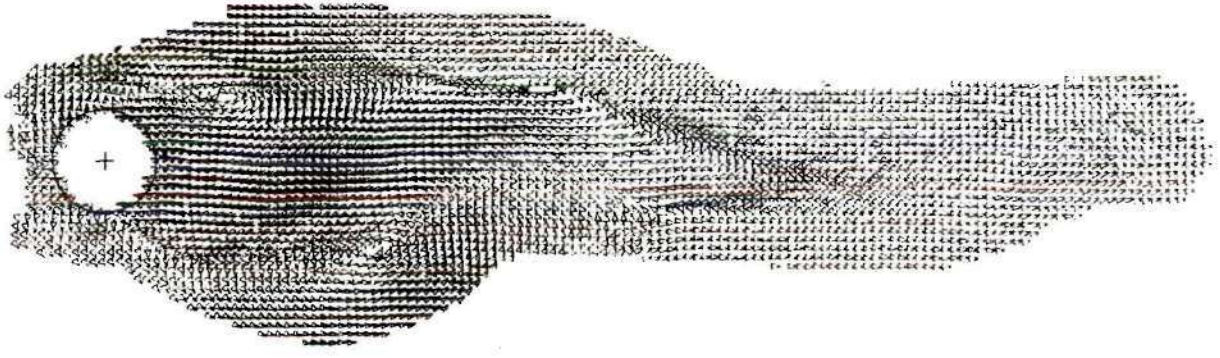

Figure 19. Vortex Street Behind Circular Cylinder (Coordinate System Moving with Street Velocity) - R = 120, T = 21.47

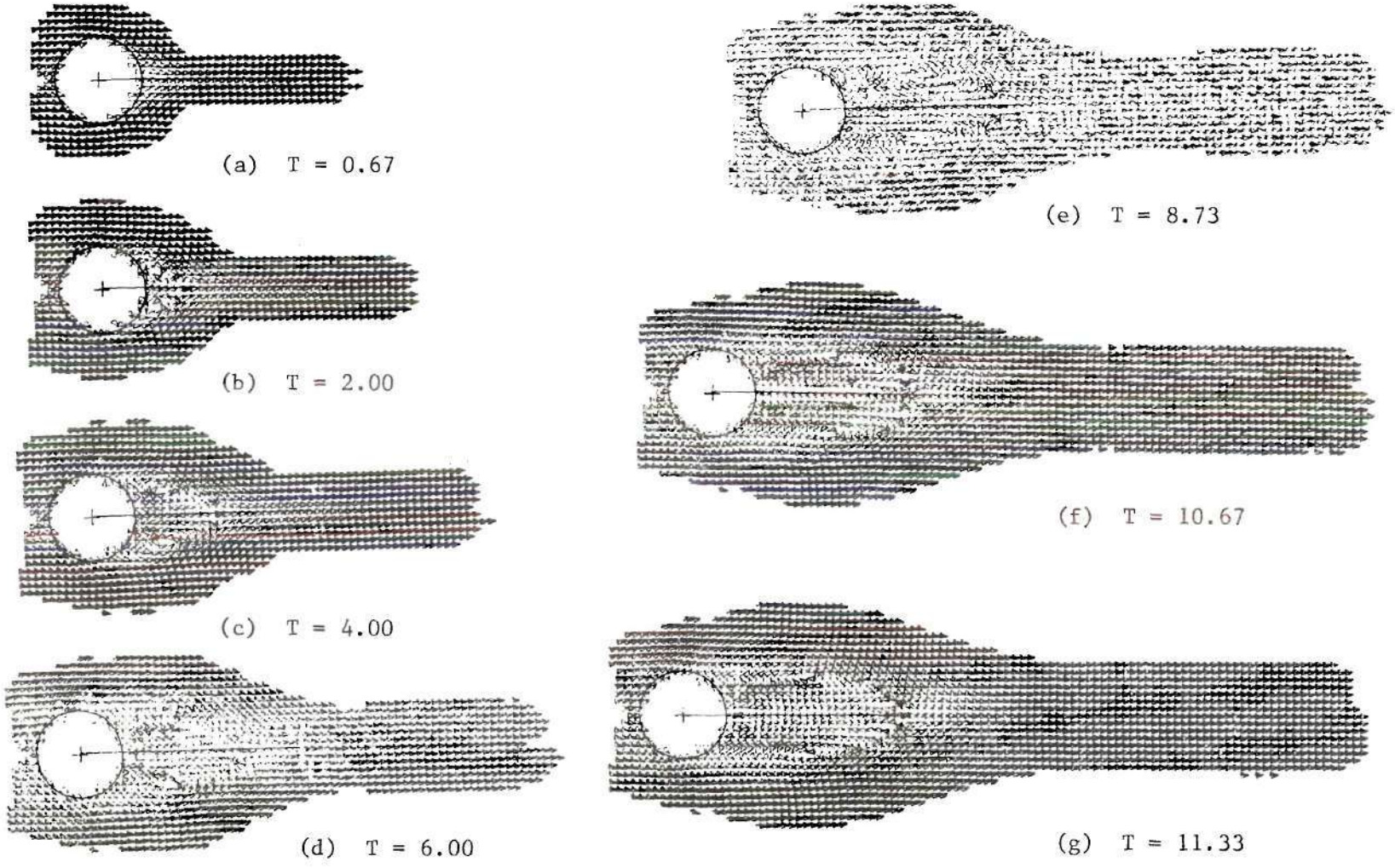

Figure 20. Standing Vortices behind Circular Cylinder with Rear Splitter Plate - R = 120

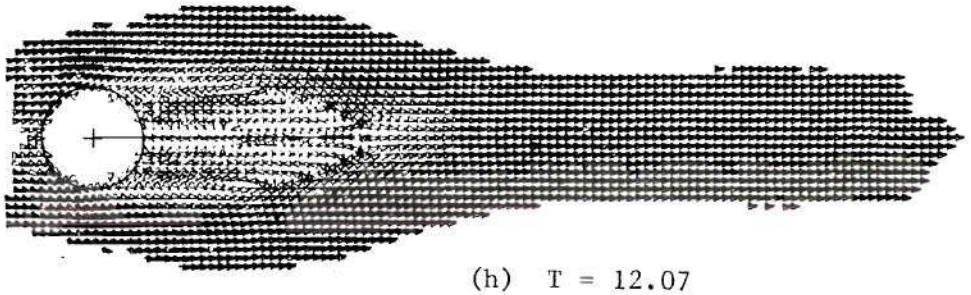

(h) T = 12.07

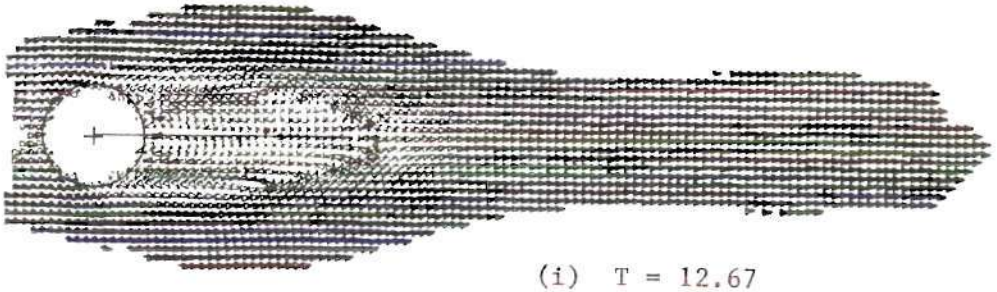

(i) T = 12.67

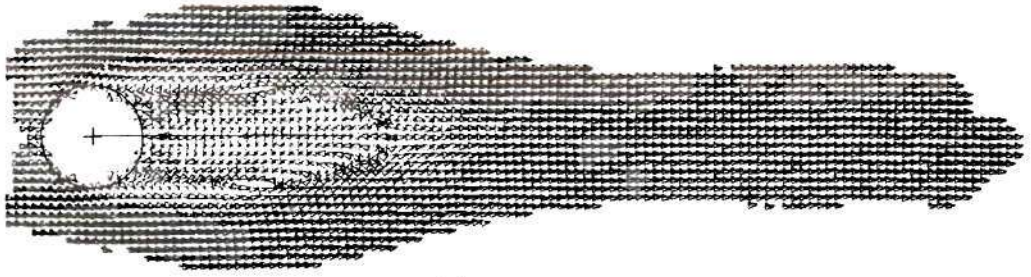

(j) T = 13.33

Figure 20. (cont.)

(k) T = 14.67

(l) T = 15.33

Figure 20. (cont.)

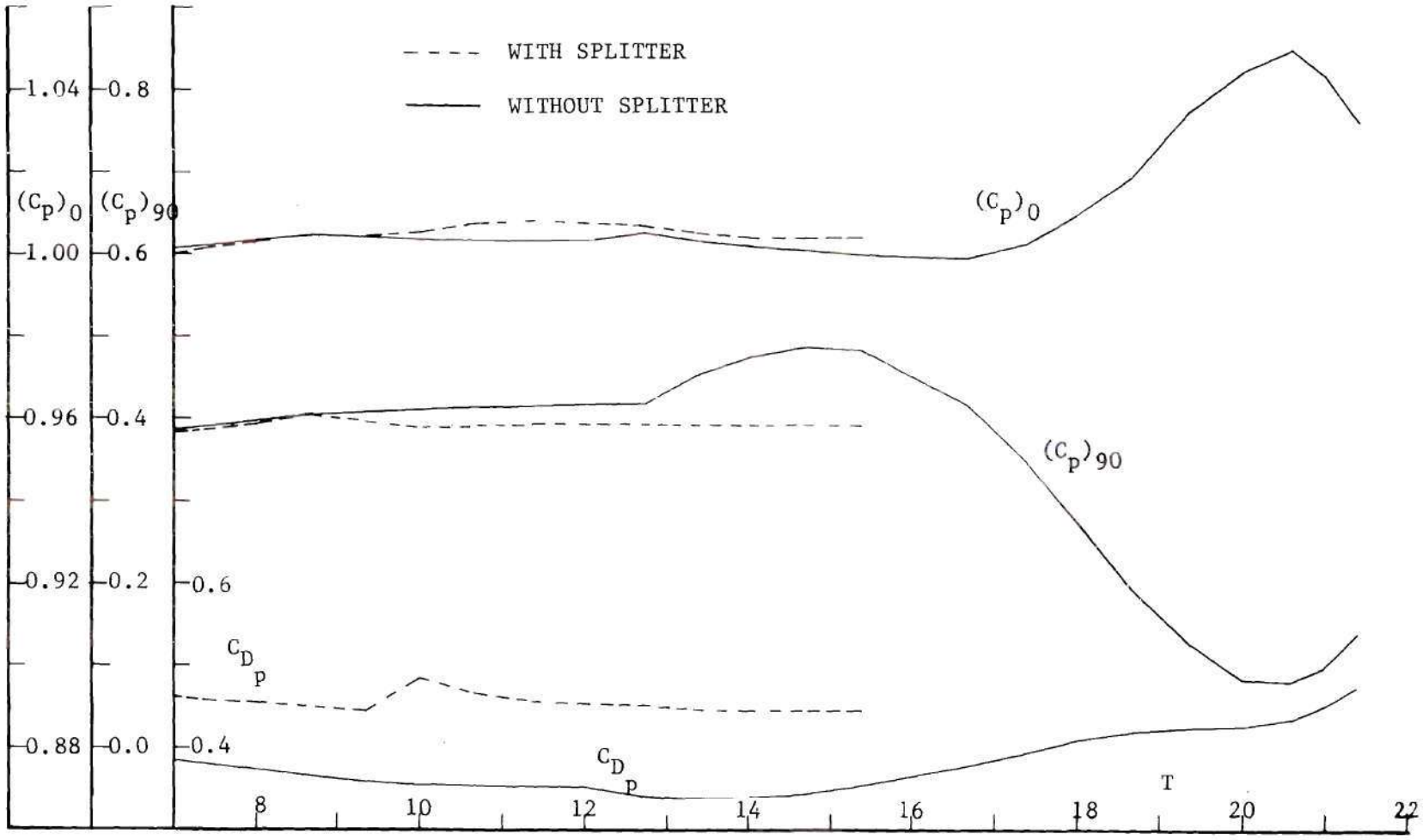

Figure 21. Effect of Rear Splitter Plate on Time Development of Circular Cylinder Pressure Drag and Surface Pressure - R = 120

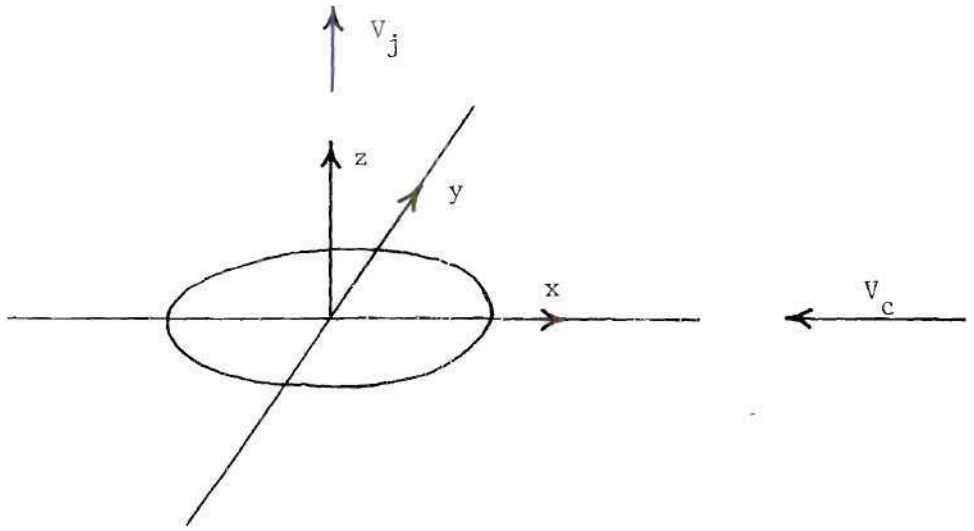

Figure 22. Coordinate System for Infinite Jet in Cross-Wind Solution

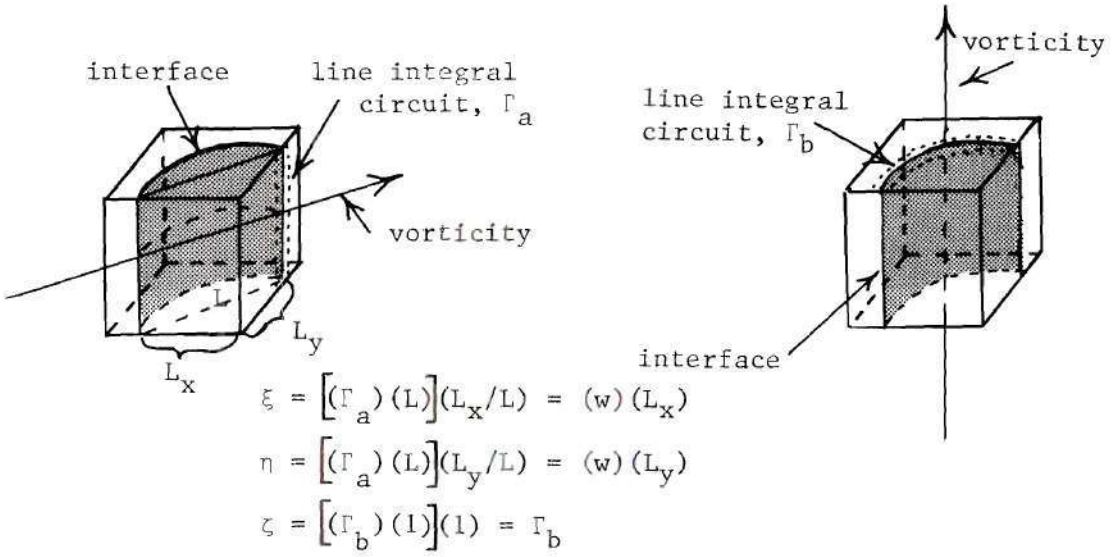

Figure 23. Determination of Initial Vorticity in Initial Vortex Cells

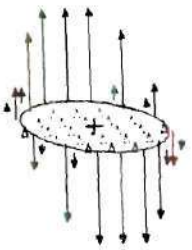

(a) Vertical Vorticity Vectors

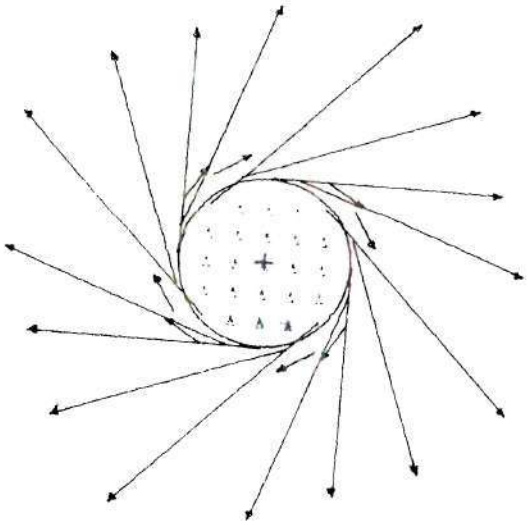

(b) Horizontal Vorticity Vectors

(c) Vertical Velocity Vectors

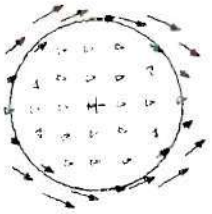

(d) Horizontal Velocity Vectors

Figure 24. Initial Solution - Infinite Jet in Cross-Wind (V_r = 8)

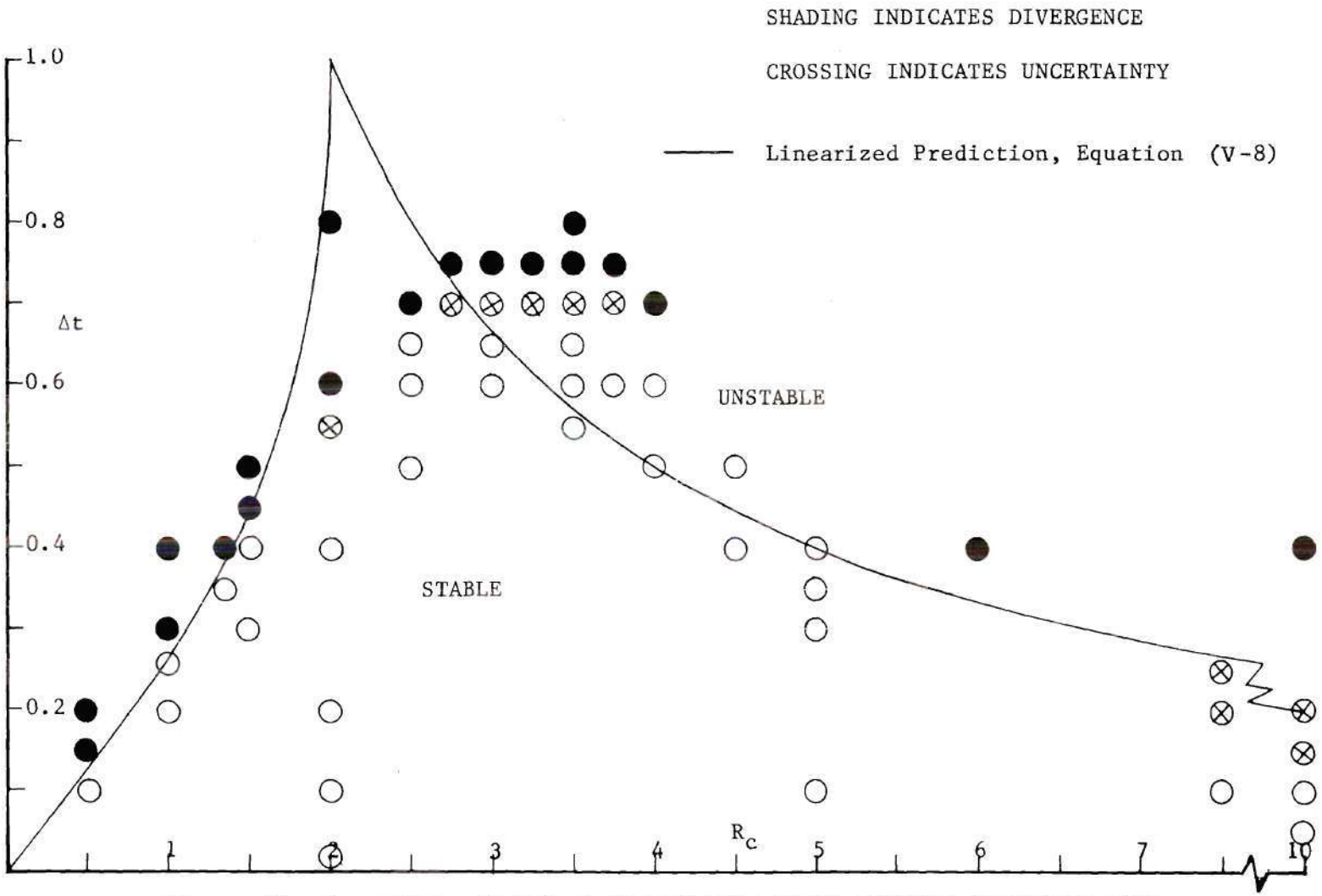

Figure 25. Comparison of Actual Straight Explicit Solution Stability with Linearized Prediction - Infinite Jet in Cross-Wind

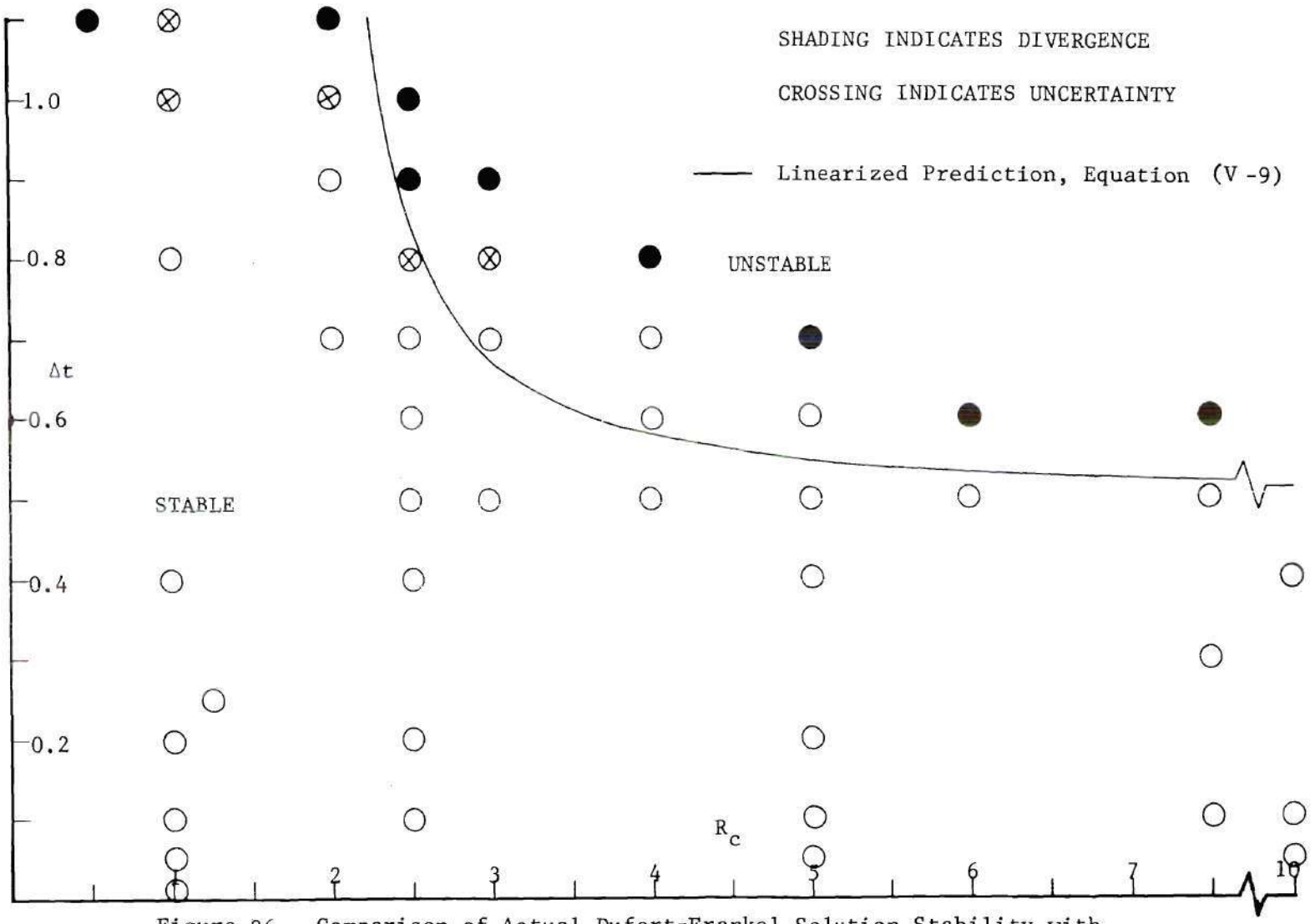

Figure 26. Comparison of Actual Dufort-Frankel Solution Stability with Linearized Prediction - Infinite Jet in Cross-Wind

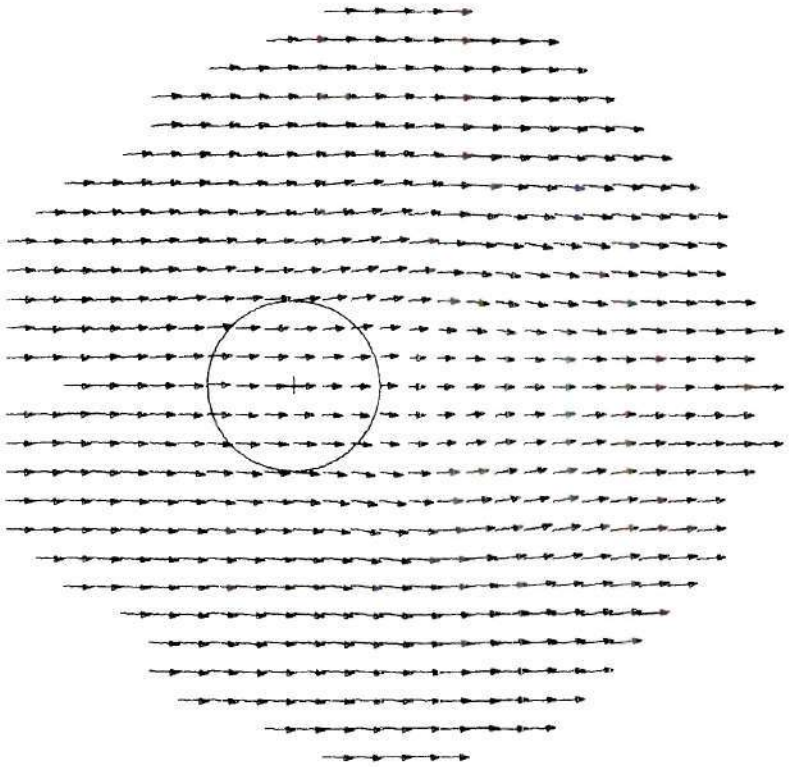

(a) $\Delta t = 0.35$

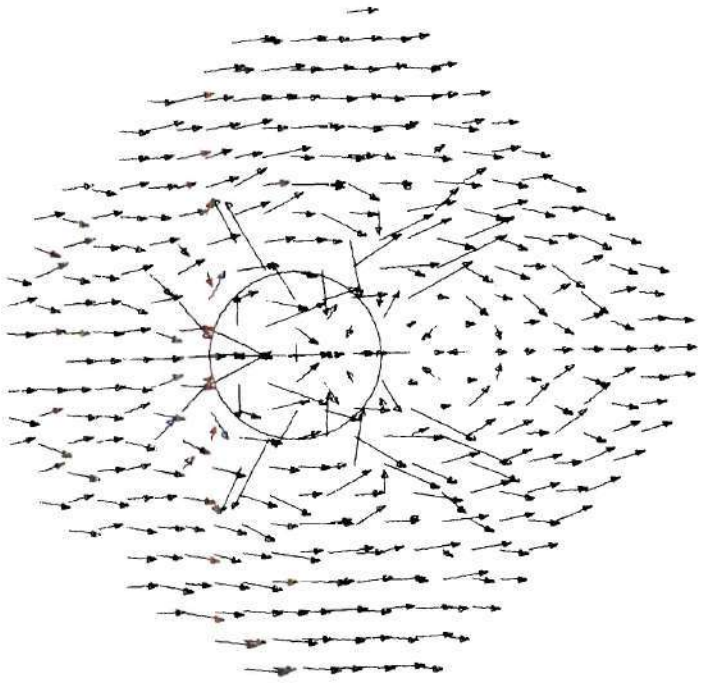

(b) $\Delta t = 0.40$

Figure 27. Effect of Time Step at Low Reynolds Number near the Stability Boundary - Infinite Jet in Cross-Wind ($V_r = 8$) - $R_c = 1.35$

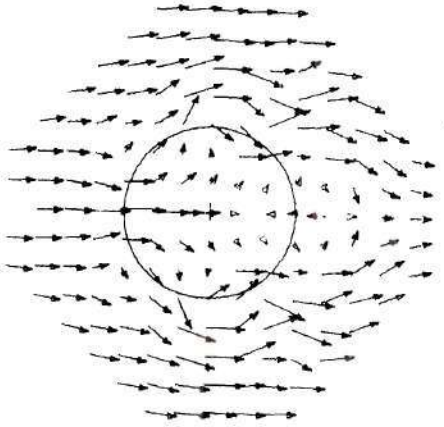

(a) t = 2.6

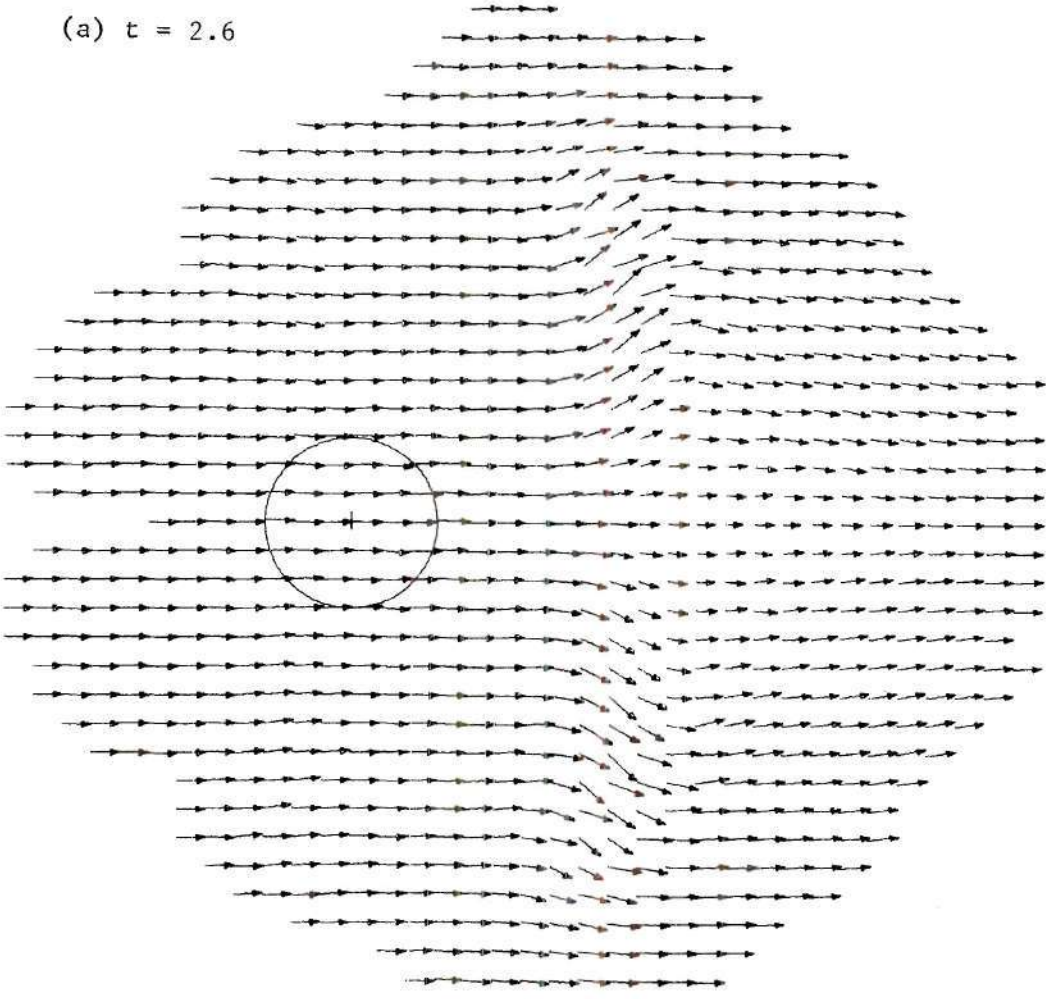

(b) t = 15.6

Figure 28. Persistence of Perturbation due to Nonlinear Instability - Infinite Jet in Cross-Wind (V_r = 8) - R_c = 2.5

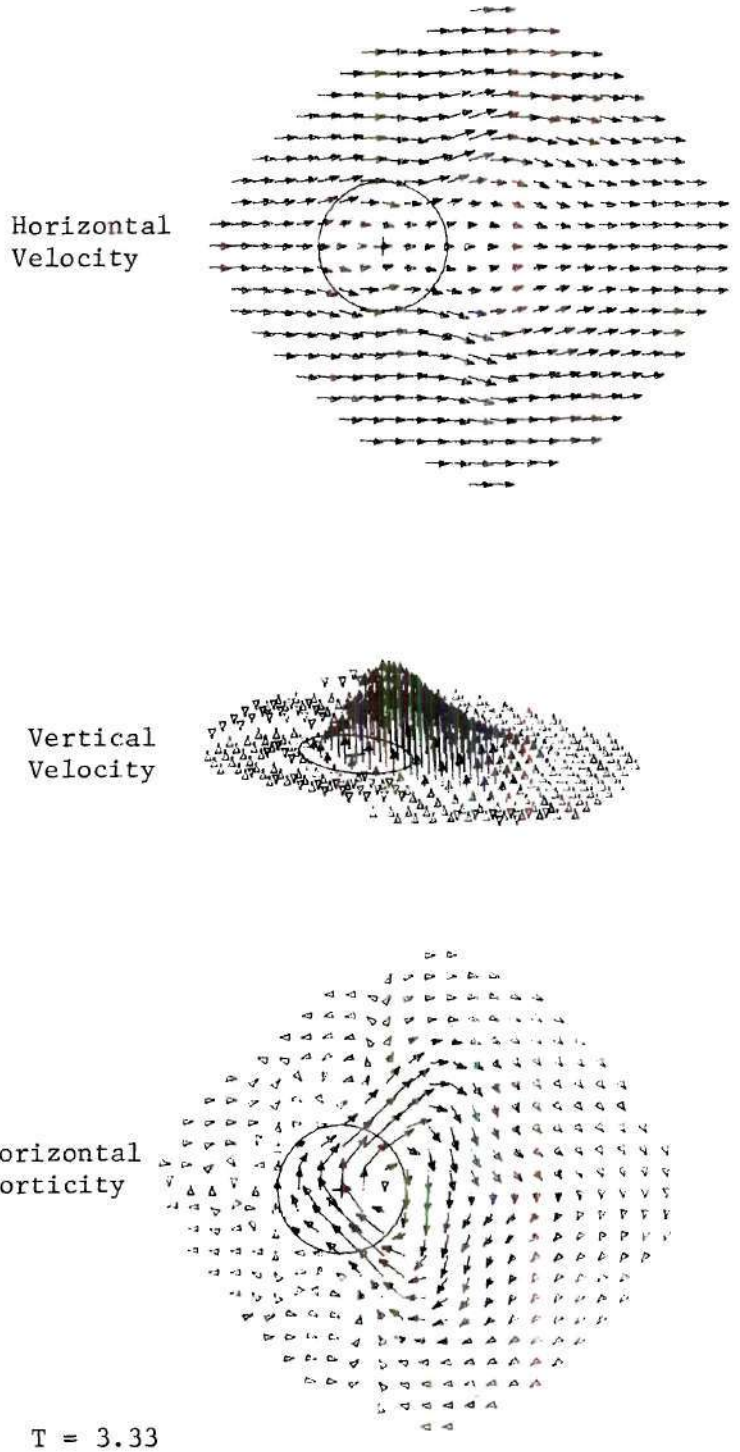

(a) T = 3.33

Figure 29. Time Development of Circular Infinite Jet in Cross-Wind (V_r = 8) - Twenty Step Gradual Start - R = 30

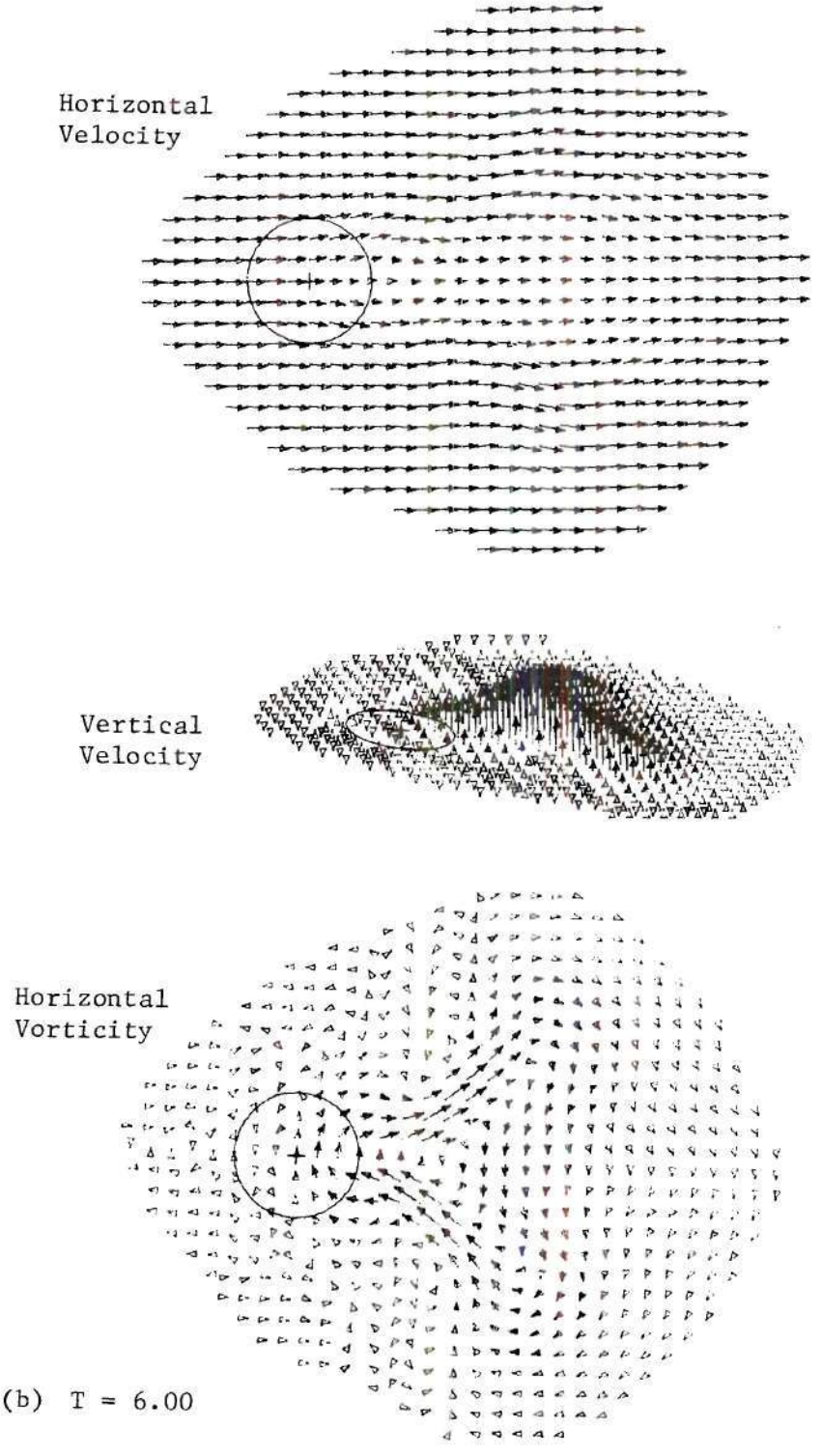

(b) T = 6.00

Figure 29. (cont.)

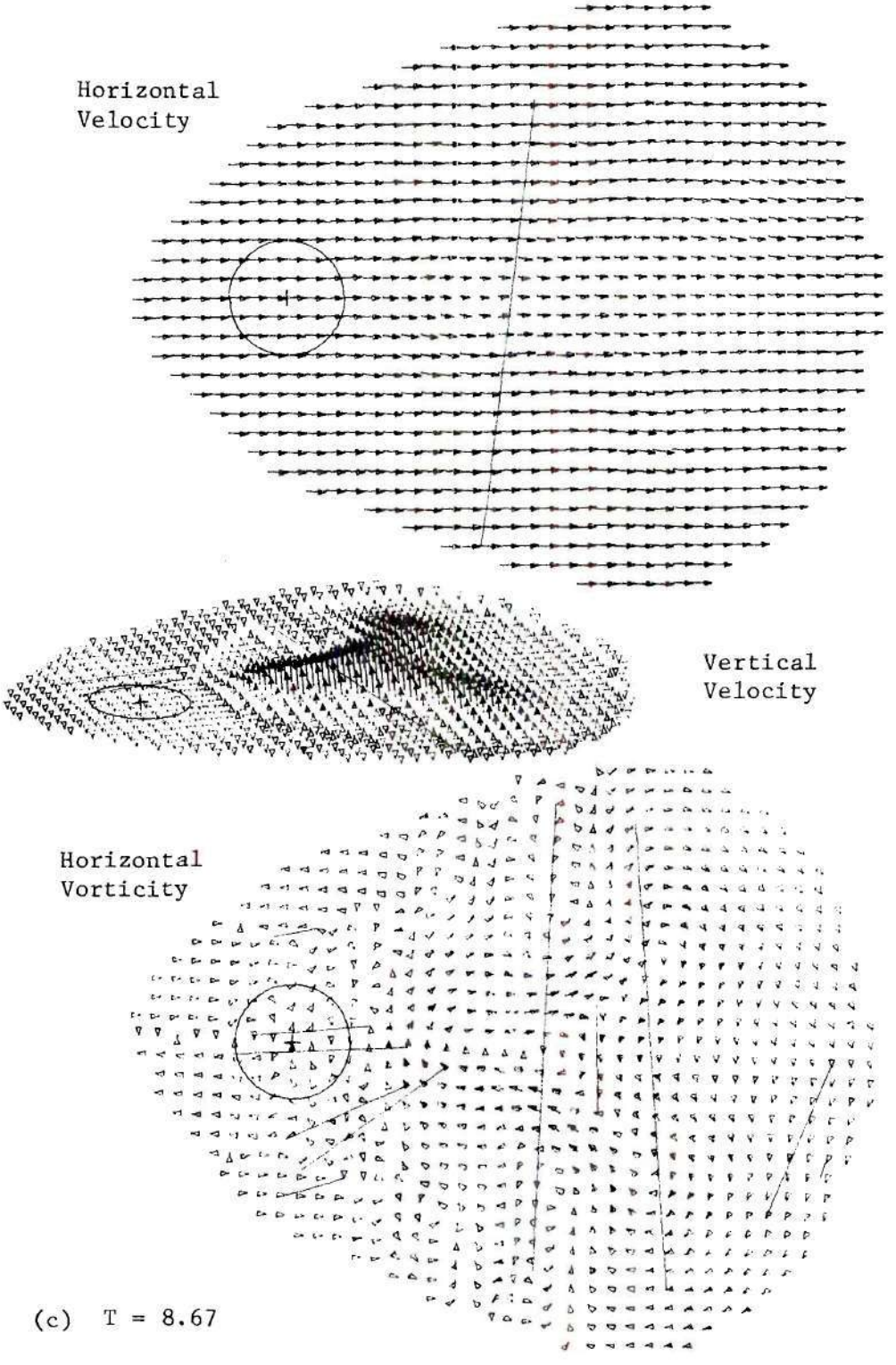

Figure 29. (cont.)

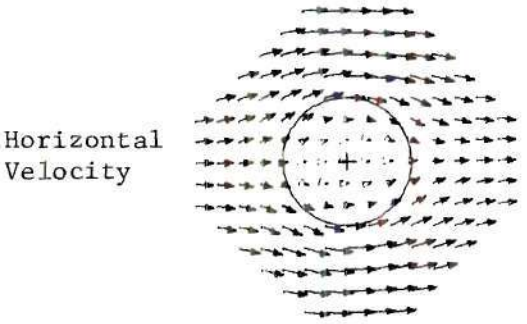

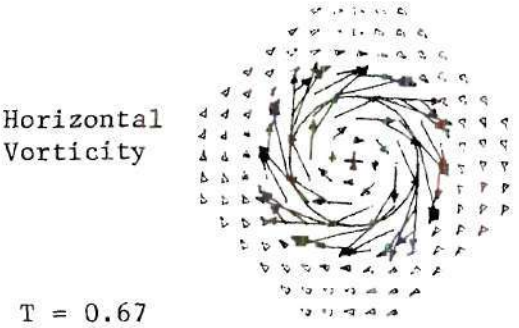

(a) T = 0.67

Figure 30. Time Development of Circular Infinite Jet in Cross-Wind (V_r = 8) - Forty Step Gradual Start - R = 30

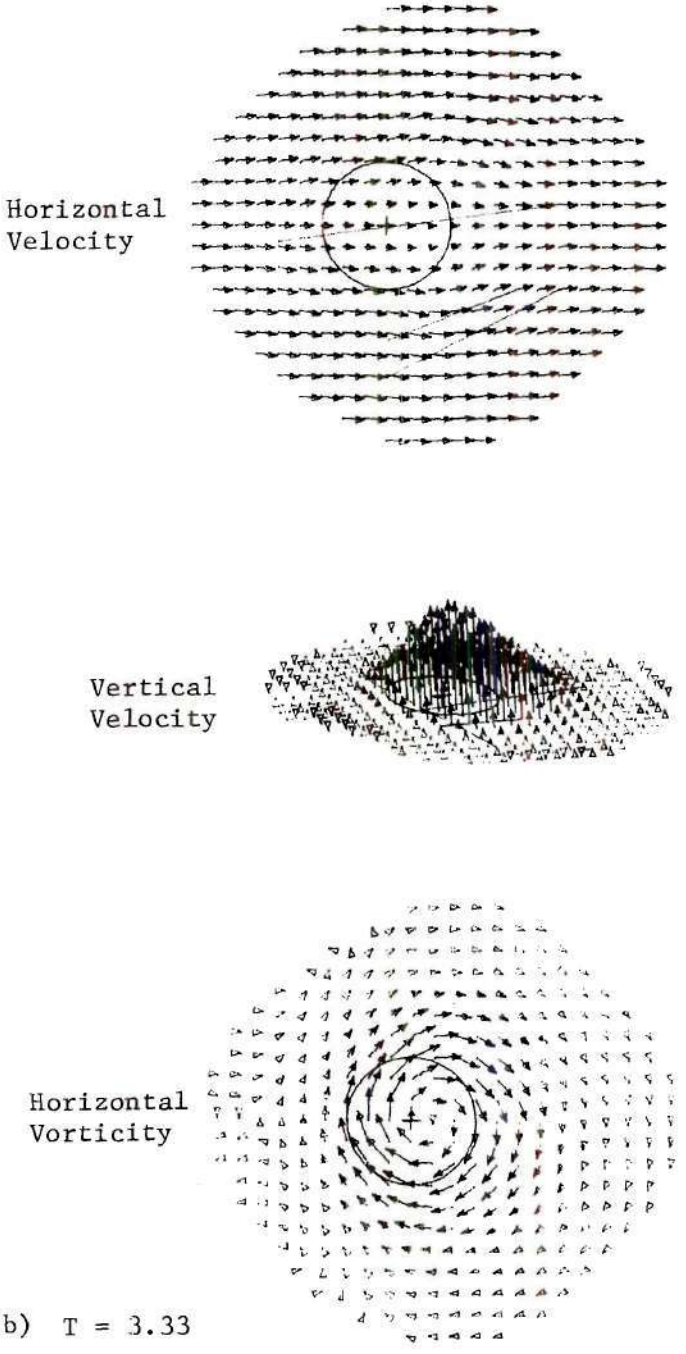

Figure 30. (cont.)

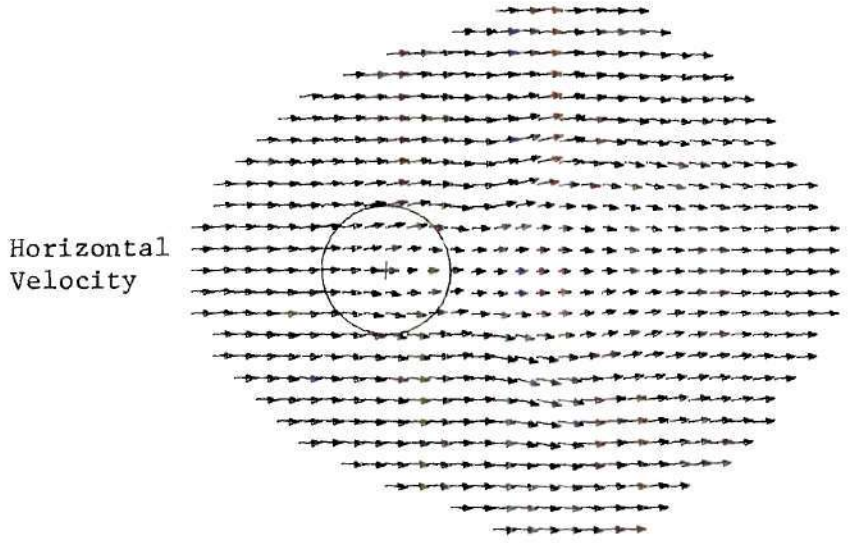

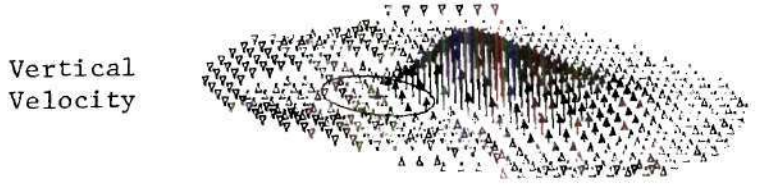

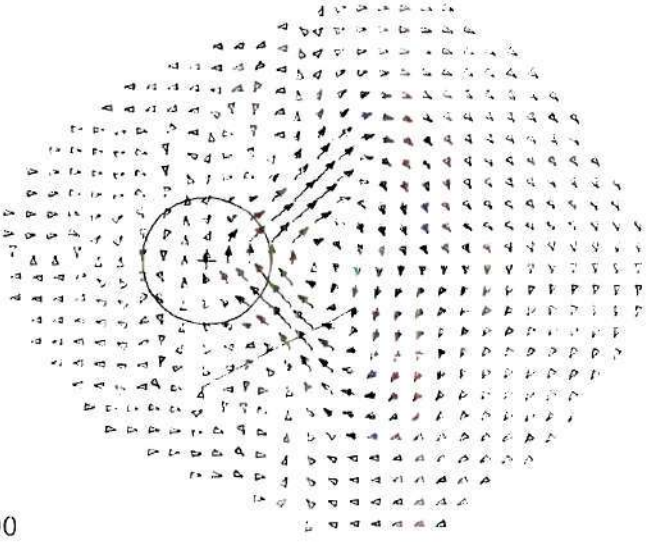

(c) T = 6.00

Figure 30. (cont.)

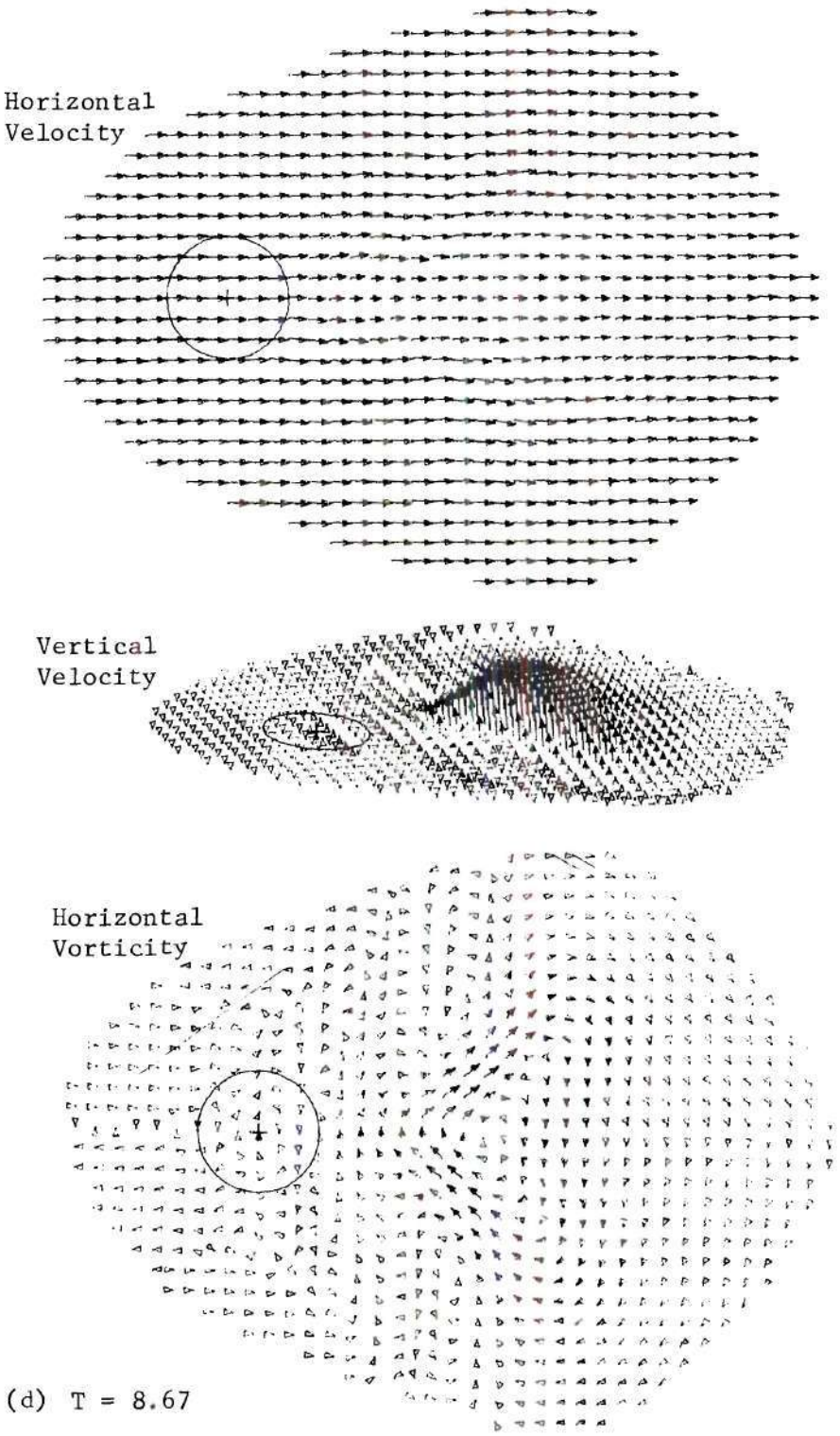

Figure 30. (cont.)

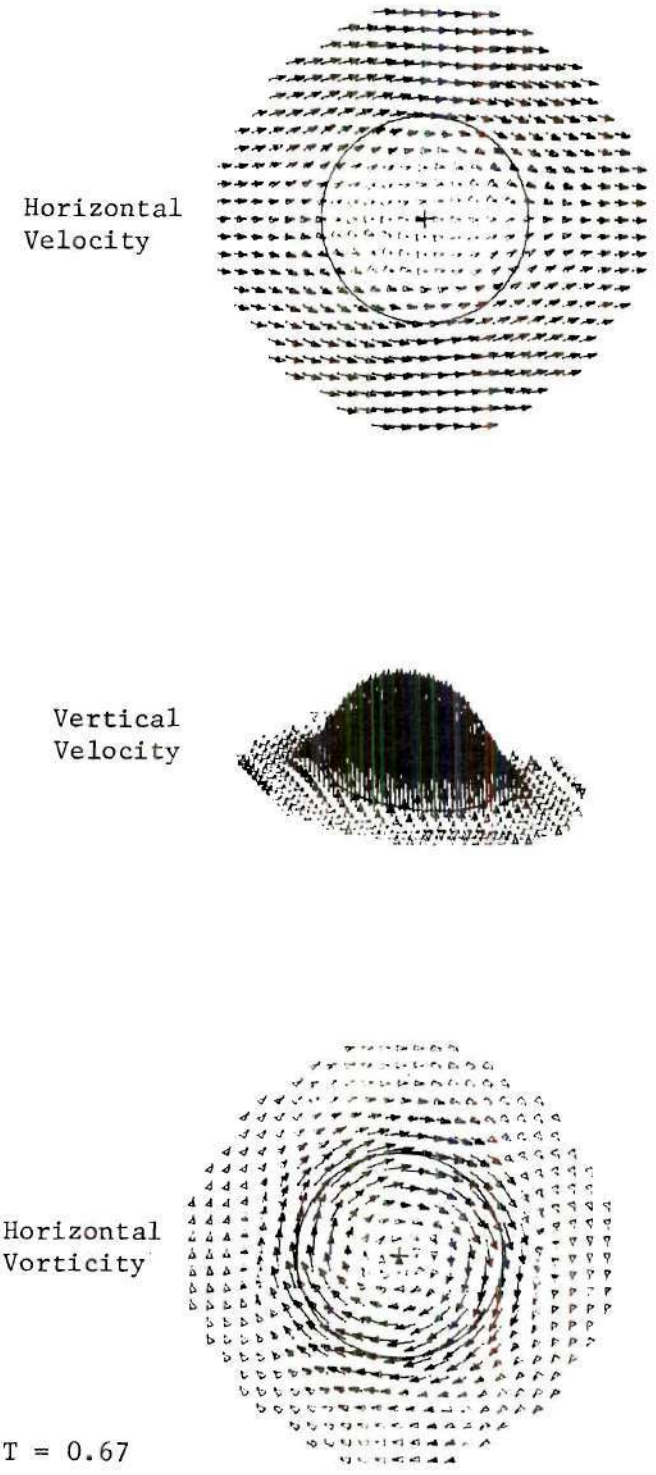

(a) T = 0.67

Figure 31. Time Development of Circular Infinite Jet in Cross-Wind (V_r = 8) - Forty Step Gradual Start with Smaller Cell Size - R = 30

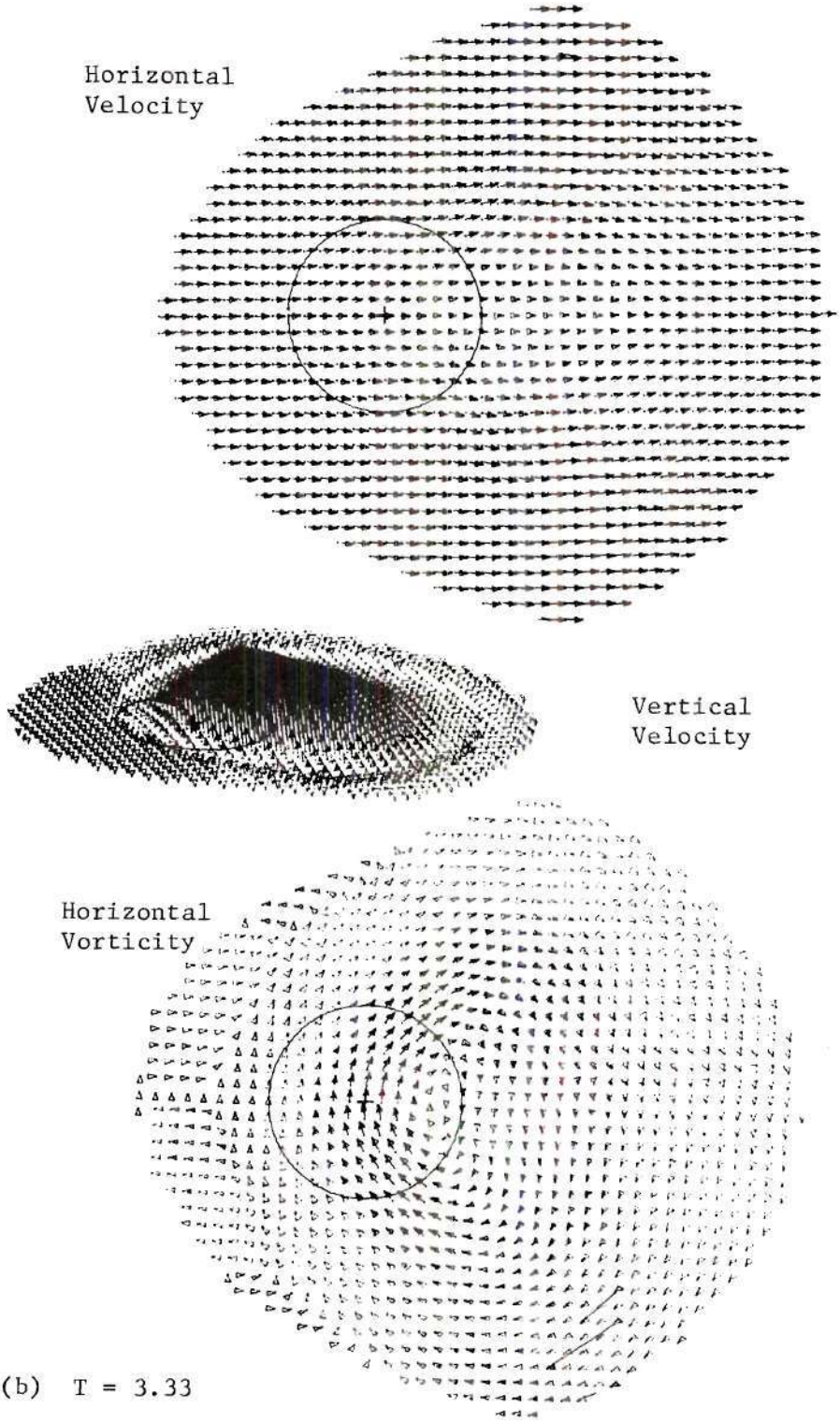

(b) T = 3.33

Figure 31. (cont.)

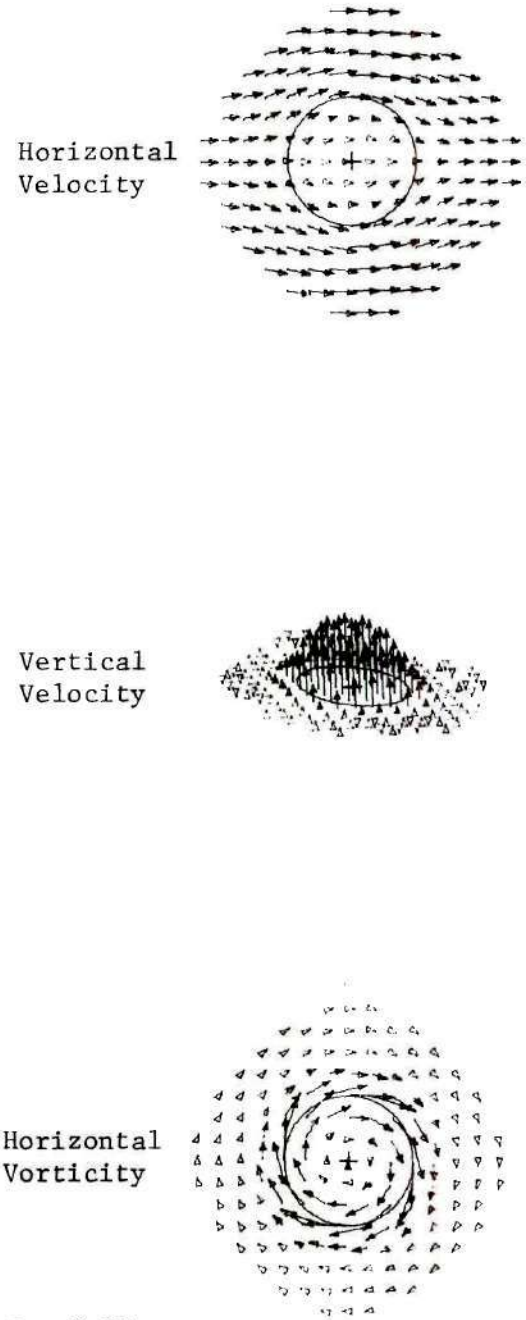

(a) T = 0.67

Figure 32. Time Development of Circular Infinite Jet in Cross-Wind (V_r = 4) - Twenty Step Gradual Start - R = 30

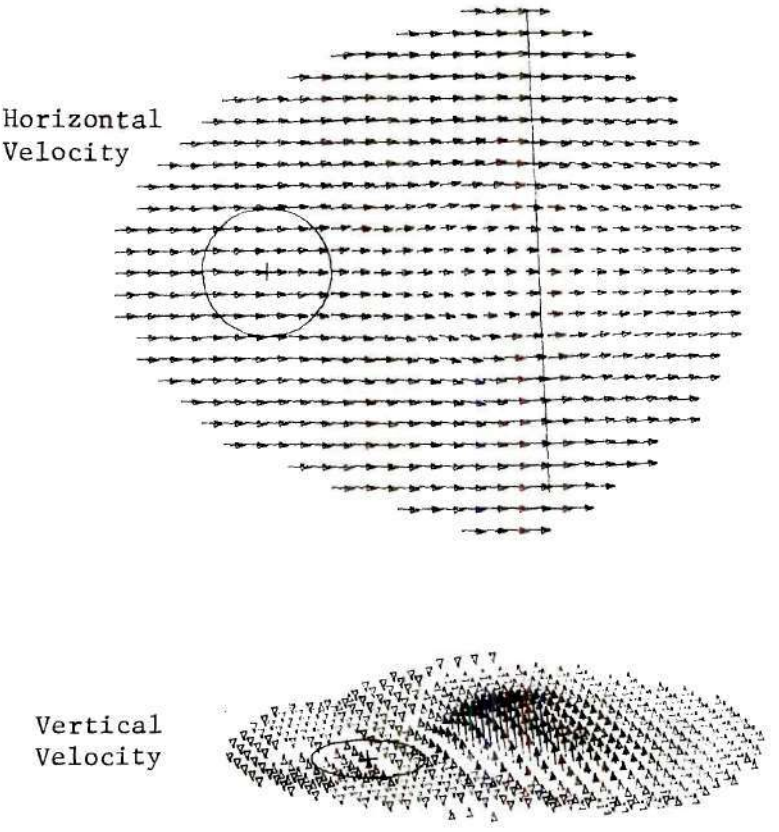

(b) T = 6.00

Figure 32. (cont.)

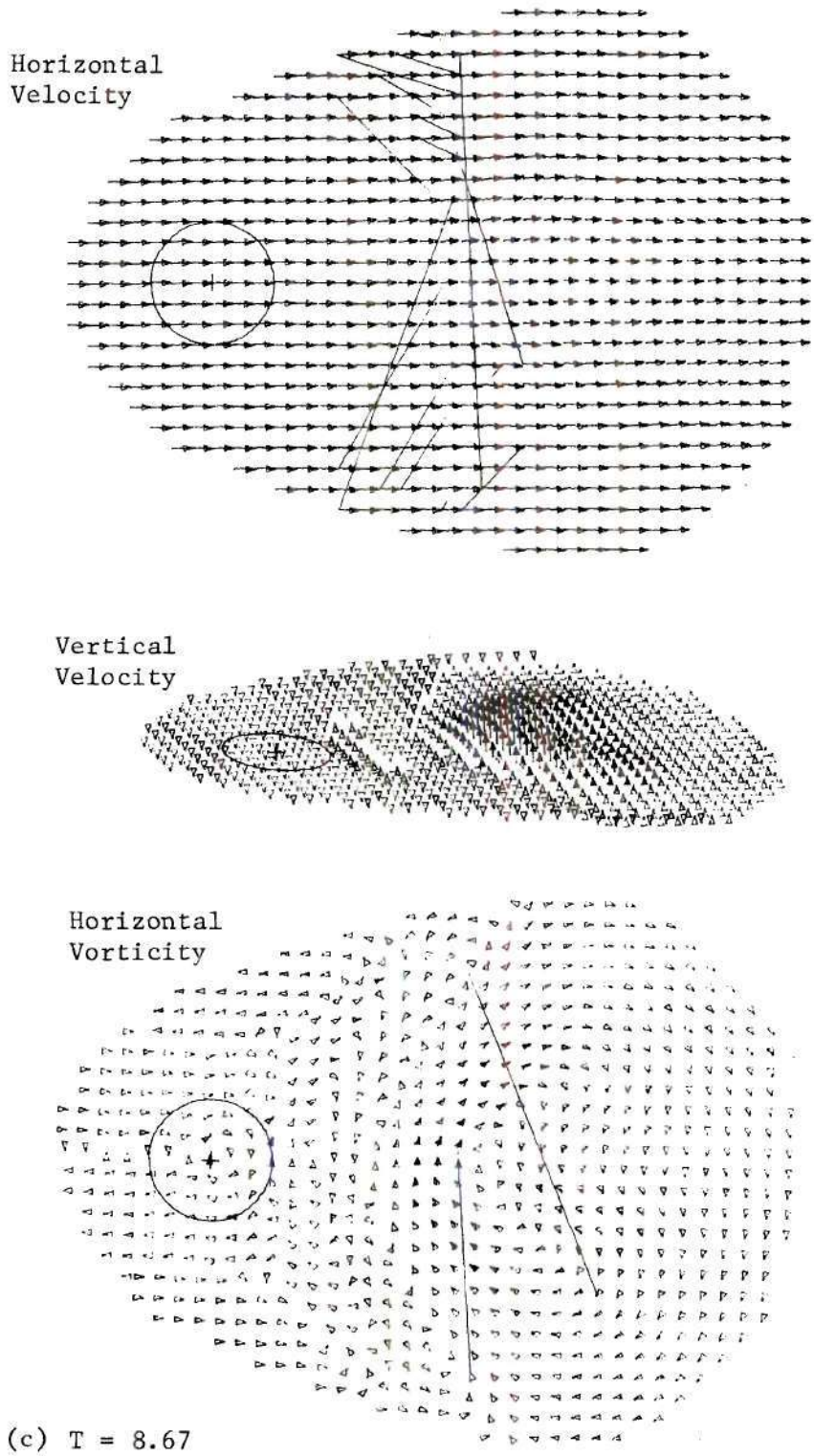

(c) T = 8.67

Figure 32. (cont.)

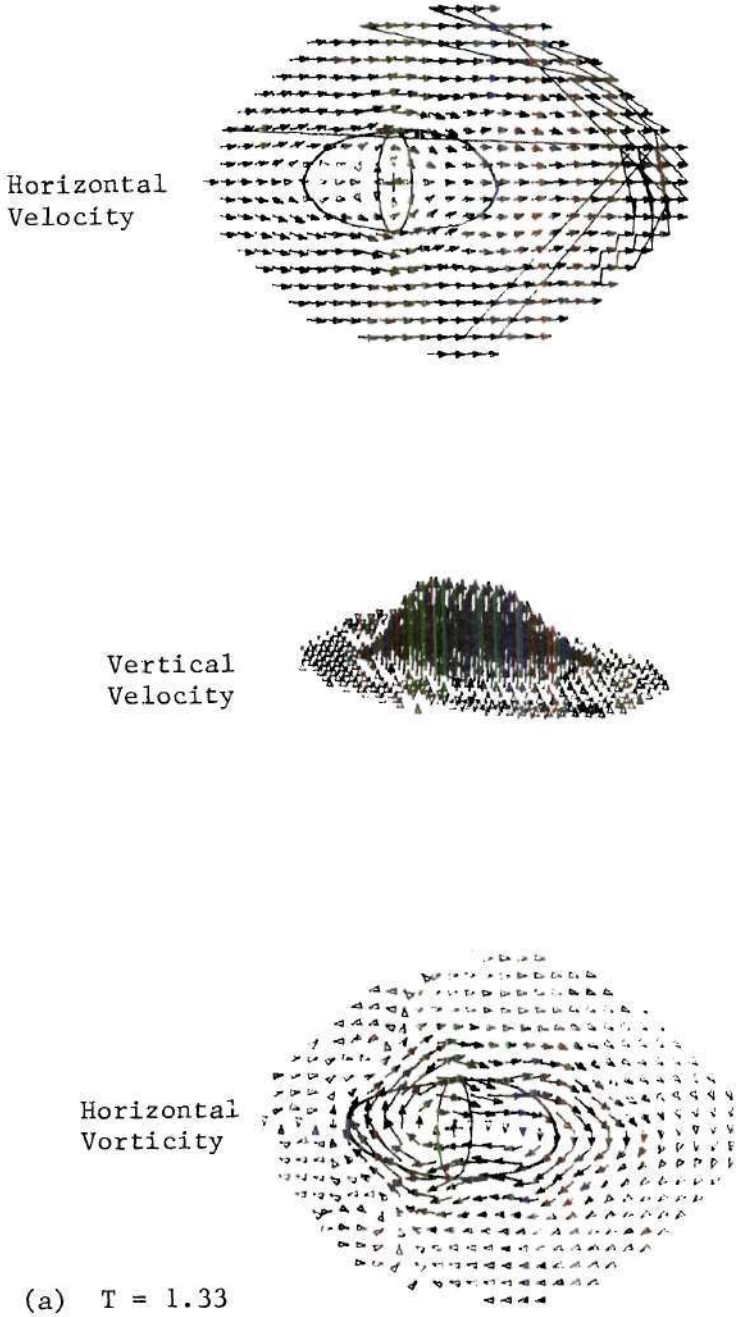

(a) T = 1.33

Figure 33. Time Development of Elliptic Infinite Jet in Cross-Wind (V_r = 8) - Twenty Step Gradual Start - R = 30 (Major Axis Parallel to Cross-Flow, Eccentricity = 5/6)

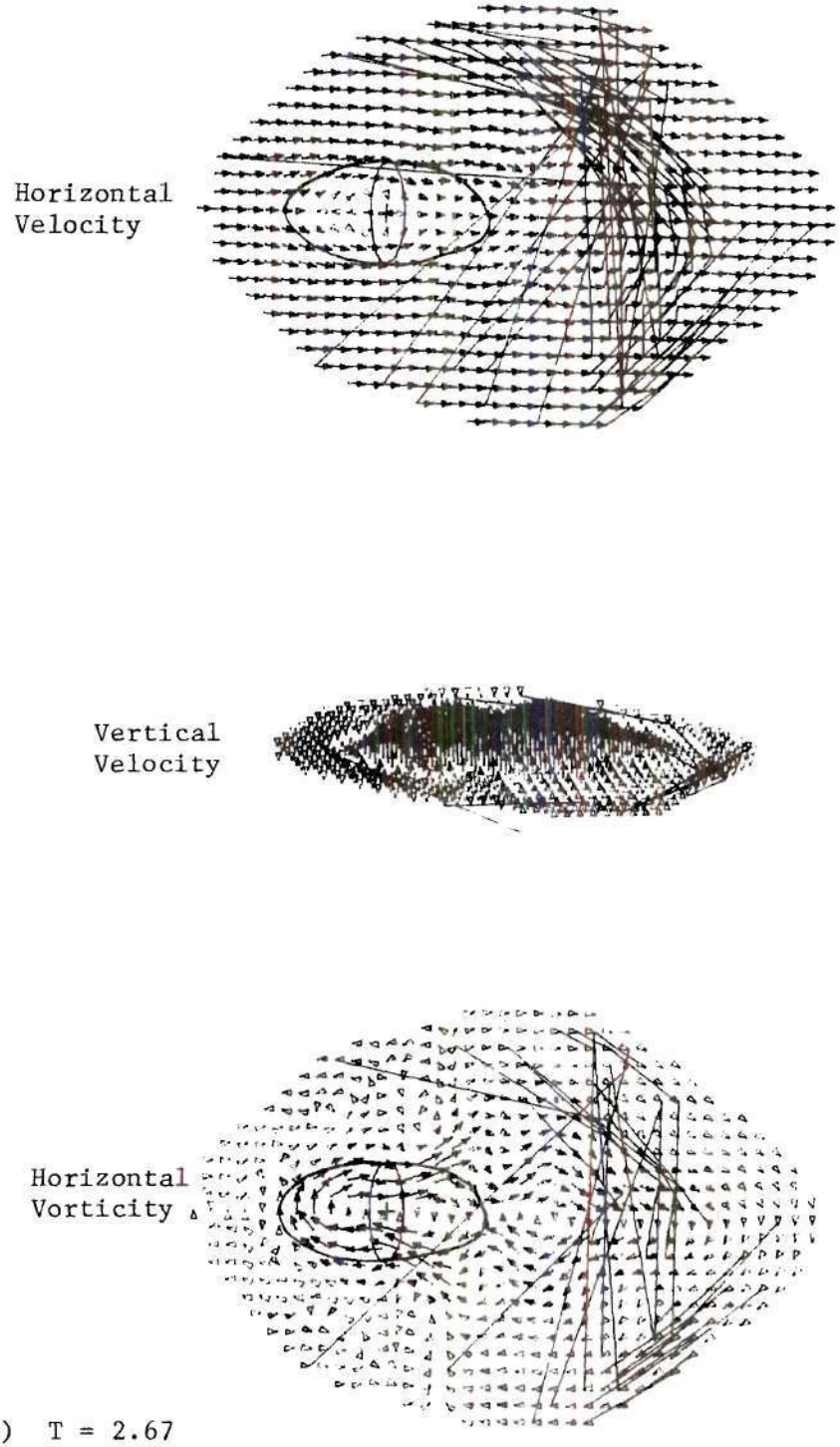

(b) T = 2.67

Figure 33. (cont.)

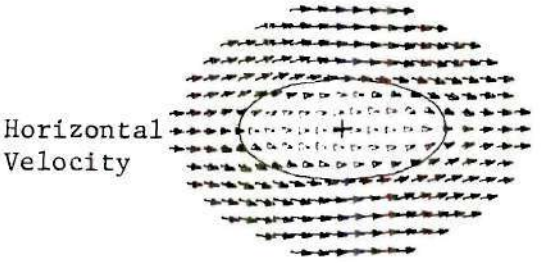

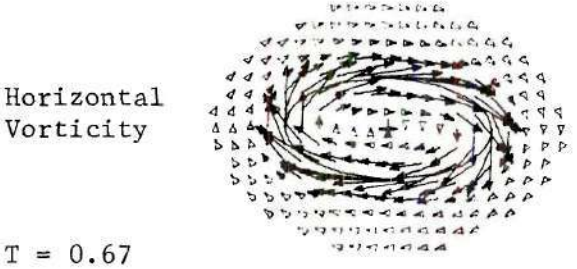

(a) T = 0.67

Figure 34. Time Development of Elliptic Infinite Jet in Cross-Wind (V_r = 8) - Forty Step Gradual Start - R = 30 (Major Axis Parallel to Cross-Flow, Eccentricity = 5/6)

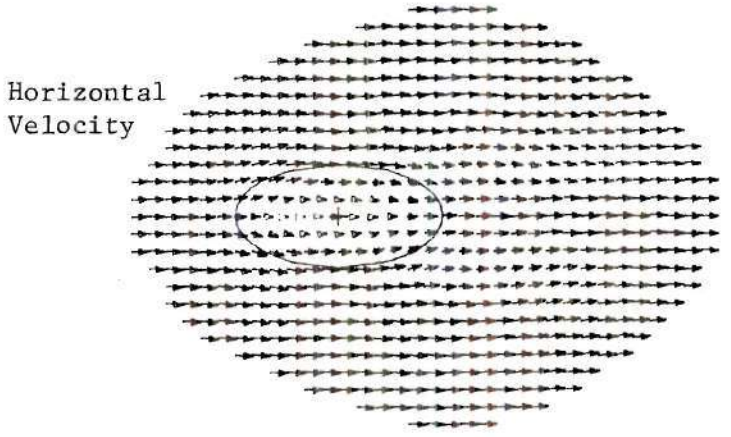

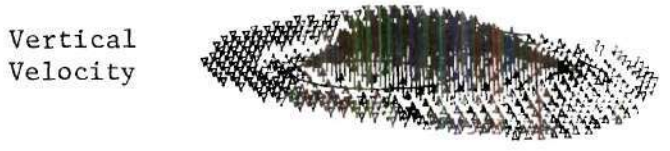

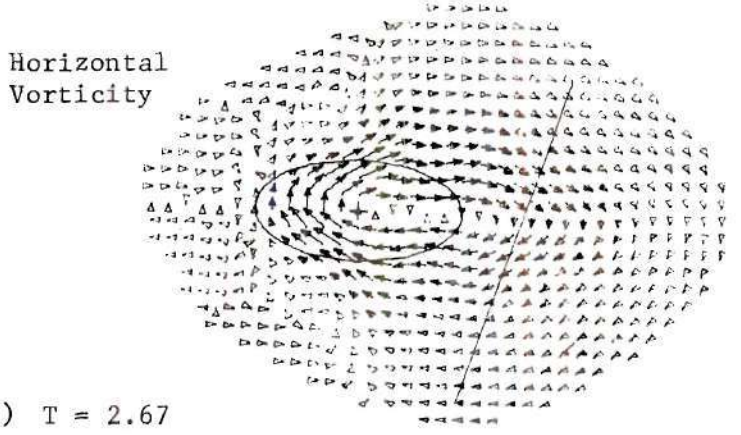

(b) T = 2.67

Figure 34. (cont.)

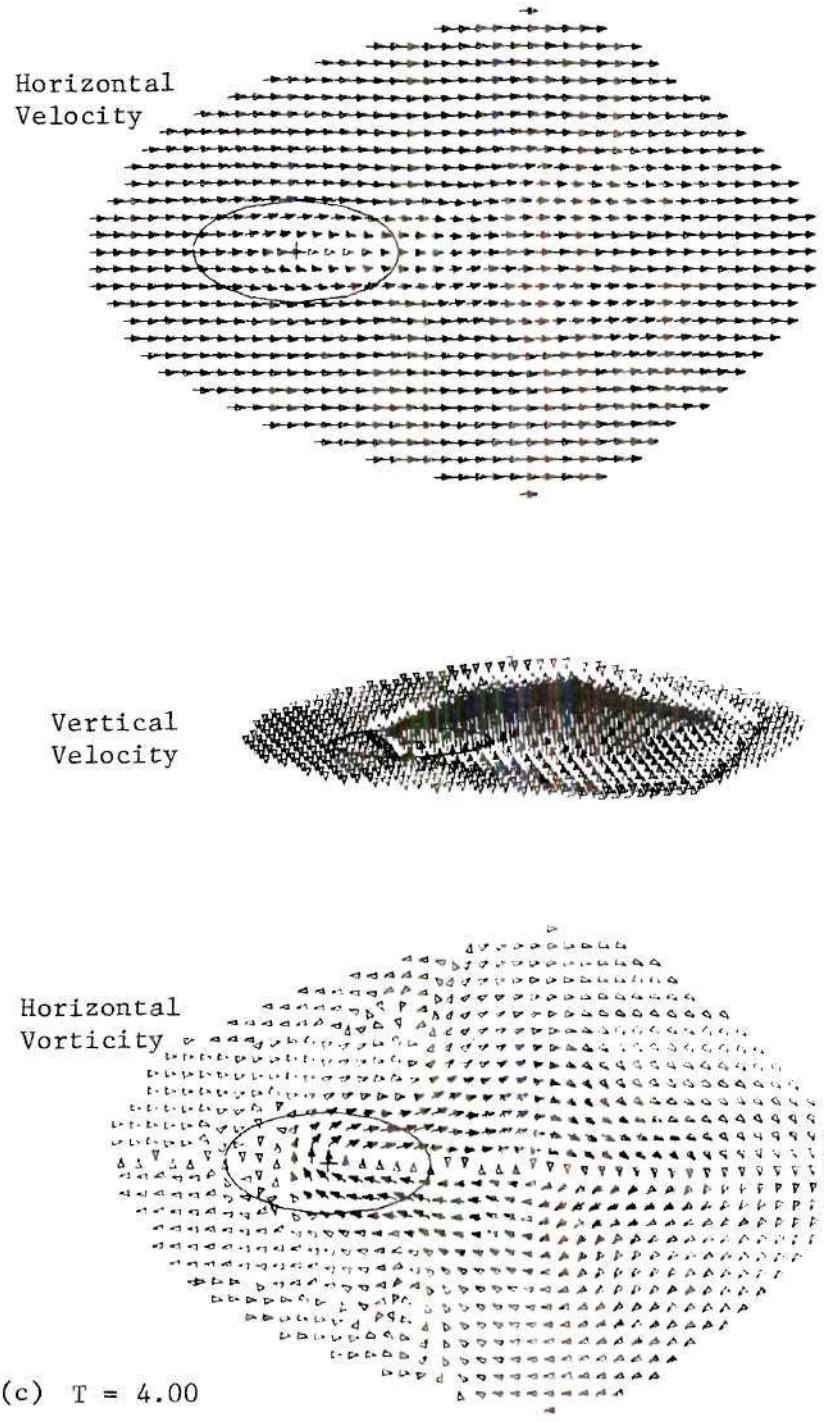

Figure 34. (cont.)

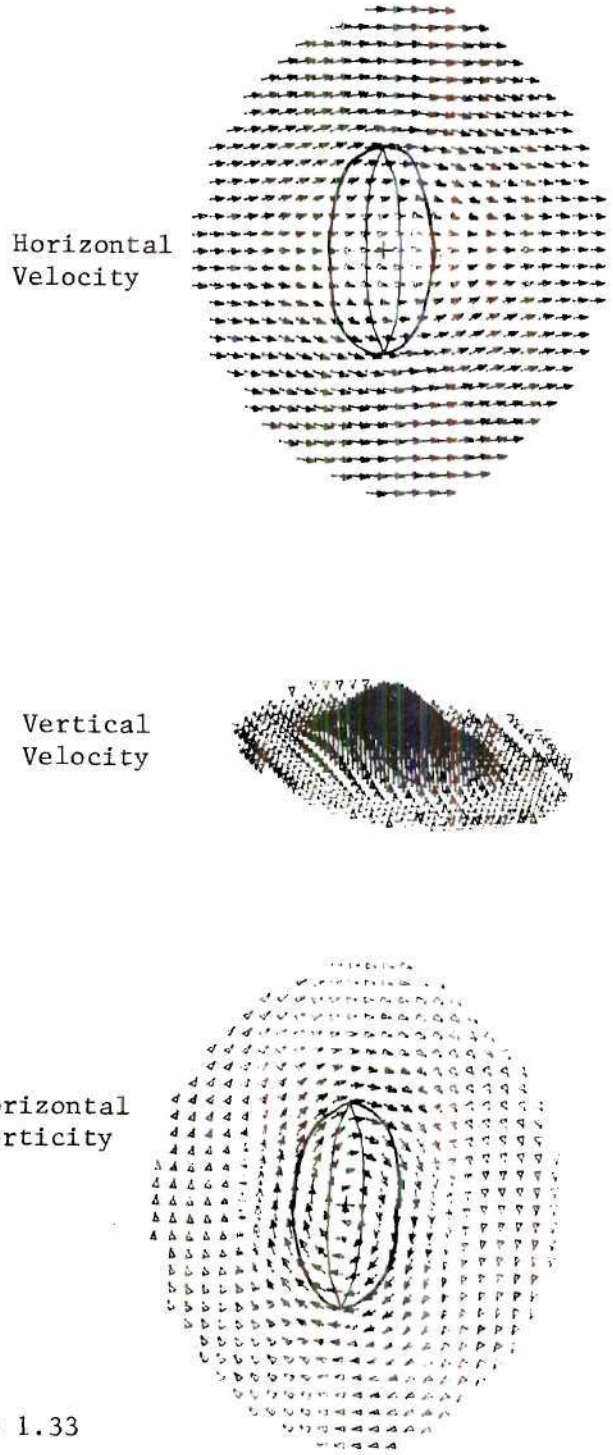

(a) T = 1.33

Figure 35. Time Development of Elliptic Infinite Jet in Cross-Wind (V_r = 8) - Forty Step Gradual Start - R = 15 (Major Axis Perpendicular to Cross-Flow, Eccentricity = 5/6)

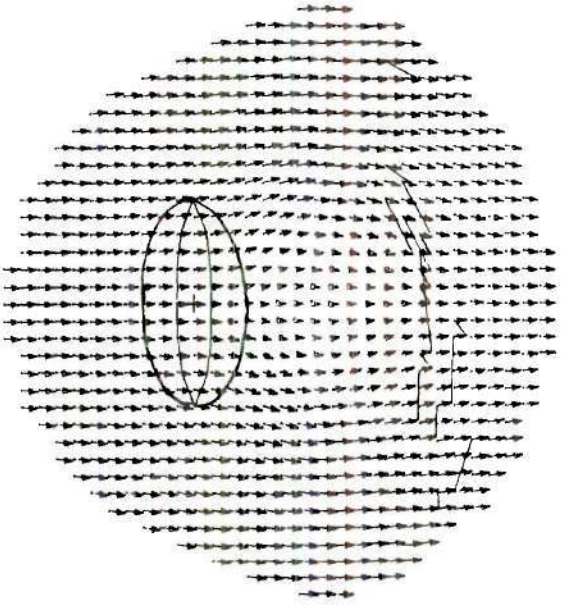

Horizontal Velocity

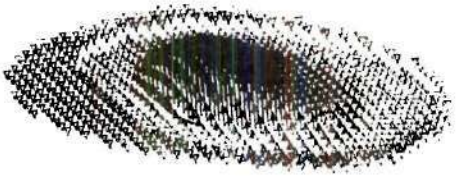

Vertical Velocity

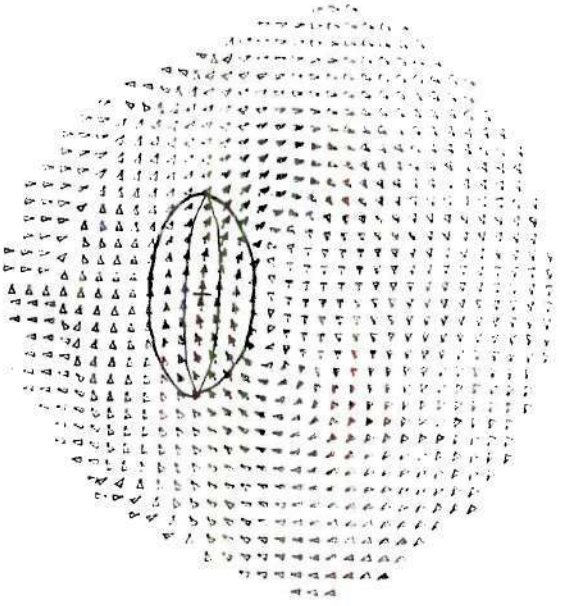

Horizontal Vorticity

(b) T = 2.67

Figure 35. (cont.)

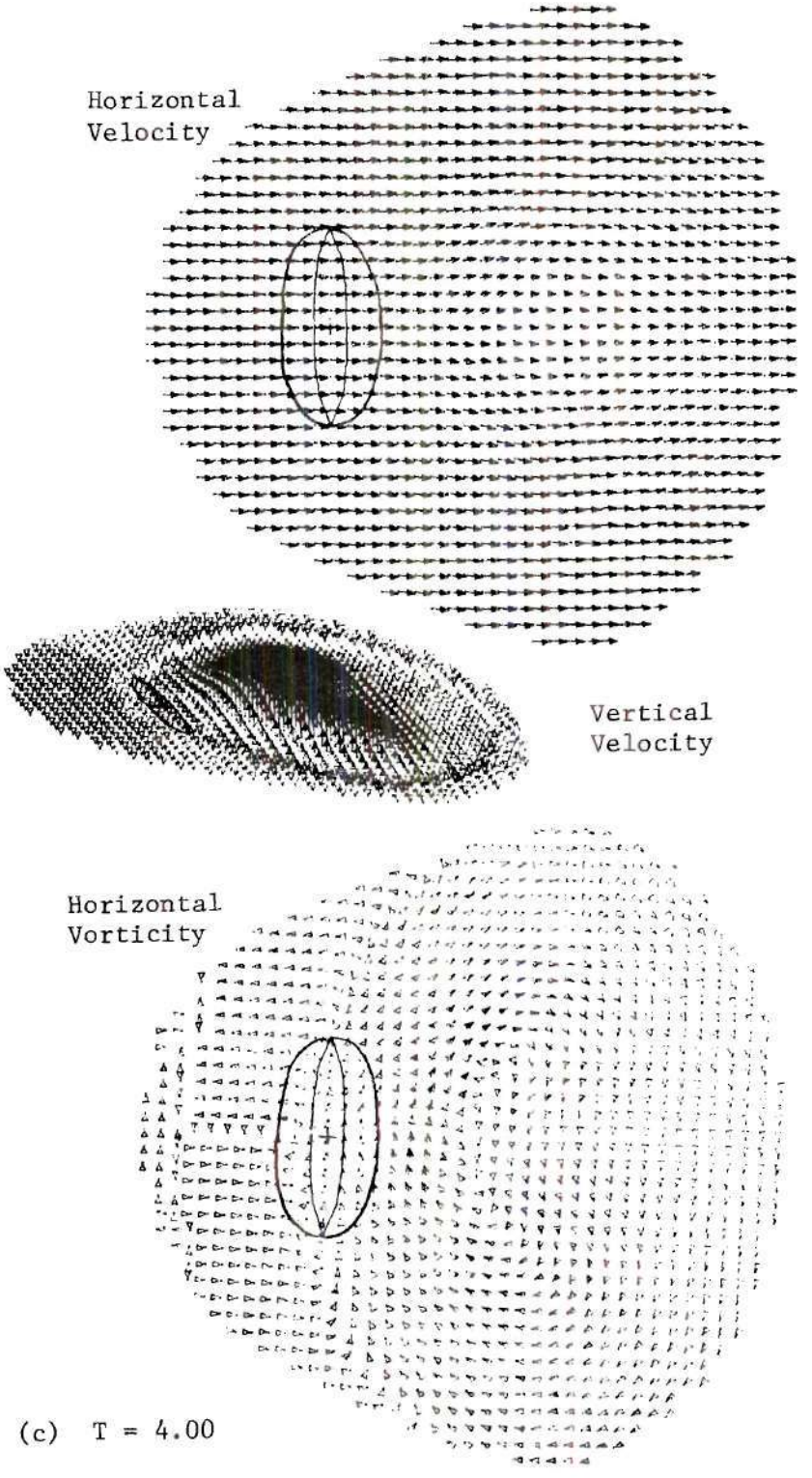

Figure 35. (cont.)

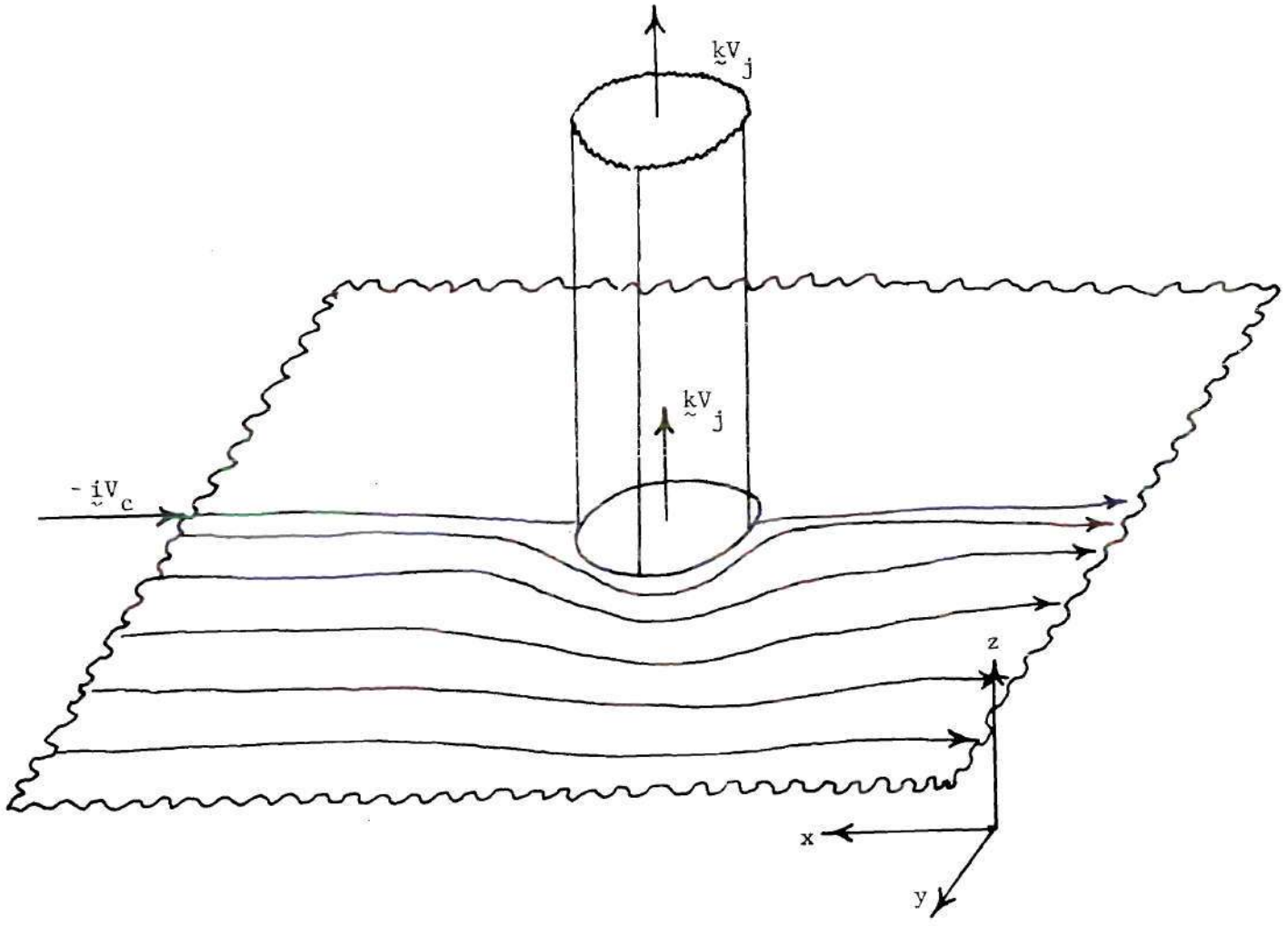

Figure 36. Coordinate System for Three-Dimensional Jet in Cross-Wind Solution and Initial Conditions for Start from Cylindrical Discontinuity

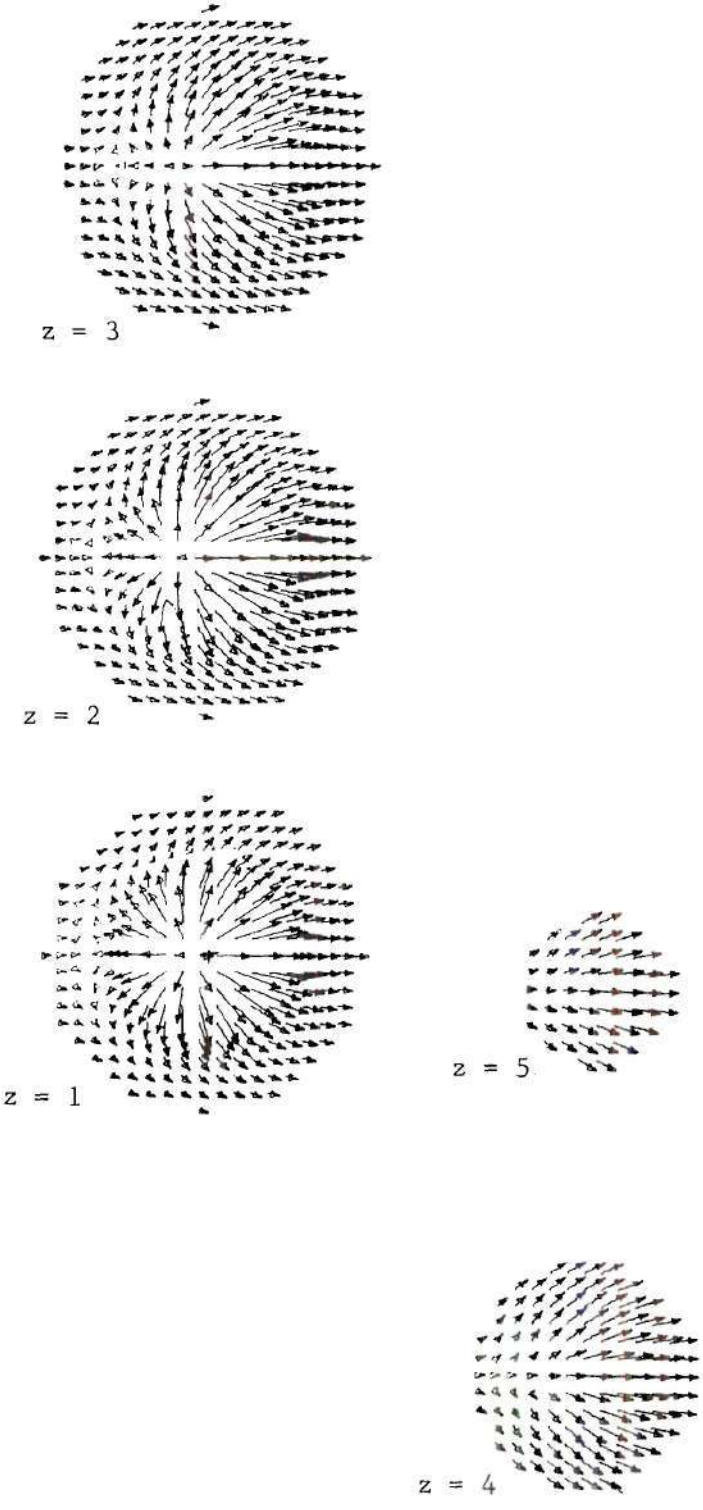

(a) T = 0.57

Figure 37. Horizontal Velocity Vectors - Start from Opening of Jet Exit (V_r = 8) - 32 Step Gradual Start, Δt = 0.05 - R = 12

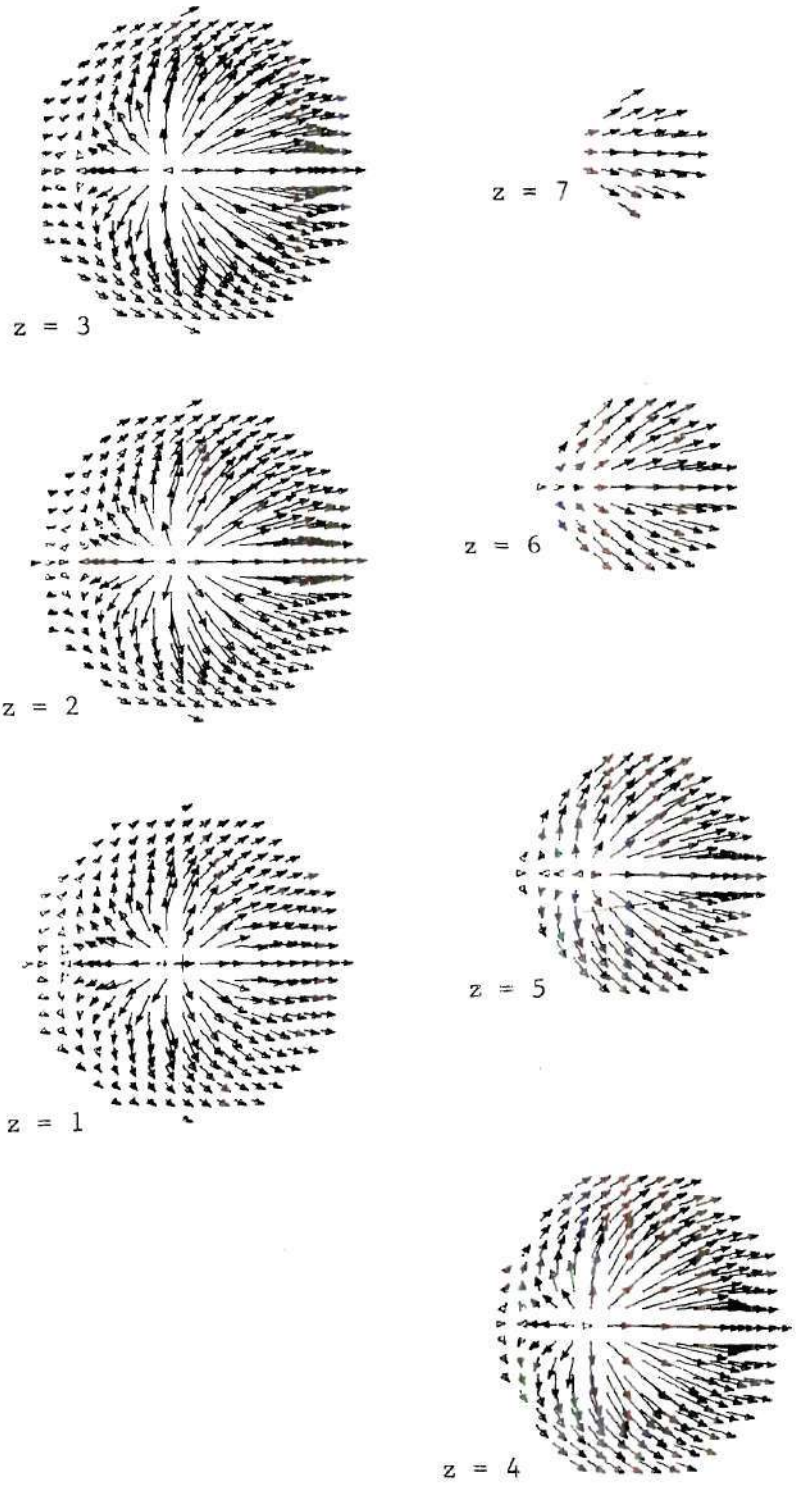

(b) T = 0.77

Figure 37. (cont.)

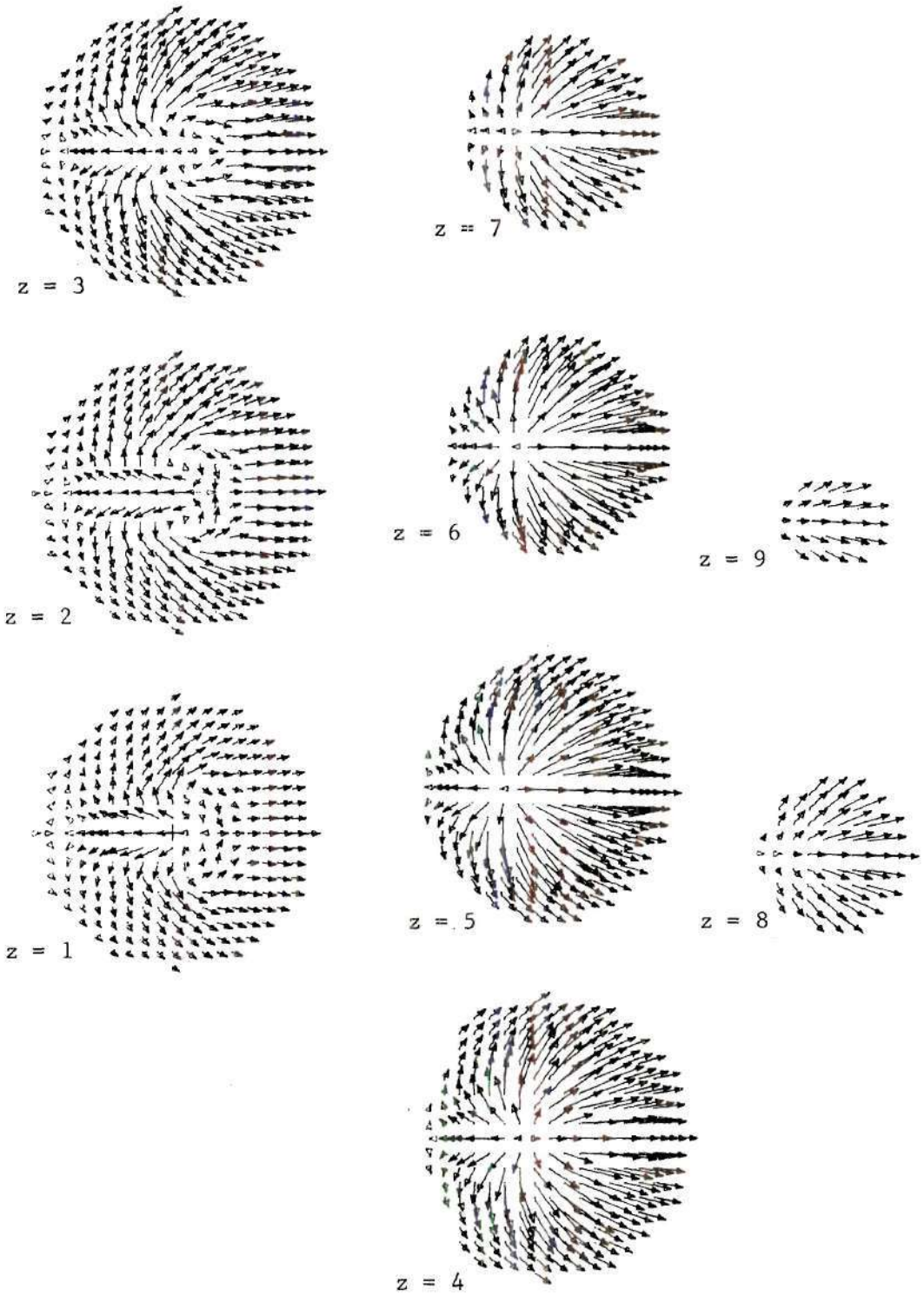

(c) T = 0.93

Figure 37. (cont.)

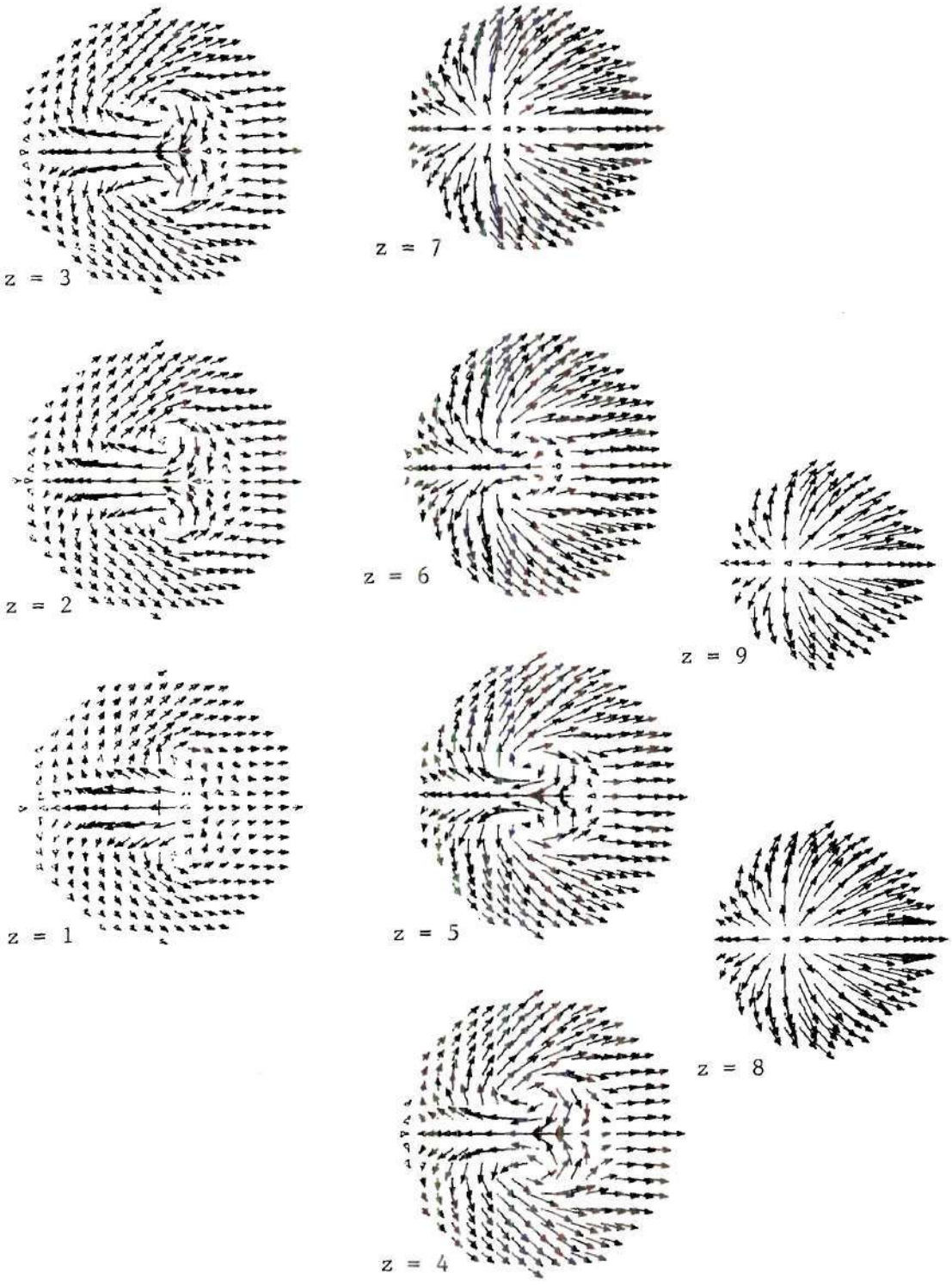

(d) T = 1.13

Figure 37. (cont.)

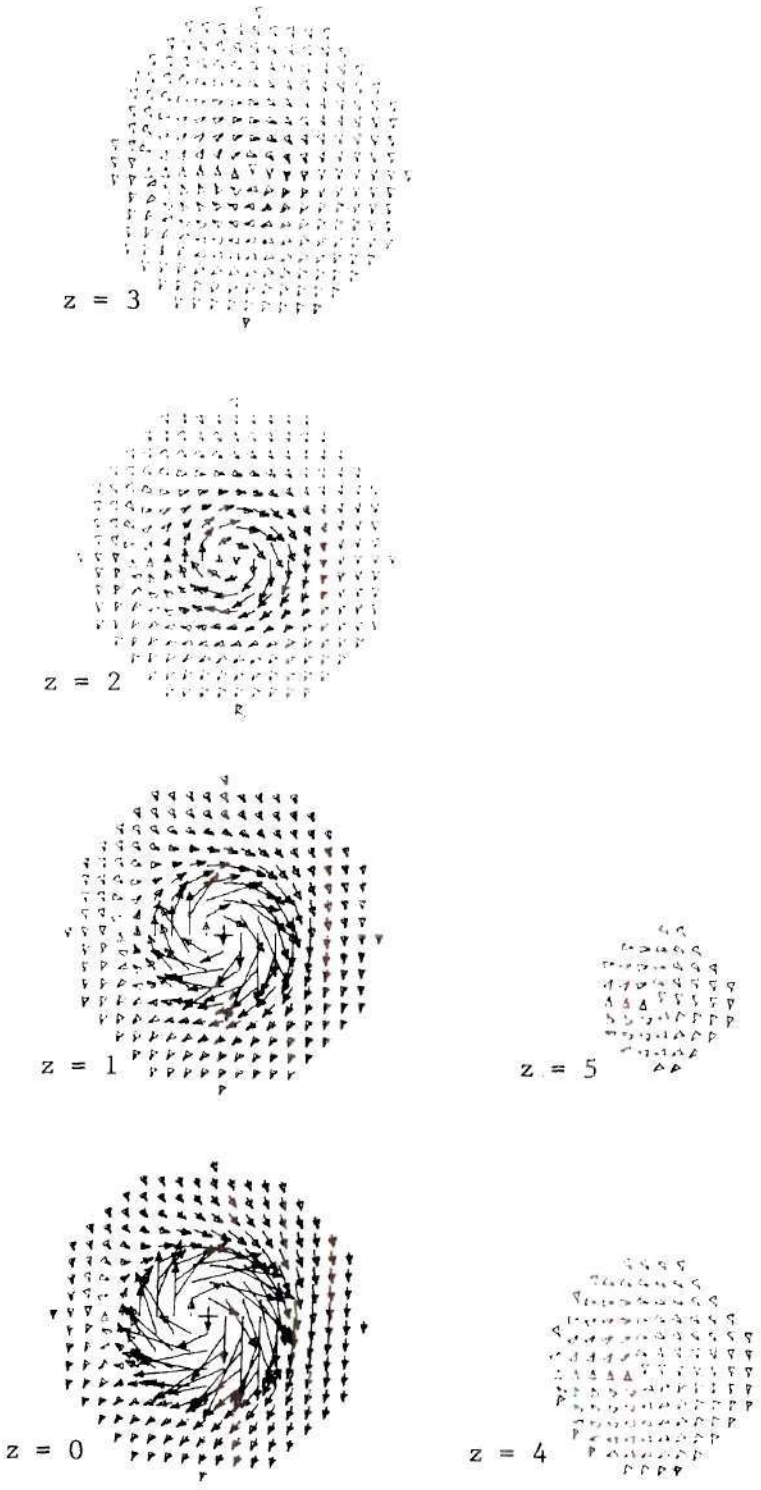

(a) T = 0.57

Figure 38. Horizontal Vorticity Vectors - Start from Opening of Jet Exit (V_r = 8) - 32 Step Gradual Start, Δt = 0.05 - R = 12

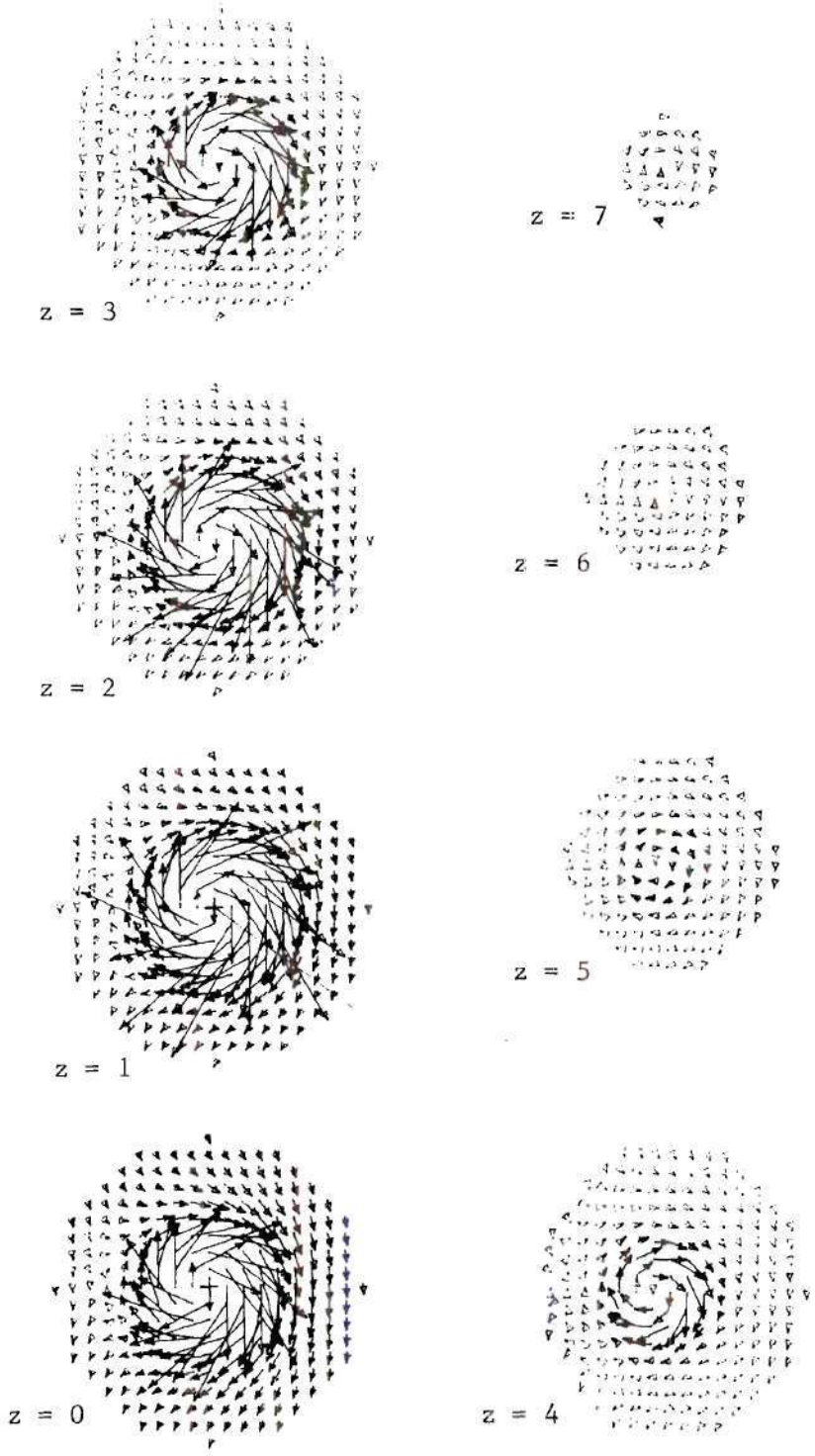

(b) T = 0.77

Figure 38. (cont.)

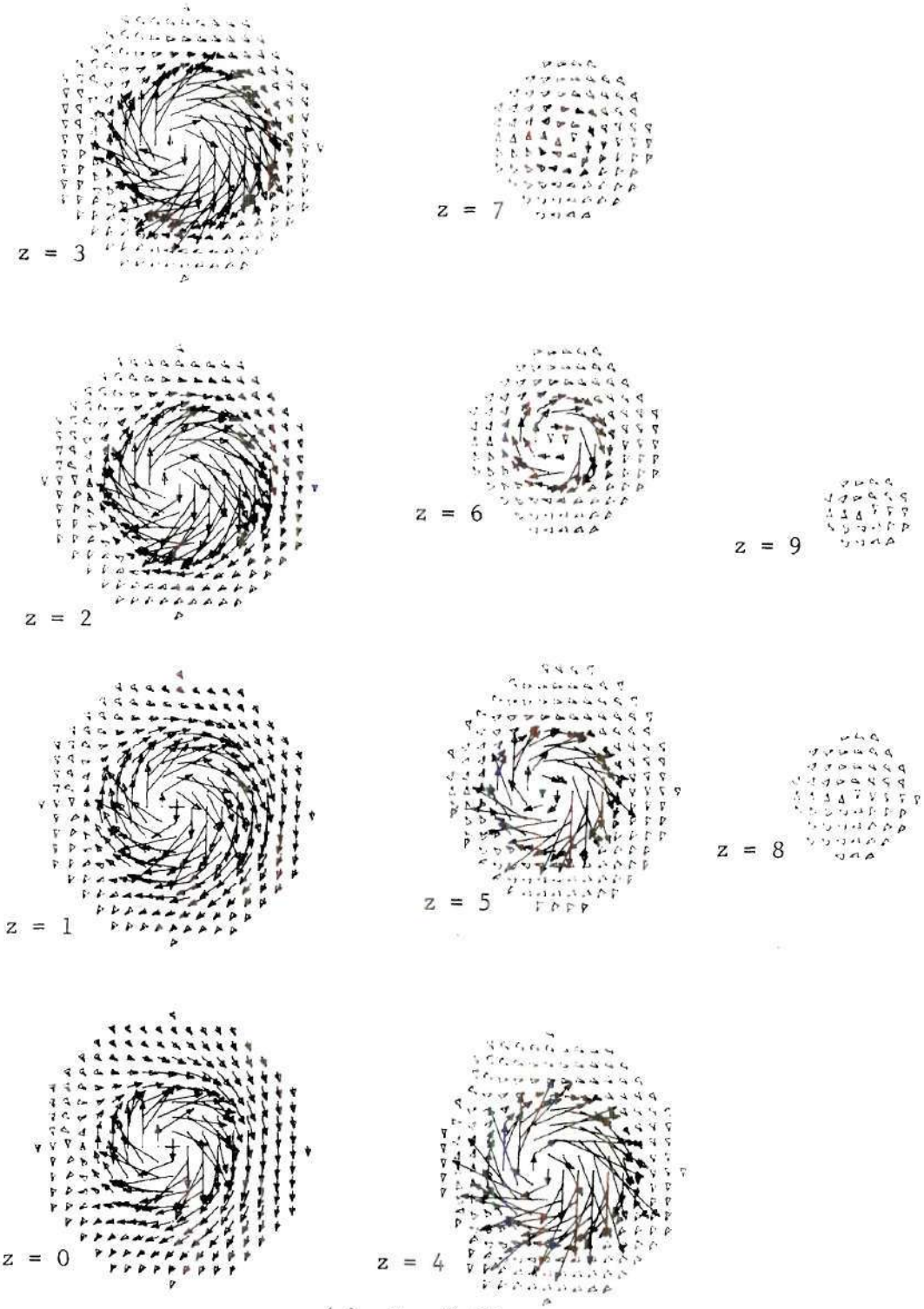

(c) T = 0.93

Figure 38. (cont.)

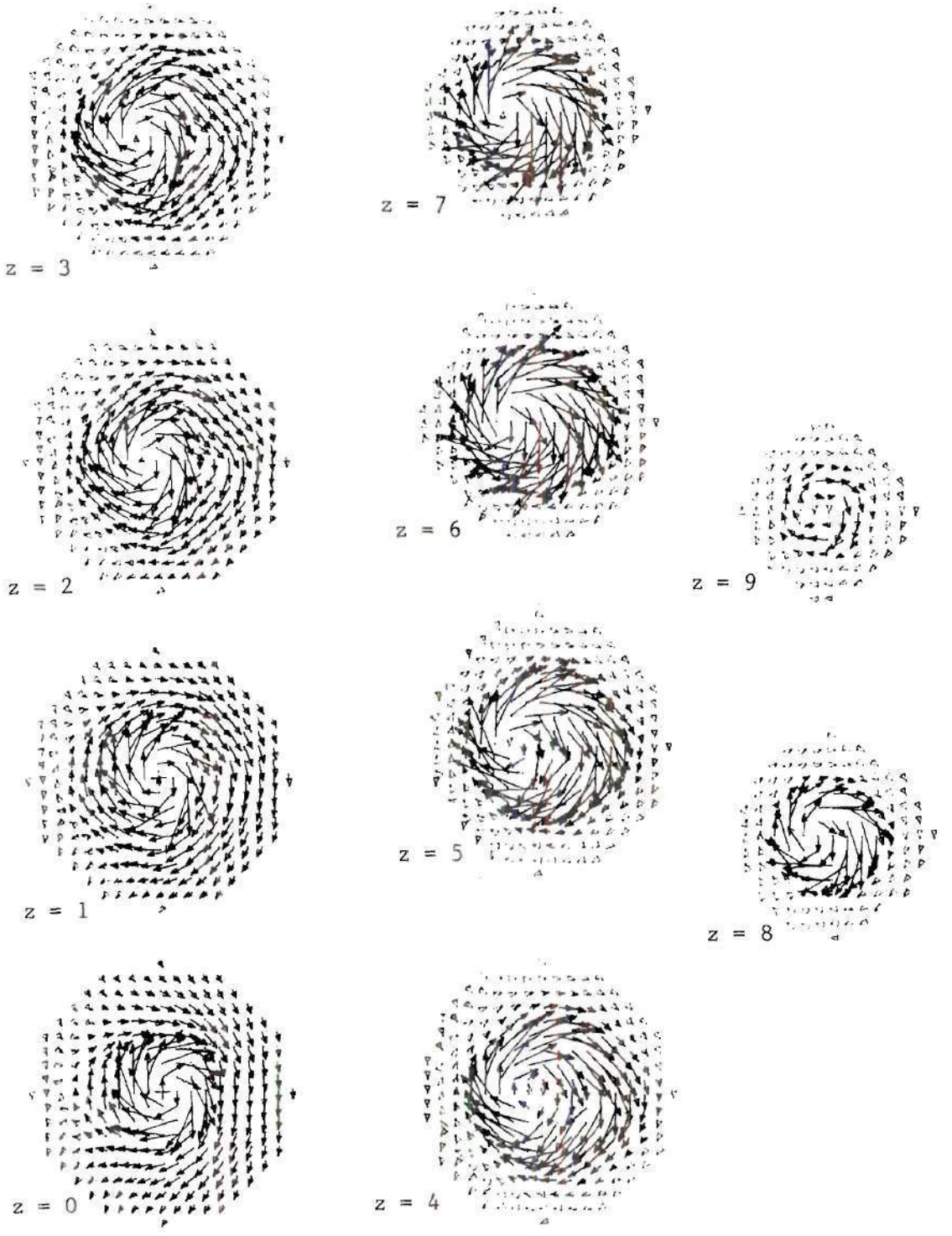

(d) T = 1.13

Figure 38. (cont.)

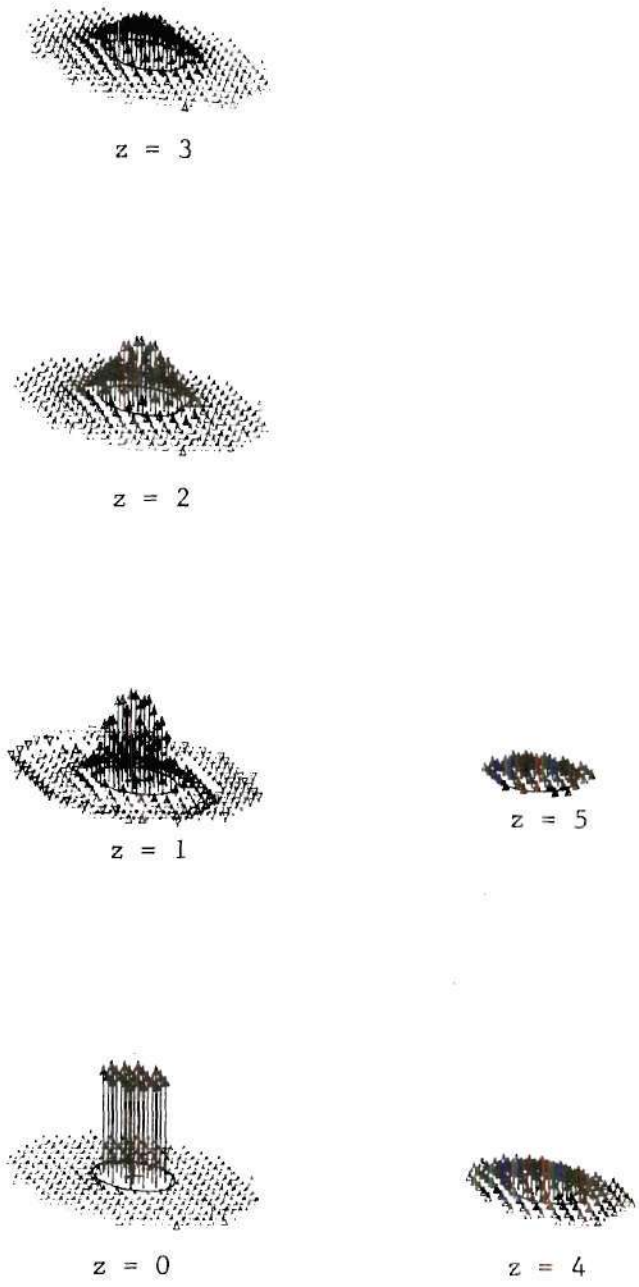

(a) T = 0.57

Figure 39. Vertical Velocity Vectors - Start from Opening of Jet Exit (V_r = 8) - 32 Step Gradual Start, Δt = 0.05 - R = 12

z = 3

z = 7

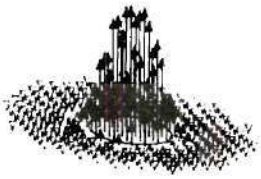

z = 2

z = 6

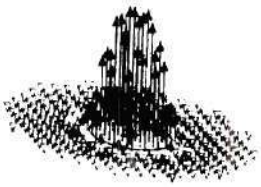

z = 1

z = 5

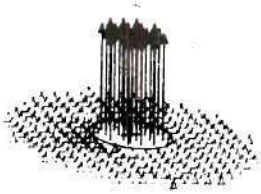

z = 0

z = 4

(b) T = 0.77

Figure 39. (cont.)

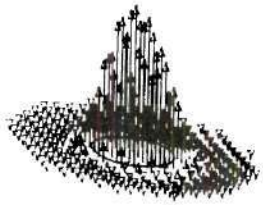

z = 3

z = 7

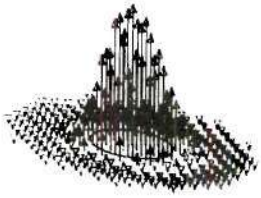

z = 2

z = 6

z = 9

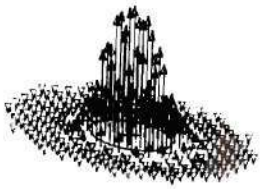

z = 1

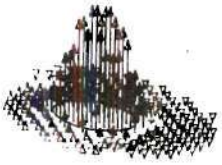

z = 5

z = 8

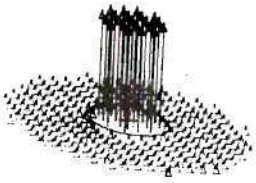

z = 0

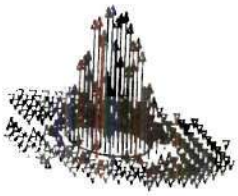

z = 4

(c) T = 0.93

Figure 39. (cont.)

z = 3

z = 7

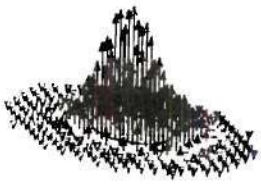

z = 2

z = 6

z = 9

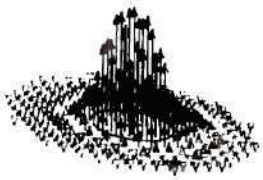

z = 1

z = 5

z = 8

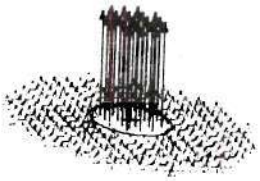

z = 0

z = 4

(d) T = 1.13

Figure 39. (cont.)

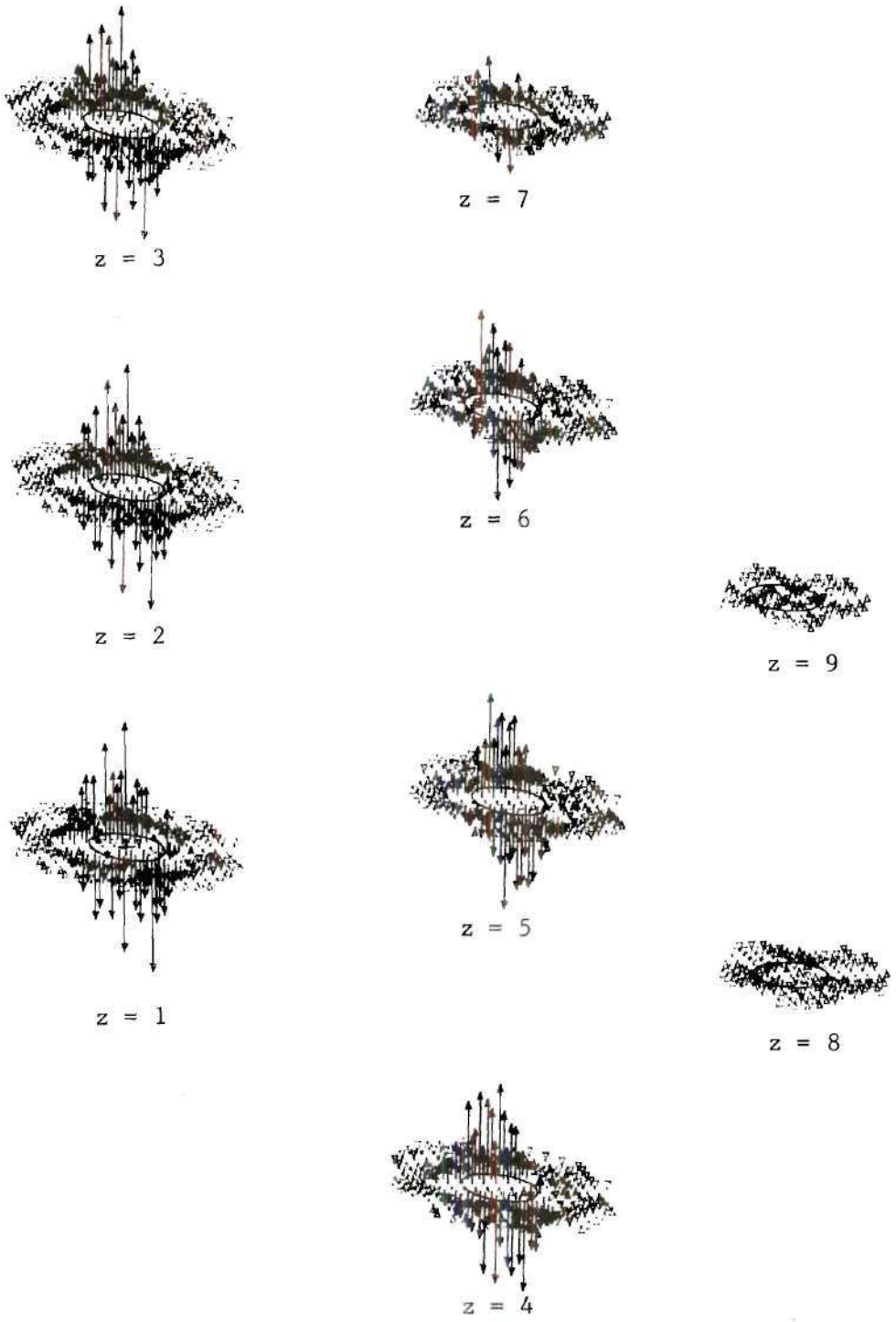

Figure 40. Vertical Vorticity Vectors - Start from Opening of Jet Exit (V_r = 8) - 32 Step Gradual Start, Δt = 0.05 - R = 12 - T = 1.13

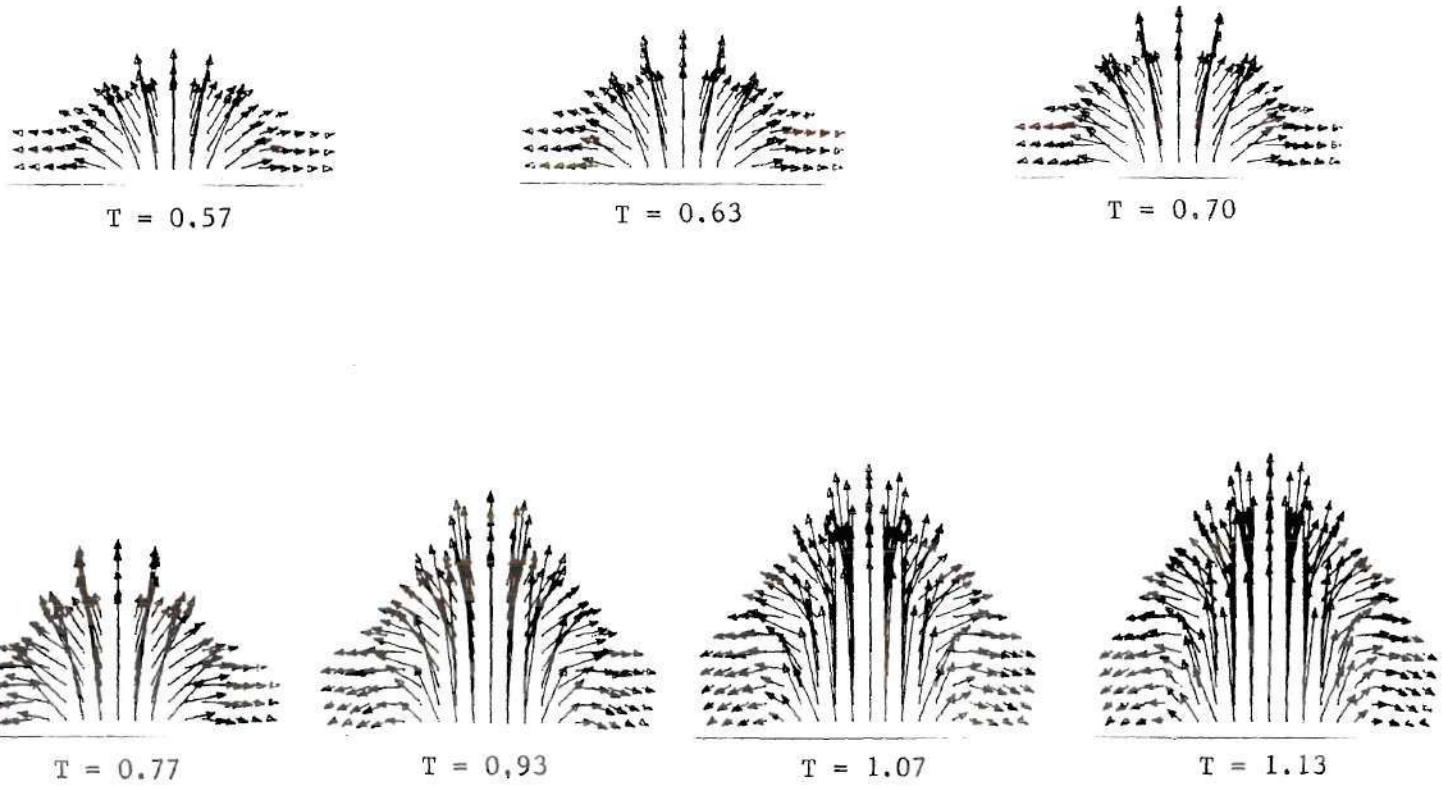

Figure 41. Velocity Vectors in Plane through Exit Center, Perpendicular to Cross-Flow - Start from Opening of Jet Exit (V_r = 8) - 32 Step Gradual Start, Δt = 0.05 - R = 12

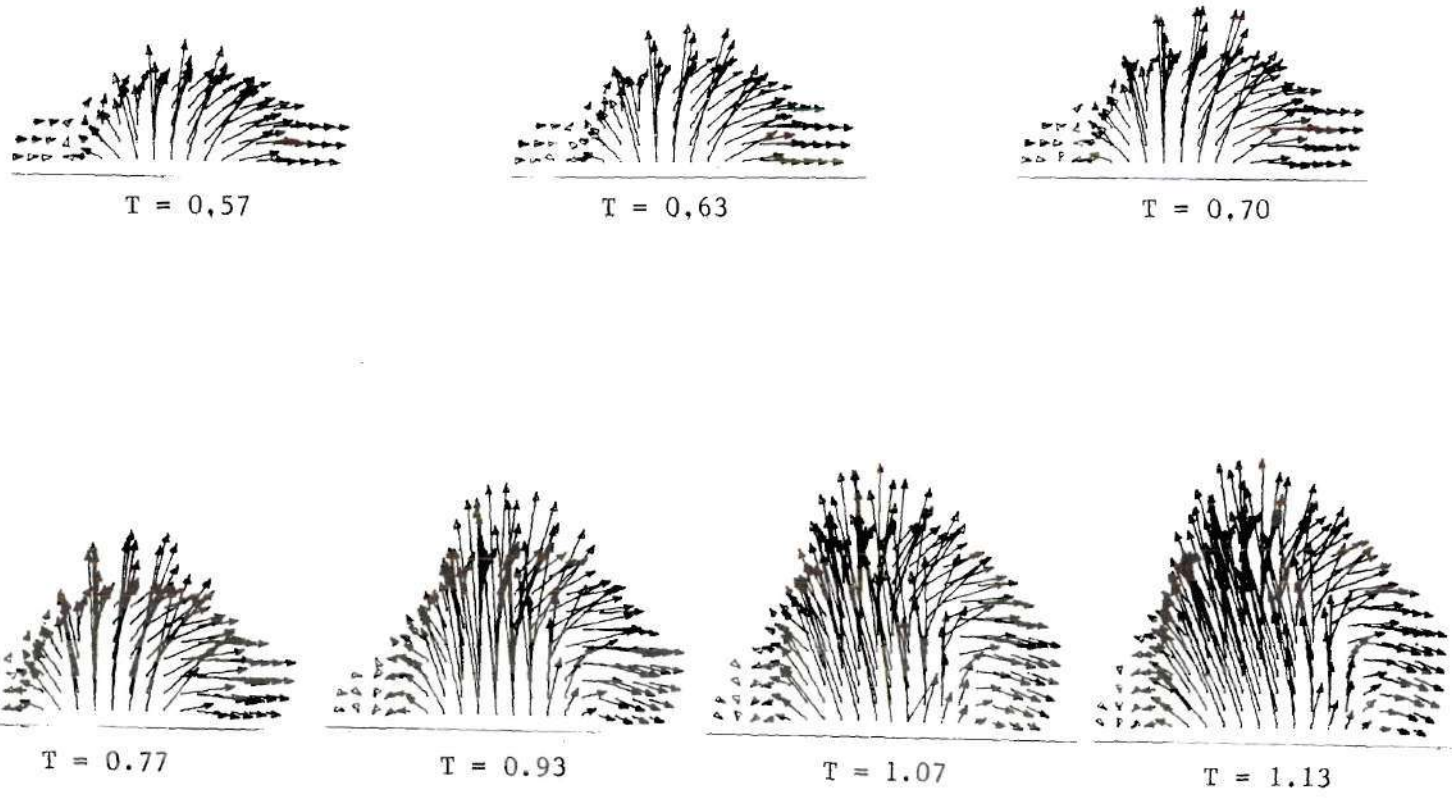

Figure 42. Velocity Vectors in Plane through Exit Center, Parallel to Cross-Flow - Start from Opening of Jet Exit (V_r = 8) - 32 Step Gradual Start, Δt = 0.05 - R = 12

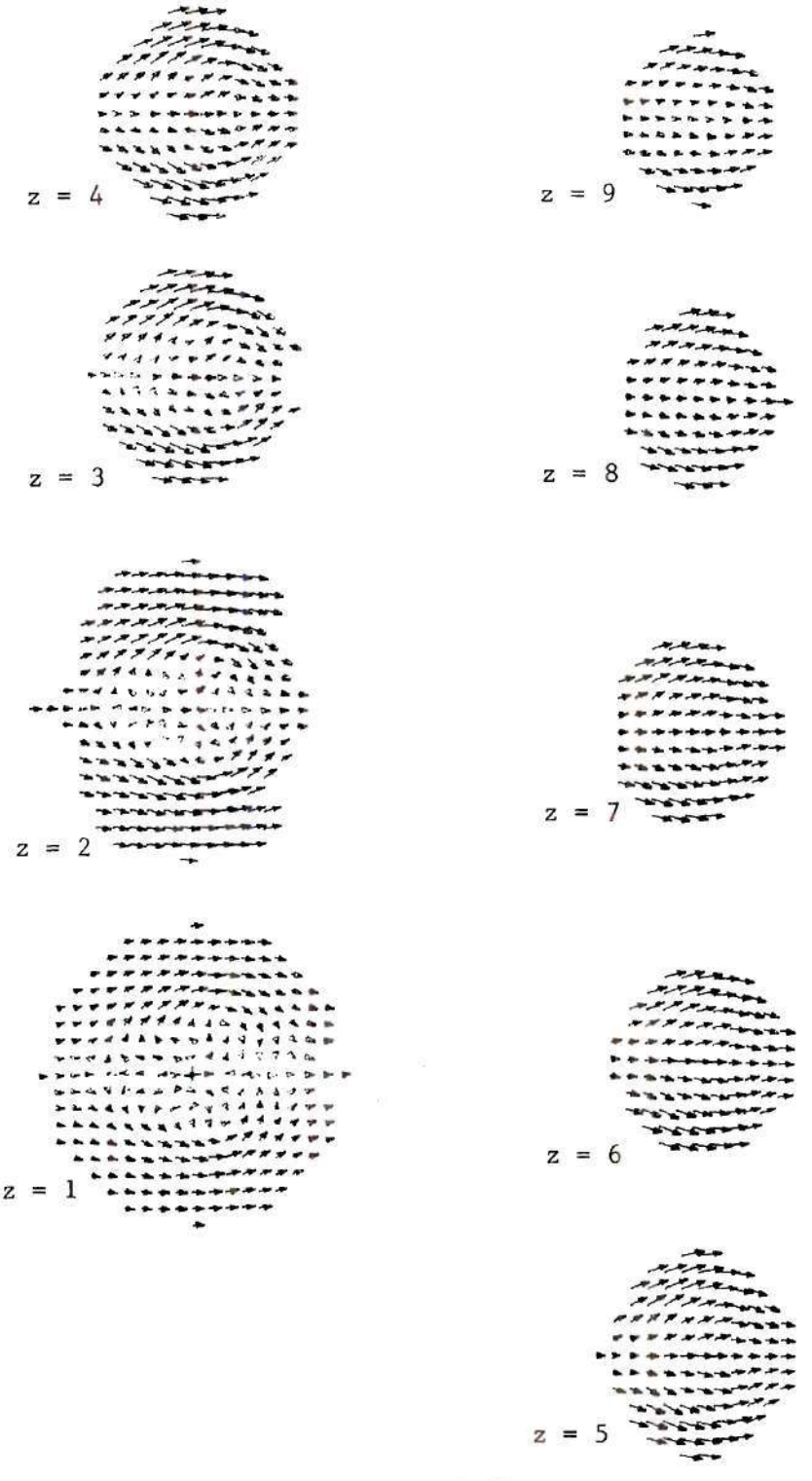

(a) T = 0.67

Figure 43. Horizontal Velocity Vectors - Start from Cylindrical Discontinuity (V_r = 8) - Eight Step Start, Δt = 0.1 - R = 12

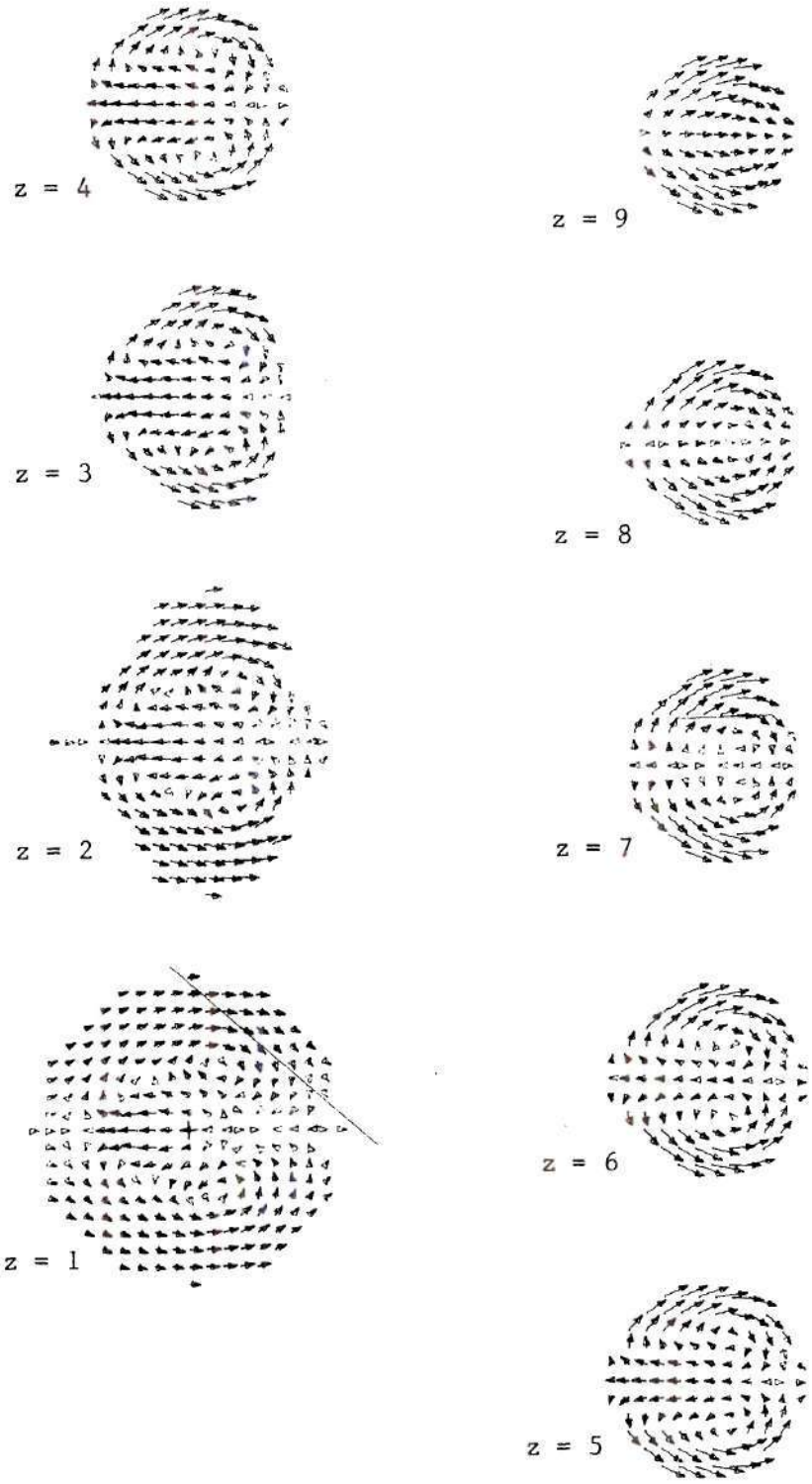

(b) T = 1.20

Figure 43. (cont.)

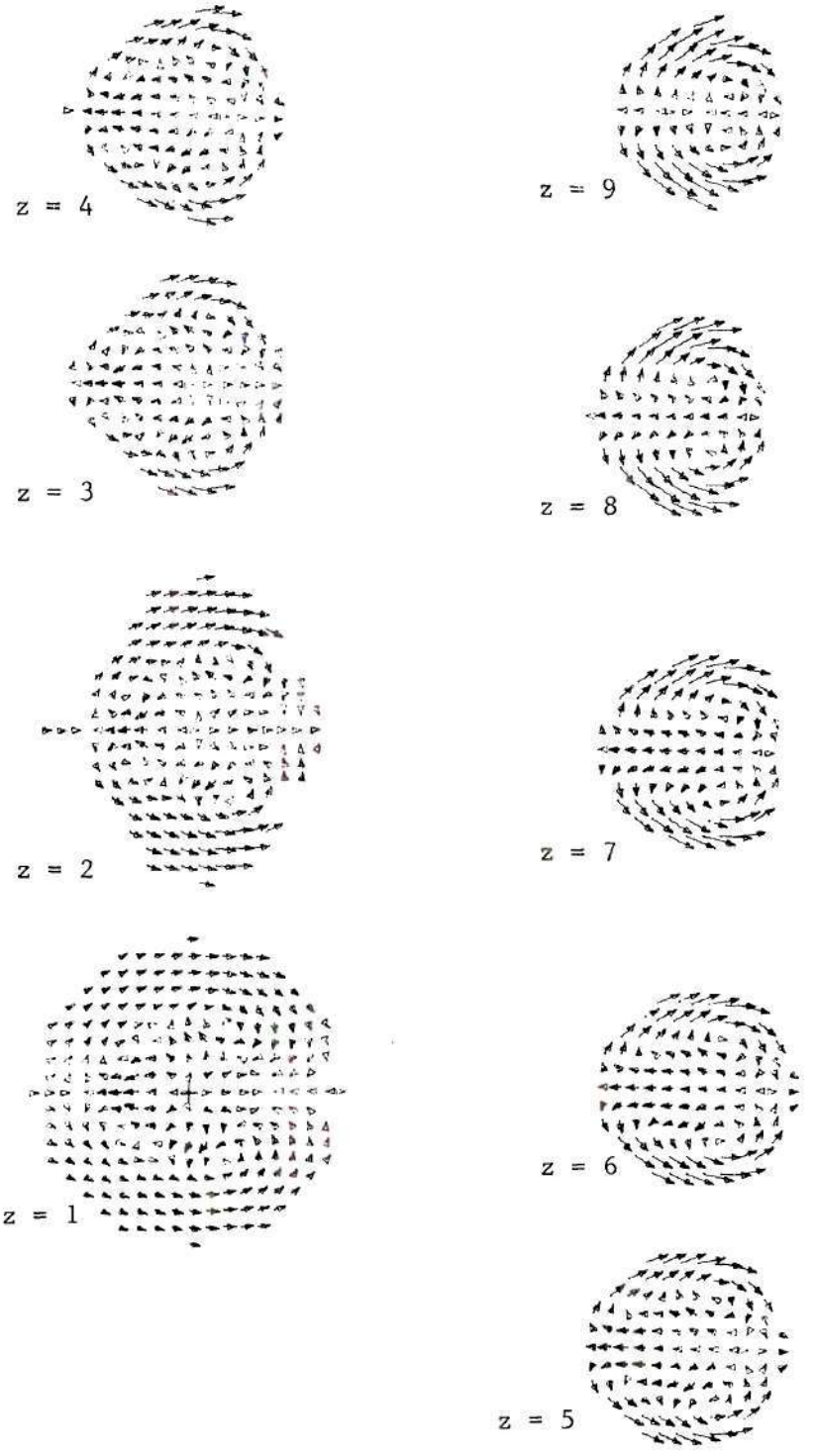

(c) T = 1.40

Figure 43. (cont.)

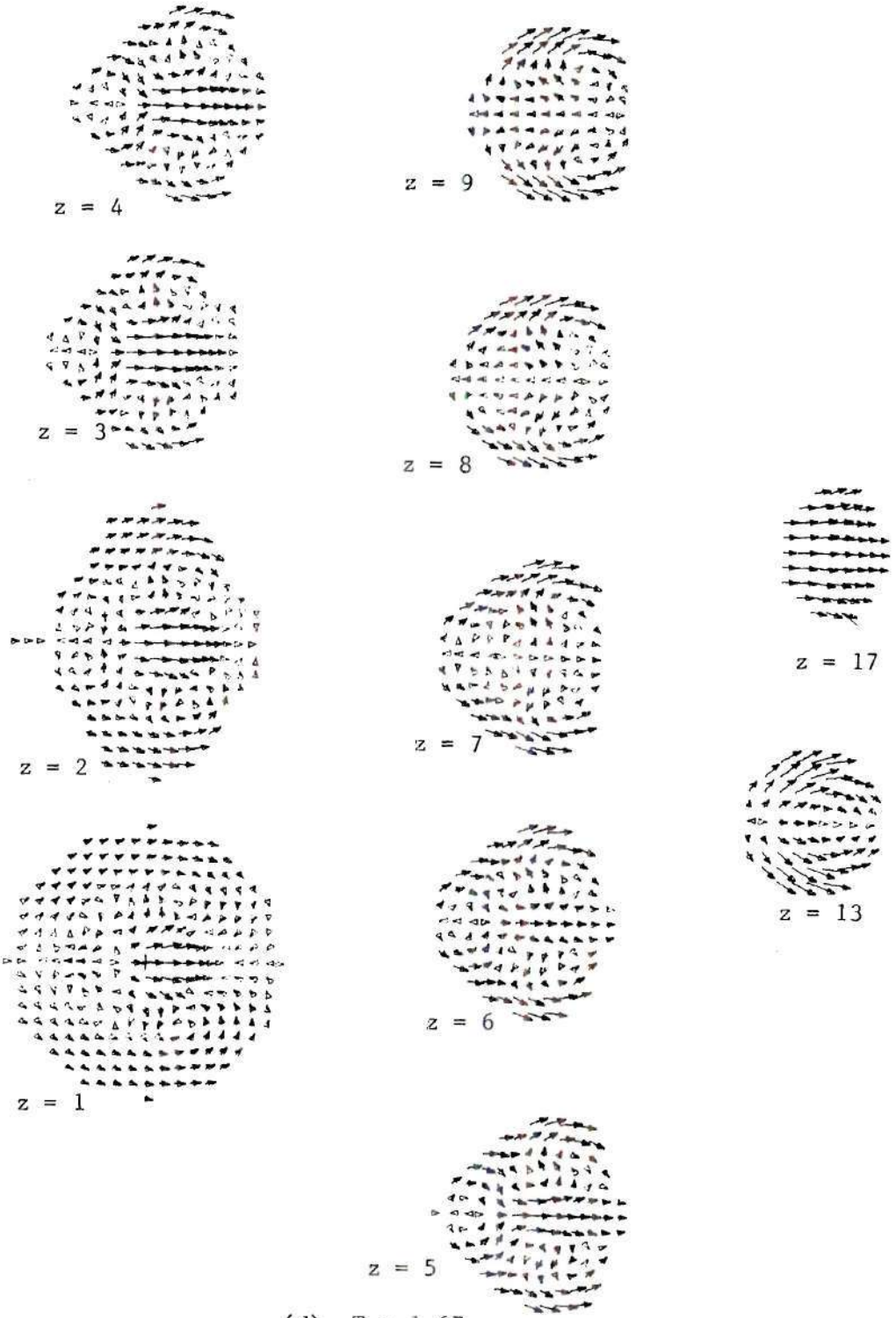

(d) T = 1.67

Figure 43. (cont.)

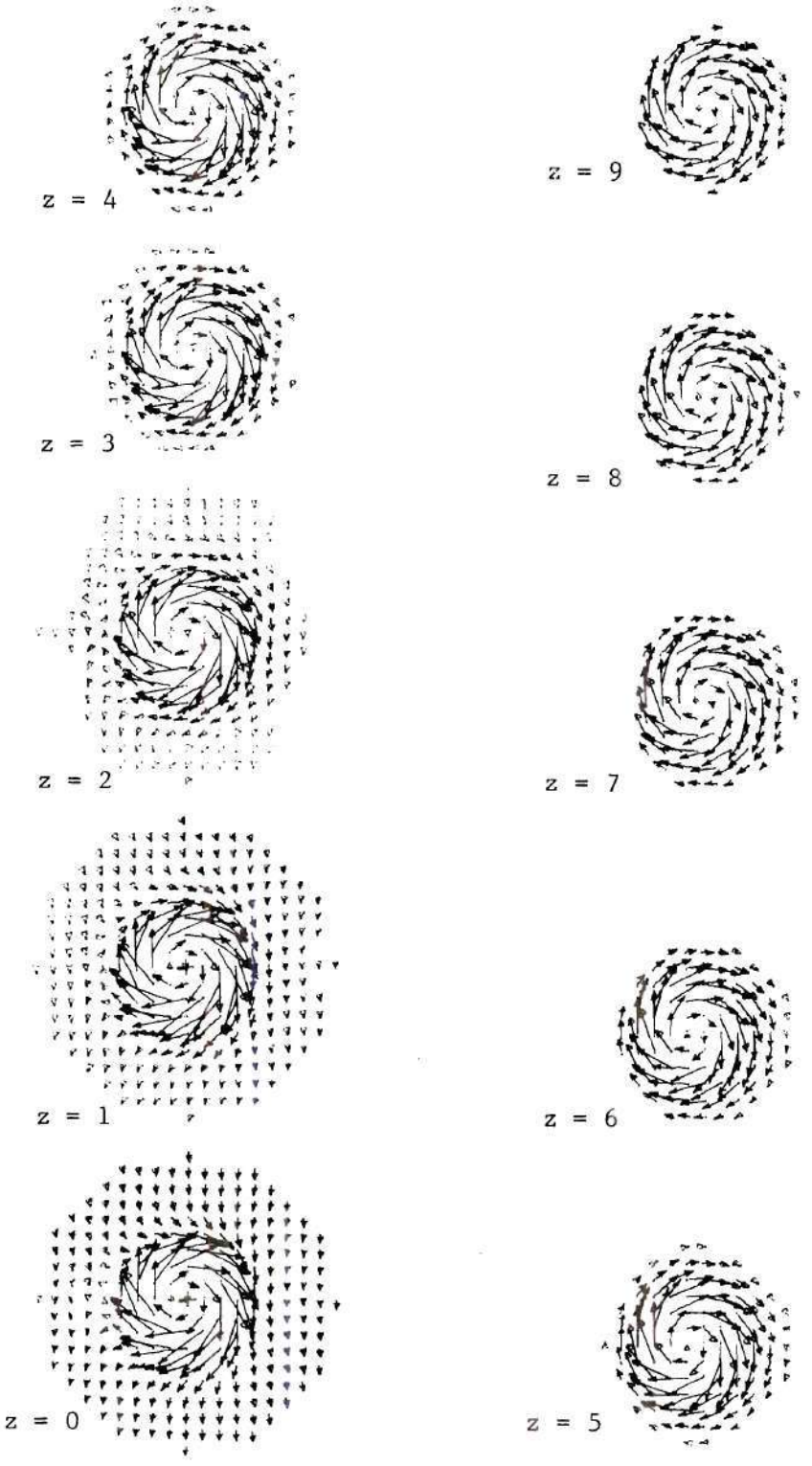

(a) T = 0.67

Figure 44. Horizontal Vorticity Vectors - Start from Cylindrical Discontinuity (V_r = 8) - Eight Step Start, Δt = 0.1 - R = 12

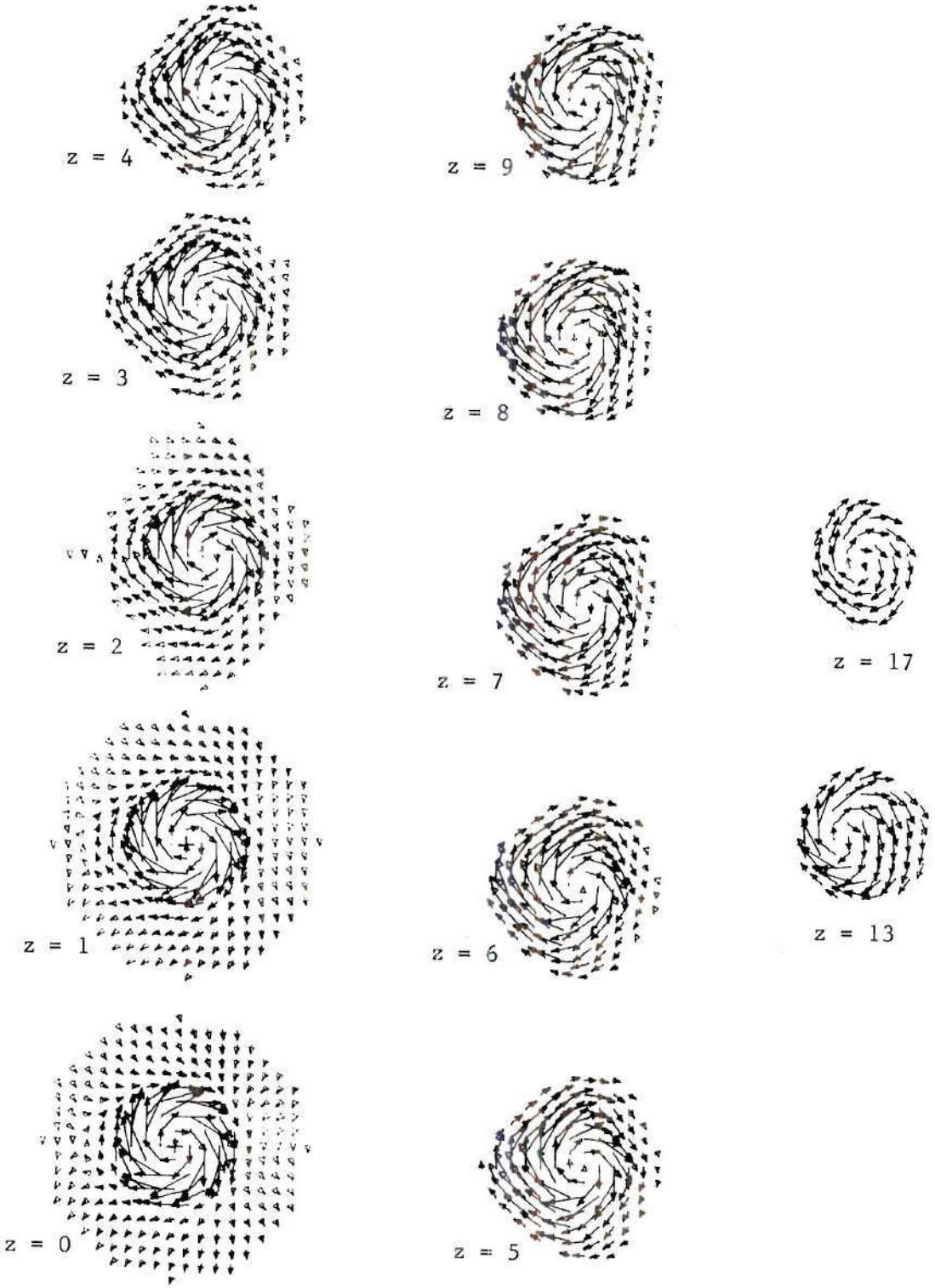

(b) T = 1.67

Figure 44. (cont.)

z = 4

z = 9

z = 3

z = 8

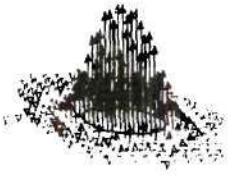

z = 2

z = 7

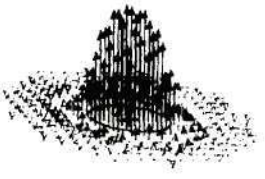

z = 1

z = 6

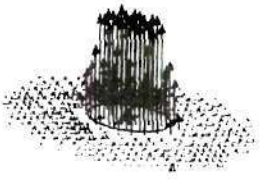

z = 0

z = 5

(a) T = 0.67

Figure 45. Vertical Velocity Vectors - Start from Cylindrical Discontinuity (V_r = 8) - Eight Step Start, Δt = 0.1 - R = 12

z = 4

z = 9

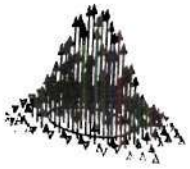

z = 3

z = 8

z = 17

z = 2

z = 7

z = 13

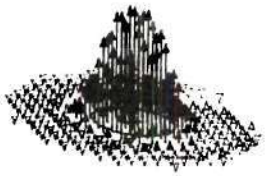

z = 1

z = 6

z = 0

z = 5

(b) T = 1.67

Figure 45. (cont.)

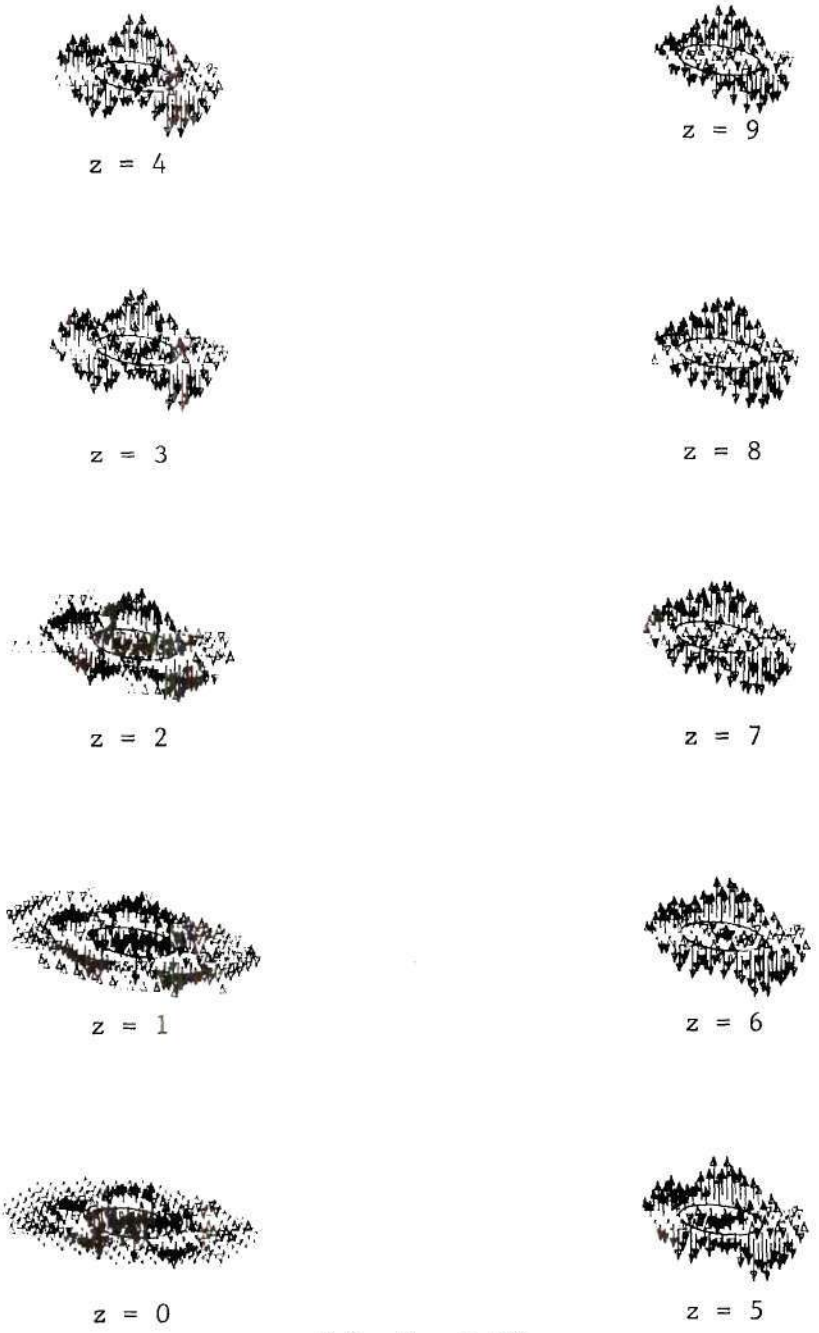

(a) T = 1.40

Figure 46. Vertical Vorticity Vectors - Start from Cylindrical Discontinuity (V_r = 8) - Eight Step Start, Δt = 0.1 - R = 12

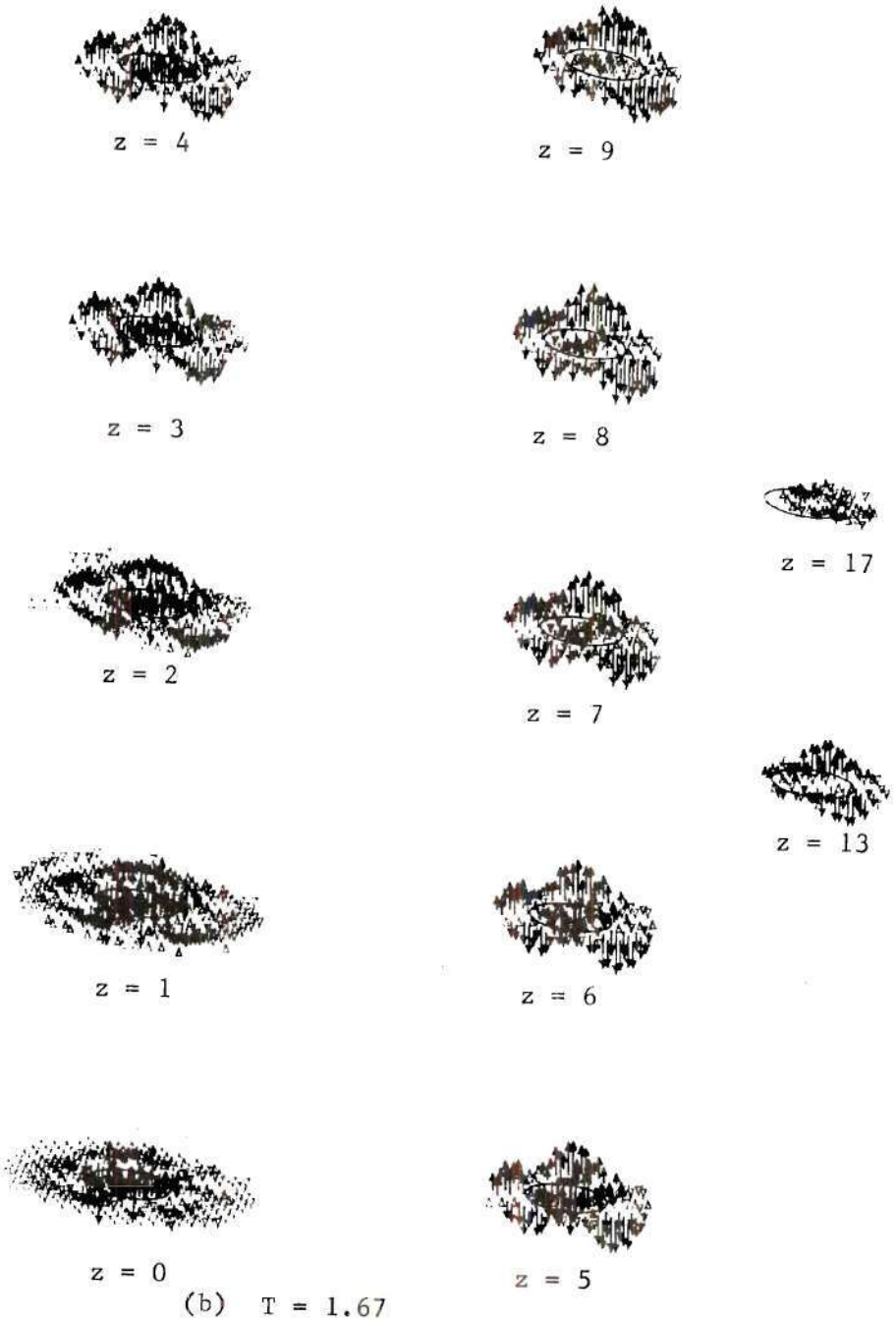

(b) T = 1.67

Figure 46. (cont.)

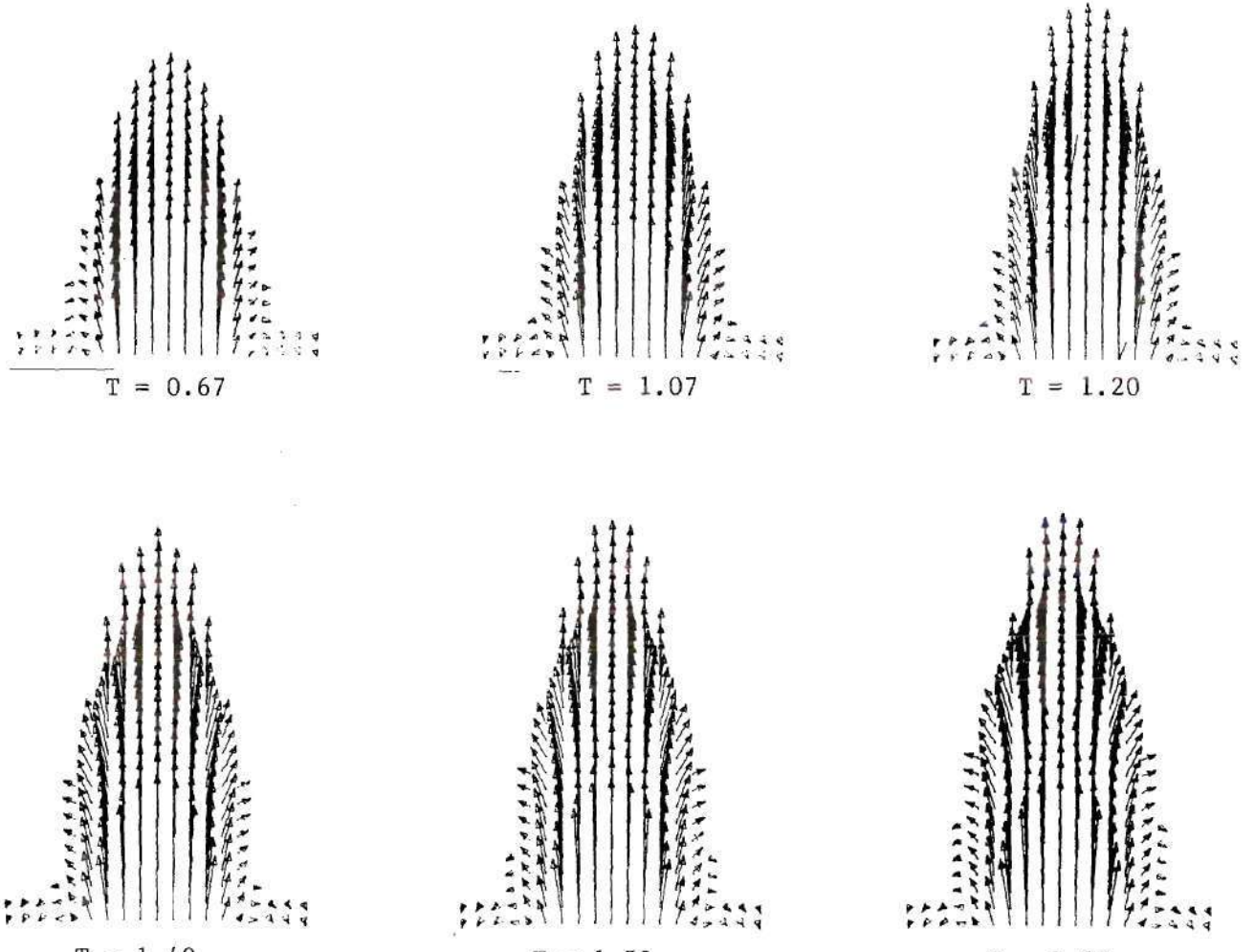

Figure 47. Velocity Vectors in Plane through Exit Center, Perpendicular to Cross-Flow - Start from Cylindrical Discontinuity (V_r = 8) - Eight Step Start, Δt = 0.1 - R = 12

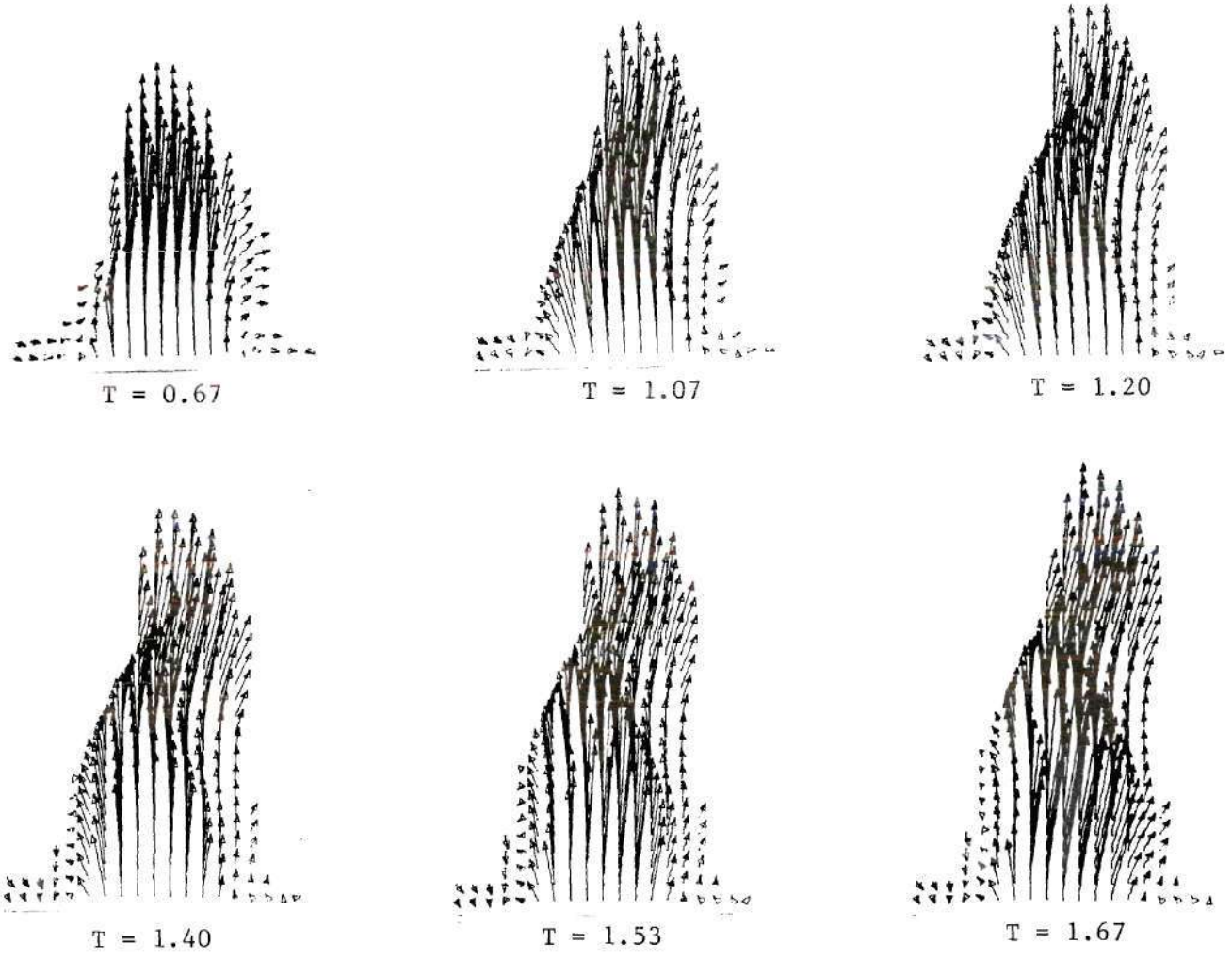

Figure 48. Velocity Vectors in Plane through Exit Center, Parallel to Cross-Flow - Start from Cylindrical Discontinuity (V_r = 8) - Eight Step Start, Δt = 0.1 - R = 12

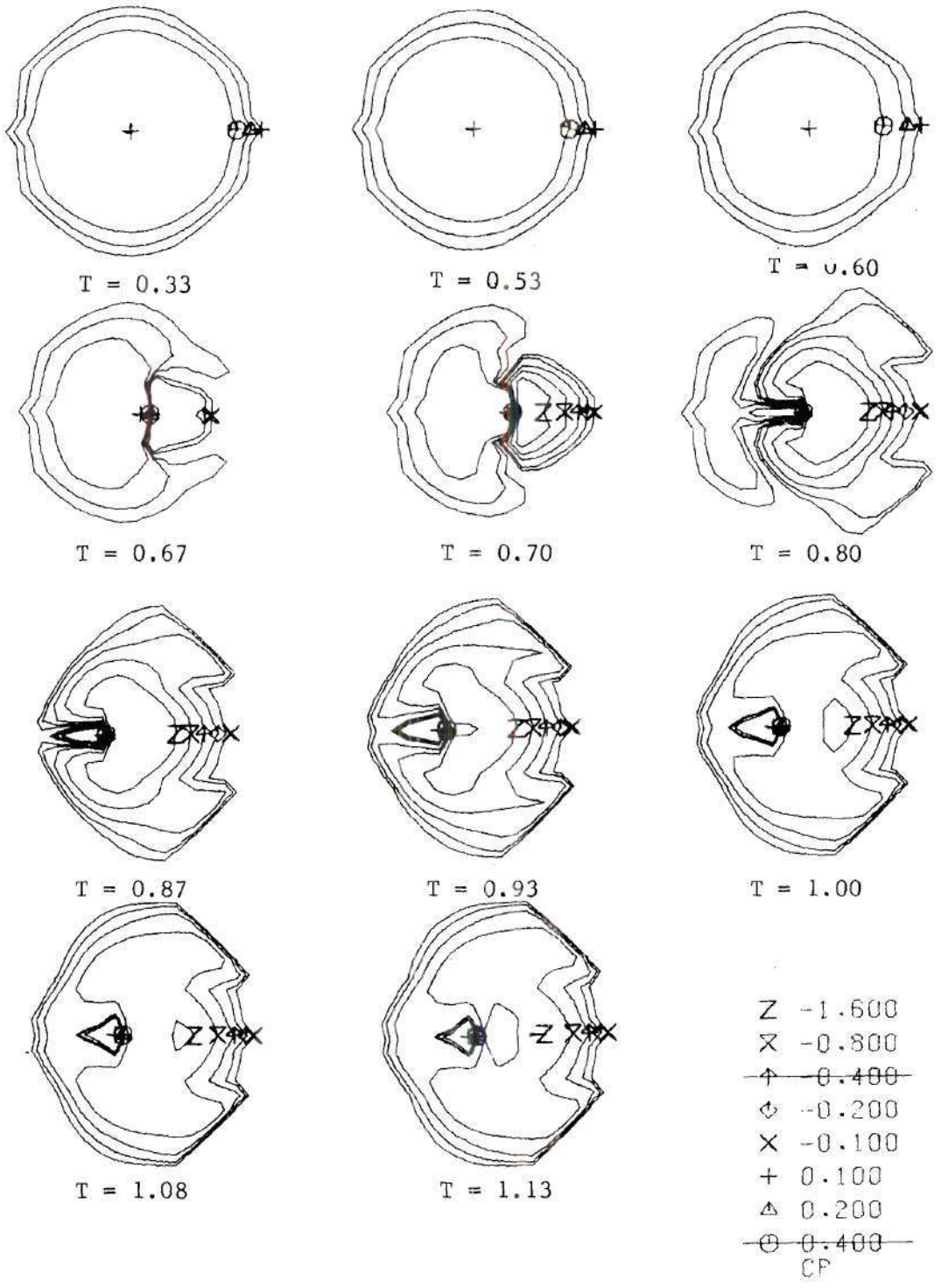

Figure 49. Surface Pressure Contours - Start from Opening of Jet Exit (V_r = 8) - 32 Step Gradual Start, Δt = 0.05 - R = 12

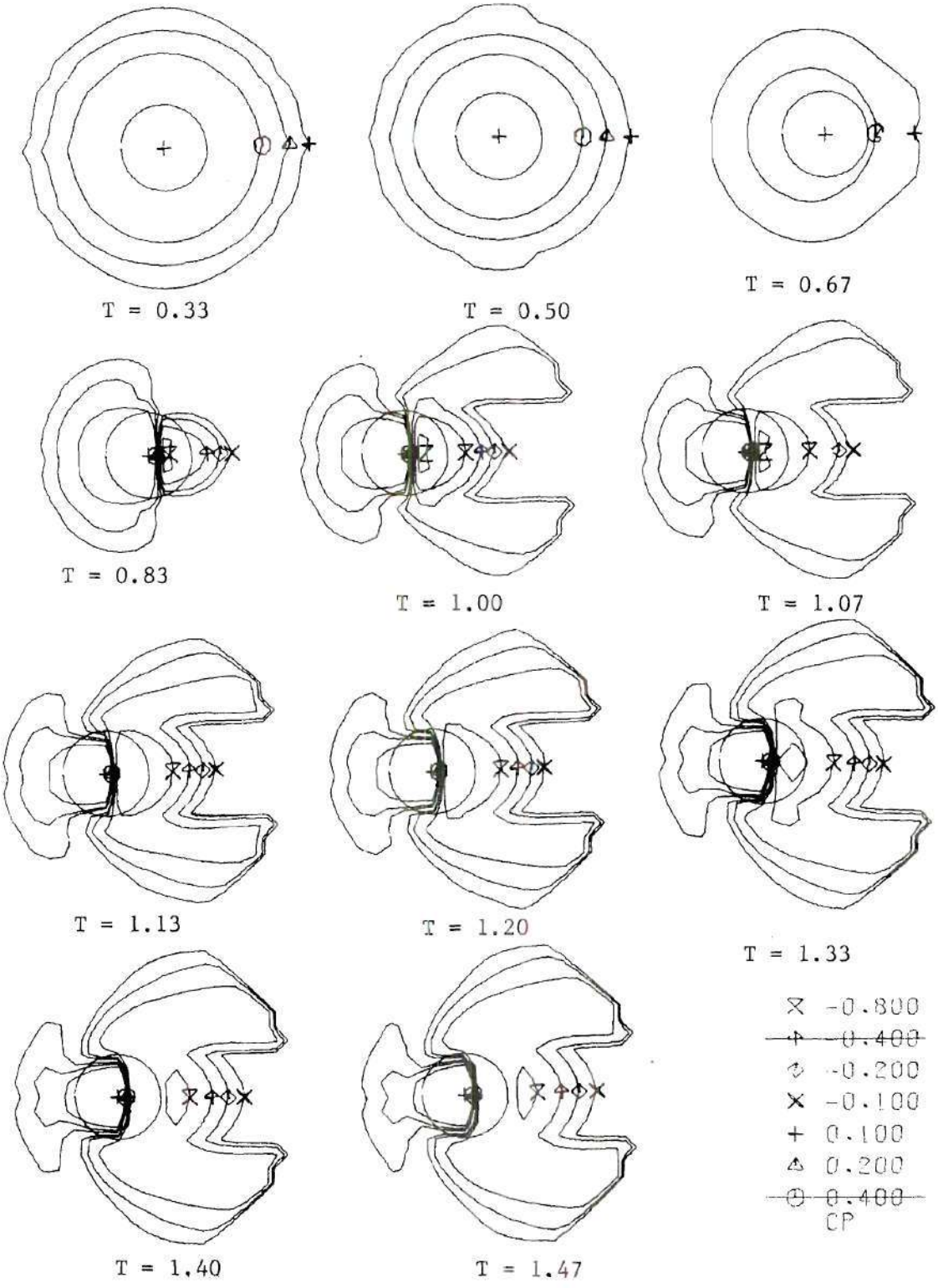

Figure 50. Surface Pressure Contours - Start from Opening of Jet Exit (V_r = 4) - 16 Step Gradual Start, Δt = 0.1 - R = 12

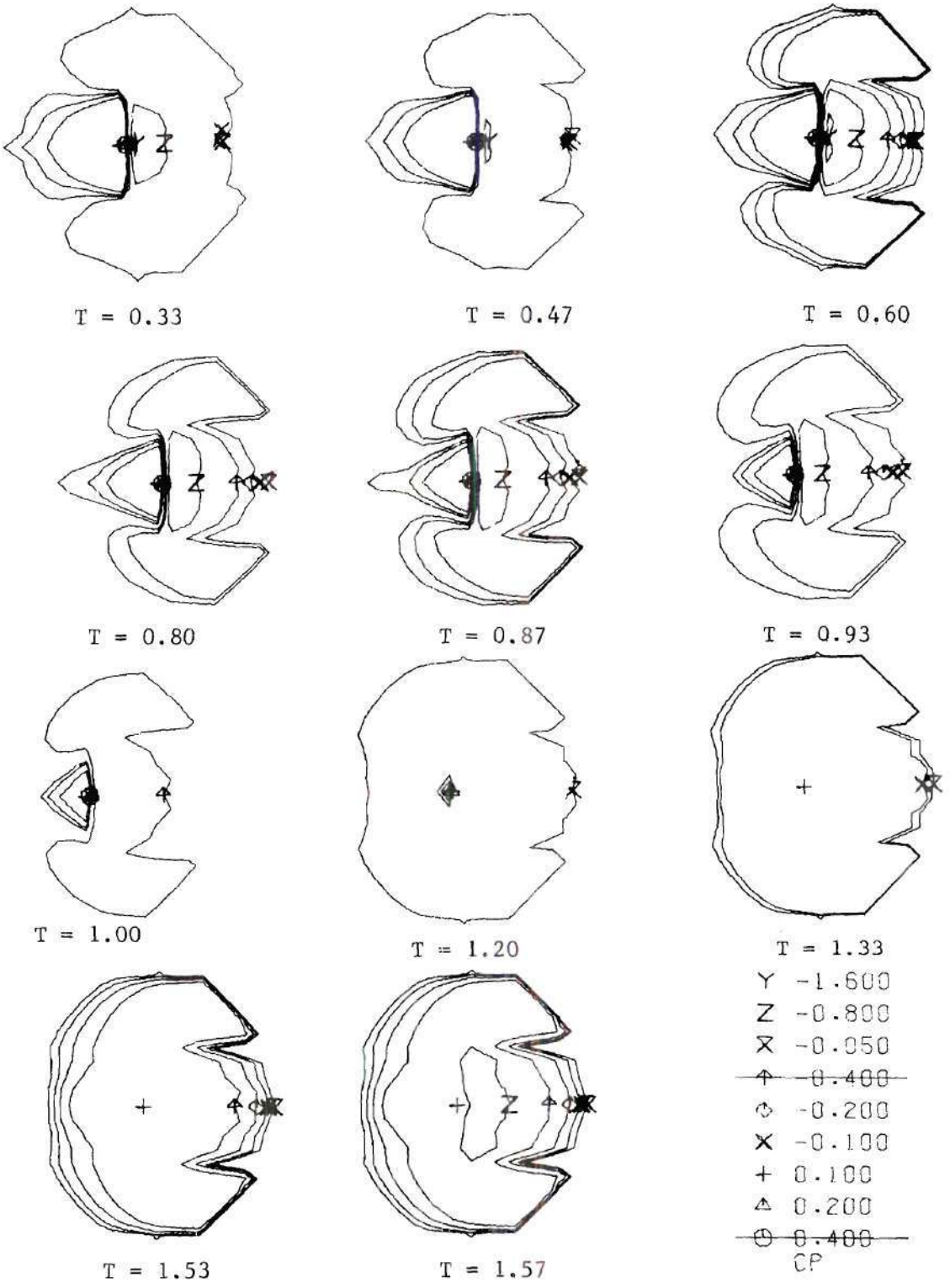

Figure 51. Surface Pressure Contours - Start from Cylindrical Discontinuity (V_r = 8) - Four Step Gradual Start, Δt = 0.2 - R = 12

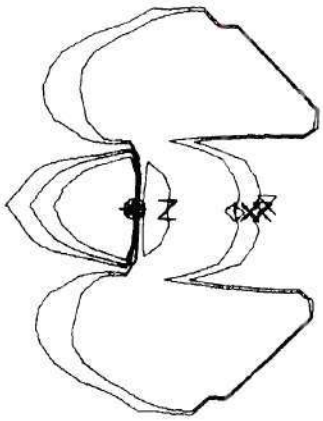

T = 0.67

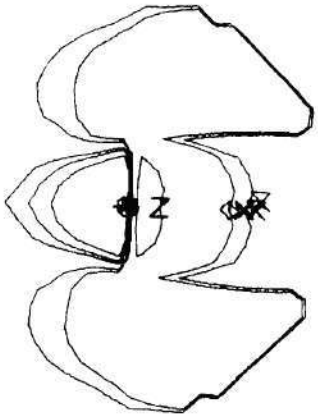

T = 0.80

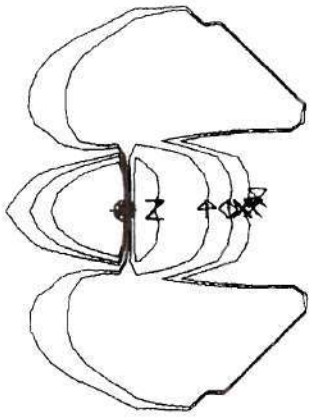

T = 0.93

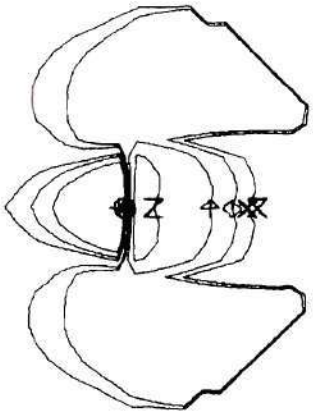

T = 1.07

Z -0.800
X -0.050
-0.400
-0.200
-0.100
+ 0.100
0.200
0.400
CP

Figure 52. Surface Pressure Contours - Start from Cylindrical Discontinuity (V_r = 4) - Four Step Start, Δt = 0.2 - R = 12

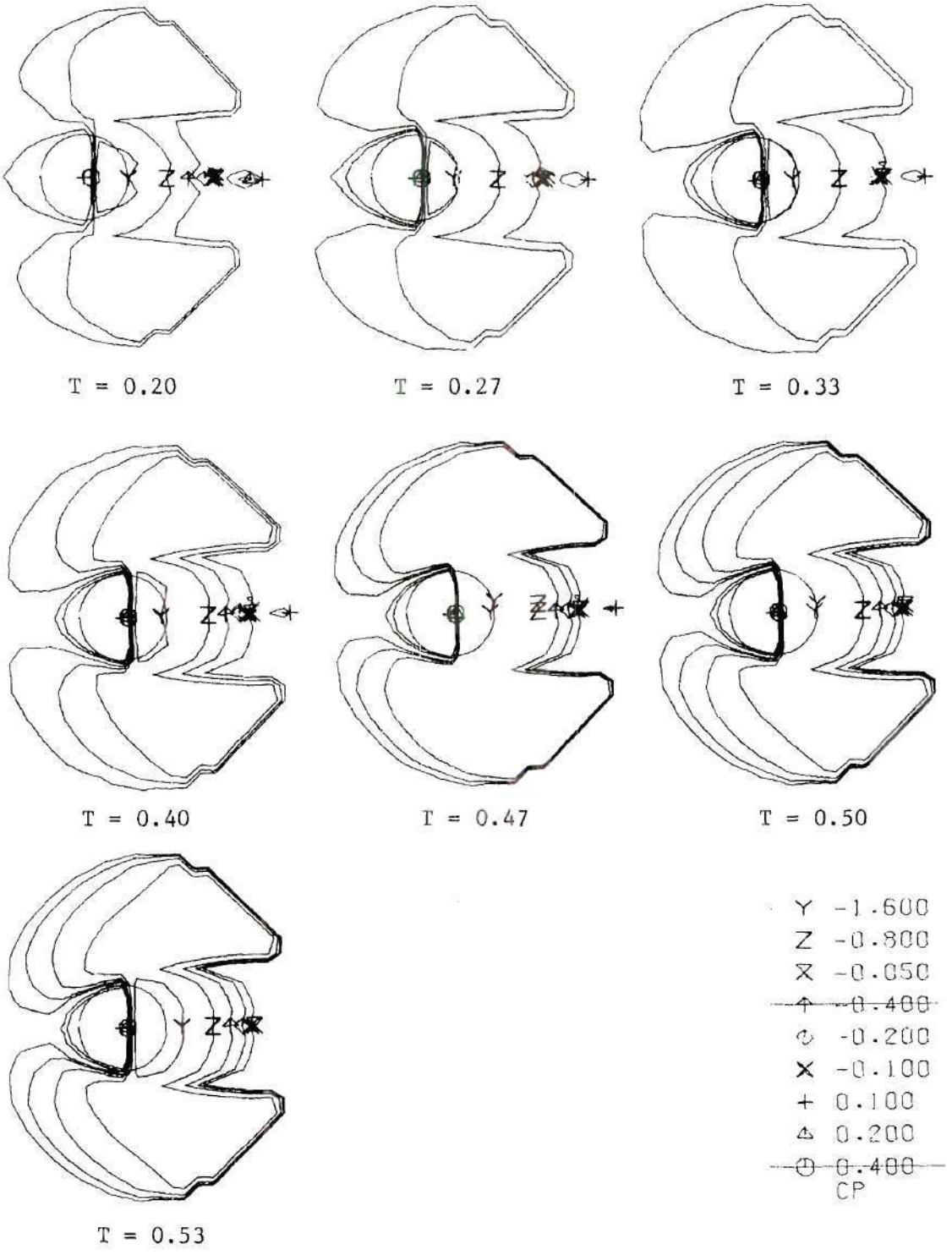

Figure 53. Surface Pressure Contours - Start from Cylindrical Discontinuity (V_r = 8) - Four Step Gradual Start, Δt = 0.1 - R = 6

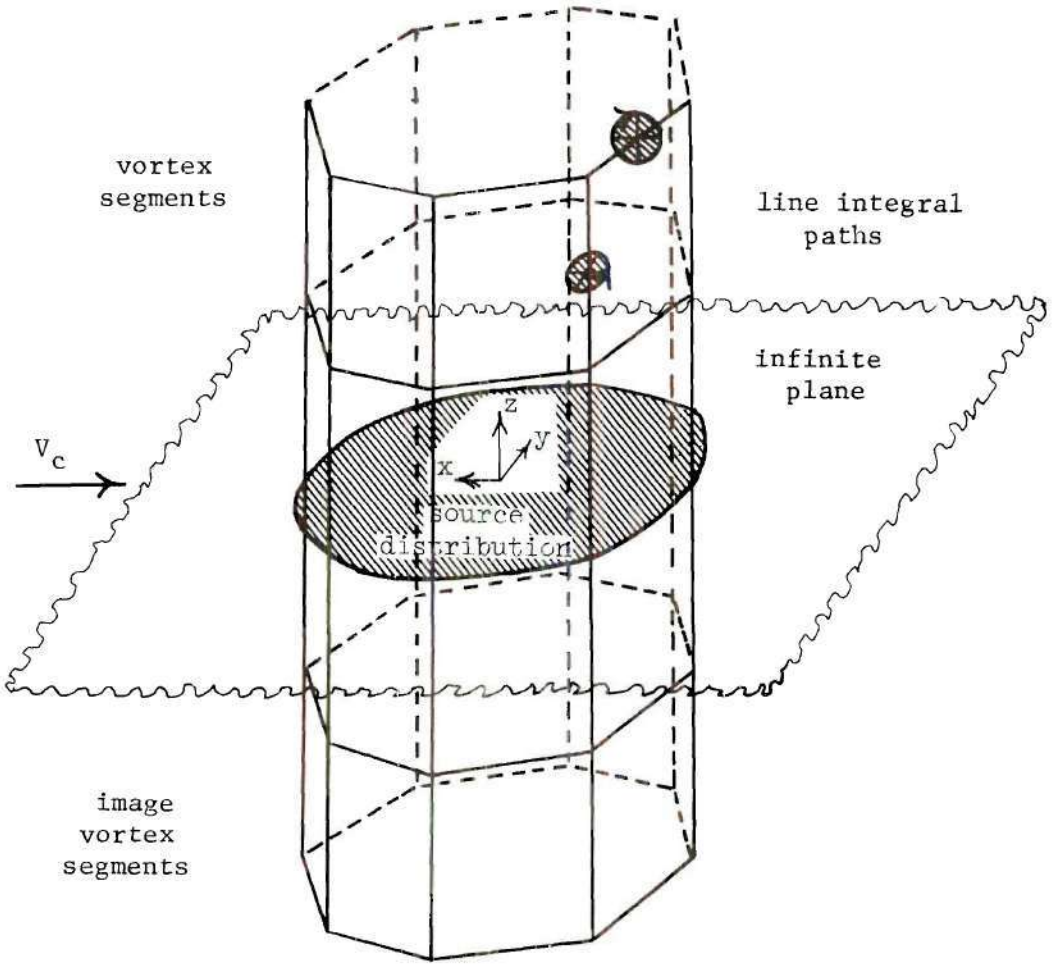

Figure 54. Initial Vortex Lattice Configuration

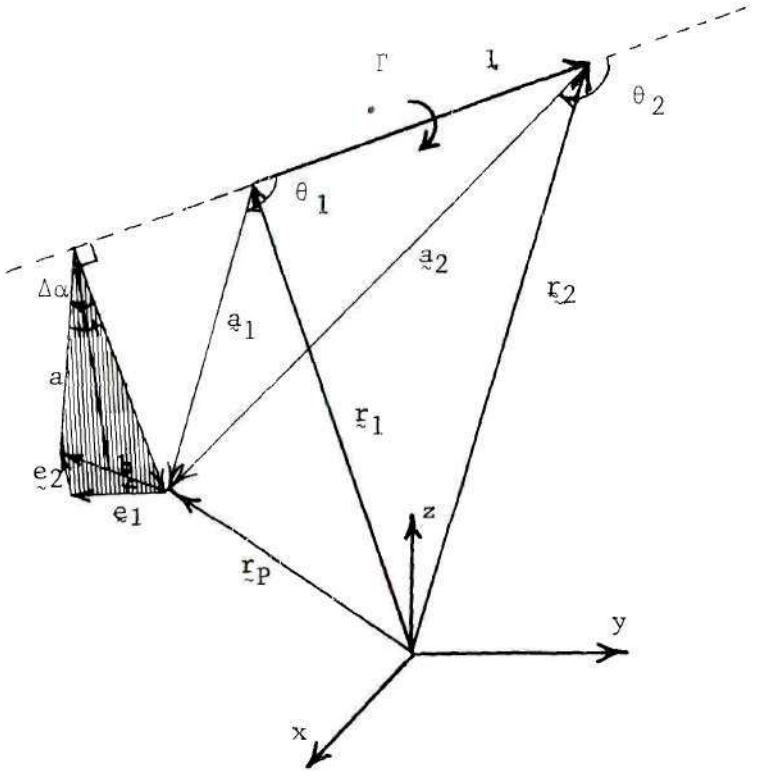

Figure 55. Velocity Induced by Vortex Segment

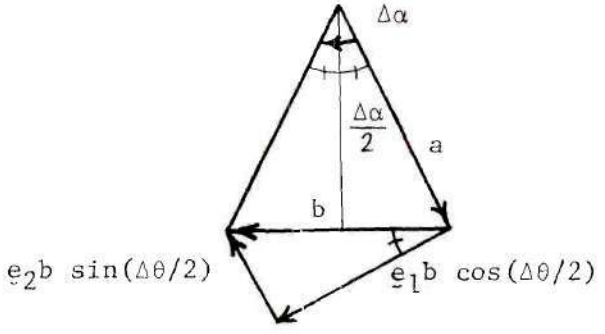

Figure 56. Correction for Spiralling Effect of Vortex Induced Velocity

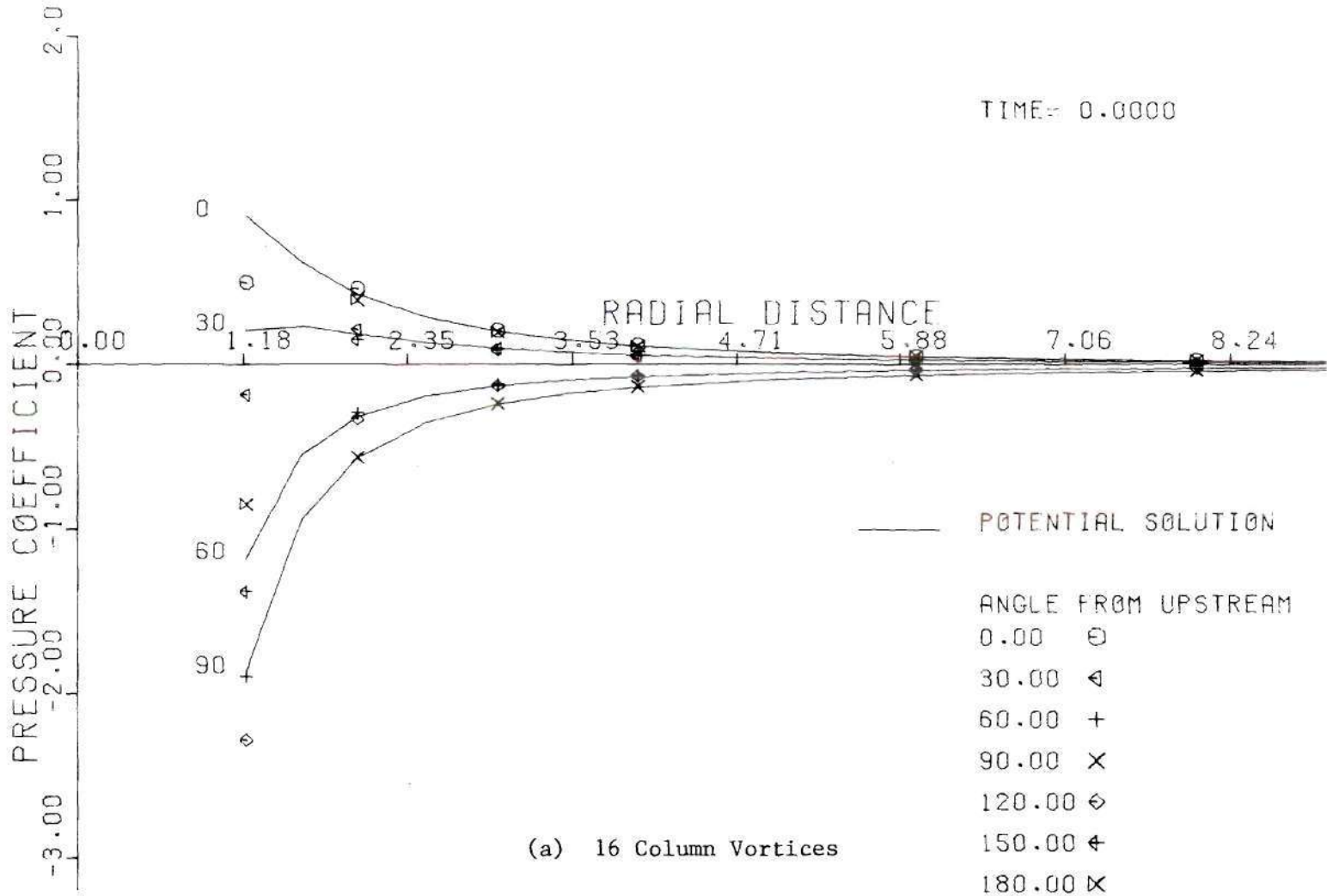

(a) 16 Column Vortices

Figure 57. Initial Surface Pressure Distribution (V_r = 8) - Vortex Lattice Model, Initial Ring Spacing = 0.5 Exit Radius

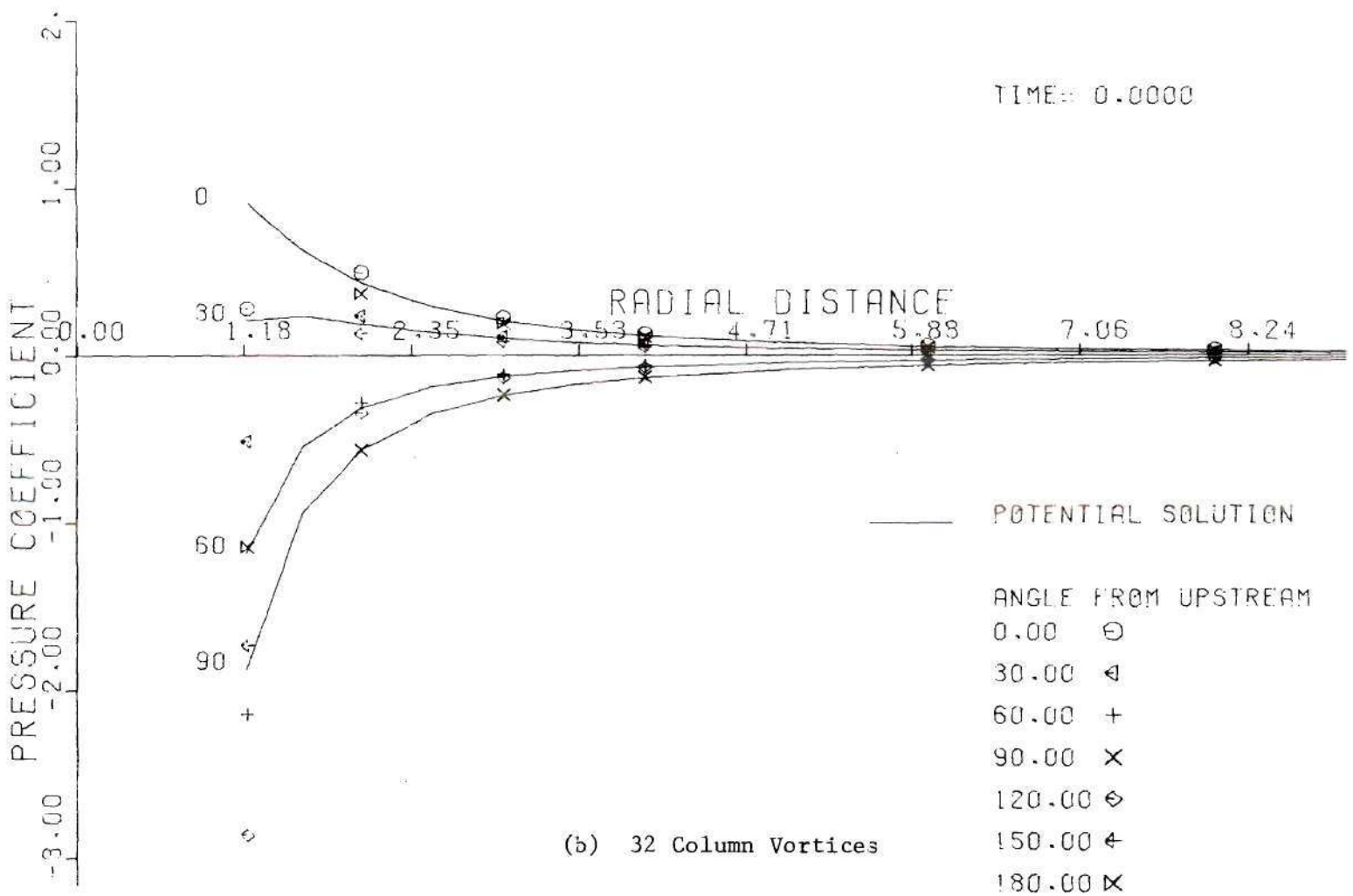

(b) 32 Column Vortices

Figure 57. (cont.)

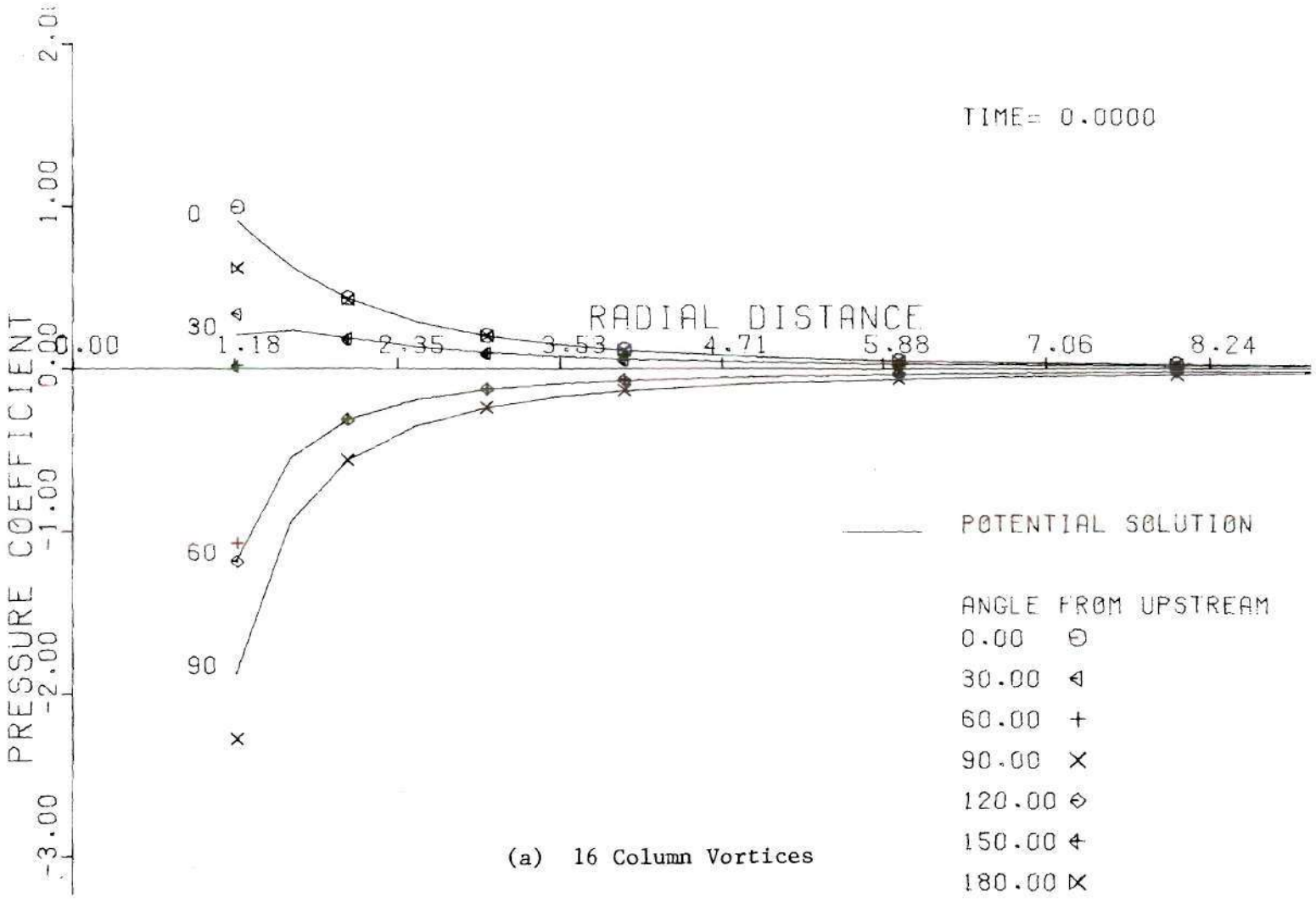

(a) 16 Column Vortices

Figure 58. Initial Surface Pressure Distribution (V_r = 8) - Vortex Lattice Model, Initial Ring Spacing = 0.25 Exit Radius

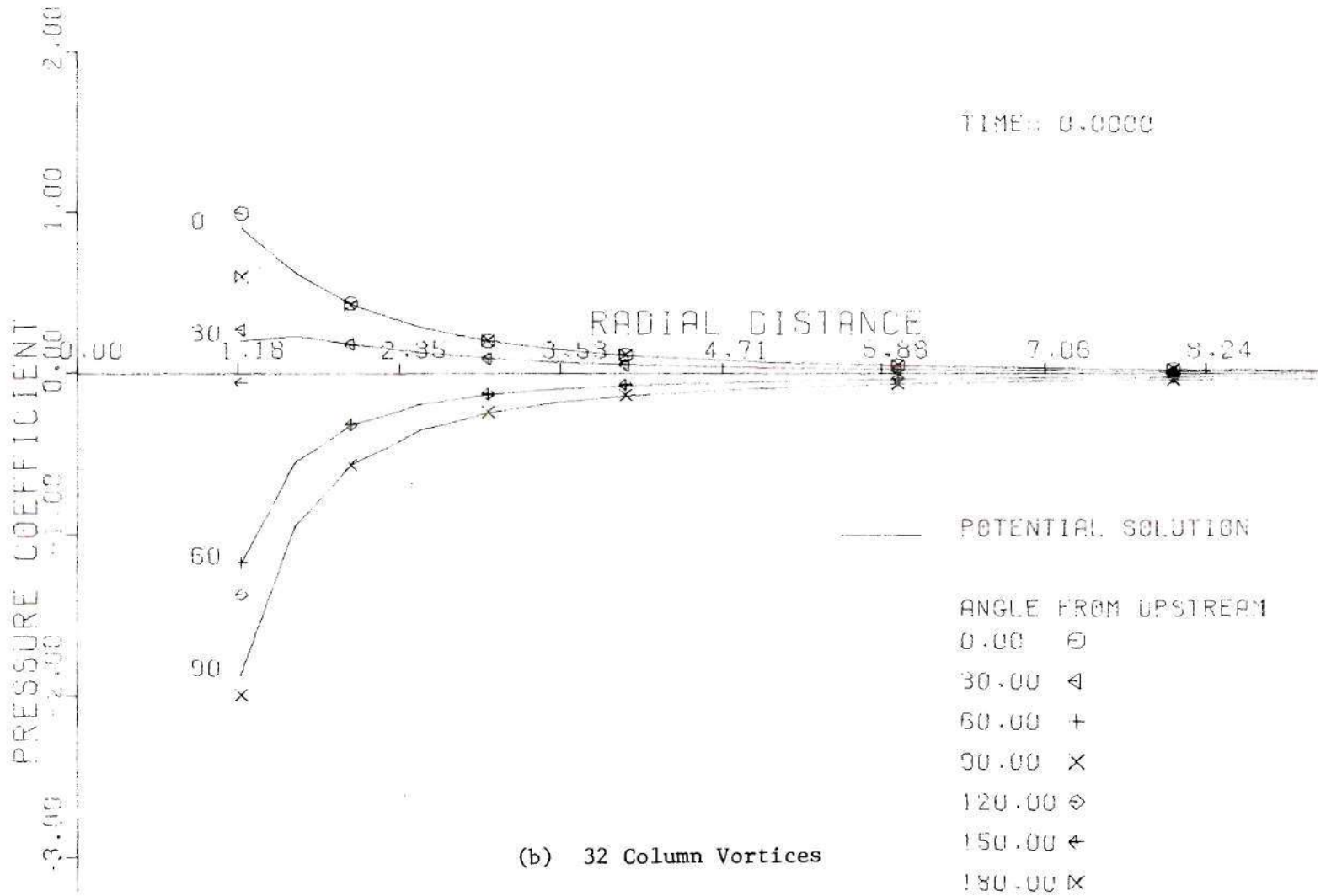

(b) 32 Column Vortices

Figure 58. (cont.)

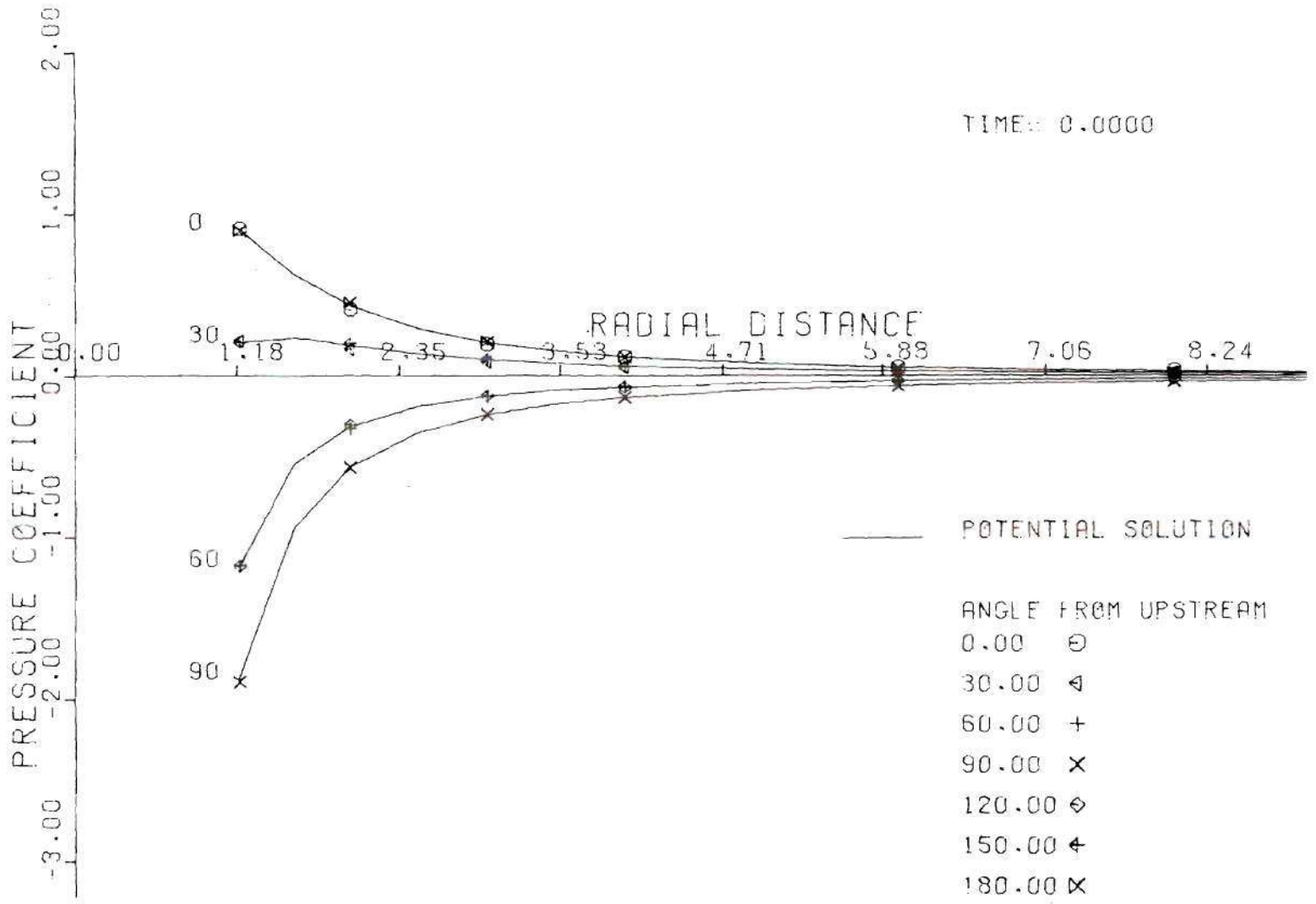

Figure 59. Initial Surface Pressure Distribution (V_r = 8) - Vortex Lattice Model, Initial Ring Spacing = 0.125 Exit Radius - 32 Column Vortices

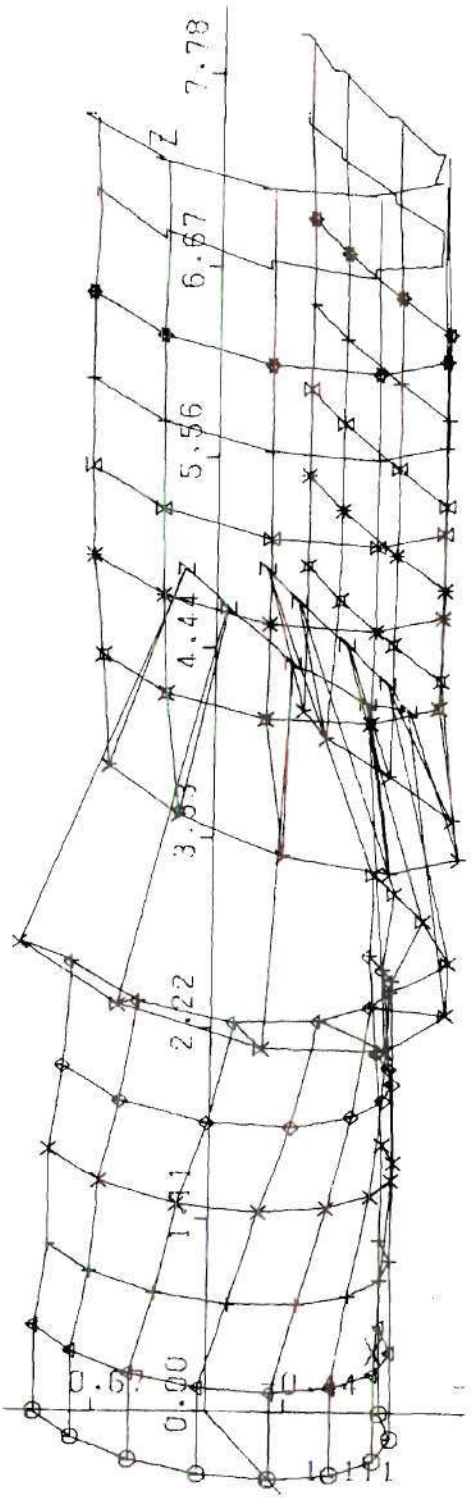

Figure 60. Roll-Up of Vortex Lattice due to Normal Perturbation (V_r = 8) - Vortex Lattice Model, Initial Ring Spacing = 0.5 Exit Radius, 16 Column Vortices - T = 0.905

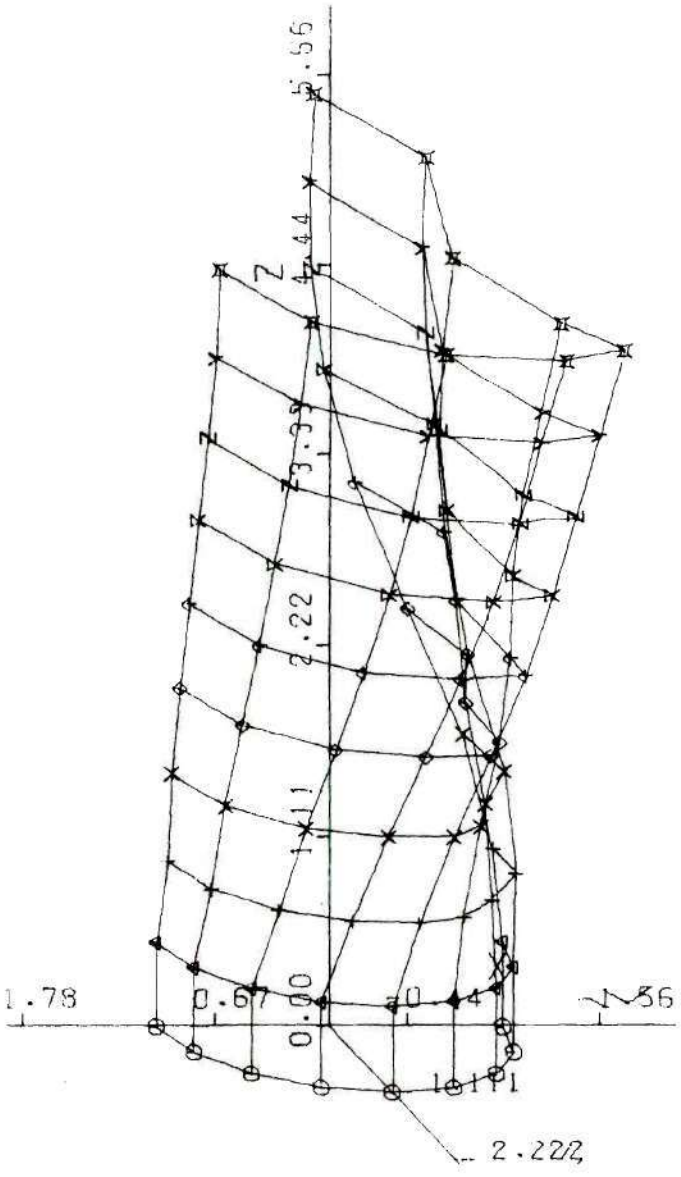

Vortex Lattice - Perspective View

Figure 61. Vortex Lattice Model (V_r = 8) - Initial Ring Spacing = 0.5 Exit Radius, 16 Column Vortices - T = 1.207

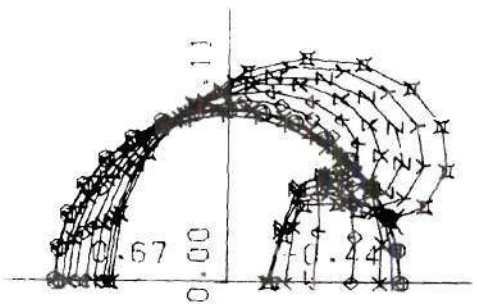

(a) Vortex Lattice - Top View

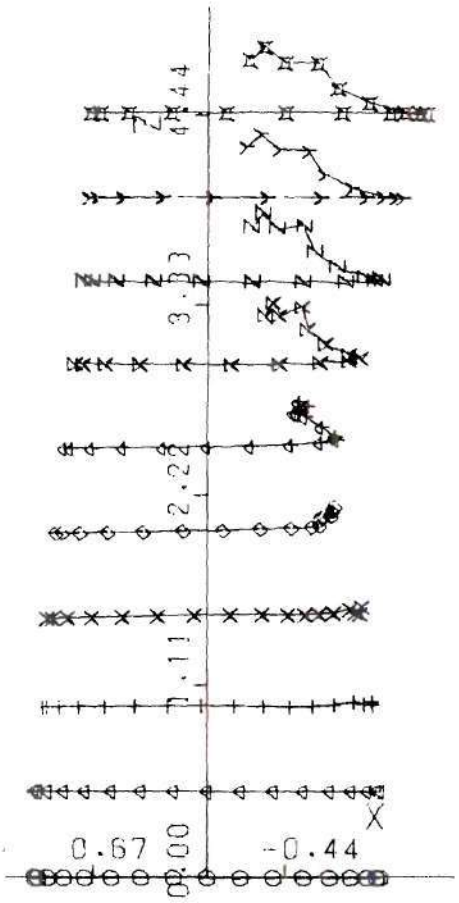

(b) Vortex Lattice - Side View

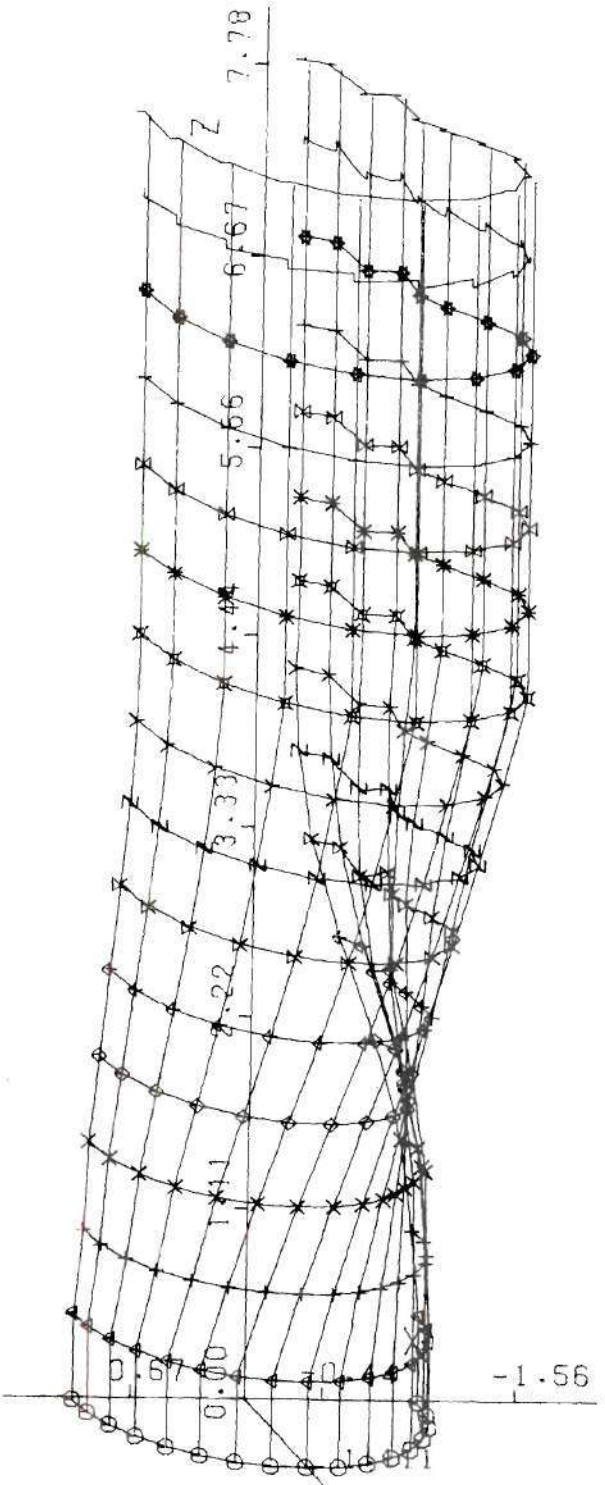

(c) Vortex Lattice - Perspective View

Figure 62. Vortex Lattice Model (V_r = 8) - Initial Ring Spacing = 0.5 Exit Radius, 32 Column Vortices - T = 1.107

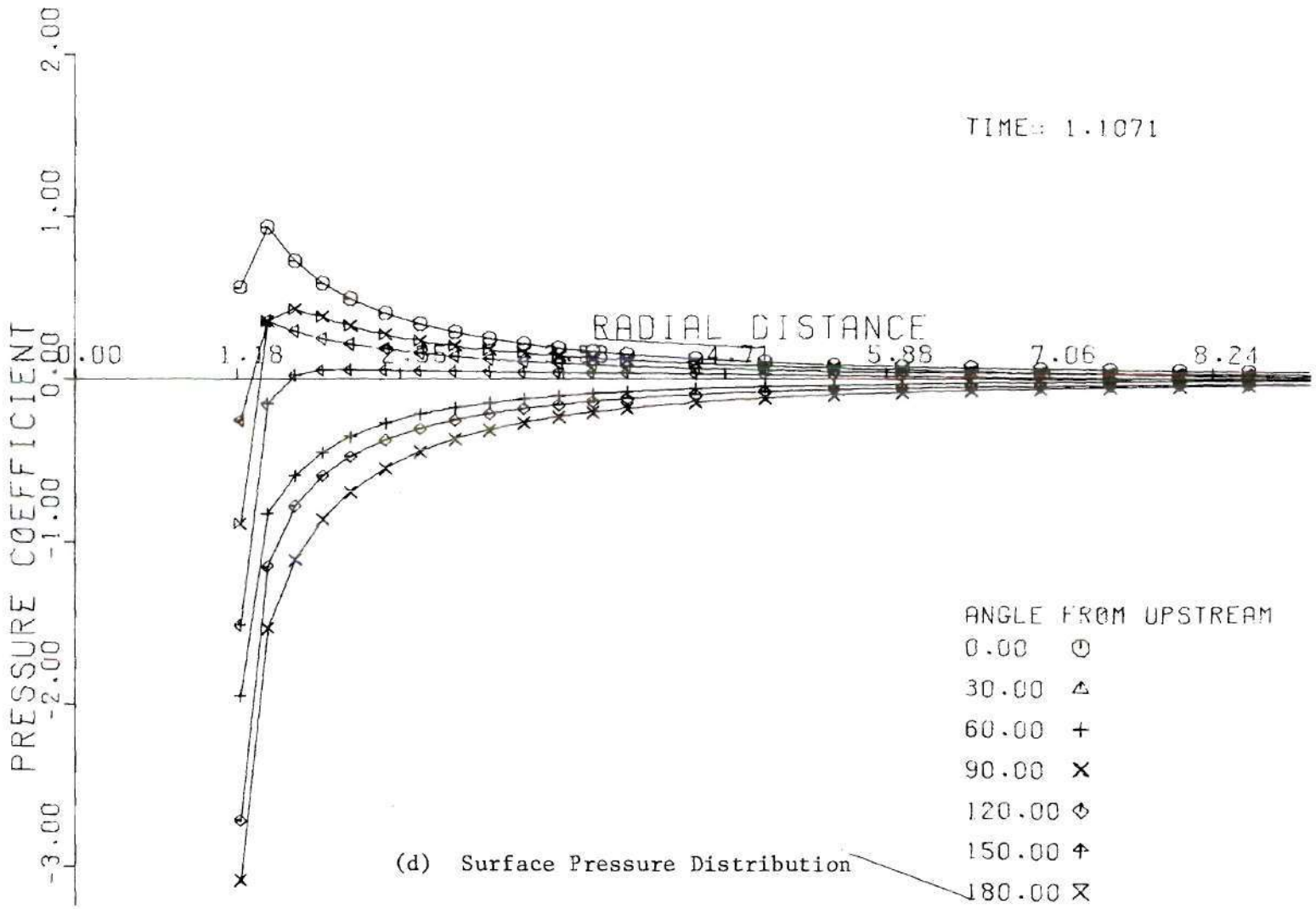

(d) Surface Pressure Distribution

Figure 62. (cont.)

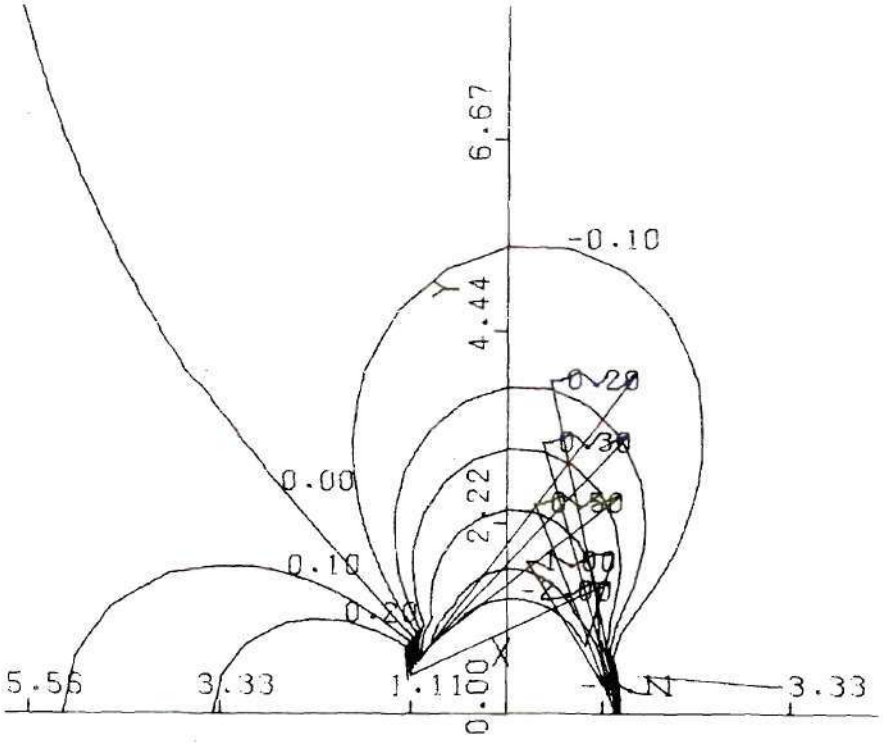

(e) Surface Pressure Contours

Figure 62. (cont.)

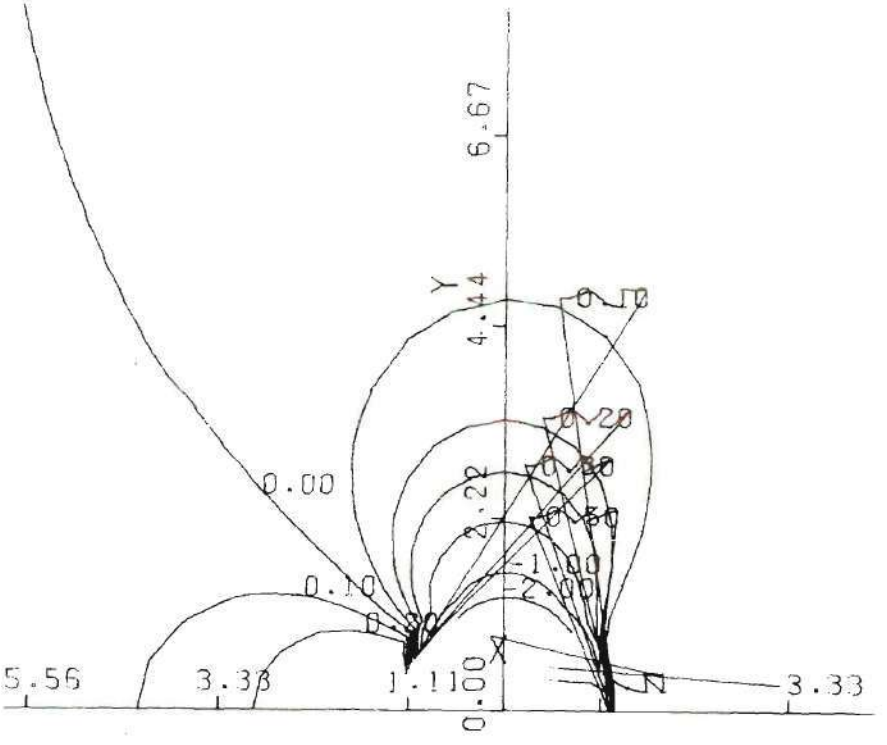

(f) Surface Pressure Contours at T =0.277

Figure 62. (cont.)

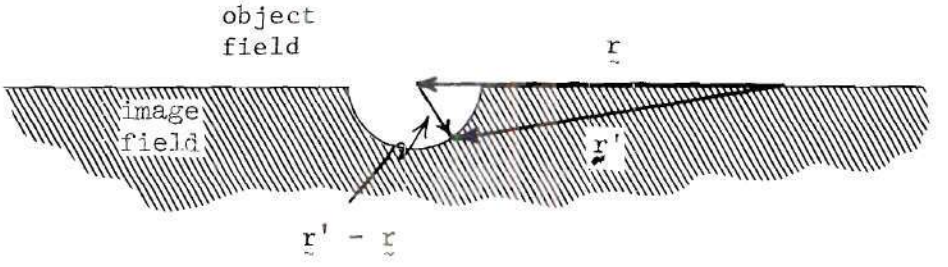

(a) Pole in Object Field

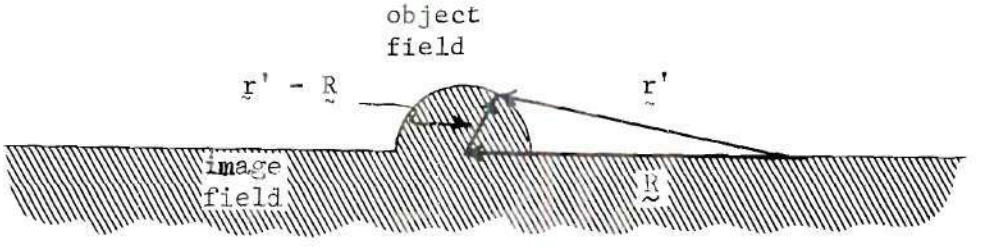

(b) Pole in Image Field

Figure 63. Integration Around Singularity on Jet Exit

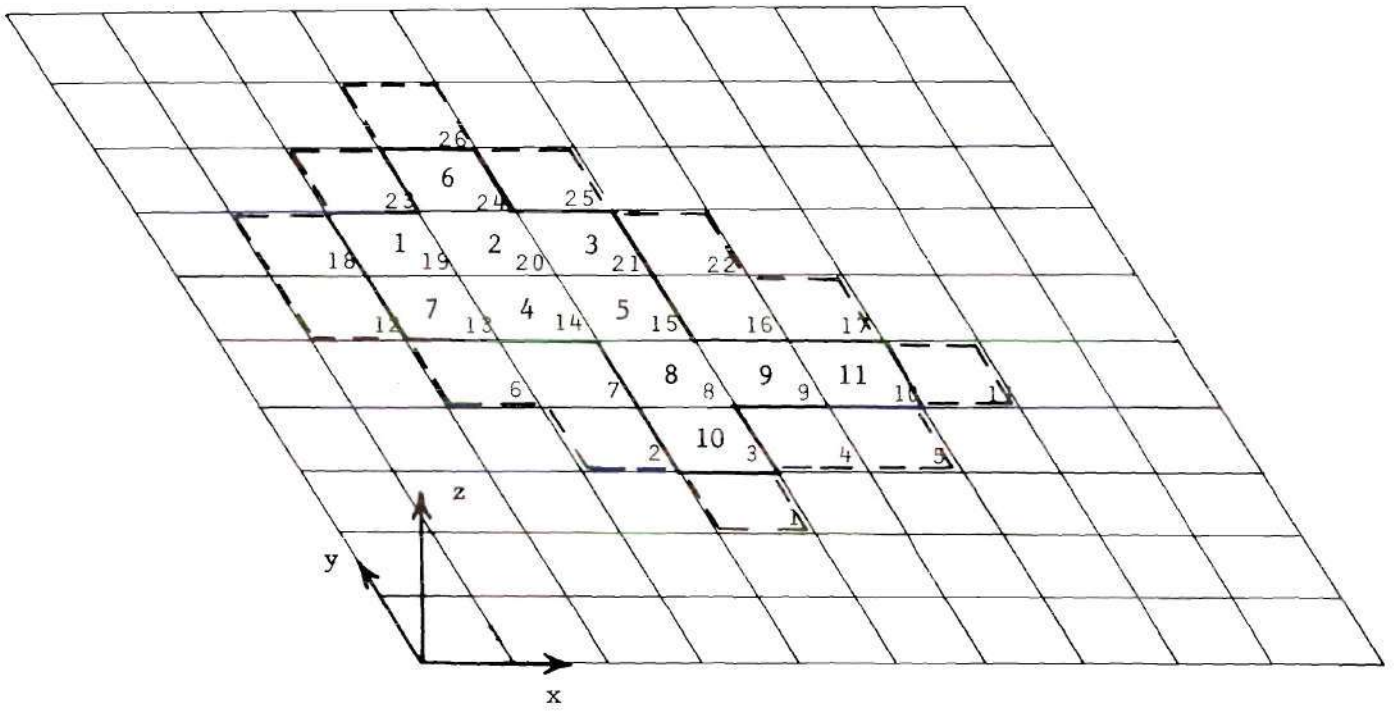

Figure 64. Cataloging of Vortex Cells

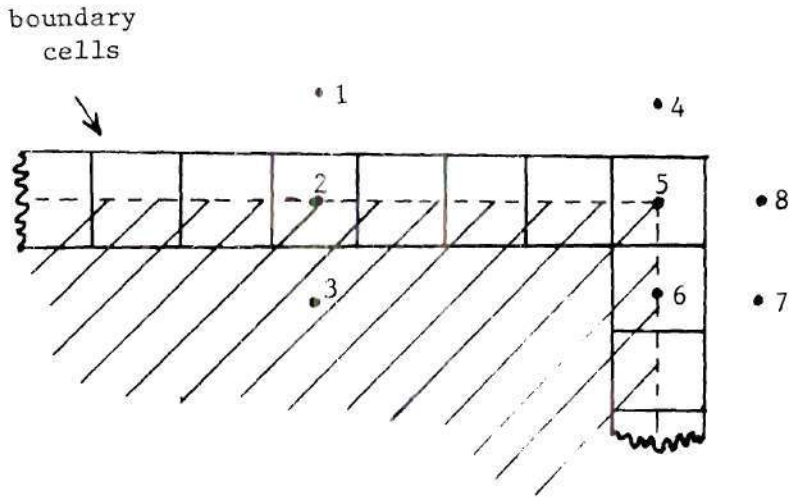

Figure 65. Points Involved in Calculation In, and Adjacent to, Boundary Cells

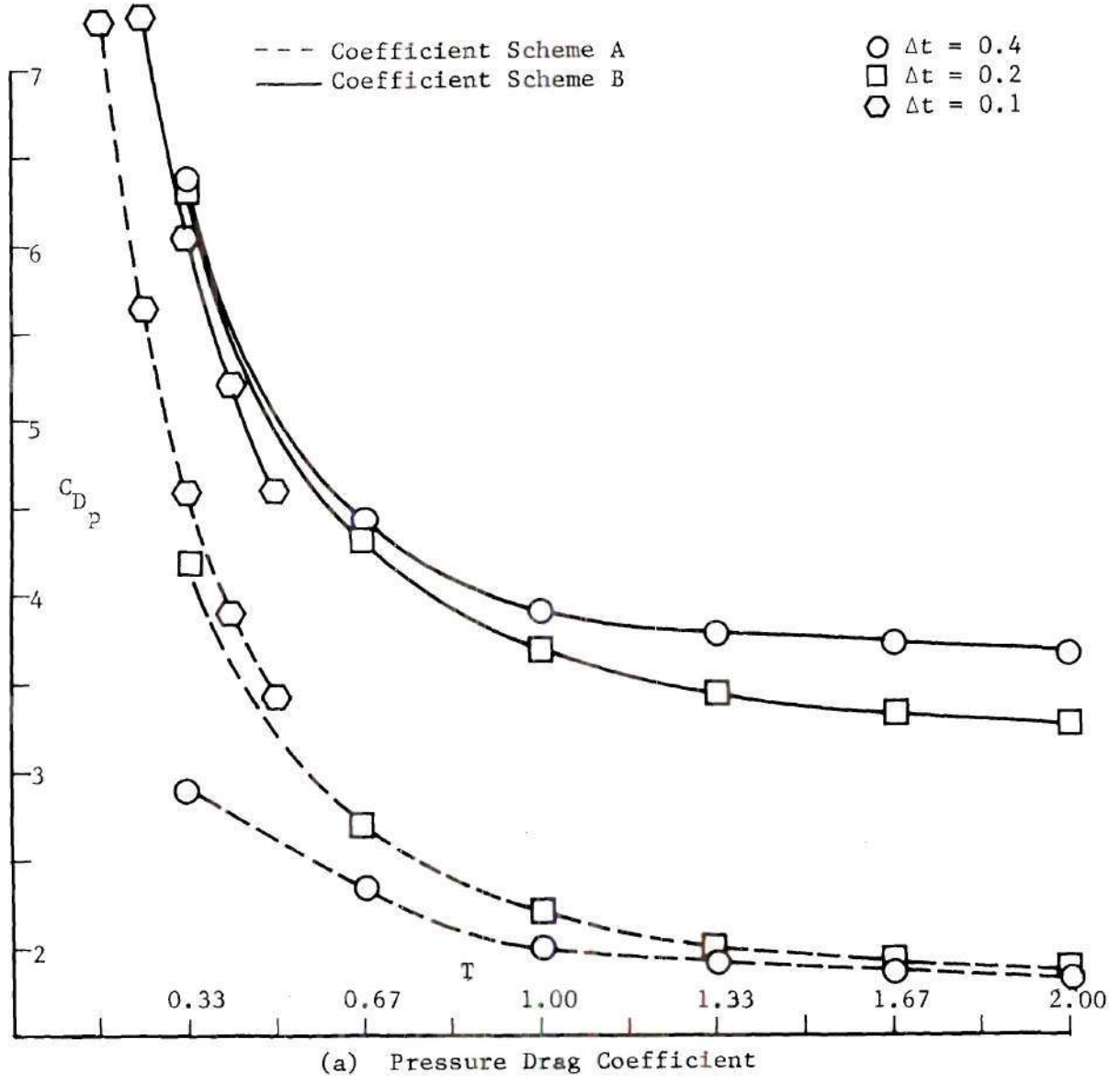

(a) Pressure Drag Coefficient

Figure 66. Comparison of Time Development of Drag Coefficients and Surface Pressure Minimum with Alternate Coefficient Schemes - Circular Cylinder (Scheme CBAC), R = 6

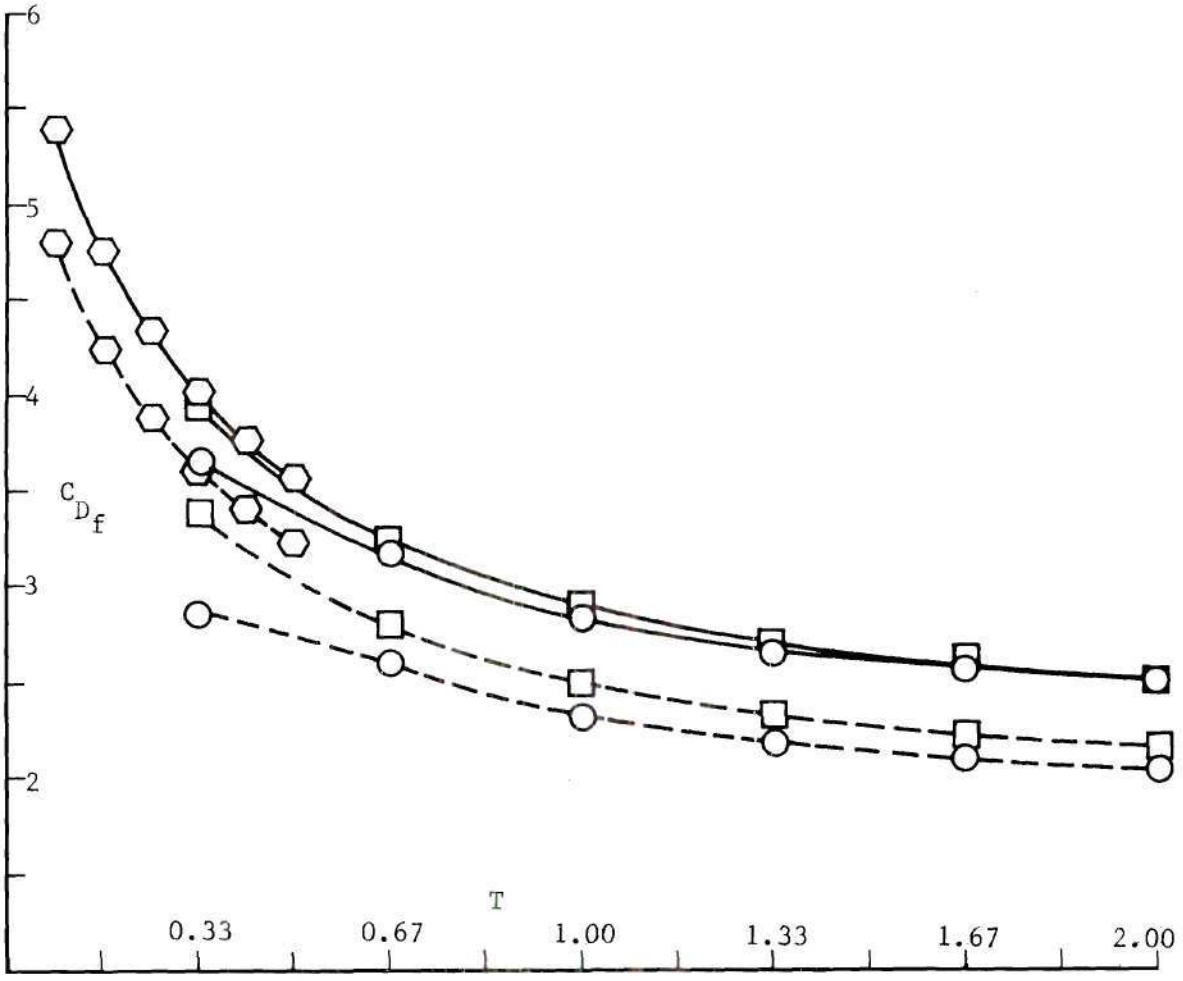

(b) Friction Drag Coefficient

Figure 66. (cont.)

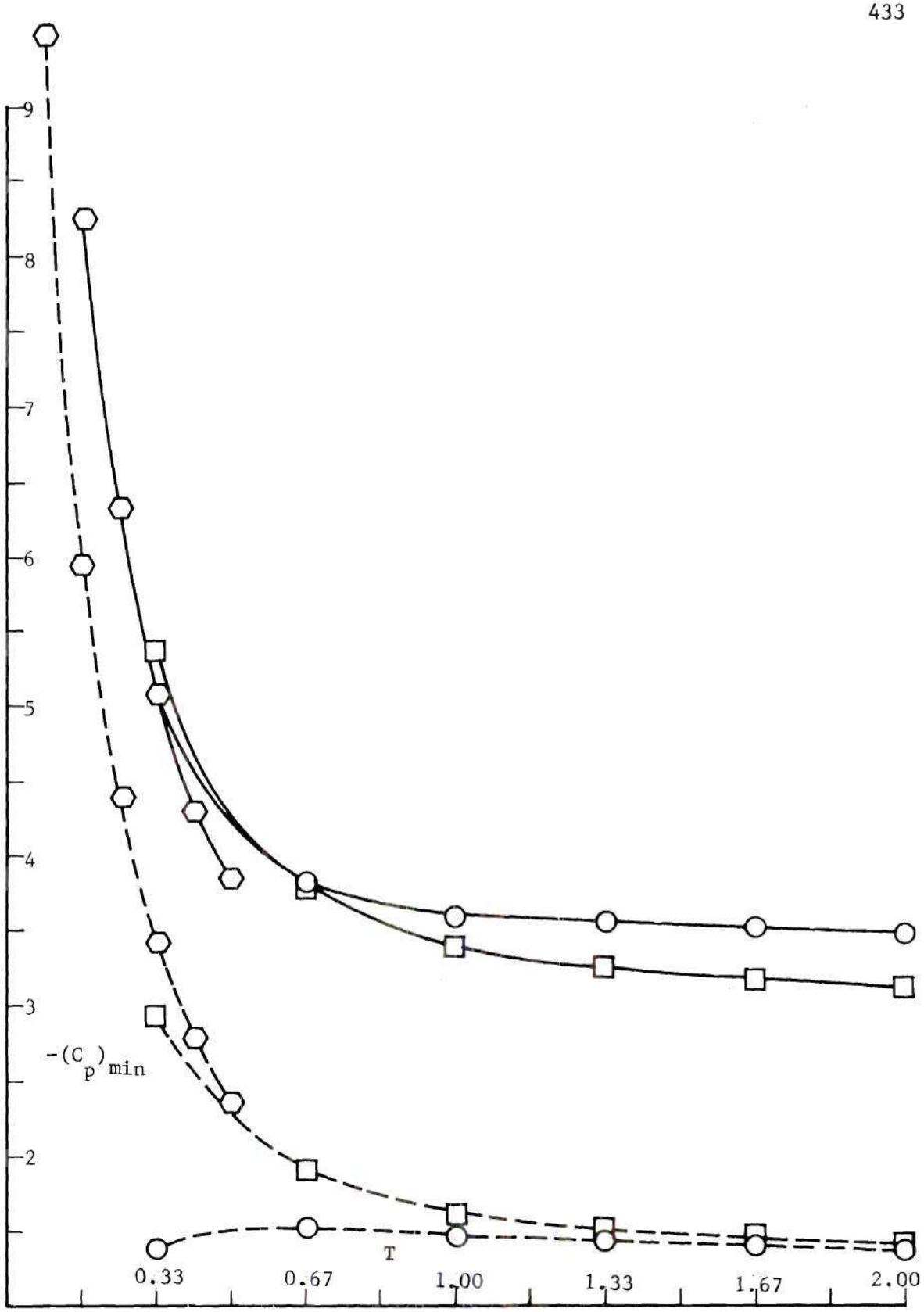

(c) Minimum Surface Pressure Coefficient

Figure 66. (cont.)

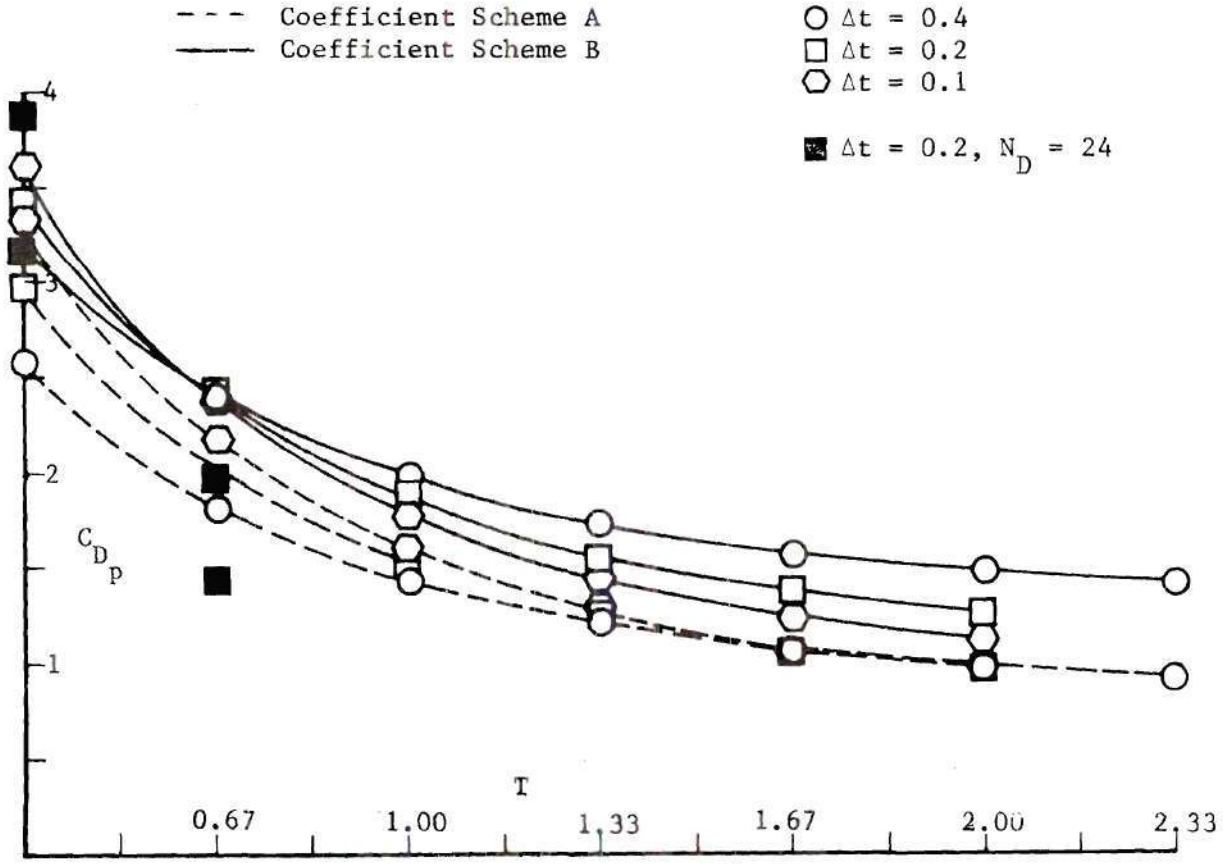

(a) Pressure Drag Coefficient

Figure 67. Comparison of Time Development of Drag Coefficients and Surface Pressure Minimum with Alternate Coefficient Schemes - Circular Cylinder (Scheme CBAC), R = 24

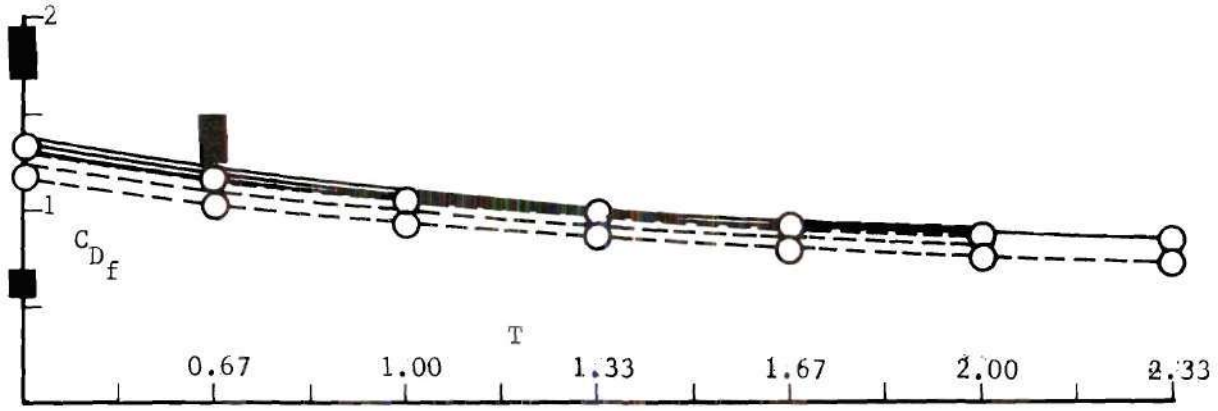

(b) Friction Drag Coefficient

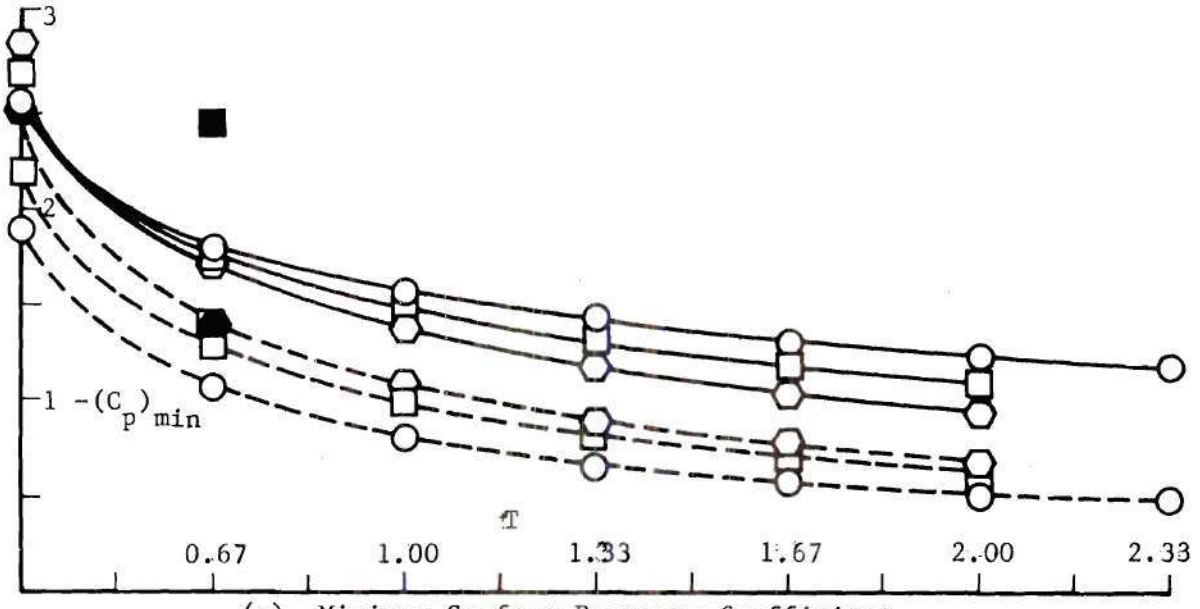

(c) Minimum Surface Pressure Coefficient

Figure 67. (cont.)

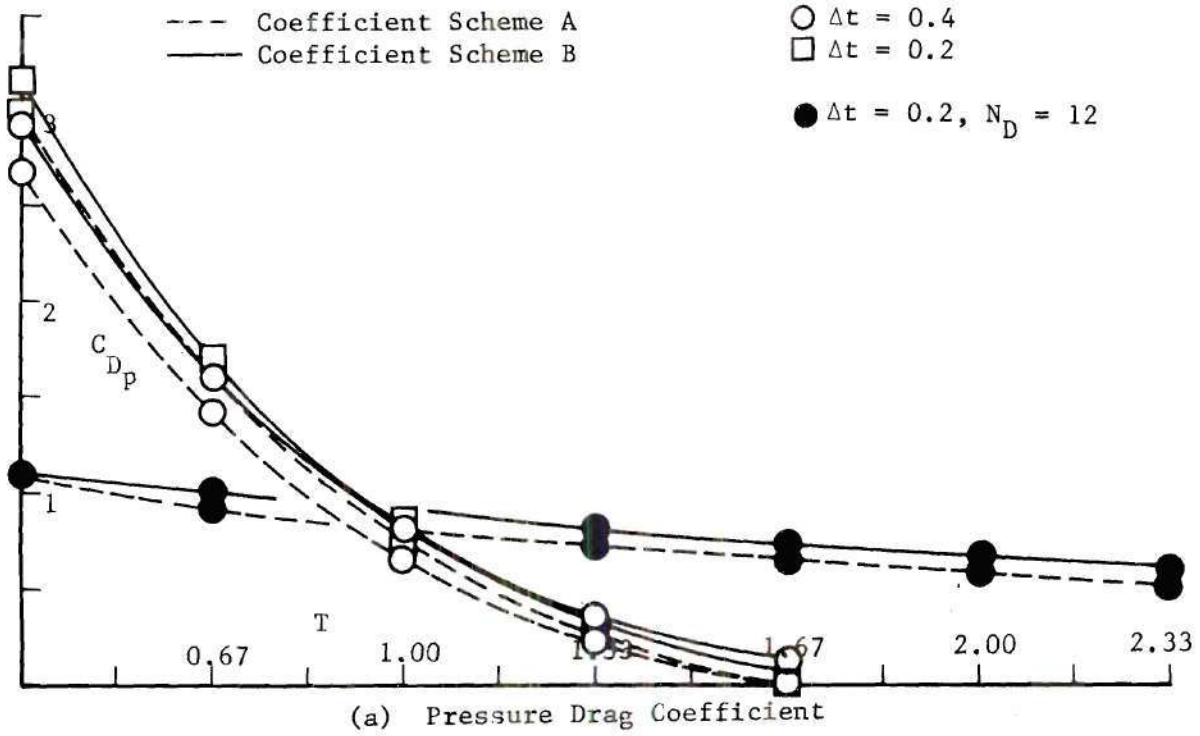

(a) Pressure Drag Coefficient

Figure 68. Comparison of Time Development of Drag Coefficients and Surface Pressure Minimum with Alternate Coefficient Schemes - Circular Cylinder (Scheme CBAC), R = 120

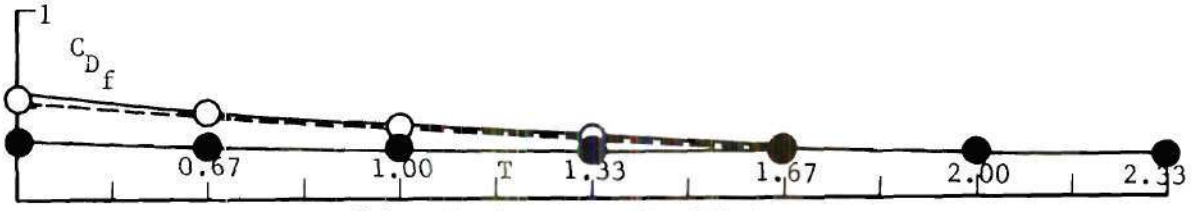

(b) Friction Drag Coefficient

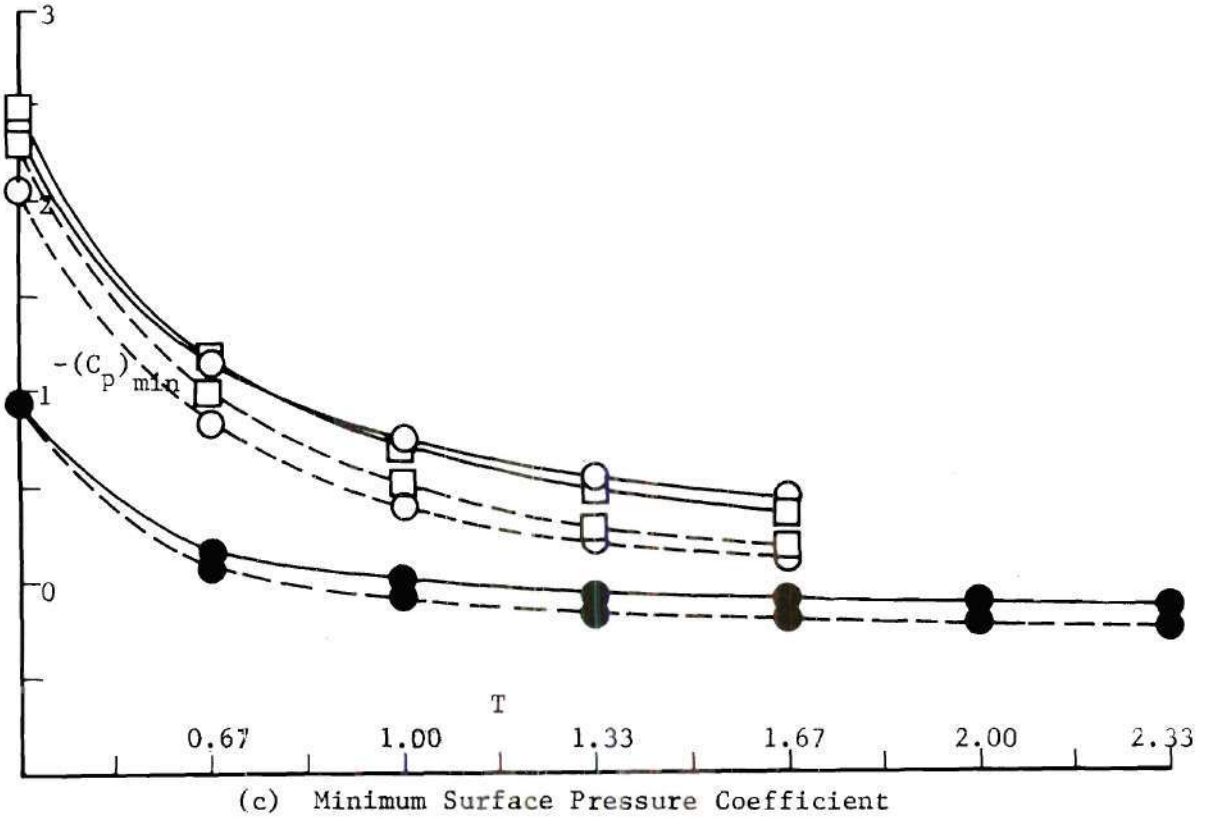

(c) Minimum Surface Pressure Coefficient

Figure 68. (cont.)

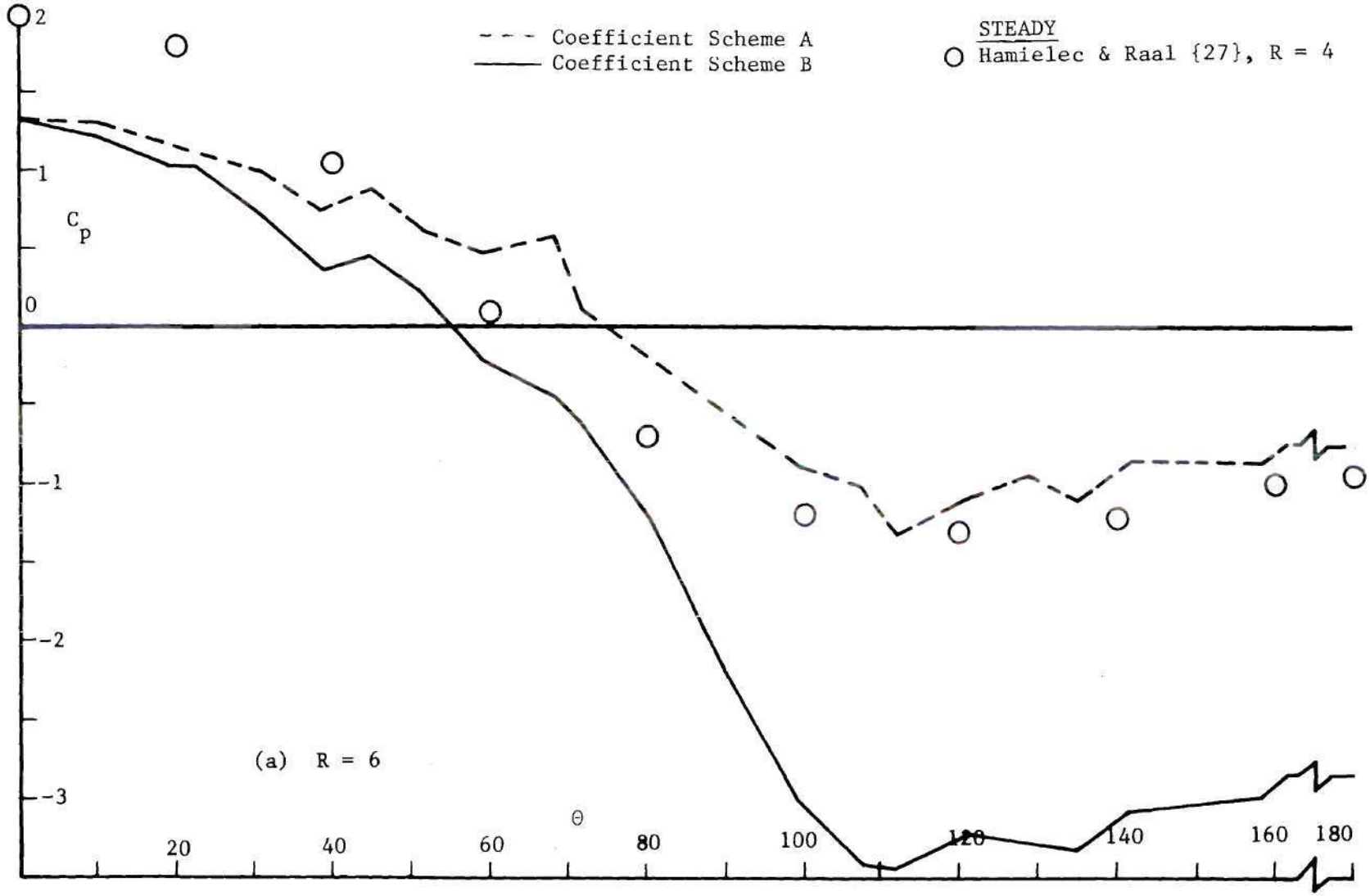

Figure 69. Comparison of Surface Pressure Distribution with Alternate Coefficient Schemes - Circular Cylinder (Scheme CBAC) - T = 2.33

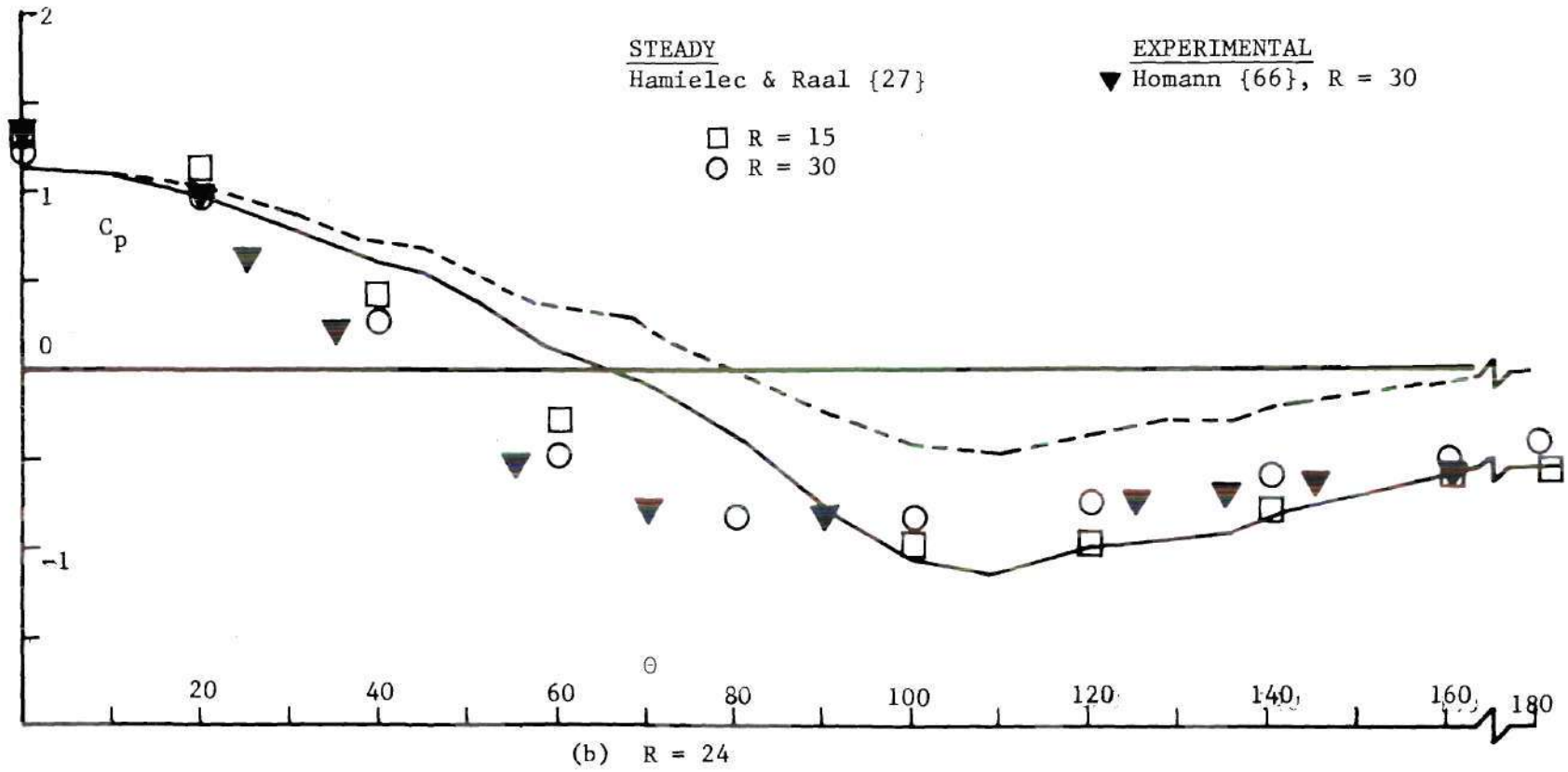

(b) R = 24

Figure 69. (cont.)

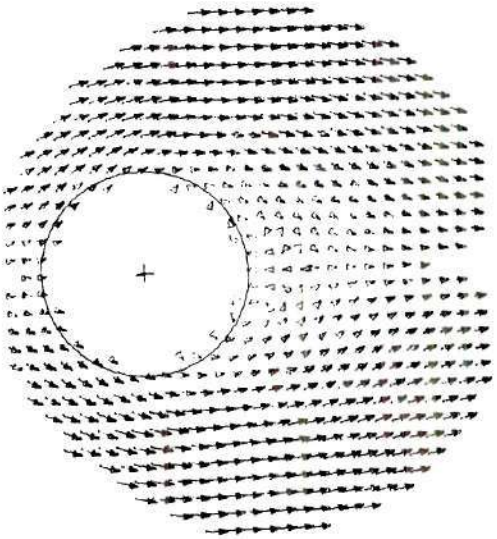

(a) $\Delta t = 0.4$

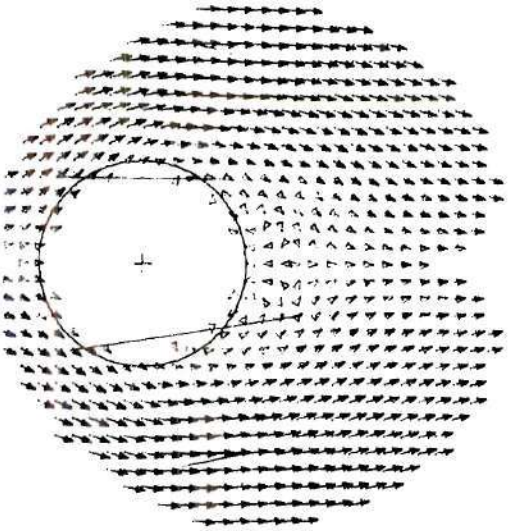

(b) $\Delta t = 0.2$

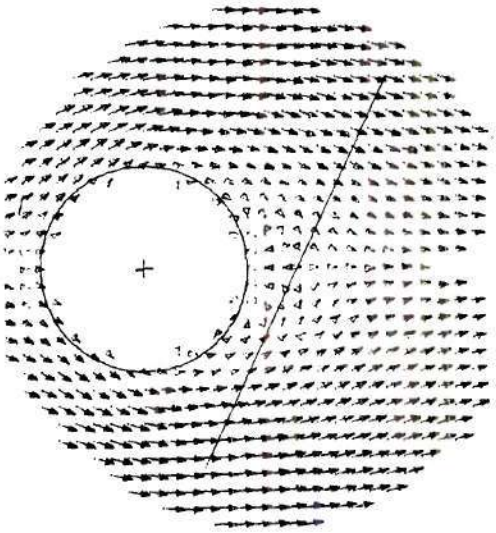

(c) $\Delta t = 0.1$

Figure 70. Convergence for Decreasing Time Step at Fixed Cell Size - Circular Cylinder, R = 24 - T = 2.0

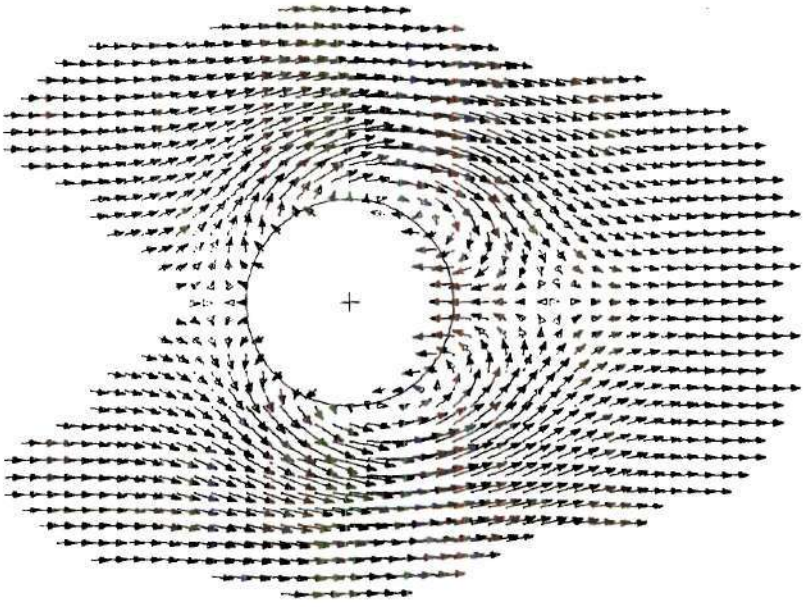

(a) $r_m = 12$

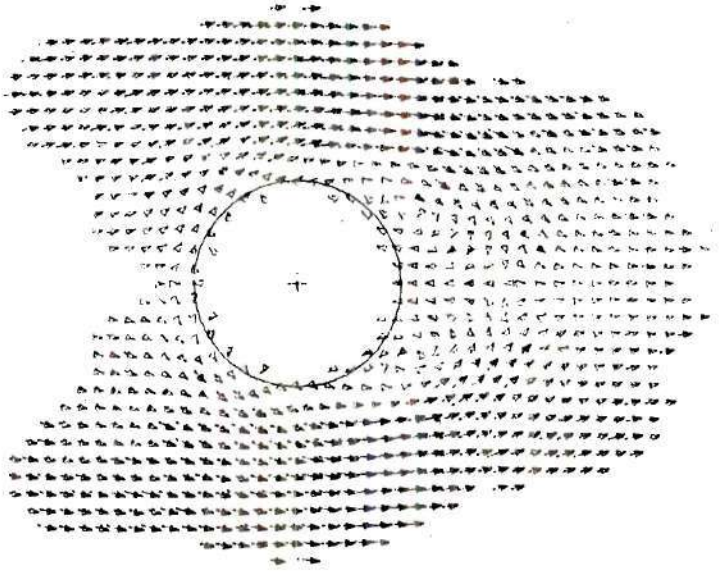

(b) $r_m = 24$

Figure 71. Effect of Influence Range, r_m, Beyond Which Vorticity is Neglected in Velocity Calculation - Circular Cylinder, R = 120 - T = 2.67

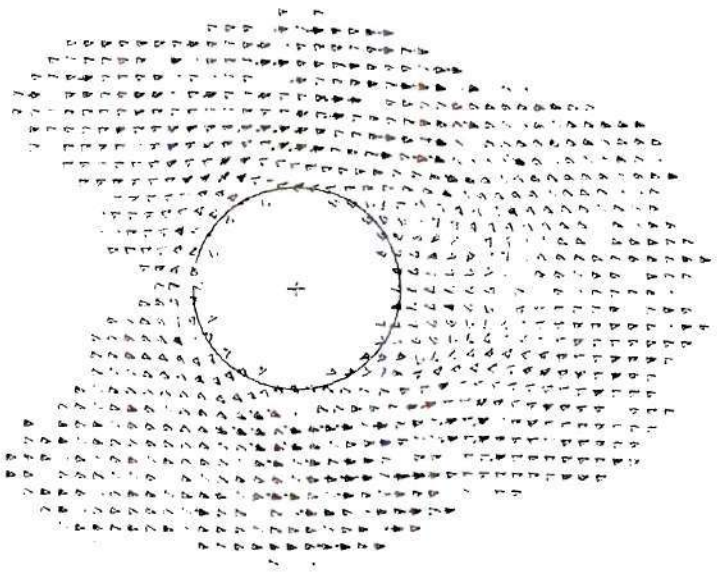

(c) $r_m = 48$

Figure 71. (cont.)

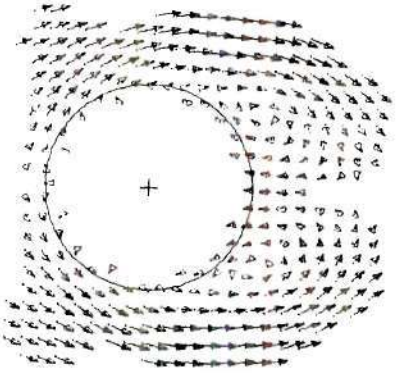

(a) $\omega_m = 0.1$

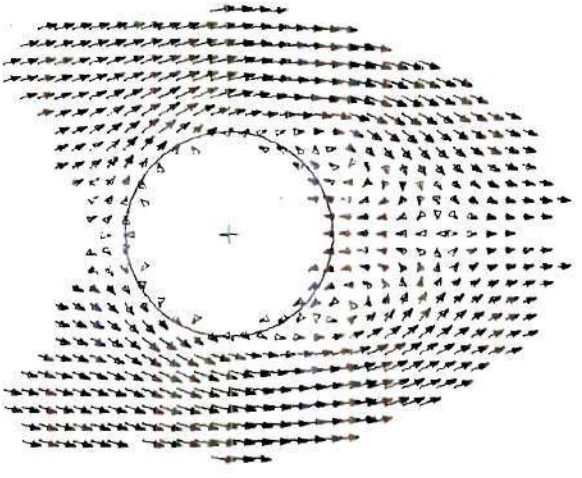

(b) $\omega_m = 0.01$

Figure 72. Effect of Minimum Vorticity, ω_m, Necessary for Creation of New Vortex Cell - Circular Cylinder, R = 120 - T = 2.67

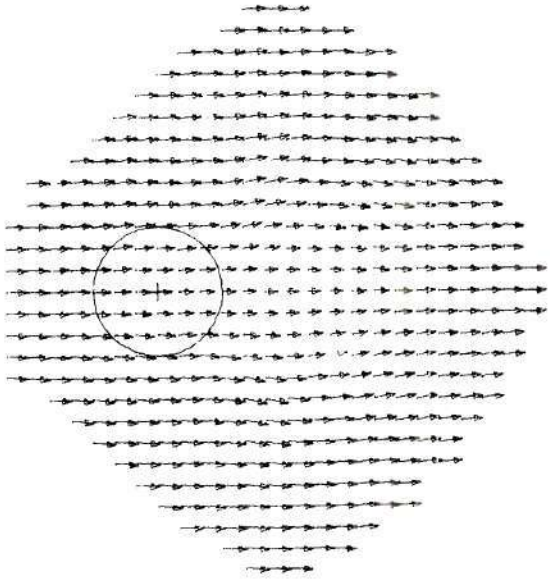

Horizontal
Velocity

Vertical
Velocity

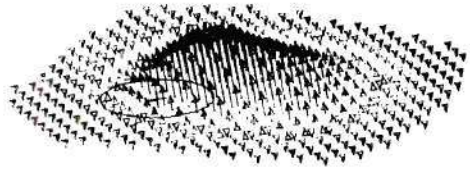

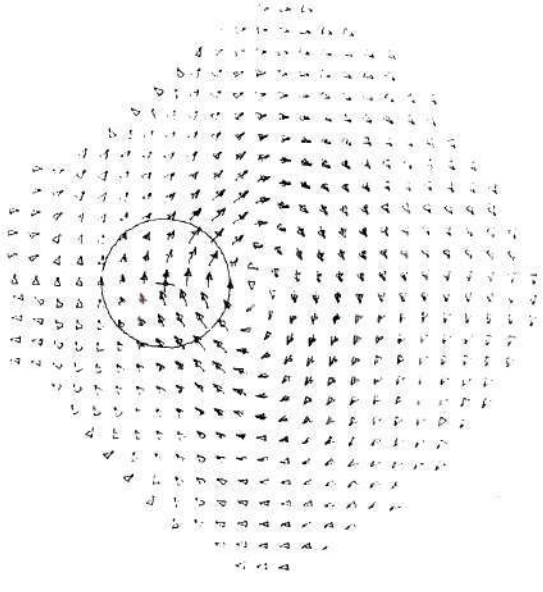

Horizontal
Vorticity

(a) $\Delta t = 0.4$

Figure 73. Convergence for Decreasing Time Step at Fixed Cell Size in Straight Explicit Formulation - Infinite Jet in Cross-Wind ($V_r = 8$), R = 12 - T = 2.67

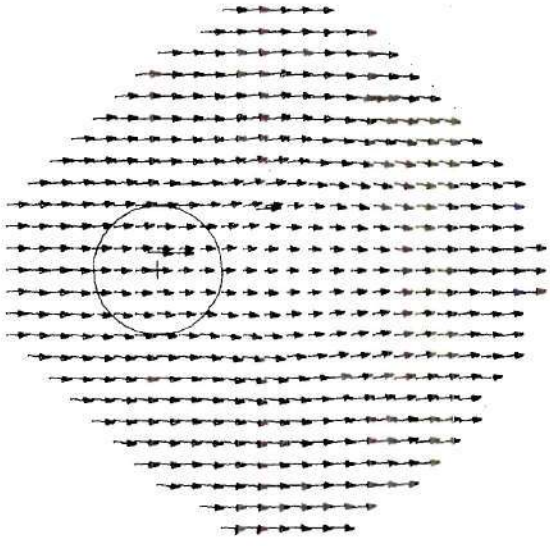

Horizontal
Velocity

Vertical
Velocity

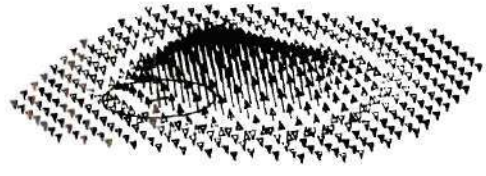

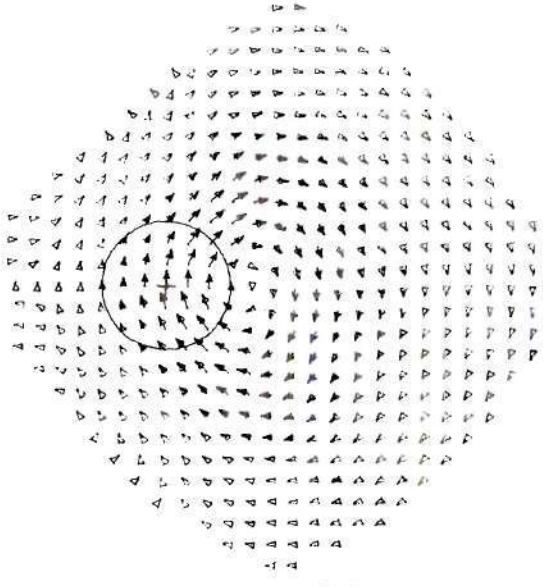

Horizontal
Vorticity

(b) $\Delta t = 0.2$

Figure 73. (cont.)

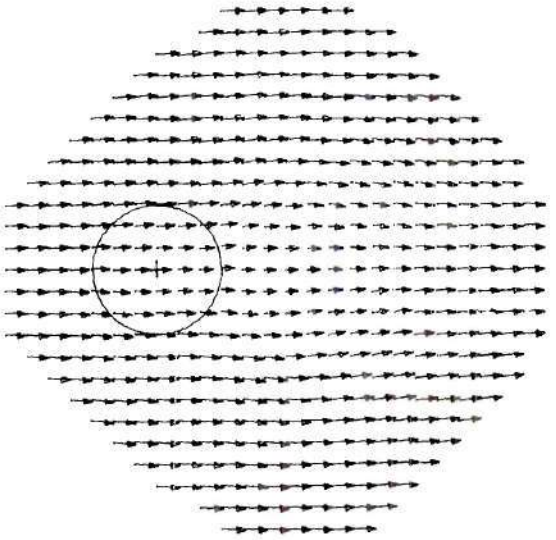

Horizontal
Velocity

Vertical
Velocity

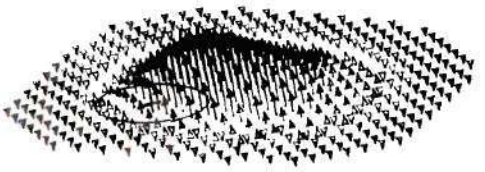

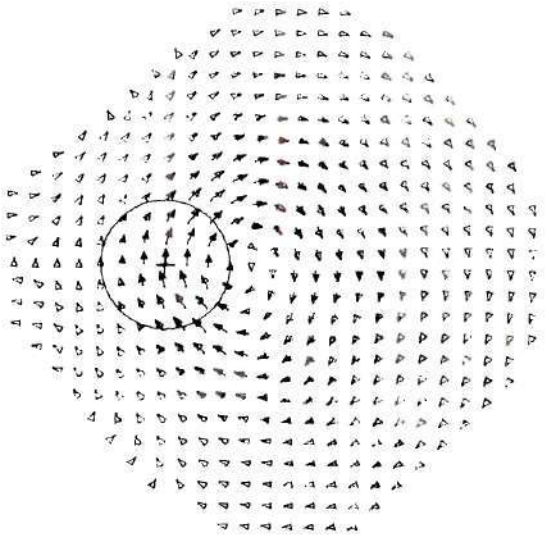

Horizontal
Vorticity

(c) $\Delta t = 0.1$

Figure 73. (cont.)

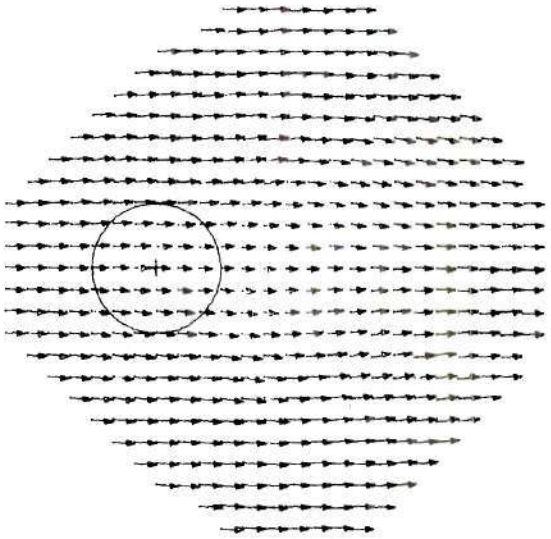

Horizontal
Velocity

Vertical
Velocity

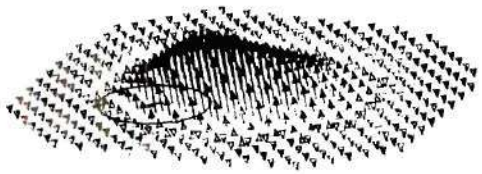

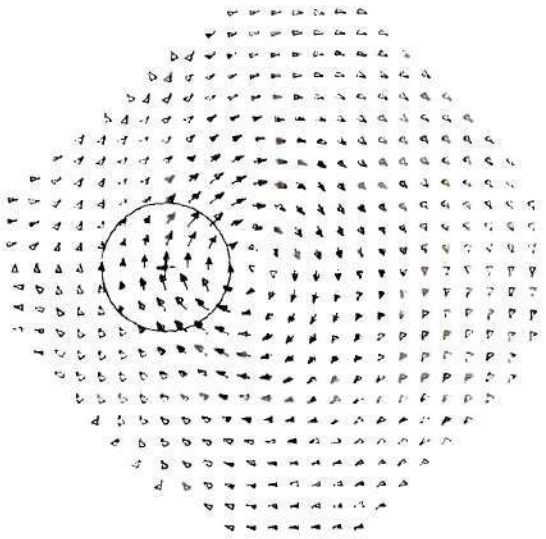

Horizontal
Vorticity

(d) $\Delta t = 0.05$

Figure 73. (cont.)

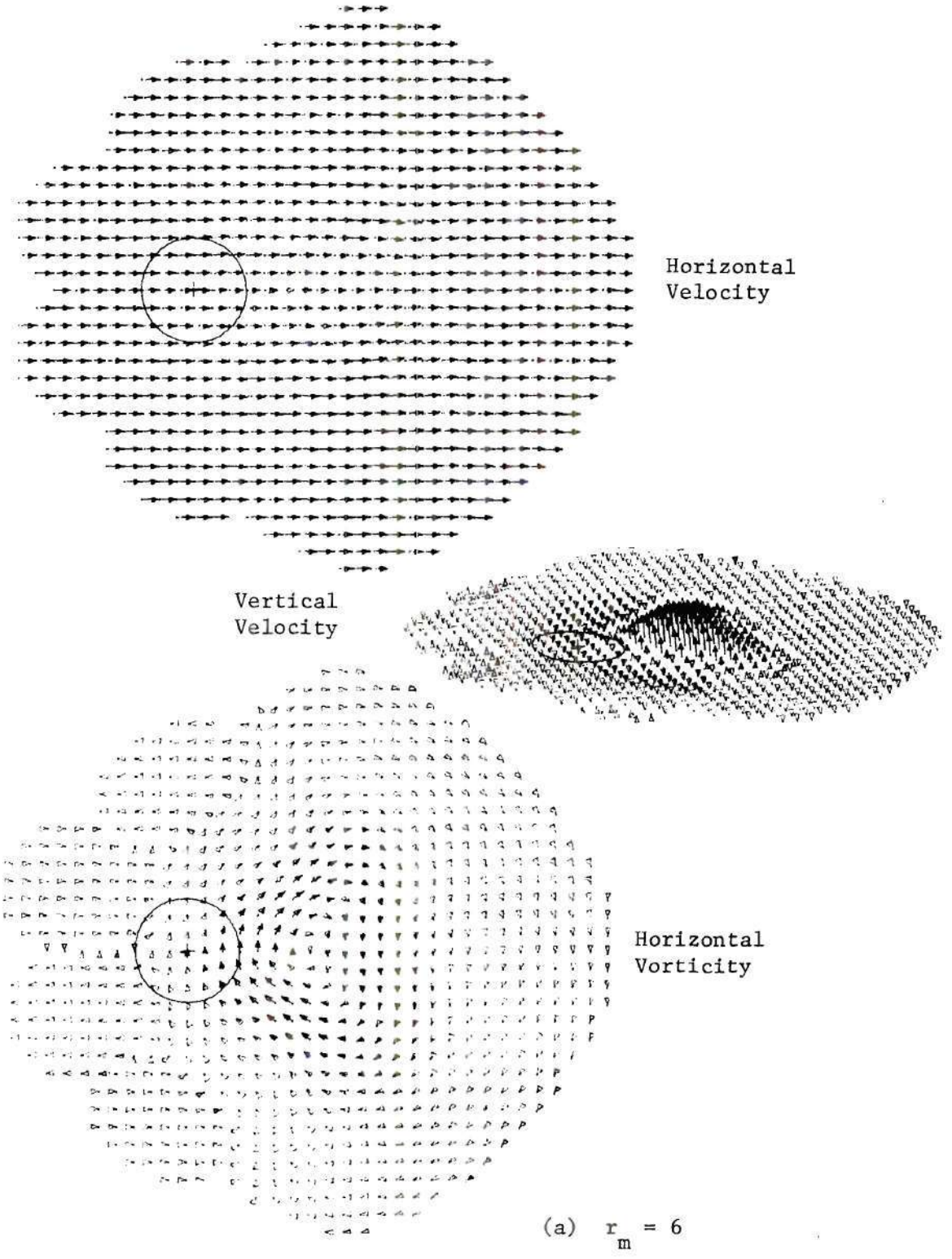

Figure 74. Effect of Influence Range, r_m, Beyond Which Vorticity is Neglected in Velocity Calculation - Infinite Jet in Cross-Wind ($V_r = 8$), R = 15 - T = 4.0

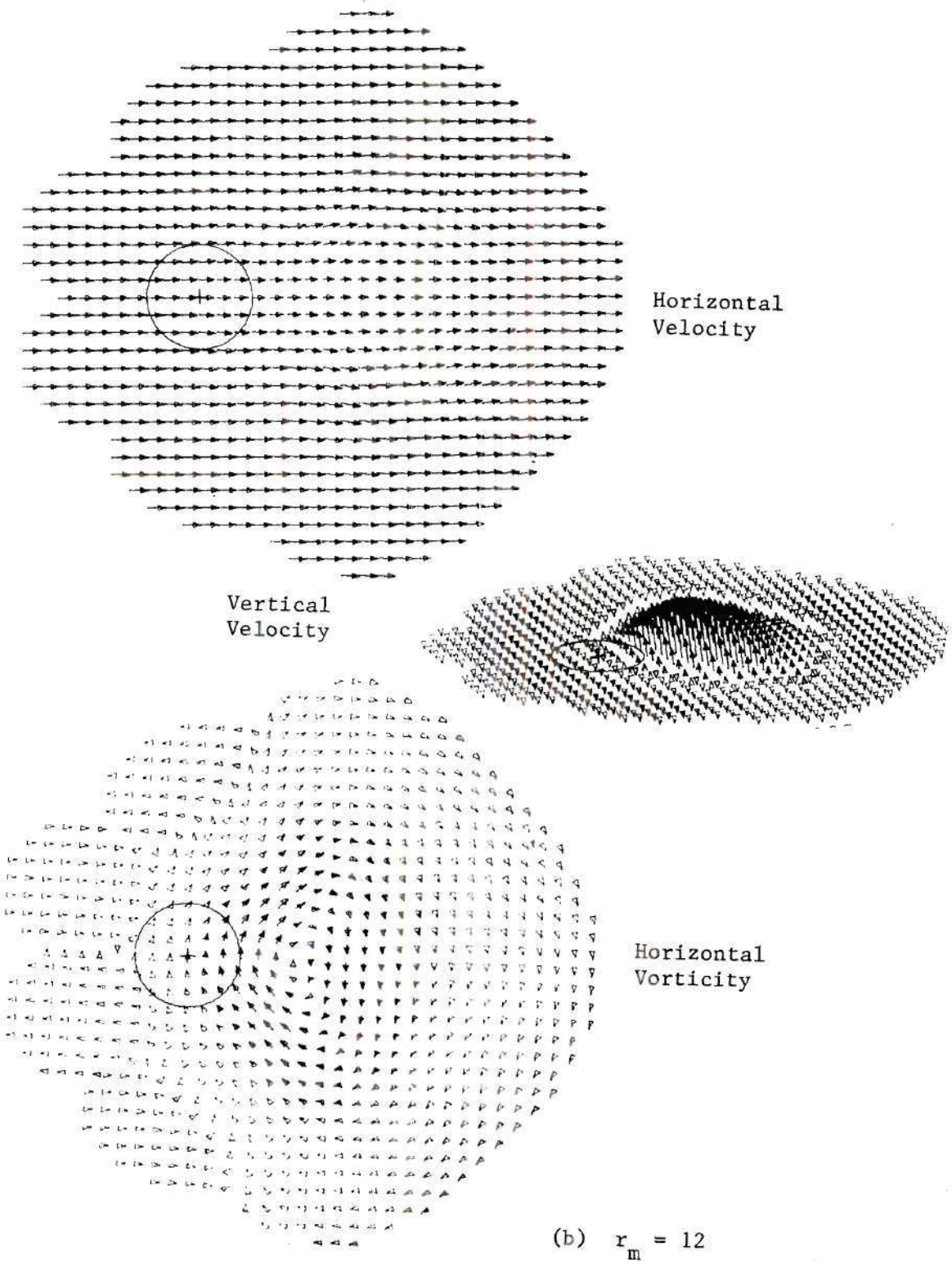

(b) $r_m = 12$

Figure 74. (cont.)

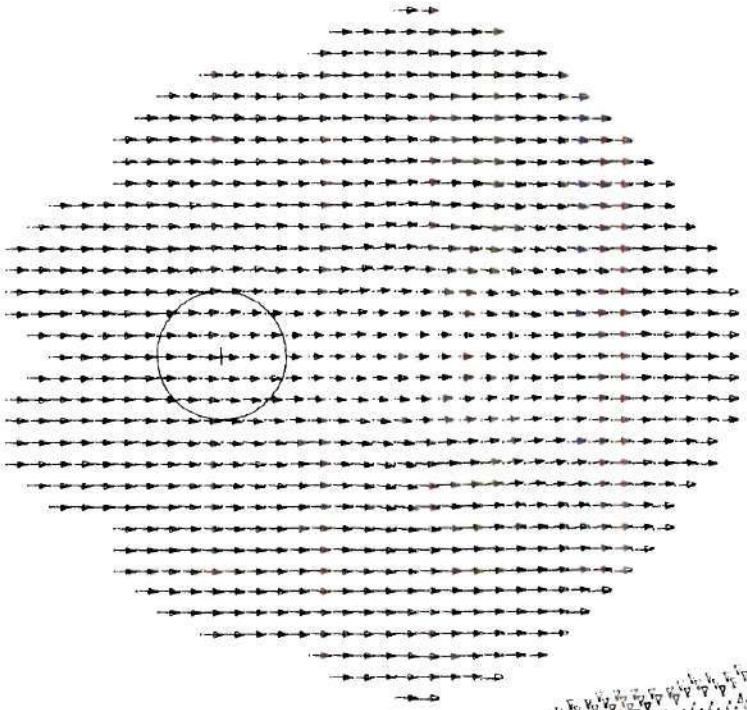

Horizontal
Velocity

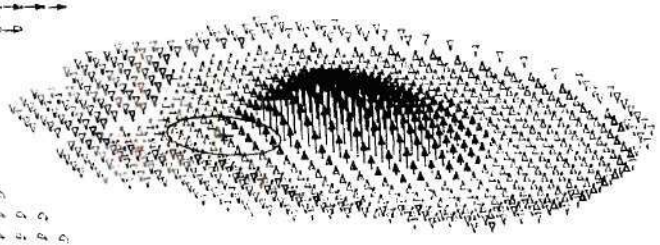

Vertical
Velocity

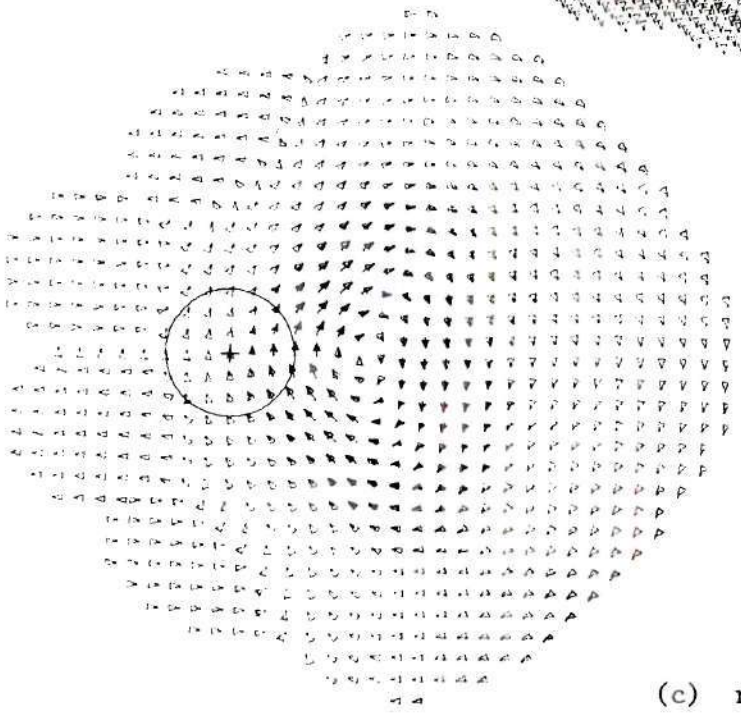

Horizontal
Vorticity

(c) $r_m = 24$

Figure 74. (cont.)

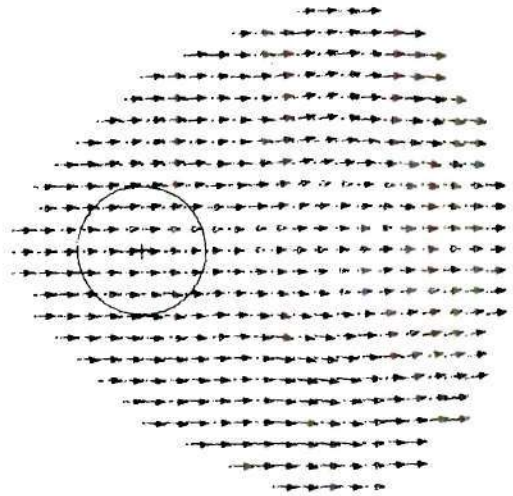

Horizontal
Velocity

Vertical
Velocity

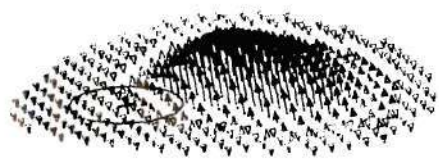

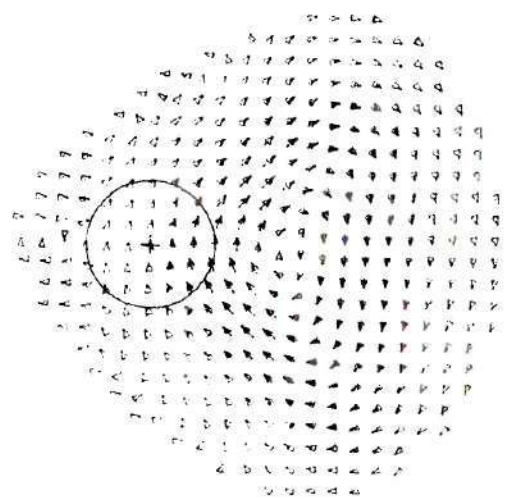

Horizontal
Vorticity

(a) $\omega_m = 0.1$

Figure 75. Effect of Minimum Vorticity, ω_m, Necessary for Creation of New Vortex Cell - Infinite Jet in Cross-Wind ($V_r = 8$), R = 15 - T = 4.0

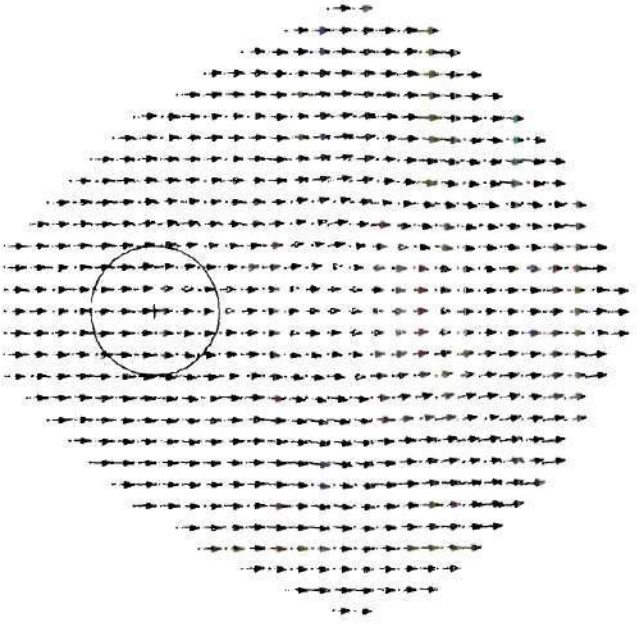

Horizontal
Velocity

Vertical
Velocity

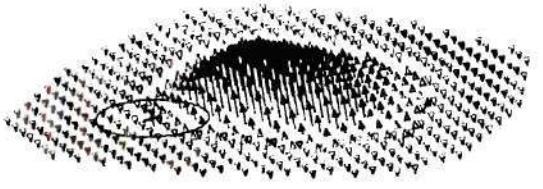

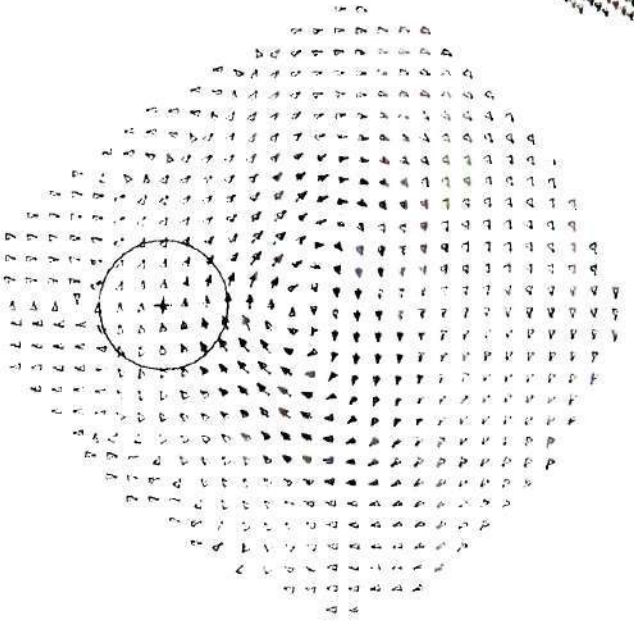

Horizontal
Vorticity

(b) $\omega_m = 0.01$

Figure 75. (cont.)

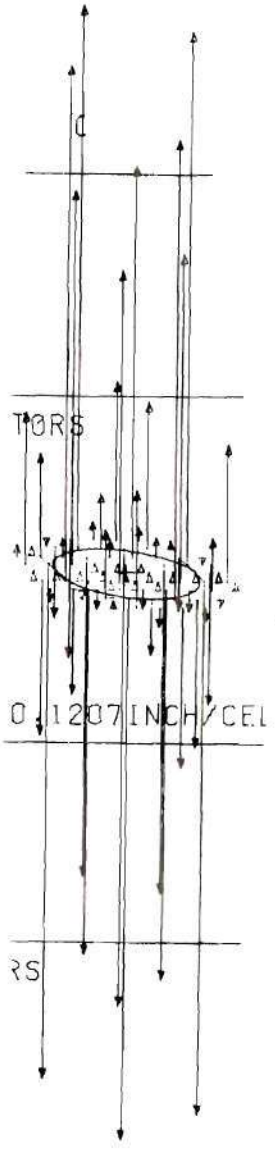

(a) Vertical Vorticity, t = 0.7

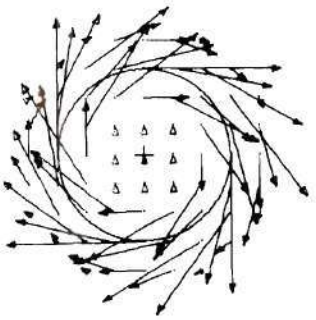

(b) Horizontal Vorticity, t = 0.7

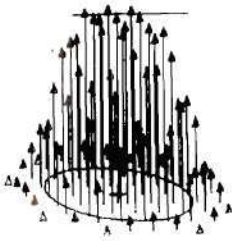

(c) Vertical Velocity, t = 0.7

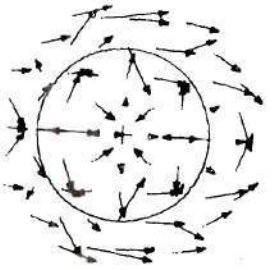

(d) Horizontal Velocity, t = 0.7

Figure 76. Time Development of Nonlinear Instability - Infinite Jet in Cross-Wind (V_r = 8) - R_c = 3.5

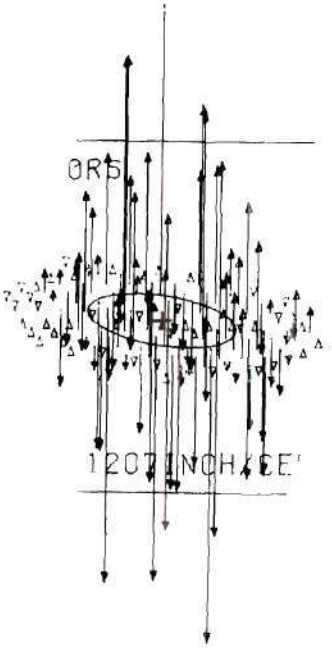

(e) Vertical Vorticity, t = 2.1

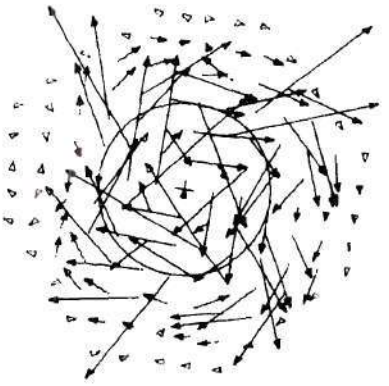

(f) Horizontal Vorticity, t = 2.1

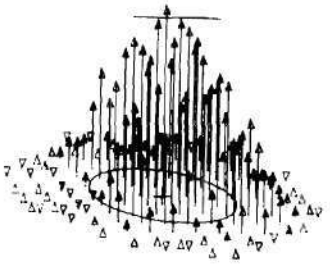

(g) Vertical Velocity, t = 2.1

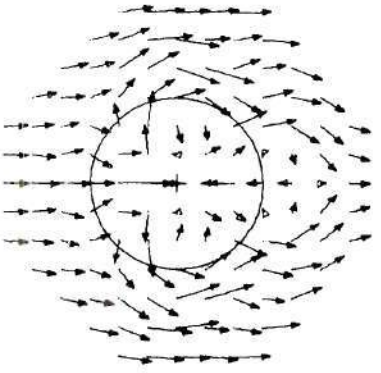

(h) Horizontal Velocity, t = 2.1

Figure 76. (cont.)

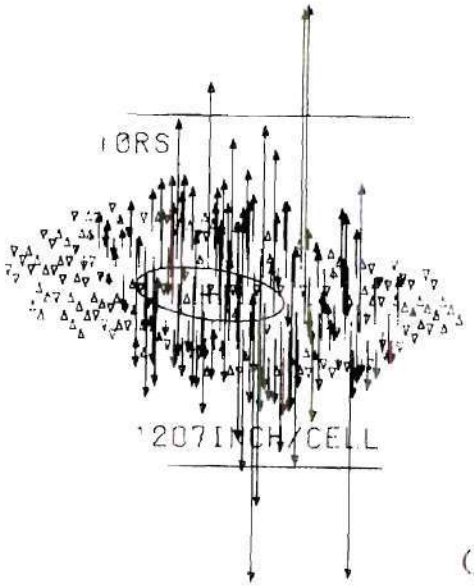

(i) Vertical Vorticity, t = 4.9

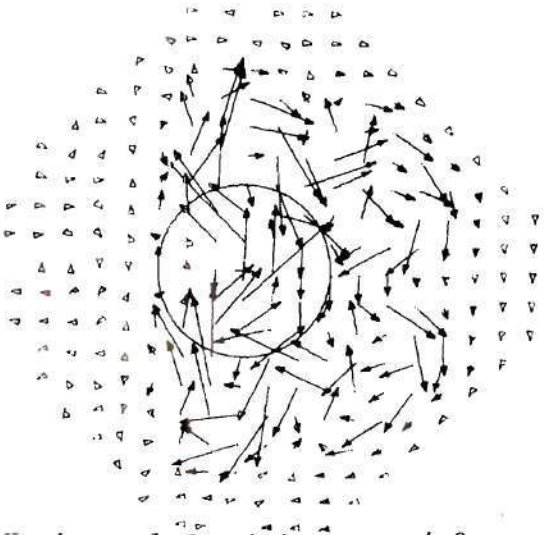

(j) Horizontal Vorticity, t = 4.9

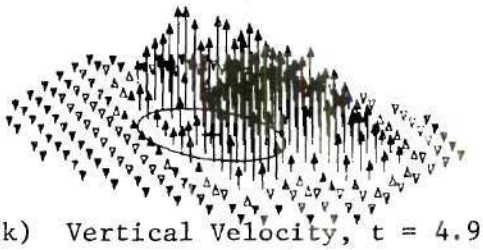

(k) Vertical Velocity, t = 4.9

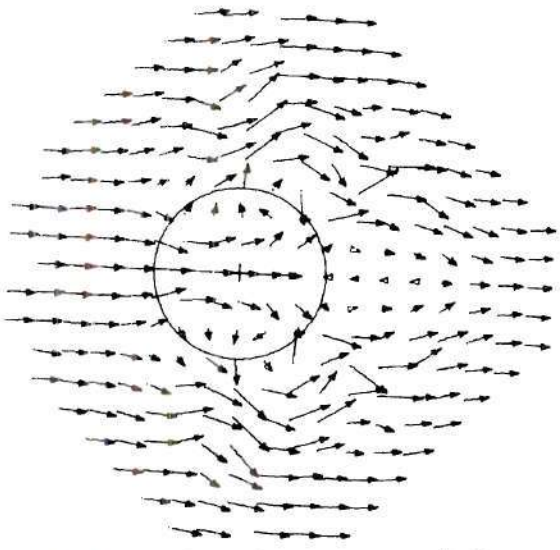

(l) Horizontal Velocity, t = 4.9

Figure 76. (cont.)

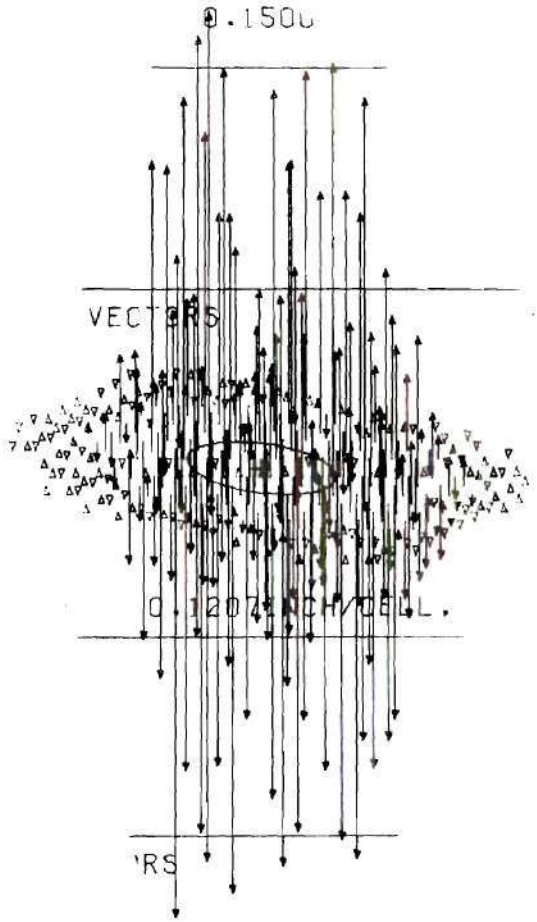

(a) Vertical Vorticity

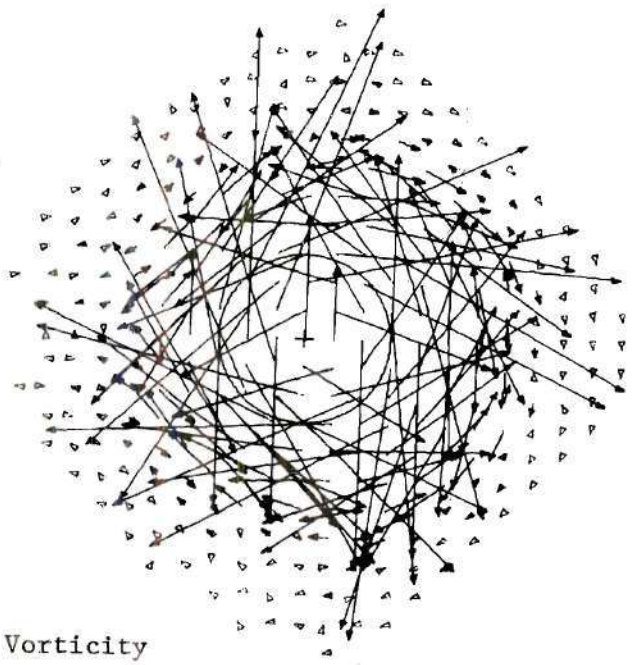

(b) Horizontal Vorticity

Figure 77. Linear Instability - Infinite Jet in Cross-Wind (V_r = 8) - R_c = 1.0

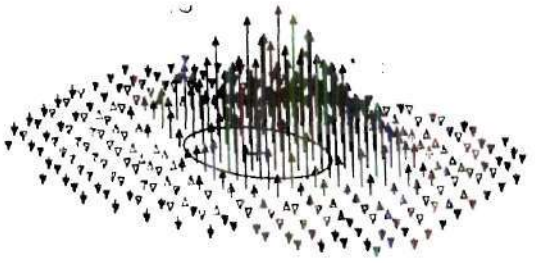

(c) Vertical Velocity

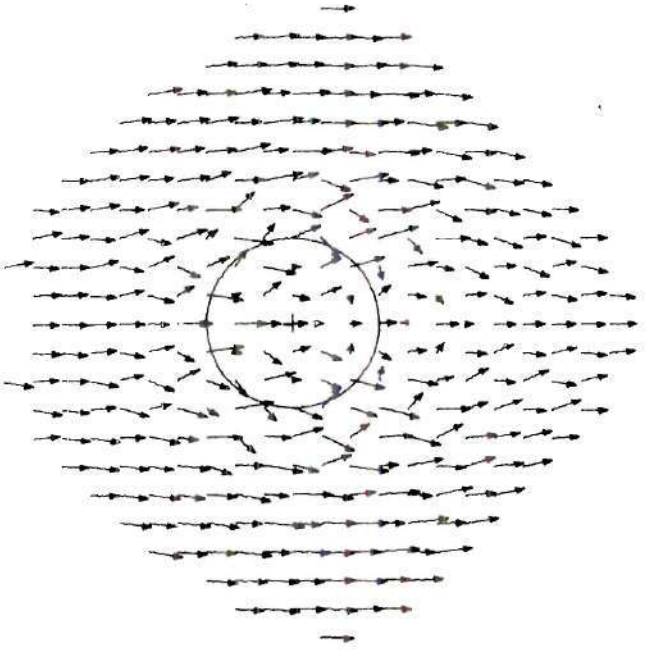

(d) Horizontal Velocity

Figure 77. (cont.)

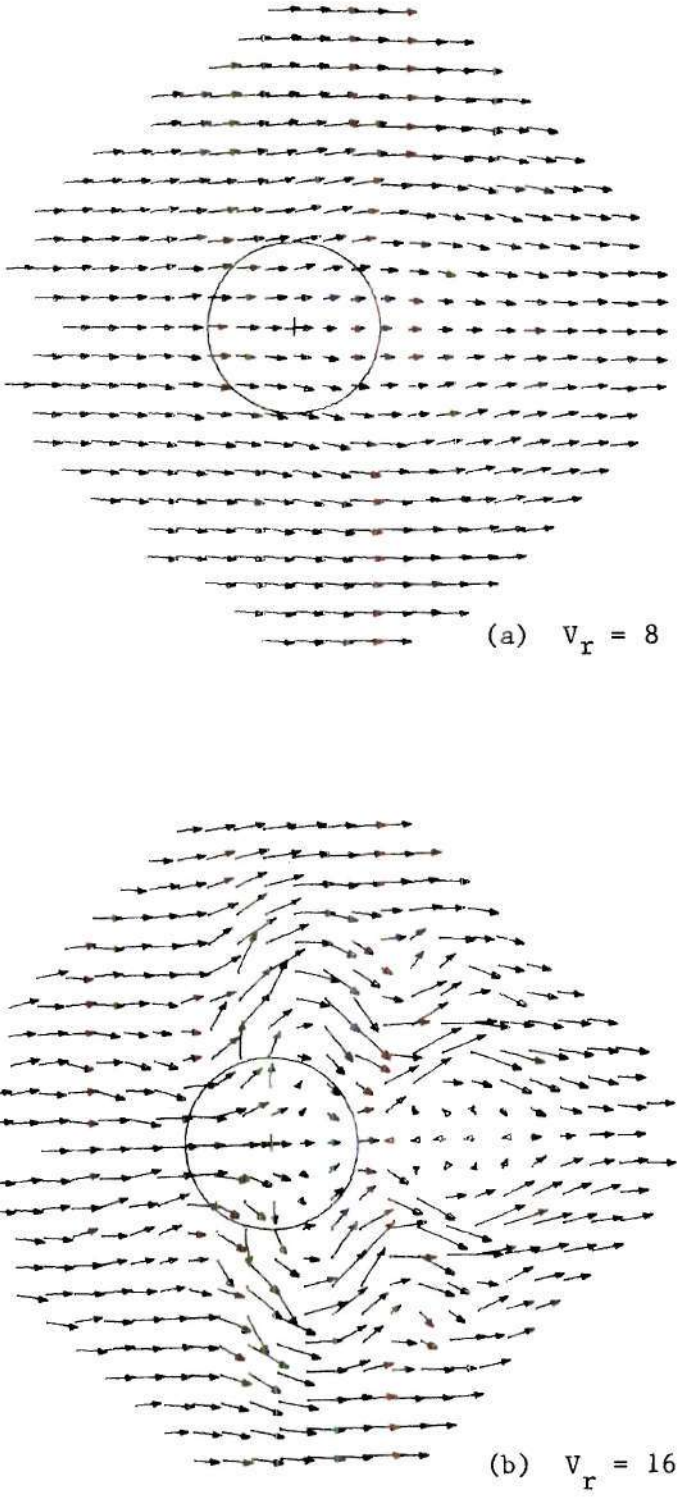

Figure 78. Effect of Velocity Ratio on Nonlinear Instability - Infinite Jet in Cross-Wind - $R_c = 1.5$

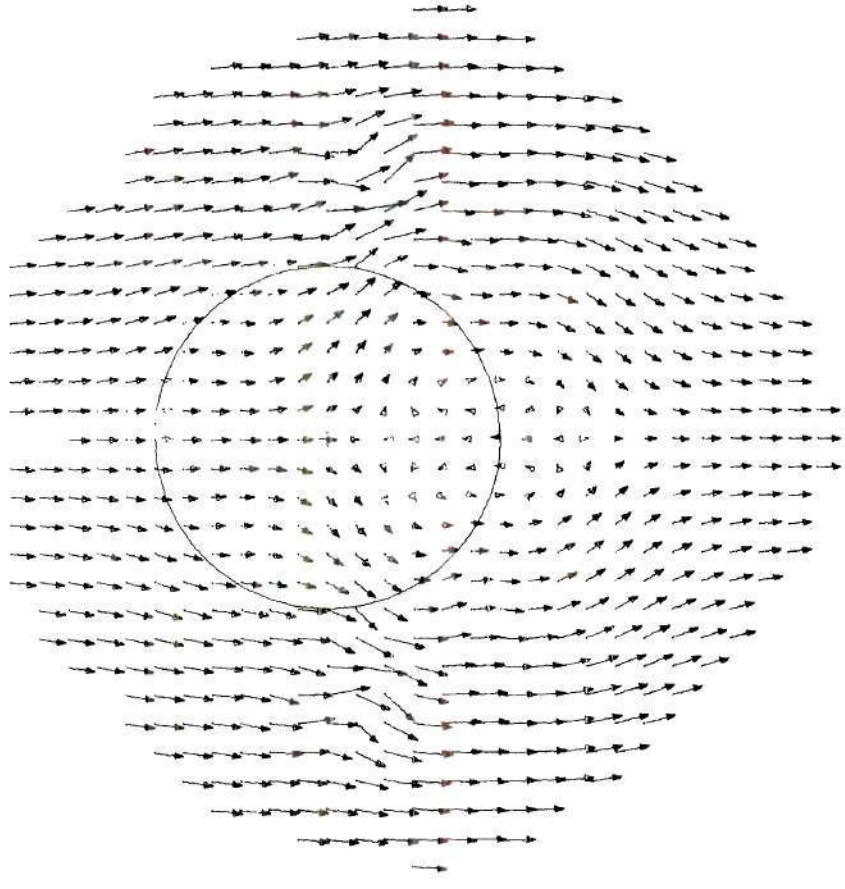

(a) Circular Jet

Figure 79. Comparisons of Nonlinear Instability with Circular and Elliptic Jets (Eccentricity 5/6) - Infinite Jet in Cross-Wind (V_r = 8) - R_c = 3.0

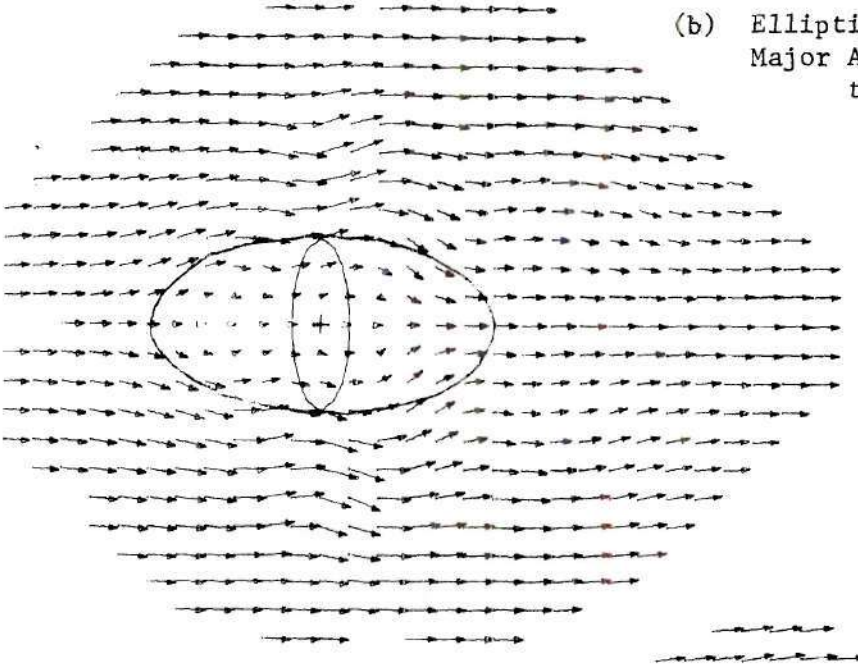

(b) Elliptic Jet,
Major Axis Parallel
to Cross-Flow

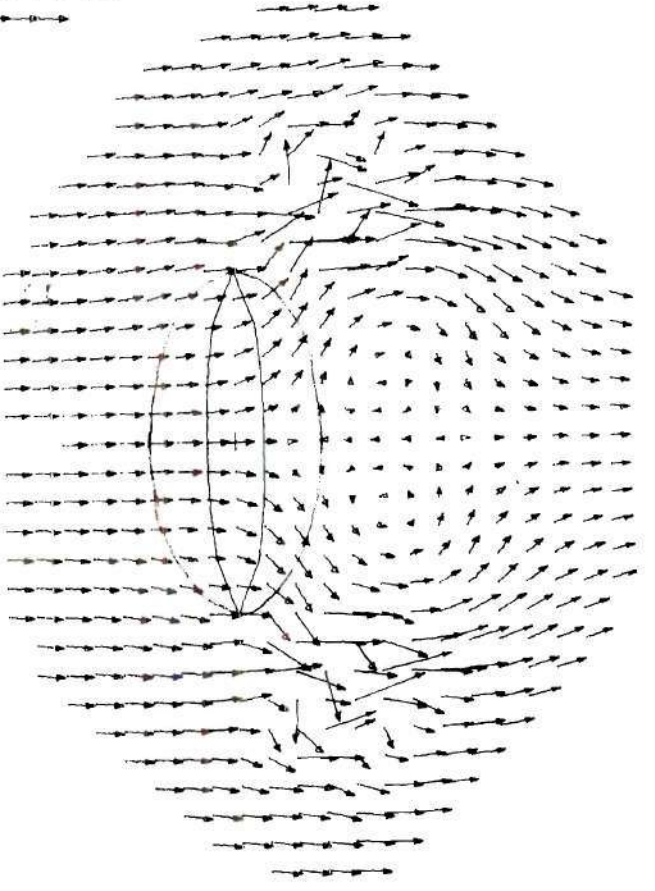

(c) Elliptic Jet,
Major Axis
Perpendicular
to Cross-Flow

Figure 79. (cont.)

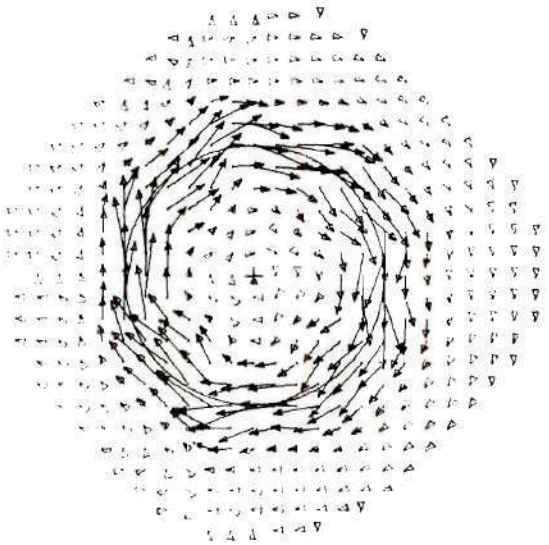

(a) t = 2.0

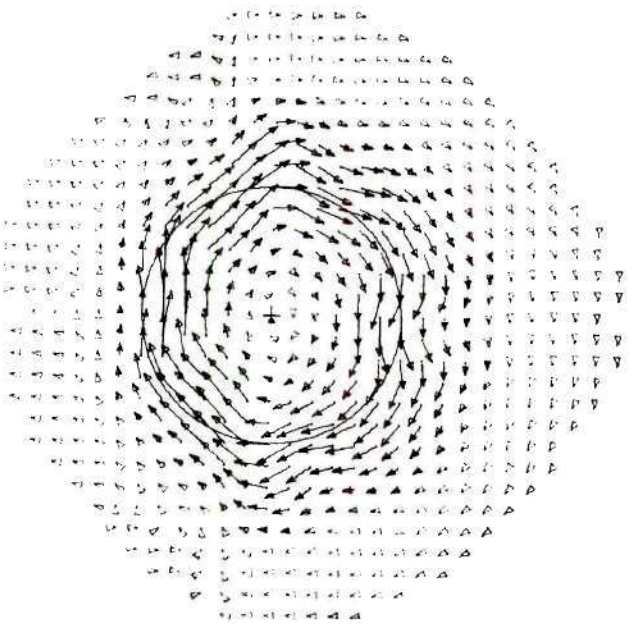

(b) t = 4.0

Figure 80. Time Development of Horizontal Vorticity with Slight Nonlinear Instability - Infinite Jet in Cross-Wind (V_r = 8) - R_c = 2.5

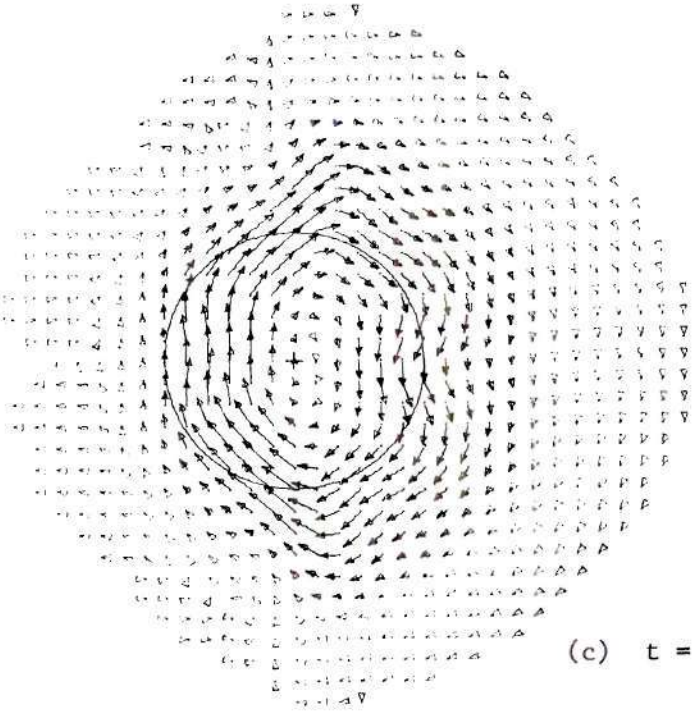

(c) t = 6.0

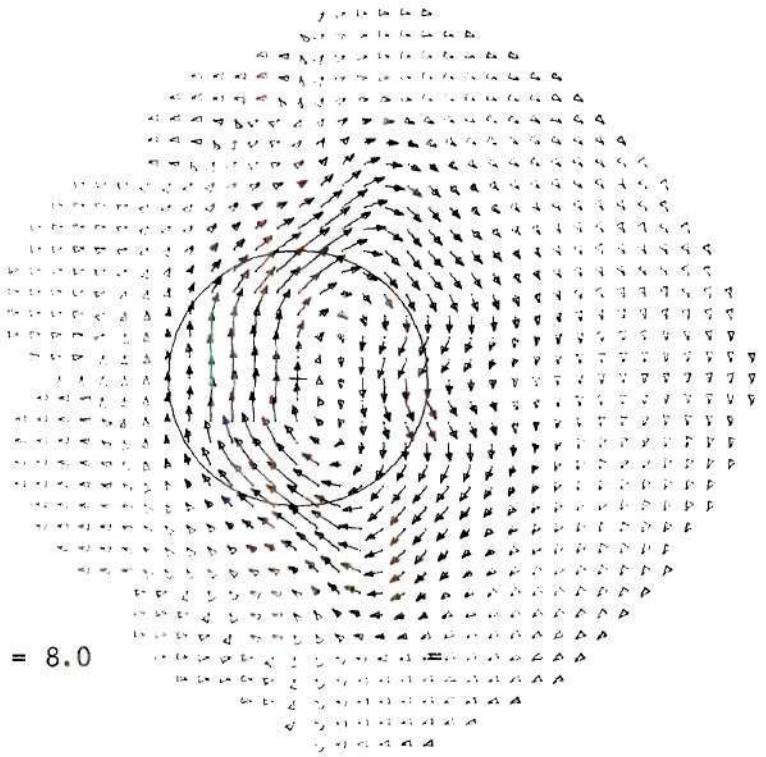

(d) t = 8.0

Figure 80. (cont.)

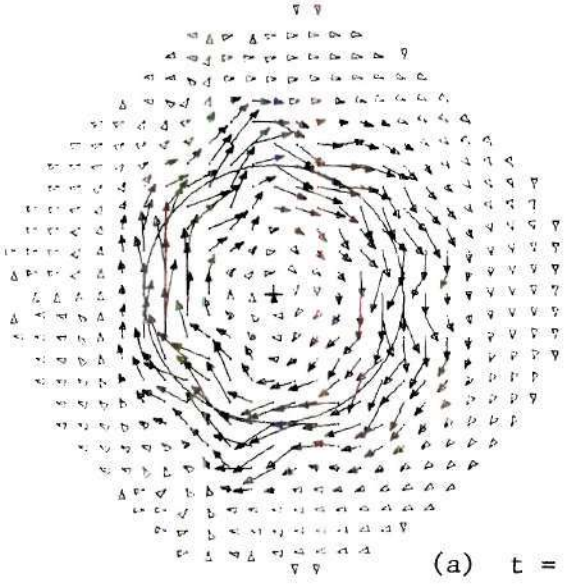

(a) t = 3.0

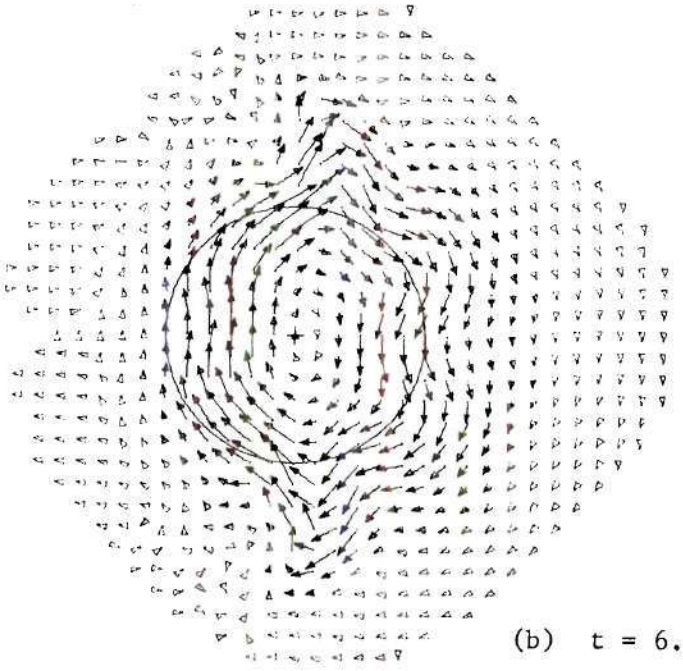

(b) t = 6.0

Figure 81. Time Development of Horizontal Vorticity with Significant Nonlinear Instability - Infinite Jet in Cross-Wind (V_r = 8) - R_c = 2.5

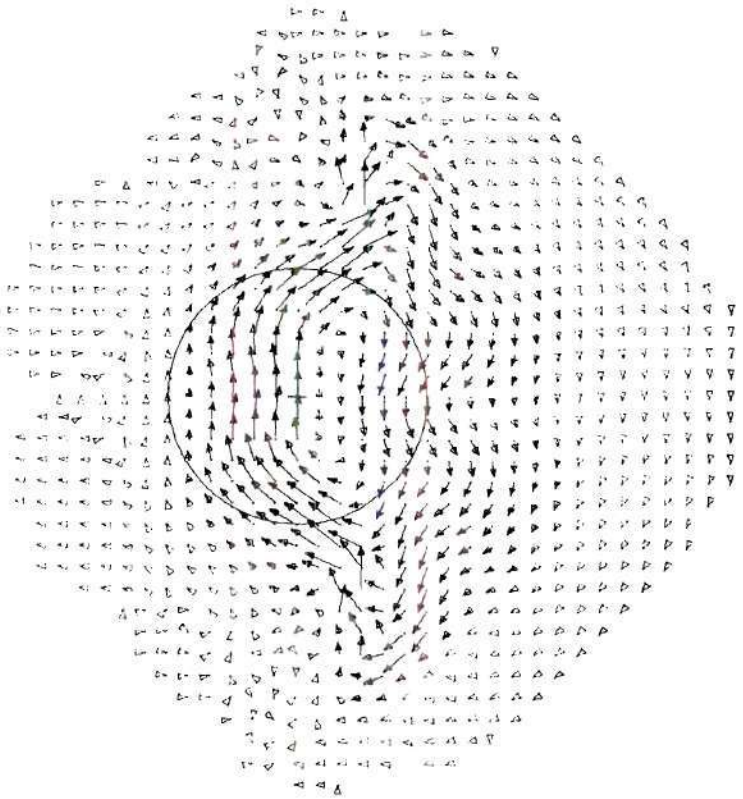

(c) t = 9.0

Figure 81. (cont.)

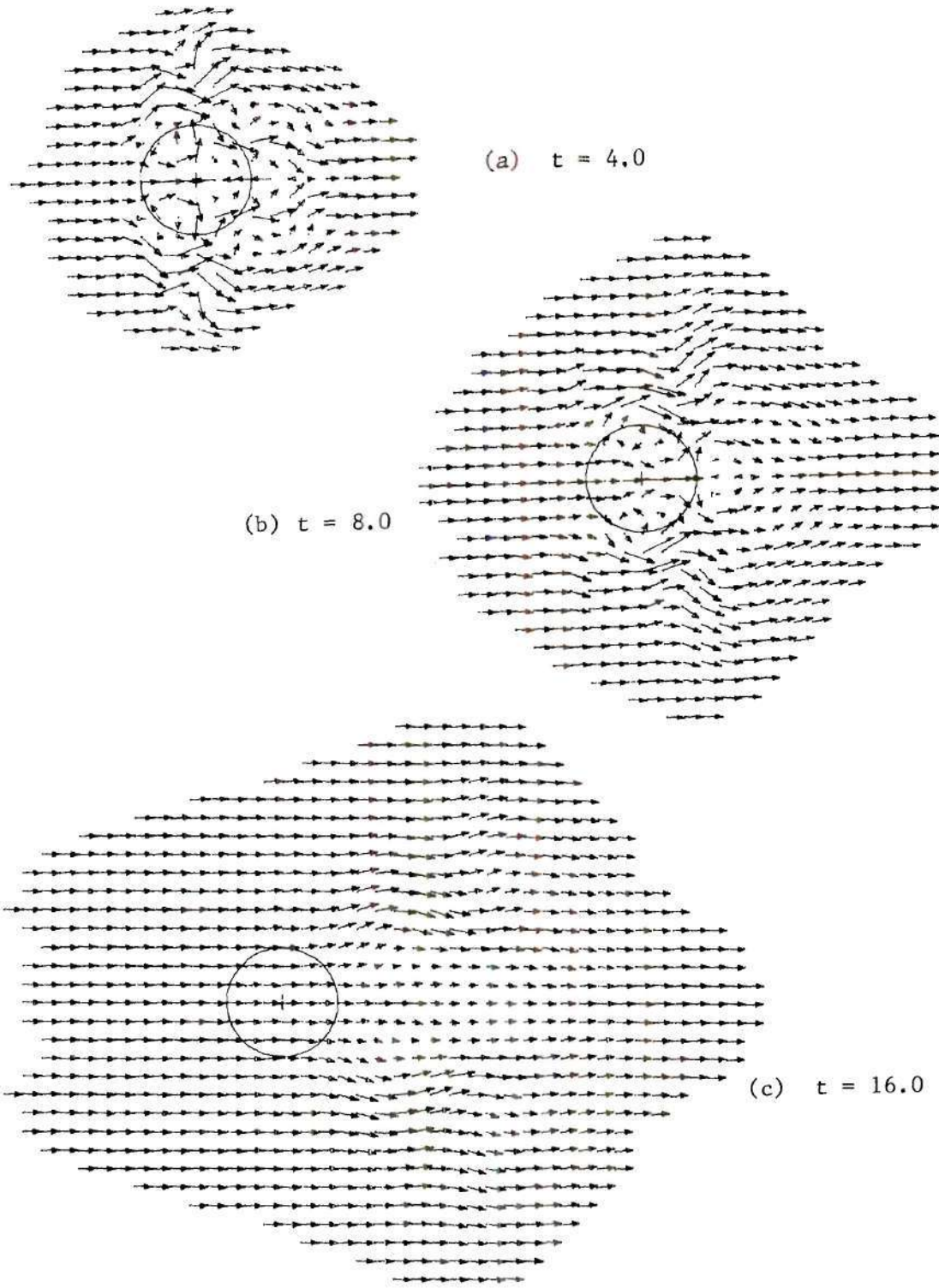

Figure 82. Damping of Early Nonlinear Instability - Infinite Jet in Cross-Wind (V_r = 8) - R_c = 10.0

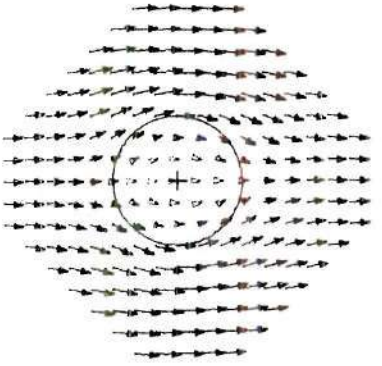

(a) t = 4.0

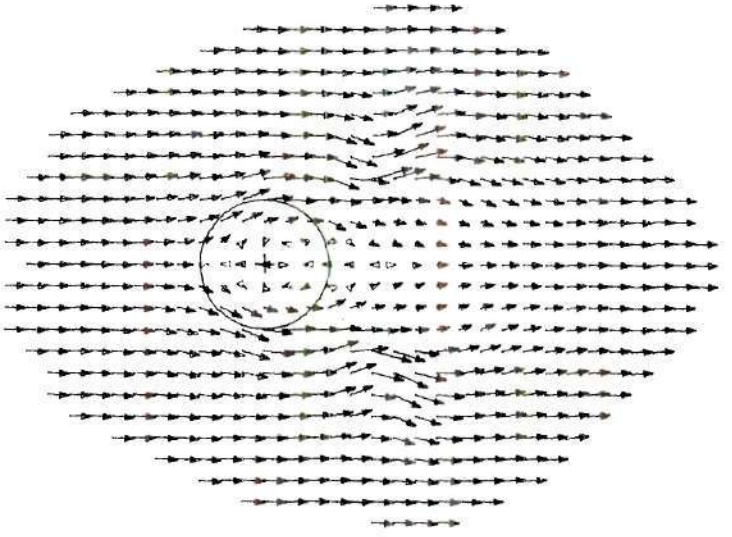

(b) t = 16.0

Figure 83. Nonlinear Instability with Twenty Step Gradual Start - Infinite Jet in Cross-Wind (V_r = 8) - R_c = 10.0

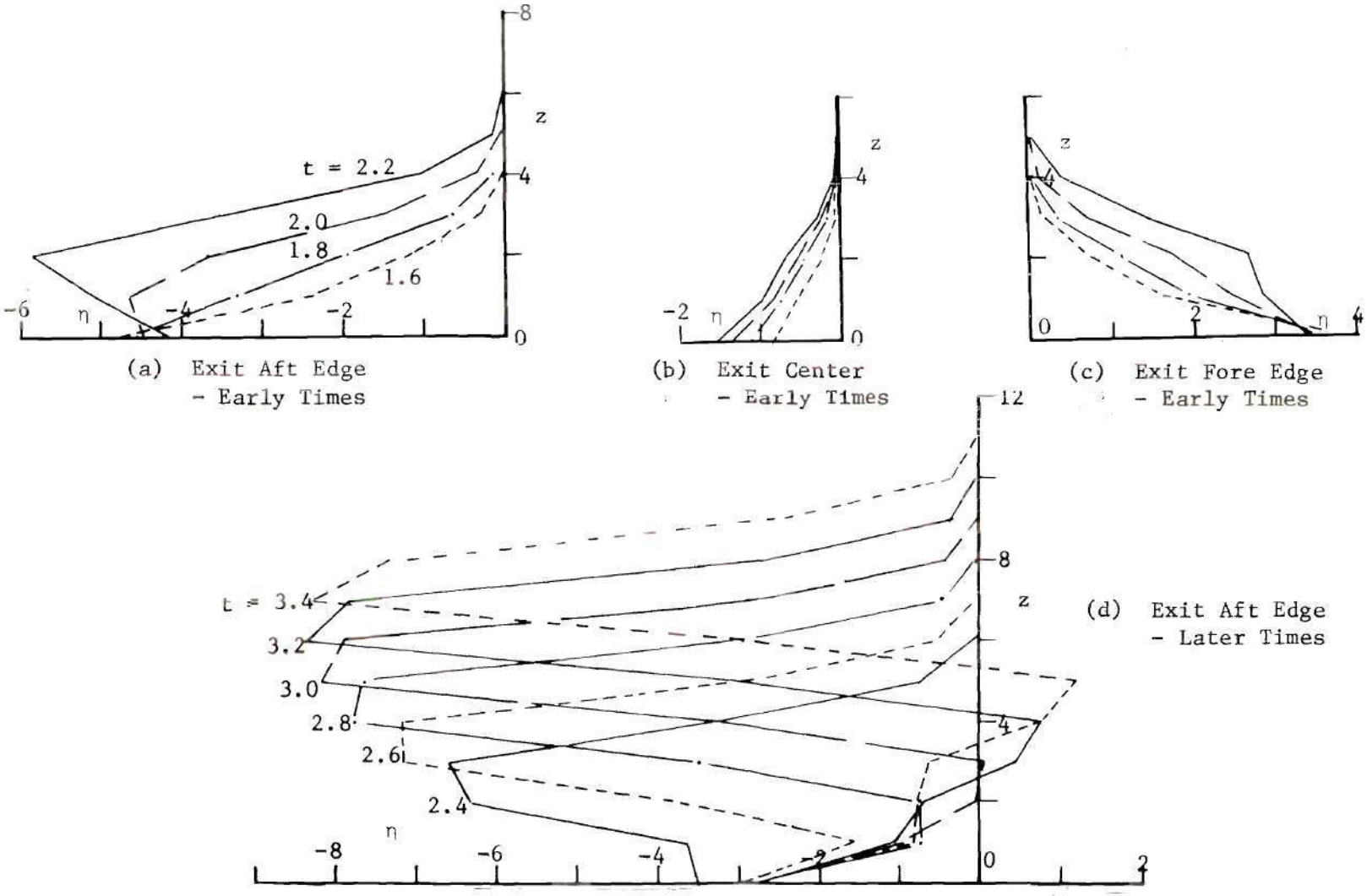

(a) Exit Aft Edge - Early Times

(b) Exit Center - Early Times

(c) Exit Fore Edge - Early Times

(d) Exit Aft Edge - Later Times

Figure 84. Horizontal Vorticity Profiles - Start from Opening of Jet Exit (V_r = 8) - 16 Step Gradual Start, Δt = 0.1 - R = 12

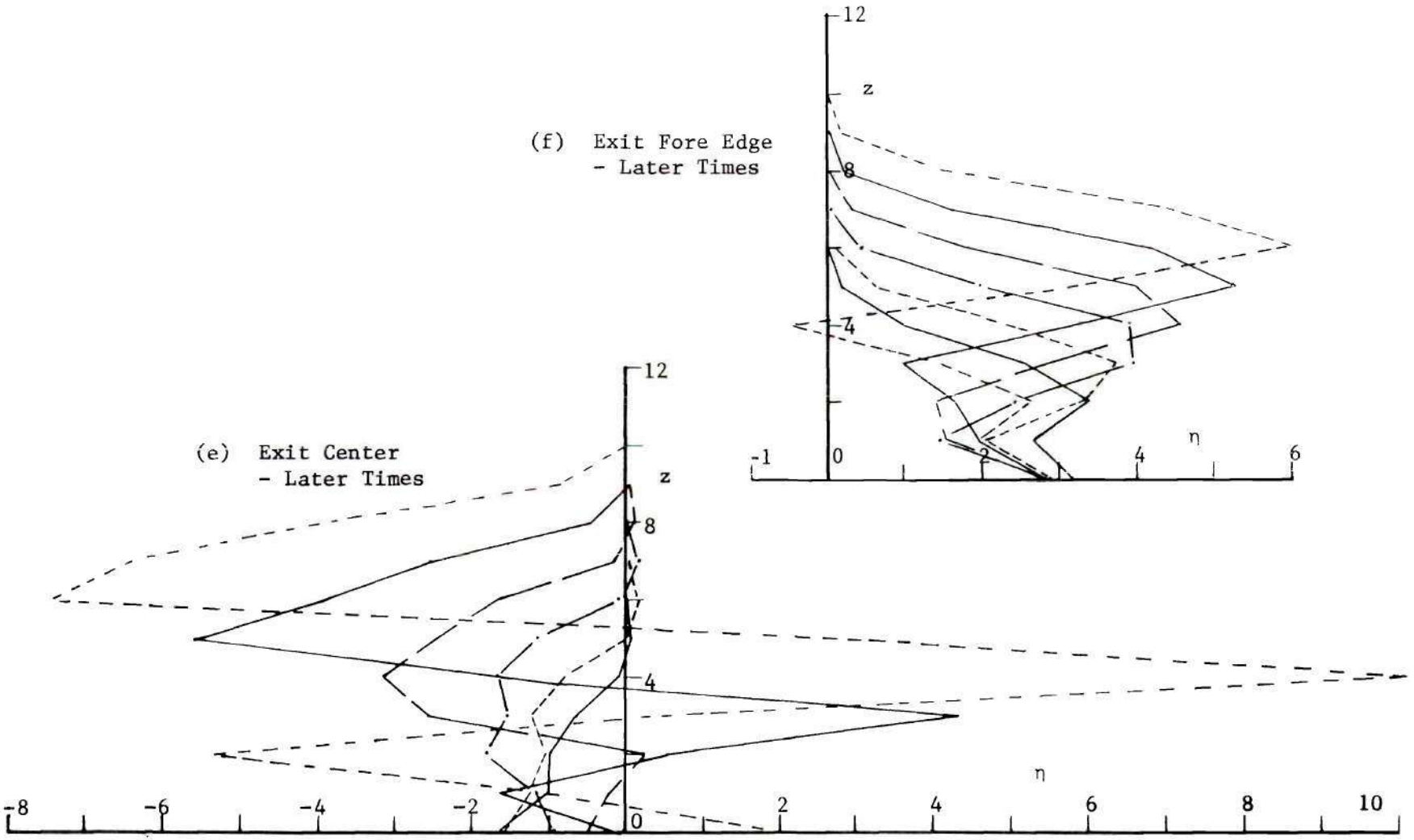

Figure 84. (cont.)

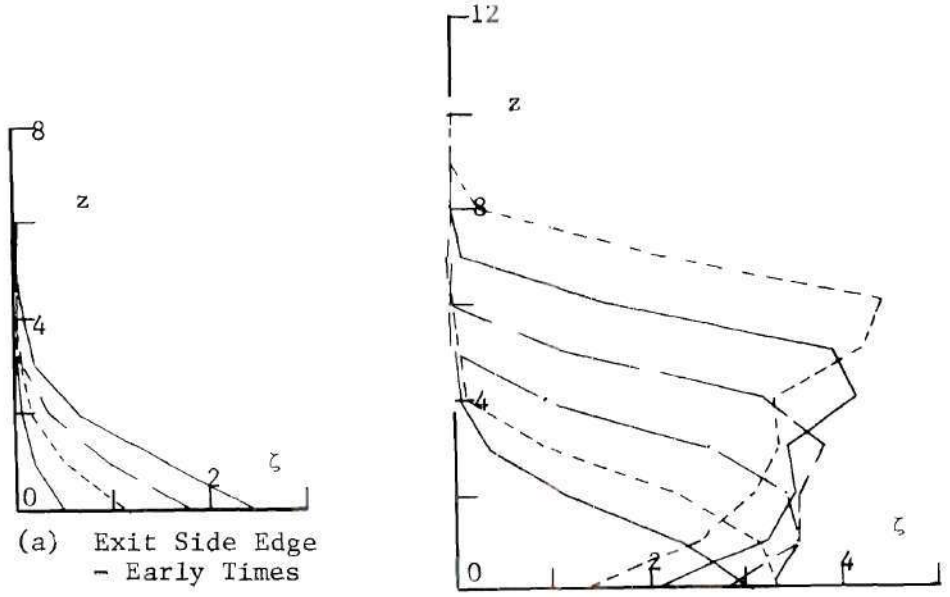

(a) Exit Side Edge - Early Times

(b) Exit Side Edge - Later Times

Figure 85. Vertical Vorticity Profiles - Start from Opening of Jet Exit (V_r = 8) - 16 Step Gradual Start, Δt = 0.1 - R = 12

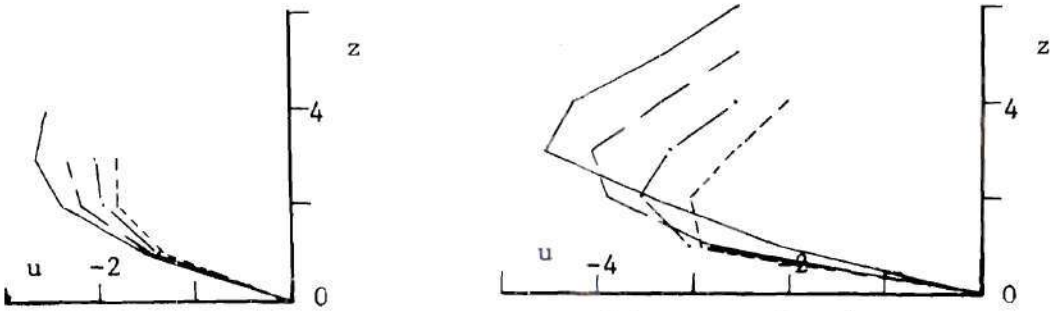

(a) One Radius Aft of Exit - Early Times

(b) Exit Aft Edge - Early Times

Figure 86. Horizontal Velocity Profiles - Start from Opening of Jet Exit (V_r = 8) - 16 Step Gradual Start, Δt = 0.1 - R = 12

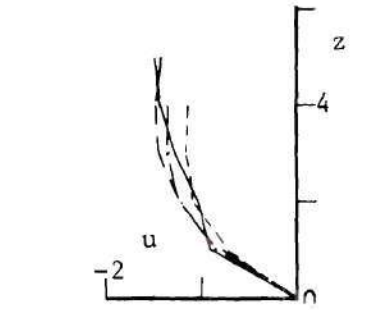

(c) Exit Center
- Early Times

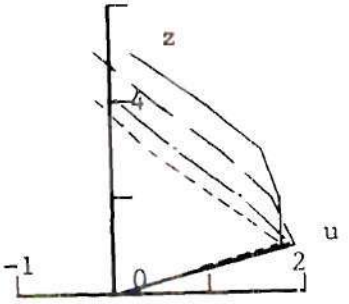

(d) Exit Fore Edge
- Early Times

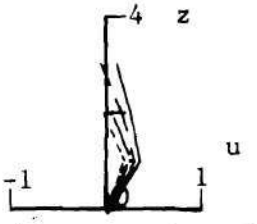

(e) One Radius Fore
of Exit
- Early Times

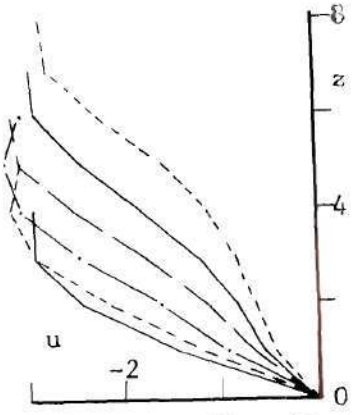

(f) One Radius Aft
of Exit
- Later Times

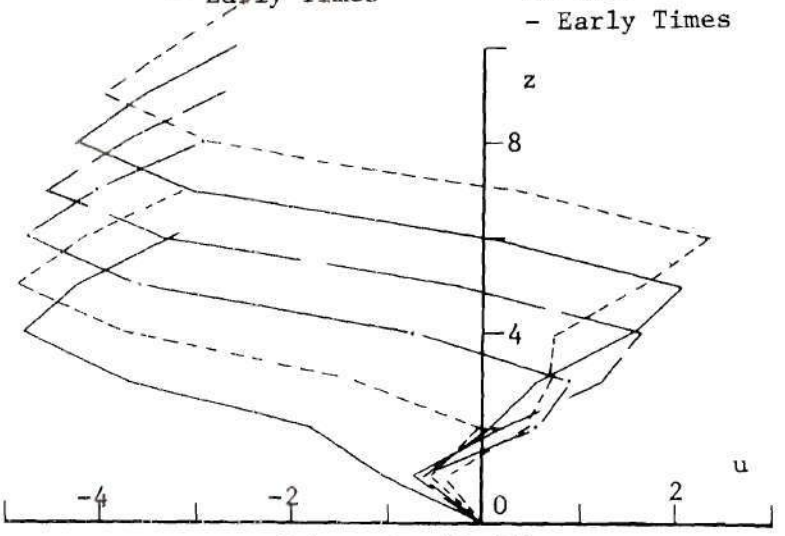

(g) Exit Aft Edge
- Later Times

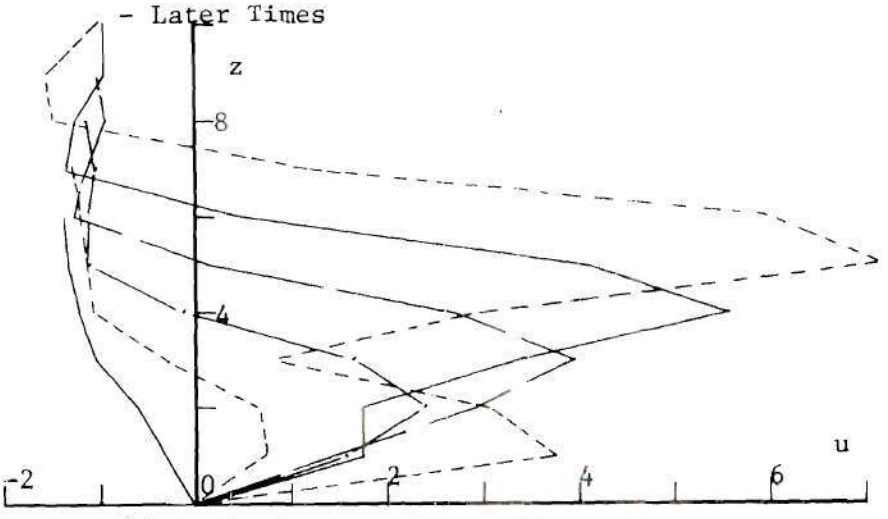

(h) Exit Center - Later Times

Figure 86. (cont.)

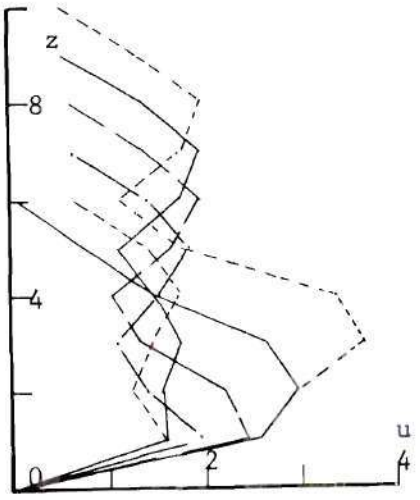

(i) Exit Fore Edge
- Later Times

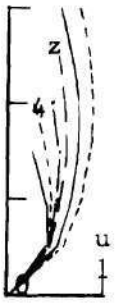

(j) One Radius Fore of Exit
- Later Times

Figure 86. (cont.)

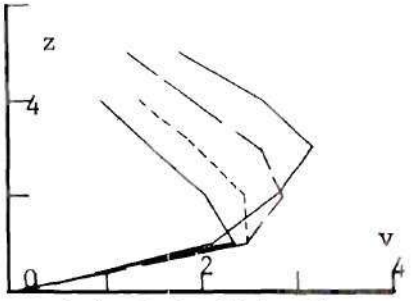

(a) Exit Side Edge
- Early Times

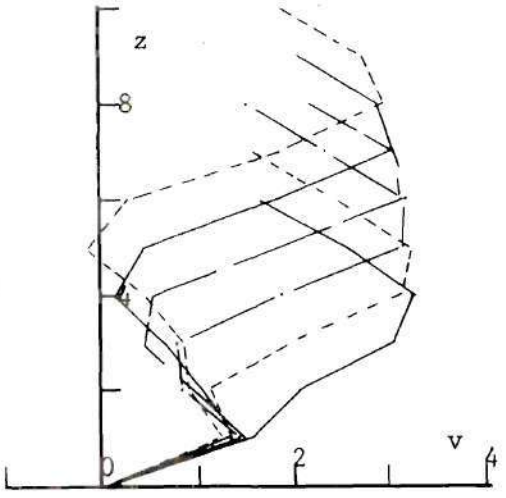

(b) Exit Side Edge
- Later Times

Figure 87. Horizontal Velocity Profiles - Start from Opening of Jet Exit (V_r = 8) - 16 Step Gradual Start, Δt = 0.1 - R = 12

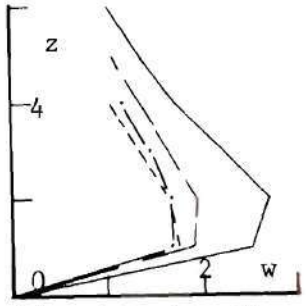

(a) Exit Aft Edge
- Early Times

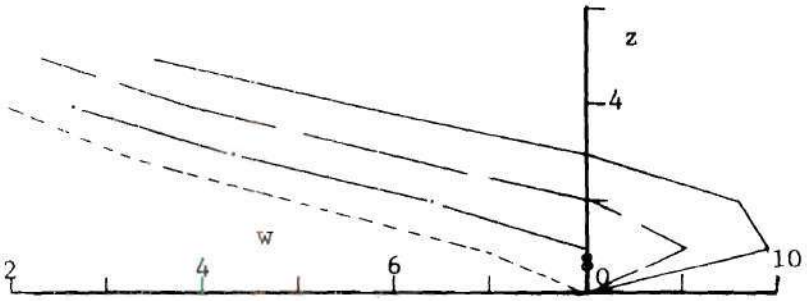

(b) Exit Center
- Early Times

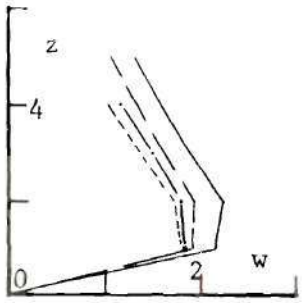

(c) Exit Fore Edge
- Early Times

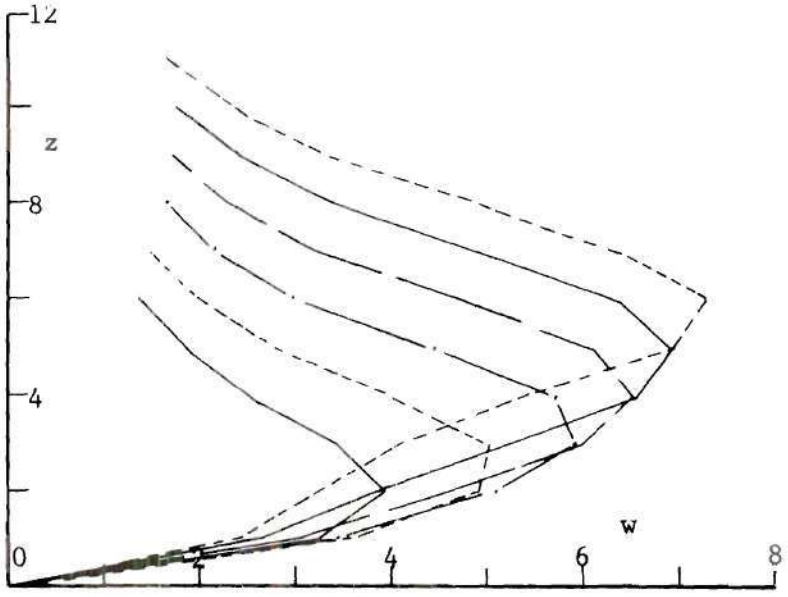

(d) Exit Aft Edge
- Later Times

Figure 88. Vertical Velocity Profiles - Start from Opening of Jet Exit (V_r = 8) - 16 Step Gradual Start, Δt = 0.1 - R = 12

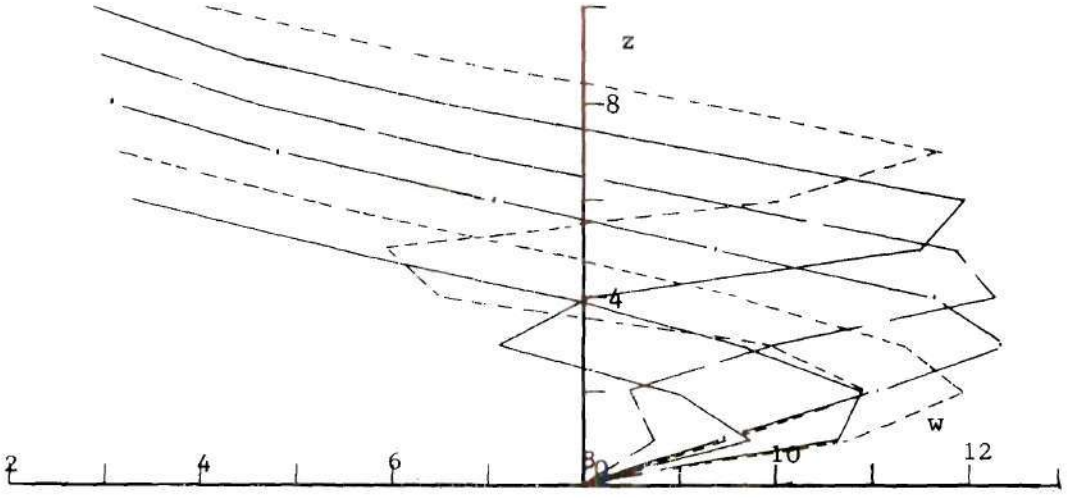

(e) Exit Center
- Later Times

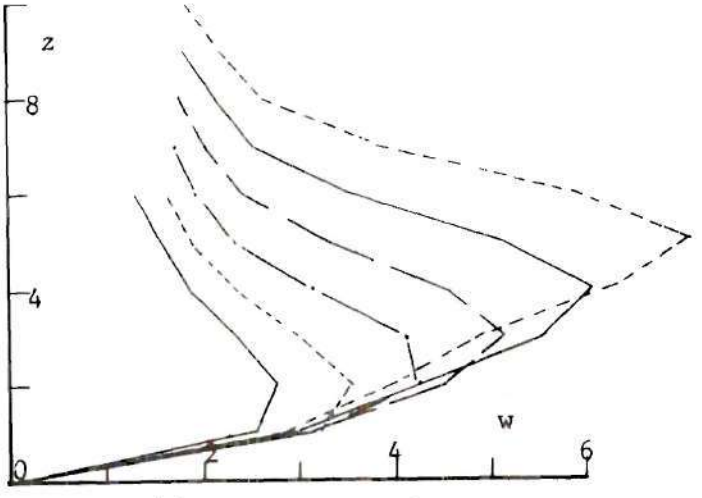

(f) Exit Fore Edge
- Later Times

Figure 88. (cont.)

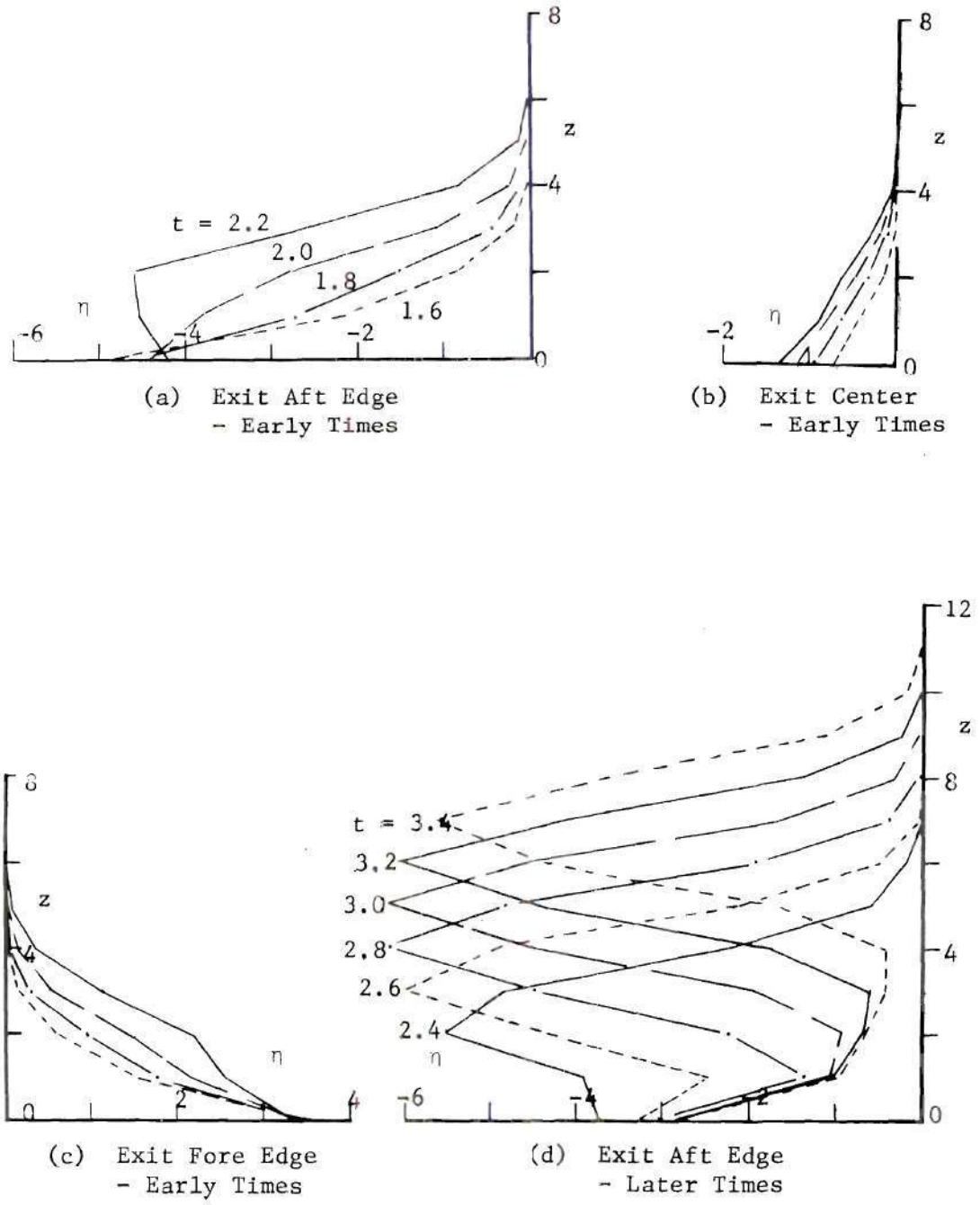

Figure 89. Horizontal Vorticity Profiles - Start from Opening of Jet Exit (V_r = 8) - 32 Step Gradual Start, Δt = 0.05 - R = 12

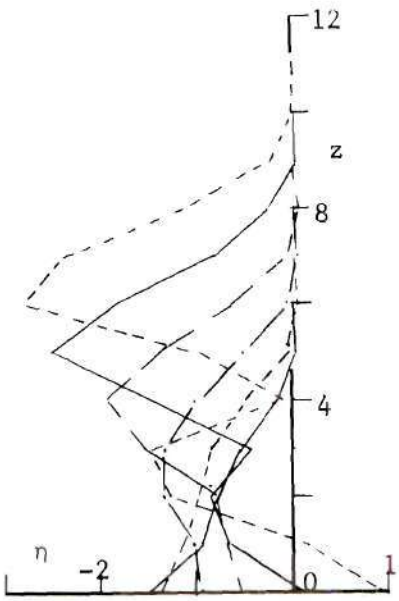

(e) Exit Center
- Later Times

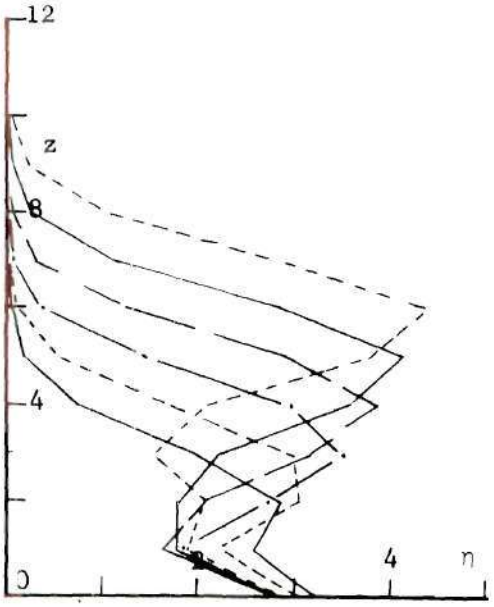

(f) Exit Fore Edge
- Later Times

Figure 89. (cont.)

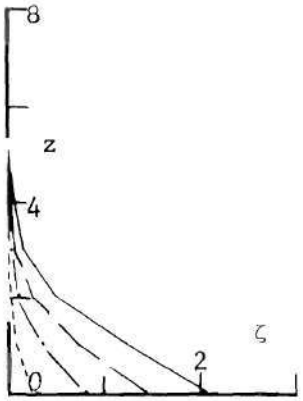

(a) Exit Side Edge
- Early Times

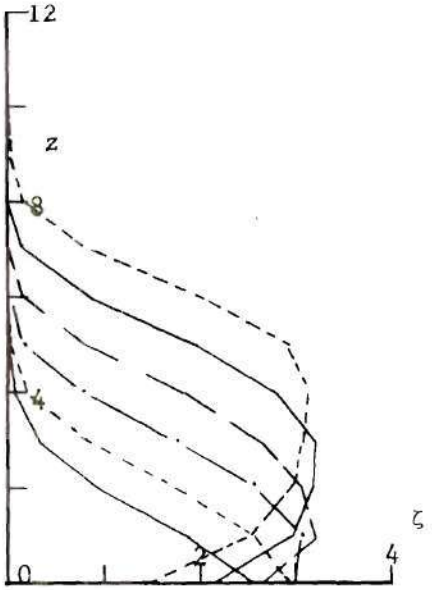

(b) Exit Side Edge
- Later Times

Figure 90. Vertical Vorticity Profiles - Start from Opening of Jet Exit (V_r = 8) - 32 Step Gradual Start, Δt = 0.05 - R = 12

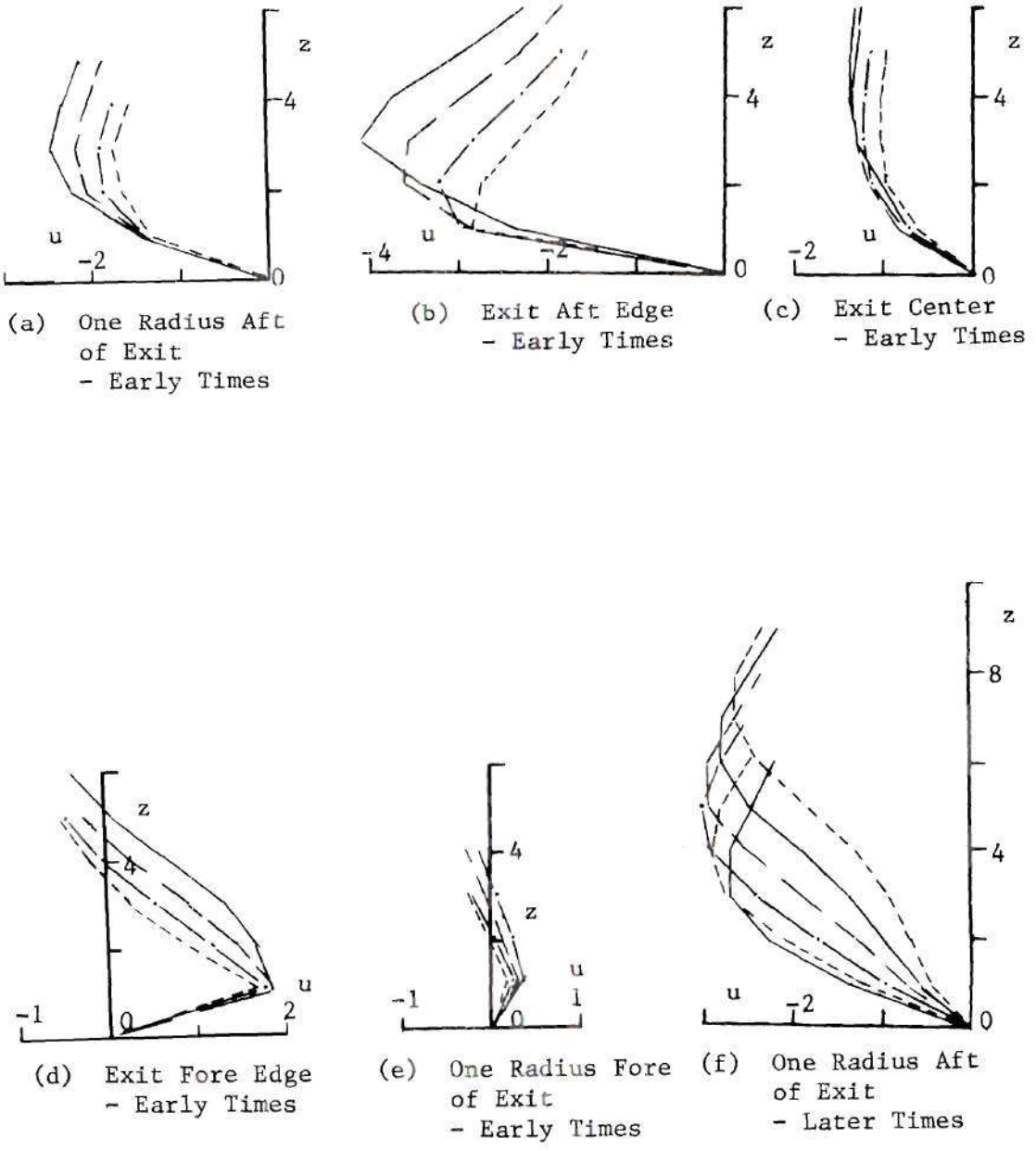

Figure 91. Horizontal Velocity Profiles - Start from Opening of Jet Exit (V_r = 8) - 32 Step Gradual Start, Δt = 0.05 - R = 12

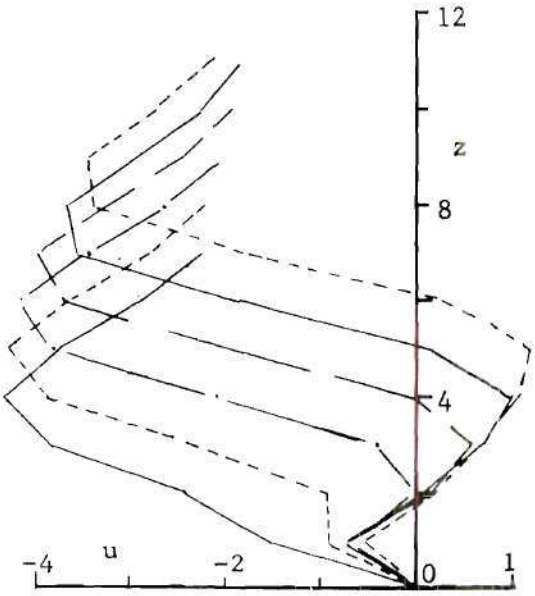

(g) Exit Aft Edge
- Later Times

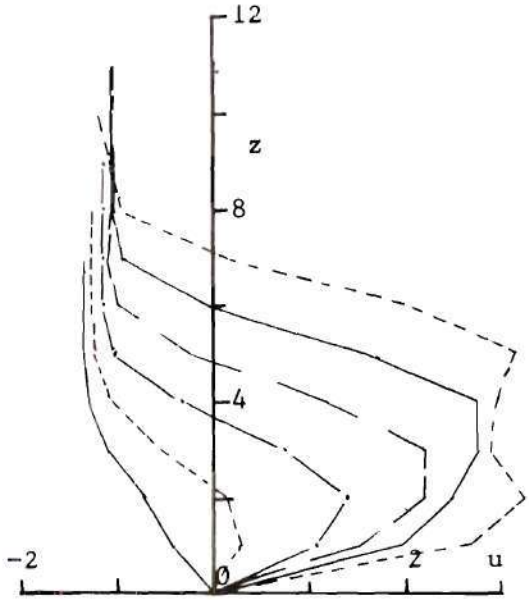

(h) Exit Center
- Later Times

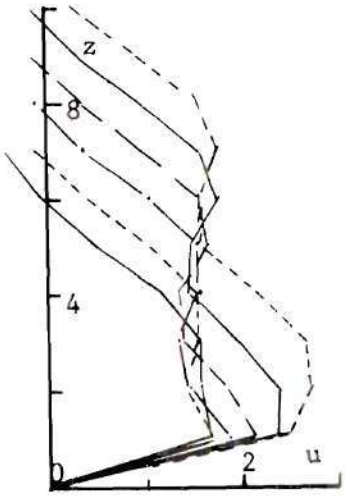

(i) Exit Fore Edge
- Later Times

(j) One Radius Fore
of Exit
- Later Times

Figure 91. (cont.)

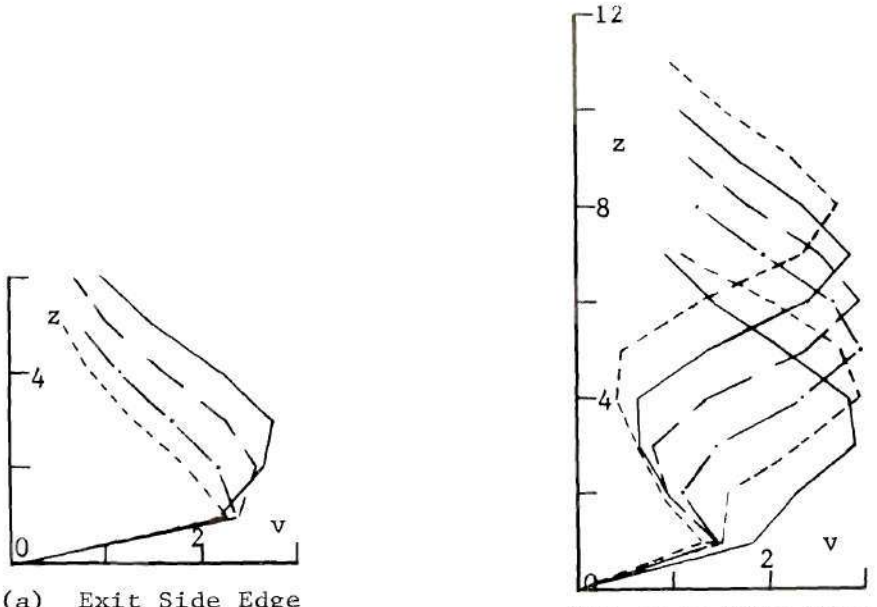

(a) Exit Side Edge - Early Times

(b) Exit Side Edge - Later Times

Figure 92. Horizontal Velocity Profiles - Start from Opening of Jet Exit (V_r = 8) - 32 Step Gradual Start, Δt = 0.05 - R = 12

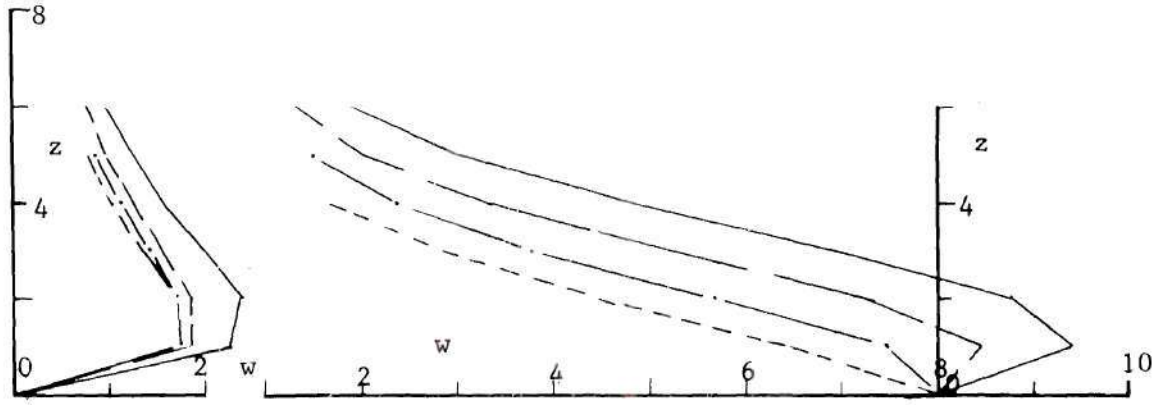

(a) Exit Aft Edge - Early Times

(b) Exit Center - Early Times

Figure 93. Vertical Velocity Profiles - Start from Opening of Jet Exit (V_r = 8) - 32 Step Gradual Start, Δt = 0.05 - R = 12

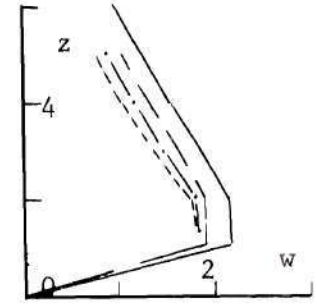

(c) Exit Fore Edge
- Early Times

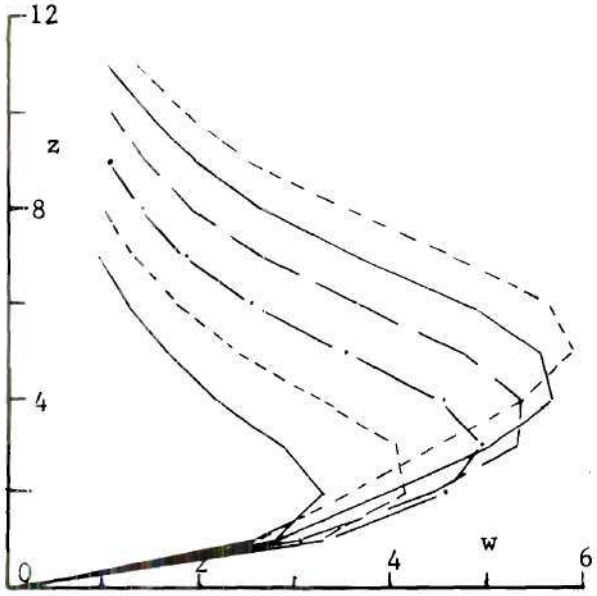

(d) Exit Aft Edge
- Later Times

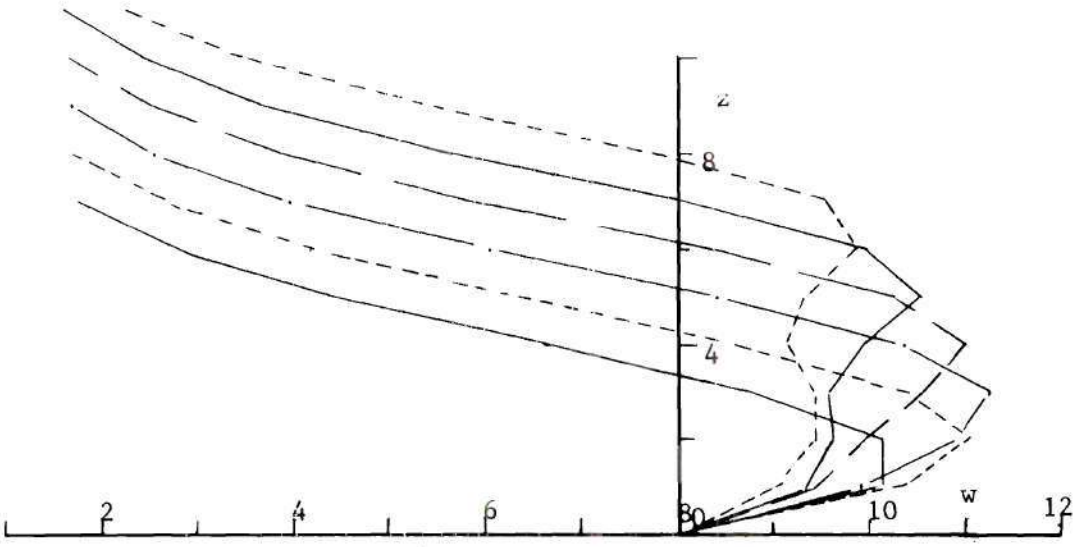

(e) Exit Center
- Later Times

Figure 93. (cont.)

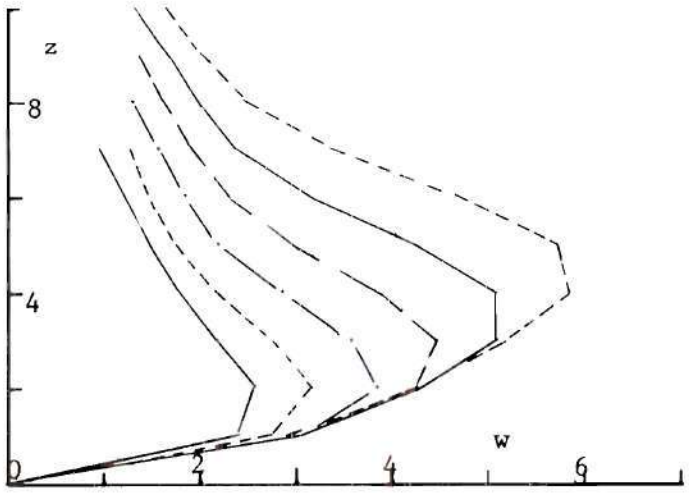

(f) Exit Fore Edge
- Later Times

Figure 93. (cont.)

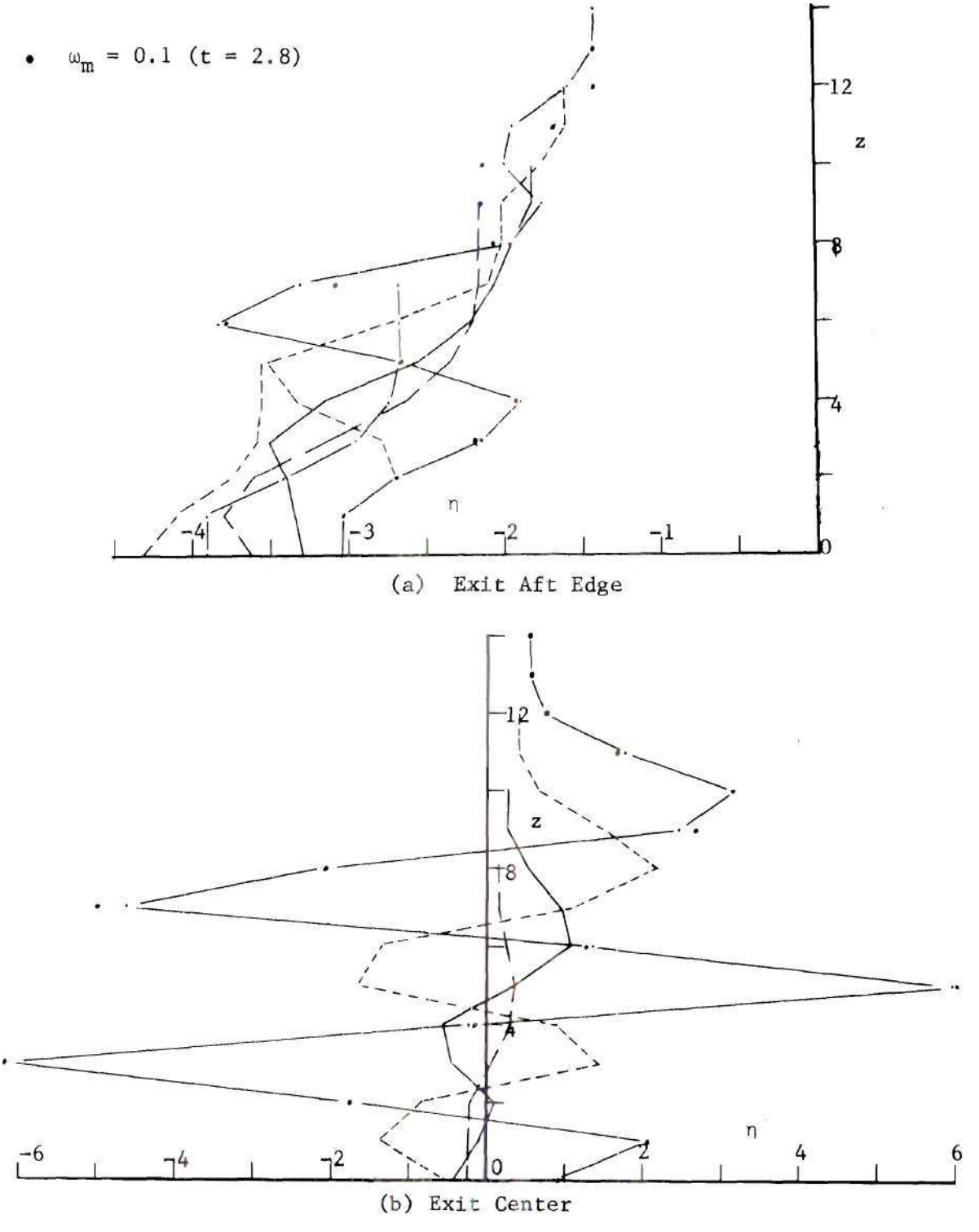

Figure 94. Horizontal Vorticity Profiles - Start from Cylindrical Discontinuity (V_r = 8) - Four Step Gradual Start, Δt = 0.2 - R = 12

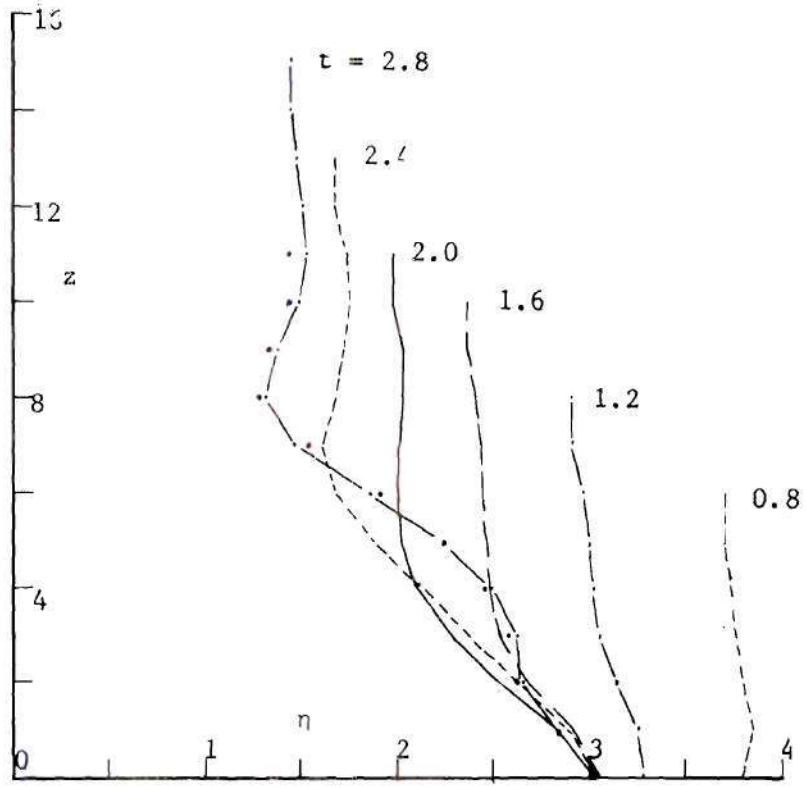

(c) Exit Fore Edge

Figure 94. (cont.)

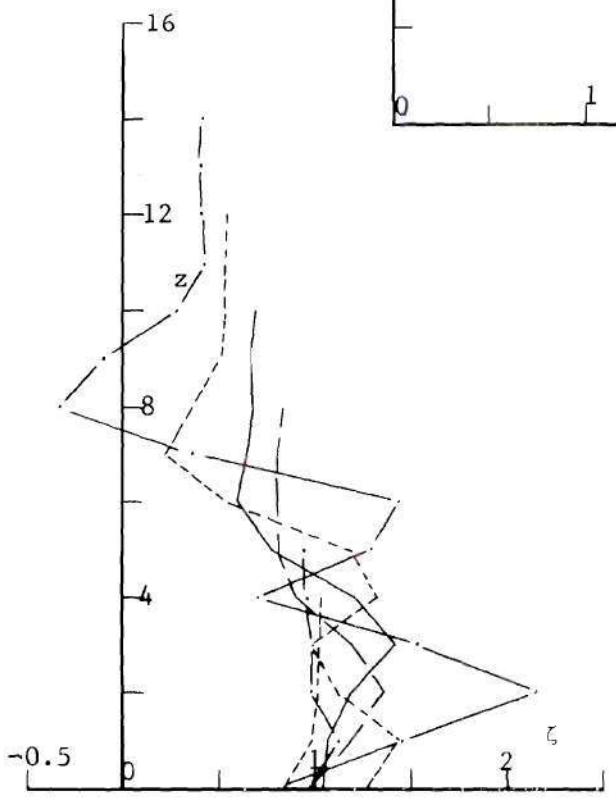

Figure 95. Vertical Vorticity Profiles - Start from Cylindrical Discontinuity (V_r = 8) - Four Step Gradual Start, Δt = 0.2 - R = 12 - Exit Side Edge

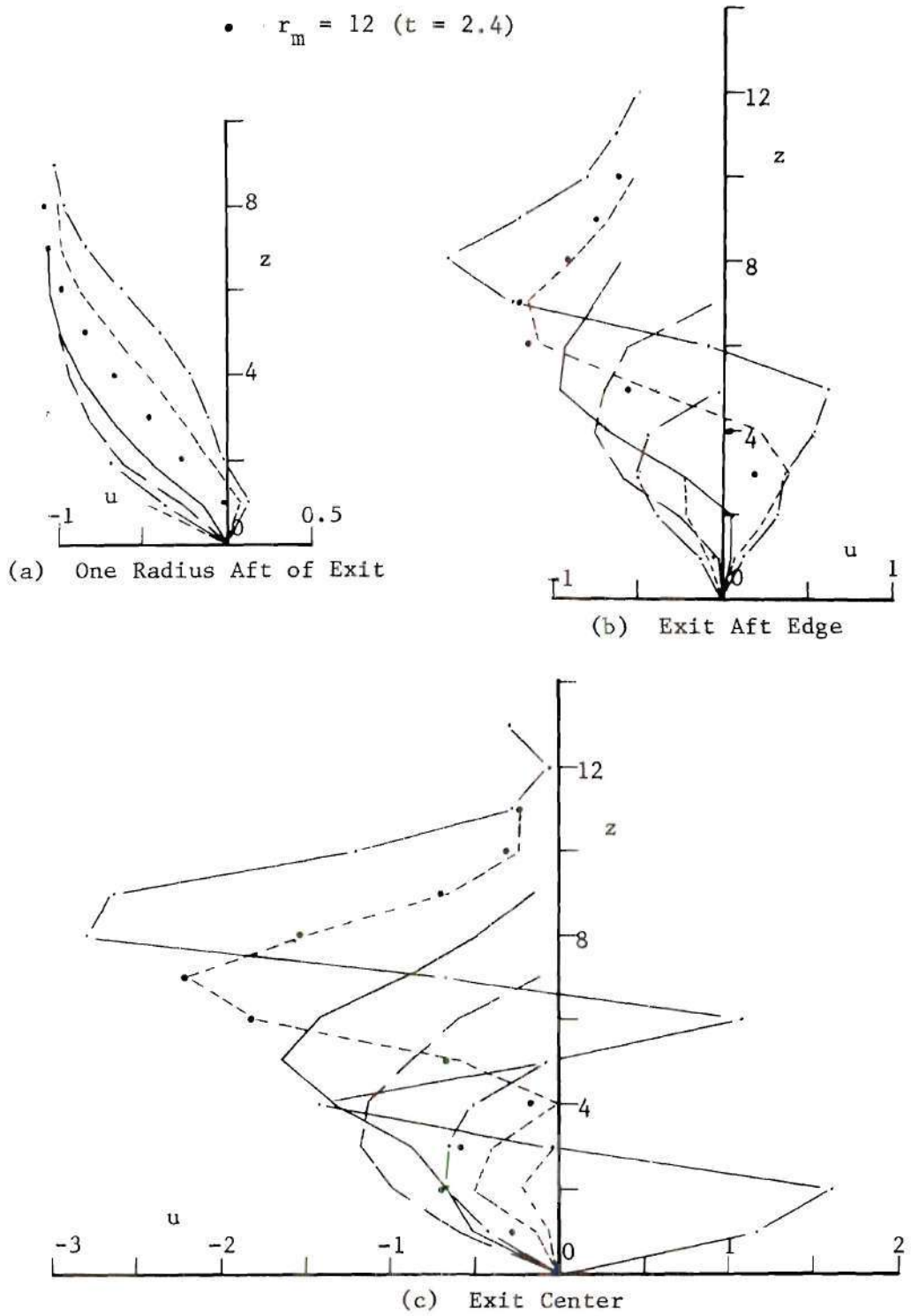

Figure 96. Horizontal Velocity Profiles - Start from Cylindrical Discontinuity (V_r = 8) - Four Step Gradual Start, Δt = 0.2 - R = 12

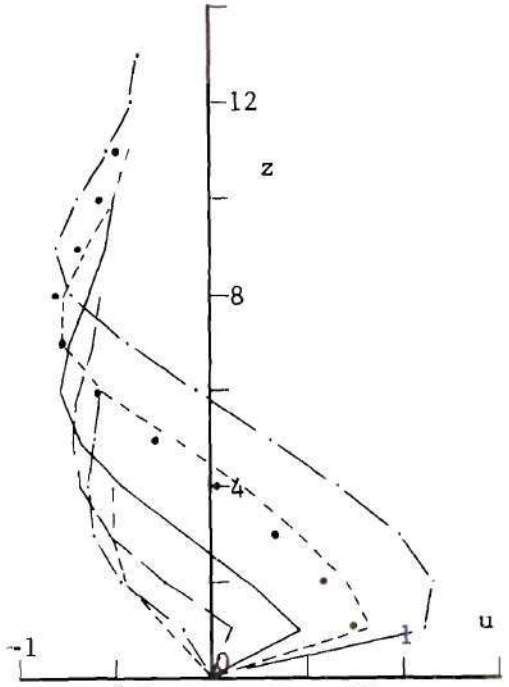

(d) Exit Fore Edge

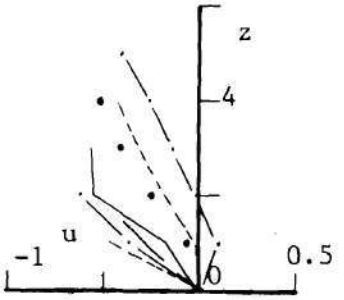

(e) One Radius Fore of Exit

Figure 96. (cont.)

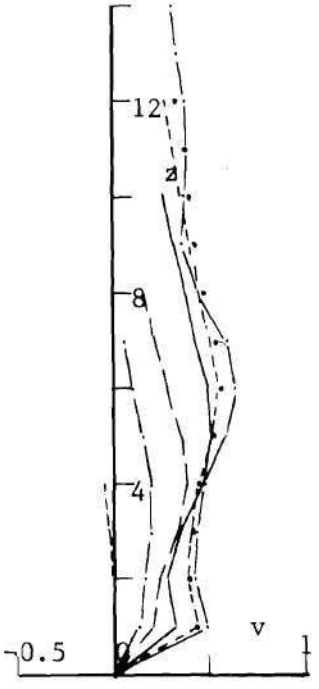

• r_m = 12 (t = 2.4)

Figure 97. Horizontal Velocity Profiles - Start from Cylindrical Discontinuity (V_r = 8) - Four Step Gradual Start, Δt = 0.2 - R = 12 - Exit Side Edge

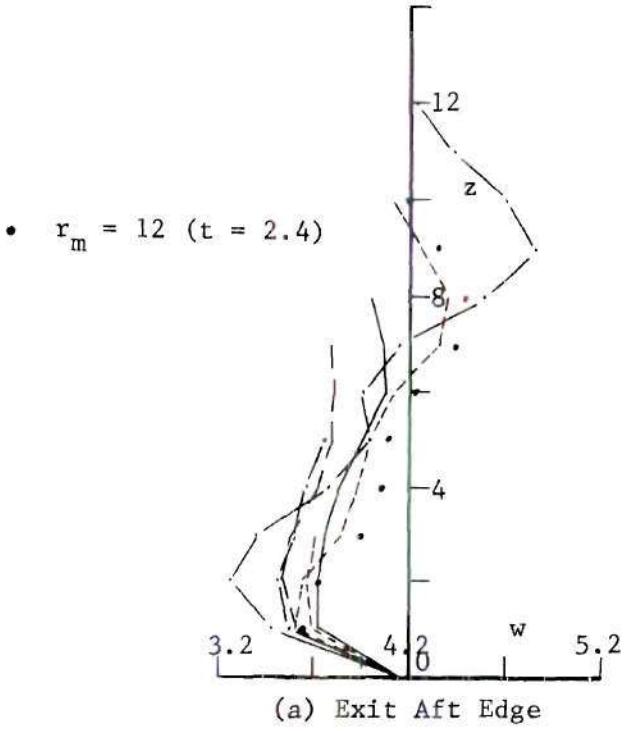

(a) Exit Aft Edge

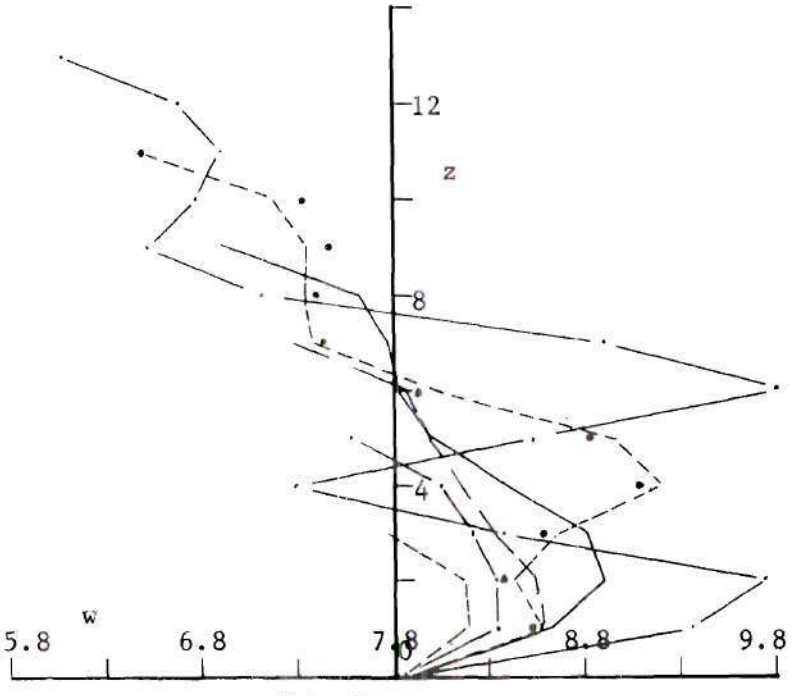

(b) Exit Center

Figure 98. Vertical Velocity Profiles - Start from Cylindrical Discontinuity (V_r = 8) - Four Step Gradual Start, Δt = 0.2 - R = 12

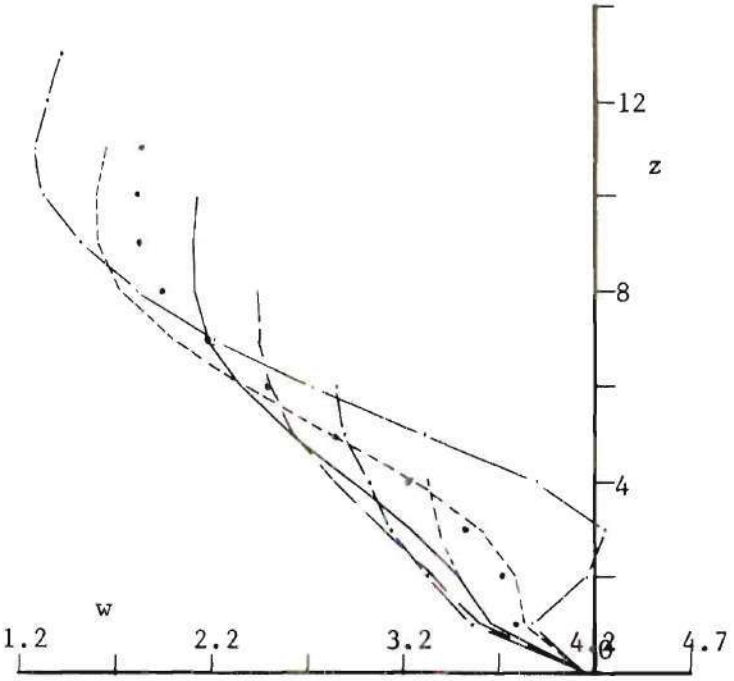

(c) Exit Fore Edge

Figure 98. (cont.)

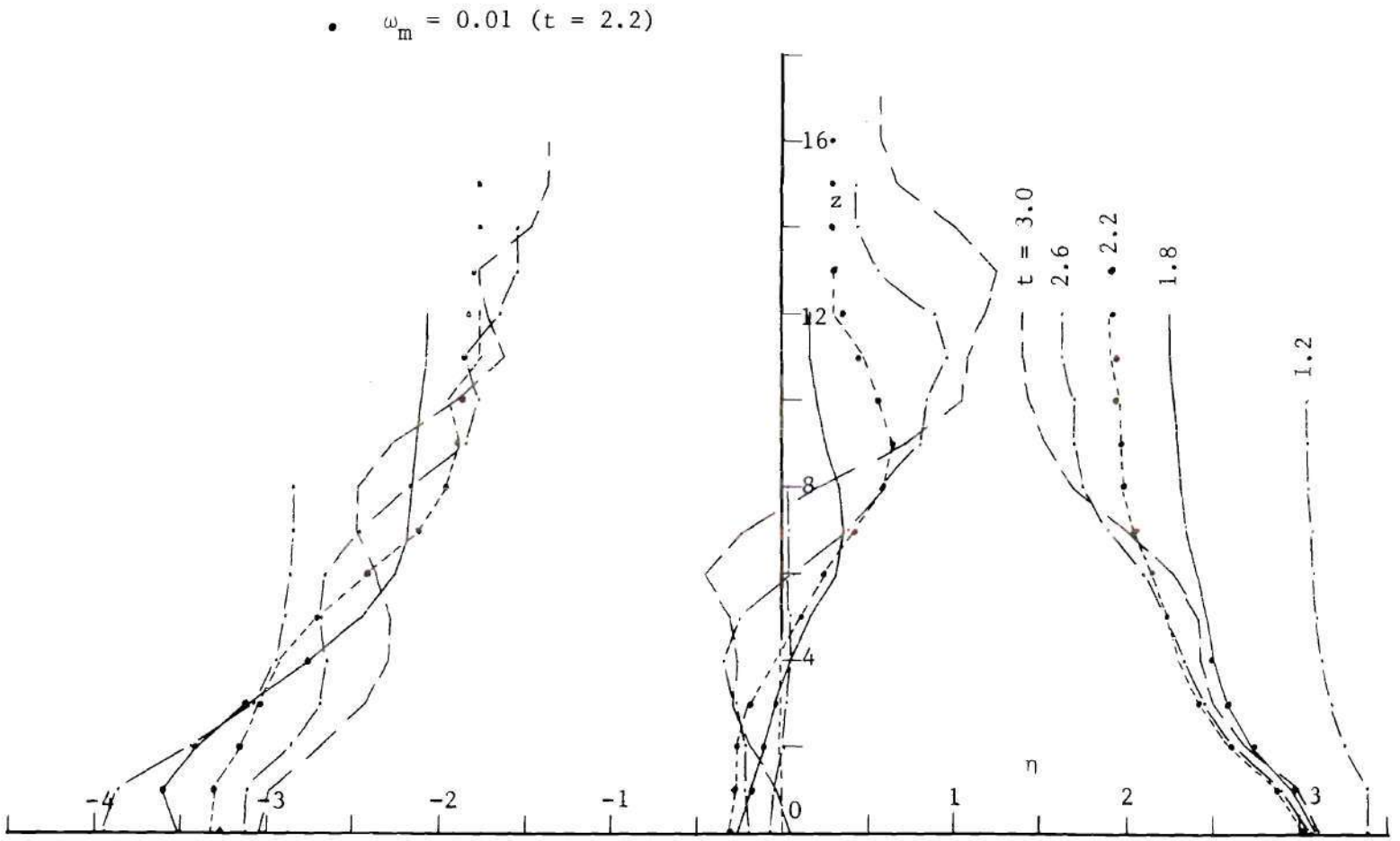

(a) Exit Aft Edge - Early Times

(b) Exit Center - Early Times

(c) Exit Fore Edge - Early Times

Figure 99. Horizontal Vorticity Profiles - Start from Cylindrical Discontinuity (V_r = 8) - Eight Step Gradual Start, Δt = 0.1 - R = 12

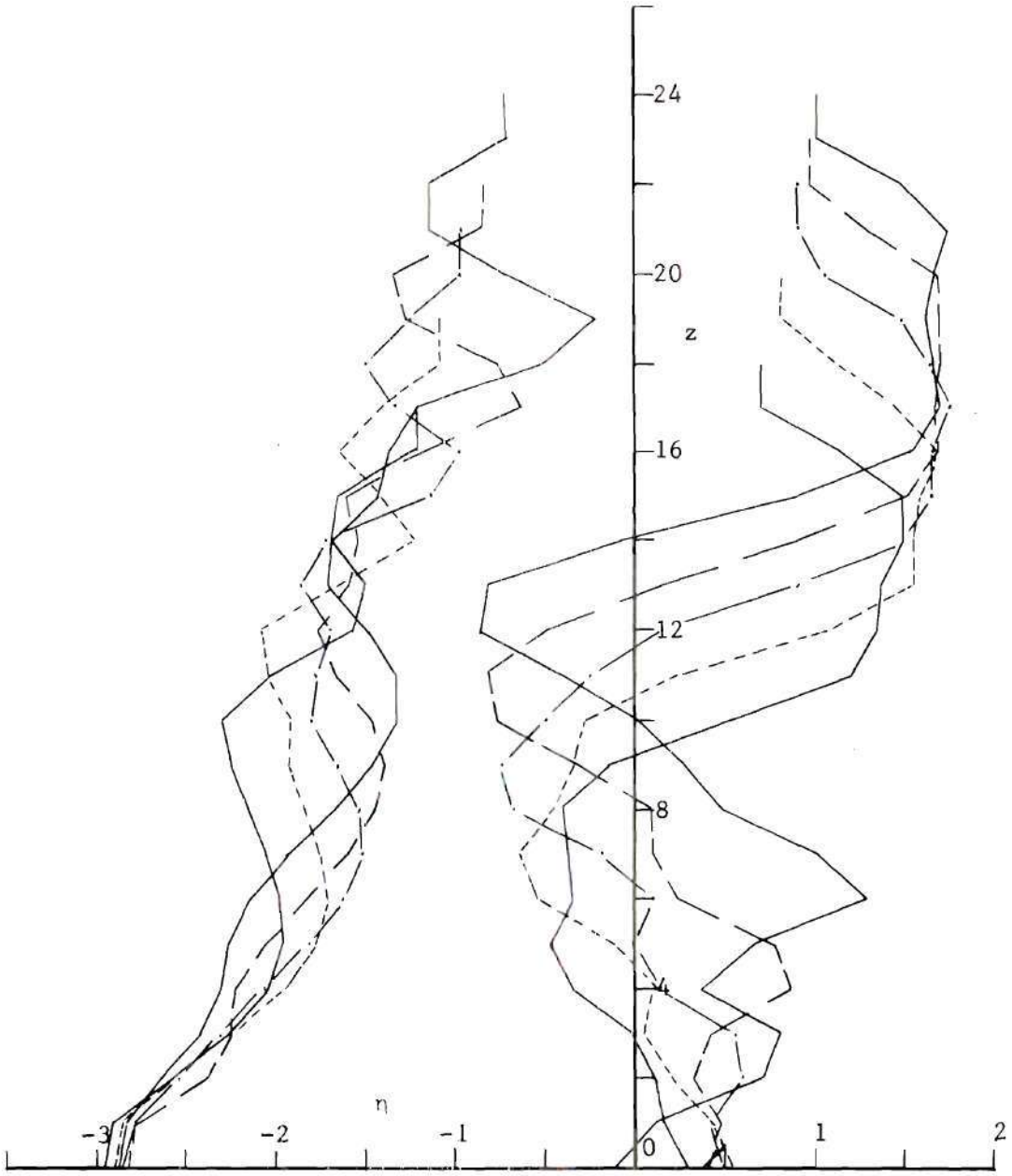

(d) Exit Aft Edge - Later Times

(e) Exit Center - Later Times

Figure 99. (cont.)

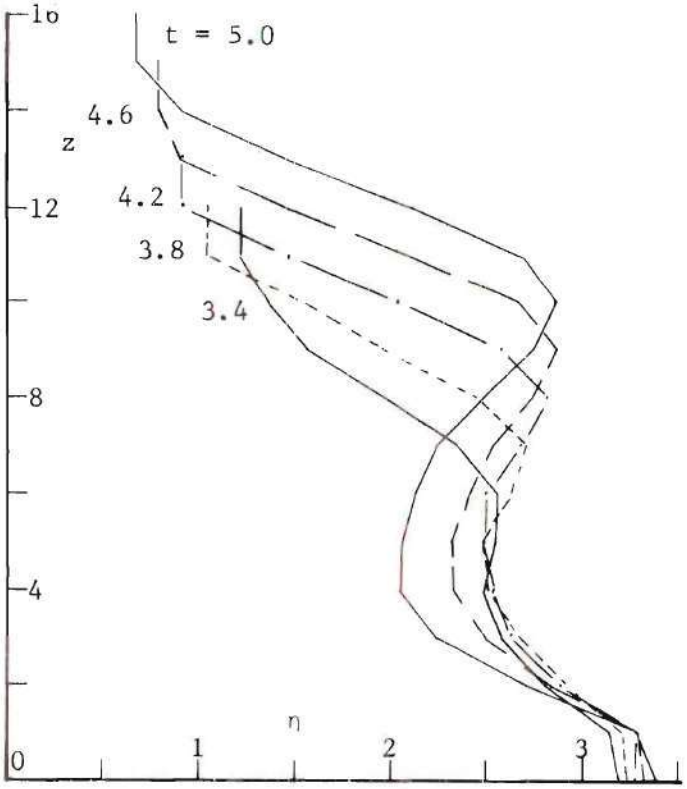

(f) Exit Fore Edge
- Later Times

Figure 99. (cont.)

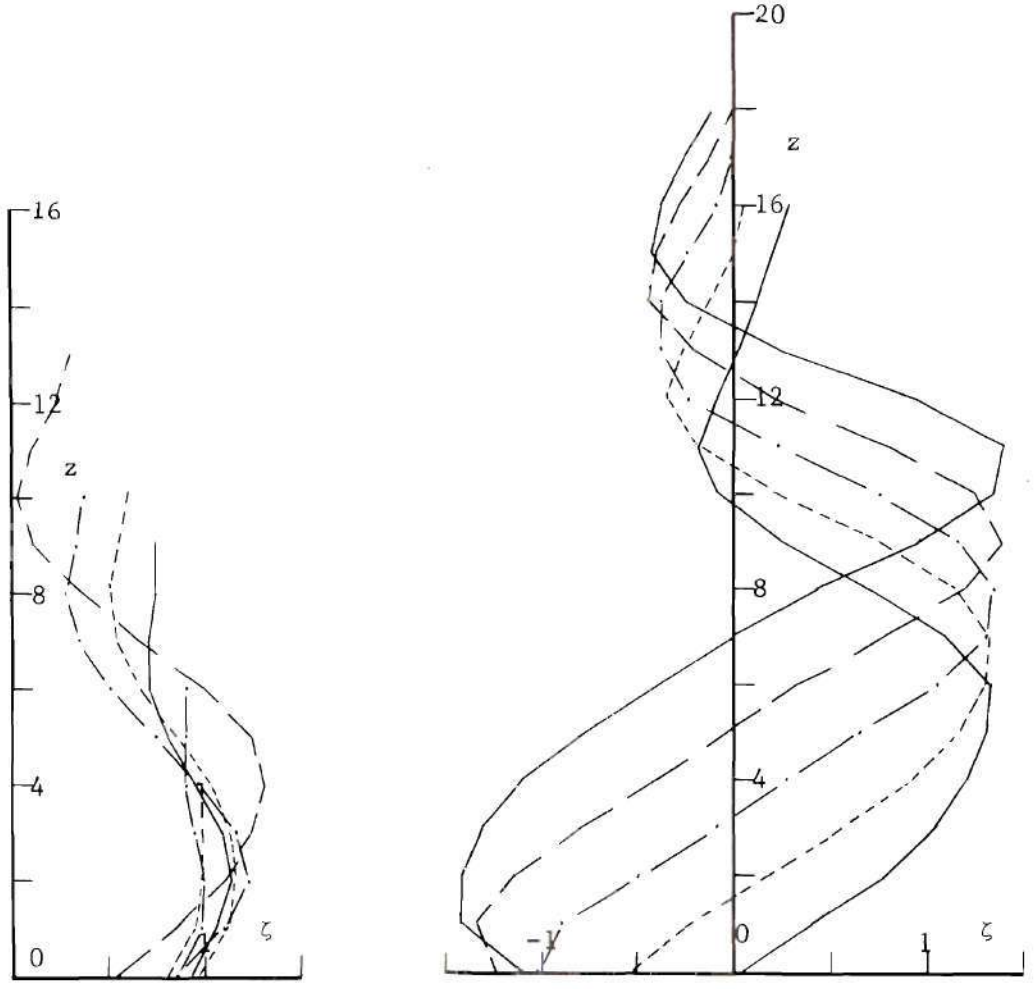

(a) Exit Side Edge - Early Times

(b) Exit Side Edge - Later Times

Figure 100. Vertical Vorticity Profiles - Start from Cylindrical Discontinuity (V_r = 8) - Eight Step Gradual Start, Δt = 0.1 - R = 12

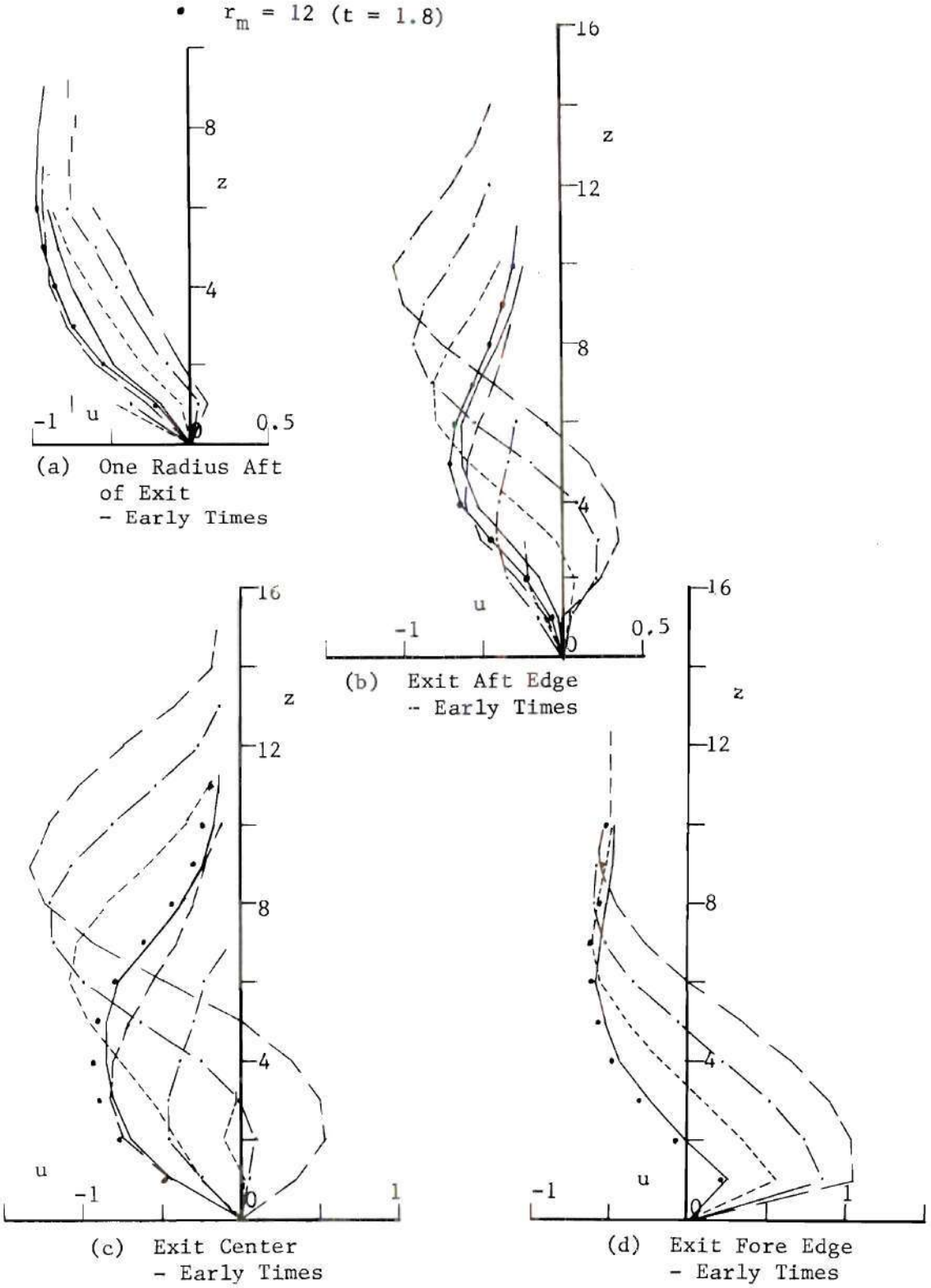

Figure 101. Horizontal Velocity Profiles - Start from Cylindrical Discontinuity (V_r = 8) - Eight Step Gradual Start, Δt = 0.1 - R = 12

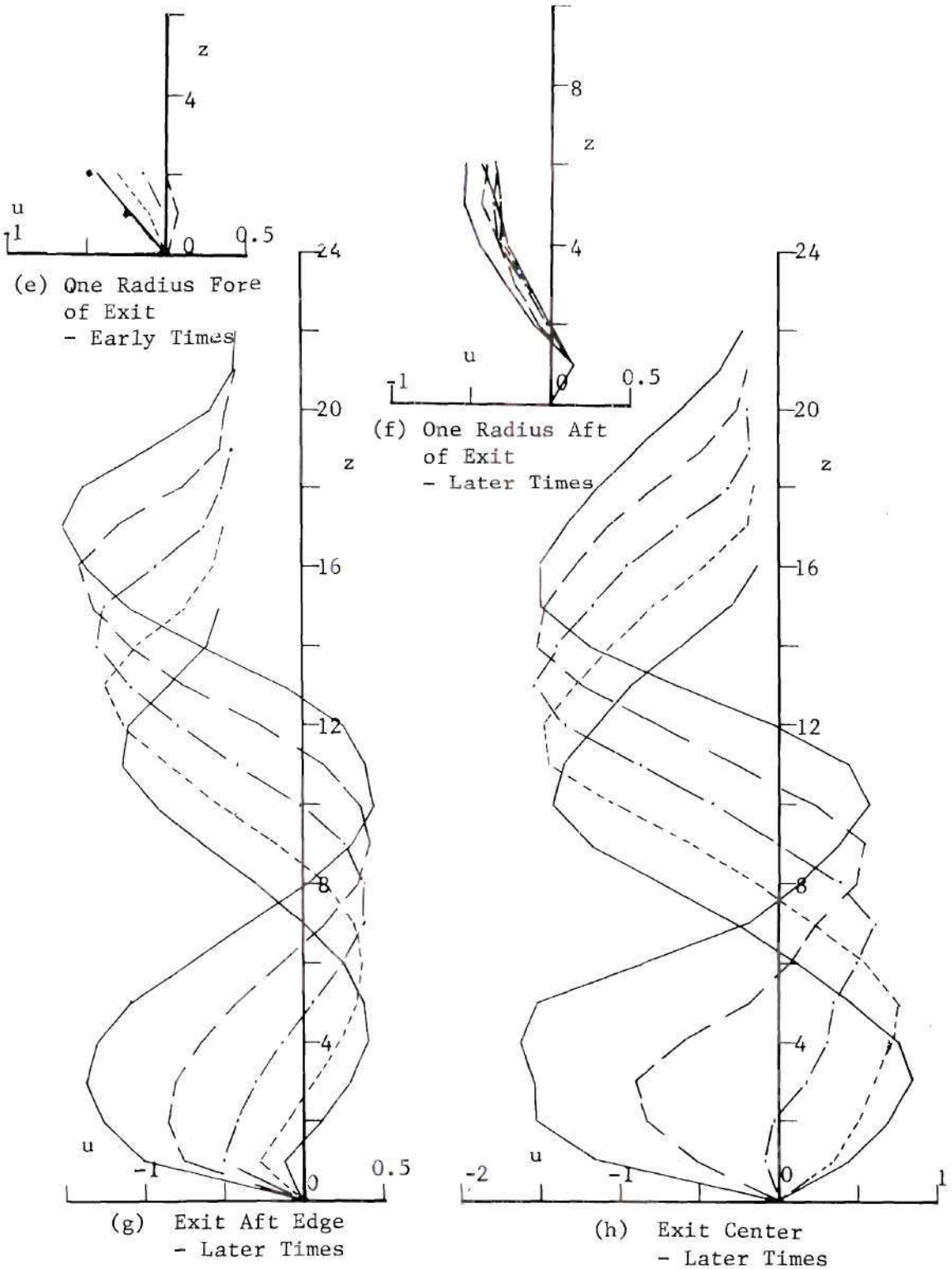

Figure 101. (cont.)

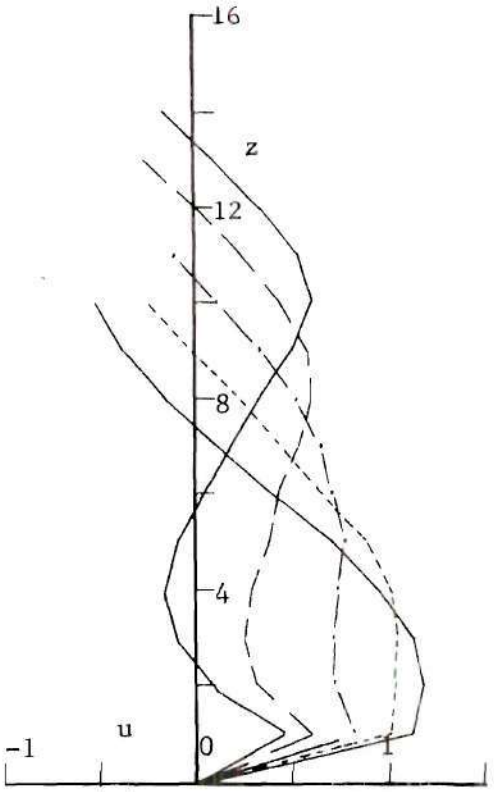

(i) Exit Fore Edge
- Later Times

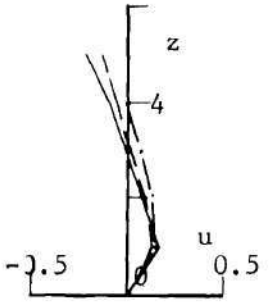

(j) One Radius Fore
of Exit
- Later Times

Figure 101. (cont.)

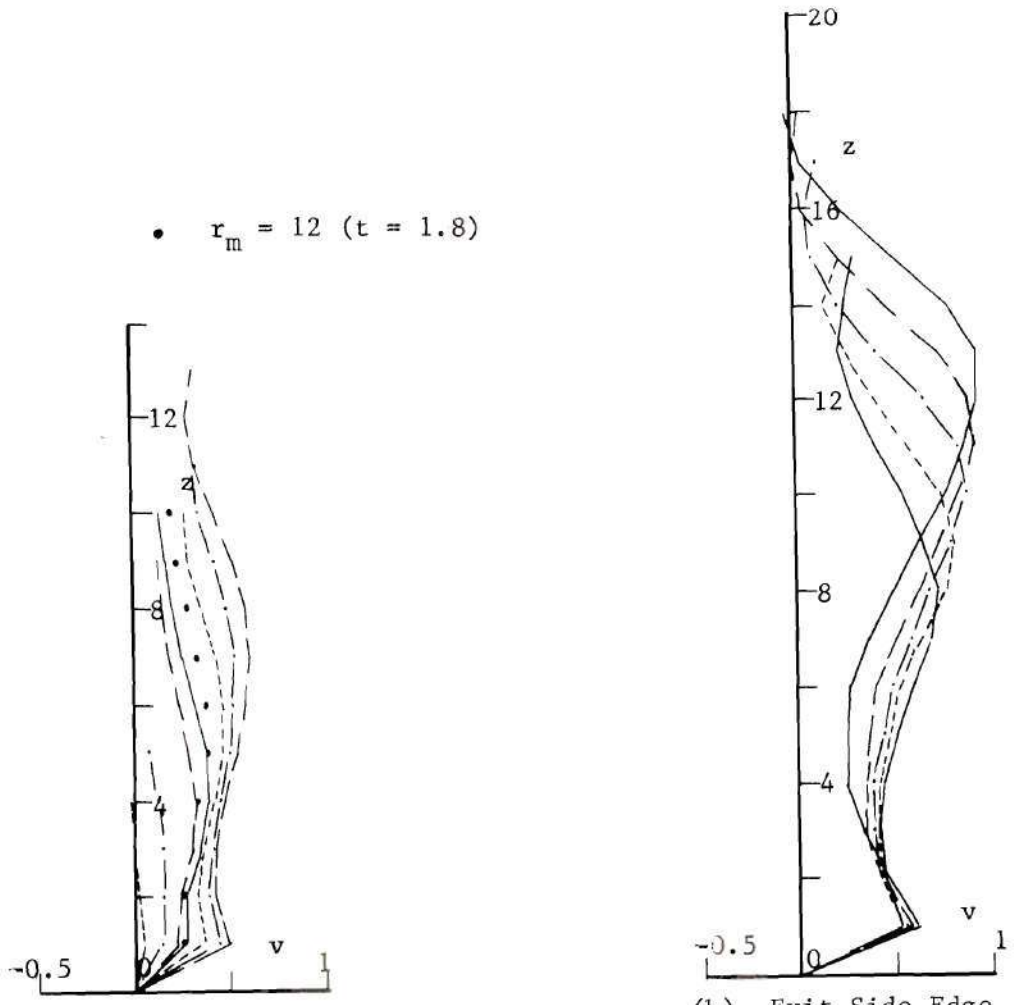

(a) Exit Side Edge - Early Times

(b) Exit Side Edge - Later Times

Figure 102. Horizontal Velocity Profiles - Start from Cylindrical Discontinuity (V_r = 8) - Eight Step Gradual Start, Δt = 0.1 - R = 12

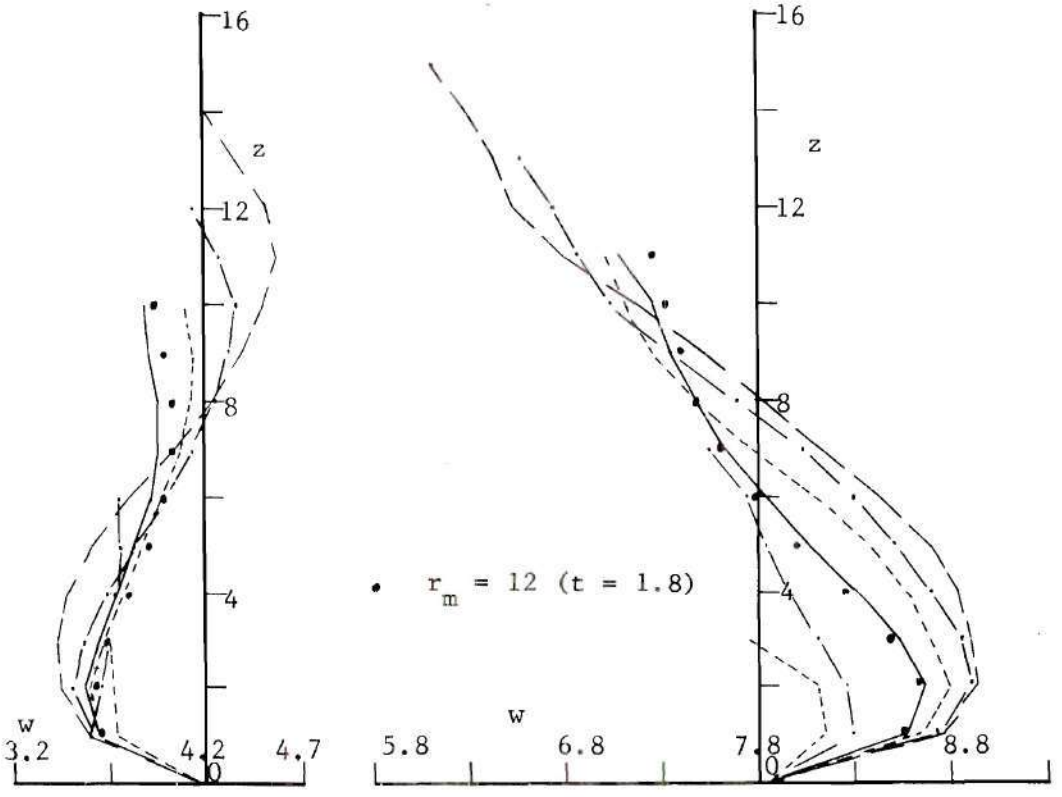

Figure 103. Vertical Velocity Profiles - Start from Cylindrical Discontinuity (V_r = 8) - Eight Step Gradual Start, Δt = 0.1 - R = 12

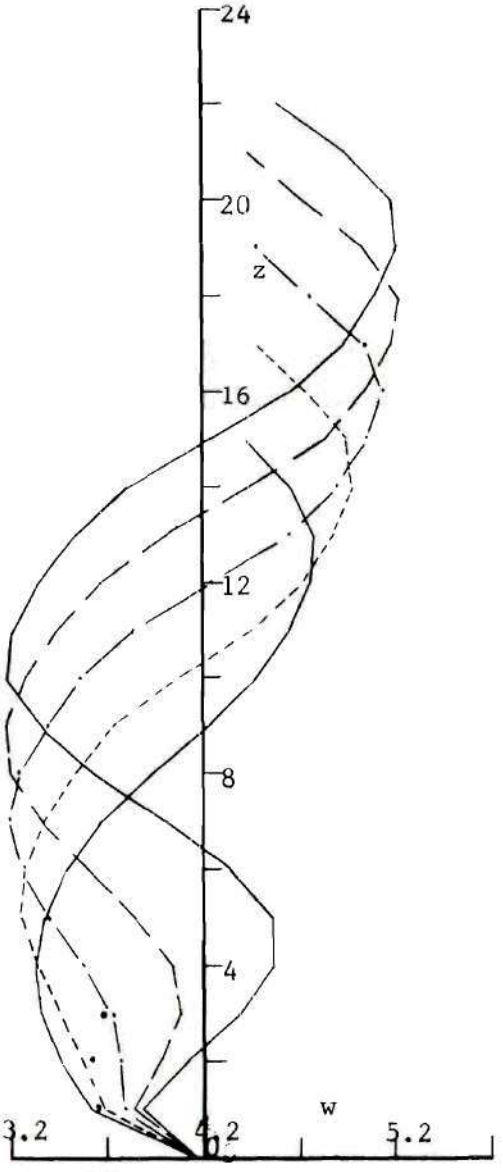

(d) Exit Aft Edge
- Later Times

Figure 103. (cont.)

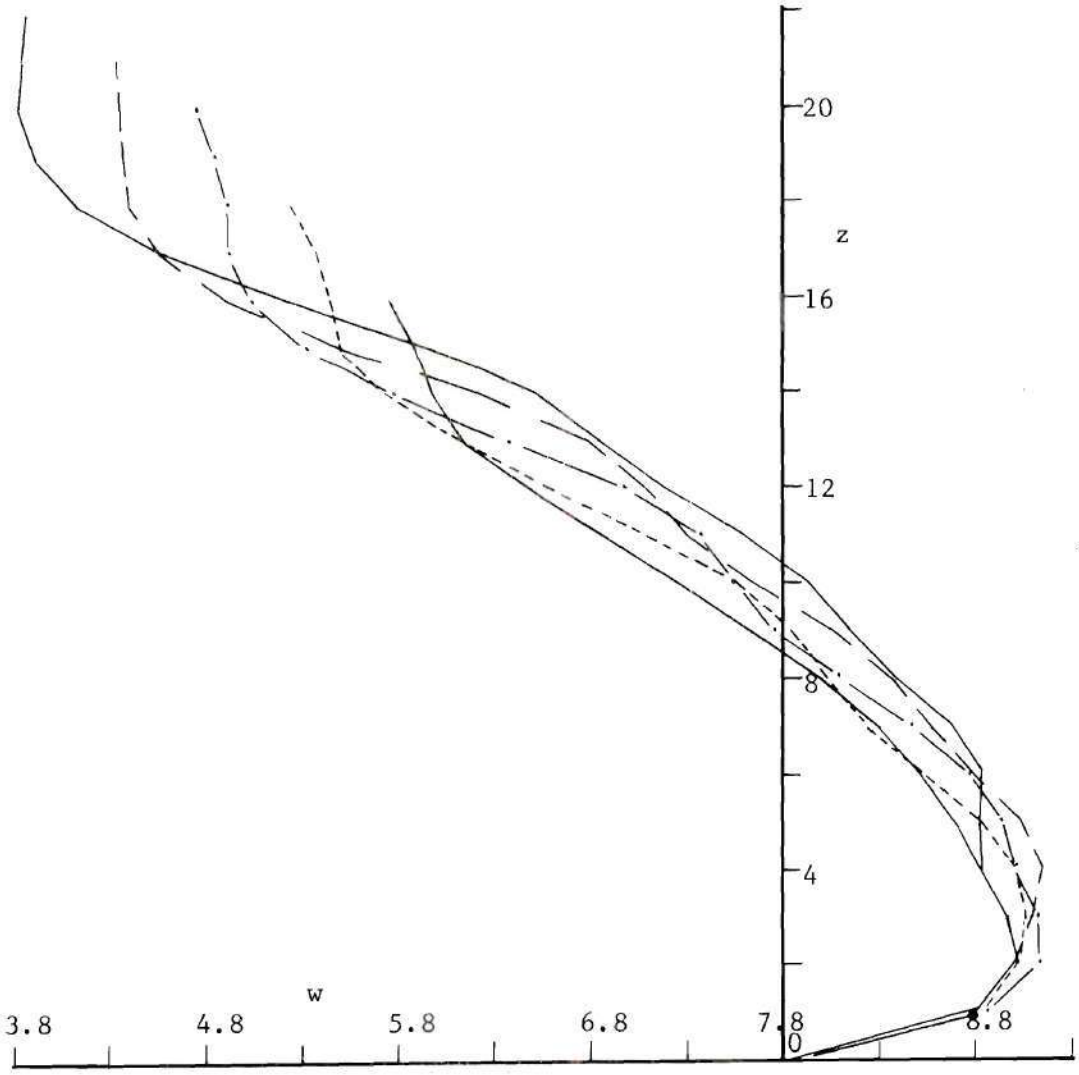

(e) Exit Center
- Later Times

Figure 103. (cont.)

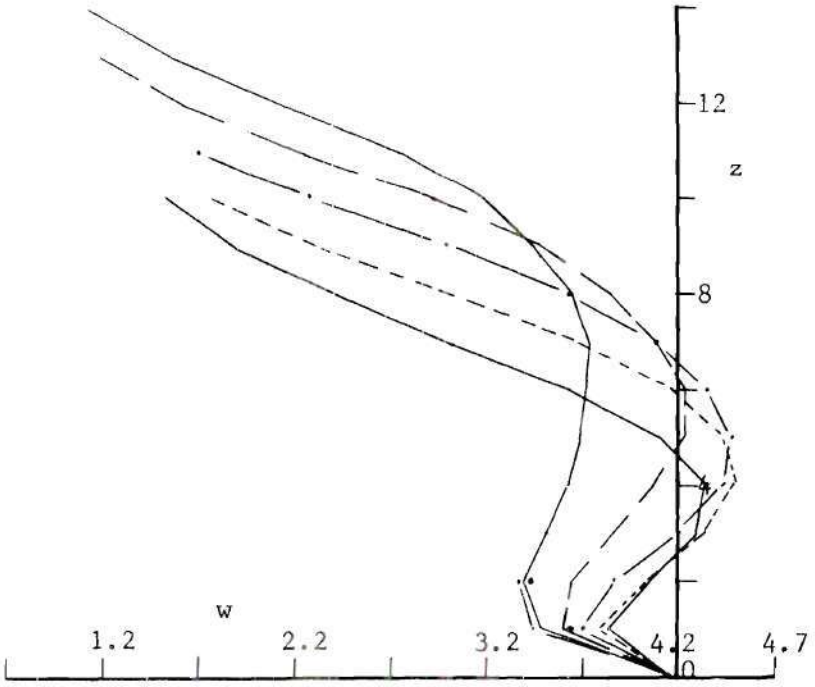

(f) Exit Fore Edge
- Later Times

Figure 103. (cont.)

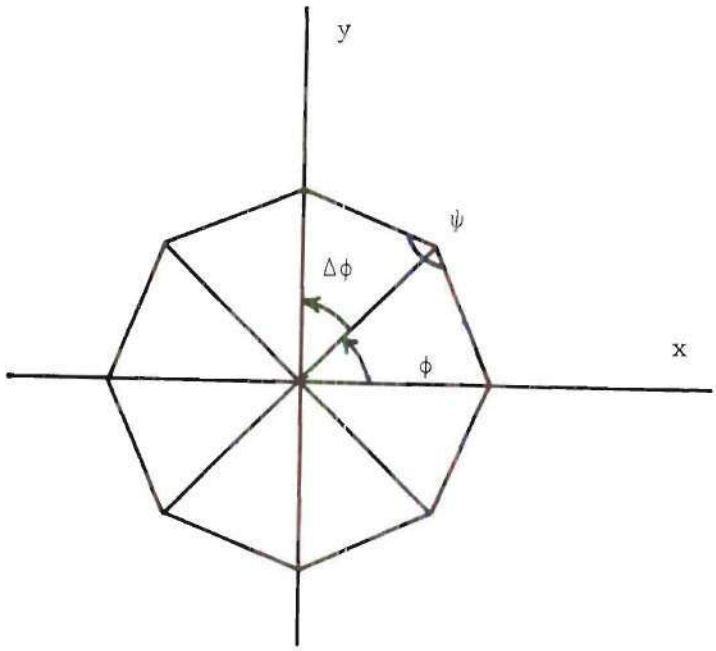

Figure 104. Exit Source Distribution - Vortex Lattice Solution

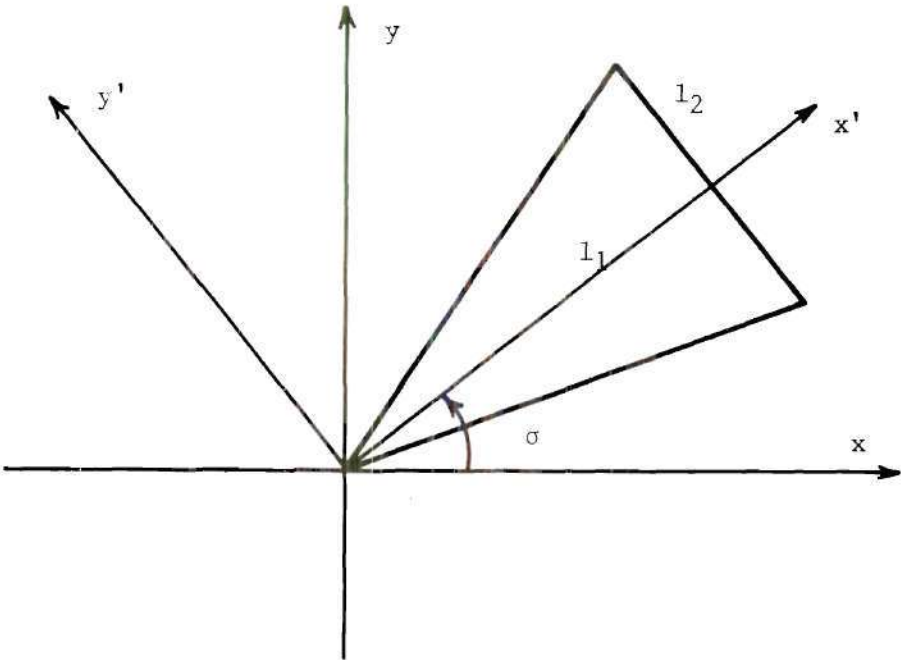

(a) Circular Exit

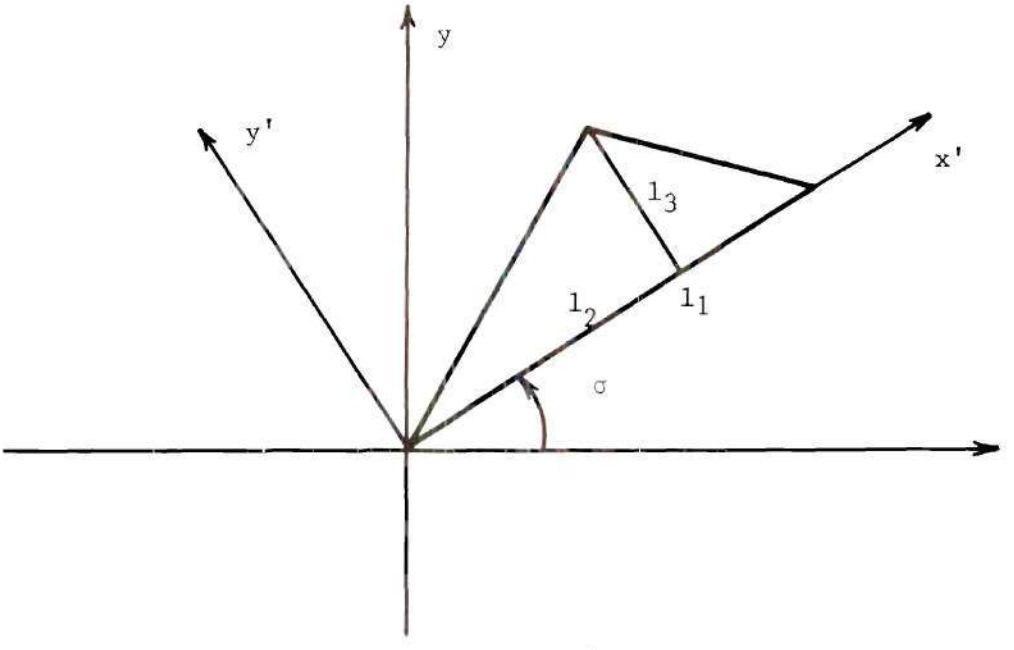

(b) General Exit

Figure 105. Exit Source Triangles - Vortex Lattice Solution

LITERATURE CITED

1. R. Rosen, N. A. Durando, and L. A. Cassel, "Inviscid Models for the Pressure Induced by a Jet Transverse to a Subsonic Stream," Analysis of a Jet in a Subsonic Crosswind, NASA SP-218, 205 (1969).

2. J. C. Wu and M. A. Wright, "A Blockage-Sink Representation of Jet Interference Effects for Noncircular Jet Orifices," Analysis of a Jet in a Subsonic Crosswind, NASA SP-218, 85 (1969).

3. J. G. Skifstad, "Numerical Treatment of Line Singularities for Modelling a Jet in a Low-Speed Cross Flow," Analysis of a Jet in a Subsonic Crosswind, NASA SP-218, 119 (1969).

4. P. E. Rubbert, "Calculation of Jet Interference Effects on V/STOL Aircraft by a Nonplanar Potential Flow Method," Analysis of a Jet in a Subsonic Crosswind, NASA SP-218, 181 (1969).

5. P. E. Rubbert, et. al., "A General Method for Determining the Aerodynamic Characteristics of Fan-in-Wing Configurations, Vol. 1 - Theory and Application," USAAVLABS Technical Report 67-61A, U. S. Army Aviation Materiel Laboratories, Ft. Eustis, Virginia (1967).

6. R. E. Monical, "A Method of Representing Fan-Wing Combinations for Three-Dimensional Potential Flow Solutions," Journal of Aircraft, 2, 527 (1965).

7. F. L. Heltsley and R. A. Kroeger, "A General Jet Efflux Simulation Model," Analysis of a Jet in a Subsonic Crosswind, NASA SP-218, 165 (1969).

8. R. J. Margason, "Analytic Description of Jet-Wake Cross Sections for a Jet Normal to a Subsonic Free Stream," Analysis of a Jet in a Subsonic Crosswind, NASA SP-218, 131 (1969).

9. J. E. Hackett and H. R. Miller, "The Aerodynamics of the Lifting Jet in a Cross Flowing Stream," Analysis of a Jet in a Subsonic Crosswind, NASA SP-218, 101 (1969).

10. P. T. Wooler, "Development of an Analytical Model for the Flow of a Jet into a Subsonic Crosswind," Analysis of a Jet in a Subsonic Crosswind, NASA SP-218, 101 (1969).

11. V. V. Baturin and I. A. Shepelev, "Air Curtains," Referenced in Chapter 12.4, The Theory of Turbulent Jets, G. N. Abramovich, MIT Press, Cambridge, Massachusetts (1963).

12. I. A. Shepelev, Referenced in Chapter 12.4, The Theory of Turbulent Jets, G. N. Abramovich, MIT Press, Cambridge, Massachusetts (1963).

13. M. S. Volinskiy, Referenced in Chapter 12.4, The Theory of Turbulent Jets, G. N. Abramovich, MIT Press, Cambridge, Massachusetts (1963).

14. G. N. Abramovich, The Theory of Turbulent Jets, Chapter 12.4, MIT Press, Cambridge, Massachusetts (1963).

15. G. S. Shandorov, "Calculation of a Jet Axis in a Drifting Flow," NASA TT F-10, 638 (1966).

16. J. F. Keffer and W. D. Baines, "The Round Turbulent Jet in a Cross-wind," Journal of Fluid Mechanics, 15, 481 (1963).

17. Y. M. Vizel and I. L. Mostinskii, "Deflection of a Jet Injected into a Stream," Journal of Engineering Physics, 8, 160 (1965).

18. G. W. Braun and J. D. McAllister, "Cross Wind Effects on Trajectory and Cross Sections of Turbulent Jets," Analysis of a Jet in a Subsonic Crosswind, NASA SP-218, 141 (1969).

19. R. L. Fearn, "Mass Entrainment of a Circular Jet in a Cross Flow," Analysis of a Jet in a Subsonic Crosswind, NASA SP-218, 239 (1969).

20. J. E. Fromm, "A Method for Computing Nonsteady Incompressible Viscous Fluid Flows," Report LA-2910, Los Alamos Scientific Lab., Los Alamos, New Mexico (1963).

21. J. E. Fromm and F. H. Harlow, "Numerical Solution of the Problem of Vortex Street Development," Physics of Fluids, 6, 975 (1963).

22. J. E. Fromm, "The Time Dependent Flow of an Incompressible Viscous Fluid," Methods in Computational Physics, 3, 346, Academic Press, New York (1964).

23. J. F. Thompson, "Numerical Solution of the Incompressible, Two-Dimensional, Time-Dependent Navier-Stokes Equations for a Body Oscillating in Pitch in a Moving Fluid," Research Report No. 86, Department of Aerophysics and Aerospace Engineering, Mississippi State University (1968).

24. S. K. Dey, "Numerical Studies of the Navier-Stokes Equations with an Application to a Circular Cylinder," Ph.D. thesis, Mississippi State University, State College, Mississippi (1970).

25. R. B. Payne, "Calculations of Unsteady Viscous Flow Past a Circular Cylinder," Journal of Fluid Mechanics, 4, 81 (1958).

26. J. G. Trulio, et. al., "Calculation of Two-Dimensional Turbulent Flow Fields," NASA CR-430 (1966)

27. A. E. Hamielec and J. D. Raal, "Numerical Studies of Viscous Flow Around Circular Cylinders," Physics of Fluids, 12, 11 (1969).

28. H. Takami and H. B. Keller, "Steady Two-Dimensional Viscous Flow of an Incompressible Fluid Past a Circular Cylinder," Physics of Fluids, 12, Supplement II, II-51 (1969).

29. P. C. Jain and K. S. Rao, "Numerical Solution of Unsteady Viscous Incompressible Fluid Flow Past a Circular Cylinder," Physics of Fluids, 12, Supplement II, II-57 (1969).

30. D. C. Thoman and A. A. Szewczyk, "Time-Dependent Viscous Flow Over a Circular Cylinder," Physics of Fluids, 12, Supplement II, II-76 (1969).

31. Y. Takaisi, "Numerical Studies of a Viscous Liquid Past a Circular Cylinder," Physics of Fluids, 12, Supplement II, II-86 (1969).

32. M. Kawaguti and P. C. Jain, "Numerical Study of a Viscous Fluid Flow Past a Circular Cylinder," Journal of the Physical Society of Japan, 21, 2055 (1966).

33. J. S. Son and T. J. Hanratty, "Numerical Solution for the Flow Around a Cylinder at Reynolds Numbers of 40, 200, and 500," Journal of Fluid Mechanics, 35, 369 (1969).

34. D. B. Ingham, "Note on the Numerical Solution for Unsteady Viscous Flow Past a Circular Cylinder," Journal of Fluid Mechanics, 31, 815 (1968).

35. M. Kawaguti, "Numerical Solution of the Navier-Stokes Equations for the Flow Around a Circular Cylinder at Reynolds Number 40," Journal of the Physical Society of Japan, 8, 747 (1953).

36. S. C. R. Dennis and G. Z. Chang, "Numerical Integration of the Navier-Stokes Equations for Steady Two-Dimensional Flow," Physics of Fluids, 12, Supplement II, II-88 (1969).

37. Y. Rimon, "Numerical Solution of the Incompressible Time-Dependent Viscous Flow Past a Thin Oblate Spheroid," Physics of Fluids, 12, SupplementII, II-65 (1969).

38. L. G. Leal and A. Acrivos, "Structure of Steady Closed Streamline Flows Within a Boundary Layer," Physics of Fluids, 12, Supplement II, II-105 (1969).

39. Y. H. Pao and R. J. Daugherty, "Time-Dependent Viscous Incompressible Flow Past a Finite Flat Plate," (Abstract), Physics of Fluids, 12, Supplement II, II-280 (1969).

40. Y. Rimon and S. I. Cheng, "Numerical Solution of a Uniform Flow over a Sphere at Intermediate Reynolds Numbers," Physics of Fluids, 12, 949 (1969).

41. J. Gillis, "Viscous Flow in the Entry Region of a Straight Channel," (Abstract), Physics of Fluids, 12, Supplement II, II-280 (1969).

42. J. E. Fromm, "Numerical Solutions of Two-Dimensional Stall in Fluid Diffusers," Physics of Fluids, 12, Supplement II, II-113 (1969).

43. P. J. Roache and T. J. Mueller, "Numerical Solutions of Laminar Separated Flows," AIAA Journal, 8, 530 (1970).

44. M. Kawaguti, "Numerical Study of the Flow of a Viscous Fluid in a Curved Channel," Physics of Fluids, 12, Supplement II, II-101 (1969).

45. L. F. Donovan, "A Numerical Solution of Unsteady Flow in a Two-Dimensional Square Cavity," AIAA Journal, 8, 524 (1970).

46. D. Greenspan, et. al., "Numerical Studies of the Navier-Stokes Equations," MRC Tech. Summary Report 482, University of Wisconsin, Madison, Wisconsin (1964).

47. Z. Lavan, et. al., "Separation and Flow Reversal in Swirling Flows in Circular Ducts," Physics of Fluids, 12, 1747 (1969).

48. K. Kuwahara and I. Imai, "Steady Viscous Flow Within a Circular Boundary," Physics of Fluids, 12, Supplement II, II-94 (1969).

49. R. B. Payne, "A Numerical Method for Calculating the Starting and Perturbation of a Two-Dimensional Jet at Low Reynolds Number," Great Britain Aeronautical Research Council R & M 3047 (1958).

50. A. K. Runchal, et. al., "Numerical Solution of the Elliptic Equations for Transport of Vorticity, Heat, and Matter in Two-Dimensional Flow," Physics of Fluids, 12, Supplement II, II-21 (1969).

51. K. D. Whitehead, "The Generation and Development of a Viscous Vortex Ring," Ph.D. Thesis, Georgia Institute of Technology (1967).

52. J. Welch, et. al., "The MAC Method," Report LA-3425, Los Alamos Scientific Lab., Los Alamos, New Mexico (1966).

53. F.H. Harlow and J. E. Welch, "Numerical Study of Large Amplitude Free-Surface Motions," Physics of Fluids, 9, 842 (1966).

54. B. J. Daly, "Numerical Study of the Two-Fluid Raleigh-Taylor Instability," Physics of Fluids, 9, 297 (1967).

55. B. J. Daly, "Numerical Study of the Effect of Density-Current Surges," Physics of Fluids, 11, 15 (1968).

56. B. J. Daly, "Numerical Study of the Effect of Surface Tension on Interface Instability," Physics of Fluids, 12, 1340 (1969).

57. W. R. Wessel, "Numerical Study of the Collapse of a Perturbation in an Infinite Density Stratified Fluid," Physics of Fluids, 12, Supplement II, II-171 (1969).

58. K. Aziz and J. D. Hellums, "Numerical Solution of the Three-Dimensional Equations of Motion for Laminar Natural Convection," Physics of Fluids, 10, 314 (1967).

59. K. A. Meyer, "Time-Dependent Numerical Study of Taylor Vortex Flow," Physics of Fluids, 10, 1874 (1967).

60. K. A. Meyer, "Three-Dimensional Study of Flow Between Concentric Rotating Cylinders," Physics of Fluids, 12, Supplement II, II-165 (1969).

61. W. Schönauer, "Numerical Experiments with a Difference Model for the Navier-Stokes Equations (Turbulence Model)," Physics of Fluids, 12, Supplement II, II-228 (1969).

62. D. J. Tritton, "Experiments on the Flow Past a Circular Cylinder at Low Reynolds Number," Journal of Fluid Mechanics, 6, 547 (1959).

63. S. Taneda, "Experimental Investigation of the Wakes Behind Cylinders and Plates at Low Reynolds Numbers," Journal of the Physical Society of Japan, 11, 302 (1956).

64. A. S. Grove, et. al., "An Experimental Investigation of the Steady Separated Flow Past a Circular Cylinder," Journal of Fluid Mechanics, 19, 60 (1964).

65. A. Thom, "The Flow Past Circular Cylinders at Low Speeds," Proceedings of the Royal Society, A, 141, 651 (1933).

66. F. Homann, "Einfluss Grösser Zähigkeit bei Stromung um Zylinder," Forschung fur Gietiete Ingenieruweiss, 67, 1 (1936).

67. H. Schlichting, Boundary Layer Theory, Fourth Edition, McGraw-Hill, New York (1960).

68. H. M. McMahon and D. K. Mosher, "Experimental Investigation of Pressures Induced on a Flat Plate by a Jet Issuing into a Subsonic Crosswind," Analysis of a Jet in a Subsonic Crosswind, NASA SP-218, 49 (1969).

69. M. R. Spiegel, Vector Analysis, Schaum Publishing Company, New York (1959).

70. H. F. Weinberger, Partial Differential Equations, Blaisdell Publishing Company, Walthan, Massachusetts (1965).

71. H. Margenau and G. M. Murphy, The Mathematics of Physics and Chemistry, Second Edition, D. Van Nostrand, Princeton, New Jersey (1956).

72. E. Isaacson and H. B. Keller, Analysis of Numerical Methods, John Wiley, New York (1966).

73. K. Karamcheti, Principles of Ideal-Fluid Aerodynamics, John Wiley, New York (1966).

74. J. L. Hess and A. M. O. Smith, "Calculation of Non-Lifting Potential Flow about Arbitrary Three-Dimensional Bodies," Report E.S. 40622, Douglas Aircraft Division, Long Beach, California (1962).

75. H. Lamb, Hydrodynamics, Cambridge University Press, Cambridge (1932).

76. A. J. Chorin, "Numerical Solution of the Navier-Stokes Equation," Mathematics of Computation, 22, 745 (1968).

77. G. P. Williams, "Numerical Integration of the Three-Dimensional Navier-Stokes Equations for Incompressible Flow," Journal of Fluid Mechanics, 37, 727 (1969).

78. M. A. Wright, "A Two-Dimensional Representation of the Crosswind for the Jet Interface Problem," Ph.D. Thesis, Georgia Institute of Technology (1970).

79. J. C. Wu, et. al., "Experimental and Analytical Investigations of Jets Exhausing into a Deflecting Stream," Journal of Aircraft, 7, 44 (1970).

80. D. K. Mosher, "An Experimental Investigation of a Turbulent Jet in a Cross Flow", Ph.D. Thesis, Georgia Institute of Technology, Atlanta, Georgia, (1970).

VITA

Joe Floyd Thompson, Jr. was born in Grenada, Mississippi, on April 13, 1939. He received a Bachelor of Science degree in physics with Highest Honors from Mississippi State University in May, 1961, and a Master of Science degree in aerospace engineering from the same institution in May, 1963. He then was employed by the Marshall Space Flight Center, NASA, as an Aerospace Engineer in the Saturn rocket program. In September 1964 he accepted an assistant professorship in the Department of Aerospace Engineering at Mississippi State University and served in that capacity until receiving a NSF Science-Faculty Fellowship for further graduate work at Georgia Tech.